

WL-TR-96-3075



DEVELOPMENT OF A HOLOGRAPHIC SYSTEM FOR AVIONICS DURABILITY ANALYSIS AND VALIDATION

Volume 1 - Text

Ryszard J. Pryputniewicz, Ph.D.
Worcester Polytechnic Institute
Department of Mechanical Engineering
Center for Holographic Studies and Laser micro-mechaTronics
Worcester, Massachusetts 01609-2280

February 1996
FINAL REPORT FOR PERIOD 01/07/91-02/29/96

APPROVED FOR PUBLIC RELEASE; DISTRIBUTION IS UNLIMITED

FLIGHT DYNAMICS DIRECTORATE
WRIGHT LABORATORY
AIR FORCE MATERIEL COMMAND
WRIGHT-PATTERSON AFB, OH 45433-7562

DTIC QUALITY INSPECTED 4

19970122 033

NOTICE

When Government drawings, specifications, or other data are used for any purpose other than in connection with a definitely Government-related procurement, the United States Government incurs no responsibility or any obligation whatsoever. The fact that the government may have formulated or in any way supplied the said drawings, specifications, or other data, is not to be regarded by implication, or otherwise in any manner construed, as licensing the holder, or any other person or corporation; or as conveying any rights or permission to manufacture, use, or sell any patented invention that may in any way be related thereto.

This report is releasable to the National Technical Information Service (NTIS). At NTIS, it will be available to the general public, including foreign nations.

This technical report has been reviewed and is approved for publication.



CHRIS E. LEAK
Project Engineer
Thermal Systems



ALBERT R. BASSO, II, CM
Chief
Transparency and Thermal Systems Branch



RICHARD E. COLCLOUGH, JR.
Chief
Vehicle Subsystems Division

If your address has changed, if you wish to be removed from our mailing list, or if the addressee is no longer employed by your organization please notify WL/FIVE, Bldg 45, 2130 Eighth St, Ste 1, Wright-Patterson AFB OH 45433-7542 to help us maintain a current mailing list.

Copies of this report should not be returned unless return is required by security considerations, contractual obligations, or notice on a specific document.

REPORT DOCUMENTATION PAGE

Form Approved
OMB No. 0704-0188

Public reporting burden for this collection of information is estimated to average 1 hour per response, including the time for reviewing instructions, searching existing data sources, gathering and maintaining the data needed, and completing and reviewing the collection of information. Send comments regarding this burden estimate or any other aspect of this collection of information, including suggestions for reducing this burden, to Washington Headquarters Services, Directorate for Information Operations and Reports, 1215 Jefferson Davis Highway, Suite 1204, Arlington, VA 22202-4302, and to the Office of Management and Budget, Paperwork Reduction Project (0704-0188), Washington, DC 20503.

1. AGENCY USE ONLY (Leave blank) 2. REPORT DATE FEB 1996 3. REPORT TYPE AND DATES COVERED FINAL 01/07/91--02/29/96

4. TITLE AND SUBTITLE DEVELOPMENT OF A HOLOGRAPHIC SYSTEM FOR AVIONICS DURABILITY ANALYSIS
VOL I - TEXT

5. FUNDING NUMBERS
C F33615-91-C-3405
PE 62201
PR 2402
TA 04
WU 74

6. AUTHOR(S)
RYSZARD J. PRYPUTNIEWICZ, PHD

7. PERFORMING ORGANIZATION NAME(S) AND ADDRESS(ES)
WORCESTER POLYTECHNIC INSTITUTE
CENTER FOR HOLOGRAPHIC STUDIES AND LASER TECHNOLOGY
WORCESTER MASSACHUSETTS 01609-2280

8. PERFORMING ORGANIZATION
REPORT NUMBER

9. SPONSORING/MONITORING AGENCY NAME(S) AND ADDRESS(ES)
CHRIS LEAK, WL/FIVE, WPAFB OH 45433; 937-255-3021
FLIGHT DYNAMICS DIRECTORATE
WRIGHT LABORATORY
AIR FORCE MATERIEL COMMAND
WRIGHT PATTERSON AFB OH 45433-7562

10. SPONSORING/MONITORING
AGENCY REPORT NUMBER
WL-TR-96-3075

11. SUPPLEMENTARY NOTES

12a. DISTRIBUTION / AVAILABILITY STATEMENT
APPROVED FOR PUBLIC RELEASE; DISTRIBUTION IS UNLIMITED.

12b. DISTRIBUTION CODE

13. ABSTRACT (Maximum 200 words)

This report documents the development of an Electro-Optic Holography (EOH) system for the measurement of mechanical displacements and strains on the micro-scale structures employed in current technology avionics. It begins with a description of the processes and mathematics of holography. This includes explanations of the illumination, observation, and sensitivity vectors as well as their relationships to the projection matrices. Next is a discussion and detailed mathematical development of the interpretation of holograms (both conventional and time-averaged) to extract displacement, rotation, and strain measurements. Experimental results illustrate the analysis. This is followed by a description of the EOH technique which includes a description of the experimental apparatus and measurement procedures, discussion of the computer-based processing used to analyze the electronically captured interference images, procedures for the determination of three-dimensional displacements, and a brief description of Electronic Shearography to contrast the two techniques. Experimental measurements of deformations in avionics are shown along with a discussion of how the EOH results can be merged with Finite Element Modeling (FEM) techniques during system design. This includes the description of a hybrid procedure to optimize the design for a specific target characteristic. Examples for the optimization of a cantilever plate are presented and discussed.

14. SUBJECT TERMS
Holography, Hologram Interferometry, Electro-Optic Holography, Nondestructive Inspection, Avionics

15. NUMBER OF PAGES
358

16. PRICE CODE

17. SECURITY CLASSIFICATION
OF REPORT
UNCLASSIFIED

18. SECURITY CLASSIFICATION
OF THIS PAGE
UNCLASSIFIED

19. SECURITY CLASSIFICATION
OF ABSTRACT
UNCLASSIFIED

20. LIMITATION OF ABSTRACT
SAR

GENERAL INSTRUCTIONS FOR COMPLETING SF 298

The Report Documentation Page (RDP) is used in announcing and cataloging reports. It is important that this information be consistent with the rest of the report, particularly the cover and title page. Instructions for filling in each block of the form follow. It is important to **stay within the lines** to meet **optical scanning requirements**.

Block 1. Agency Use Only (Leave blank).

Block 2. Report Date. Full publication date including day, month, and year, if available (e.g. 1 Jan 88). Must cite at least the year.

Block 3. Type of Report and Dates Covered. State whether report is interim, final, etc. If applicable, enter inclusive report dates (e.g. 10 Jun 87 - 30 Jun 88).

Block 4. Title and Subtitle. A title is taken from the part of the report that provides the most meaningful and complete information. When a report is prepared in more than one volume, repeat the primary title, add volume number, and include subtitle for the specific volume. On classified documents enter the title classification in parentheses.

Block 5. Funding Numbers. To include contract and grant numbers; may include program element number(s), project number(s), task number(s), and work unit number(s). Use the following labels:

C - Contract	PR - Project
G - Grant	TA - Task
PE - Program Element	WU - Work Unit Accession No.

Block 6. Author(s). Name(s) of person(s) responsible for writing the report, performing the research, or credited with the content of the report. If editor or compiler, this should follow the name(s).

Block 7. Performing Organization Name(s) and Address(es). Self-explanatory.

Block 8. Performing Organization Report Number. Enter the unique alphanumeric report number(s) assigned by the organization performing the report.

Block 9. Sponsoring/Monitoring Agency Name(s) and Address(es). Self-explanatory.

Block 10. Sponsoring/Monitoring Agency Report Number. (If known)

Block 11. Supplementary Notes. Enter information not included elsewhere such as: Prepared in cooperation with...; Trans. of...; To be published in.... When a report is revised, include a statement whether the new report supersedes or supplements the older report.

Block 12a. Distribution/Availability Statement. Denotes public availability or limitations. Cite any availability to the public. Enter additional limitations or special markings in all capitals (e.g. NOFORN, REL, ITAR).

DOD - See DoDD 5230.24, "Distribution Statements on Technical Documents."

DOE - See authorities.

NASA - See Handbook NHB 2200.2.

NTIS - Leave blank.

Block 12b. Distribution Code.

DOD - Leave blank.

DOE - Enter DOE distribution categories from the Standard Distribution for Unclassified Scientific and Technical Reports.

NASA - Leave blank.

NTIS - Leave blank.

Block 13. Abstract. Include a brief (*Maximum 200 words*) factual summary of the most significant information contained in the report.

Block 14. Subject Terms. Keywords or phrases identifying major subjects in the report.

Block 15. Number of Pages. Enter the total number of pages.

Block 16. Price Code. Enter appropriate price code (*NTIS only*).

Blocks 17. - 19. Security Classifications. Self-explanatory. Enter U.S. Security Classification in accordance with U.S. Security Regulations (i.e., UNCLASSIFIED). If form contains classified information, stamp classification on the top and bottom of the page.

Block 20. Limitation of Abstract. This block must be completed to assign a limitation to the abstract. Enter either UL (unlimited) or SAR (same as report). An entry in this block is necessary if the abstract is to be limited. If blank, the abstract is assumed to be unlimited.

TABLE OF CONTENTS

List of figures	vi
List of tables	xii
Acknowledgments	xiii
1. Introduction	1-1
1.1. Objective	1-1
1.2. Background	1-1
1.3. Organization of this report	1-2
2. Illumination, observation, and sensitivity vectors	2-1
2.1. Mathematical considerations	2-1
2.2. References	2-3
3. Projection matrices: definition and properties	3-1
3.1. Normal projection	3-1
3.2. Oblique projection	3-3
3.3. References	3-5
4. Determination of displacements	4-1
4.1. Determination of displacements when fringe order is known	4-2
4.2. Determination of displacements when fringe order unknown	4-9
4.3. Determination of displacements from multiple holograms	4-13
4.4. References	4-15
5. Determination of rigid-body motions	5-1
5.1. Mathematical considerations	5-1
5.2. References	5-5
6. Determination of strains and rotations	6-1
6.1. Spatial dependence of the fringe-locus function	6-2
6.2. Rigid-body rotations and homogeneous strains	6-4
6.3. References	6-6
7. Interpretation of time-average holograms	7-1
7.1. Introduction	7-1
7.2. Mathematical considerations	7-3
7.3. Quantitative interpretation of time-average holograms of a cantilever beam	7-6
7.4. Experimental setup	7-11
7.5. Experimental results	7-12
7.6. Conclusions	7-14
7.7. References	7-15

8. Electro-optic holography	8-1
8.1. Fundamentals of EOH	8-1
8.2. Electronic processing of holograms	8-2
8.2.1. Static measurements	8-2
8.2.2. Dynamic measurements	8-8
8.2.2.1. Determination of the fringe-locus function for the vibrating object	8-11
8.2.2.2. Generation of a lookup table	8-13
8.3. EOH system and procedure	8-14
8.3.1. Description of the system	8-14
8.3.2. Setting the bias vibration	8-20
8.4. Representative applications of the EOH system	8-21
8.4.1. Development of an automated fringe unwrapper	8-21
8.4.2. Determination of three-dimensional displacements by EOH	8-22
8.5. Conclusions	8-23
8.6. References	8-25
9. Electronic shearography	9-1
9.1. Electronic holography	9-2
9.2. Electronic shearography	9-3
9.3. Representative results and discussion	9-6
9.4. Conclusions	9-8
9.5. References	9-11
10. Hybrid approach to deformation analysis	10-1
10.1. ACES methodology	10-1
10.2. Finite element method	10-2
10.2.1. Unification in error analysis	10-3
10.2.2. Unification in evaluating element matrices	10-5
10.3. Hologram interferometry	10-6
10.3.1. Electronic holography	10-7
10.4. Representative applications	10-8
10.5. Conclusions	10-12
10.6. References	10-12
11. Quantitative EOH and FEM hybrid study of vibration characteristics of avionics	11-1
11.1. Introduction	11-1
11.2. Time-average hologram interferometry	11-2
11.3. Electro-optic holography	11-4
11.3.1. Quantitative analysis of electro-optic holograms	11-4
11.3.2. Description of the EOH system	11-6
11.4. Test samples	11-7
11.5. Representative results and discussion	11-8
11.6. Conclusions and recommendations	11-16
11.7. References	11-17

12. Hybrid, EOH and FEM, study and optimization of a cantilever plate dynamics	12-1
12.1. Analytical considerations	12-1
12.1.1. Terminology	12-1
12.1.2. Mathematical programming methods	12-2
12.1.3. Modal analysis	12-2
12.2. Description of the optimization procedure	12-4
12.2.1. Optimization procedure	12-4
12.2.2. Description of the computational model	12-6
12.2.3. Description of the experimental model	12-6
12.3. Results and discussion	12-7
12.3.1. Cantilever plate with a single hole having as design variables the vertical location and diameter of the hole	12-7
12.3.2. Cantilever plate with two holes having as design variables the diameters of the holes	12-11
12.4. Conclusions and recommendations	12-13
12.5. References	12-14
13. Overall summary, conclusions, and recommendations	13-1
Appendix A. Electro-optic holography	A-1
Appendix B. Automated fringe unwrapping by energy minimization	B-1
Appendix C. Three-dimensional graphics techniques applied to the rendering of holographic interferometric data	C-1
Appendix D. Phase unwrapping by least-squares error minimization of phase curvature	D-1
Appendix E. Vibration studies using electro-optic holography and finite element method	E-1
Appendix F. Quantitative electro-optic holography study of dynamics of electronic components	F-1

LIST OF FIGURES

Fig. 2.1. Illumination and observation geometry in hologram interferometry	2-1
Fig. 3.1. Normal projection onto a surface	3-2
Fig. 3.2. Oblique projection onto a surface	3-4
Fig. 4.1. Typical appearances of the two types of holographic fringes: (a) and (c) cosinusoidal fringes, (b) and (d) J_0 (Bessel) fringes	4-1
Fig. 4.2. Multiple observations of a holographically reconstructed image from three different directions	4-4
Fig. 4.3. Multiple observations of a holographically reconstructed image from five different directions	4-6
Fig. 4.4. Multiple observations of a holographically reconstructed image with the first direction of observation chosen arbitrarily	4-10
Fig. 4.5. Multiple observations of a holographically reconstructed image with the first direction of observation being in the center of all points through which observations are made	4-13
Fig. 4.6. Use of multiple holograms in analysis of a single image	4-16
Fig. 4.7. Multiple observations of an image through a single hologram	4-16
Fig. 5.1. Schematic representation of the geometry for holographic determination of rigid-body motions	5-2
Fig. 6.1. A photograph of a reconstruction from a double-exposure hologram recording a rigid-body rotation of the object	6-2
Fig. 6.2. Formation of fringes in hologram interferometry: the surface of the object appears to be intersected by a set of equally spaced fringe-locus planes which are represented by \mathbf{K}_f	6-2
Fig. 6.3. Illumination and observation geometry for interpretation of holograms using the fringe-vector theory	6-3
Fig. 7.1. Schematic representation of a setup for recording and reconstruction of continuous time-average holograms	7-2

Fig. 7.2.	The zero-order Bessel function of the first kind and its square, defining locations of centers of dark fringes seen during reconstruction of continuous time-average holograms of vibrating objects	7-6
Fig. 7.3.	Fringes obtained during reconstruction of: (a) conventional double-exposure hologram, showing cosinusoidal intensity variation (note, the zero-order fringe (ZOF) is as bright as other fringes), (b) continuous time-average holograms, showing J_0^2 intensity variation (note that the ZOF's are much brighter than the higher order fringes)	7-7
Fig. 7.4.	Values of $(K_{2z} - K_{1z})$ as a function of γ_1 and γ_2	7-10
Fig. 7.5.	Percentage error in L_{tz} , with respect to $L_{t_{zrr}}$, as a function of $(K_{2z} - K_{1z})$	7-11
Fig. 7.6.	Resonance frequency of a vibrating cantilever beam as a function of mode number: comparison between the experimental results obtained from the time-average holograms and those based on the beam theory	7-12
Fig. 7.7.	Shape of the first flexure mode of a vibrating cantilever beam: comparison between the experimental results obtained from the time-average hologram and those based on the beam theory	7-13
Fig. 7.8.	Shape of the second flexure mode of a vibrating cantilever beam: comparison between the experimental results obtained from the time-average hologram and those based on the beam theory	7-14
Fig. 7.9.	Shape of the third flexure mode of a vibrating cantilever beam: comparison between the experimental results obtained from the time-average hologram and those based on the beam theory	7-15
Fig. 8.1.	Optical configuration of the EOH system	8-3
Fig. 8.2.	Electronic configuration of the EOH system	8-14
Fig. 8.3.	Overall view of the EOH system with three cameras	8-15
Fig. 8.4.	Close up view of the optomechanical setup of the EOH system with three cameras	8-16
Fig. 8.5.	Close up view of the three cameras of the EOH system	8-16
Fig. 8.6.	Generation of the object and three reference beams for the EOH system with three cameras	8-17

Fig. 8.7. Multiple beam generation subsystem and camera-1 of the EOH system with three cameras	8-17
Fig. 8.8. Close up view of the multiple beam generation subsystem of the EOH system with three cameras	8-18
Fig. 8.9. Close up view of the beamsplitters and the beam shaping lenses of the EOH system with three cameras	8-18
Fig. 8.10. Display monitor of the EOH system with three cameras	8-19
Fig. 8.11. Cantilever plate vibrating at its third flexure mode, three non-coplanar EOH images simultaneously recorded by: (a) camera-1, (b) camera-2, and (c) camera-3	8-22
Fig. 8.12. Typical wrapped phase, corresponding to the EOH image of Fig. 8.11a	8-23
Fig. 8.13. Unwrapped phase maps, corresponding to the EOH images of Fig. 8.11, as recorded by: (a) camera-1, (b) camera-2, and (c) camera-3	8-23
Fig. 8.14. Wire frame representation of the three-dimensional displacements computed from the unwrapped phase maps of Fig. 8.13: (a) x -component, (b) y -component, and (c) z -component	8-24
Fig. 9.1. A typical configuration of the electronic shearography system	9-4
Fig. 9.2. Double-exposure electronic holograms of the cantilever plate in bending by a static load of: (a) 1 gram, (b) 2 grams, and (c) 5 grams	9-6
Fig. 9.3. Shearographic interferograms of the cantilever plate in bending by a static load of 5 grams: (a) $s_y = 15$ mm, (b) $s_x = 15$ mm	9-7
Fig. 9.4. Shearographic interferograms of the cantilever plate in bending by a static load of 5 grams: (a) $s_y = 25$ mm, (b) $s_x = 25$ mm	9-7
Fig. 9.5. Shearographic interferograms of the cantilever plate in bending by a static load of 10 grams: (a) $s_y = 25$ mm, (b) $s_x = 25$ mm	9-9
Fig. 9.6. Shearographic interferograms of the cantilever plate in bending by a static load of 10 grams: (a) $s_y = 10$ mm, (b) $s_x = 10$ mm	9-9
Fig. 9.7. Shearographic interferograms of the cantilever plate in bending by a static load of 10 grams: (a) $s_y = 3$ mm, (b) $s_x = 3$ mm	9-9

- Fig. 9.8. Cantilever plate vibrating at 425 Hz: (a) the time-average electronic hologram, (b) the electronic shearogram displaying displacement derivative in the y -direction, and (c) the electronic shearogram displaying displacement derivative in the x -direction 9-10
- Fig. 9.9. Cantilever plate vibrating at 1591 Hz: (a) the time-average electronic hologram, (b) the electronic shearogram displaying displacement derivative in the y -direction, and (c) the electronic shearogram displaying displacement derivative in the x -direction 9-10
- Fig. 10.1 FEM and holographic study of a gas turbine engine: (a) typical finite element discretization of a turbine blade, (b) displacements of a turbine blade - a comparison between the results obtained from holograms and the FEM results, (c) a fringe pattern showing abrupt discontinuity in the fringe pattern indicating stress concentration in the root area 10-8
- Fig. 10.2. Study of dynamics of the NASA's GAW-2 wing section: (a) profile of the airfoil, (b) a typical image reconstructed from a stroboscopic hologram of the airfoil vibrating at 3,994 Hz, (c) FEM mode shape corresponding to the conditions under which the image shown in (b) was recorded 10-9
- Fig. 10.3. Study of the tooth-ligament-bone system: (a) typical FEM discretization zones, (b) distance from the theoretical center of resistance to the center of rotation as a function of time 10-10
- Fig. 10.4. Miniature star-connector: (a) interconnection concept, (b) FEM simulation of displacement versus position of a typical arm of the microcontact as a function of contact force, (c) FEM estimates of von Mises stress (in Mpsi) for a load of 25 g at each tip - the microcontact is shown in its deformed state, (d) a prototype microcontact, (e) and (f) EOH images of a single arm of the microcontact while loaded with a force increasing from (e) to (f), respectively 10-11
- Fig. 11.1. Optomechanical configuration of the EOH system 11-3
- Fig. 11.2. TS1: a multilayer board with eight identical surface mounted chip modules arranged in two rows with four modules per row 11-7
- Fig. 11.3. TS2: a multilayer board with surface mounted chip modules of different sizes 11-8
- Fig. 11.4. Full field of view EOH images of the TS1 vibrating at: (a) 6,720 Hz, (b) 13,685 Hz, and (c) 20,011 Hz 11-9

Fig. 11.5.	Summary of the EOH images of a single lidded chip module of the TS1 vibrating at nine different resonance frequencies ranging from 6,720 Hz to 31,005 Hz	11-10
Fig. 11.6.	Summary of the FEM results, equivalent to the results shown in Fig. 11.5, for a single lidded chip module of the TS1 vibrating at nine different resonance frequencies ranging from 6,752 Hz to 30,724 Hz	11-11
Fig. 11.7.	Summary of the measured frequencies for TS1	11-12
Fig. 11.8.	Full field of view EOH images of the TS2 vibrating at four different resonance frequencies ranging from 18.7 Hz to 148 Hz	11-13
Fig. 11.9.	EOH images of the TS2 vibrating at 682 Hz: (a) full field of view, and (b) a close up of the central module and its vicinity	11-14
Fig. 11.10.	Full field of view EOH images of the TS2 vibrating at: (a) 4,690 Hz, (b) 6,890 Hz, and (c) 9,330 Hz	11-14
Fig. 11.11.	EOH and FEM study of vibration characteristics of the TS2: (a) and (b) represent EOH images recorded at the excitation frequency of 4,830 Hz and at amplitudes lower than that corresponding to Fig. 11.10a, (c) and (d) show equivalent FEM mode shapes determined at 4,809 Hz, and (e) wire frame representation of the fundamental mode shape	11-15
Fig. 12.1.	Flowchart of the optimization procedure	12-5
Fig. 12.2.	Optical configuration of the EOH system used in the optimization study	12-6
Fig. 12.3.	Configuration of the Al-2024 plate with a single hole considered for optimization. The objective function is the minimization/maximization of the fundamental natural frequencies of the plate: D and C_y are the constrained design variables	12-8
Fig. 12.4.	Typical finite element model and convergence behavior to the first resonance frequency with respect to the number of elements utilized for performing the computational modal analyses	12-8
Fig. 12.5.	Sensitivity of the first three resonance frequencies with respect to normalized design variables D and C_y , W and H are the width and the height of the plate, respectively	12-9

Fig. 12.6.	EOH fringe patterns and computational mode shapes of the first five resonance frequencies for <i>minimization</i> of the objective function of the cantilever plate with a single hole	12-10
Fig. 12.7.	EOH fringe patterns and computational mode shapes of the first five resonance frequencies for <i>maximization</i> of the objective function of the cantilever plate with a single hole	12-10
Fig. 12.8.	Configuration of the Al-2024 plate with two holes considered for optimization. The objective function is the minimization/maximization of the fundamental natural frequencies of the plate: $D1$ and $D2$ are the constrained design variables	12-12
Fig. 12.9.	Typical finite element model and convergence behavior to the first resonance frequency with respect to the number of elements utilized for performing the computational modal analyses	12-12
Fig. 12.10.	Sensitivity of the first three resonance frequencies with respect to the normalized design variables $D1$ and $D2$, W is the width of the plate	12-13
Fig. 12.11.	EOH fringe patterns and computational mode shapes for the first five resonance frequencies for <i>minimization</i> of the objective function of the cantilever plate with two holes	12-15
Fig. 12.12.	EOH fringe patterns and computational mode shapes for the first five resonance frequencies for <i>maximization</i> of the objective function of the cantilever plate with two holes	12-15

LIST OF TABLES

Table 7.1. Zeros of J_o and values of the corresponding L_{irr}	7-9
Table 12.1. Summary of computational and experimental values of the first 12 resonance frequencies of the initial configuration of the cantilever plate with a single hole	12-9
Table 12.2. Summary of computational and experimental values of the first 12 resonance frequencies of the cantilever plate with a single hole optimized for minimization of the objective function	12-11
Table 12.3. Summary of computational and experimental values of the first 12 resonance frequencies of the cantilever plate with a single hole optimized for maximization of the objective function	12-11
Table 12.4. Summary of computational and experimental values of the first 12 resonance frequencies of the initial configuration of the cantilever plate with two holes	12-13
Table 12.5. Summary of computational and experimental values of the first 12 resonance frequencies of the cantilever plate with two holes optimized for minimization of the objective function	12-14
Table 12.6. Summary of computational and experimental values of the first 12 resonance frequencies of the cantilever plate with two holes optimized for maximization of the objective function	12-14

ACKNOWLEDGMENTS

The support and contributions of WL by Mr. Chris E. Leak and Dr. Alan H. Burkhard are gratefully acknowledged.

This project was supported by the Flight Dynamics Directorate, Wright Laboratory, Aeronautical Systems Center (AFMC), United States Air Force, Wright-Patterson AFB, OH 45433-7126.

1. INTRODUCTION

This is the final report on the project relating to the *development of a holographic system for avionics durability analysis and validation*. This report covers the 36 months duration of the project.

1.1. Objective

The objective of this project was to develop and apply, to micro-scale electronic assemblies, a quantitative measurement approach using electro-optic holography (EOH) that is able to simultaneously measure three-dimensional displacements and deformations under either static, quasi-static, or vibration conditions.

1.2. Background

Modern avionics are complex assemblies of micro-scale structural elements that must withstand the applied and/or generated mechanical, thermal, chemical, and/or electrical stresses. The durability of the micro-scale elements controls the overall durability of the avionic components, modules, assemblies, etc.

Validated durability prediction methods are needed for the design assessment phases to allow engineers to predict, within engineering confidence, the available failure free life of avionics systems based on the materials and geometries of the micro-scale structural elements common to current and future electronic components and assemblies. Predictions of this type are additionally complicated, in contrast to large structural systems, by the fact that the geometric features of the micro-scale structural elements are on the same size and order of magnitude as the microstructure of the materials.

Ever increasing demands for optimum design of avionics, in particular in respect to electronic packaging, require accurate knowledge of the behavior of the components under actual operating conditions. This information, however, is difficult to obtain experimentally because of the small size of today's electronic components. Also, the conventional experimental procedures involving strain gauges, photoelasticity, mechanical probing, etc., are generally not applicable to these measurements because they are invasive in nature and, therefore, interfere with the performance of the tested components. An alternative to the conventional experimental methods, however, can be provided using recent developments in laser technology. Out of a number of existing laser methods, available today, the methods of heterodyne hologram interferometry (HHI), electro-optic holography (EOH), pulsed electro-optic holography (PEOH), and their variations, including hologram interferometry with multiple illuminations and a single

observation point, and hologram interferometry with multiple observations for a single illumination, are the most applicable to the studies of electronic components. This stems from the fact that displacements and/or deformations of today's electronic components are very small and take place over the entire component, which itself is very small. The measurements, therefore, made on such components, must be accurate and precise. Otherwise, experimental uncertainties will constitute an appreciable percentage of the measured quantity and the experimental results might not be useful from the designer's point of view.

Of particular interest to this project was the EOH method. In this method, no photographic recording is necessary and interferometric data are acquired by a CCD camera at high spatial resolution and at 30 frames per second. These data are entered directly into the host computer and are ready for subsequent processing.

At the time of initiation of this project, the state-of-the-art EOH system, existing at the Center for Holographic Studies and Laser μ mechTronics (CHSLT), was equipped with only one CCD camera. In order to be able to measure displacements and deformations in three-dimensions, the system was expanded to include three CCD cameras for simultaneous, non-coplanar viewing of the object. To facilitate operation of the expanded EOH system with three-dimensional measurement capabilities, developments of this project were combined with prior developments at the CHSLT and implemented to study avionics, as described in this report.

1.3. Organization of this report

This report consists of three volumes. Volume one contains the text. Volumes two and three contain the presentation materials.

The text, contained in Volume 1 of this report, presents fundamentals of holography, description of the electro-optic holography (EOH) system, and case studies demonstrating applicability of the system to study of avionics. The appendices of the report contain reprints of publications resulting from this project.

More specifically, this report gives a brief introduction to mathematical fundamentals and definitions necessary to quantitatively apply hologram interferometry. This presentation relates to projection matrices, illumination, observation, and sensitivity vectors, determination of displacements from holograms, including interpretation of time-average interferograms. This is followed by description of the EOH system for automated, quantitative interpretation of holograms based on direct electronic acquisition and processing of holographic data, as developed in the course of this project. Use of the EOH system is demonstrated by representative case studies of avionics.

Basic definitions of the parameters defining hologram recording and reconstruction geometries are given in Chapter 2. This is followed by Chapter 3 presentation of the concepts of

the projection matrices necessary for quantitative interpretation of interferograms with special emphasis on electronic holograms. Based on these concepts, Chapters 4, 5, and 6 detail procedures for determination of displacements, rigid-body motions, and strains and rotations directly from holograms, respectively. These procedures are general in nature and apply to all types of interferograms. Chapter 7 concentrates on interpretation of time-average holograms of vibrating objects. Electro-optic holography (EOH) is described in Chapter 8, including description of the system and presentation of representative results. Complementary discussion of electro-optic shearography (EOS) is given in Chapter 9 and its relationship to EOH is illustrated with representative examples. Modern hybrid approach to structural deformation analysis by ACES methodology, which is based on a combined use of analytical, computational, and experimental solution methodologies, is introduced in Chapter 10. Chapter 11 addresses quantitative EOH and FEM hybrid study of vibration characteristics of avionics. Preliminary results of the state-of-the-art hybrid, EOH and FEM, study and optimization of cantilever plate dynamics are presented in Chapter 12. Chapter 13 gives overall summary, conclusions, and recommendations for the project.

Reprints of the publications, which resulted from this project, are included in Appendices A to F. Appendix A presents description and initial results obtained using the EOH system. Automated fringe unwrapping by energy minimization, as developed during this project and implemented in the EOH system, is discussed in Appendix B. Three-dimensional graphics techniques applied to the rendering of holographic interferometric data are presented in Appendix C. Appendix D details phase unwrapping by least-squares error minimization of phase curvature. Vibration studies using EOH and FEM methodologies are described in Appendix E. Appendix F presents quantitative EOH study of dynamics of electronic components.

Presentation materials, consisting of selected sections of this report, are contained in Volumes 2 and 3. Volume 2 contains overhead transparencies, while Volume 3 contains VHS tape recordings of representative case studies performed during this project.

2. ILLUMINATION, OBSERVATION, AND SENSITIVITY VECTORS

Quantitative interpretation of holograms depends on knowledge of the illumination and observation directions used during recording and reconstruction of the holograms. These directions are defined by illumination and observation vectors, \mathbf{K}_1 and \mathbf{K}_2 , respectively, as shown in Fig. 2.1. The projection matrices are based on the unit vectors defining these directions of illumination and observation¹⁻⁴. The vectors \mathbf{K}_1 and \mathbf{K}_2 , in turn, are used to define the sensitivity vector, \mathbf{K} , as detailed in Section 2.1.

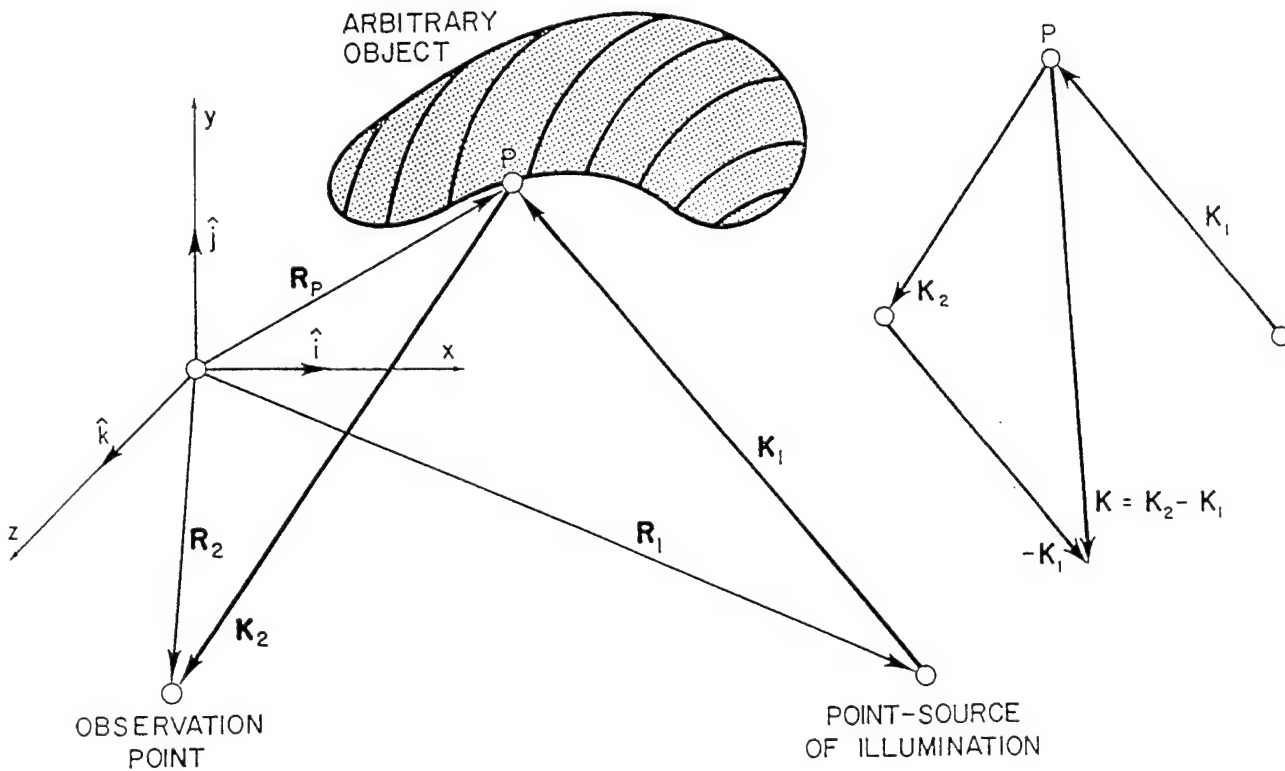


Fig. 2.1. Illumination and observation geometry in hologram interferometry.

2.1. Mathematical considerations

The vectors \mathbf{K}_1 and \mathbf{K}_2 are defined as propagation vectors of light from the point source of illumination to the object and from the object to the "observer" (photosensitive medium, or the sensing element of a CCD camera), respectively, Fig. 2.1. Therefore, \mathbf{K}_1 and \mathbf{K}_2 can be readily

described in terms of position vectors, \mathbf{R}_1 , \mathbf{R}_p , and \mathbf{R}_2 , which are defined with respect to the origin of the Cartesian x - y - z coordinate system. These position vectors, defining the locations of the point source of illumination, a point on the object, and a point of observation, are:

$$\mathbf{R}_1 = x_1 \hat{i} + y_1 \hat{j} + z_1 \hat{k} \quad , \quad (2.1)$$

$$\mathbf{R}_p = x_p \hat{i} + y_p \hat{j} + z_p \hat{k} \quad , \quad (2.2)$$

and

$$\mathbf{R}_2 = x_2 \hat{i} + y_2 \hat{j} + z_2 \hat{k} \quad , \quad (2.3)$$

respectively, where \hat{i} , \hat{j} , and \hat{k} represent unit vectors, which are parallel to the axis of the coordinate system.

Using Eqs 2.1 to 2.3 and the geometry shown in Fig. 2.1, the vectors \mathbf{K}_1 and \mathbf{K}_2 can be defined as

$$\begin{aligned} \mathbf{K}_1 &= k \hat{K}_1 = k \left(K_{1x} \hat{i} + K_{1y} \hat{j} + K_{1z} \hat{k} \right) = k \frac{\mathbf{R}_p - \mathbf{R}_1}{|\mathbf{R}_p - \mathbf{R}_1|} \\ &= k \frac{(x_p - x_1) \hat{i} + (y_p - y_1) \hat{j} + (z_p - z_1) \hat{k}}{[(x_p - x_1)^2 + (y_p - y_1)^2 + (z_p - z_1)^2]^{\frac{1}{2}}} \\ &= k K_{1x} \hat{i} + k K_{1y} \hat{j} + k K_{1z} \hat{k} \end{aligned} \quad (2.4)$$

and

$$\begin{aligned} \mathbf{K}_2 &= k \hat{K}_2 = k \left(K_{2x} \hat{i} + K_{2y} \hat{j} + K_{2z} \hat{k} \right) = k \frac{\mathbf{R}_2 - \mathbf{R}_p}{|\mathbf{R}_2 - \mathbf{R}_p|} \\ &= k \frac{(x_2 - x_p) \hat{i} + (y_2 - y_p) \hat{j} + (z_2 - z_p) \hat{k}}{[(x_2 - x_p)^2 + (y_2 - y_p)^2 + (z_2 - z_p)^2]^{\frac{1}{2}}} \\ &= k K_{2x} \hat{i} + k K_{2y} \hat{j} + k K_{2z} \hat{k} \quad . \end{aligned} \quad (2.5)$$

In Eqs 2.4 and 2.5, \hat{K}_1 and \hat{K}_2 are the unit illumination and observation vectors, respectively, while k is the magnitude of the \mathbf{K}_1 and \mathbf{K}_2 vectors defined as

$$|\mathbf{K}_1| = |\mathbf{K}_2| = k = \frac{2\pi}{\lambda} \quad , \quad (2.6)$$

with λ being the wavelength of the laser light.

Finally, definition of the sensitivity vector \mathbf{K} , as a difference between the observation and illumination vectors, yields

$$\begin{aligned}\mathbf{K} &= K_x \hat{i} + K_y \hat{j} + K_z \hat{k} \\ &= \mathbf{K}_2 - \mathbf{K}_1 = k(\hat{K}_2 - \hat{K}_1) \\ &= k(K_{2x} - K_{1x})\hat{i} + k(K_{2y} - K_{1y})\hat{j} + k(K_{2z} - K_{1z})\hat{k} \quad ,\end{aligned}\tag{2.7}$$

where \mathbf{K}_1 and \mathbf{K}_2 are as defined in Eqs 2.4 and 2.5, respectively.

2.2. References

- 2.1. R. J. Pryputniewicz, "Determination of the sensitivity vectors directly from holograms," *J. Opt. Soc. Am.*, 67:1351-1353, 1977.
 - 2.2. R. J. Pryputniewicz and K. A. Stetson, *Fundamentals and applications of laser speckle and hologram interferometry*, Center for Holographic Studies and Laser Technology, Department of Mechanical Engineering, Worcester Polytechnic Institute, Worcester, MA 1980.
 - 2.3. R. J. Pryputniewicz and K. A. Stetson, "Determination of sensitivity vectors in hologram interferometry from two known rotations of the object," *Appl. Opt.*, 19:2201-2205, 1980.
 - 2.4. R. J. Pryputniewicz, "Projection matrices in specklegraphic displacement analysis," *Proc. SPIE*, 243:158-164, 1980.
-

3. PROJECTION MATRICES: DEFINITION AND PROPERTIES

Quantitative interpretation of holograms is based on one's ability to delineate various parameters which characterize recording and reconstruction processes in hologram interferometry¹. These parameters, being vectorial in nature, can be most clearly defined by matrix transformations. These transformations map fields of three-dimensional vectors from one space into corresponding fields of vectors in another space by means of projection matrices¹⁻⁴.

The matrix transformation which is of primary interest in quantitative interpretation of holograms is that which transforms a vector into its shadow on a surface. This transformation may fall into either of two categories: if the direction from which the shadow is cast is parallel to the surface normal, the operation is called a *normal projection*; if it is not, then it is called an *oblique projection*.

3.1. Normal projection

Referring to Fig. 3.1, where \mathbf{A} is a vector, $\hat{\mathbf{b}}$ is a unit vector normal to a surface, and \mathbf{A}_b is the projection of \mathbf{A} onto a surface normal to $\hat{\mathbf{b}}$, it is seen that all that is required to obtain \mathbf{A}_b is to subtract from \mathbf{A} its component in the direction of $\hat{\mathbf{b}}$. The magnitude of that component is given by a scalar product $\hat{\mathbf{b}} \cdot \mathbf{A}$, and its direction is that of $\hat{\mathbf{b}}$, so that the result is

$$\mathbf{A}_b = \mathbf{A} - \hat{\mathbf{b}}(\hat{\mathbf{b}} \cdot \mathbf{A}) \quad . \quad (3.1)$$

We may recognize the right-hand side of Eq. 3.1 as the expansion of the triple vector product, that is,

$$\mathbf{A}_b = -\hat{\mathbf{b}} \times (\hat{\mathbf{b}} \times \mathbf{A}) \quad . \quad (3.2)$$

Because the vector product of two vectors yields a third vector, vector multiplication may be described as a transformation and it may be represented by a matrix. This is achieved by arranging the components of the vector $\hat{\mathbf{b}}$ as an antisymmetric matrix $\tilde{\mathbf{b}}$, which can be written as

$$\tilde{\mathbf{b}} = \begin{bmatrix} 0 & -b_z & b_y \\ b_z & 0 & -b_x \\ -b_y & b_x & 0 \end{bmatrix} \quad . \quad (3.3)$$

Using the matrix defined by Eq. 3.3, we may rewrite Eq. 3.2 as

$$\mathbf{A}_b = -\tilde{\hat{b}} \tilde{\hat{b}} \mathbf{A} = \tilde{P}_b \mathbf{A} \quad , \quad (3.4)$$

where

$$\tilde{P}_b = -\tilde{\hat{b}} \tilde{\hat{b}} \quad , \quad (3.5)$$

is the matrix transformation that projects the vector \mathbf{A} onto the surface which is normal to \hat{b} to form the shadow \mathbf{A}_b .

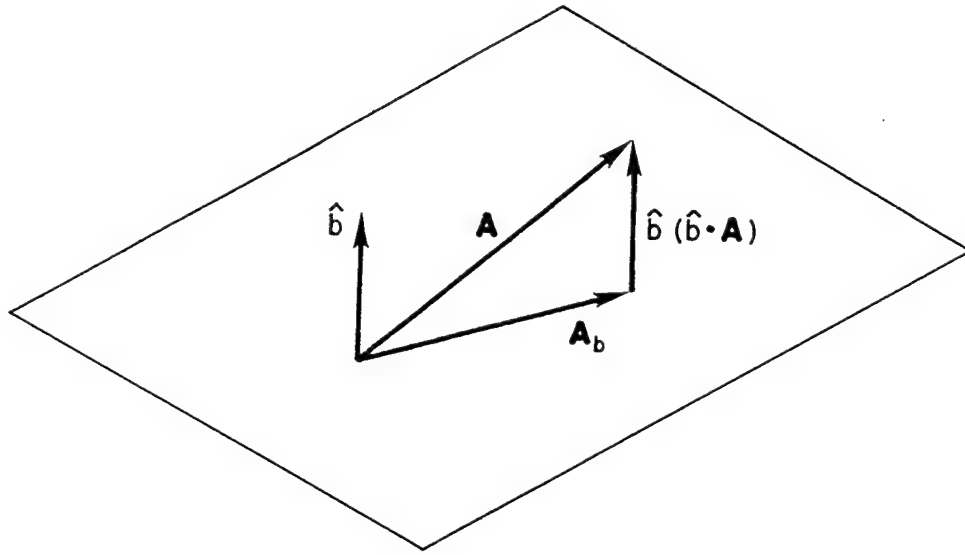


Fig. 3.1. Normal projection onto a surface.

In an alternate way, we can rewrite Eq. 3.1 in a matrix form such that

$$\mathbf{A}_b = \tilde{I} \mathbf{A} - \begin{bmatrix} b_x & 0 & 0 \\ b_y & 0 & 0 \\ b_z & 0 & 0 \end{bmatrix} \begin{bmatrix} b_x & b_y & b_z \\ 0 & 0 & 0 \\ 0 & 0 & 0 \end{bmatrix} \begin{bmatrix} A_x & 0 & 0 \\ A_y & 0 & 0 \\ A_z & 0 & 0 \end{bmatrix} \quad , \quad (3.6)$$

where A_x , A_y , and A_z are the components of \mathbf{A} , b_x , b_y , and b_z are the components of \hat{b} , and \tilde{I} is the identity matrix. The product of the first two matrices in the second term on the right hand side of Eq. 3.6 yields a 3×3 matrix whose elements are all nine possible products of the three components of \hat{b} . This operation defines the third type of product between two vectors, in addition to the well known *scalar product* and *vector product*. In this text, this operation will be called a *matric product* of two vectors, with the word *matric* meaning *of or pertaining to a matrix*, and it will be represented by an encircled cross, that is, \otimes . Thus, using the definition of the matric product, we may rewrite Eq. 3.6 as

$$\mathbf{A}_b = (\tilde{\mathbf{I}} - \hat{\mathbf{b}} \otimes \hat{\mathbf{b}}) \mathbf{A} = \tilde{\mathbf{P}}_b \mathbf{A} \quad , \quad (3.7)$$

from which it follows that

$$\tilde{\mathbf{P}}_b = \tilde{\mathbf{I}} - \hat{\mathbf{b}} \otimes \hat{\mathbf{b}} \quad . \quad (3.8)$$

Equation 3.8 defines the matrix transformation which describes the normal projection along the unit vector $\hat{\mathbf{b}}$ onto a plane whose normal is parallel to the direction of the projection. It should be noted that based on Eqs 3.5 and 3.8,

$$\tilde{\mathbf{P}}_b = -\tilde{\mathbf{b}}\tilde{\mathbf{b}} = \tilde{\mathbf{I}} - \hat{\mathbf{b}} \otimes \hat{\mathbf{b}} \quad . \quad (3.9)$$

3.2. Oblique projection

Now, let us define an oblique projection of the vector \mathbf{A} along the direction $\hat{\mathbf{b}}$ onto a surface that is normal to $\hat{\mathbf{c}}$, to produce the resultant vector \mathbf{A}_{bc} , as shown in Fig. 3.2. In this case, we must subtract from \mathbf{A} such a component in the direction of $\hat{\mathbf{b}}$ that the resultant has no component in the direction of $\hat{\mathbf{c}}$, that is,

$$\mathbf{A}_{bc} = \mathbf{A} - \frac{\hat{\mathbf{b}}(\hat{\mathbf{c}} \cdot \mathbf{A})}{\hat{\mathbf{b}} \cdot \hat{\mathbf{c}}} \quad , \quad (3.10)$$

where \mathbf{A}_{bc} is the projection of \mathbf{A} from the direction of $\hat{\mathbf{b}}$ onto a plane perpendicular to $\hat{\mathbf{c}}$.

Equation 3.10 may be expressed in terms of the vector triple product as

$$\mathbf{A}_{bc} = -\frac{1}{\hat{\mathbf{b}} \cdot \hat{\mathbf{c}}} \hat{\mathbf{c}} \times (\hat{\mathbf{b}} \times \mathbf{A}) \quad . \quad (3.11)$$

Using Eq. 3.3 and defining $\hat{\mathbf{c}}$ as an antisymmetric matrix $\tilde{\mathbf{c}}$, expressed as

$$\tilde{\mathbf{c}} = \begin{bmatrix} 0 & -c_z & c_y \\ c_z & 0 & -c_x \\ -c_y & c_x & 0 \end{bmatrix} \quad , \quad (3.12)$$

we can rewrite Eq. 3.11 to obtain

$$\mathbf{A}_{bc} = -\frac{1}{\hat{\mathbf{b}} \cdot \hat{\mathbf{c}}} \tilde{\mathbf{c}} \hat{\mathbf{b}} \mathbf{A} = \tilde{\mathbf{P}}_{bc} \mathbf{A} \quad . \quad (3.13)$$

where

$$\tilde{P}_{bc} = -\frac{1}{\hat{b} \cdot \hat{c}} \tilde{c} \tilde{b} \quad , \quad (3.14)$$

is the transformation matrix that projects a vector along the direction of \hat{b} onto a plane normal to \hat{c} , to form the shadow \mathbf{A}_{bc} . Furthermore, we can easily express Eq. 3.10 in the form analogous to Eq. 3.7, that is,

$$\mathbf{A}_{bc} = \tilde{I} \mathbf{A} - \frac{1}{\hat{b} \cdot \hat{c}} \hat{b} \otimes \hat{c} \mathbf{A} = \left(\tilde{I} - \frac{1}{\hat{b} \cdot \hat{c}} \hat{b} \otimes \hat{c} \right) \mathbf{A} = \tilde{P}_{bc} \mathbf{A} \quad , \quad (3.15)$$

from which it clearly follows that

$$\tilde{P}_{bc} = \tilde{I} - \frac{1}{\hat{b} \cdot \hat{c}} \hat{b} \otimes \hat{c} \quad . \quad (3.16)$$

Finally, comparing Eqs 3.14 and 3.16, we obtain

$$\tilde{P}_{bc} = -\frac{1}{\hat{b} \cdot \hat{c}} \tilde{c} \tilde{b} = \tilde{I} - \frac{1}{\hat{b} \cdot \hat{c}} \hat{b} \otimes \hat{c} \quad . \quad (3.17)$$

Equation 3.17 represents the transformation matrix defining the oblique projection that projects a vector along the direction of \hat{b} onto the plane normal to \hat{c} , to form the shadow \mathbf{A}_{bc} . It should be noted that the order of subscripts b and c in specification of the transformation matrix \tilde{P}_{bc} , given by Eq. 3.17, is that of vectors \hat{b} and \hat{c} in the matrix product $\hat{b} \otimes \hat{c}$. It should also be noted that in the special case when $\hat{b} = \hat{c}$, Eq. 3.17 reduces to Eq. 3.9.

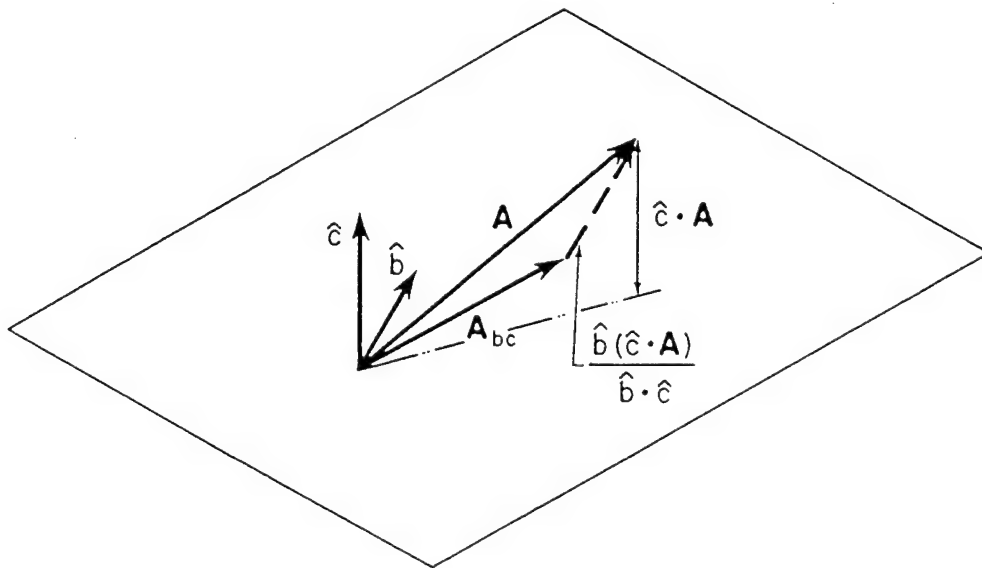


Fig. 3.2. Oblique projection onto a surface.

It must be noted that the order of multiplication is not interchangeable for the matrix products because $\hat{c} \otimes \hat{b}$ yields a matrix not equal to $\hat{b} \otimes \hat{c}$, but equal instead to its transpose. From this it may be deduced that the transpose of an oblique projection matrix simply exchanges the role of the two unit vectors. Therefore,

$$\tilde{P}_{bc}^T = \tilde{P}_{cb} \quad , \quad (3.18)$$

where \tilde{P}_{cb} is the transformation matrix that projects a vector along the direction of \hat{c} onto a plane normal to \hat{b} .

In addition, all projection matrices are singular and do not possess inverses. There is one property, however, that they do have and which is extensively used in holographic analysis. This property is based on the fact that if a vector is projected from a given direction onto a plane, and then if this result is projected from the same direction onto the second plane, the final result is the same as having projected the original vector onto the second plane directly. Thus, for example, if a vector is first projected from the direction \hat{b} onto a plane normal to \hat{c} , and then if this result is projected again from the same direction \hat{b} onto a plane normal to \hat{b} , the result is

$$\tilde{P}_b \tilde{P}_{bc} = \tilde{P}_b \quad , \quad (3.19)$$

where it should be noted that the second projection premultiplies the first projection.

In another case, when \tilde{P}_{bc} is the transformation matrix defining the first projection and \tilde{P}_{ba} is the matrix characterizing the second projection, then

$$\tilde{P}_{ba} \tilde{P}_{bc} = \tilde{P}_{ba} \quad . \quad (3.20)$$

It is important to keep in mind that in these sequences the direction along which the projection is made does not change. However, it should be observed that the sequence of two normal projections, first onto one surface, \tilde{P}_a , and then onto another, \tilde{P}_b , is not the same as the oblique projection \tilde{P}_{ba} , that is,

$$\tilde{P}_b \tilde{P}_a \neq \tilde{P}_{ba} \quad . \quad (3.21)$$

3.3. References

- 3.1. R. J. Pryputniewicz and K. A. Stetson, *Fundamentals and applications of laser speckle and hologram interferometry*, Center for Holographic Studies and Laser Technology, Department of Mechanical Engineering, Worcester Polytechnic Institute, Worcester, MA, 1980.

- 3.2. R. J. Pryputniewicz, "Projection matrices in specklegraphic displacement analysis," *Proc. SPIE*, 243:158-164, 1980.
 - 3.3. K. A. Stetson, "The use of projection matrices in hologram interferometry," *J. Opt. Soc. Am.*, 71:1248-1257, 1981.
 - 3.4. W. Schuman, J. -P. Zürcher, and D. Cuhe, *Holography and deformation analysis*, Springer-Verlag, Berlin, 1985.
-

4. DETERMINATION OF DISPLACEMENTS

Hologram interferometry is used to measure displacements of objects subjected to static and/or dynamic loads. Depending on the loading method used and the methods for recording/reconstruction of holograms and readout of the interferometric information, fringe patterns produced during these reconstructions can be classified either as cosinusoidal fringes or Bessel (J_0) fringes. Typical appearances of these two types of holographic fringes are shown in Fig. 4.1.

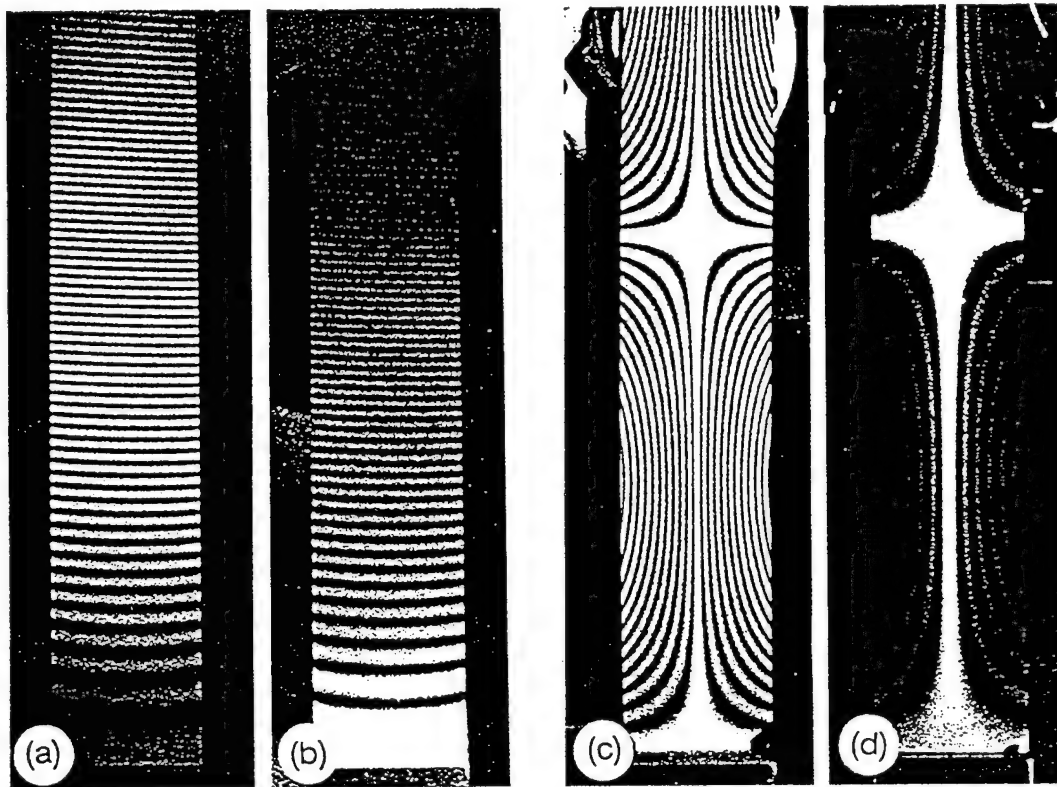


Fig. 4.1. Typical appearances of the two types of holographic fringes: (a) and (c) show cosinusoidal fringes - note that the zero-order fringes are as bright as the higher order cosinusoidal fringes, while (b) and (d) show J_0 fringes - note that the zero-order fringes are much brighter than the higher order J_0 fringes.

The cosinusoidal fringes are of equal brightness across the image, regardless of the fringe order, and are normally associated with a response of the object to the static load. The Bessel fringes are of unequal brightness, which decreases as the fringe order increases, across the image. These fringes are normally associated with a response of the object to dynamic loading, especially periodic excitation causing objects to resonate. Interpretation of the cosinusoidal fringes is a subject of this chapter, while interpretation of the Bessel fringes is discussed in Chapter 7.

Holographic numerical analysis depends on knowledge of the illumination and the observation directions used while recording and/or reconstructing the holograms¹. These directions are described by the illumination and observation vectors, \mathbf{K}_1 and \mathbf{K}_2 , respectively, as discussed in Chapter 2, and define propagation of light from the point source of illumination via the object to the observation point. As the object displaces/deforms, while recording a hologram, the phase difference between the light beams arriving at a specific observation point, from the object and its displaced/deformed copy, is encoded in form of fringe patterns. These fringes are described by a *fringe-locus function*, Ω , constant values of which define fringe loci on the surface of the object. The fringe-locus function relates directly to the fringe orders, n , via

$$\Omega = 2\pi n \quad . \quad (4.1)$$

The fringe-locus function can also be related to the scalar product of the sensitivity vector \mathbf{K} with the displacement vector \mathbf{L} , that is,

$$\mathbf{K} \cdot \mathbf{L} = \Omega \quad . \quad (4.2)$$

The sensitivity vector \mathbf{K} , appearing in Eq. 4.2, can be varied by changing either the direction of illumination, \mathbf{K}_1 , or the direction of observation, \mathbf{K}_2 , or both \mathbf{K}_1 and \mathbf{K}_2 simultaneously. Because of different approaches employed to vary \mathbf{K} and because of different approaches used in determination of Ω , the problem of extracting displacement vectors, \mathbf{L} , directly from cosinusoidal fringes has been solved in a number of ways¹⁻⁹. In this section, we will discuss some of these ways for determination of the object displacements directly from the fringe patterns observed during reconstruction of holograms. We will begin with interpretation of a single hologram when the fringe order is known, then, we will follow with interpretation of a single hologram when the fringe order is unknown and, finally, we will present a method, based on the projection matrices, for determination of displacements from multiple holograms.

4.1. Determination of displacements when fringe order is known

Determination of displacements when the fringe order is known represents a special case, in holographic numerical analysis, when the zero-order fringe is identifiable within the holographically reconstructed image. Then, orders are unambiguously assigned to fringes, with respect to the zero-order fringe. The most popular of the existing techniques, used to assign the fringe order numbers, is based on multiple observations of images reconstructed from a single hologram or, in the case of electro-optic holography (EOH), "single observations" of multiple holograms, i. e., by varying \mathbf{K}_2 .

Multiple observations of a holographically reconstructed image must be made from various, noncoplanar directions. This can be accomplished by noting that the fringes and the surface of the object can nearly always be viewed in focus by simply using a sufficiently small observing aperture, i. e., one having a sufficiently large f /number.

The three-dimensional displacement vector, \mathbf{L} , appearing in Eq. 4.2, is defined in terms of its Cartesian components as

$$\mathbf{L} = L_x \hat{i} + L_y \hat{j} + L_z \hat{k} \quad , \quad (4.3)$$

Therefore, in order to completely determine its unknown components L_x , L_y , and L_z , an "ideal" system of three equations of the type of Eq. 4.2 must be solved simultaneously. Such equations can be generated using the observation geometry shown in Fig. 4.2. Therefore, writing one equation of the type of Eq. 4.2, for each of the three observations shown in Fig. 4.2, we obtain

$$\mathbf{K}^1 \cdot \mathbf{L} = \Omega^1 \quad , \quad (4.4)$$

$$\mathbf{K}^2 \cdot \mathbf{L} = \Omega^2 \quad , \quad (4.5)$$

and

$$\mathbf{K}^3 \cdot \mathbf{L} = \Omega^3 \quad , \quad (4.6)$$

where the superscripts identify quantities corresponding to the specific directions of observation and where, according to Eq. 2.7, the sensitivity vectors are

$$\begin{aligned} \mathbf{K}^1 &= K_x^1 \hat{i} + K_y^1 \hat{j} + K_z^1 \hat{k} \\ &= \mathbf{K}_2^1 - \mathbf{K}_1 = k(K_{2x}^1 - K_{1x}) \hat{i} + k(K_{2y}^1 - K_{1y}) \hat{j} + k(K_{2z}^1 - K_{1z}) \hat{k} \quad , \end{aligned} \quad (4.7)$$

$$\begin{aligned} \mathbf{K}^2 &= K_x^2 \hat{i} + K_y^2 \hat{j} + K_z^2 \hat{k} \\ &= \mathbf{K}_2^2 - \mathbf{K}_1 = k(K_{2x}^2 - K_{1x}) \hat{i} + k(K_{2y}^2 - K_{1y}) \hat{j} + k(K_{2z}^2 - K_{1z}) \hat{k} \quad , \end{aligned} \quad (4.8)$$

and

$$\begin{aligned} \mathbf{K}_3 &= K_x^3 \hat{i} + K_y^3 \hat{j} + K_z^3 \hat{k} \\ &= \mathbf{K}_2^3 - \mathbf{K}_1 = k(K_{2x}^3 - K_{1x}) \hat{i} + k(K_{2y}^3 - K_{1y}) \hat{j} + k(K_{2z}^3 - K_{1z}) \hat{k} \quad . \end{aligned} \quad (4.9)$$

Therefore, based on Eqs 4.7 to 4.9, we have

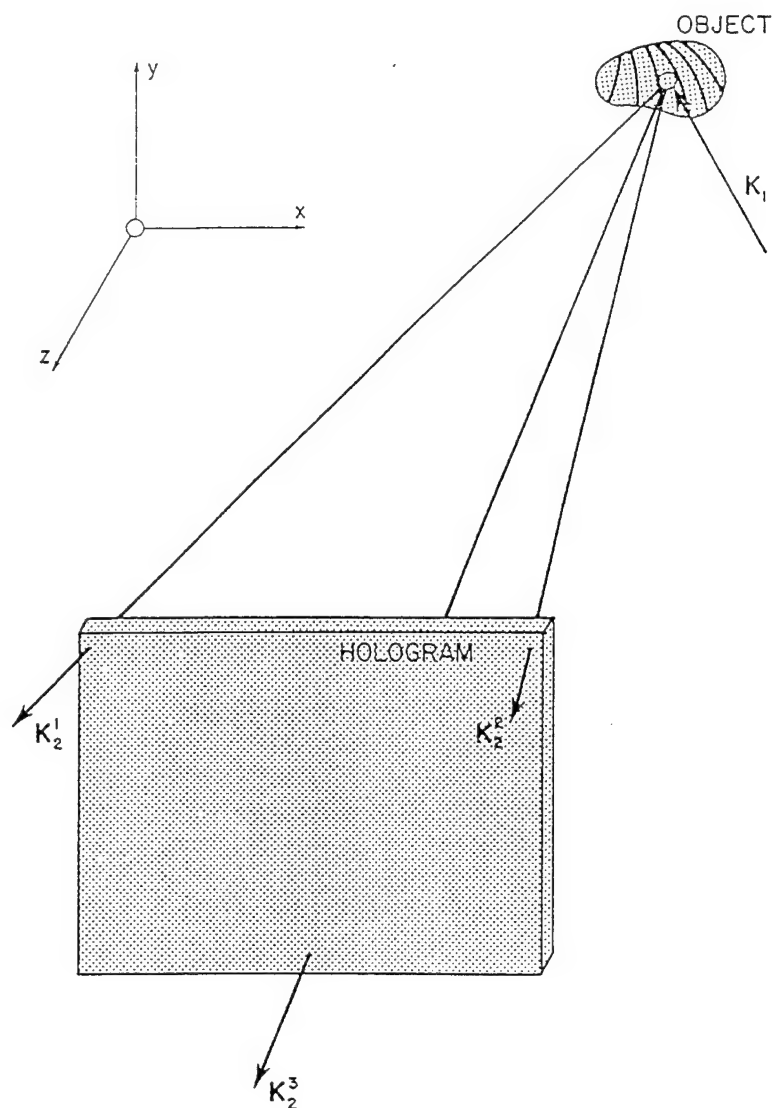


Fig. 4.2. Multiple observations of a holographically reconstructed image from three different directions.

$$\begin{aligned}
 K_x^1 &= k \left(K_{2x}^1 - K_{1x} \right) , \\
 K_y^1 &= k \left(K_{2y}^1 - K_{1y} \right) , \\
 K_z^1 &= k \left(K_{2z}^1 - K_{1z} \right) , \\
 K_x^2 &= k \left(K_{2x}^2 - K_{1x} \right) , \\
 &\cdot \quad \cdot \quad \cdot \\
 &\cdot \quad \cdot \quad \cdot \\
 &\cdot \quad \cdot \quad \cdot \\
 K_z^3 &= k \left(K_{2z}^3 - K_{1z} \right) .
 \end{aligned}
 \tag{4.10}$$

Expanding Eqs 4.4 to 4.6, we obtain

$$K_x^1 L_x + K_y^1 L_y + K_z^1 L_z = \Omega^1 \quad , \quad (4.11)$$

$$K_x^2 L_x + K_y^2 L_y + K_z^2 L_z = \Omega^2 \quad , \quad (4.12)$$

and

$$K_x^3 L_x + K_y^3 L_y + K_z^3 L_z = \Omega^3 \quad . \quad (4.13)$$

The set of Eqs 4.11 to 4.13 can be rewritten as a single matrix equation

$$\begin{bmatrix} K_x^1 & K_y^1 & K_z^1 \\ K_x^2 & K_y^2 & K_z^2 \\ K_x^3 & K_y^3 & K_z^3 \end{bmatrix} \begin{pmatrix} L_x \\ L_y \\ L_z \end{pmatrix} = \begin{pmatrix} \Omega^1 \\ \Omega^2 \\ \Omega^3 \end{pmatrix} \quad , \quad (4.14)$$

Providing that \mathbf{K}^1 , \mathbf{K}^2 , and \mathbf{K}^3 are independent, the 3×3 matrix of the sensitivity vectors is nonsingular and the solution to Eq. 4.14 becomes

$$\begin{pmatrix} L_x \\ L_y \\ L_z \end{pmatrix} = \begin{bmatrix} K_x^1 & K_y^1 & K_z^1 \\ K_x^2 & K_y^2 & K_z^2 \\ K_x^3 & K_y^3 & K_z^3 \end{bmatrix}^{-1} \begin{pmatrix} \Omega^1 \\ \Omega^2 \\ \Omega^3 \end{pmatrix} \quad , \quad (4.15)$$

where the superscript -1 indicates the inverse of the matrix of the sensitivity vectors; the elements of this matrix are defined by Eqs 4.10.

Equation 4.15 gives solution for the three components of \mathbf{L} when three noncoplanar sensitivity vectors are used to obtain the corresponding fringe-locus functions. This is the ideal case. In general, however, the matrix of the sensitivity vectors used in Eq. 4.14 is ill-conditioned because of the limited size of the hologram. As a result of this, substantial errors result in \mathbf{L} . In order to overcome this drawback, more than three observations of the reconstructed image are made. This generates an overdetermined set of simultaneous equations, with one equation for each observation, that is,

$$\begin{aligned} \mathbf{K}^1 \cdot \mathbf{L} &= \Omega^1 \\ \mathbf{K}^2 \cdot \mathbf{L} &= \Omega^2 \\ . & . . \\ . & . . \\ . & . . \\ \mathbf{K}^r \cdot \mathbf{L} &= \Omega^r \quad , \end{aligned} \quad (4.16)$$

where r is the total number of observations, e. g., five, as shown in Fig. 4.3. To facilitate solution of this overdetermined set of equations, Eqs 4.16 can be rewritten using the index notation as

$$\mathbf{K}^m \cdot \mathbf{L} = \Omega^m, \quad m = 1, 2, \dots, r, \quad (4.17)$$

Obviously, no matter how careful and how many observations are made, there will always be some error E inherent in the measurements. Therefore, Eq. 4.17 may be expressed as

$$E^m = \mathbf{K}^m \cdot \mathbf{L} - \Omega^m, \quad m = 1, 2, \dots, r. \quad (4.18)$$

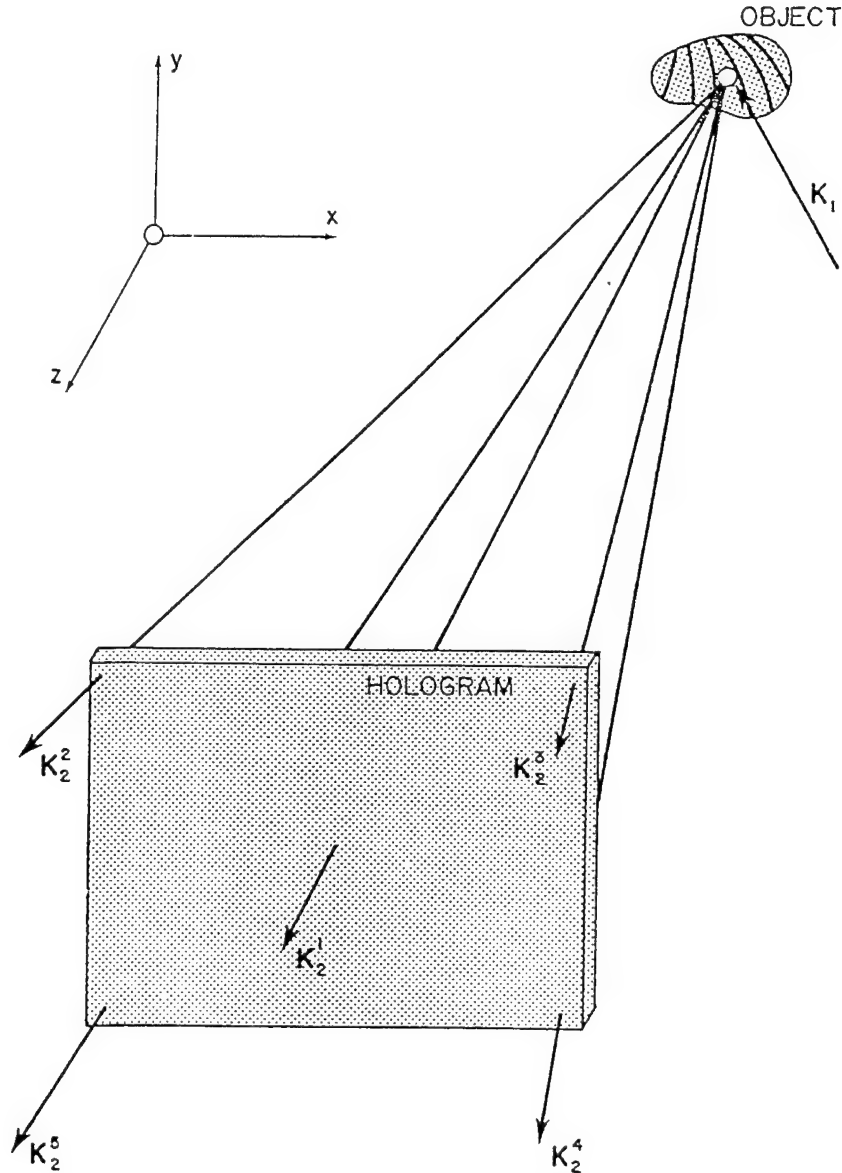


Fig. 4.3. Multiple observations of a holographically reconstructed image from five different directions.

The goal of the analysis is to adjust the coefficients in Eq. 4.18 in such a way as to minimize the sum of all the errors squared, i. e.,

$$\sum_{m=1}^r (E^m)^2 = \sum_{m=1}^r (\mathbf{K}^m \cdot \mathbf{L} - \Omega^m)^2, \quad m = 1, 2, \dots, r. \quad (4.19)$$

In order for the

$$\sum_{m=1}^r (E^m)^2$$

to be minimum, the partial derivatives of Eq. 4.19 with respect to the components L_x , L_y , and L_z of the displacement vector \mathbf{L} must be zero, that is,

$$\frac{\partial}{\partial L_i} \left[\sum_{m=1}^r (E^m)^2 \right] = \frac{\partial}{\partial L_i} \left[\sum_{m=1}^r (\mathbf{K}^m \cdot \mathbf{L} - \Omega^m)^2 \right] = 0, \quad m = 1, 2, \dots, r \quad i = x, y, z, \quad (4.20)$$

which results in the following system of three simultaneous equations

$$\begin{aligned} \sum_{m=1}^r (K_x^m L_x + K_y^m L_y + K_z^m L_z) K_x^m &= \sum_{m=1}^r K_x^m \Omega^m, \\ \sum_{m=1}^r (K_x^m L_x + K_y^m L_y + K_z^m L_z) K_y^m &= \sum_{m=1}^r K_y^m \Omega^m, \\ \sum_{m=1}^r (K_x^m L_x + K_y^m L_y + K_z^m L_z) K_z^m &= \sum_{m=1}^r K_z^m \Omega^m. \end{aligned} \quad (4.21)$$

Equations 4.21 can be written in the matrix form as

$$\begin{bmatrix} \sum_{m=1}^r K_x^m K_x^m & \sum_{m=1}^r K_x^m K_y^m & \sum_{m=1}^r K_x^m K_z^m \\ \sum_{m=1}^r K_y^m K_x^m & \sum_{m=1}^r K_y^m K_y^m & \sum_{m=1}^r K_y^m K_z^m \\ \sum_{m=1}^r K_z^m K_x^m & \sum_{m=1}^r K_z^m K_y^m & \sum_{m=1}^r K_z^m K_z^m \end{bmatrix} \begin{pmatrix} L_x \\ L_y \\ L_z \end{pmatrix} = \begin{pmatrix} \sum_{m=1}^r K_x^m \Omega^m \\ \sum_{m=1}^r K_y^m \Omega^m \\ \sum_{m=1}^r K_z^m \Omega^m \end{pmatrix}, \quad (4.22)$$

and can be readily solved to obtain

$$\begin{pmatrix} L_x \\ L_y \\ L_z \end{pmatrix} = \begin{bmatrix} \sum_{m=1}^r K_x^m K_x^m & \sum_{m=1}^r K_x^m K_y^m & \sum_{m=1}^r K_x^m K_z^m \\ \sum_{m=1}^r K_y^m K_x^m & \sum_{m=1}^r K_y^m K_y^m & \sum_{m=1}^r K_y^m K_z^m \\ \sum_{m=1}^r K_z^m K_x^m & \sum_{m=1}^r K_z^m K_y^m & \sum_{m=1}^r K_z^m K_z^m \end{bmatrix}^{-1} \begin{pmatrix} \sum_{m=1}^r K_x^m \Omega^m \\ \sum_{m=1}^r K_y^m \Omega^m \\ \sum_{m=1}^r K_z^m \Omega^m \end{pmatrix}. \quad (4.23)$$

The result shown in Eq. 4.23 can be obtained in a much more direct way if we write Eq. 4.17 in a condensed matrix form as

$$\tilde{K}\mathbf{L} = \bar{\Omega} \quad , \quad (4.24)$$

where \tilde{K} is a rectangular $r \times 3$ matrix of the sensitivity vectors and $\bar{\Omega}$ is a column $r \times 1$ matrix of the fringe-locus functions.

Defining the error vector E in much the same way as it was done in Eq. 4.18, we can rewrite Eq. 4.24 as

$$E = \tilde{K}\mathbf{L} - \bar{\Omega} \quad (4.25)$$

and write the equivalent of Eq. 4.19 as

$$E^2 = \mathbf{E} \cdot \mathbf{E} = E^T E = (\tilde{K}\mathbf{L} - \bar{\Omega})^T (\tilde{K}\mathbf{L} - \bar{\Omega}) \quad . \quad (4.26)$$

Noting that the transpose of a product of two matrices is equal to the product of the transposes of the two matrices with the order of multiplication reversed, Eq. 4.26 can be rewritten to obtain

$$E^2 = (L^T \tilde{K}^T - \bar{\Omega}^T) (\tilde{K}\mathbf{L} - \bar{\Omega}) = L^T \tilde{K}^T \tilde{K}\mathbf{L} - \bar{\Omega}^T \tilde{K}\mathbf{L} - L^T \tilde{K}^T \bar{\Omega} + \bar{\Omega}^T \bar{\Omega} \quad . \quad (4.27)$$

In order to minimize E^2 , the partial derivatives of Eq. 4.27 with respect to the components of \mathbf{L} must be zero, that is,

$$\frac{\partial(E^2)}{\partial L_i} = 0 \quad , \quad i = x, y, z \quad . \quad (4.28)$$

Therefore, applying Eq. 4.28 to Eq. 4.27 we obtain

$$\tilde{K}^T \tilde{K}\mathbf{L} + L^T \tilde{K}^T \tilde{K} - \bar{\Omega}^T \tilde{K} - \tilde{K}^T \bar{\Omega} = 0 \quad , \quad (4.29)$$

wherefrom, after rearranging, we get

$$(\tilde{K}^T \tilde{K}\mathbf{L} - \tilde{K}^T \bar{\Omega}) + (L^T \tilde{K}^T \tilde{K} - \bar{\Omega}^T \tilde{K}) = 0 \quad , \quad (4.30)$$

or

$$\tilde{K}^T (\tilde{K}\mathbf{L} - \bar{\Omega}) + (\tilde{K}\mathbf{L} - \bar{\Omega})^T \tilde{K} = 0 \quad . \quad (4.31)$$

Examining Eq. 4.31, it becomes apparent that both terms on the left-hand side of the equality sign are identical to each other. Therefore, in order for Eq. 4.31 to be satisfied, both of these terms must be zero. Hence, we obtain

$$\tilde{K}^T (\tilde{K}\mathbf{L} - \bar{\Omega}) = \tilde{K}^T \tilde{K}\mathbf{L} - \tilde{K}^T \bar{\Omega} = 0 \quad , \quad (4.32)$$

or

$$\tilde{K}^T \tilde{K} \mathbf{L} = \tilde{K}^T \overline{\Omega} \quad . \quad (4.33)$$

It should be noted, at this time, that Eq. 4.33 is nothing more than Eq. 4.24 with both sides premultiplied by the transpose of the rectangular matrix \tilde{K} . This procedure decreased the rank of the rectangular matrix \tilde{K} to a square 3×3 matrix $\tilde{K}^T \tilde{K}$ and yields the solution for the displacement vector \mathbf{L} which has the least-squares-error, that is,

$$\mathbf{L} = [\tilde{K}^T \tilde{K}]^{-1} (\tilde{K}^T \overline{\Omega}) \quad . \quad (4.34)$$

It is interesting to note that the square matrix $\tilde{K}^T \tilde{K}$ of Eq. 4.34 may be expressed as the sum of all r matrix products of the sensitivity vectors \mathbf{K}^m , that is,

$$\tilde{K}^T \tilde{K} = \sum_{m=1}^r \mathbf{K}^m \otimes \mathbf{K}^m \quad , \quad (4.35)$$

where the procedures of Chapter 3 were used. Therefore, combining Eqs 4.34 and 4.35, we obtain

$$\mathbf{L} = \left[\sum_{m=1}^r \mathbf{K}^m \otimes \mathbf{K}^m \right]^{-1} (\tilde{K}^T \overline{\Omega}) \quad . \quad (4.36)$$

Comparing Eqs 4.23 and 4.36 it becomes obvious that both equations are identical. However, Eq. 4.36 is much more compact than Eq. 4.23 and, therefore, greatly facilitates holographic numerical analysis.

4.2. Determination of displacements when fringe order is unknown

In holographic analysis of objects for which the entire surface has moved and/or deformed it is often impossible to identify the zero-order fringe and, therefore, procedures of Section 4.1 do not apply. Instead, we may only determine the fringe orders to within an additive constant. With this in mind, we will set up a system of equations of the type of Eq. 4.24 and solve for the displacement vector. To reduce measurement errors, we will use an overdetermined set of equations and solve for \mathbf{L} which has the least-squares-error.

To set up the system of equations, we must determine the fringe-locus functions to within an additive constant. Let us call this constant Ω_o and let us bear in mind that this constant comes from the lack of knowledge of the absolute fringe order. Then, for the first "observation" of the holographically reconstructed image, as shown in Fig. 4.4, we can write an equation relating Ω_o to the scalar product of \mathbf{L} with \mathbf{K}^1 , corresponding to the observation along the direction specified by the vector \mathbf{K}_2^1 , as

$$\mathbf{K}^1 \cdot \mathbf{L} = \Omega_o \quad , \quad (4.37)$$

where the sensitivity vector is as defined by Eq 4.7. Next, "counting" the fringes that pass across the point of interest on the object as the view is being changed from the observation along the direction of \mathbf{K}_2^1 to the observation along the direction of \mathbf{K}_2^2 , while continuously observing the

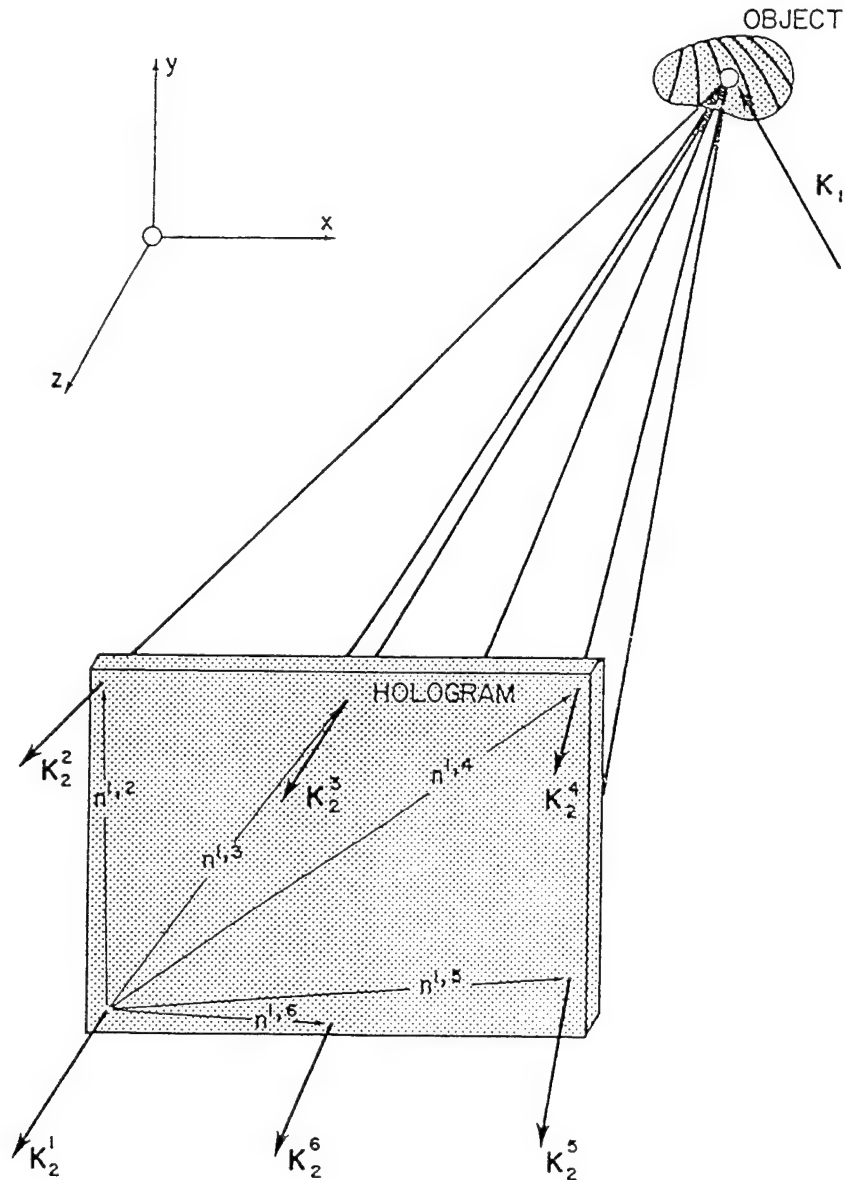


Fig. 4.4. Multiple observations of a holographically reconstructed image with the first direction of observation chosen arbitrarily.

point of interest on the object, we determine the (observed) fringe order, more commonly known as the fringe shift, $n^{1,2}$, which relates to the change, $\Delta\Omega^{1,2}$, in the fringe-locus function via

$$\Delta\Omega^{1,2} = 2\pi n^{1,2} \quad , \quad (4.38)$$

thus giving

$$\mathbf{K}^2 \cdot \mathbf{L} = \Omega_o + \Delta\Omega^{1,2} \quad (4.39)$$

Following the procedure used to obtain Eq. 4.39, we can determine the fringe shifts $n^{1,m}$ for other changes in the direction of observation from that along the direction of \mathbf{K}_2^1 to those along the directions of \mathbf{K}_2^m , one at a time. The sensitivity vectors corresponding to these observations can be described by the system of equations, similar to Eqs 4.7 to 4.9, that is,

$$\begin{aligned} \mathbf{K}^m &= K_x^m \hat{i} + K_y^m \hat{j} + K_z^m \hat{k} = \mathbf{K}_2^m - \mathbf{K}_1 \\ &= k(K_{2x}^m - K_{1x})\hat{i} + k(K_{2y}^m - K_{1y})\hat{j} + k(K_{2z}^m - K_{1z})\hat{k} \quad (4.40) \end{aligned}$$

$$m = 1, 2, \dots, r \quad ,$$

where r is the total number of observations.

Based on Eq. 4.40, the components of the sensitivity vectors can be defined as

$$\begin{aligned} K_x^m &= k(K_{2x}^m - K_{1x}) \quad , \quad m = 1, 2, \dots, r \quad , \\ K_y^m &= k(K_{2y}^m - K_{1y}) \quad , \quad m = 1, 2, \dots, r \quad , \\ K_z^m &= k(K_{2z}^m - K_{1z}) \quad , \quad m = 1, 2, \dots, r \quad . \end{aligned} \quad (4.41)$$

The changes in the fringe-locus function, corresponding to the sensitivity vectors defined by Eq. 4.40, can be expressed as

$$\Delta\Omega^{1,m} = 2\pi n^{1,m} \quad , \quad m = 1, 2, \dots, r \quad , \quad (4.42)$$

where it should be realized that when $m = 1$, $\Delta\Omega^{1,1} = 0$.

Equations relating the sensitivity vectors of Eq. 4.40 and the changes in the fringe-locus functions of Eq. 4.42 to the displacement vector \mathbf{L} are

$$\mathbf{K}^m \cdot \mathbf{L} = \Omega_o + \Delta\Omega^{1,m} \quad , \quad m = 1, 2, \dots, r \quad . \quad (4.43)$$

It should be noted that in the approach described by Eqs 4.40 to 4.43, the number of observations must be equal to or greater than four (i. e., $r \geq 4$) because in addition to the three unknown components of the displacement vector \mathbf{L} we must also account for Ω_o which is an unknown. Therefore, from Eq. 4.43 we have

$$\mathbf{K}^m \cdot \mathbf{L} - \Omega_o = \Delta\Omega^{1,m} \quad , \quad m = 1, 2, \dots, r \quad . \quad (4.44)$$

Since \mathbf{L} and Ω_o are common to all r equations, Eq. 4.44 can be rewritten in a matrix form as

$$[\tilde{K}, -1](\mathbf{L}, \Omega_o) = \Delta\bar{\Omega} \quad , \quad (4.45)$$

where $[\tilde{K}, -1]$ is a rectangular $r \times 4$ matrix, (\mathbf{L}, Ω_o) is a column 4×1 matrix, and $\Delta\bar{\Omega}$ is a column $r \times 1$ matrix. Renaming the $[\tilde{K}, -1]$ matrix of the sensitivity vectors as \tilde{G} , that is,

$$[\tilde{K}, -1] = \tilde{G} \quad , \quad (4.46)$$

we can rewrite Eq. 4.45 as

$$\tilde{G}(\mathbf{L}, \Omega_o) = \Delta\bar{\Omega} \quad . \quad (4.47)$$

Finally, Eq. 4.47 can be solved to obtain

$$(\mathbf{L}, \Omega_o) = [\tilde{G}^T \tilde{G}]^{-1} (\tilde{G}^T \Delta\bar{\Omega}) \quad , \quad (4.48)$$

or

$$(\mathbf{L}, \Omega_o) = \left[\sum_{m=1}^r \mathbf{G}^m \otimes \mathbf{G}^m \right]^{-1} (\tilde{G}^T \Delta\bar{\Omega}) \quad . \quad (4.49)$$

It should be noted that the usual methods of holographic displacement analysis eliminate the unknown Ω_o from the system of equations by subtracting one member of the set from the rest, or by subtracting pairs of equations. The method given in this section is preferred because, in the subtraction process, the effects of some measurement errors can be escalated. However, we should realize that in the case when the first observation is made through a point lying within the center of all points through which observations are made, as shown in Fig. 4.5, it does not matter whether we introduce the additive constant Ω_o and use Eq. 4.49 in determination of displacements, or simply use the fringe shifts alone. The results will be the same.

The mathematical developments of this section require that all changes in the fringe-locus function be determined in reference to the initial direction of observation. This requirement is not a result of a mere mathematical convenience, but rather of a crucial practical need. This need is based on recognition that in order to minimize influence of the measurement errors, the initial direction of observation, \mathbf{K}_2^1 , be established in such a way that the greatest changes in the observation perspective(s), for a given holographic setup, can be achieved. This, in turn, allows determination of the largest changes in the fringe-locus function, $\Delta\Omega$, corresponding to the changes in the directions of observation, in reference to the \mathbf{K}_2^1 , and leads to minimization of the effects that the measurement errors have on the $\Delta\Omega$. Finally, minimization of errors in determination of $\Delta\Omega$, for a known sensitivity vector \mathbf{K} , yields (\mathbf{L}, Ω_o) from Eq. 4.49 that gives the best results for the particular holographic setup used.

It is stressed that in the cases when we want to make observations in an arbitrary fashion, with the first observation not being through the central point, only Eq. 4.49 can be used to determine the displacements. Use of other equations will give incorrect results.

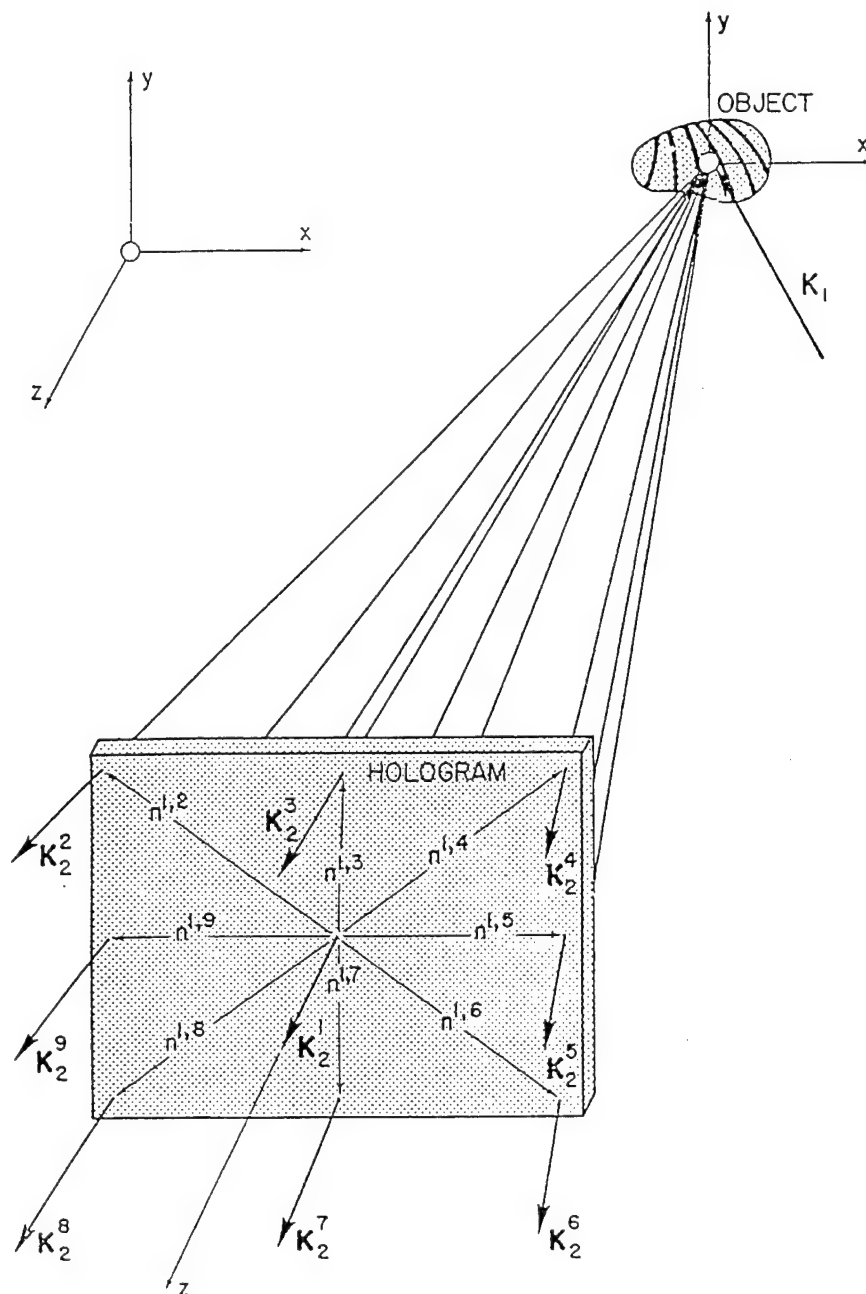


Fig. 4.5. Multiple observations of a holographically reconstructed image with the first direction of observation being in the center of all points through which observations are made.

4.3. Determination of displacements from multiple holograms

In certain applications, it is either not practical or, even, not possible to record holograms large enough to allow multiple observations of the reconstructed images. In some other

applications, the holograms do not exhibit any parallax at all. This is certainly the case with electro-optic (also referred to as electronic, and/or TV) holography, discussed in Chapter 8, where holograms are recorded electronically on CCD arrays and exhibit no parallax. Therefore, procedures discussed in Sections 4.1 and 4.2 cannot be used in these applications. However, even in the case of holograms that do not exhibit parallax, we can easily determine two components of the object displacement vectors in the directions transverse to the direction from which the hologram was recorded. The vector sum of these two components may be referred to as the *observed displacement vector* and it can be denoted as \mathbf{L}_{ob} . This vector is a result of a projection of the actual (unknown) displacement vector \mathbf{L} onto a plane normal to the direction of observation, i. e., the plane normal to the direction from which the hologram was recorded. As such, \mathbf{L}_{ob} provides only a two-dimensional information on the displacement of the object, in a local coordinate system which is based on the local direction of observation. However, if we are able to record more than one hologram, each from a different, non collinear direction, then each of these holograms can be interpreted to determine the corresponding observed displacement vectors. A set of simultaneous equations representing these observed displacement vectors can be solved for the unknown \mathbf{L} using projection matrices, as follows.

Let us assume that r observations are made of the holographically reconstructed image. If each of these observations is made along a direction of a unit vector $\hat{\mathbf{K}}_2^m$, which, based on Eqs 2.5 and 2.6, can be defined as

$$\hat{\mathbf{K}}_2^m = \frac{\lambda}{2\pi} \mathbf{K}_2^m, \quad (4.50)$$

where \mathbf{K}_2^m is the average direction of the m -th ($m=1, 2, \dots, r$) recording, then the corresponding projection matrices $\tilde{\mathbf{P}}_{K_2}^m$ can be expressed as

$$\tilde{\mathbf{P}}_{K_2}^m = \tilde{\mathbf{I}} - \hat{\mathbf{K}}_2^m \otimes \hat{\mathbf{K}}_2^m. \quad (4.51)$$

Therefore, for each of the r observations, the observed displacements \mathbf{L}_{ob}^m (i. e., the displacement vectors which are completely defined by two components transverse to the direction of observation) can be related to the actual (unknown) displacement vector \mathbf{L} (i. e., the vector which requires three components for a complete definition) by means of the corresponding projection matrices, $\tilde{\mathbf{P}}_{K_2}^m$, i. e.,

$$\begin{aligned} \mathbf{L}_{ob}^1 &= \tilde{\mathbf{P}}_{K_2}^1 \mathbf{L} \\ \mathbf{L}_{ob}^2 &= \tilde{\mathbf{P}}_{K_2}^2 \mathbf{L} \\ &\vdots \\ \mathbf{L}_{ob}^r &= \tilde{\mathbf{P}}_{K_2}^r \mathbf{L} \end{aligned} \quad (4.52)$$

Since the displacement \mathbf{L} is common to all Eqs 4.52, this system of equations can be written in a matrix form as

$$\begin{bmatrix} \mathbf{L}_{bb}^1 \\ \mathbf{L}_{ob}^2 \\ \cdot \\ \cdot \\ \cdot \\ \mathbf{L}_{ob}^r \end{bmatrix} = \begin{bmatrix} \tilde{P}_{K_2}^1 \\ \tilde{P}_{K_2}^2 \\ \cdot \\ \cdot \\ \cdot \\ \tilde{P}_{K_2}^r \end{bmatrix} \mathbf{L} , \quad (4.53)$$

and Eq. 4.53 can be solved to obtain

$$\mathbf{L} = \left[\sum_{m=1}^r \tilde{P}_{K_2}^m \right]^{-1} \left(\sum_{m=1}^r \mathbf{L}_{ob}^m \right) . \quad (4.54)$$

Equation 4.54 shows that the actual object displacement \mathbf{L} is equal to the product of the inverse of a 3×3 matrix formed by summation of all r projection matrices $\tilde{P}_{K_2}^m$ with a column matrix of the sum of all r observed displacements \mathbf{L}_{ob}^m .

The only parameters that are needed to evaluate Eq. 4.54 are the unit vectors \hat{K}_2^m and the corresponding observed displacements \mathbf{L}_{ob}^m . The unit observation vectors are easily determined from the illumination/observation geometry, as discussed in Chapter 2, while the observed displacements relate directly to the fringe patterns seen during reconstruction of the holographic interferograms and are determined from the spatial distributions of the fringe-locus function Ω .

It should be realized, at this time, that Eq. 4.54 applies not only to the cases when the single observations are made through multiple holograms, Fig. 4.6, but also when fringe parallax is used in analysis of a single holographic image, Fig. 4.7.

4.4. References

- 4.1. R. J. Pryputniewicz and K. A. Stetson, *Fundamentals and applications of laser speckle and hologram interferometry*, Center for Holographic Studies and Laser Technology, Department of Mechanical Engineering, Worcester Polytechnic Institute, Worcester, MA, 1980.
- 4.2. E. B. Aleksandrov and A. M. Bonch-Bruевич, "Investigation of surface strains by the hologram technique," *Sov. Phys. Tech. Phys.*, 12:258-265, 1967.

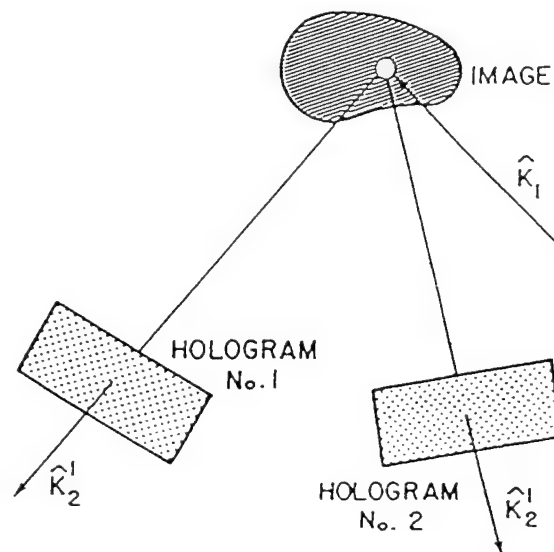


Fig. 4.6. Use of multiple holograms in analysis of a single image.

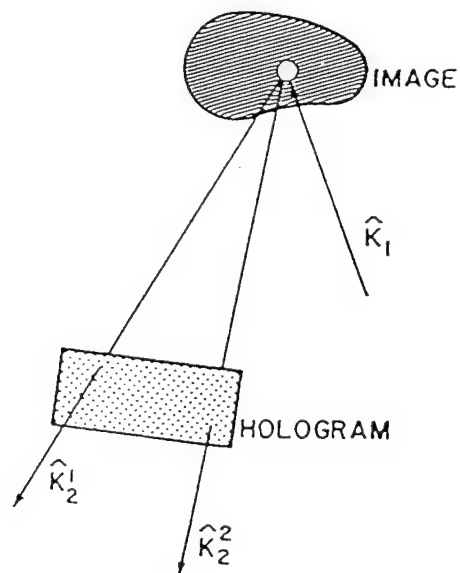


Fig. 4.7. Multiple observations of an image through a single hologram.

- 4.3. J. E. Sollid, "Holographic interferometry applied to measurements of small static displacements of diffusely reflecting surfaces," *Appl. Opt.*, 8:1587-1595, 1969.
 - 4.4. K. Shibayama and H. Uchiyama, "Measurement of three-dimensional displacement by hologram interferometry," *Appl. Opt.*, 10:2150-2154, 1971.
 - 4.5. E. Archbold and A. E. Ennos, "Displacement measurement from double-exposure holography," *Optica Acta*, 19:253-271, 1972.
 - 4.6. S. K. Dhir and J. P. Sikora, "An improved method for obtaining the general-displacement field from a holographic interferogram," *Exp. Mech.*, 12:323-327, 1972.
 - 4.7. P. M. Boone and L. C. De Backer, "Determination of three orthogonal displacement components from one double-exposure hologram," *Optik*, 37:61-81, 1973.
 - 4.8. K. A. Stetson, "Fringe interpretation for holographic interferometry of rigid-body motions and homogeneous deformations," *J. Opt. Soc. Am.*, 64:1-10, 1974.
 - 4.9. R. J. Pryputniewicz and W. W. Bowley, "Techniques of holographic displacement measurement: an experimental comparison," *Appl. Opt.*, 17:1748-1756, 1978.
-

5. DETERMINATION OF RIGID-BODY MOTIONS

Development of modern avionics requires rapid, full surface inspection techniques that can lead to quick identification of areas experiencing severe vibrations and high stress concentrations. Recent developments in holography and speckle interferometry have allowed development of such techniques. However, application of these techniques is often limited by the fact that fringe patterns yield undesired information due to rigid-body motions of the entire assembly, superimposed on the motion of the component studied. It should be noted that use of ultra-fast pulsed lasers does not preclude formation of fringes due to rigid-body motions. It is not the exposure time (duration of a pulse) which is usually several nanoseconds, but the time between the exposures, normally several orders of magnitude higher, that plays an important role in recording of holograms.

In this chapter, a method for determination of rigid-body motions is presented¹. In addition, a procedure that allows use of the rigid-body motions in subsequent analysis of relative motions of deformed points on the object is also presented.

5.1. Mathematical considerations

Rigid-body motions of any object may be resolved into bulk body translation \mathbf{L}_o and rotation θ , therefore, we can write that the motion \mathbf{L}_i at any point i on the object can be defined as

$$\mathbf{L}_i = \mathbf{L}_o + \mathbf{R}_i \times \theta, \quad i = 1, 2, \dots, r, \quad (5.1)$$

where r is the total number of points considered and \mathbf{R}_i is the position vector, Fig. 5.1, from the origin of arbitrarily chosen coordinate system to the i -th point on the object defined as

$$\mathbf{R}_i = x_i \hat{i} + y_i \hat{j} + z_i \hat{k}, \quad i = 1, 2, \dots, r, \quad (5.2)$$

with x_i , y_i , and z_i being components of \mathbf{R}_i in directions of unit vectors \hat{i} , \hat{j} , and \hat{k} of the Cartesian coordinate system, respectively.

In Eq. 5.1, the vectors \mathbf{L}_i , \mathbf{L}_o , and θ , defining rigid-body motion, bulk body translation, and body rotation, respectively, are defined as

$$\mathbf{L}_i = L_{ix} \hat{i} + L_{iy} \hat{j} + L_{iz} \hat{k}, \quad i = 1, 2, \dots, r, \quad (5.3)$$

$$\mathbf{L}_o = L_{ox} \hat{i} + L_{oy} \hat{j} + L_{oz} \hat{k}, \quad (5.4)$$

and

$$\theta = \theta_x \hat{i} + \theta_y \hat{j} + \theta_z \hat{k}. \quad (5.5)$$

Now, we may write matrix equivalent of Eq. 5.1 as

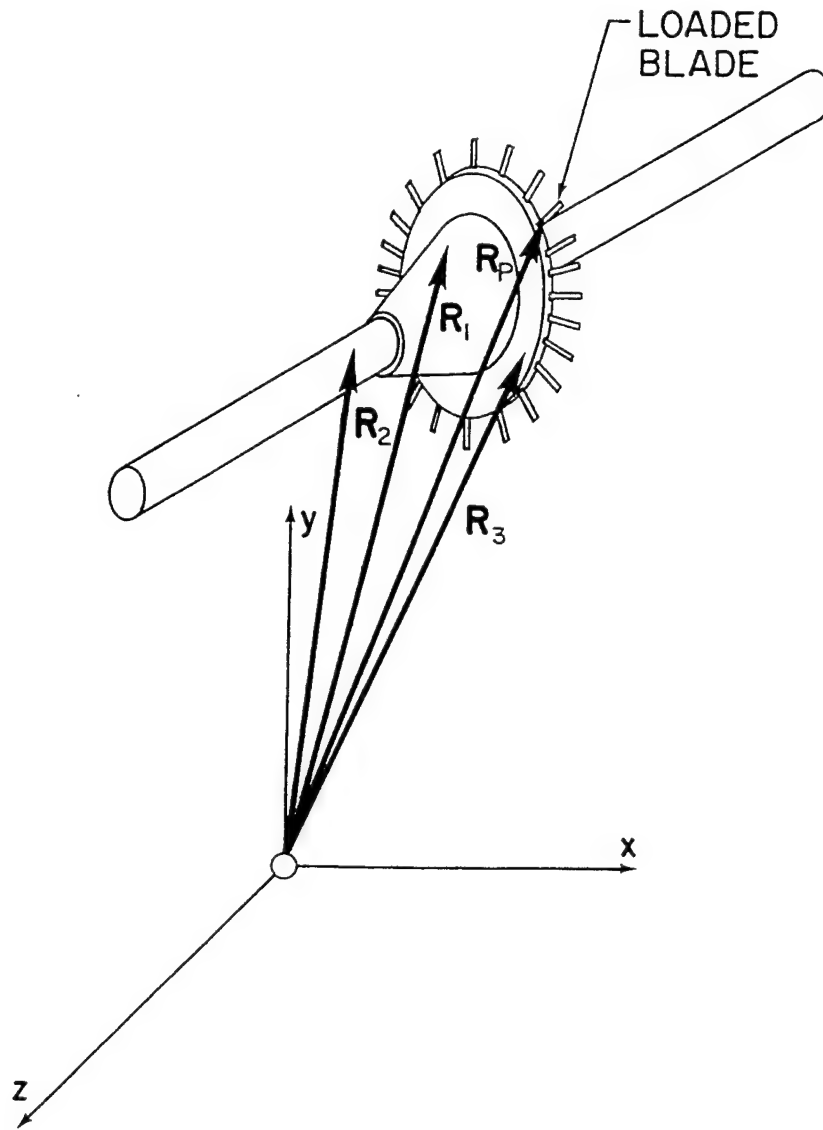


Fig. 5.1. Schematic representation of the geometry for holographic determination of rigid-body motions.

$$\mathbf{L}_i = [\tilde{I} \quad \tilde{R}_i] \begin{pmatrix} \mathbf{L}_o \\ \theta \end{pmatrix}, \quad i = 1, 2, \dots, r, \quad (5.6)$$

where the i -th displacement vector \mathbf{L}_i was written as a column matrix

$$\mathbf{L}_i = \begin{pmatrix} L_{ix} \\ L_{iy} \\ L_{iz} \end{pmatrix}, \quad i = 1, 2, \dots, r, \quad (5.7)$$

identity matrix \tilde{I} was defined as

$$\tilde{I} = \begin{bmatrix} 1 & 0 & 0 \\ 0 & 1 & 0 \\ 0 & 0 & 1 \end{bmatrix}, \quad (5.8)$$

the i -th space vector \mathbf{R}_i was rewritten in a matrix form, viz.,

$$\tilde{\mathbf{R}}_i = \begin{bmatrix} 0 & -z_i & y_i \\ z_i & 0 & -x_i \\ -y_i & x_i & 0 \end{bmatrix}, \quad i = 1, 2, \dots, r, \quad (5.9)$$

and the components of \mathbf{L}_o and $\boldsymbol{\theta}$ vectors, given in Eqs 5.3 and 5.4, respectively, were combined in a six by one matrix $\begin{pmatrix} \mathbf{L}_o \\ \boldsymbol{\theta} \end{pmatrix}$ defined as

$$\begin{pmatrix} \mathbf{L}_o \\ \boldsymbol{\theta} \end{pmatrix} = \begin{pmatrix} L_{ox} \\ L_{oy} \\ L_{oz} \\ \theta_x \\ \theta_y \\ \theta_z \end{pmatrix}. \quad (5.10)$$

One might think that two equations of the type of Eq. 5.6 would be sufficient to determine the six unknowns, that is, L_{ox} , L_{oy} , L_{oz} , θ_x , θ_y , and θ_z . However, the square matrix $[\tilde{I} \tilde{\mathbf{R}}_i]$, which results when $r = 2$ in Eq. 5.6, is singular and, therefore, does not have an inverse. Hence, in the foregoing analysis we need three or more object points (that is, $r \geq 3$ in Eq. 5.6 which results in a rectangular $3r \times 6$ matrix $[\tilde{I} \tilde{\mathbf{R}}_i]$, $i = 1, 2, \dots, r$. The use of an overdetermined set of equations is also advantageous when we realize that because of the limited solid angle the hologram subtends at the object large errors might result in determination of the rigid-body motions. Hence, expanding Eq. 5.6 for r points on the object we obtain

$$\begin{pmatrix} \mathbf{L}_1 \\ \mathbf{L}_2 \\ \vdots \\ \mathbf{L}_r \end{pmatrix} = \begin{bmatrix} \tilde{I} & \tilde{\mathbf{R}}_1 \\ \tilde{I} & \tilde{\mathbf{R}}_2 \\ \vdots & \vdots \\ \tilde{I} & \tilde{\mathbf{R}}_r \end{bmatrix} \begin{pmatrix} \mathbf{L}_o \\ \boldsymbol{\theta} \end{pmatrix}. \quad (5.11)$$

Equation 5.11 can be written in a more condensed form as

$$\tilde{L} = \tilde{\Xi} \begin{pmatrix} \mathbf{L}_o \\ \boldsymbol{\theta} \end{pmatrix}, \quad (5.12)$$

where we have defined

$$\tilde{L} = \begin{pmatrix} \mathbf{L}_1 \\ \mathbf{L}_2 \\ \vdots \\ \mathbf{L}_r \end{pmatrix}, \quad (5.13)$$

and

$$\tilde{\Xi} = \begin{bmatrix} \tilde{I} & \tilde{R}_1 \\ \tilde{I} & \tilde{R}_2 \\ \vdots & \vdots \\ \tilde{I} & \tilde{R}_r \end{bmatrix}. \quad (5.14)$$

Premultiplying both sides of Eq. 5.12 by a transpose of the rectangular matrix $\tilde{\Xi}$ we obtain

$$\tilde{\Xi}^T \tilde{L} = \tilde{\Xi}^T \tilde{\Xi} \begin{pmatrix} \mathbf{L}_o \\ \boldsymbol{\theta} \end{pmatrix}. \quad (5.15)$$

This procedure reduces the rectangular $3r \times 6$ matrix $\tilde{\Xi}$ to a square 6×6 matrix $\tilde{\xi}$, that is,

$$\tilde{\xi} = \tilde{\Xi}^T \tilde{\Xi}, \quad (5.16)$$

and gives the solution of the matrix of rigid-body translation and rotation, which has the least-square-error, which can be expressed as

$$\begin{pmatrix} \mathbf{L}_o \\ \boldsymbol{\theta} \end{pmatrix} = \tilde{\xi}^{-1} (\tilde{\Xi}^T \tilde{L}), \quad (5.17)$$

where $\tilde{\xi}^{-1}$ is an inverse of the matrix defined by Eq. 5.16. Using Eq. 5.17 and considering three or more points on the surface of the object that experienced rigid-body motion, the corresponding translations and rotations can be determined from holograms. If we are also able to determine total translation \mathbf{L}_P and total rotation $\boldsymbol{\theta}_P$ of a deformed point P on the object, then, we can determine motions $\mathbf{L}_{P_{rel}}$ and $\boldsymbol{\theta}_{P_{rel}}$ of this point P relative to the rest of the object. In order to do so, we must first determine the rigid-body translation $\mathbf{L}_{P_{rig}}$ at the point P on the object, defined by the position vector \mathbf{R}_P as shown in Fig. 5.1, because translations are position dependent. Therefore, using an equivalent of Eq. 5.6, we can write an expression for rigid-body translation of point P as

$$\mathbf{L}_{P_{rig}} = [\tilde{I} \quad \tilde{\mathbf{R}}_P] \begin{pmatrix} \mathbf{L}_o \\ \boldsymbol{\theta} \end{pmatrix}, \quad (5.18)$$

where \mathbf{L}_o and $\boldsymbol{\theta}$ have values determined from Eq. 5.17 and \mathbf{R}_P is the position vector from the origin of the coordinate system to the point of interest on the object. Next, we subtract the $\mathbf{L}_{P_{rig}}$, given by Eq. 5.18, from the total translation \mathbf{L}_P which results in a translation $\mathbf{L}_{P_{rel}}$ of P relative to the rest of the object, i. e.,

$$\mathbf{L}_{P_{rel}} = \mathbf{L}_P - \mathbf{L}_{P_{rig}}. \quad (5.19)$$

Noting that the rigid-body rotations are independent of the position on the surface of the object we can subtract $\boldsymbol{\theta}$ (computed from Eq. 5.17) directly from total rotation $\boldsymbol{\theta}_P$ which will result in a relative rotation $\boldsymbol{\theta}_{P_{rel}}$ of point P , viz.,

$$\boldsymbol{\theta}_{P_{rel}} = \boldsymbol{\theta}_P - \boldsymbol{\theta}. \quad (5.20)$$

Equations 5.19 and 5.20 allow determination of translations and rotations at any deformed point on the object relative to the rest of the body. For example, if we wish to determine motions of a point on a blade constituting a part of a turbine stage assembly, we can solve Eq. 5.17 by choosing three points on the disk and shaft. Let us assume that we have decided to compute translations and rotations of the disk assembly based on motions of points defined by position vectors \mathbf{R}_1 , \mathbf{R}_2 , and \mathbf{R}_3 . Then, solution of Eq. 5.17 will result in the components of vectors \mathbf{L}_o and $\boldsymbol{\theta}$. Next, using Eq. 5.18, rigid-body translation of point P at a known \mathbf{R}_P , on the blade, can be determined. Finally from Eq. 5.19 we can compute $\mathbf{L}_{P_{rel}}$ and using computed value of $\boldsymbol{\theta}_P$ we can calculate $\boldsymbol{\theta}_{P_{rel}}$ from Eq. 5.20. Vectors $\mathbf{L}_{P_{rel}}$ and $\boldsymbol{\theta}_{P_{rel}}$ relate directly to the force system that was acting on the blade when the measurements were made.

5.2. References

- 5.1. R. J. Pryputniewicz, "Holographic determination of rigid-body motions," *Appl. Opt.*, 18:1442-1444, 1979.

6. DETERMINATION OF STRAINS AND ROTATIONS

Accurate determination of object's strain is of great interest in mechanics because it may correlate with the structural failure. As a direct outcome of this need, numerous methods were developed to perform the necessary diagnosis. Some of these methods are based on the principles of hologram interferometry which, with its high sensitivity, has found strong applications in analysis of small strains. This becomes obvious when we realize that object deformations, on the order of a fraction of a wavelength, will cause fringes to be formed during reconstruction of a hologram which recorded this deformation. In this way, any changes in the object's state of stress, which cause changes in its shape and/or deformation, can be measured.

Holographic strain analysis has been introduced in a classical paper by Ennos¹ in 1968. Since then, a number of different applications for measurement of small strains were developed²⁻⁶. For example, Dändliker et al.^{3,4} have developed a sophisticated optoelectronic fringe interpolation method, Schumann and Dubas^{5,6} have advanced a complicated theory of fringe localization together with a complex apparatus of coupled telescopes, while Stetson^{7,8} presented a theory, based on a concept of a fringe-vector, that permits determination of strain when it can be assumed to be homogeneous over a sufficiently large region of a sufficiently three-dimensional object.

The Stetson's approach is called the *fringe-vector method of holographic strain analysis*. This method recognizes that any combination of a homogeneous strain, shear, and rotation of an object, yields fringes on the surface of the object, which can be described by a single vector, the *fringe-vector*. The fringe-vector method was generalized by Pryputniewicz and Stetson^{8,9} by introducing a procedure which accounts for variations of the sensitivity vector across the object and this, therefore, allows application of the method even in the presence of a perspective variation in the illumination or observation directions.

If an object undergoes a homogeneous deformation and/or rotation while a hologram is being recorded, then, during the reconstruction of the hologram, the object will be seen covered by a pattern of fringes that would appear to be generated along the lines of intersection of the surface of the object with a set of parallel, equally spaced planes called *fringe-locus planes*. For example, holographically reconstructed three-dimensional object with flat surfaces will be seen covered by a pattern of parallel, equally spaced fringes, Fig. 6.1, as though it were intersected by a set of the fringe-locus planes. These fringe-locus planes are uniquely defined by a fringe-vector, \mathbf{K}_f , whose magnitude is inversely proportional to the spacing between the planes and whose direction is normal to them, Fig. 6.2. Therefore, observation of the fringe patterns allows determination of the fringe-vector. Since fringe-vectors are related to the holographic sensitivity vectors by a matrix transformation which describes strains, shears, and rotations of the object, multiple observations, from noncoplanar directions, of the holographically reconstructed image allow determination of the desired strain-rotation matrix.

The procedures for determination of the fringe-vectors, strains, and rotations, from holographically reconstructed images, are discussed in this Chapter.

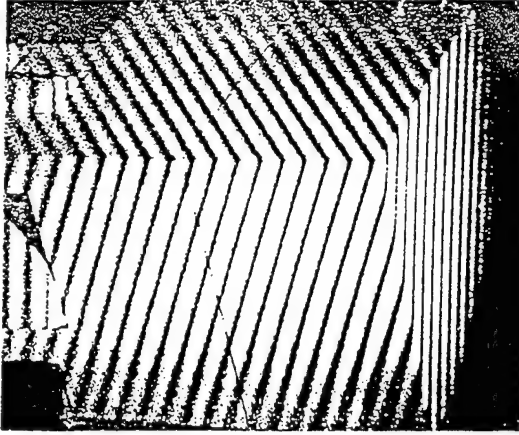


Fig. 6.1. A photograph of a reconstruction from a double-exposure hologram recording a rigid-body rotation of the object.

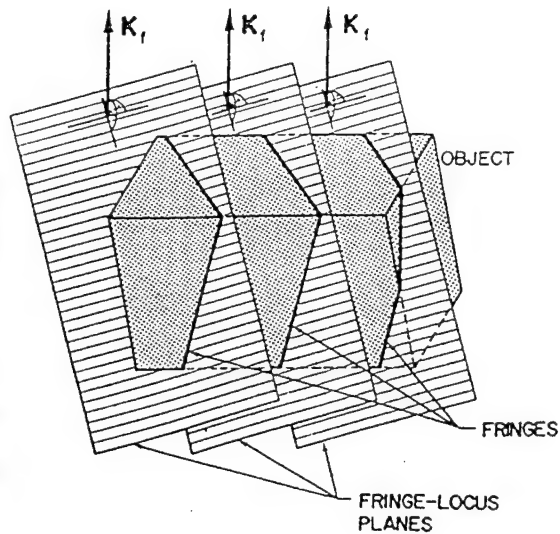


Fig. 6.2. Formation of fringes in hologram interferometry: the surface of the object appears to be intersected by a set of equally spaced fringe-locus planes which are represented by \mathbf{K}_f .

6.1. Spatial dependence of the fringe-locus function

Let us assume that an object is illuminated with spherical wavefronts from a point defined by a position vector \mathbf{R}_1 and observed with a spherical perspective from a point given by \mathbf{R}_2 , Fig. 6.3.

As a result of some deformation and/or rotation between exposures of, e. g., a double-exposure hologram, the object would be reconstructed covered with fringes. These fringes will be generated by the fringe-locus function which is a scalar function of space.

Let us also assume that the value of this fringe-locus function at a point P on the object, $\Omega(\mathbf{K}, \mathbf{R}_P)$, is known, where \mathbf{R}_P is the position vector from the origin of the Cartesian coordinate system to the point of interest and \mathbf{K} is the sensitivity vector, as defined in Chapter 2. Then, the fringe-locus function Ω_Q , at a nearby point Q on the object, may be expressed in terms of the value of Ω and its derivatives at P , by means of the Taylor series expansion, that is,

$$\Omega(\mathbf{K}, \mathbf{R}_Q) = \Omega(\mathbf{K}, \mathbf{R}_P) + \Delta\mathbf{R}_{PQ}$$

$$= \Omega(\mathbf{K}, \mathbf{R}_P) + \Delta\mathbf{R}_{PQ} \cdot \mathbf{K}_f + \frac{1}{2} \Delta\mathbf{R}_{PQ} \tilde{T}_f \Delta\mathbf{R}_{PQ} + \dots, \quad (6.1)$$

where the third and higher order terms were neglected.

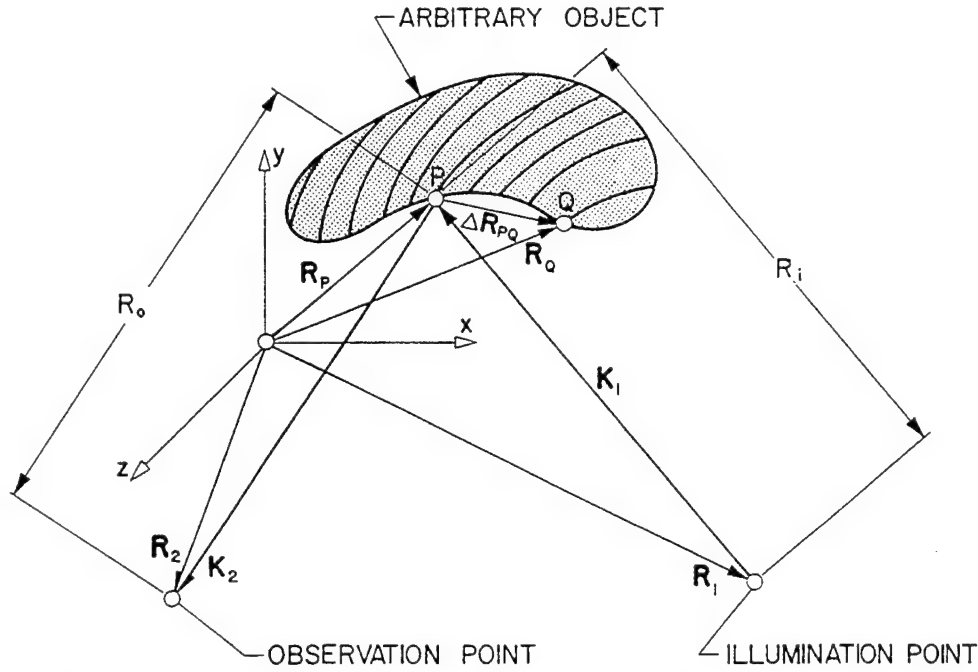


Fig. 6.3. Illumination and observation geometry for interpretation of holograms using the fringe-vector theory.

The second term on the right side of Eq. 6.1 represents a scalar product of the differential position vector,

$$\Delta\mathbf{R}_{PQ} = \Delta x_{PQ} \hat{i} + \Delta y_{PQ} \hat{j} + \Delta z_{PQ} \hat{k}, \quad (6.2)$$

with the fringe vector, which is defined as the gradient of Ω , that is,

$$\begin{aligned} \mathbf{K}_f &= K_{fx} \hat{i} + K_{fy} \hat{j} + K_{fz} \hat{k} \\ &= \Omega^{xP} \hat{i} + \Omega^{yP} \hat{j} + \Omega^{zP} \hat{k} = \frac{\partial \Omega}{\partial x_P} \hat{i} + \frac{\partial \Omega}{\partial y_P} \hat{j} + \frac{\partial \Omega}{\partial z_P} \hat{k} \\ &= \nabla_R \Omega = \nabla_R (\mathbf{K} \cdot \mathbf{L}) = (\nabla_R \otimes \mathbf{L}) \mathbf{K} + (\nabla_R \otimes \mathbf{K}) \mathbf{L}, \end{aligned} \quad (6.3)$$

where ∇_R is the gradient operator in the real space,

$$\nabla_R = \hat{i} \frac{\partial}{\partial x_P} + \hat{j} \frac{\partial}{\partial y_P} + \hat{k} \frac{\partial}{\partial z_P} \quad , \quad (6.4)$$

and where \otimes denotes the matric product which was defined in Chapter 3.

It should be noted that Eq. 6.3 takes into account the first order (i. e., linear) variations in Ω . The second order variations in Ω are accounted for by the last term on the right side of Eq. 6.1, where the *fringe-tensor*, \tilde{T}_f , represents the linear variations in \mathbf{K}_f . Therefore, expansion of the first two terms on the right side of Eq. 6.1 leads to formulations allowing holographic numerical analysis of rigid-body motions and homogeneous deformations, while all three terms let us interpret inhomogeneous strains.

6.2. Rigid-body rotations and homogeneous strains

The second term on the right side of Eq. 6.1 describes a change in Ω between points P and Q . On the surface of the object, where fringes are visible, Ω is defined as

$$\begin{aligned} \Omega &= \mathbf{K} \cdot \mathbf{L} = (K_x \hat{i} + K_y \hat{j} + K_z \hat{k}) \cdot (L_x \hat{i} + L_y \hat{j} + L_z \hat{k}) \\ &= K_x L_x + K_y L_y + K_z L_z \quad . \end{aligned} \quad (6.5)$$

Differentiating Eq. 6.5, as required by Eq. 6.3, we obtain 18 terms which can be described as a sum of the products of two vectors and two matrices, that is,

$$\mathbf{K}_f = \mathbf{K} \tilde{f} + \mathbf{L} \tilde{g} \quad , \quad (6.6)$$

where

$$\tilde{g} = \tilde{g}_2 - \tilde{g}_1 = \frac{k}{R_o} (\tilde{I} - \hat{K}_2 \otimes \hat{K}_2) - \frac{k}{R_i} (\hat{I} - \hat{K}_1 \otimes \hat{K}_1) = \frac{k}{R_o} \tilde{P}_{K_2} - \frac{k}{R_i} \tilde{P}_{K_1} \quad . \quad (6.7)$$

In Eq. 6.7, R_o and R_i are radii of curvature of the illumination and observation perspectives, respectively, Fig. 6.3, while \tilde{P}_{K_1} and \tilde{P}_{K_2} represent the projection matrices based on the unit vectors defining average illumination and observation directions, respectively.

What is of interest in Eq. 6.6 is the transformation matrix \tilde{f} , which can be decomposed into a matrix of strains and shears, $\tilde{\epsilon}$, and a matrix of rotations, $\tilde{\theta}$, that is,

$$\tilde{f} = \tilde{\epsilon} + \tilde{\theta} \quad . \quad (6.8)$$

In order to solve Eq. 6.7, for the transformation matrix \tilde{f} , multiple observations of the holographically produced image must be made. For each observation, the sensitivity vector \mathbf{K} and the fringe vector \mathbf{K}_f must be determined that best fit data for the entire region examined. Also, multiple views are used to obtain displacement \mathbf{L} at a point of interest on the object. For each view, the matrix \tilde{g} is computed and multiplied by \mathbf{L} to obtain perspective correction to \mathbf{K}_f . From multiple views, a set of equations of the type of Eq. 6.7, with the matrix \tilde{f} common to all, is generated and solved to obtain

$$\tilde{f} = [\tilde{K}^T \tilde{K}]^{-1} [\tilde{K}^T \tilde{K}_{fc}] \quad , \quad (6.9)$$

where

$$\tilde{K}_{fc} = \tilde{K}_f - \mathbf{L} \tilde{g} \quad , \quad (6.10)$$

is the matrix formed by the fringe-vectors corrected for perspective. Decomposition of the matrix \tilde{f} , computed from Eq. 6.9, into a symmetric part $\tilde{\epsilon}$ and the antisymmetric part $\tilde{\theta}$, that is,

$$\tilde{\epsilon} = \frac{1}{2} [\tilde{f} + \tilde{f}^T] \quad , \quad (6.11)$$

and

$$\tilde{\theta} = \frac{1}{2} [\tilde{f} - \tilde{f}^T] \quad , \quad (6.12)$$

gives strains and shears, and rotations, respectively.

When the object deformations are not homogeneous over the entire body under study, they may, nonetheless, be approximately so over a small region of its surface, and projection matrices are very helpful in formulating the solution to this problem. It can be shown that, in this case, the surface strain-rotation matrix \tilde{f} is

$$\tilde{f}_s = \tilde{f} \tilde{P}_n \quad , \quad (6.13)$$

where \tilde{P}_n is the projection matrix defined as

$$\tilde{P}_n = \tilde{I} - \hat{n} \otimes \hat{n} \quad , \quad (6.14)$$

with \hat{n} being the local surface normal.

It should be noticed that derivatives of the observed displacement are not generally equal to surface strains and rotations of the object. They become approximately equal to the extent that the viewing direction can be made parallel to the surface normal.

6.3. References

- 6.1. A. E. Ennos, "Measurement of in-plane strain by hologram interferometry," *J. Phys. E (Sci. Instr.)*, 1:731-746, 1968.
 - 6.2. A. E. Ennos, "Strain measurement," in *Holographic nondestructive testing*, R. K. Erf, ed., Academic Press, New York, pp. 275-287, 1974.
 - 6.3. R. Dändliker, B. Ineichen, and F. M. Mottier, "High resolution hologram interferometry by electronic phase measurement," *Opt. Commun.*, 9:412-416, 1973.
 - 6.4. R. Dändliker and B. Ineichen, "Strain measurement through hologram interferometry," *Proc. SPIE*, 99:90-98, 1976.
 - 6.5. W. Schumann and M. Dubas, "On direct measurement of strain in holographic interferometry using the line of complete localization," *Optica Acta*, 22:807, 1975.
 - 6.6. W. Schumann, J. P. Zürcher, and D. Cuche, *Holography and deformation analysis*, Springer-Verlag, Berlin, 1985.
 - 6.7. K. A. Stetson, "Homogeneous deformations: determination by fringe vectors in hologram interferometry," *Appl. Opt.*, 14:2256-2259, 1975.
 - 6.8. R. J. Pryputniewicz and K. A. Stetson, "Holographic strain analysis: extension of fringe vector method to include perspective," *Appl. Opt.*, 15:725-728, 1976.
 - 6.9. R. J. Pryputniewicz, "Holographic strain analysis: an experimental implementation of the fringe-vector theory," *Appl. Opt.*, 17:3613-3618, 1978.
-

7. INTERPRETATION OF TIME-AVERAGE HOLOGRAMS

7.1. Introduction

Transverse vibrations of beams are of primary interest in many engineering applications. However, the conventional methods, both analytical and experimental, are rather limited when it comes to vibration analysis. In general, the analytical methods, including the finite element methods (FEM), require accurate knowledge of boundary conditions and material properties. The experimental techniques, on the other hand, are in general invasive and frequently take into consideration only a few points, on the studied structure. The results obtained from analysis of these limited experimental data are then "extrapolated" to predict the dynamic behavior of the entire structure. Also, as the vibration frequency increases, the corresponding displacement amplitude decreases making it difficult to measure with conventional instrumentation. In 1965, however, the method of hologram interferometry was developed¹ which provided means of measuring vibrations of very small amplitudes.

In hologram interferometry of vibrating objects, two (or more) waves, correlated in frequency and phase (e. g., emitted from a single laser), interact with each other because of the differences in their path lengths. The most popular technique for recording of holograms is the off-axis method². In this arrangement, Fig. 7.1, the highly coherent and monochromatic laser light is divided into two beams by means of a beamsplitter. One of the beams, in the case shown that transmitted through the beamsplitter, is expanded and filtered (by means of a microscope objective and a pin-hole assembly) and is directed (by mirrors) to illuminate the object to be recorded. This beam, modulated by reflection from the scene being recorded, is called the object beam. It carries instantaneous information about the configuration of the object. The other beam, i. e., that reflected from the beamsplitter, is also expanded and spatially filtered, but it is directed by mirror(s) in such a way that it does not interfere with the object. This is the reference beam. The reference beam is also directed to overlap with the object beam. The two beams interfere in the regions of space where they overlap. A photosensitive medium placed in this region records the resulting interference pattern. The developed medium, when reilluminated with the original reference beam, faithfully reconstructs the image of the recorded object.

In practice, multiple object configurations are recorded in the same medium. Therefore, during reconstruction of such holograms multiple images are produced, i. e., one image for each recorded object configuration. Since each of these images is reconstructed in coherent light, they interfere with each other in any region of space where they superpose. As a result of this, the reconstructed image of the object is seen covered by a set of bright and dark interference fringes. These fringes are a direct measure of changes in the object's position and/or shape that occurred while the hologram was being recorded, as discussed in Chapters 4 to 6.

Depending on the particular application, the interference fringes may be recorded using one of the following techniques³: (i) double-exposure hologram interferometry, (ii) real-time hologram interferometry, (iii) time-average hologram interferometry; the time-average technique can be further subdivided into (i) stroboscopic time-average hologram interferometry and (ii)

continuous time-average hologram interferometry. Each of the above techniques has certain advantages over the others in specific vibration measurement applications.

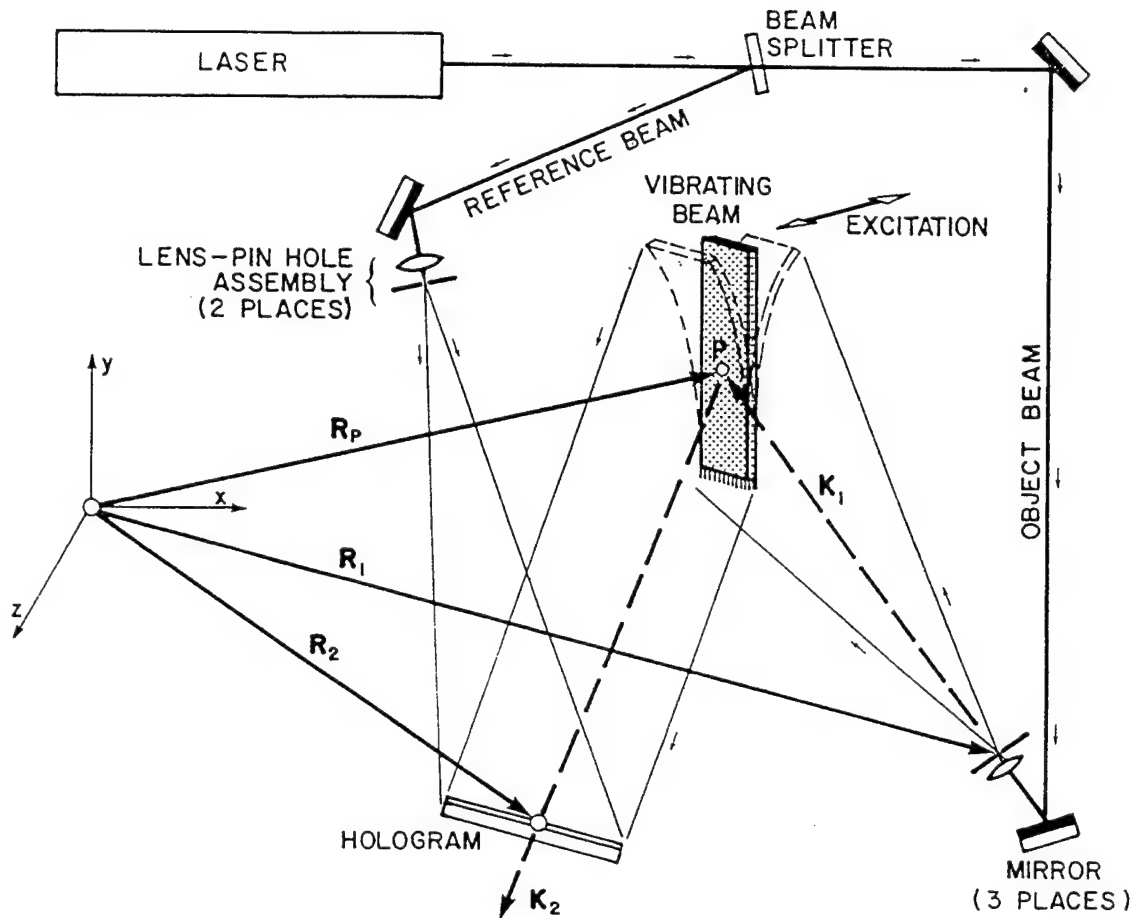


Fig. 7.1. Schematic representation of a setup for recording and reconstruction of continuous time-average holograms. K_1 is the vector giving direction of illumination (during recording of a hologram), from point source defined by position vector R_1 to a point P on the object specified by R_P . The observation vector K_2 is propagating from P to a point on hologram at R_2 , through which the reconstructed image is viewed.

The *double-exposure method* is uniquely suited for studies of transient vibrations; it can be used equally well in studies of resonating objects. However, it depends on the use of a pulsed laser which delivers two submicrosecond pulses synchronized with motion of the object. During reconstruction of a double-exposure hologram, the image of the object is modulated by cosinusoidal fringes. Although interpretation of such fringes is straightforward, cost of the pulsed laser system is rather high.

The *real-time method* requires the use of a liquid gate plate holder, or some mechanical micropositioner, to precisely locate/relocate a developed hologram. The image reconstructed

from this hologram, when superposed onto the original object, interferes with the light field modulated by vibrating object, at the instant the object moves. This method is particularly useful in identification of object resonances.

The *stroboscopic time-average method* is really an extension of the double-exposure method, except that now a continuous wave (CW) laser can be used to record a hologram. In this application, the CW laser beam is "chopped" into short pulses synchronized with the object frequency; the pulse length depends on the nature of the vibration studied. To effectively use this method, object vibration must be monitored continuously to assure proper characteristics of the illuminating beam. This synchronization must be maintained over many vibration cycles, to provide for sufficient exposure of the recording medium. Although interference fringes produced during reconstruction of a stroboscopic hologram are cosinusoidal and are straight-forward to analyze, the electronic apparatus, needed to produce good quality images, may be complex and expensive.

In *continuous time-average method*, a single holographic recording of an object, undergoing a cyclic vibration, is made. With the (continuous) exposure time long in comparison to one period of the vibration cycle, the hologram effectively records an ensemble of images corresponding to the time-average of all positions of the object while it is vibrating. During reconstruction of such a hologram, the interference occurs between the entire ensemble of images with those recorded near zero velocity (i. e., maximum displacement) contributing most strongly to the reconstruction. The interference fringes observed are of unequal brightness. In fact, they vary according to the square of the zero order Bessel function of the first kind, J_0^2 , as shown in Fig. 7.2 and as will be demonstrated mathematically in this chapter.

The continuous time-average method is the most popular of the holographic methods discussed herein, when it comes to vibration analysis. The existing holographic laboratories are, in general, well equipped to perform continuous time-average studies. The apparatus is the same as that used in recording of conventional holograms, except for the mechanism to "drive" the object. The driving mechanism can be a piezoelectric shaker, a loud speaker, a magnetic oscillator, a flowing fluid, etc. However, regardless of the method used to excite the object, the (continuously) time-averaged interference fringes are the same in nature. In the following sections, the discussion will center on quantitative interpretation of the (continuous) time-average holograms.

7.2. Mathematical considerations

The time-average holograms can be recorded using a setup similar to that shown in Fig. 7.1. The time varying displacement vector, $\mathbf{L}_t(x, y, z, t)$, of a vibrating object is a function of spatial Cartesian coordinates x , y , and z , and also a function of time t . For cosinusoidal excitation, this time varying displacement vector can be expressed as³⁻⁵

$$\mathbf{L}_t(x, y, z, t) = \mathbf{L}_t(x, y, z) \cos(\omega t) \quad . \quad (7.1)$$

In Eq. 7.1, L_o is the magnitude of the displacement of the object which is vibrating at a circular frequency ω . This object motion causes temporal changes, $\Omega_t(x, y, z, t)$, in phase of the light field modulated by interaction with the vibrating object. These phase changes can be represented by the scalar product of $\mathbf{L}_t(x, y, z, t)$ with the sensitivity vector $\mathbf{K}(x, y, z)$, that is,

$$\Omega_t(x, y, z, t) = \mathbf{K}(x, y, z) \cdot \mathbf{L}_t(x, y, z, t) \quad , \quad (7.2)$$

where \mathbf{K} is as defined in Chapter 2. Therefore, the complex light field, $\mathbf{F}_v(x, y, z, t)$, propagating away from the vibrating object, can be represented as

$$\mathbf{F}_v(x, y, z, t) = A_o(x, y, z) \exp[i\phi(x, y, z) + i\Omega_o(x, y, z, t)] \quad . \quad (7.3)$$

Holograms of vibrating objects are recorded by interfering the time varying field defined by Eq. 7.3 with the temporally invariant reference field. As a result of this interference, the complex light field, $\mathbf{F}_h(x, y, z, t)$, in the plane of the hologram, or some recording medium, is

$$\begin{aligned} \mathbf{F}_h(x, y, z, t) = & A_o(x, y, z) \exp[i\phi_o(x, y, z) + i\Omega_t(x, y, z, t)] \\ & + A_r(x, y, z) \exp[i\phi_r(x, y, z)] \quad , \end{aligned} \quad (7.4)$$

where A_o and ϕ_o are the amplitude and phase, respectively, of the (object) illuminating light field propagating in the space defined by the x , y , and z coordinates, Ω_t is the fringe-locus function which represents temporal changes in phase of the light reflected from the object, and A_r and ϕ_r are the amplitude and phase, respectively, of the reference beam.

The medium, in which a hologram is recorded, responds to intensity $I_h(x, y, z, t)$ of the field given by Eq. 7.4. The value of this time-varying intensity is expressed as the product of $\mathbf{F}_h(x, y, z, t)$ and its conjugate $\mathbf{F}_h^*(x, y, z, t)$, that is,

$$\begin{aligned} I_h = \mathbf{F}_h \mathbf{F}_h^* &= [A_o \exp(i\phi_o + i\Omega_t) + A_r \exp(i\phi_r)] [A_o \exp(-i\phi_o - i\Omega_t) + A_r \exp(-i\phi_r)] \\ &= A_o^2 + A_r^2 + \mathbf{F}_r \mathbf{F}_v^* + \mathbf{F}_r^* \mathbf{F}_v \quad , \end{aligned} \quad (7.5)$$

where the arguments (x, y, z) and (x, y, z, t) were omitted for simplification.

The image recorded within the photosensitive medium is the time-average of I_h over the exposure time T , thus

$$\frac{1}{T} \int_0^T I_h dt = A_o^2 + A_r^2 + \frac{1}{T} \mathbf{F}_r \int_0^T \mathbf{F}_v^* dt + \frac{1}{T} \mathbf{F}_r^* \int_0^T \mathbf{F}_v dt \quad . \quad (7.6)$$

When the time-average hologram is developed and illuminated by the original reference field \mathbf{F}_r , we obtain

$$\mathbf{F}_r \frac{1}{T} \int_0^T I_h dt = A_o^2 \mathbf{F}_r + A_r^2 \mathbf{F}_r + A_r^2 \exp(2i\phi_r) \frac{1}{T} \int_0^T \mathbf{F}_v^* dt + A_r^2 \frac{1}{T} \int_0^T \mathbf{F}_v dt \quad (7.7)$$

The first two terms on the right hand side of Eq. 7.7 represent an attenuated undiffracted reconstruction field, the third term gives rise to the conjugate image, while the fourth term is proportional to the time-average of the original object field and describes formation of the virtual image. Therefore, the developed hologram, when illuminated by \mathbf{F}_r , produces an object wave which has a complex amplitude proportional to the time-average of \mathbf{F}_v over the time interval T , that is,

$$\begin{aligned} \frac{1}{T} \int_0^T \mathbf{F}_v dt &= \frac{1}{T} \int_0^T A_o(x, y, z) \exp[i\phi(x, y, z) + i\Omega_t(x, y, z, t)] dt \\ &= \mathbf{F}_o(x, y, z) \frac{1}{T} \int_0^T \exp[i\Omega_t(x, y, z, t)] dt \quad (7.8) \end{aligned}$$

The time-average integral appearing in Eq. 7.8 is called the characteristic function⁶ and is denoted by \mathbf{M}_T , that is,

$$\frac{1}{T} \int_0^T \exp[i\Omega_t(x, y, z, t)] dt = \mathbf{M}_T(x, y, z) \quad (7.9)$$

The time-average integral of Eq. 7.9 may be evaluated as $J_o(|\Omega_t|)$, the zero-order Bessel function of the first kind of the magnitude of the argument Ω_t . Based on Eq. 7.2, the magnitude of Ω_t is

$$\begin{aligned} |\Omega_t| &= |\mathbf{K} \cdot \mathbf{L}_t| = |(\mathbf{K}_2 - \mathbf{K}_1) \cdot \mathbf{L}_t| \\ &= |k[(K_{2x} - K_{1x})L_{tx} + (K_{2y} - K_{1y})L_{ty} + (K_{2z} - K_{1z})L_{tz}]| \quad (7.10) \end{aligned}$$

where the arguments (x, y, z) and (x, y, z, t) were omitted for simplification, $K_{1x}, K_{2x}, K_{1y}, \dots$, are the components of the unit illumination and observation vectors defining average directions of \mathbf{K}_1 and \mathbf{K}_2 , respectively, while L_{tx}, L_{ty} , and L_{tz} represent the Cartesian components of \mathbf{L}_t .

Thus, according to Eqs 7.8 and 7.9, the reconstructed complex amplitude responsible for formation of the virtual image is proportional to $\mathbf{F}_o \cdot \mathbf{M}_T$, while the corresponding intensity $I_{im}(x, y, z)$, of the reconstructed image, is

$$I_{im} = \mathbf{F}_o^2 \mathbf{M}_T^2 = A_o^2 J_o^2(|\Omega_t|) \quad (7.11)$$

Equation 7.11 shows that the virtual image obtained during reconstruction of the time-average hologram is modulated by a system of fringes described by the square of the zero-order Bessel function of the first kind. Thus, for nontrivial values of A_o , centers of the dark fringes will be located at those points on the surface of the object where $J_o(|\Omega_t|)$ equals zero, Fig. 7.2.

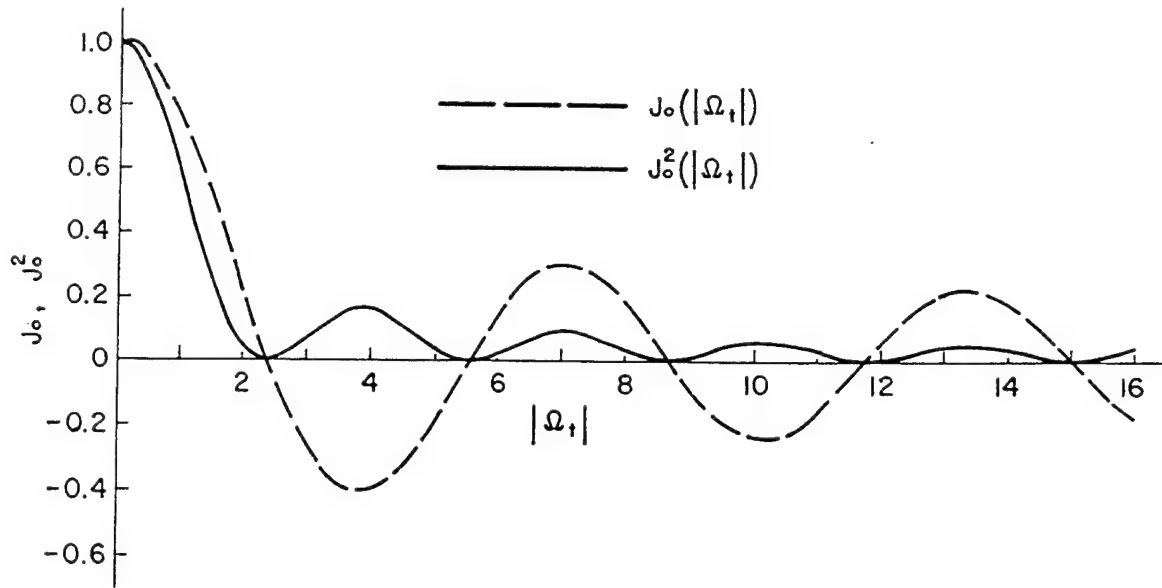


Fig. 7.2. The zero order Bessel function of the first kind and its square, defining location of centers of dark fringes seen during reconstruction of continuous time-average holograms of vibrating objects.

The images formed during reconstruction of the time-average holograms of objects undergoing periodic motions are modulated according to the variations of J_0 . The J_0 fringes differ from cosinusoidal fringes obtained in conventional double-exposure hologram interferometry, see Fig. 4.1. One of these differences is that the zero-order J_0 fringe is much brighter than the higher order J_0 fringes, while all cosinusoidal fringes, regardless of their order, show equal brightness, Fig. 7.3. Furthermore, the zero-order fringes represent the stationary points on the vibrating object and thus allow easy identification of nodes. The brightness of the higher order J_0 fringes decreases with increasing fringe order and can be directly related to the mode shapes.

Application of the foregoing analysis, to quantitative interpretation of transverse vibrations of a cantilever beam, is discussed in Sections 7.3 to 7.5.

7.3. Quantitative interpretation of time-average holograms of a cantilever beam

Following is a representative example of a cantilever beam that was fixed at the lower end while its upper end was free. The cosinusoidal excitation was applied at the free end, by means of a loud speaker. The excitation was always set in such a way that the motion of the beam was in the direction parallel to the z -axis, Fig. 7.1. For this case, Eq. 7.1 can be written as

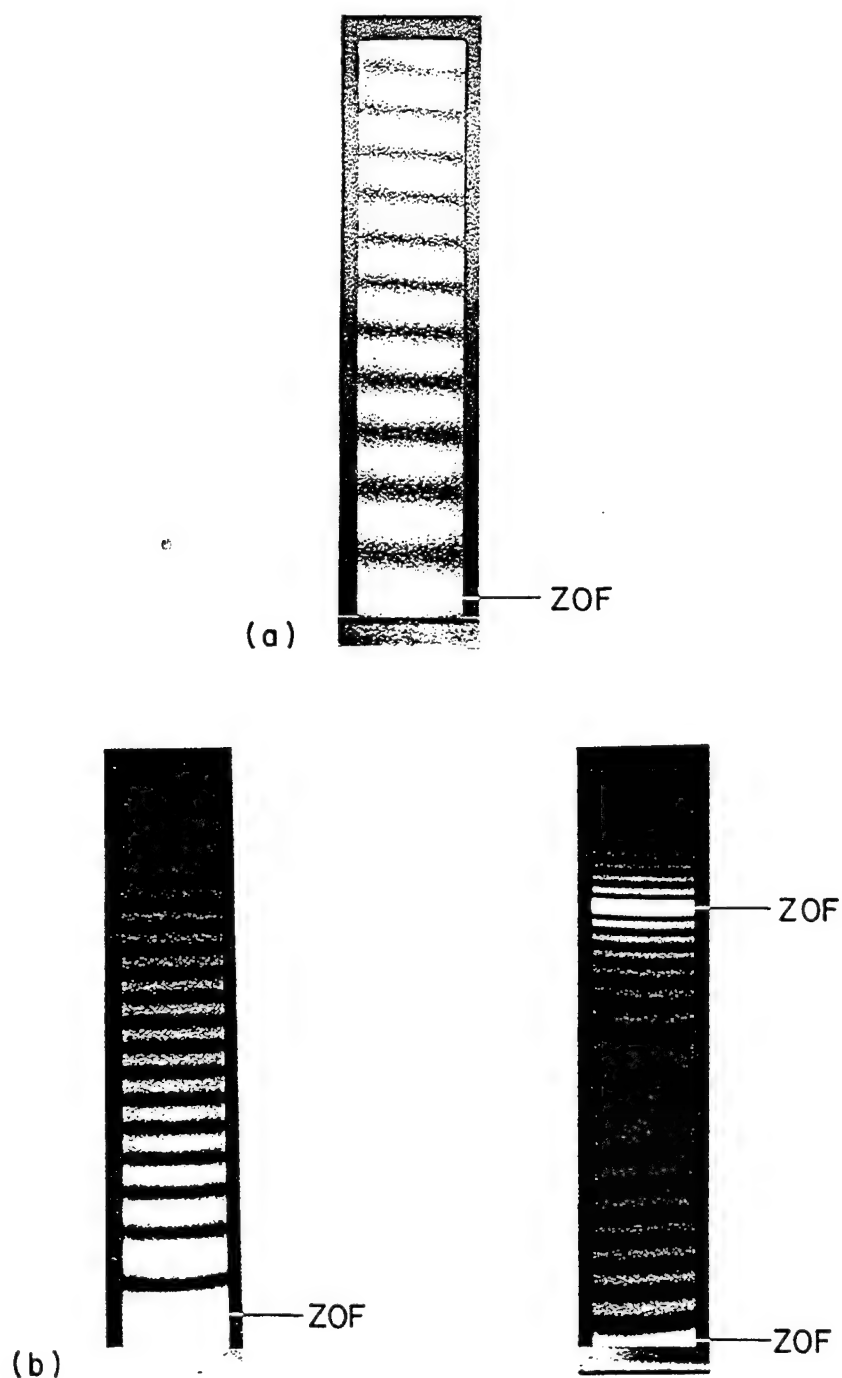


Fig. 7.3. Fringes obtained during reconstruction of: (a) conventional double-exposure hologram, showing cosinusoidal intensity variation (note, the zero-order-fringe (ZOF) is as bright as other fringes), (b) continuous time-average holograms, showing J_0^2 intensity variation (note that the ZOF's are much brighter than the higher order fringes).

$$L_t(0, 0, z, t) = L_t(0, 0, z) \cos(\omega t) \quad , \quad (7.12)$$

while Eq. 7.10 yields

$$|\Omega_t| = k(K_{2z} - K_{1z})L_{tz} \quad , \quad (7.13)$$

where k is given by Eq. 2.6, K_{1z} and K_{2z} can be computed from Eqs 2.4 and 2.5 as

$$K_{1z} = \frac{z_P - z_1}{\left[(x_P - x_1)^2 + (y_P - y_1)^2 + (z_P - z_1)^2 \right]^{1/2}} \quad , \quad (7.14)$$

and

$$K_{2z} = \frac{z_2 - z_P}{\left[(x_2 - x_P)^2 + (y_2 - y_P)^2 + (z_2 - z_P)^2 \right]^{1/2}} \quad , \quad (7.15)$$

respectively, and L_{tz} is the vibration amplitude.

The goal of the analysis is to determine L_{tz} which gives the mode shape. However, before this can be done, Eqs 7.14 and 7.15 have to be evaluated, at every point of interest on the vibrating object.

For the case of retro-reflective illumination and observation, parallel to the z -axis, the quantity $(K_{2z} - K_{1z})$ has the maximum value of 2, as determined from Eqs 7.14 and 7.15. Thus, combination of Eqs 2.6 and 7.13, yields

$$L_{tz} = \frac{\lambda}{4\pi} |\Omega_t| \quad . \quad (7.16)$$

The values of L_{tz} , for various orders of the J_0 fringes and $\lambda = 0.6328 \mu\text{m}$, as computed from Eq. 7.16, are shown in Table 7.1.

For any other geometry, where the directions of illumination and observation are not parallel to the z -axis, the quantity $(K_{2z} - K_{1z})$ will always be less than 2. Its actual magnitude will depend on the magnitudes of angles γ_1 and γ_2 that the directions of \mathbf{K}_1 and \mathbf{K}_2 , respectively, make with the direction of \mathbf{L} , as shown in Fig. 7.4. That is, for every case when directions of illumination and observation deviate from being parallel to the direction of motion, the L_{tz} computed from Eq. 7.13 will always be greater than that given by Eq. 7.16, for the same order of the J_0 fringe. The percentage error, PE , between the value of L_{tz} , for the non retro-reflective case, and the value of $L_{t_{zrr}}$, for the retro-reflective case, can be defined as

$$PE = \left(\frac{L_{tz} - L_{t_{zrr}}}{L_{t_{zrr}}} \right) \times 100\% \quad . \quad (7.17)$$

Table 7.1. Zeros of J_0 and values of the corresponding $L_{t_{zrr}}$. (The values of $L_{t_{zrr}}$ were determined for the case of retroreflective illumination and observation and for $\lambda = 0.6328 \mu\text{m}$.)

n	$ \Omega_t $	$L_{t_{zrr}}$ (μm)
1	2.40438	0.121
2	5.52008	0.278
3	8.65373	0.438
4	11.79153	0.594
5	14.93092	0.752
6	18.07106	0.910
7	21.21264	1.068
8	24.35247	1.226
9	27.49348	1.385
10	30.63461	1.543
11	33.77582	1.701
12	36.91710	1.859
13	40.05843	2.017
14	43.19979	2.175
15	46.34119	2.334
16	49.48261	2.492
17	52.62405	2.650
18	55.76551	2.808
19	58.90698	2.966
20	62.04847	3.125
21	65.18996	3.283
22	68.33147	3.441
23	71.47298	3.599
24	71.61450	3.757
25	77.75603	3.916
26	80.89756	4.074
27	84.03909	4.232
28	87.18063	4.390
29	90.32217	4.548
30	93.46372	4.707

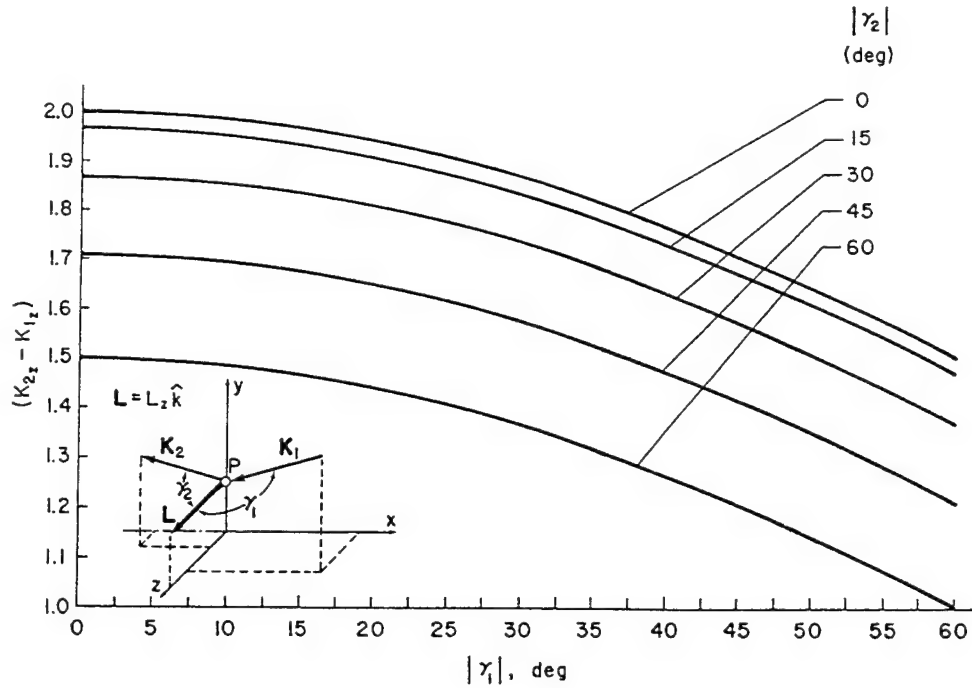


Fig. 7.4. Values of $(K_{2z} - K_{1z})$ as a function of γ_1 and γ_2 .

Equation 7.17 was evaluated for various values of $(K_{2z} - K_{1z})$ and the results are shown in Fig. 7.5. This figure indicates that Eq. 7.16 will yield L_z to within 5% of the value actually experienced by the object as long as $(K_{2z} - K_{1z}) > 1.9$. This result, in turn, allows to determine, from Fig. 7.4, that when $|\gamma_2| = 0^\circ$, $|\gamma_1|$ should be less than or equal to 26° , while for $|\gamma_2| = 15^\circ$, $|\gamma_1| \leq 21^\circ$. By reciprocity, the following pairs of angles will be true: $|\gamma_1| = 0^\circ$, $|\gamma_2| \leq 26^\circ$ and $|\gamma_1| = 15^\circ$, $|\gamma_2| \leq 26^\circ$. Figure 7.4 also indicates that experimental setups with $|\gamma_1| > 26^\circ$ (or, by reciprocity, with $|\gamma_2| > 26^\circ$) will always yield $(K_{2z} - K_{1z}) < 1.9$, which will result in errors (as defined by Eq. 7.17) in excess of 5%.

One way to compensate for the errors resulting from the setup geometry is to use the following formula

$$L_{tz} = \left(1 + \frac{PE}{100}\right) L_{t_{zrr}} \quad , \quad (7.18)$$

where $L_{t_{zrr}}$ is the displacement corresponding to the order of the J_o fringe crossing the point of interest on the particular object, as given in Table 7.1, while PE is determined from Figs 7.4 and 7.5. Therefore, L_{tz} obtained from Eq. 7.18 is the displacement at a given point on the object, compensated for geometry of the system used to record and reconstruct the hologram.

Another way to achieve the same result is to use Eqs 7.13 to 7.15 directly, as discussed in Section 7.5.

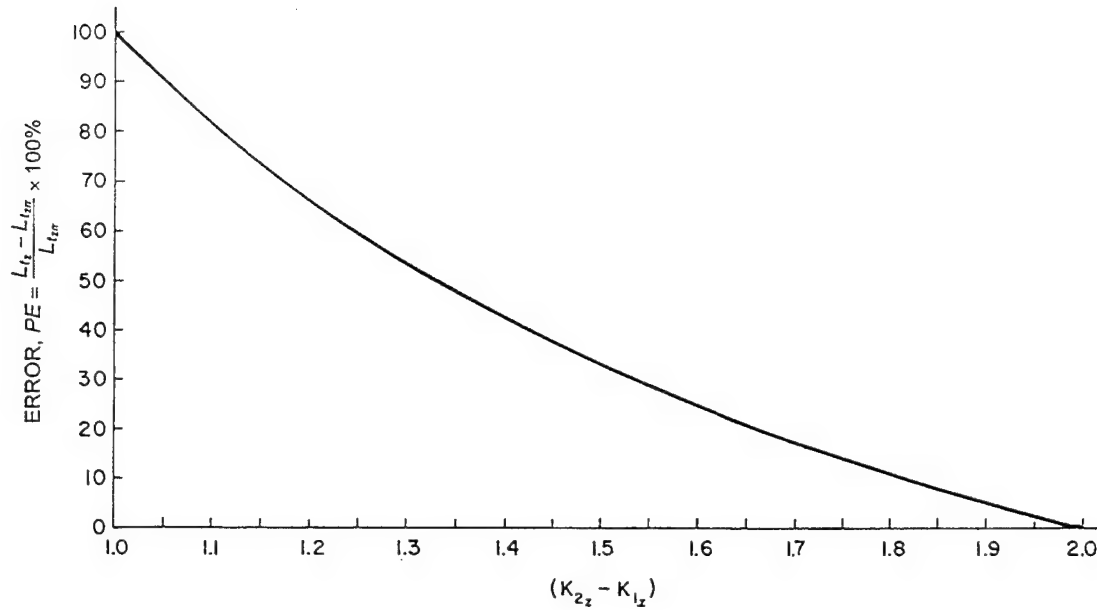


Fig. 7.5. Percentage error in L_{tz} , with respect to L_{ttr} , as a function of $(K_{2z} - K_{1z})$.

7.4. Experimental setup

The cantilever beam used in this example was rigidly fixed at the bottom and free at the top. Its free length was 160 mm (6.3 in), it was 28.58 mm (1.125 in) wide and 3.18 mm (0.125 in) thick. The cantilever beam, made of 6061-T6 aluminum, was excited acoustically at its free end. The origin of the right-handed rectangular Cartesian coordinate system was located at the fixed end of the cantilever beam with the positive z -axis pointing toward the hologram. In this coordinate system, the position vectors \mathbf{R}_1 and \mathbf{R}_2 defining point source of illumination and point of observation, respectively, were determined to be

$$\mathbf{R}_1 = 216\hat{i} + 23\hat{j} + 1321\hat{k} \quad (7.19)$$

and

$$\mathbf{R}_2 = -13\hat{i} + 38\hat{j} + 806\hat{k} \quad , \quad (7.20)$$

where coefficients are distances in millimeters. The experimental setup, shown schematically in Fig. 7.1, was used to record time-average holograms of the vibrating cantilever beam. These holograms were analyzed and the results are discussed in Section 7.5.

7.5. Experimental results

The excitation frequency was varied until the cantilever beam resonance was achieved. These experimentally obtained resonance frequencies compared very well with the frequencies computed using the beam theory, Fig. 7.6.

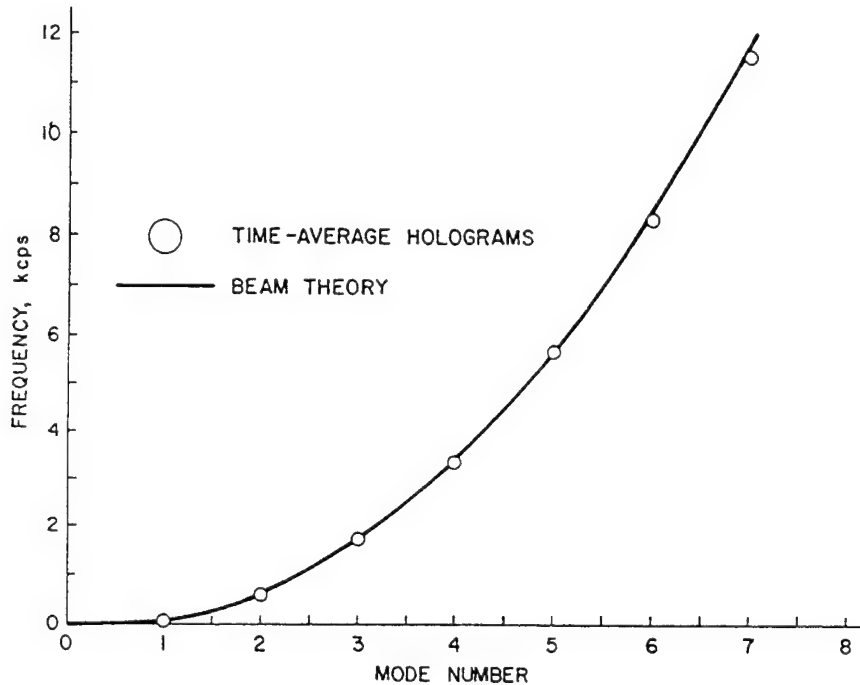


Fig. 7.6. Resonance frequency of a vibrating cantilever beam as a function of mode number: comparison between the experimental results obtained from the time-average holograms and those based on the beam theory.

Representative time-average holograms were recorded at the first three resonance frequencies with the corresponding results shown in Figs 7.7 to 7.9, respectively. For example, for the first flexure mode, Fig. 7.7, the center of the fifth dark fringe was located 67 mm above the fixed end. That is, for this point on the object,

$$R_P = 67j \quad , \quad (7.21)$$

Substitution of Eqs 7.19 to 7.21 into Eqs 7.14 and 7.15 yielded

$$K_{1z} = -0.9864 \quad (7.22)$$

and

$$K_{2z} = 0.9992 \quad , \quad (7.23)$$

respectively.

Subsequent substitution of Eqs 2.6, 7.22, and 7.23 into Eq. 7.13, together with the values of $\lambda = 0.6328 \mu\text{m}$ (wavelength of the He-Ne laser used to record and reconstruct the time-average holograms, in this study) and $|\Omega_t| = 14.93092$ (corresponding to the fifth J_0 fringe, Table 7.1) gave the following result:

$$L_{tz} = \frac{\lambda}{2\pi(K_{2z} - K_{1z})} |\Omega_t| = 0.757 \mu\text{m} \quad (7.24)$$

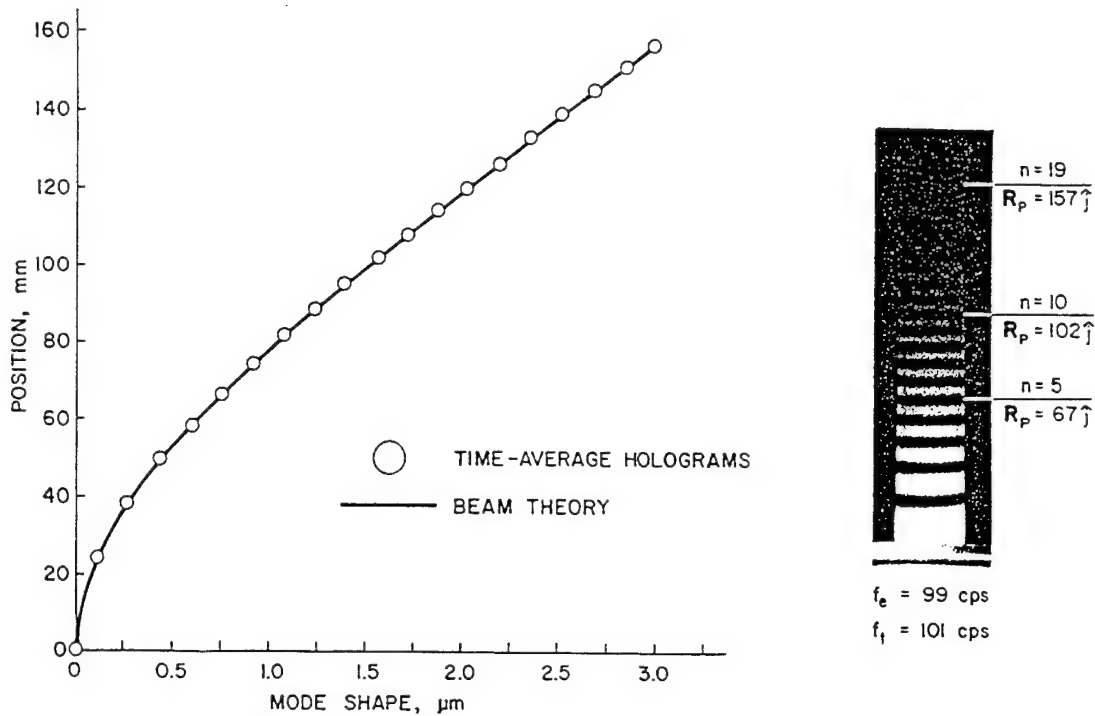


Fig. 7.7. Shape of the first flexure mode of a vibrating cantilever beam: comparison between the experimental results obtained from the time-average hologram and those based on the beam theory.

Equation 7.24 indicates that the L_{tz} corrected for setup geometry is only 0.7% greater than that for the retro-reflective illumination and observation case. For the center of the 10th dark fringe, located 102 mm above the fixed end of the cantilever beam, we obtain $L_{tz} = 1.557 \mu\text{m}$ which is 0.9% greater than the value given in Table 7.1. Finally, the center of the 19th dark fringe, at 157 mm, corresponds to the displacement of $3.010 \mu\text{m}$ which is 1.5% larger than the displacement for the retro-reflective illumination and observation for $n=19$, as given in Table 7.1.

In a similar manner, displacements at other points on the cantilever beam were determined, Fig. 7.7. For comparison, the mode shape of the cantilever beam vibrating at its first flexure

frequency was determined analytically using the beam theory. The agreement between the theory and experiments is very good.

Following the procedure described above, mode shapes for the second and the third flexure frequencies were determined, Figs 7.8 and 7.9, respectively. Again, the agreement between the theoretical and the experimental results, obtained from the time-average holograms, is very good.

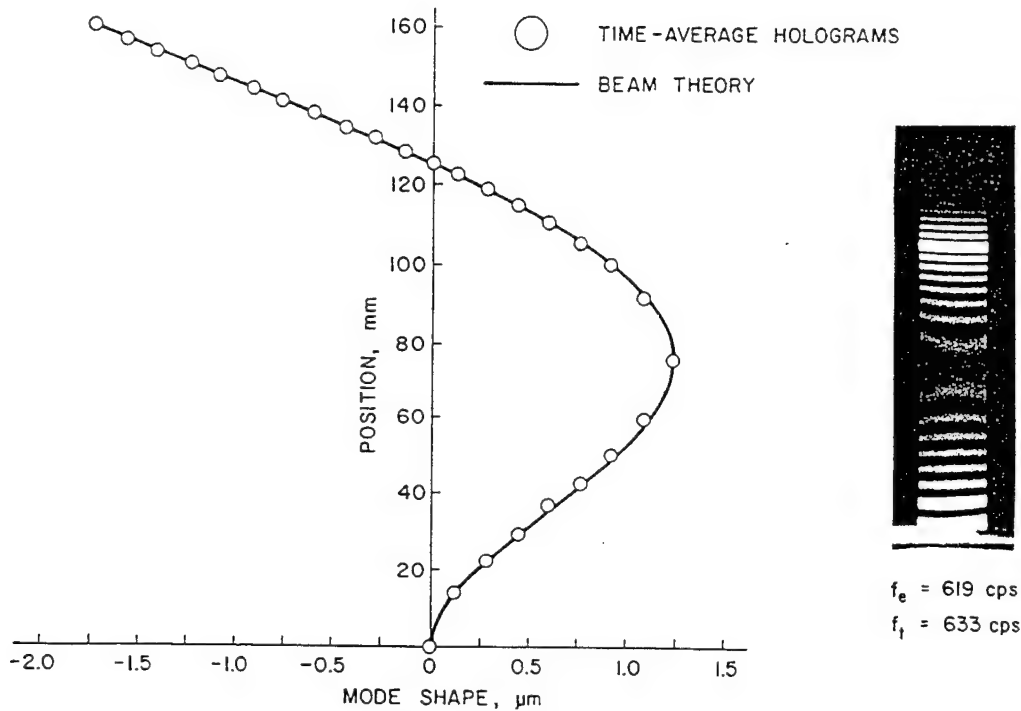


Fig. 7.8. Shape of the second flexure mode of a vibrating cantilever beam: comparison between the experimental results obtained from the time-average hologram and those based on the beam theory.

7.6. Conclusions

The results presented in this chapter indicate that images obtained during reconstruction of the time-average holograms are modulated by a system of fringes described by the square of the zero-order Bessel function of the first kind. These images can be readily interpreted to obtain quantitative information on resonance frequencies and corresponding mode shapes of vibrating objects. The representative examples show very good agreement between the experimental results obtained from time-average holograms and the analytical results based on the beam theory. It should be remembered, that these results were determined for a cantilever beam of

constant cross section for which an exact solution of the differential equation can be obtained. However, for beams of varying cross section, as well as for objects of complex geometry or with complicated boundary conditions, exact analytical solutions may be unobtainable. The experimental procedures of time-average holography, on the other hand, are independent of object geometry or its boundary conditions. As such, once a hologram of a vibrating object has been recorded, it can be interpreted to obtain quantitative results following the procedure described in this chapter. Furthermore, the experimental results obtained from time-average holograms can be used to define boundary conditions needed to "run" the analytical or computational methods, e. g., finite element computer codes. This combination of the time-average holography (or other optical methods) with the finite element method will lead to the development, of new design methodologies. Such hybrid methodologies, possessing both experimental and analytical capabilities, will be the next generation of tools that engineers will use to create new designs for the future (see, e. g., Chapter 10).

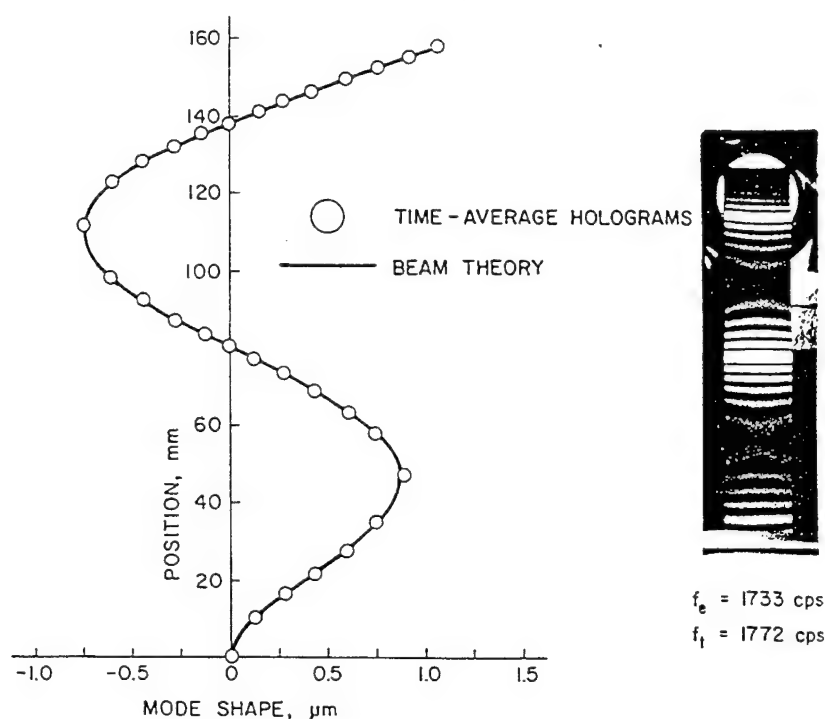


Fig. 7.9. Shape of the third flexure mode of a vibrating cantilever beam: comparison between the experimental results obtained from the time-average hologram and those based on the beam theory.

7.7. References

- 7.1. R. L. Powell and K. A. Stetson, "Interferometric analysis by wave-front reconstruction," *J. Opt. Soc. Am.*, 55:1593-1598, 1965.

- 7.2. E. N. Leith and J. Upatnieks, "Wavefront reconstruction with continuous-tone objects," *J. Opt. Soc. Am.*, 53:1377-1381, 1963.
- 7.3. R. J. Pryputniewicz, "Quantitative interpretation of time-average holograms in vibration analysis," *Optical metrology*, NATO ASI Series E: Applied Sciences - No. 131, Martius Nijhoff Publishers, Dordrecht, The Netherlands, pp. 296-316, 1987.
- 7.4. R. J. Pryputniewicz, "Time-average holography in vibration analysis," *Opt. Engrg.*, 24:843-848, 1985.
- 7.5. R. J. Pryputniewicz, "Holographic and finite element studies of vibrating beams," *Proc. SPIE*, 599:54-62, 1985.
- 7.6. K. A. Stetson, "Effects of beam modulation on fringe loci and localization in time-average hologram interferometry," *J. Opt. Soc. Am.*, 60:1378-1384, 1970.
-

8. ELECTRO-OPTIC HOLOGRAPHY

Recent advances in the phase step hologram interferometry, speckle metrology, and computer technology allowed development of a system for direct electronic recording of holograms and transmission of holographic interferograms by television systems for real-time display of interference fringes¹⁻¹⁶. This Electro-Optic Holography (EOH) system, in addition to other electronic and optical components, consists of a modified speckle interferometer, which produces speckles large enough to be resolved by the TV camera. The output of the TV camera is fed to a system that computes and stores the magnitude and phase, relative to the reference beam, of each picture element in the image of the illuminated object.

Any of the usual phenomena that generate characteristic fringes in hologram interferometry will do so in this process also, and the characteristic fringe functions will be impressed on the magnitudes of the values stored.

8.1. Fundamentals of EOH

Measurements of displacements of objects undergoing static and dynamic loads have been solved in a number of ways, as discussed in Chapters 4 to 7. Recently, this problem has been addressed using advances in phase step hologram interferometry, speckle metrology, and computer technology. One of these ways is based on the method of Electro-Optic Holography (EOH) and is the subject of this chapter.

Today, the displacement/deformation analysis of objects undergoing either static or dynamic loads are, to a great extent, satisfied by application of the finite element method (FEM)¹⁰. In these applications, the FEM is used to solve problems for which exact solutions do not exist, or are very difficult to obtain. Also, the FEM provides the only means to analyze complex three-dimensional structures, for which the response to the applied loads cannot be predicted by any other computational method. However, results obtained by the FEM depend on boundary conditions, rely greatly on the accurate knowledge of material properties, depend on accurate representation of the geometry of the structure, and are sensitive to the shape and the size of elements employed in modeling of the structure. All the information necessary to run the finite element models can be obtained, directly or indirectly, from experimental studies.

Currently, there are a number of experimental methods used to study displacements/deformations of objects. These methods are primarily based on the use of mechanical probes, strain gauges, and accelerometers and, in general, are invasive because they may affect the object's response to the load. In 1965, however, the method of hologram interferometry was invented¹¹ and provided means for noninvasive measurement of the displacements/deformations of the objects. Although this method provided means by which holograms of objects could readily be recorded, quantitative interpretation of interference fringes has traditionally been tedious and prone to considerable inaccuracy. This has led to the use of

heterodyne and phase step methods to read out the interferometric fringes produced during reconstruction of holograms of vibrating objects. Although these methods¹²⁻¹⁵ allowed high accuracy, 1/1000 and 1/100 of one fringe, respectively, in measurements of local phase differences, they still require physical recording of a permanent hologram in some type of photosensitive medium, which needs lengthy processing. Therefore, the methods requiring lengthy processing do not qualify for fully automated holographic analysis. Recently, an automated method for processing of vibration fringes has been developed⁶. In this method, measurements of irradiances produced by mutual interference of the object and a reference fields are made electronically by a detector array. Processing of this interferometric information and display of the computational results are carried out concomitantly with measurements of irradiation. Because this method does not depend on recording of holograms in conventional media, but rather relies on electronic acquisition, processing, and display of optical interference information, it is called Electro-Optic Holography (EOH), also referred to as Electronic Holography, or TV Holography⁹. In the following sections, application of EOH to static and dynamic measurements is described; more detailed description of selected applications are described in the subsequent chapters

The EOH method allows automated processing of fringes of statically and dynamically loaded objects^{5,8}. In this method, measurements of irradiances produced by mutual interference of the object and the reference fields are made electronically by a CCD camera, Fig. 8.1. Processing of this interferometric information and display of the computational results are carried out concomitantly with measurements of irradiation. The EOH method does not depend on recording of holograms in conventional media, but rather relies on electronic acquisition, processing, and display of optical interference information.

In the following sections, principles of EOH are outlined and its implementation to static and dynamic measurements is presented.

8.2. Electronic processing of holograms

The EOH system is capable of performing either static or dynamic measurements. In the discussion which follows, static measurements are implemented using the double-exposure hologram interferometry method, while dynamic measurements are implemented by the time-average method.

8.2.1. Static measurements

Static measurements are characterized by recording "single-exposure" holograms of an object at two different states of stress. As a result of interference between a set of two

"single-exposure" holograms, fringes form, if there are any optical path differences between the corresponding points on the object as recorded in the two holograms.

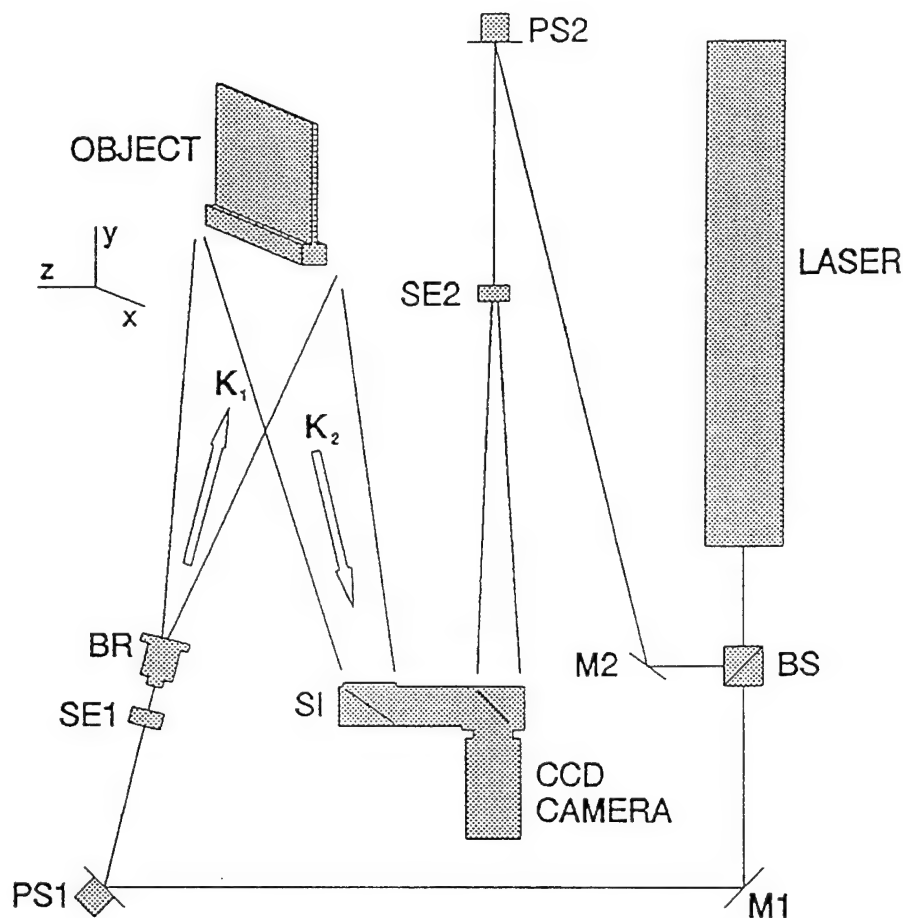


Fig. 8.1. Optical configuration of the EOH system: BS is the beamsplitter, M1 and M2 are the mirrors, PS1 and PS2 are the phase steppers, SE1 and SE2 are the spatial filter beam expander assemblies, BR is the object beam rotator, and SI is the speckle interferometer.

In EOH, this process is carried out by recording sequential frames of images of the object corresponding to the two states of stress. Typically, four sequential frames are recorded, with a finite phase step - imposed on the reference beam - between each frame, for every single-exposure image of the object. In the following discussion, in order to simplify derivation of equations describing the EOH process for static measurements, the object will be initially unstressed; results would be the same if the object was stressed initially but mathematics would be much more complicated.

The image of an unstressed (i. e., unloaded) object can be described by the irradiance distribution for the n -th sequential frame, $I_n(x,y)$, at the detector array of a CCD camera in the EOH system setup, as

$$I_n(x,y) = I_o(x,y) + I_r(x,y) + 2A_o(x,y)A_r(x,y)\cos[\Delta\phi(x,y) + \Delta\theta_n] \quad , \quad (8.1)$$

while the corresponding image of the stressed (i. e., loaded) object can be described by the irradiance distribution, $I'_n(x,y)$, as

$$I'_n(x,y) = I'_o(x,y) + I_r(x,y) + 2A'_o(x,y)A_r(x,y)\cos[\Delta\phi(x,y) + \Omega(x,y) + \Delta\theta_n] \quad . \quad (8.2)$$

In Eqs 8.1 and 8.2, x and y identify coordinates of the detectors in the array, I_o and I_r , are the irradiances of the object and the reference beams and are squares of the amplitudes A_o and A_r , respectively, $\Delta\phi$ is the phase difference between the object and the reference fields, $\Delta\theta_n$ is the finite phase step imposed on the reference beam between sequential frames recording individual images, and Ω is the fringe-locus function, constant values of which define fringe loci on the surface of the object.

Since I and I' are measured at known coordinates x and y , Eqs 8.1 and 8.2 contain four unknowns, that is, irradiances (which are squares of the amplitudes) of the two fields, the phase differences between these fields, and the fringe-locus function. The goal of the analysis is to determine Ω because it relates directly to displacements and deformations of the object.

In EOH, $\Delta\phi$ is eliminated by recording sequentially four TV frames with an introduction of a 90° phase step between each frame. That is, $\Delta\theta_n$, appearing in Eqs 8.1 and 8.2, takes on the values of 0° , 90° , 180° , and 270° . This process can be represented by two sets of four simultaneous equations corresponding to Eqs 8.1 and 8.2, respectively, that is,

$$I_1 = I_o + I_r + 2A_oA_r\cos(\Delta\phi + 0^\circ) \quad , \quad (8.3)$$

$$I_2 = I_o + I_r + 2A_oA_r\cos(\Delta\phi + 90^\circ) \quad , \quad (8.4)$$

$$I_3 = I_o + I_r + 2A_oA_r\cos(\Delta\phi + 180^\circ) \quad , \quad (8.5)$$

$$I_4 = I_o + I_r + 2A_oA_r\cos(\Delta\phi + 270^\circ) \quad , \quad (8.6)$$

and

$$I'_1 = I'_o + I_r + 2A'_oA_r\cos(\Delta\phi + \Omega + 0^\circ) \quad , \quad (8.7)$$

$$I'_2 = I'_o + I_r + 2A'_oA_r\cos(\Delta\phi + \Omega + 90^\circ) \quad , \quad (8.8)$$

$$I'_3 = I'_o + I_r + 2A'_oA_r\cos(\Delta\phi + \Omega + 180^\circ) \quad , \quad (8.9)$$

$$I'_4 = I'_o + I_r + 2A'_oA_r\cos(\Delta\phi + \Omega + 270^\circ) \quad , \quad (8.10)$$

where the arguments (x, y) were omitted for simplification. Evaluation of Eqs 8.3 to 8.10 yields

$$I_1 = I_o + I_r + 2A_o A_r \cos \Delta\phi \quad , \quad (8.11)$$

$$I_2 = I_o + I_r + 2A_o A_r \sin \Delta\phi \quad , \quad (8.12)$$

$$I_3 = I_o + I_r - 2A_o A_r \cos \Delta\phi \quad , \quad (8.13)$$

$$I_4 = I_o + I_r - 2A_o A_r \sin \Delta\phi \quad , \quad (8.14)$$

and

$$I'_1 = I'_o + I_r + 2A'_o A_r \cos(\Delta\phi + \Omega) \quad , \quad (8.15)$$

$$I'_2 = I'_o + I_r + 2A'_o A_r \sin(\Delta\phi + \Omega) \quad , \quad (8.16)$$

$$I'_3 = I'_o + I_r - 2A'_o A_r \cos(\Delta\phi + \Omega) \quad , \quad (8.17)$$

$$I'_4 = I'_o + I_r - 2A'_o A_r \sin(\Delta\phi + \Omega) \quad . \quad (8.18)$$

It should be noted that systems of equations similar to Eqs 8.11 to 8.14 and Eqs 8.15 to 8.18 could be obtained using any value of the phase step, however, use of the 90° phase step results in the simplest computations.

Subtracting Eqs 8.11 and 8.13 as well as Eqs 8.12 and 8.14 we obtain, for the unstressed object, the following set of two equations:

$$(I_1 - I_3) = 4A_o A_r \cos \Delta\phi \quad , \quad (8.19)$$

and

$$(I_2 - I_4) = 4A_o A_r \sin \Delta\phi \quad . \quad (8.20)$$

Following the above procedure and subtracting Eqs 8.15 and 8.17 and Eqs 8.16 and 8.18, a set of two equations is obtained for the stressed object, that is,

$$(I'_1 - I'_3) = 4A'_o A_r \cos(\Delta\phi + \Omega) \quad , \quad (8.21)$$

and

$$(I'_2 - I'_4) = 4A'_o A_r \sin(\Delta\phi + \Omega) \quad . \quad (8.22)$$

Addition of Eqs 8.19 and 8.21 yields

$$(I_1 - I_3) + (I'_1 - I'_3) = 4A_o A_r \cos \Delta\phi + 4A'_o A_r \cos(\Delta\phi + \Omega) \quad . \quad (8.23)$$

Because object displacements and deformations are small, it can be assumed that $A'_o \approx A_o$. Therefore, Eq. 8.23 becomes

$$(I_1 - I_3) + (I'_1 - I'_3) = 4A_o A_r [\cos \Delta\phi + \cos(\Delta\phi + \Omega)] \quad . \quad (8.24)$$

Recognizing that $\cos(\Delta\phi + \Omega) = \cos \Delta\phi \cos \Omega - \sin \Delta\phi \sin \Omega$, Eq. 8.24 can be rewritten as

$$\begin{aligned} D_1 &= (I_1 - I_3) + (I'_1 - I'_3) \\ &= 4A_o A_r [(1 + \cos \Omega) \cos \Delta\phi - \sin \Delta\phi \sin \Omega] \quad . \end{aligned} \quad (8.25)$$

In a similar way, addition of Eqs 8.20 and 8.22 simplifies to

$$\begin{aligned} D_2 &= (I_2 - I_4) + (I'_2 - I'_4) \\ &= 4A_o A_r [(1 + \cos \Omega) \sin \Delta\phi + \cos \Delta\phi \sin \Omega] \quad . \end{aligned} \quad (8.26)$$

Finally, addition of the squares of Eqs 8.25 and 8.26 yields

$$\begin{aligned} D_1^2 + D_2^2 &= \{4A_o A_r [(1 + \cos \Omega) \cos \Delta\phi - \sin \Delta\phi \sin \Omega]\}^2 \\ &\quad + \{4A_o A_r [(1 + \cos \Omega) \sin \Delta\phi + \cos \Delta\phi \sin \Omega]\}^2 \quad , \end{aligned}$$

which reduces to

$$D_1^2 + D_2^2 = 16A_o^2 A_r^2 [(1 + \cos \Omega)^2 + \sin^2 \Omega] \quad ,$$

wherefrom

$$D_1^2 + D_2^2 = 32A_o^2 A_r^2 (1 + \cos \Omega) \quad . \quad (8.27)$$

Furthermore, recognizing that $(1 + \cos \Omega) = 2 \cos^2(\Omega/2)$, Eq. 8.27 can be reduced to

$$\sqrt{D_1^2 + D_2^2} = 8A_o A_r \cos\left(\frac{\Omega}{2}\right) \quad , \quad (8.28)$$

which represents the static viewing image displayed by the EOH. In Eq. 10.28, Ω is the fringe-locus function corresponding to the static displacements and/or deformations of the object. The fringe-locus function can be determined by processing the sequential EOH images as described below.

In order to obtain data from the EOH images, we will again employ Eqs 8.19 to 8.22 and follow the procedure used to derive Eq. 8.27. The result of this procedure is

$$\begin{aligned}
D_3 &= (I_1 - I_3) - (I'_1 - I'_3) \\
&= 4A_o A_r [(1 - \cos \Omega) \cos \Delta\phi + \sin \Delta\phi \sin \Omega] \quad , \quad (8.29)
\end{aligned}$$

$$\begin{aligned}
D_4 &= (I_2 - I_4) - (I'_2 - I'_4) \\
&= 4A_o A_r [(1 - \cos \Omega) \sin \Delta\phi - \cos \Delta\phi \sin \Omega] \quad , \quad (8.30)
\end{aligned}$$

and

$$D_3^2 + D_4^2 = 32A_o^2 A_r^2 (1 - \cos \Omega) \quad . \quad (8.31)$$

Subtracting Eq. 8.31 from Eq. 8.27 we obtain

$$\begin{aligned}
D &= (D_1^2 + D_3^2) - (D_1^2 + D_4^2) = 32A_o^2 A_r^2 (1 + \cos \Omega) - 32A_o^2 A_r^2 (1 - \cos \Omega) \quad , \\
\text{or} \quad D &= 64A_o^2 A_r^2 \cos \Omega \quad . \quad (8.32)
\end{aligned}$$

Starting with Eqs 8.19 to 8.22, we can also determine

$$\begin{aligned}
N_1 &= (I_1 - I_3) + (I'_2 - I'_4) \\
&= 4A_o A_r [(1 + \sin \Omega) \cos \Delta\phi + \sin \Delta\phi \cos \Omega] \quad , \quad (8.33)
\end{aligned}$$

$$\begin{aligned}
N_2 &= (I_2 - I_4) - (I'_1 - I'_3) \\
&= 4A_o A_r [(1 + \sin \Omega) \sin \Delta\phi - \cos \Delta\phi \cos \Omega] \quad , \quad (8.34)
\end{aligned}$$

$$\begin{aligned}
N_3 &= (I_1 - I_3) - (I'_2 - I'_4) \\
&= 4A_o A_r [(1 - \sin \Omega) \cos \Delta\phi - \sin \Delta\phi \cos \Omega] \quad , \quad (8.35)
\end{aligned}$$

$$\begin{aligned}
N_4 &= (I_2 - I_4) + (I'_1 - I'_3) \\
&= 4A_o A_r [(1 - \sin \Omega) \sin \Delta\phi + \cos \Delta\phi \cos \Omega] \quad , \quad (8.36)
\end{aligned}$$

$$N_1^2 + N_2^2 = 32A_o^2 A_r^2 (1 + \sin \Omega) \quad , \quad (8.37)$$

$$N_3^2 + N_4^2 = 32A_o^2 A_r^2 (1 - \sin \Omega) \quad , \quad (8.38)$$

and

$$N = (N_1^2 + N_2^2) - (N_3^2 + N_4^2) = 64A_o^2 A_r^2 \sin \Omega \quad . \quad (8.39)$$

Finally, dividing Eq. 8.39 by Eq. 8.32, we obtain

$$\frac{N}{D} = \frac{64A_o^2A_r^2\sin\Omega}{64A_o^2A_r^2\cos\Omega} ,$$

from which it follows that

$$\Omega = \tan^{-1}\left(\frac{N}{D}\right) . \quad (8.40)$$

It should be noted that Ω , computed from Eq. 8.40, is a spatial function that depends on coordinates x and y . Therefore, its values are determined for every coordinate pair (x,y) in the object space. Once the values of Ω are determined, they can be used to compute object displacements using procedures discussed in Chapter 4.

8.2.2. Dynamic measurements

In this section, application of EOH to dynamic measurements is made based on time-average hologram interferometry (Chapter 7). To facilitate this presentation, time-average recording of a sinusoidally vibrating object will be considered. For this case, the irradiance distribution for the n -th sequential frame, I_{tn} , can be represented by a relationship similar to those shown in Eqs 8.1 and 8.2, that is,

$$I_{tn} = I_o + I_r + 2A_oA_r\cos(\Delta\phi_t + \Delta\theta_n)M(\Omega_t) . \quad (8.41)$$

In Eq. 8.41, the arguments (x,y) were omitted for simplification, subscript t indicates time varying parameters, M is the characteristic function (see Chapter 7) which modulates the interference of the two fields due to the motion of the object, Ω_t is the fringe-locus function defining fringe loci on the surface of a vibrating object, and other parameters are as defined for Eqs 8.1 and 8.2.

Equation 8.41, like Eqs 8.1 and 8.2, has four unknowns: I_o and I_r , which are squares of A_o and A_r , respectively, $\Delta\phi_t$, and Ω_t . The goal of the analysis is to determine Ω_t because it relates directly to the displacements of the vibrating object.

In order to determine Ω_t from the electronic holograms of a vibrating object, four sequential frames are recorded with the phase steps equal to multiples of 90° imposed on the reference beam between each frame, see also Section 8.2.1. This process can be represented by the following set of four simultaneous equations:

$$I_{t_1} = I_o + I_r + 2A_o A_r \cos(\Delta\phi_t + 0^\circ) M(\Omega_t) \quad , \quad (8.42)$$

$$I_{t_2} = I_o + I_r + 2A_o A_r \cos(\Delta\phi_t + 90^\circ) M(\Omega_t) \quad , \quad (8.43)$$

$$I_{t_3} = I_o + I_r + 2A_o A_r \cos(\Delta\phi_t + 180^\circ) M(\Omega_t) \quad , \quad (8.44)$$

$$I_{t_4} = I_o + I_r + 2A_o A_r \cos(\Delta\phi_t + 270^\circ) M(\Omega_t) \quad , \quad (8.45)$$

Following the procedure used to derive Eqs 8.19 and 8.20 and operating on Eqs 8.42 to 8.45, we obtain

$$I_{t_1} = I_o + I_r + 2A_o A_r \cos(\Delta\phi_t) M(\Omega_t) \quad , \quad (8.46)$$

$$I_{t_2} = I_o + I_r + 2A_o A_r \sin(\Delta\phi_t) M(\Omega_t) \quad , \quad (8.47)$$

$$I_{t_3} = I_o + I_r - 2A_o A_r \cos(\Delta\phi_t) M(\Omega_t) \quad , \quad (8.48)$$

$$I_{t_4} = I_o + I_r - 2A_o A_r \sin(\Delta\phi_t) M(\Omega_t) \quad , \quad (8.49)$$

Then, from Eqs 8.46 to 8.49, it follows that

$$(I_{t_1} - I_{t_3}) = 4A_o A_r \cos(\Delta\phi_t) M(\Omega_t) \quad , \quad (8.50)$$

and

$$(I_{t_2} - I_{t_4}) = 4A_o A_r \sin(\Delta\phi_t) M(\Omega_t) \quad , \quad (8.51)$$

If the viewing mode is selected, then, based on the input described by Eqs 8.50 and 8.51, the EOH system produces an image which can be represented by

$$\sqrt{(I_{t_1} - I_{t_3})^2 + (I_{t_2} - I_{t_4})^2} = 4A_o A_r M(\Omega_t) \quad . \quad (8.52)$$

The image represented by Eq. 8.52 is displayed live on a TV monitor and it can be stored in a processor memory.

This storage can be of two types. If the image is to be recalled in the future for visual observation, then an 8-bit image is stored and occupies approximately one-quarter megabyte of memory - this is image storage. If the image is to be processed quantitatively, then the lookup table for the data mode is loaded into the operating system and produces a data image which can be represented by

$$(I_{t_1} - I_{t_3})^2 + (I_{t_2} - I_{t_4})^2 = 16I_o I_r M^2(\Omega_t) \quad . \quad (8.53)$$

The result of Eq. 8.53 is stored as the 16-bit data image and occupies one-half megabyte of memory - this is data storage. Either type of image may then be down-loaded to the memory of the host computer for further processing.

Equations 8.52 and 8.53 indicate that the viewing and the data images are proportional to the characteristic function and to the square of the characteristic function, respectively. The characteristic function is determined by the temporal motion of the object, and for sinusoidal vibrations, assuming that the vibration period is much shorter than the TV framing time,

$$M[\Omega_t(x, y)] = J_o[|\Omega_t(x, y)|] \quad , \quad (8.54)$$

where J_o is the zero-order Bessel function of the first kind, as discussed in Chapter 7. Therefore, Eqs 8.52 and 8.57 become

$$\sqrt{(I_{t_1} - I_{t_3})^2 + (I_{t_2} - I_{t_4})^2} = 4A_o A_r |J_o(|\Omega_t|)| \quad , \quad (8.55)$$

and

$$(I_{t_1} - I_{t_3})^2 + (I_{t_2} - I_{t_4})^2 = 16I_o I_r J_o^2(|\Omega_t|) \quad , \quad (8.56)$$

respectively. Equation 8.55 results in a viewed image that is modulated by a system of fringes described by the zero-order Bessel function of the first kind, while Eq. 8.56 shows that the data image is modulated by the square of this function. Thus, centers of the dark fringes are located at those points on the surface of the object where $J_o(|\Omega_t|)$ equals zero, as shown in Fig. 7.2. This figure indicates that the zero-order fringe is much brighter than the other J_o fringes. Since the zero-order fringes represent the stationary points on the vibrating object they allow easy identification of nodes. The brightness of other fringes decreases with increasing fringe order and can be directly related to the mode shapes. It should be noted that higher order zeros are nearly equally spaced giving the J_o function an almost periodic nature which is the characteristic that is utilized in quantitative interpretation of images recorded by the EOH system as discussed in Section 8.2.2.1.

In the EOH system, the data provided by the CCD camera are processed to produce results shown by Eq. 8.55 for every pixel in the image frame at the rate of 30 frames per second. Each frame contains 512×480 8-bit numbers so that each image consists of 245,760 points. For visual examination of the vibration modes, time-average hologram images corresponding to Eq. 8.55 are displayed on the TV monitor. These images are generated concomitantly by the pipeline processor of the EOH system. To produce data suitable for quantitative analysis of time-average holograms, 16-bit images represented by Eq. 8.56 are stored. These data are stored in two 8-bit bytes per pixel and produce a frozen image which can be displayed on the TV monitor one byte at a time, that is, either as a high-byte image or a low-byte image.

8.2.2.1. Determination of the fringe-locus function for the vibrating object

To interpret electronically recorded time-average holograms quantitatively, the argument of the J_o^2 function, appearing in Eq. 8.56, must be determined. One method to determine this argument, suitable for the time-average images recorded by EOH, was developed by Stetson and Brohinsky⁶. This method uses the fact that it is possible to shift J_o fringes in a manner similar to that in which phase modulation shifts cosinusoidal fringes in conventional double-exposure hologram interferometry. In time-average holography, this is done by modulating the phase of either the object or the reference beams sinusoidally at the same frequency and phase as the object vibration. Such a process can be represented mathematically by addition of a phasor bias, B , to the argument of the Bessel function, resulting in the characteristic function

$$M[\Omega_t(x, y), B] = J_o[|\Omega_t(x, y) - B|] \quad (8.57)$$

For purposes of analysis, the object must be made to vibrate in only one vibration mode at a time so that the motions of its various parts are either in or out of phase with one another. If the phase of the sinusoidal beam modulation is adjusted to coincide with that of the object vibration, the phasor bias becomes a simple additive term within the argument of the Bessel function, that is,

$$M[\Omega_t(x, y), B] = J_o[|\Omega_t(x, y) - B|] \quad (8.58)$$

Therefore, Eq. 8.56 becomes

$$\begin{aligned} [I_{t_1}(x, y) - I_{t_3}(x, y)]^2 + [I_{t_2}(x, y) - I_{t_4}(x, y)]^2 = \\ = 16I_o(x, y)I_r(x, y)J_o^2[|\Omega_t(x, y) - B|] \end{aligned} \quad (8.59)$$

For comparison, a general equation representing the irradiance, I_{h_t} , of an image reconstructed from a time-average hologram is

$$I_{h_t}(x, y) = I_{a_t}(x, y) + I_{m_t}(x, y)J_o^2[|\Omega_t(x, y) - B|] \quad (8.60)$$

where I_{a_t} represents local average background irradiance from scattered light and I_{m_t} is the local maximum irradiance. Therefore, Eq. 8.59 is the special case of Eq. 8.60 with

$$I_{h_t}(x, y) = [I_{t_1}(x, y) - I_{t_3}(x, y)]^2 + [I_{t_2}(x, y) - I_{t_4}(x, y)]^2 \quad (8.61)$$

$$I_{a_t}(x, y) = 0 \quad (8.62)$$

and

$$I_{m_t}(x, y) = 16I_o(x, y)I_r(x, y) \quad (8.63)$$

The output of the processor in the data mode, I_{h_t} , is stored in the host computer for different values of B , while I_{a_t} , I_{m_t} , and Ω_t constitute three unknowns, and the goal of the analysis is to determine Ω_t . Unfortunately, the Bessel function is not separable in terms of Ω_t and B , so a straightforward solution is not possible. However, the nearly periodic nature of the J_0 function (see discussion following Eq. 8.56) allows an approximate solution for the fringe-locus function. This approximate solution recognizes that Eq. 8.60 is similar to the general equation for the irradiance distribution, I_h , for an image reconstructed from a conventional double-exposure hologram with sinusoidal fringes, that is,

$$I_h(x, y) = I_a(x, y) + I_m(x, y) \cos^2[\Omega(x, y) - B] \quad , \quad (8.64)$$

where J_0^2 in Eq. 8.60 has been replaced by \cos^2 and Ω_t has been replaced by Ω .

Examination of Eq. 8.64 shows that it, just like Eq. 8.60, also has three unknowns: I_a , I_m , and Ω . However, the $\cos^2[\Omega(x, y) - B]$ term, appearing in Eq. 8.64, unlike the $J_0^2[|\Omega_t(x, y) - B|]$ term of Eq. 8.60, is separable in its component arguments. To facilitate solution for Ω , Eq. 8.64 is rewritten as

$$I_h(x, y) = I'_a(x, y) + I'_m(x, y) \cos[2\Omega(x, y) - 2B] \quad , \quad (8.65)$$

where

$$I'_a(x, y) = I_a(x, y) + \frac{I_m(x, y)}{2} \quad (8.66)$$

and

$$I'_m(x, y) = \frac{I_m(x, y)}{2} \quad . \quad (8.67)$$

With three values of B , three simultaneous equations of the type of Eq. 8.65, can be solved uniquely for a given value of the Ω . The three simultaneous equations are

$$I_{h_1}(x, y) = I'_a(x, y) + I'_m(x, y) \cos[2\Omega(x, y)] \quad , \quad (8.68)$$

$$I_{h_2}(x, y) = I'_a(x, y) + I'_m(x, y) \cos[2\Omega(x, y) - 2B] \quad , \quad (8.69)$$

$$I_{h_3}(x, y) = I'_a(x, y) + I'_m(x, y) \cos[2\Omega(x, y) + 2B] \quad , \quad (8.70)$$

corresponding to the zero-, positive-, and negative-shifts, respectively. Solution of Eqs 8.68 to 8.70 yields

$$\Omega(x, y) = \frac{1}{2} \tan^{-1} \left\{ \left[\frac{1 - \cos(2B)}{\sin(2B)} \right] \times \frac{I_{h_3}(x, y) - I_{h_2}(x, y)}{2I_{h_1}(x, y) - I_{h_2}(x, y) - I_{h_3}(x, y)} \right\} \quad . \quad (8.71)$$

If the three irradiance distributions $I_{h_1}(x, y)$, $I_{h_2}(x, y)$, and $I_{h_3}(x, y)$, corresponding to three time-average holograms, are substituted into Eq. 8.71 the result is $\Omega_{t_{approx}}(x, y)$. This value of $\Omega_{t_{approx}}$ differs from the correct argument, Ω_t , of the J_o function, because of inequality between the J_o^2 and \cos^2 functions, and should be expressed as

$$\Omega_{t_{approx}}(x, y) = \Omega_t(x, y) + \epsilon(x, y) \quad . \quad (8.72)$$

Equation 8.71 yields values of $\Omega_{t_{approx}}$ modulo 180° . By adding or subtracting 180° , depending on the sign of the numerator in Eq. 8.71, whenever the denominator is negative, $\Omega_{t_{approx}}$ can be obtained modulo 360° . The image can be searched by the computer to locate discontinuities to define areas where the missing multiples of the 360° should be added to unwrap function $\Omega_{t_{approx}}$. By further identifying pixels within the zero-order fringe, an overall level shift can be applied to make those pixels have values between $\pm 180^\circ$.

Errors ϵ can be computed for any value of Ω_t for specific values of B to create a lookup table. This lookup table is used to correct the values computed from Eq. 8.71 which have been unwrapped and level shifted. In this way, vibratory deformations can be obtained from time-average hologram reconstructions with little more mathematical computation than is required for static deformations. Once the correct values of Ω_t are determined, they can be used in any one of the equations for quantitative interpretation of time-average holograms, as discussed in Chapter 7.

8.2.2.2. Generation of a lookup table

The lookup table is computed from Eqs 8.60 and 8.71. First, three values of I_{h_i} are computed by using Eq. 8.60 for three values of B , for example, 0 and $\pm\pi/3$, that is,

$$I_{h_1}(x, y) = I_{a_t}(x, y) + I_{m_t}(x, y) J_o^2[|\Omega_t(x, y)|] \quad , \quad (8.73)$$

$$I_{h_2}(x, y) = I_{a_t}(x, y) + I_{m_t}(x, y) J_o^2[|\Omega_t(x, y) - B|] \quad , \quad (8.74)$$

$$I_{h_3}(x, y) = I_{a_t}(x, y) + I_{m_t}(x, y) J_o^2[|\Omega_t(x, y) + B|] \quad . \quad (8.75)$$

Substitution of the values of Eqs 8.73 to 8.75 into Eq. 8.71 yields

$$\begin{aligned} \Omega_{t_{approx}}(x, y) = & \frac{1}{2} \tan^{-1} \left\{ \left[\frac{1 - \cos(2B)}{\sin(2B)} \right] \times \right. \\ & \times \left. \frac{J_o^2[|\Omega_t(x, y) + B|] - J_o^2[|\Omega_t(x, y) - B|]}{2J_o^2[|\Omega_t(x, y)|] - J_o^2[|\Omega_t(x, y) - B|] - J_o^2[|\Omega_t(x, y) + B|]} \right\} \quad . \quad (8.76) \end{aligned}$$

To construct a lookup table corresponding to the specific value of B , Eq. 8.76 is used to compute $\Omega_{t_{approx}}$ for the designated range of values of Ω_t . Tabulating Ω_t versus $\Omega_{t_{approx}}$ produces the lookup table for the given value of the bias vibration. If the magnitude of phase modulation of the bias vibration changes, new lookup table must be constructed and used in quantitative interpretation of the corresponding holograms.

8.3. EOH system and procedure

In this section, physical description of the EOH system is given and its operation is presented.

8.3.1. Description of the system

Schematic representation of the optical and electronic configurations of the EOH system are shown in Figs 8.1 and 8.2, respectively. Laboratory implementation of these configurations is shown in Figs 8.3 to 8.10.

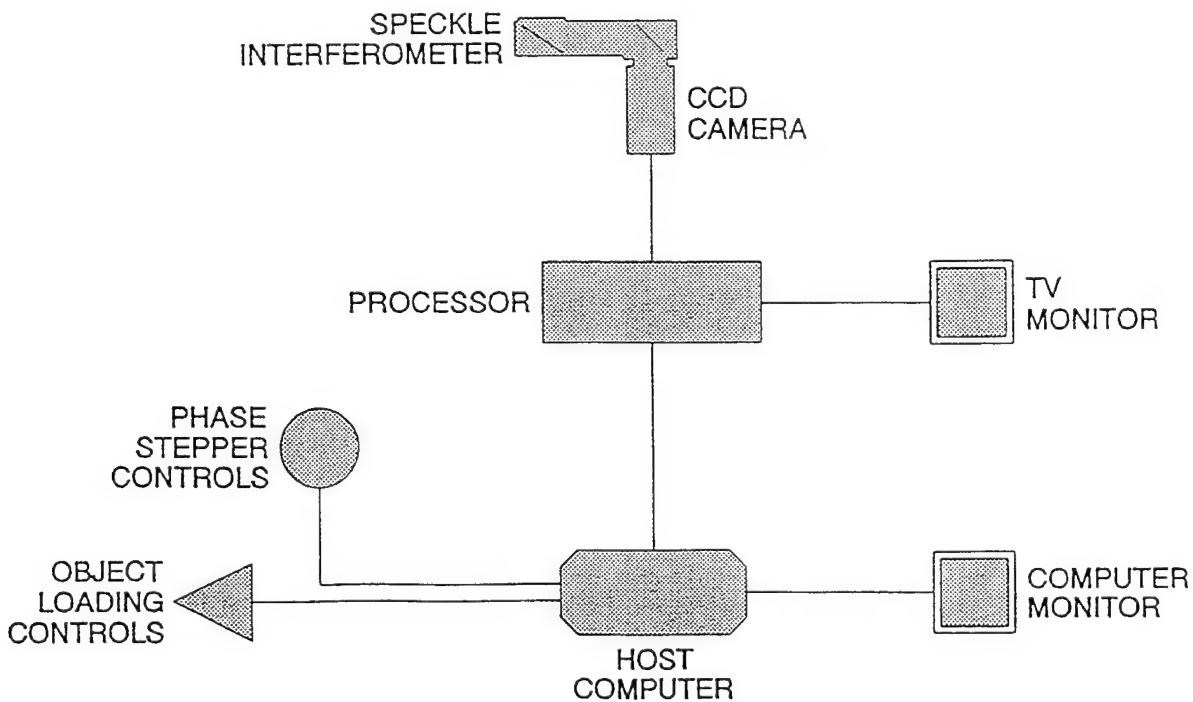


Fig. 8.2. Electronic configuration of the EOH system.

In the EOH system with three cameras, developed during this project, the laser output is divided into four beams, Figs 8.6 to 8.9, by means of continuously variable beamsplitters. One of these beams is directed via a piezoelectrically driven mirror and is shaped by the spatial filter beam expander assembly to illuminate the object uniformly, Fig. 8.1; this mirror can be driven at the same frequency as the object excitation to provide bias vibration. The other three beams, also spatially filtered and expanded, are directed toward the reference inputs of the speckle interferometers by three other piezoelectrically driven mirrors which introduce 90° phase steps between consecutive frames.

It should be noted that each of the three cameras of the EOH system is equipped with its own speckle interferometer. The speckle interferometers combine the object beam with the reference beam, associated with the specific camera, and direct them collinearly toward the detector arrays of the CCD cameras.

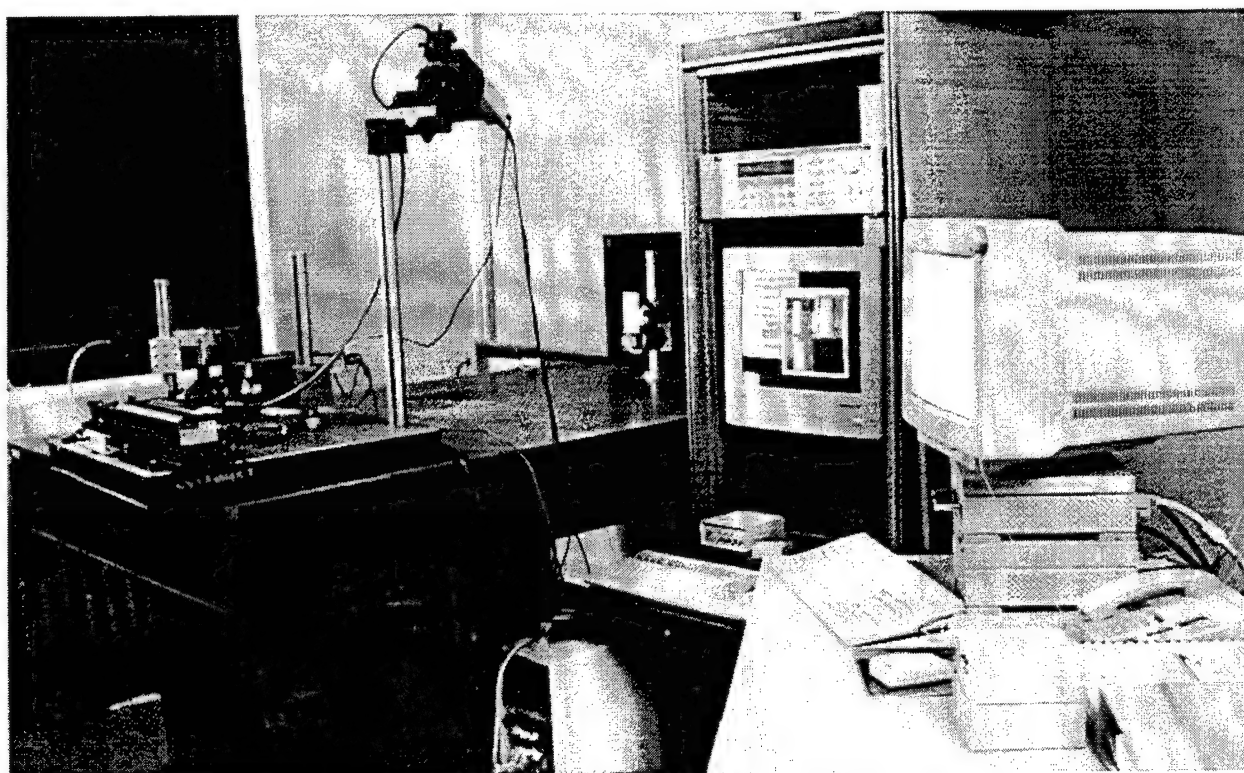


Fig. 8.3. Overall view of the EOH system with three cameras.

In the EOH system, the CCD cameras detect the interference patterns, corresponding to the cameras' directions of observation as defined by the vectors \mathbf{K}_2^m , where the superscript $m = 1, 2, 3$ designates the number of the camera, and send the signals to the pipeline processor, Fig. 8.2. In the processor, the sequential frames obtained from each of the three cameras are processed as discussed in Section 8.2. All computations are done in a pipeline processor which

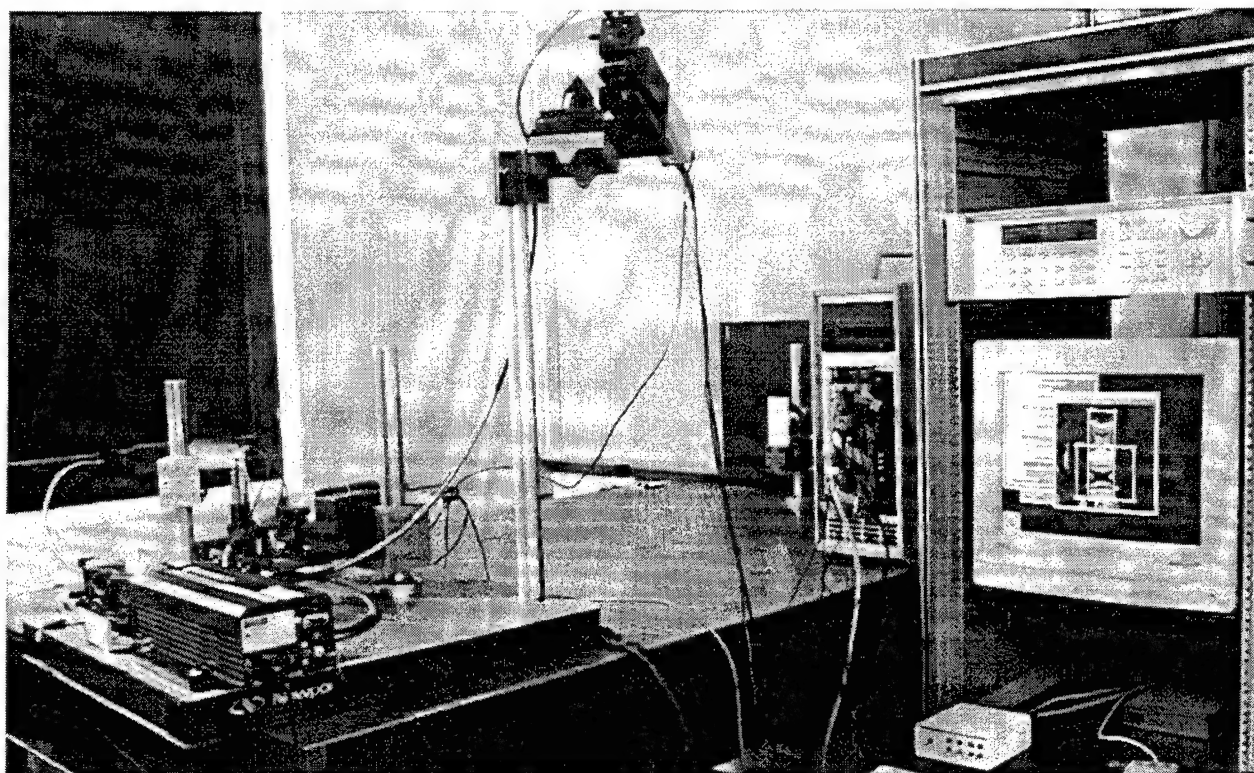


Fig. 8.4. Close up view of the optomechanical setup of the EOH system with three cameras.

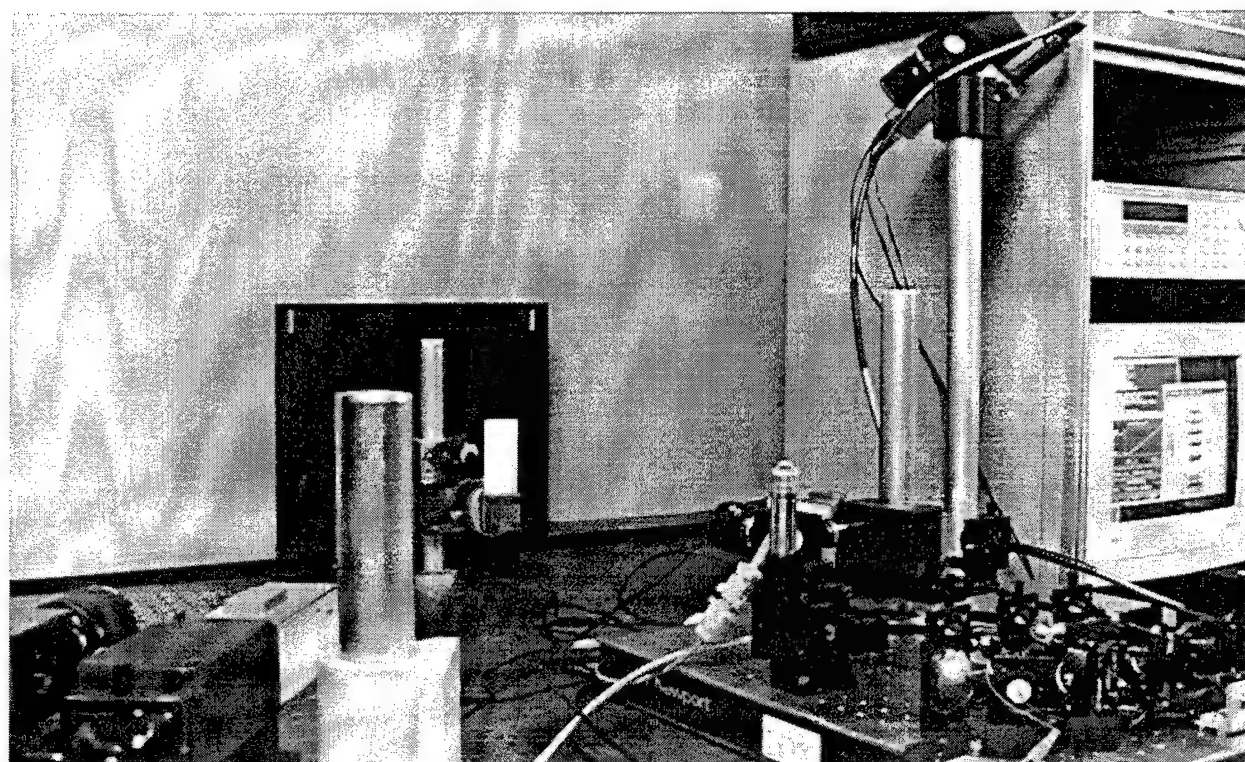


Fig. 8.5. Close up view of the three cameras of the EOH system.

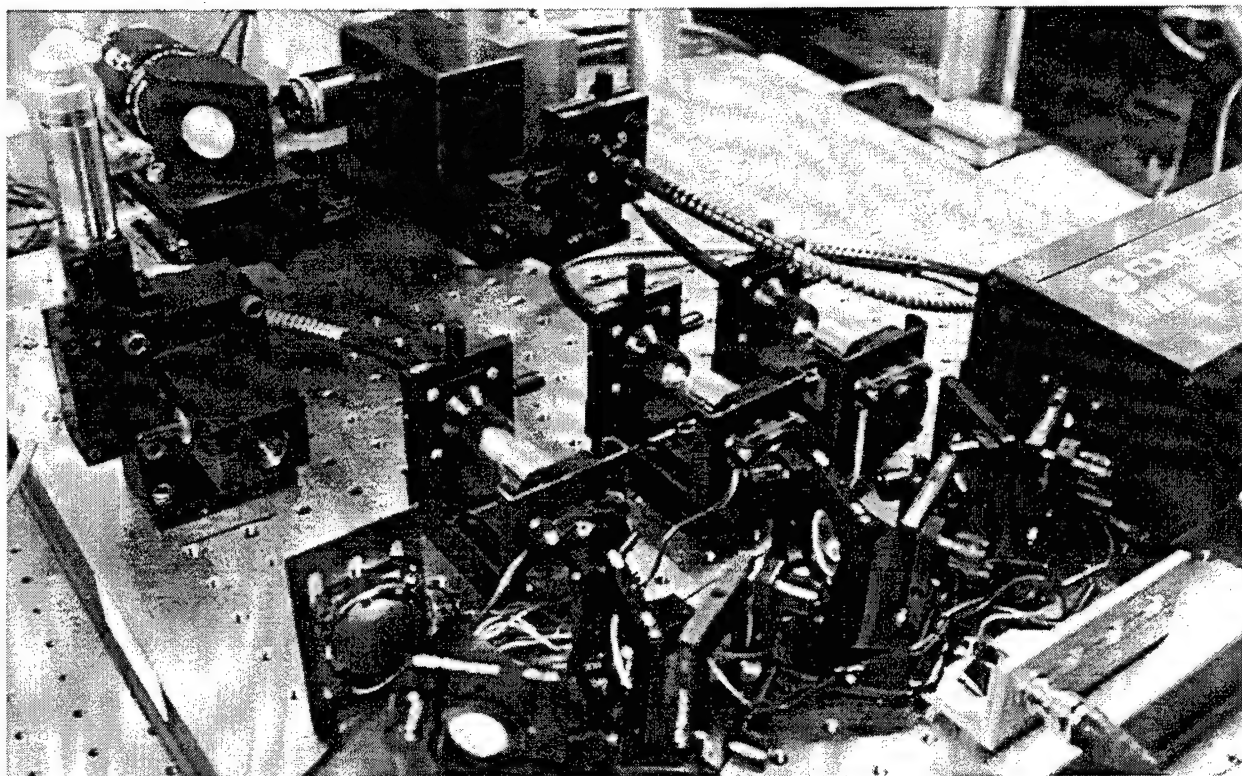


Fig. 8.6. Generation of the object and three reference beams for the EOH system with three cameras.

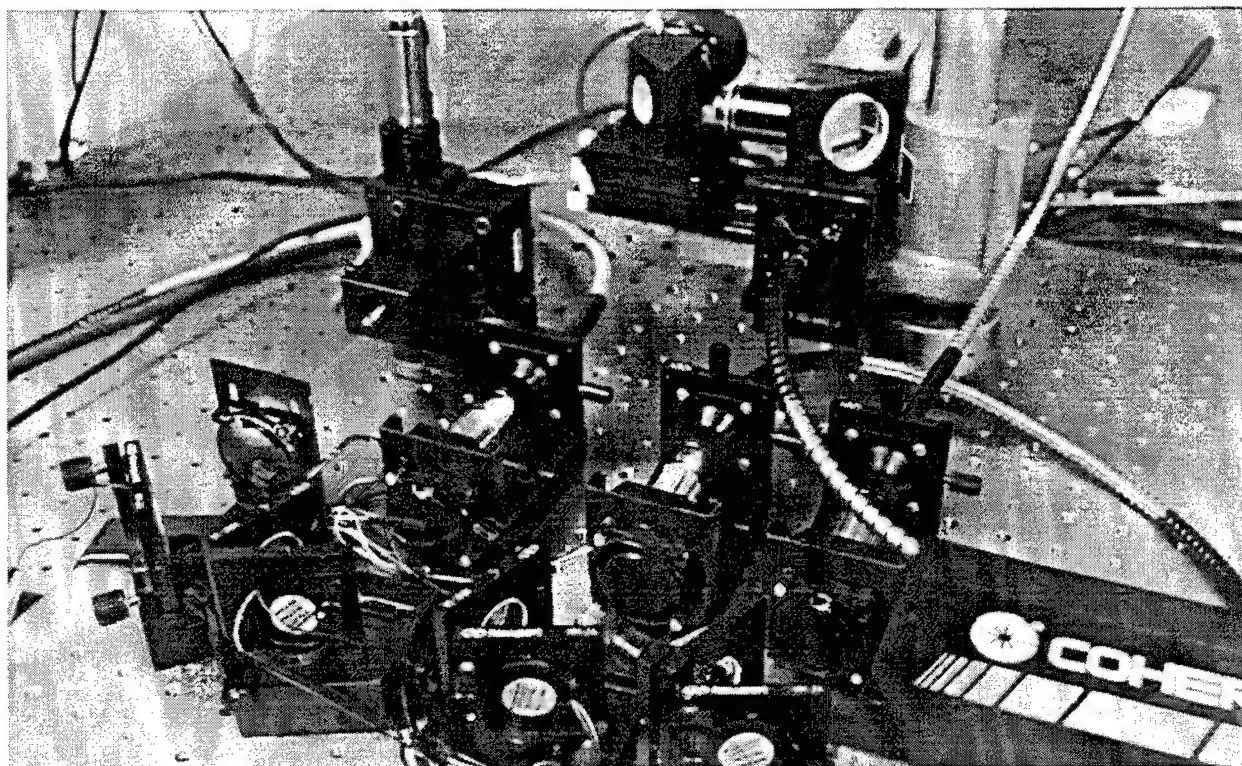


Fig. 8.7. Multiple beam generation subsystem and camera-1 of the EOH system with three cameras.

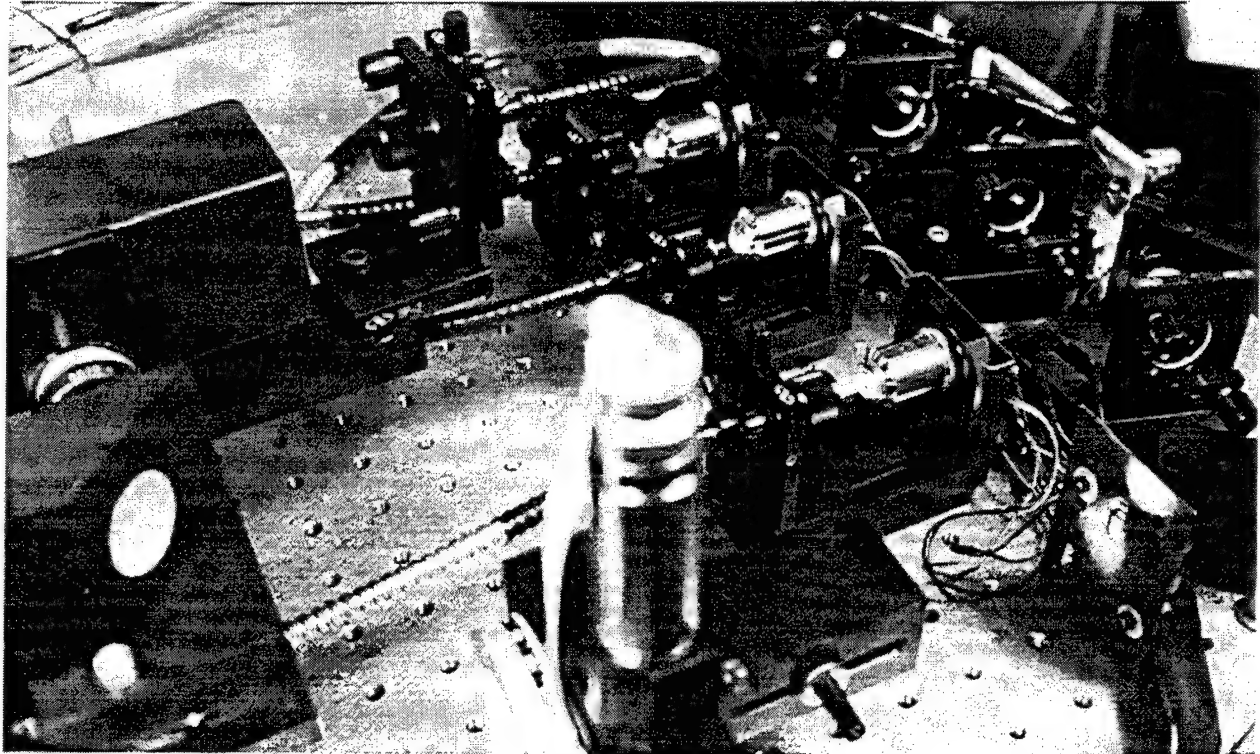


Fig. 8.8. Close up view of the multiple beam generation subsystem of the EOH system with three cameras.

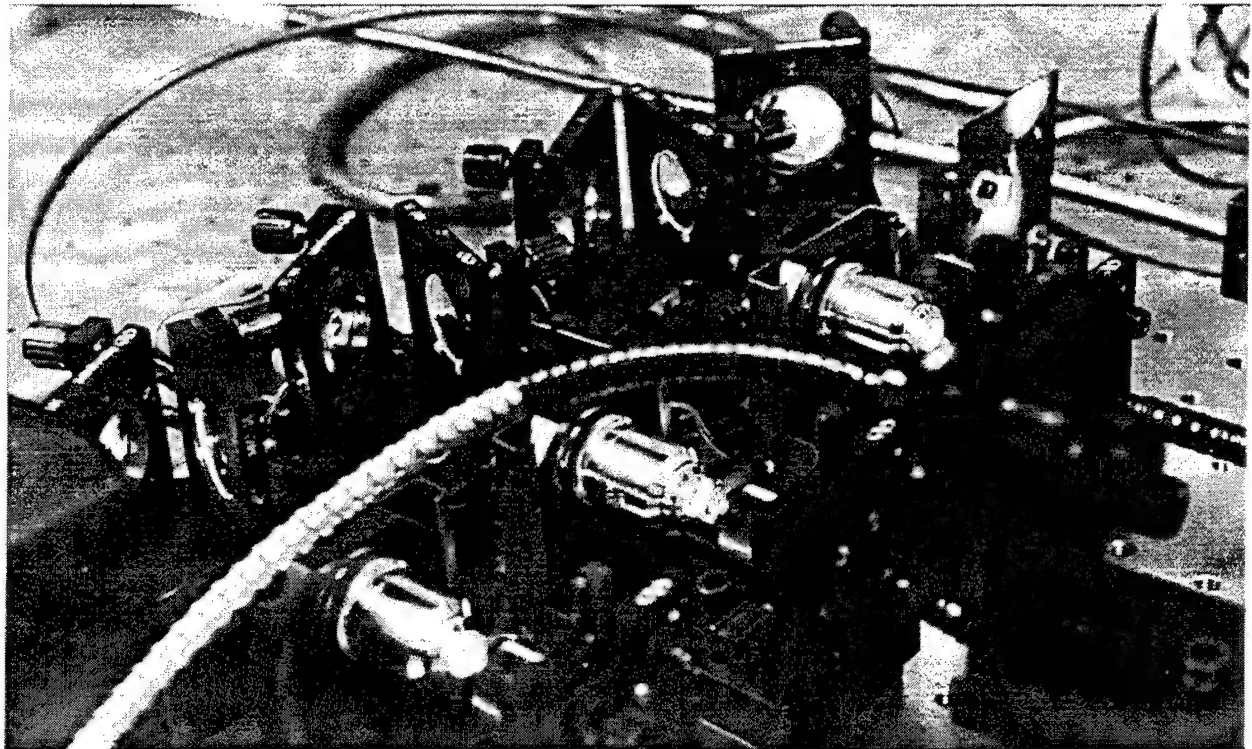


Fig. 8.9. Close up view of the beamsplitters and the beam shaping lenses of the EOH system with three cameras.

operates under control of a host computer. The host computer also controls excitation of the object, coordinates it with the bias vibration imposed on the object beam, and keeps track of the 90° phase stepping between the frames.

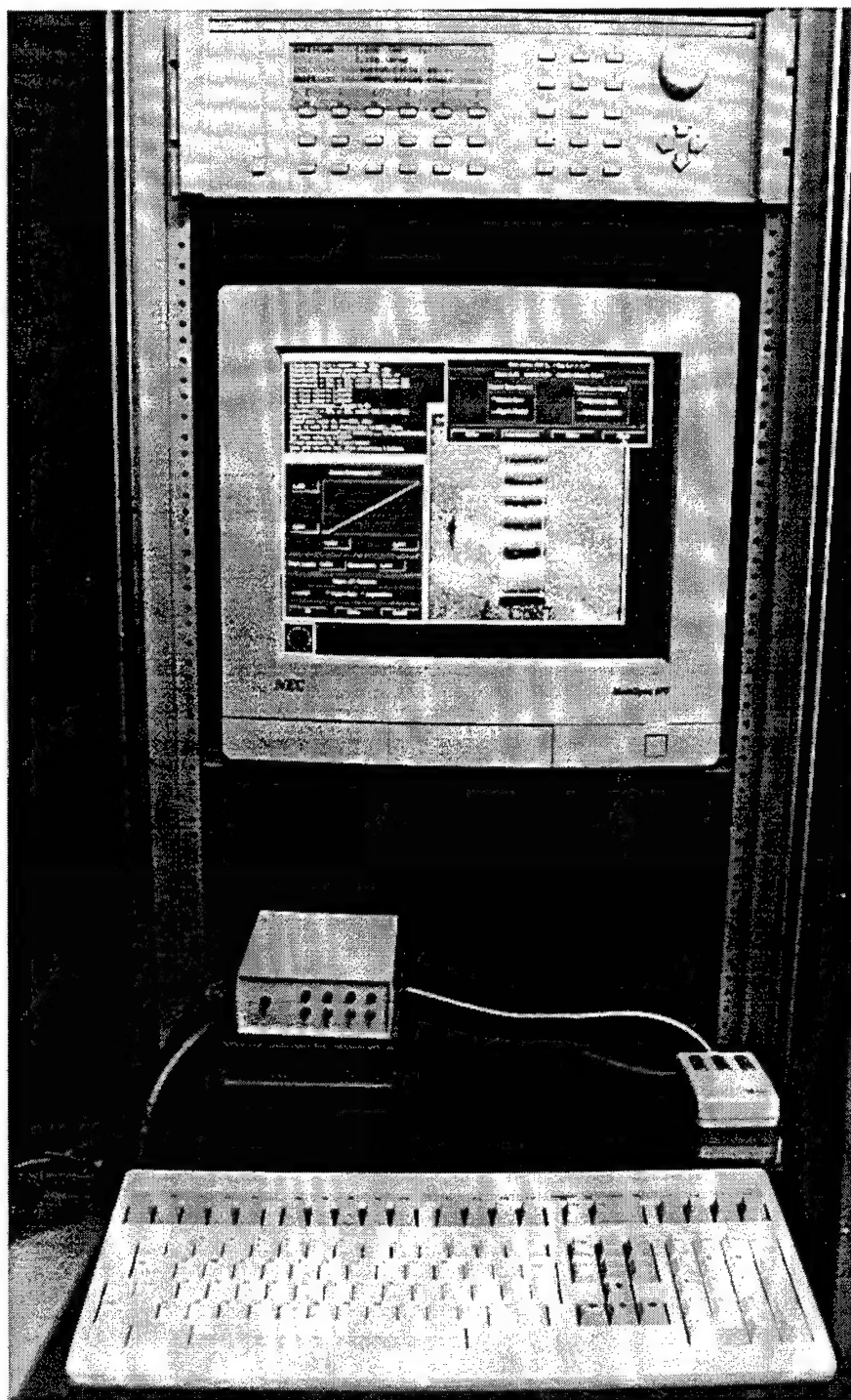


Fig. 8.10. Display monitor of the EOH system with three cameras.

By operating on each input image and its three predecessors, the pipeline processor produces a hologram of the object being studied for each of the three noncoplanar views of the three cameras, respectively. The resulting three holograms, i. e., one hologram for each of the three cameras of the EOH system, can be viewed concomitantly on the TV monitor. Such holograms are produced for the zero, as well as the positive and the negative bias vibrations, for each resonance frequency of the object; a procedure for setting up the bias vibration is discussed in Section 8.3.2. The resulting three electronic holograms, for each of the three cameras of the EOH system, i. e., a set of nine holograms for a given loading condition of the object, are then processed by the host computer to determine spatial distribution of the displacement vectors which can be viewed directly on the computer monitor.

Representative results obtained using the EOH system are included in Appendices A to F and in Section 8.4.

8.3.2. Setting the bias vibration

In order to interpret electronically recorded time-average holograms quantitatively, both the magnitude and the phase of the bias vibration must be known. One method to set the bias vibration is as follows.

Adjust object excitation so that several J_o fringes are seen across the object and the zero-order fringe is well identified. Then, increase magnitude of the bias vibration until the zero-order fringe is lost. Following this, adjust phase of the bias vibration until the zero-order fringe is regained and its width is maximum. At this point, phase of the bias modulation equals the phase of the vibrating object.

Next, turn off object excitation and reduce magnitude of the bias vibration to zero - do not, however, change the bias phase! Then, slowly increase magnitude of the bias vibration until the entire object goes black, that is, when the first null of J_o occurs. At this point, the value of B is 2.40438, which is the argument of the first zero of the J_o , as shown in Fig. 7.2 and Table 7.1. Record the voltage output of the bias modulation controller for this condition and reset it by a scaling factor. The scaling factor is the desired magnitude of the bias vibration (e. g., $\pi/3$) divided by 2.40438. The phase of this bias vibration should be recorded; it corresponds to the positive-shift modulation. This completes calibration of the magnitude and the phase of the bias vibration. At this time, the sequence of the three holograms can be recorded. Before this is done, however, the bias excitation should be turned off, the object excitation should be turned on, and the excitation magnitude should be adjusted to the desired level.

When the desired object excitation is achieved, the first time-average hologram is recorded without the bias excitation; this is the zero-bias modulation. Then, the second hologram is recorded after switching on the bias excitation with the magnitude and phase as set

above; this is the positive-shift bias modulation. Finally, the phase of the bias excitation is shifted 180° with respect to that used during recording of the second hologram, the bias magnitude is kept the same, and the third hologram is recorded; this is the negative-shift bias modulation. Irradiances of the three time-average holograms recorded in this way are represented by Eqs 8.73 to 8.75, respectively. Note that the bias vibration should be recalibrated for each vibration frequency of the object.

8.4. Representative applications of the EOH system

The EOH procedures discussed in this chapter were implemented and representative results of this implementation are included in this section and in Appendices A to F.

8.4.1. Development of an automated fringe unwrapper

It should be noted that implementation of the EOH required development of a new method for unwrapping two-dimensional periodically discontinuous phase data generated by the EOH system while recording images of the objects being investigated. Detailed description of the method is given in Appendices B to D.

The method, foundations of which lie in the minimization of the energy of the surface determined by the unwrapped data, fits planar surface patches to EOH acquired data, then uses the parameters of the planar patches to estimate the value of the pixel under consideration. At each pixel, a new value composed of the sum of the original value and an integral multiple of the magnitude of the phase discontinuity is assigned. Processing proceeds along an expanding wavefront originating from a seed point chosen as the reference for the measurements. The facet based fringe number selection method has been found highly reliable even for incomplete, noisy data.

The phase unwrapping method is based on the definition of the energy of a surface as being proportional to the change in slope over a surrounding neighborhood. Since full field iterative approaches were deemed to be inappropriate for the inherently sequential problem of assigning fringe orders, techniques for estimating surface characteristics based on a set of known neighbors' values seemed the best approach to pursue. Facet based surface modeling provides a means of estimating an unknown value at a given location based on known values of its neighbors. The facet model was generalized to work on the sparse, weighted neighborhoods available in the unwrapping problem to construct the facet based phase unwrapper. Energy minimization was accomplished by finding a complete set of fringe order assignments over the non-zero weighted locations such that no other arrangement of assignments can be found to give a smaller total deviation of the surface from planarity. As such, the energy minimization

approach gave a solid framework for the construction of the phase unwrapper developed during this project. The preliminary results obtained using this unwrapper show great promise for future applications.

8.4.2. Determination of three-dimensional displacements by EOH

Typical results obtained using the EOH system with three cameras are shown in Figs 8.11 to 8.14. All interferograms shown in these figures, as well as those included in Appendices A to F were produced electronically using the EOH system developed during this project.

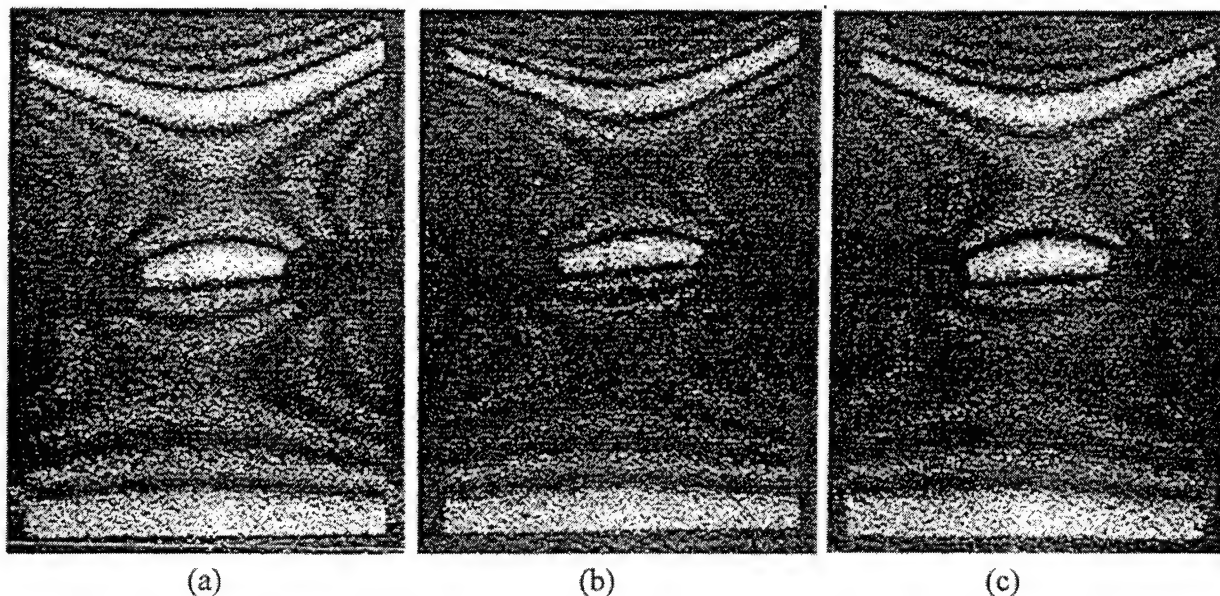


Fig. 8.11. Cantilever plate vibrating at its third flexure mode, three non-coplanar EOH images simultaneously recorded by: (a) camera-1, (b) camera-2, and (c) camera-3.

It should be noted that the three camera EOH system, developed during this project, acquires the three non-coplanar images, Fig. 8.11, simultaneously, one image per each camera, respectively. The interferometric data are processed electronically to produce wrapped (i. e., discontinuous) phase distributions, Fig. 8.12. These phase distributions are, in turn, unwrapped to generate (continuous) phase maps, Fig. 8.13, representing the digitally acquired images. Finally, the set of three phase maps, corresponding to the specific loading condition of the object being studied, is processed electronically to obtain the three-dimensional displacement fields, Fig. 8.14. This figure shows primary displacement component in the z -direction, with negligible x - and y -components of the displacement, indicating out-of-plane (transverse) vibration of the plate.

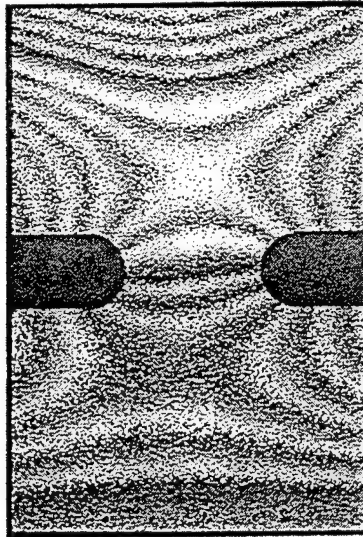


Fig. 8.12. Typical wrapped phase, corresponding to the EOH image of Fig. 8.11a.

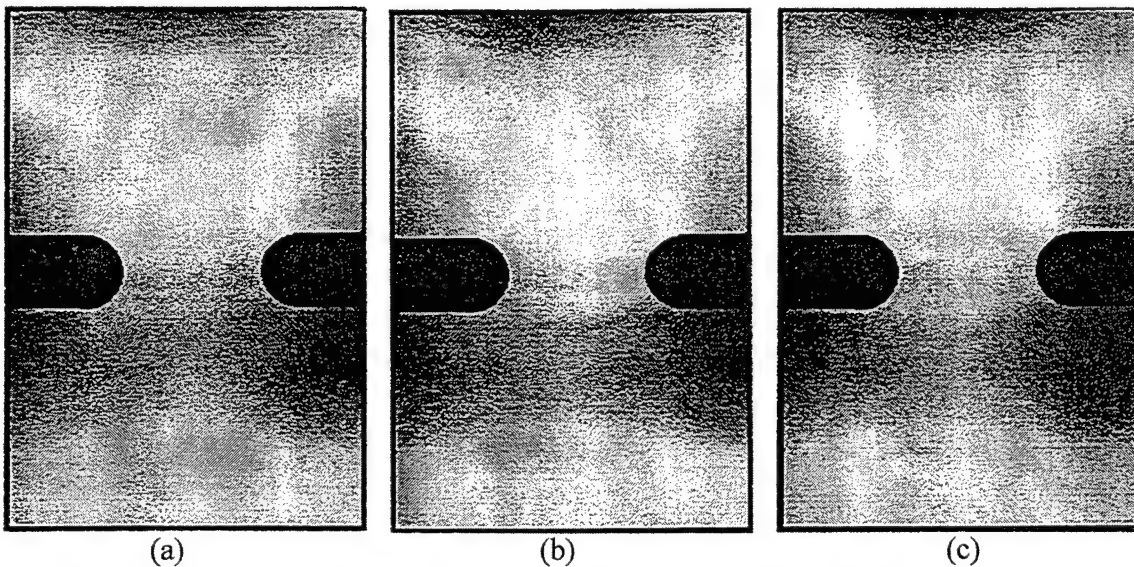


Fig. 8.13. Unwrapped phase maps, corresponding to the EOH images of Fig. 8.11, as recorded by: (a) camera-1, (b) camera-2, and (c) camera-3.

8.5. Conclusions

The results presented in Section 8.4.2 and Appendices A to F show that the EOH system effectively records high quality electronic holograms of objects subjected to static and dynamic

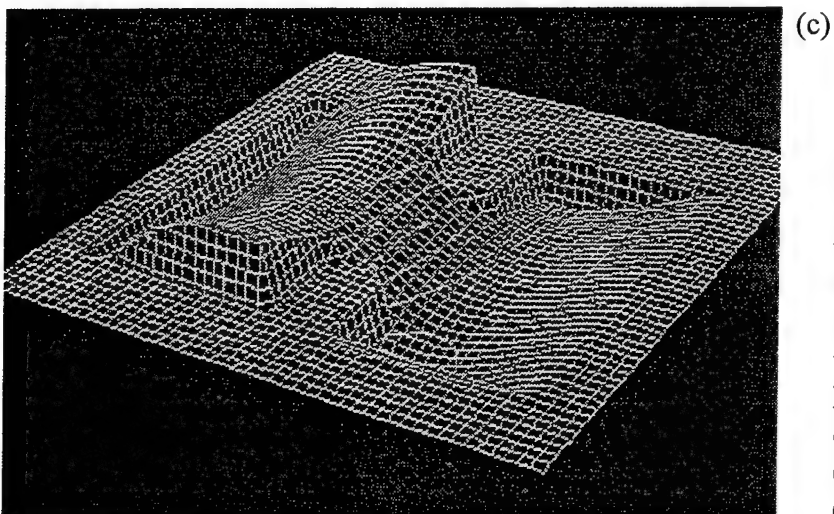
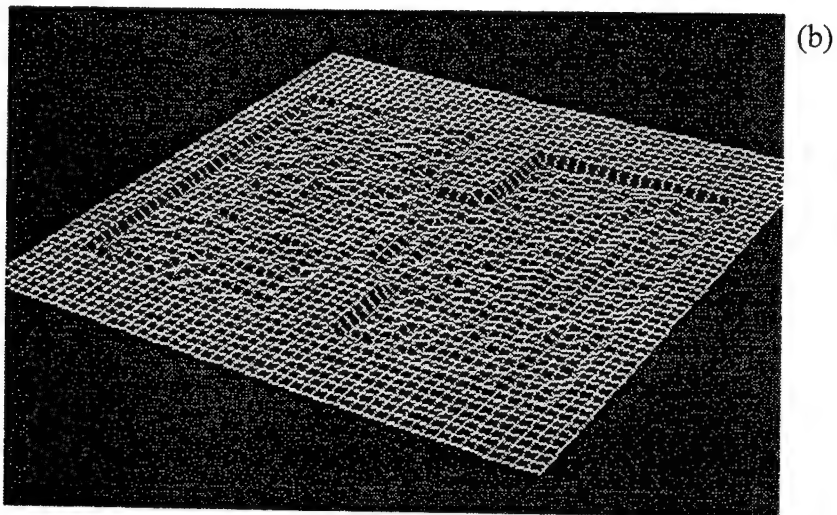
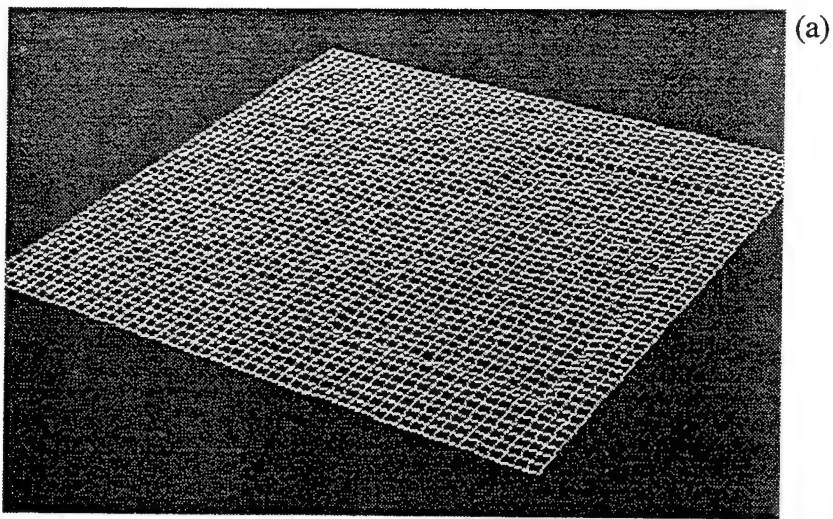


Fig. 8.14. Wire frame representation of the three-dimensional displacements computed from the unwrapped phase maps of Fig. 8.13:
(a) x -component,
(b) y -component, and
(c) z -component.

loads. These results also show that displacements can be extracted from the electronically recorded holograms using the procedures described in this report.

Using the EOH system, developed during this project, results are obtained in a truly totally automated manner. The interferometric information is recorded electronically at the rate of 30 frames per second, it is processed in a pipeline fashion, and produces results which have very high spatial density - currently at up to 512×480 points per image (frame). These results correlate well with the computational (i. e., FEM) predictions of the displacement fields of the objects subjected to static and dynamic loads.

The results presented in this chapter and in Appendices A to F demonstrate viability of the EOH system for avionics durability analysis and validation.

Continued work is needed to merge, within the host computer, the results obtained from the EOH system with the computational procedures of the FEM. This will result in a hybrid system which will allow totally automated, quantitative approach for avionics durability analysis and validation.

8.6. References

- 8.1. J. E. Berrang, "Television transmission of holograms using narrow-band video signal," *Bell System Technical Journal*, 49:879-887, 1970.
- 8.2. A. Makovski, S. D. Ramsey, and L. F. Schaefer, "Time lapse interferometry and contouring with television systems," 10:2711-2727, 1971.
- 8.3. K. A. Stetson and W. R. Brohinsky, "Electro-optic holography and its application to hologram interferometry," *Appl. Opt.*, 24:3631-3637, 1985.
- 8.4. S. Nakadate, "Vibration measurement using phase-shifting time-average holographic interferometry," *Appl. Opt.*, 25:4162-4167, 1986.
- 8.5. K. A. Stetson and W. R. Brohinsky, "An electro-optic holography system for vibration analysis and nondestructive testing," *Proc. SPIE*, 746:44-51, 1987.
- 8.6. K. A. Stetson and W. E. Brohinsky, "Fringe-shifting technique for numerical analysis of time-average holograms of vibrating objects," *J. Opt. Soc. Am.-A*, 5:1472-1476, 1988.
- 8.7. K. Creath, "Phase-measurement interferometry," in *Progress in optics*, E. Wolf, ed., North-Holland, Vol. 26, 1988.

- 8.8. R. J. Pryputniewicz and K. A. Stetson, "Measurement of vibration patterns using electro-optic holography," *Proc. SPIE*, 1162:456-467, 1989.
 - 8.9. R. J. Pryputniewicz, "Automated systems for quantitative analysis of holograms," *SPIE-IS8*:215-246, 1991.
 - 8.10. R. J. Pryputniewicz, "Holographic and finite element studies of vibrating beams," *Proc. SPIE*, 599:54-62, 1985.
 - 8.11. R. L. Powell and K. A. Stetson, "Interferometric vibration analysis by wavefront reconstruction," *J. Opt. Soc. Am.*, 55:1593, 1965.
 - 8.12. B. Ineichen and J. Mastner, "Vibration analysis by stroboscopic two-reference-beam heterodyne holographic interferometry," *Optics Applied to Metrology*, SPIE-210:207-212, 1980.
 - 8.13. K. A. Stetson, "Method of vibration measurements in heterodyne interferometry," *Opt. Lett.*, 7:233-234, 1982.
 - 8.14. P. Hariharan and B. F. Oreb, "Stroboscopic holographic interferometry: application of digital techniques," *Opt. Commun.*, 59:83, 1986.
 - 8.15. R. J. Pryputniewicz, "Vibration studies using heterodyne hologram interferometry," *Industrial Laser Interferometry II*, SPIE-955:154-161, 1988.
 - 8.16. K. A. Stetson, "Effects of beam modulation on fringe loci and localization in time-average hologram interferometry," *J. Opt. Soc. Am.*, 60:1378-1384, 1970.
-

9. ELECTRONIC SHEAROGRAPHY

Design optimization of the load resisting structures requires analysis of stresses in their components. These stresses are related, via the governing equations, to the structural components' boundary, initial, and loading conditions, their dimensions, geometries, and material properties. The governing equations also relate the stresses to surface strains and curvatures, which, in turn, are related to the first and the second spatial derivatives of displacement, respectively.

One way to obtain the derivatives necessary to analyze stresses in the structures is by differentiation of displacements that these structures undergo in response to the applied loads. Differentiation, however, is very laborious and, in general, is a source of considerable errors. The magnitude of the differentiation errors depends on the accuracy with which the displacements are measured.

The most desirable way, however, to obtain the displacement derivatives, is to measure them directly, without differentiation of the displacements. Although direct mechanical differentiation is possible, its accuracy is not adequate to satisfy the measurement requirements. However, various approaches, based on optical methodologies, have been advanced successfully¹.

In 1954, a reflective moiré method has been presented and allowed direct measurements of the displacement derivatives². However, in order for the method to work, a cylindrical grating had to be used and the measured surfaces of the test specimen had to be of mirror quality. In the mid 1960's, this method was improved when the cylindrical grating was replaced by a planar grating³. In 1970, the method was further improved by using a projected grating which allowed selection of the measurement sensitivity⁴. However, the method still required mirror like surface preparation of the specimen, which was a handicap.

The handicap of the reflective moiré method has been overcome, in an elegant way, in 1974, when Hung and Taylor proposed a new method⁵, which they called *speckle-shearing interferometry*. This method does not require that the surfaces of the specimens be of mirror quality. In fact, it requires that the measured surfaces be optically rough so that the coherent light scattered by them interferes randomly to form alternating bright and dark patches. These patches are known as *speckles*, and these, in turn, form *speckle patterns*. The speckle patterns give a grainy appearance to the surface illuminated by a coherent light. This grainy appearance is known as the *speckle effect*.

In the speckle-shearing interferometry, double-exposure interferograms are made recording changes in the speckle patterns, in response to the corresponding changes in the applied loads⁵⁻⁸. At the time the method was proposed, these recordings were made by using a shearing mechanism which comprised of pieces of glass installed in front of an imaging lens. Also, the sheared images were recorded in high resolution photographic media. This process was laborious, time consuming, and not suitable for real-time applications.

Current trend in the speckle-shearing interferometry is to perform all of its operations electronically. That is, the trend is to electronically: 1) record the interferometric data, 2) store these data, 3) process them, and 4) display the results in real-time. Because in its current implementation each operation of the method is performed electronically, this method is known as *electronic shearography*.

The same trend toward direct electronic recording and processing of the interferometric data is evident in the methods of hologram interferometry. As a result, the method of *electronic holography* has evolved.

In the following sections, fundamentals of the electronic holography and electronic shearography are outlined, their implementation is discussed, and representative results, obtained by working these systems side by side, are presented.

9.1. Electronic holography

Electronic holography, also known as Electro-Optic Holography (EOH), or TV holography, measures irradiances produced by mutual interference of the object and the reference fields recorded electronically by a CCD camera⁹⁻¹², see also Chapter 8. These measurements can be made either under static or dynamic loading conditions¹²⁻¹⁴. The static measurements are implemented using the double-exposure hologram interferometry, while the dynamic measurements are implemented by the time-average method. Processing of this interferometric information and display of the results are carried out concomitantly with measurements of the irradiances, as discussed in Chapter 8.

The image of a loaded object, in the case of the electronic recording of a double-exposure hologram, can be described by the irradiance distribution for the $n - th$ sequential frame, at the detector array of a CCD camera, as

$$I_n = I_o + I_r + 2A_o A_r \cos(\Delta\phi + \Omega + \Delta\theta_n) \quad , \quad (9.1)$$

where the coordinates x and y were omitted for simplification, I_o and I_r are the irradiances of the object and the reference fields whose amplitudes are A_o and A_r , respectively, $\Delta\phi$ is the phase difference between the two fields, $\Delta\theta_n$ is the $n - th$ finite phase step imposed on the reference beam between the sequential frames, and Ω is the fringe-locus function, constant values of which define fringe loci on the surface of the object. The irradiance for the unloaded object is described by an equation similar to Eq. 9.1, except that the fringe-locus function equals zero, in this case.

Operating on the irradiances given by Eq. 9.1, corresponding to a sequence of four frames recorded with a known phase step imposed between each frame, we obtain an electronic hologram that is modulated by a fringe pattern, FP , which is described by the equation¹⁴

$$FP = 32A_o^2A_r^2(1 + \cos \Omega) \quad (9.2)$$

The fringe-locus function, appearing in Eq. 9.2, is defined as

$$\Omega = \mathbf{K} \cdot \mathbf{L} \quad (9.3)$$

where \mathbf{L} is the unknown displacement of the object and \mathbf{K} is the sensitivity vector defined as a difference between vectors \mathbf{K}_2 and \mathbf{K}_1 , specifying the directions of illumination and observation in the holographic setup, that is, $\mathbf{K} = \mathbf{K}_2 - \mathbf{K}_1$, as discussed in Chapter 2. Since the sensitivity and displacement vectors have three Cartesian components, Eq. 9.3 can be rewritten as

$$\Omega = K_x L_x + K_y L_y + K_z L_z \quad (9.4)$$

Procedures for the solution of Eq. 9.4 for the components of \mathbf{L} have been worked out and are discussed in Chapter 4 and in References 9.15 and 9.16.

Quantitative data on the object displacements are obtained by processing the images using procedures of Reference 9.14 and of this chapter. These procedures extract data from electronically recorded holograms by a method of optical fringe shifting¹⁰.

9.2. Electronic shearography

Electronic shearography is an interferometric technique that permits full field observation of surface displacement derivatives. It employs an image shearing device which brings two neighboring points on the object surface to interfere in the image plane. By comparing the interference patterns before and after deformation, a fringe pattern depicting derivatives of the surface displacement is produced.

Electronic shearography is a computerized process that depends on concomitant processing of interferometric data to generate fringe patterns representing derivatives of the surface displacements. A typical configuration of the electronic shearography system is shown in Fig. 9.1. In this configuration, the object is illuminated by a coherent laser light from a point source, PSI. The light modulated by interaction with the object is imaged by the lens IL. The imaged light is split into two parts by a cube beamsplitter (CBS). In the configuration shown in Fig. 9.1, one of these parts is sheared by SA, while the other part is modulated by imposition of discrete phase steps by PS. Then, both beams are combined and redirected by the CBS to collinearly impinge on the sensing element of the CCD camera. The irradiance distribution recorded by the camera is described by Eq. 9.1, which defines a speckle pattern that is unique for a given set of the shearogram recording conditions.

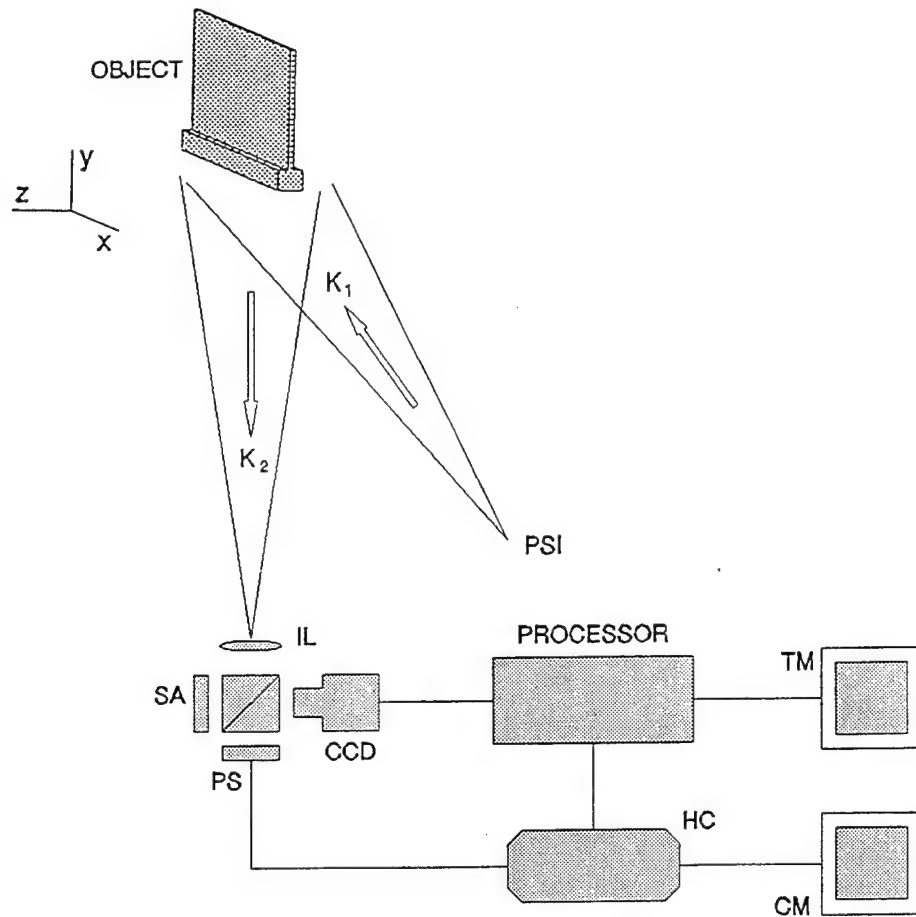


Fig. 9.1. A typical configuration of the electronic shearography system: PSI is the point source of illumination, K_1 and K_2 are the vectors defining the directions of illumination and observation, respectively, IL is the imaging lens, SA is the shear adjusting mirror, PS is the phase stepper controlled mirror, CCD is the TV camera, TM is the TV monitor, HC is the host computer, and CM is the computer monitor.

In the configuration shown in Fig. 9.1, the IL, CBS, SA, PS, and CCD comprise an *image shearing camera*. The role of the image shearing camera, in the electronic shearography process, is to bring the light rays scattered from one point on the surface of the object to interfere with those scattered from a neighboring point. Since the object is illuminated by a laser light, the rays from the two points interfere producing a speckle pattern. When the object is displaced and/or deformed, a relative displacement between the two points occurs. This relative displacement induces a corresponding phase change that modifies the interference speckle pattern. That is, the speckle patterns change as the object loading conditions change. Comparison of the two slightly different speckle patterns results in moiré fringes that depict the derivatives of surface displacement with respect to the direction of shearing.

The procedure for the electronic recording, processing, and display of the interferometric data in electronic shearography is the same as that described in Section 9.1 and Chapter 8.

If the shearing direction is parallel to the x -axis, then, two points separated in the x -direction are brought to interfere. If the magnitude of this shearing is s_x , the derivatives (with respect to x) of the displacement vector \mathbf{L} can be related, using Eq. 9.4, to the fringe-locus function and the sensitivity vector as

$$\Omega = (K_x \frac{\partial L_x}{\partial x} + K_y \frac{\partial L_y}{\partial x} + K_z \frac{\partial L_z}{\partial x}) s_x \quad (9.5)$$

Similarly, if the shearing is in the y -direction, the derivatives (with respect to y) of \mathbf{L} can be related to Ω and \mathbf{K} as

$$\Omega = (K_x \frac{\partial L_x}{\partial y} + K_y \frac{\partial L_y}{\partial y} + K_z \frac{\partial L_z}{\partial y}) s_y \quad (9.6)$$

where s_y is the magnitude of the shearing in the y -direction.

There are a number of implementations of Eqs 9.5 and 9.6 in specific applications. The application of particular interest to this study relates to characterization of the out-of-plane displacements of a cantilever plate. In this case, the in-plane displacement derivatives are negligible in comparison with the out-of-plane displacement derivative. Therefore, recalling that the fringe-locus function is proportional to the fringe order, n , with the proportionality constant equal to 2π , it can be shown, using Eq. 9.6, that

$$n = \frac{1}{2\pi} K_z \frac{\partial L_z}{\partial y} s_y \quad (9.7)$$

In general, the shearograms are recorded using a setup having the directions of illumination and observation optimized for the specific application. That is, the sensitivity vector is known and remains invariant during the sequential recording of the shearograms. Furthermore, a specific loading condition also remains invariant during the data acquisition sequence. As a result, using the equations defining elastic behavior of a cantilever plate in bending, we can show that the out-of-plane displacement derivative is given by the relationship

$$\frac{\partial L_z}{\partial y} = \frac{6F}{Eb^3h^3} y (2L - y) \quad (9.8)$$

which indicates that $\partial L_z / \partial y$, or the local surface slope at a specific position y on the cantilever plate, is uniquely defined by the magnitude of the loading force F , the dimensions L , b , and h of the plate, and the modulus of elasticity E of the plate's material. Clearly, the displacement derivative at a specific position y is invariant, for a given set of parameters defining the right hand side of Eq. 9.8.

The foregoing discussion indicates that the values of K_z and $\partial L_z / \partial y$, appearing in Eq. 9.7, are constant for a given application and a specific loading condition. Therefore, according to Eq. 9.7, the number of fringes seen during observation of a shearogram will be directly proportional to the magnitude of the shear s_y .

Starting with Eq. 9.5, we can also show that for a given application and a specific loading condition, the number of fringes seen during observation of a shearogram will be directly proportional to the magnitude of the shear s_x .

In the electronic shearography system, described in this chapter, the magnitudes of s_x and s_y can be adjusted independent of each other. This feature allows convenient means for selection of measurement sensitivity, over a wide range of values, which is a particular advantage that the electronic shearography has over other optical measurement methods.

9.3. Representative results and discussion

Representative results, obtained during this study, are shown in Figs 9.2 to 9.10. These results are for the cantilever plate which was subjected to static and dynamic loads. The interferograms corresponding to these loads were recorded using the electronic holography and the electronic shearography systems working side by side.

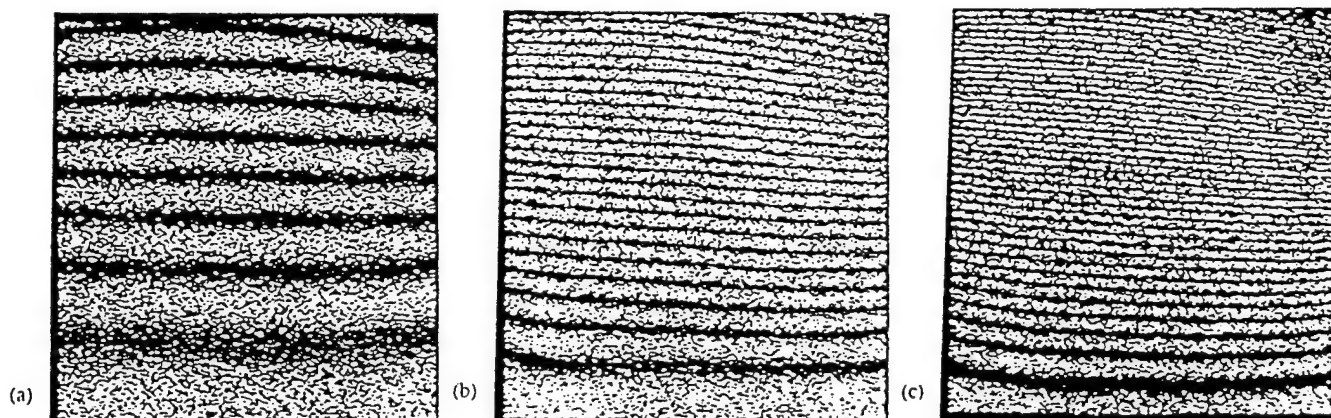


Fig. 9.2. Double-exposure electronic holograms of the cantilever plate in bending by a static load of: (a) 1 gram, (b) 3 grams, and (c) 5 grams.

Figure 9.2 shows reconstructions of three double-exposure electronic holograms of the cantilever plate under static loads which ranged from 1 gram to 5 grams in 2 gram increments, respectively. Note that the number of fringes increases from approximately 8, in Fig. 9.2a, to approximately 40, in Fig. 9.2c, as should be expected. In fact, the number of fringes determined directly from the electronic holograms correlated to within 0.1 fringe with the number of fringes estimated using the theoretical procedures based on the elastic deformation of the cantilever plate, under the static loading conditions for which the holograms of Fig. 9.3 were recorded.

This resulted in the correlation to better than 1% between the displacements determined from electronic holograms and those estimated theoretically.

The images shown in Fig. 9.2 indicate almost pure out of plane bending, except in the regions close to the free end of the plate, in the vicinity of the point of the force application. These changes can be related to the displacement derivatives, i. e., to the local surface slopes that can be detected by the electronic shearography.

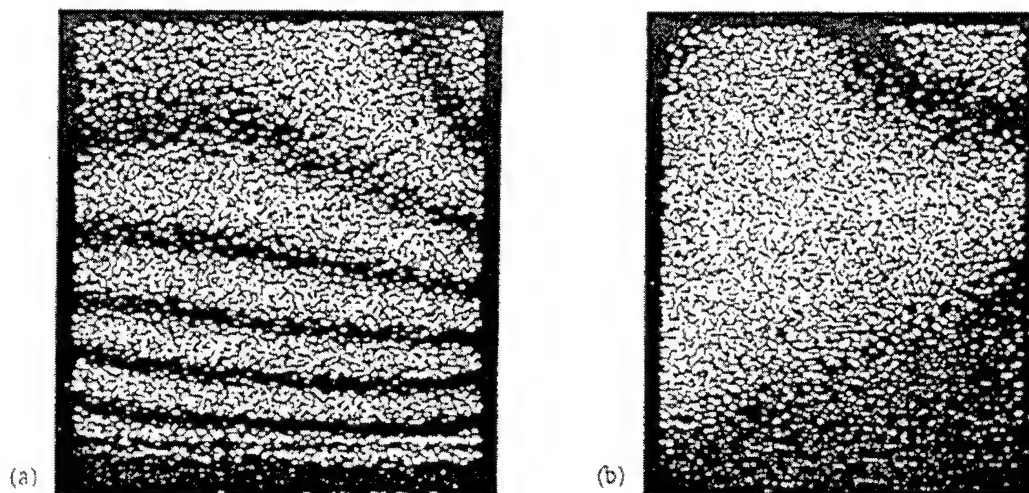


Fig. 9.3. Shearographic interferograms of the cantilever plate in bending by a static load of 5 grams: (a) $s_y = 15$ mm, (b) $s_x = 15$ mm.

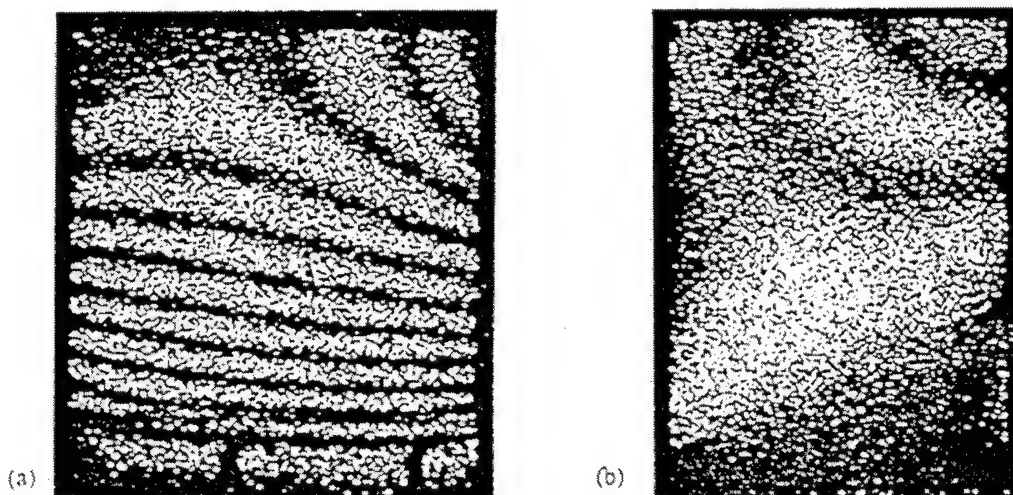


Fig. 9.4. Shearographic interferograms of the cantilever plate in bending by a static load of 5 grams: (a) $s_y = 25$ mm, (b) $s_x = 25$ mm.

Figures 9.3 and 9.4 show the shearographic interferograms, recorded for two different magnitudes of the shear, corresponding to the static loading condition of Fig. 9.2c. The

shearograms of Fig. 9.3 were recorded for the case of $s_x = s_y = 15$ mm, while those shown in Fig. 9.4 were recorded when $s_x = s_y = 25$ mm. These results clearly show that the number of fringes increased in proportion to the increase in the magnitude of the shear, which is in agreement with the arguments presented in Section 9.2. However, it should be noted that as the magnitude of the shear increases, so does the difference between the theoretically estimated local displacement derivatives and those determined directly from the electronic shearograms.

For the object and the loading conditions presented in this chapter, the displacement derivatives determined from the electronic holograms were lower than the theoretically estimated ones.

Figures 9.5 to 9.7 show the shearographic images for the cantilever plate loaded with a static load of 10 grams and the magnitudes of shear equal to 25 mm, 10 mm, and 3 mm, respectively.

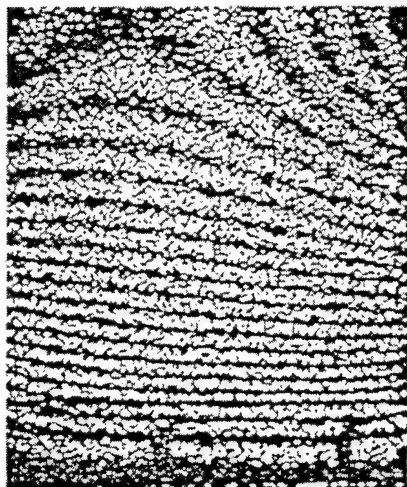
Comparison of Fig. 9.4 (static load of 5 grams) with Fig. 9.5 (static load of 10 grams), both of which were recorded with the shear of 25 mm, indicates doubling in the number of the shearographic fringes because of the doubling in the static loading force, in accordance with the discussion in Section 9.2. However, the magnitude of the local slope determined from these shearograms was approximately 16% lower than the slope estimated theoretically.

As the shear reduced, while maintaining a static load of 10 grams and holding other characteristic parameters constant, so did the difference between the magnitudes of the local slopes determined from the electronic shearograms and those estimated. For the case shown in Fig. 9.7 (shear equal to 3 mm), the corresponding difference was approximately 1%.

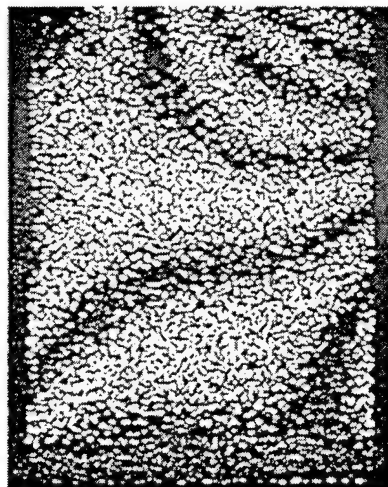
Although electronic shearography is primarily used to study structures under static, or quasi-static loads, it can also be very effective while studying dynamic behavior of resonating structures. Figures 9.8 and 9.9 show side by side results obtained by the electronic holography and the electronic shearography recording the cantilever plate (the same as that used to obtain results shown in Figs 9.2 to 9.7) resonating at 425 Hz and 1591 Hz, respectively. The holographic images vividly demark the mode shapes characteristic of the specific resonance frequency while the shearographic images show the displacement derivatives in the lateral directions parallel to the plane of the cantilever plate. Comparison of the holographic and the shearographic results shows good correlation.

9.4. Conclusions

In this chapter, viability of electronic shearography to study behavior of a cantilever plate under static and dynamic loading conditions was investigated, with reference to electronic holography (see Chapter 8) and a preliminary comparison of their respective results was made while the methods were working side by side. In particular, examination of parameters characterizing recording of images by electronic shearography was made.

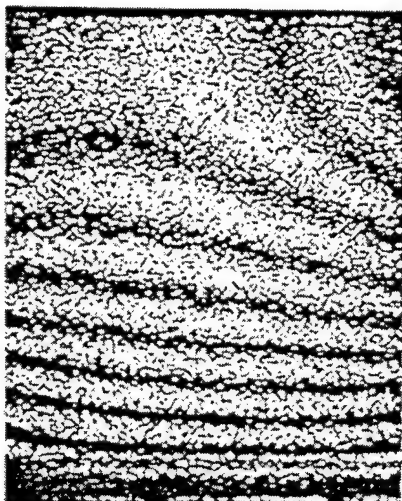


(a)

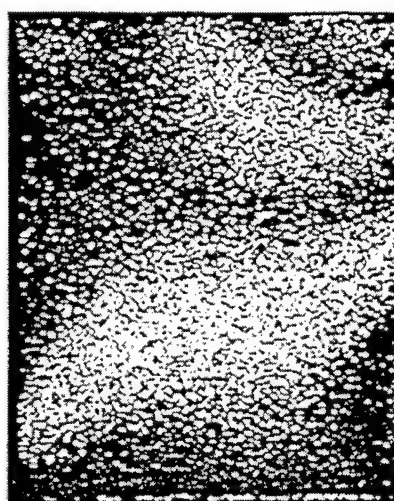


(b)

Fig. 9.5. Shearographic interferograms of the cantilever plate in bending by a static load of 10 grams: (a) $s_y = 25$ mm, (b) $s_x = 25$ mm.

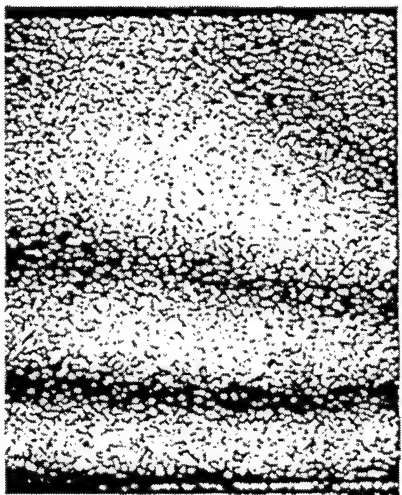


(a)

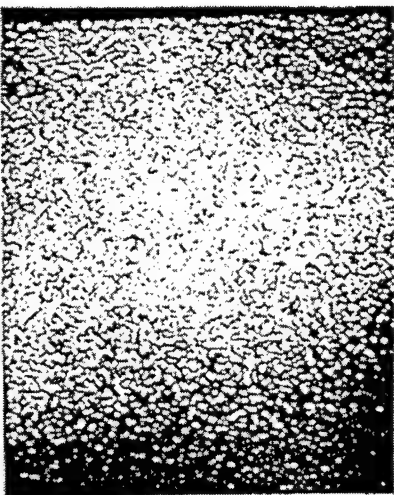


(b)

Fig. 9.6. Shearographic interferograms of the cantilever plate in bending by a static load of 10 grams: (a) $s_y = 10$ mm, (b) $s_x = 10$ mm.



(a)



(b)

Fig. 9.7. Shearographic interferograms of the cantilever plate in bending by a static load of 10 grams: (a) $s_y = 3$ mm, (b) $s_x = 3$ mm.

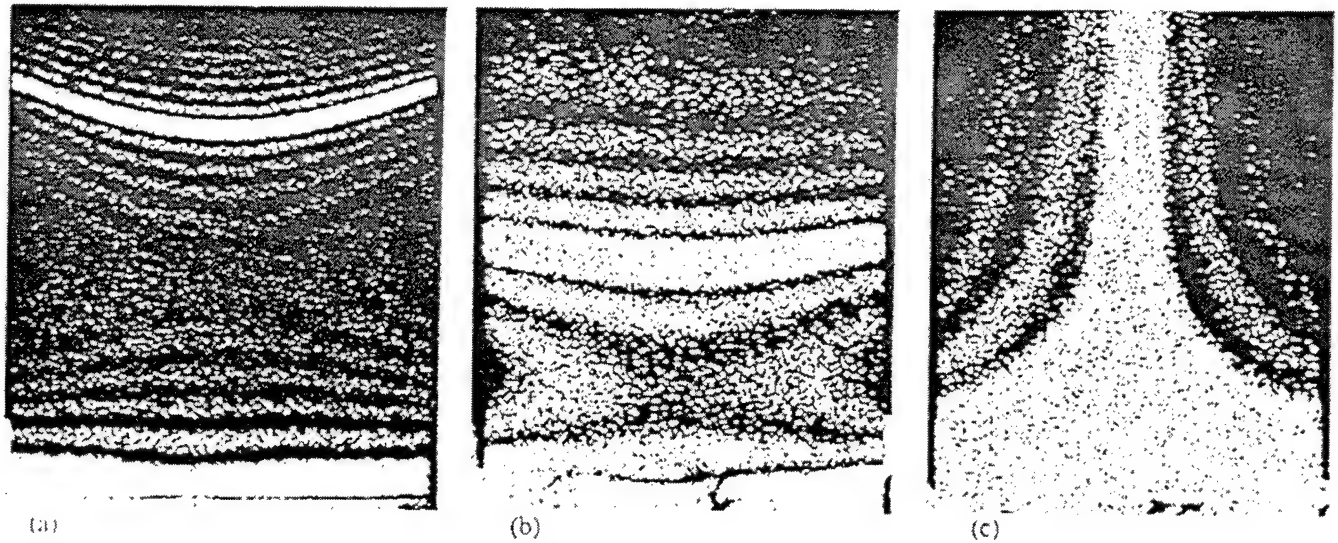


Fig. 9.8. Cantilever plate vibrating at 425 Hz: (a) the time-average electronic hologram, (b) the electronic shearogram displaying displacement derivative in the y-direction, and (c) the electronic shearogram displaying displacement derivative in the x-direction.

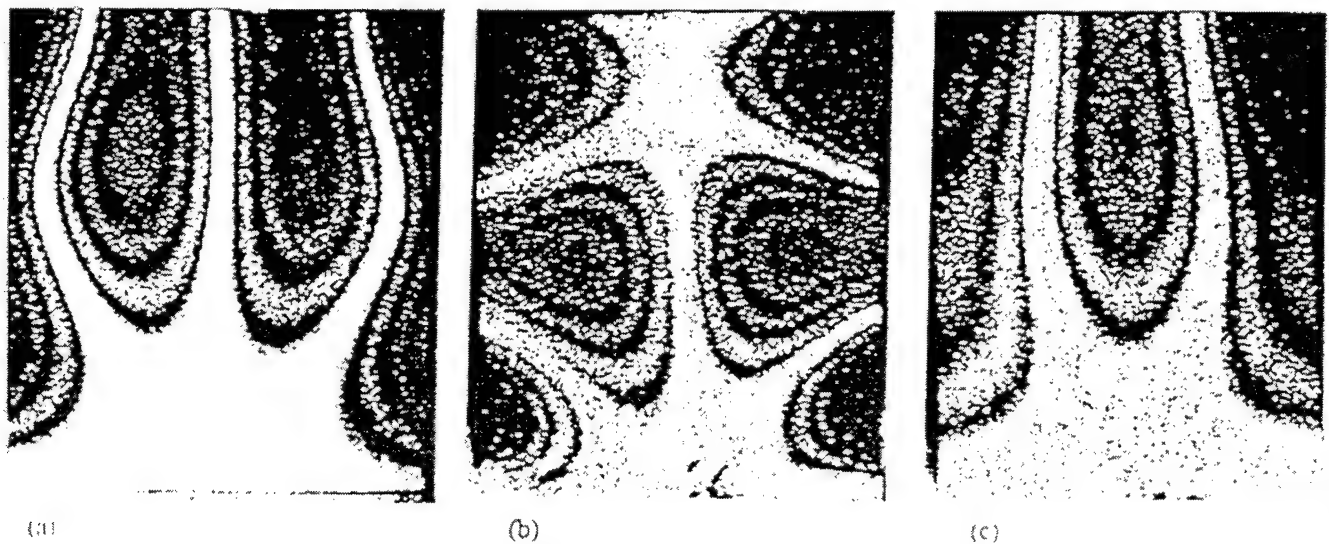


Fig. 9.9. Cantilever plate vibrating at 1591 Hz: (a) the time-average electronic hologram, (b) the electronic shearogram displaying displacement derivative in the y-direction, and (c) the electronic shearogram displaying displacement derivative in the x-direction.

The results shown in this chapter indicate that because of the electronic holography's inherent sensitivity, fringe frequencies become very high rapidly and often hinder determination of local deformations which are of interest. This obstacle is overcome, to a certain degree, by electronic shearography which is particularly suitable for determination of the local displacement derivative fields.

The results presented indicate that the accuracy in the shearographic determination of the local displacement derivatives depends on the magnitude of the shear introduced while recording the interferograms. In this study, shears ranging from 3 mm to 25 mm were used. The preliminary data show that the difference between the shearographic and the theoretical results decreases as the magnitude of the shear decreases, from approximately 16% for 25 mm shear to approximately 1% for the 3 mm shear.

In addition, this study demonstrates the viability of the electronic shearography for studies of objects under the condition of resonance. It is particularly interesting to see a side by side comparison of the fringe patterns produced electronically while imposing shears in the directions normal to the direction of the predominant component of the displacement vector and how they relate to the conventional mode shapes obtained by the electronic holography.

Work on side by side developments of electronic holography and electronic shearography will continue.

9.5. References

- 9.1. R. J. Pryputniewicz, "Electronic shearography and electronic holography working side by side," *Proc. SPIE*, 1821A:142-151, 1992.
- 9.2. F. K. Lightenberg, "The moiré method: a new experimental method for the determination of moments in small slab models," *Proc. SESA*, 12:83-98, 1954.
- 9.3. P. S. Theocaris, *Moiré fringes in strain analysis*, Pergamon Press, New York, pp. 249-250, 1969.
- 9.4. F. P. Chiang and J. Treiber, "A note on Lightenberg's reflective moiré method," *Exp. Mech.*, 10:537-538, 1970.
- 9.5. Y. Y. Hung and C. E. Taylor, "Measurement of slopes of structural deflections by speckle-shearing interferometry," *Exp. Mech.*, 14:281-285, 1974.
- 9.6. J. A. Leendertz and J. N. Butters, "An image-shearing speckle-pattern interferometer for measuring bending moments," *J. Phys. E: Sci. Instrum.*, 6:1107-1109, 1973.
- 9.7. Y. Y. Hung, "Shearography: a novel and practical approach for nondestructive inspection," *J. Nondestr. Eval.*, 8:55-67, 1989.
- 9.8. Y. Y. Hung, "Electronic shearography versus ESPI for nondestructive evaluation," *Proc. SPIE*, 1554B:692-700, 1992.

- 9.9. K. A. Stetson and W. R. Brohinsky, "An electro-optic holography system for vibration analysis and nondestructive testing," *Proc. SPIE*, 746:44-51, 1987.
 - 9.10. K. A. Stetson and W. R. Brohinsky, "Fringe-shifting technique for numerical analysis of time-average holograms of vibrating objects," *J. Opt. Soc. Am. - A*, 5:1472-1476, 1988.
 - 9.11. R. J. Pryputniewicz and K. S. Stetson, "Measurement of vibration patterns using electro-optic holography," *Proc. SPIE*, 1162:456-467, 1989.
 - 9.12. R. J. Pryputniewicz, "Electro-optic holography," in *Critical reviews of optical science and technology*, *SPIE*, CR47:148-174, 1993.
 - 9.13. R. J. Pryputniewicz, "Applications of electro-optic holography in vibration studies," *Proc. Spring Conf. on Exp. Mech.*, SEM, Bethel, CT, pp. 912-919, 1991.
 - 9.14. R. J. Pryputniewicz, "Static and dynamic measurements using electro-optic holography," *Proc. SPIE*, 1554B:790-798, 1991.
 - 9.15. R. J. Pryputniewicz, "Computer-aided fringe analysis," *Proc. SPIE*, 673:250-257, 1986.
 - 9.16. R. J. Pryputniewicz, "Hologrammetry: systems and applications," Ch. 14 in *Non-topographic photogrammetry*, H. M. Karara, editor-in-chief, 2nd ed., Am. Soc. for Photogramm. and Remote Sensing, Falls Church, VI, pp. 203-230, 1989.
-

10. HYBRID APPROACH TO DEFORMATION ANALYSIS

Current trends in development of components, structures, and systems place unprecedented requirements on their designers. To satisfy these demands, new, highly efficient materials and structural designs are being employed and integrated utilization of the most sophisticated technologies is being made. This chapter addresses some of the pertinent issues relating to this integration and explores how to take advantage of the analytical, computational, and experimental solution methodologies in relation to a given problem. More specifically, a hybrid approach to deformation analysis is described, based on recent developments in merging, or unifying, of the finite element method with experimental methodologies, and especially with optical metrology. This approach emphasizes the analogy between the methodologies used and employs them to obtain solutions that may not have been otherwise obtainable, to ease the existing solution procedures, or to attain improvements in the results. The chapter begins with an introduction to the methodologies used, continues with a discussion of the analytical fundamentals, and concludes with a presentation of representative results.

10.1. ACES methodology

Continued demands for development of optimum and reliable designs have led to advancement of a number of solution methodologies. These methodologies can, in general, be classified as Analytical, Computational, and Experimental Solutions, and constitute, what this author calls, **ACES** approach to design problems, or, in fact, any type of problems which can be solved either by analytical, or computational, or experimental method, or a combination of these methods; depending on the needs of a specific problem, this combination involves at least two methodologies from one or more of the three classifications. Certainly, each methodology has a considerable advantage over the others, for a given class of problems. In many cases, the data furnished by one methodology have been utilized by the other methodologies to make the solutions possible¹⁻¹⁰.

Analytical methodologies are characterized by *exact* closed form solutions and make use of infinitesimal elements. Computational methodologies make use of finite size elements in discretization of the physical domain and provide *approximate* solutions. Experimental methodologies employ, in general, *actual* objects subjected to *real* operating conditions, to provide information on responses of the objects to the applied loads.

Because of increased availability and capability of the number crunching equipment, in recent years, formulation of problems has shifted from exact to approximate. This shift has also developed an increasing dependence on the experimental methodologies to "*bridge the gap*" between the other two methodologies. In fact, the need for processes for unifying, or merging, some or all of these methodologies was recognized a number of years ago. One of these processes, with which this author is most familiar, was initiated in 1972 and resulted in the *International Invitational Symposium Series* dedicated to *Unification of Solution Methodologies*.

The theme of each symposium in this series relates to a topic of current interest at the time of the symposium. For example, the 1991 Symposium dealt with unification of finite element methods through parallelism in analysis and experimentation¹¹, while the 1993 and 1995 Symposia addressed unification of analytical, computational, and experimental solution methodologies in micromechanics and microsystems^{12,13}. Continued trends in unification of the solution methodologies indicate that in spite of recent advances in number crunching equipment, which have drawn considerable attention to the computational methodologies, including finite difference methods (FDM), finite element methods (FEM), and boundary element methods (BEM), the importance of experimental and analytical methodologies has not diminished.

Out of the computational methodologies available today, demands for optimum and reliable design are, to a great extent, satisfied by application of FEM. In these applications, the FEM are used to solve problems for which exact solutions are nonexistent, or, at the best, are very difficult to obtain. Also, the FEM are the only way to analyze complex three-dimensional structures, response of which to applied load system cannot be predicted in any other way. However, results obtained by the FEM are subject to the boundary conditions used, rely greatly on the accurate knowledge of material properties, depend on accurate representation of geometry of the objects being modeled, and are sensitive to the shape and size of elements employed in modeling. The information necessary to "run" the finite element models is obtained either from published data, or from design specifications, or from experimental studies, or from a combination of any of these sources.

As is often the case with new and powerful methods, the FEM have been over-used, perhaps even misused. Only recently have we begun to realize that virtually all versions of FEM contain shortcomings. As a result, the need for unifying (merging, coupling, or hybridizing) FEM in the physical and time domains with other methods has begun to manifest itself¹⁴⁻¹⁷. This need has led to merging of FEM with experimental methods. Initially, this merging involved "electro-mechanical" approaches to experimentation via, e. g., strain gage and accelerometer methods. Then, optical methods have begun to play more and more prominent role in this merging. One of these merging efforts is based on unification of the optical methods, employing laser experimentation, with FEM in space and time simultaneously^{18,19}.

In the following, the FEM is briefly described with emphasis on unification in error analysis and in evaluation of element matrices. Next, fundamentals of laser experimentation are introduced based on the modern methods of hologram interferometry. Then, a unified, or hybrid, approach to solution of specific problems is discussed and illustrated with representative results.

10.2. Finite element method

The finite element method²⁰⁻²⁵ is a computational analysis technique for obtaining approximate solutions to a wide variety of engineering problems. In a continuum problem of any dimension the *field variables*, such as displacement, stress, temperature, etc., possess infinitely many values because they are functions of each generic point in the body, or solution region.

Consequently, the problem is one with an infinite number of unknowns. The finite element discretization procedures reduce the problem to one of a finite number of unknowns by dividing the problem into *elements* and by expressing the unknown field variables in terms of *assumed approximate functions* within each element. The approximate functions, sometimes called *interpolation functions*, are defined in terms of the values of the field variables at specified points called *nodes* or *nodal points*. Nodes usually lie on the *element boundaries* where adjacent elements are considered to be *connected*. In addition to *boundary nodes*, an element may have a number of *internal nodes*. The nodal values of the field variables and the interpolation functions for the elements define the behavior of the field variables within the elements. For the finite element representation of a problem, the nodal values of the field variables become the unknowns. Once these unknowns are found, the interpolation functions define field variables throughout the assemblage of elements.

Clearly, the nature of the solution and the degree of approximation depend not only on the size and number of the elements used, but also on the interpolation function selected. As one would expect, we cannot choose the functions arbitrarily, because certain compatibility conditions must be satisfied. Often, functions are chosen so that the field variables, or their derivatives, are continuous across the adjoining element boundaries.

An important feature of FEM, that sets it apart from other computational methods, is its ability to formulate solutions for individual elements before putting them together to represent the entire problem. This means that if we are treating a problem in stress analysis, we can find the force-displacement, or stiffness, characteristics of each individual element and then assemble the elements to find stiffness of the whole structure. In essence, the solution of a problem reduces to a process of considering a series of greatly simplified problems. At the end of this process, field variables are known and constitute an approximate solution to the problem. However, a very important issue relating to the FEM solution, or, in general, to any approximate solution, is the accuracy of the results, which relates to the unification in error analysis, as discussed in Section 10.2.1.

10.2.1. Unification in error analysis

How good are the approximate results? What are the upper bounds of errors? Such questions have often been asked though answers have not always been found¹⁹. Nevertheless, problems were solved and systems were put into service. The easiest response to these questions has always been the use of a factor of safety (FS) big enough to account for all uncertainties. How big should it be has, of course, been another question. If it was big enough, the engineer was successful; if not, the engineer was doomed.

An alternative approach to these questions has been to experiment (full scale, half scale, whatever) before putting the system into service. Recognizing that things designed and built yesterday were not as complex as those designed and built today, experimentation and the choice

of FS were relatively easier tasks then than they are today. In recent years, however, the availability of computational tools, both in respect to methodology and equipment, has enabled engineers to design very complicated systems by successfully solving very difficult problems. Nevertheless, one question raised above still remains: *how good are the results?*

Development of fully automatic self-adaptive processes is one of the most crucial needs of finite element computations today. To achieve this, one must not develop algorithms based on the computed information alone. Instead, information based on actual measurements, made during the processing, must also be incorporated into the algorithms. These measurements, or observations, should be employed not only for verification of the computed values of the unknown function, as is often done, but also for estimating or even controlling errors.

When discretizing the domain, engineers generally pay attention to certain regions of the domain which are critical or very sensitive to changes in parameters. Localized error norms in these regions may fluctuate drastically, or even diverge, as in the case of ill-conditioned systems of equations. If u_c and u_m represent the computed and the measured values of the unknown function, respectively, then the error e_c or e_m , corresponding to these values, can be defined as either

$$e_c = u_c - u \quad \text{or} \quad e_m = u_m - u, \quad (10.1)$$

where u is the correct answer. Moreover, if the measurements are of very high accuracy and precision, then it is suggested that e_m be employed for error estimates and for adaptive processes in the critical regions of the domain rather than e_c .

In structural mechanics problems, the energy of the error, η , corresponding to a particular solution over a region A , can be represented as¹⁹

$$\eta = \int_A e r dA, \quad (10.2)$$

where r represents the residual forces. One way to obtain a possible refinement on u is by using a hierarchic mode N_{p+1} , i. e., the finite element basis function for the polynomial of degree $p+1$. Since the energy absorbed by this additional mode is assumed to be directly proportional to the corresponding force and inversely proportional to the stiffness, Eq. 10.2 can be written, for the i -th element, as

$$\eta_i^2 = \frac{(\int N_{p+1} r_i dA_i)^2}{S_{ii}^{p+1}}, \quad (10.3)$$

where r_i represents the residual forces, N_{p+1} denotes the mode for the polynomial of degree $p+1$, and S_{ii} are the elements of the stiffness matrix. Equation 10.3 suggests that among all the available N_{p+1} solutions the one that gives the greatest error decrease should be chosen as the

new refinement. One should, however, make sure that N_{p+1} is not orthogonal, otherwise $\eta_i = 0$ may lead to a deceptive estimate of error.

10.2.2. Unification in evaluating element matrices

Experimental techniques can be used not only for error estimates, but also for direct evaluation of the element stiffness and/or flexibility coefficients. In particular, when an element's shape is irregular, i. e., when it possesses curved lines and surfaces, which is often the case at the free boundaries, even using higher order isoparametric elements may not yield the accuracy desired. The mesh refinements for those elements would, on the other hand, increase the number of equations to be solved, thereby decreasing the accuracy of the results. In the case of solid elements, whether one-, two-, or three-dimensional, the stiffness matrices can be obtained experimentally. For this we shall refer to Castigliano's theorem in tensor notation²⁶, i. e.,

$$p^{iq} = \frac{\partial W}{\partial u_{iq}} , \quad (10.4)$$

where

$$W = \frac{1}{2} p^{iq} u_{iq} , \quad i = 1, 2, \dots, n , \quad q = 1, 2, 3 \quad (10.5)$$

represents strain energy stored in the element. Substituting Eq. 10.5 into Eq. 10.4 and keeping in mind that

$$\frac{\partial u_{jr}}{\partial u_{iq}} = 1 \quad \text{for } i, q = j, r , \quad \text{respectively, and zero otherwise,} \quad (10.6)$$

the results is

$$p^{iq} = \frac{\partial p^{iq}}{\partial u_{jr}} u_{jr} , \quad (10.7)$$

which can be rewritten as

$$p^{iq} = S^{ijqr} u_{jr} . \quad (10.8)$$

The quadrivalent tensor of Eq. 10.8 represents the stiffness matrix of the element. Furthermore, Eq. 10.8 indicates that the stiffness, or flexibility, matrix coefficients can be determined by observing, or measuring, the changes in p^{iq} with respect to changes in u_{jr} , or vice versa. Note that in Eq. 10.8 i and j represent the nodes, i. e., the integration points in the standard FEM, of the element, while q and r denote the directions of (local and global) coordinate axes.

Today, there are a number of procedures that can be used to evaluate the stiffness, or flexibility, matrix coefficients of an element of any shape and material. In this chapter, however, the procedures utilizing optical techniques are emphasized. Since the measurements are continuous, i. e., they are independent of time and path, the stiffness matrix coefficients for those elements, highly nonlinear both in respect to time and path, can be determined at any increment of time and/or load. These coefficients can then be incorporated into the global S prior to the solution procedure.

Let us assume that the overall stiffness matrix is partitioned as follows:

$$\begin{bmatrix} p_1 \\ p_2 \\ p_3 \end{bmatrix} = \begin{bmatrix} [S_{1,1}]_{c,m} & [S_{1,2}]_{c,m} & [S_{1,3}]_c \\ & [S_{2,2}]_{c,m} & [S_{2,3}]_c \\ \text{symm.} & & [S_{3,3}]_c \end{bmatrix} \begin{bmatrix} u_{1,c} \\ u_{2,c} \\ u_{3,m} \end{bmatrix}, \quad (10.9)$$

where the subscripts c and m identify the *computed* and *measured* quantities, respectively, and where, in certain portions of the stiffness matrix, the measured and computed elements are coupled and identified with subscripts c,m . Equation 10.9 can be further reduced to

$$\begin{bmatrix} p_1 - [S_{1,3}]_c u_{3,m} \\ p_2 - [S_{2,3}]_c u_{3,m} \end{bmatrix} = \begin{bmatrix} [S_{1,1}]_{c,m} & [S_{1,2}]_{c,m} \\ [S_{2,1}]_{c,m} & [S_{2,2}]_{c,m} \end{bmatrix} \begin{bmatrix} u_{1,c} \\ u_{2,c} \end{bmatrix}. \quad (10.10)$$

Since the left side of Eq. 10.10 contains all the known entities, whether given, computed, or measured, its solution is possible and will yield the unknown values of the function at the nodes where no measurements have been taken. Once we have determined $u_{1,c}$ and $u_{2,c}$, we can compute the residual force vector r as

$$r = p_3 - [S_{3,1}]_c u_{1,c} - [S_{3,2}]_c u_{2,c} - [S_{3,3}]_c u_{3,m} \neq 0. \quad (10.11)$$

The components of the vector expressed by Eq. 10.11, corresponding to the i -th element, can then be substituted into Eq. 10.3 to determine the next refinement. In the text which follows, laser based experimental methods for obtaining measurements are presented.

10.3. Hologram interferometry

Hologram interferometry is a two-step process. During the first step, a holographic interferogram of an object being studied is recorded in some photosensitive medium. During the second step, the interferogram is reconstructed from the medium by producing an image of the object. The image obtained during the reconstruction has all the visual effects that the original object would have if it were observed directly. However, in addition to these visual effects, the

holographically produced image appears covered by alternating bright and dark bands, known as *fringes*. These fringes encode, in a very elaborate manner, information about displacements and deformations that the object has undergone while the hologram was being recorded. Decoding, or reading out, the information stored in the holographic fringe patterns leads to very accurate quantification of displacement and deformation fields characterizing behavior of the object while the hologram was being recorded. The displacement and deformation fields measured from holograms can be merged, or unified, i. e., hybridized, with computational methodologies to facilitate their solutions. Of particular interest to the developments presented in this chapter are the hybrid approaches based on hologram interferometry and FEM. However, the quality of this hybridization depends on our ability to accurately and precisely determine orders of fringes in the fringe patterns produced during reconstruction of holograms. More specifically, this determination relates to accurate and precise measurements of optical phase distributions within the holographically produced image and has received considerable attention, over the years, resulting in a number of methods which have reached high degrees of sophistication and automation and are usually based on one of, but are not limited to, the following ways²⁷: (1) line scan, (2) video digitization, (3) heterodyne readout, (4) phase step readout, or (5) direct electronic recording and processing of holograms. Although each one of these ways has been used, to a varying degree of implementation, in hybrid approaches to deformation analysis, only the method based on the direct electronic recording and processing of holograms, will be considered in this chapter, for the sake of brevity. This method is known as the Electro-Optic Holography (EOH), or simply Electronic Holography, and is the subject of Section 10.3.1; more detailed description of the EOH is given in Chapter 8.

10.3.1. Electronic holography

Electronic holography is the method based on recent advances in hologram interferometry, speckle metrology, and computer technology, Chapter 8. In this method, interferometric information is captured by a CCD camera. The output from the camera is fed into the electronic system which acquires, processes, and displays optical interference information. The EOH method allows automated processing of fringes recorded under either static or dynamic loading conditions. In the EOH system, measurements of irradiances produced by mutual interference of the object and reference fields are made electronically by a CCD camera. Processing of this interferometric information and display of the results are carried concomitantly with measurements of irradiation.

The EOH system is capable of operating in either a viewing mode, used for visual examination of the interference patterns, or a data mode, used for quantitative interpretation of the EOH images.

The EOH system is capable of performing either static or dynamic measurements²⁸. The static measurements are implemented using the double-exposure hologram interferometry method, while the dynamic measurements are implemented by the time-average hologram interferometry method, Chapter 8.

10.4. Representative applications

The examples presented in this section are only representative and, by no means, imply exhaustive enumeration relating to the unified, or hybrid, applications of FEM and hologram interferometry. Hybridization of FEM with hologram interferometry has its start, at least in this author's experience, with aerospace applications, particularly as they relate to development of gas turbine engines and wing sections. These problems are rather difficult to solve and computational methodologies depend on a number of simplifying assumptions and approximations which, to be effective, ought to be based on physical data. In these studies, the data have been provided by holographic studies based on which the boundary conditions have been accurately identified and trends in displacement rates have been visualized directly from the fringe patterns. Figures 10.1 and 10.2 show typical holographic images recorded and the quantitative results obtained based on the data obtained from these images^{1,2,29,30}.

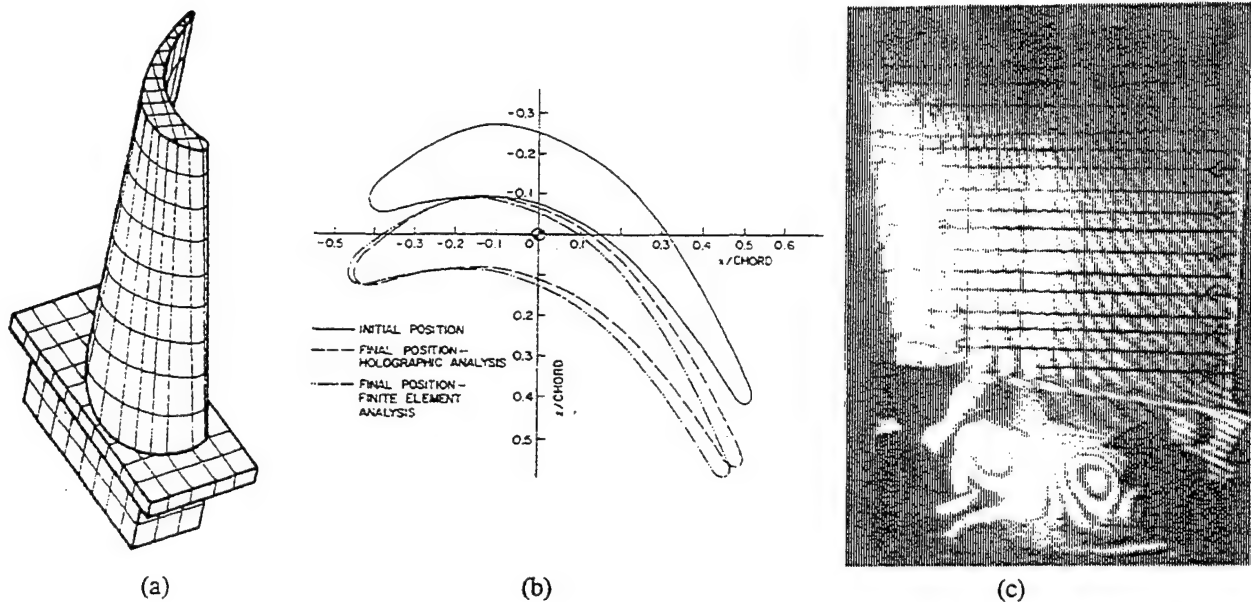


Fig. 10.1. FEM and holographic study of a gas turbine engine: (a) typical finite element discretization of a turbine blade, (b) displacements of a turbine blade - a comparison between the results obtained from holograms and the FEM results, (c) a fringe pattern showing abrupt discontinuity in the fringe pattern indicating stress concentration in the root area.

Slender structural components are of considerable importance in developing high strength to weight structures^{31,32}. Durability of these structures depends, to a large degree, on the dynamic characteristics of the slender components. These components are, in general, thin walled and are formed into three-dimensional shapes. One of most popular shapes is a channel cross section. This shape can be controlled by appropriate selection of the wall thickness and optimization of

its length to width and to depth ratios. The shape and the boundary conditions define dynamic response characteristics of the thin wall channel beams to the loads acting upon them³².

Knowledge of the relationship between the applied force system and the resulting tooth displacement plays an ever-increasing role in prediction of tooth movement, estimating stress in the periodontal ligament, and standardizing histologic studies of tooth movement³³⁻³⁵. FEM simulation of orthodontic tooth movement depends on knowledge of mutual interrelationship between various sections of the tooth-ligament-bone system, Fig. 10.3. These sections consist of various structures: compact bone, spongy bone, periodontal ligament, cementum, dentin, pulp, gingival fibers, and enamel. Each of these materials have different (nonlinear, visco-elastic) properties which change as a function of daily functions. Monitoring of these properties is very difficult using conventional methodologies. However, hologram interferometry, used both *in-vitro* and *in-vivo*, allowed characterization of tooth response to the applied force systems and led to quantification of the effects of time and force on tooth movement.

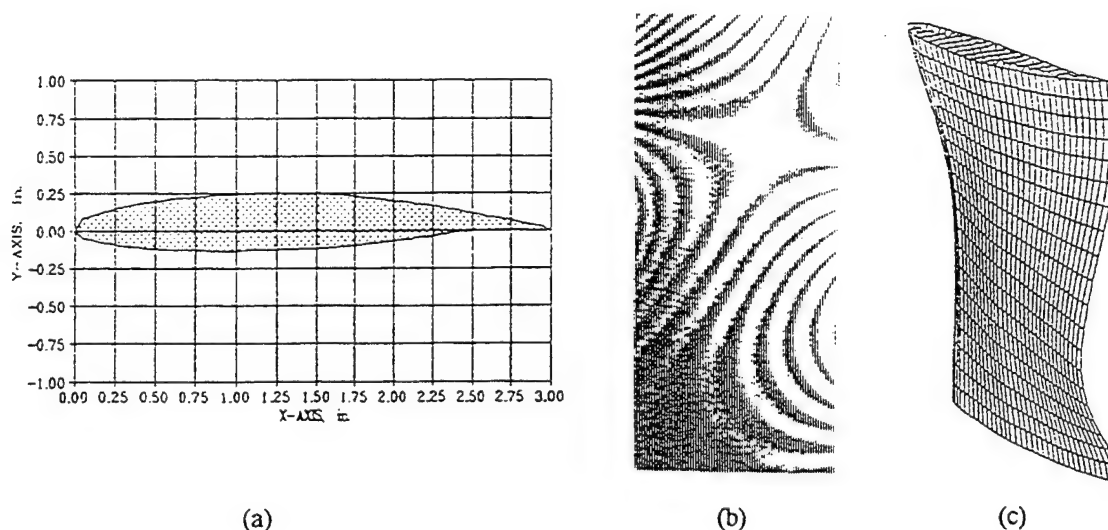


Fig. 10.2. Study of dynamics of the NASA's GAW-2 wing section: (a) profile of the airfoil, (b) a typical image reconstructed from a stroboscopic hologram of the airfoil vibrating at 3,994 cps, (c) FEM mode shape corresponding to the conditions under which the image shown in (b) was recorded.

Advances in integrated circuit (IC) technologies drive electronic packaging requirements. The trend toward miniaturization, which begun with the transistor and progressed rapidly with the IC, continues unabated. Designers are constantly attempting to squeeze faster and faster processing power out of computers. The methods are numerous: use of wider word widths, use of faster clock rates, implementation of higher density packaging in order to decrease propagation delays, as well as the use of novel architectures such as parallel processing in order to overcome the bottlenecks of traditional serial processing schemes. In attempt to satisfy the demanding packaging needs of such applications, the connector designer must develop a trade-off solution by balancing various requirements in order to produce a connector combining

reliability and performance. In view of these requirements and in addition to manufacturing issues, the designer must consider the properties of available materials, the means for practically meeting the tolerances of such a high-density design, and the means for modeling and simulating the performance of a design with accuracy and reliability. One solution to this need is shown in Fig. 10.4. The design represents a departure from conventional designs in that the contact resembles a four-armed starfish: one set of arms points downward while the other points upward. These orientations of the contacts are formed by bending the arms into arcs located in two mutually orthogonal planes which divide the star into four equal quadrants. The contacts are designed to act as interposers between two planar surfaces such that two of the arms of each star make contacts with each surface; when compressed, the overall height of the starfish is approximately 0.5 mm. Development of such a small contact presents several challenges. Foremost is the inadequacy of published data for materials. Material properties are generally published for bulk test samples whose dimensions are orders of magnitude greater than the sizes of the microelectronic contacts. Properties of materials which were required for FEM of the contact were simply not available as the project began. Use of the techniques of hologram interferometry, however, provided needed characterization of the properties of small test samples³⁶⁻³⁹. The data obtained allowed computational analysis leading to a detailed determination of a load-deflection characteristics and stress fields for the contact experiencing large deflections and exhibiting nonlinear behavior.

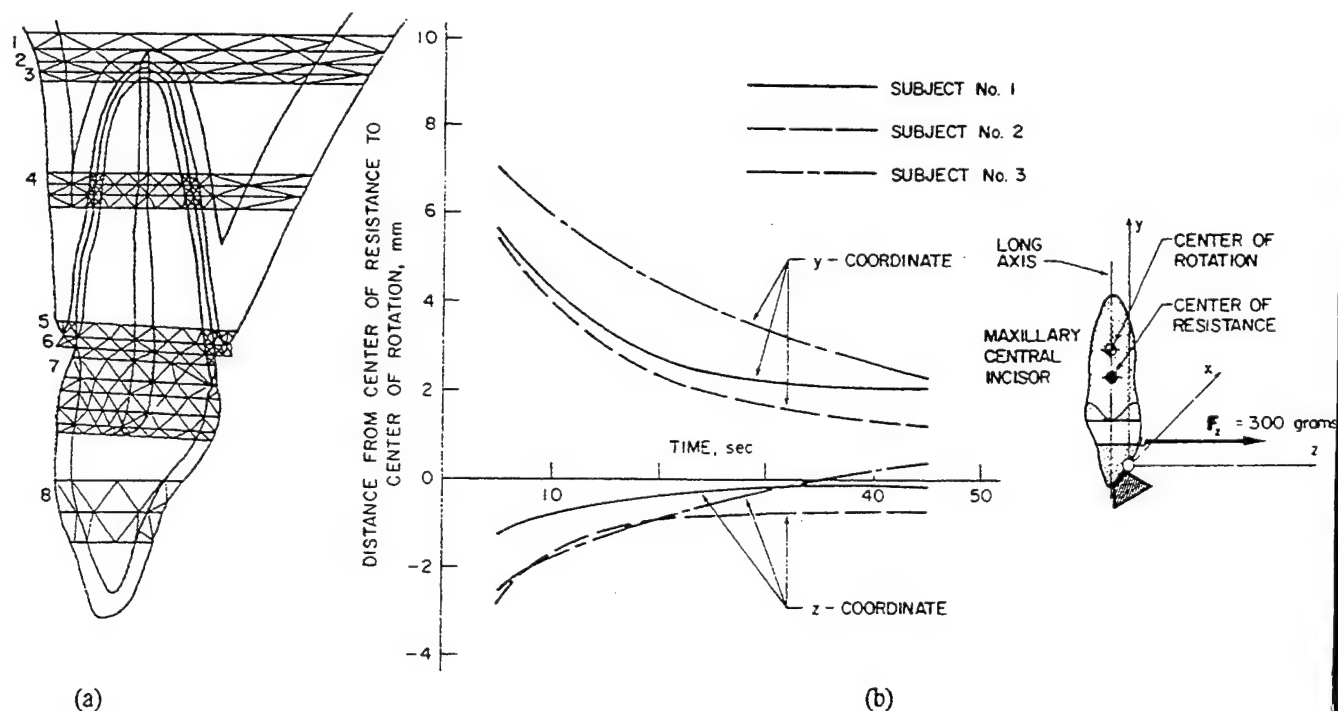
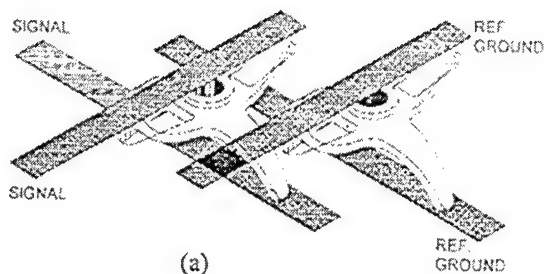
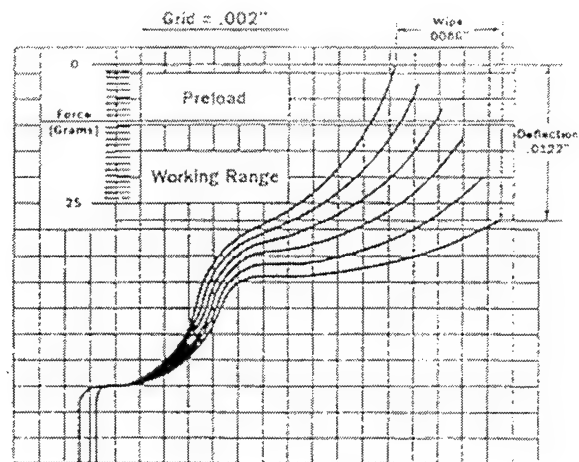


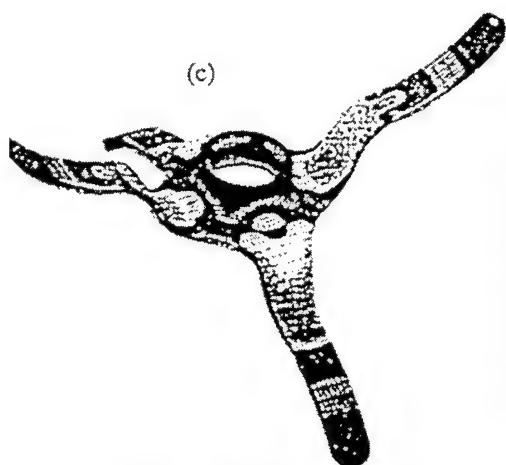
Fig. 10.3. Study of the tooth-ligament-bone system: (a) 1 to 8 are typical FEM discretization zones, (b) distance from the theoretical center of resistance to the center of rotation as a function of time.



(a)



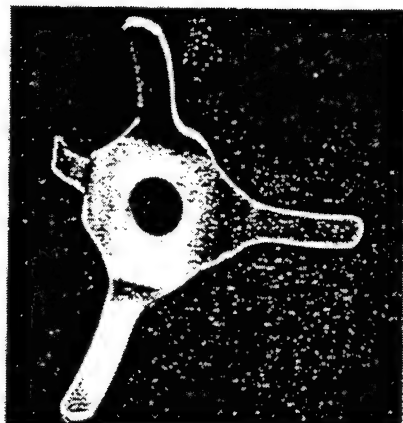
(b)



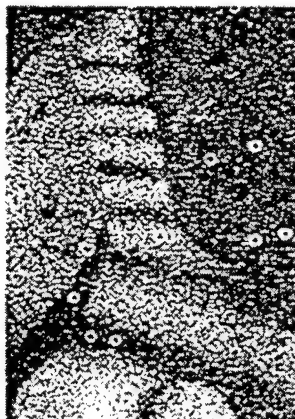
(c)

Fig. 10.4. Miniature star-connector: (a) interconnection concept, (b) FEM simulation of displacement versus position for a typical arm of the microcontact as a function of contact force, (c) FEM estimate of von Misses stress (in Mpsi) for a load of 25 g at each tip - the microcontact is shown in its deformed state, (d) a prototype microcontact, (e) and (f) EOH images of a single arm of the microcontact while loaded with a force increasing from (e) to (f), respectively.

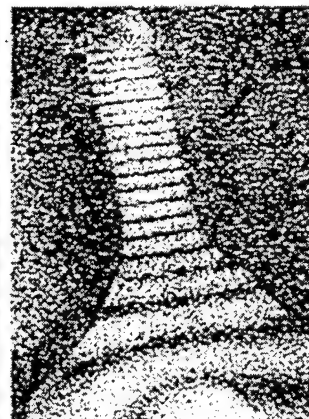
(d)



(e)



(f)



10.5. Conclusions

This chapter presents some of the developments relating to hybridization of hologram interferometry and FEM methods. This hybrid approach to deformation analysis is a part of what we call ACES methodologies, which emphasize the analogy between analytical, computational, and experimental methodologies and employs them to obtain solutions that may not have been otherwise obtainable, to ease the existing solution procedures, or to attain improvements in the results. Use of these methodologies to solution of real problems is illustrated with representative examples.

Continued advances on hybridization of experimental, especially optical, methods with the computational methods will lead to development of new tools that will facilitate solution of problems hampered by lack of knowledge on behavior of new materials, large deformations, and/or inherent nonlinearities.

10.6. References

- 10.1. R. J. Pryputniewicz, "A hybrid approach to deformation analysis," *Proc. SPIE*, 2342:282-296, 1994.
- 10.2. R. J. Pryputniewicz and W. W. Bowley, "Holographic analysis of airfoils," *Proc. ISP Comm. V Symposium*, pp. 22-30, Stockholm, Sweden, 1978.
- 10.3. K. H. Laermann, "Recent developments and further aspects of experimental stress analysis in the Federal Republic of Germany and Western Europe," *Exp. Mech.*, 21:49-57, 1981.
- 10.4. A. S. Kobayashi, "Hybrid experimental-numerical stress analysis," *Exp. Mech.*, 23:338-347, 1983.
- 10.5. R. J. Pryputniewicz, "Holographic and numerical studies of convective heat transfer from horizontal cylinders," *Conf. Digest, ICO-13*, pp. 40-41, Sapporo, Japan, 1984.
- 10.6. J. S. Sirkis and C. E. Taylor, "Displacement pattern matching and boundary-element methods for elastic-plastic stress analysis," *Exp. Mech.*, 30:26-33, 1990.
- 10.7. J. Morton, D. Post, P. Han, and M. Y. Tsai, "A localized hybrid method of stress analysis: a combination of moiré interferometry and FEM," *Exp. Mech.*, 30:195-200, 1990.
- 10.8. T. Nowak and R. J. Pryputniewicz, "Theoretical and experimental investigation of laser drilling in a partially transparent medium," *J. Electronic Packaging - Transactions of the ASME*, 114:71-80, 1992.

- 10.9. D. G. Grabbe, H. Merkelo, and R. J. Pryputniewicz, "Project AMPSTAR connector," *AMP J. Technology*, 2:4-13, 1992.
- 10.10. R. J. Pryputniewicz, *Holographic numerical analysis*, Center for Holographic Studies and Laser Technology, Department of Mechanical Engineering, Worcester Polytechnic Institute, Worcester, MA 01609-2280, 1992.
- 10.11. R. J. Pryputniewicz, ed., *Proc. 10th Internat. Invitational UFEM Symp.*, WPI, ME-CHSLT, Worcester, MA, 1991.
- 10.12. R. J. Pryputniewicz, ed., *Proc. 11th Internat. Invitational UACEM Symp.*, Soc. Exp. Mech., Bethel, CT, 1993.
- 10.13. R. J. Pryputniewicz, ed., *Proc. Abstr. 12th Internat. Invitational UACEM Symp.*, WPI, ME-CHSLT, Worcester, MA, 1995.
- 10.14. H. Kardestuncer, *Discrete mechanics: a unified approach*, Springer-Verlag, Vienna, 1975.
- 10.15. O. C. Zienkiewicz, D. W. Kelly, and P. Bettess, "The coupling of the finite element method and boundary solution procedures," *Internat. J. Num. Meth. Engr.*, 11:355-373, 1977.
- 10.16. O. C. Zienkiewicz, D. W. Kelly, and P. Bettess, "Marriage ala mode - the best of both worlds (Finite elements and boundary integrals)," Ch. 5 in *Energy methods in finite element methods*, R. Glowinski, E. Y. Rodin, and O. C. Zienkiewicz, eds, Wiley, New York, 1980.
- 10.17. I. Babuska, O. C. Zienkiewicz, J. Gago, and E. R. de A. Oliveira, eds, *Accuracy estimates and adaptive refinements in finite element computations*, Wiley, New York, 1986.
- 10.18. R. J. Pryputniewicz, "Unification of FEM modeling with laser experimentation," Ch. 11 in *Proc. 6th Invitational Symp. on the Unification of Finite Elements, Finite Differences, and Calculus of Variations*, H. Kardestuncer, ed., Storrs, CT 1982.
- 10.19. H. Kardestuncer and R. J. Pryputniewicz, "Unification of FEM with laser experimentation," Ch. 9 in *Unification of finite element methods*, H. Kardestuncer, ed., North-Holland, Amsterdam, 1984.
- 10.20. K. J. Bathe, *Finite element procedures in engineering analysis*, Prentice-Hall, Englewood Cliffs, NJ, 1982.
- 10.21. H. Kardestuncer, Editor-in-Chief, *Finite element handbook*, McGraw-Hill, New York, 1987.

- 10.22. W. Weaver, Jr., and P. R. Johnston, *Structural dynamics by finite elements*, Prentice-Hall, Englewood Cliffs, NJ, 1987.
- 10.23. T. J. R. Hughes, *The finite element method: linear static and dynamic finite element analysis*, Prentice-Hall, Englewood Cliffs, NJ, 1987.
- 10.24. O. C. Zienkiewicz and R. L. Taylor, *The finite element method*, 4th ed., Vol. 1: *Basic formulation and linear problems*, McGraw-Hill, New York, 1989.
- 10.25. O. C. Zienkiewicz and R. L. Taylor, *The finite element method*, 4th ed., Vol. 2: *Solid and fluid mechanics, dynamics, and nonlinearity*, McGraw-Hill, New York, 1989.
- 10.26. H. Kardestuncer, "Tensors versus matrices in discrete mechanics," in *Problem analysis in science and engineering*, F. H. Branin, Jr., and K. Huseyin, eds, Academic Press, New York, 1977.
- 10.27. R. J. Pryputniewicz, "Automated systems for quantitative analysis of holograms," *SPIE Institute for Advanced Optical Technologies*, IS8:215-246, 1991.
- 10.28. R. J. Pryputniewicz, "Static and dynamic measurements using electro-optic holography," *Proc. SPIE*, 1554B:790-798, 1991.
- 10.29. R. J. Pryputniewicz, "Time-average holography in vibration analysis," *Opt. Engrg.*, 24:843-848, 1985.
- 10.30. S. W. Biederman and R. J. Pryputniewicz, "Holographic study of vibrations of a wing section," *Proc. SPIE*, 1756:153-163, 1992.
- 10.31. B. W. Cranton and R. J. Pryputniewicz, "Numerical and experimental study of wave propagation in metals," *Proc. SPIE*, 1756:164-175, 1992.
- 10.32. M. J. Klausbruckner and R. J. Pryputniewicz, "Theoretical and experimental study of coupled vibrations of channel beams," *J. Sound and Vibration - Transactions of the ASME*, 183:239-252, 1995.
- 10.33. C. J. Burstone, R. J. Pryputniewicz, and W. W. Bowley, "Holographic measurement of tooth mobility in three dimensions," *J. Periodontal Res.*, 13:283-294, 1978.
- 10.34. R. J. Pryputniewicz and C. J. Burstone, "The effect of time and force magnitude on orthodontic tooth movement," *J. Dental Res.*, 58:1754-1764, 1979.
- 10.35. R. J. Pryputniewicz, "Pulsed laser holography in studies of bone motions and deformations," *Opt. Engrg.*, 24:832-839, 1985.

- 10.36. R. J. Pryputniewicz, "Heterodyne holography application in studies of small components," *Opt. Engrg.*, 24:849-854, 1985.
- 10.37. G. C. Brown and R. J. Pryputniewicz, "Investigation of submillimeter components by heterodyne holographic interferometry and computational methods," *Proc. SPIE*, 1755:120-130, 1992.
- 10.38. G. M. Brown and R. J. Pryputniewicz, "Nanomeasurements by heterodyne hologram interferometry," *Proc. SPIE*, 1756:301-310, 1992.
- 10.39. G. C. Brown and R. J. Pryputniewicz, "Measurement of Young's modulus on thin films under static and dynamic loading conditions," *Proc. SPIE*, 2004:302-312, 1993.
-

11. QUANTITATIVE EOH AND FEM HYBRID STUDY OF VIBRATION CHARACTERISTICS OF AVIONICS

One of the major challenges in the development of avionics is the requirement to assure their reliable functionality while subjected to actual operating conditions which are static and dynamic in nature. Of particular interest, to the developments presented in this chapter, are the dynamic loading conditions. Because the avionics have certain mass and elasticity, they respond to the loads encountered during operation with a specific vibration behavior. Therefore, development of reliable avionics packages depends upon our ability to determine the dynamic characteristics which define and control their vibration behavior, particularly as it relates to the dynamic environment within an aircraft which is a major contributor to the failure of airborne avionic systems. In this chapter, computational and experimental hybrid methodology is used to quantitatively study the vibration characteristics of avionics. The computational methodology is based on the finite element method (FEM). The experimental methodology is based on the electro-optic holography (EOH) method, which allows direct electro-optic recording, processing, and display of the laser holograms at the rate of 30 holograms per second, making it capable of producing quantitative data in nearly real-time. Using the EOH method, displacement magnitudes in the submicron range are measured noninvasively over the full field of view, as a function of the resonance frequencies. Although some of the experimentally observed mode shapes were not predicted using the computational model employed in this study, the correlation between the results obtained using the finite element and the electro-optic holography methods was otherwise good and the agreement between the corresponding resonance frequencies was within 2%.

11.1. Introduction

The dynamic environment within an aircraft is a major contributor to the failure of airborne avionic systems. Estimates are that 20% of experienced field failures can be attributed to the damaging influence of vehicle vibrations¹. The level of concern over the influence of vibrations on the durability of avionics is reflected in the depth with which this environment is covered in military standards on equipment test and design² and reliability³. Also, as a result of this concern, a number of computational tools^{1,4-9} and experimental methodologies¹⁰⁻¹³ have been developed to assess the impact of vibration on the durability of specific avionic designs.

Economic considerations combined with the requirements of the Avionics Integrity Program¹⁴ (AVIP) to predict a specific failure-free life based on a tailored environmental profile have resulted in primary reliance on FEM as the computational means to assess the durability of avionics in the early stages of their design¹⁵⁻¹⁷. Fundamentals of the FEM have been discussed in great detail elsewhere¹⁸⁻²³ and the reader is referred to the appropriate publications. However, for the FEM to be effective, in addition to other input parameters, a priori knowledge of the mechanical properties of the materials used in the construction of the avionics is required for the size of the structures employed in the design²⁴. In many cases, these properties are neither

available nor well defined²⁵ which is mainly because the traditional measurement techniques cannot be applied to the structures on the scale of those used in the construction of the modern avionics without inherently affecting the outcome. One way to circumvent this difficulty is to employ recent developments in laser holographic interferometry methods which allow noninvasive measurements of the quantities of interest. Out of a number of the laser methods available today, the most suitable one for the study of vibrations of the avionics is the time-average hologram interferometry^{26,27} (TAHI), particularly as it is implemented via electro-optic holography²⁸⁻³¹ (EOH).

In the following sections, fundamentals of the TAHI as implemented via EOH are presented, with special emphasis on the quantitative analysis of the vibrating objects. Discussion of this analysis is illustrated by representative examples from a study of vibration characteristics of avionics.

11.2. Time-average hologram interferometry

Time-average hologram interferometry is characterized by a single holographic recording of an object undergoing a cyclic vibration. With the continuous exposure time long in comparison to one period of the vibration, the hologram effectively records an ensemble of images corresponding to the time-average of all positions on the vibrating object^{26,27,32}. In a classical implementation of TAHI, the two beam off-axis setup, shown in Fig. 11.1, is used to produce the time-average holograms. During production of such holograms, the interference occurs between the entire ensemble of images, with the images recorded near zero velocity, i. e., the maximum displacement, contributing most strongly to the resulting image. As a result, the image of the object, seen during reconstruction of the time-average hologram, is overlaid with interference fringes of unequal brightness. In fact, these fringes vary according to the square of the zero-order Bessel function of the first kind, as discussed in this Chapter 7.

Time varying displacement, $L_t(x, y, z, t)$, of a vibrating object can be related to temporal changes in the fringe-locus function, $\Omega_t(x, y, z, t)$, constant values of which define fringe loci on the surface of the object. Using the holographic setup shown in Fig. 11.1, it was shown^{26,27} that this relationship can be written as

$$\Omega_t(x, y, z, t) = \mathbf{K}(x, y, z) \bullet \mathbf{L}_t(x, y, z, t) \quad , \quad (11.1)$$

where t is the time and $\mathbf{K}(x, y, z)$ is the sensitivity vector defined as the difference between the observation and illumination vectors, $\mathbf{K}_2(x, y, z)$ and $\mathbf{K}_1(x, y, z)$, respectively, with x , y , and z representing the Cartesian coordinates characterizing the holographic setup. The time varying light field propagating from the vibrating object, along the direction specified by the vector \mathbf{K}_2 , interferes with a reference field to produce a spatial distribution of image irradiance, $I_{im}(x, y, z)$, which is proportional to the square of the zero-order Bessel function of the first kind of the

argument $\Omega_t(x, y, z, t)$, with the proportionality factor being the amplitude squared of the object field, $A_o^2(x, y, z)$, i. e.,

$$I_{im}(x, y, z) = A_o^2(x, y, z) J_o^2[\Omega_t(x, y, z, t)] \quad (11.2)$$

Equation 11.2 shows that the image obtained during reconstruction of the time-average hologram is modulated by a system of fringes of unequal brightness described by the square of the zero-order Bessel function of the first kind. Thus, for nontrivial values of A_o , centers of the dark fringes will locate at those points on the surface of the object where $J_o(\Omega_t)$ equals zero.

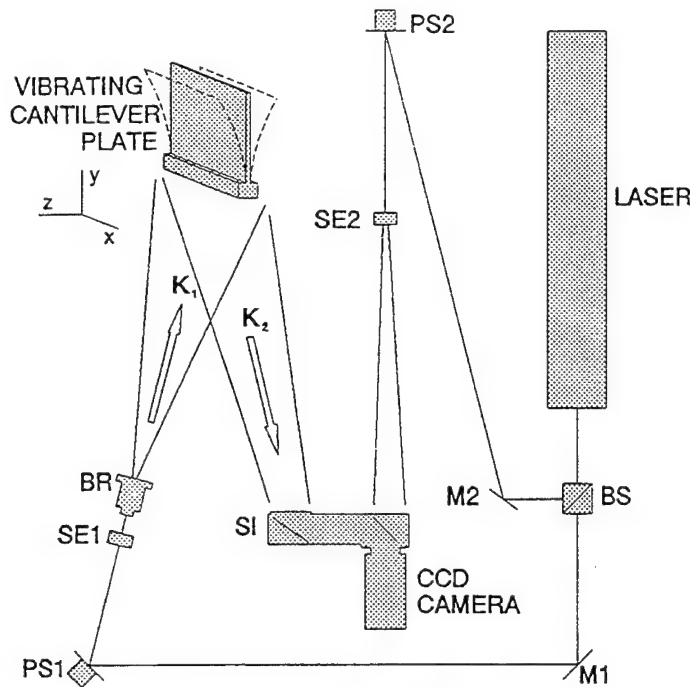


Fig. 11.1. Opto-mechanical configuration of the EOH system: BS is the beamsplitter, M1 and M2 are the mirrors, PS1 and PS2 are the phase steppers, SE1 and SE2 are the spatial filter beam expander assemblies, BR is the object beam rotator, SI is the speckle interferometer, and K_1 and K_2 are the directions of object illumination and observation, respectively.

In the case of the out-of-plane (transverse) vibrations of the object, i. e., when motion of the object is in the direction parallel to the z -axis, Fig. 11.1, the vibration amplitude, L_{tz} , can be shown^{26,27} to be

$$L_{tz} = \frac{\lambda}{2\pi(K_{2z} - K_{1z})} |\Omega_t| \quad (11.3)$$

In Eq. 11.3, L_{tz} is the z -component of the displacement vector, λ is the wavelength of the laser light used to produce the holograms, K_{1z} and K_{2z} are the components of the illumination and observation unit vectors defining directions of \mathbf{K}_1 and \mathbf{K}_2 , respectively, and $|\Omega_t|$ is the magnitude of the time varying fringe-locus function.

In order to evaluate Eq. 11.3, the wavelength of the laser light must be known, the illumination and the observation geometry must be known in terms of the components of the unit illumination and observation vectors, and the spatial distribution of the fringe-locus function must also be known. The wavelength of the laser light is usually very well known for the specific type of the laser being used. The illumination and the observation vectors are computed based on the measurements of x , y , and z coordinates of the position vectors specifying locations of the point source of the illumination, the point(s) of interest on the object, and the point along the optical axis of the viewing system^{33,34}. Finally, the spatial distribution of Ω_t is determined directly from the holograms and, for the case of TAHI by means of EOH, this determination is the subject of Section 11.3; more detailed discussion can be found in Section 8.2.2.

11.3. Electro-optic holography

Unlike traditional forms of holographic interferometry, EOH does not use a photographic medium to record the fringe patterns. Rather, a CCD camera is used to convert the light intensity patterns into a digital bit map, making this method capable of producing quantitative data in nearly real-time. That is, in the EOH method, the irradiances produced by mutual interference of the object and the reference fields are recorded electronically by the CCD camera^{28,29}. Processing of this interferometric information and display of the experimental results are carried out concomitantly with the measurements of irradiation. In order to achieve this, the EOH method relies on electronic acquisition, processing, and display of optical interference information, and allows automated processing of fringes of objects subjected to static and dynamic loads^{35,36}.

In the following sections, principles of the EOH, as they apply to vibrations, are outlined and their implementation to the study of the vibration characteristics of avionics is presented. In order to facilitate development of the governing equations, this presentation considers time-average recording of sinusoidally vibrating objects.

11.3.1. Quantitative analysis of electro-optic holograms

In the EOH, the holographic process is carried out by recording sequential frames of images of an object as it vibrates. Typically, four sequential frames are recorded, with a finite phase step, imposed on the reference beam, between each frame. It should be noted that the number of the sequentially recorded frames is equal to the number of unknowns in Eq. 11.4

which describes irradiance distribution of a typical frame recorded in the EOH system. For the case of a sinusoidally vibrating object, the irradiance distribution for the n -th sequential frame, i. e., $I_{t_n}(x, y)$, at the detector array of the CCD camera in the EOH system, can be represented^{29,37} by

$$I_{t_n}(x, y) = I_o(x, y) + I_r(x, y) + 2A_o(x, y)A_r(x, y)\cos[\Delta\phi(x, y) + \Delta\theta_n]J_o[\Omega_t(x, y, t)] \quad (11.4)$$

In Eq. 11.4, x and y identify the coordinates of the pixels in the CCD array, t indicates the time, I_o and I_r denote the irradiances of the object and reference fields, whose amplitudes are A_o and A_r , respectively, $\Delta\phi$ is the phase difference between the two fields, $\Delta\theta_n$ is the n -th finite phase step - in this study, the phase step equals 90° and is introduced between the sequential frames, J_o is the zero-order Bessel function of the first kind, and Ω_t is the time dependent fringe-locus function defining loci on the surface of a vibrating object.

It was shown²⁹ that, for any set of four sequentially recorded frames, the sum of the squares of the differences between pairs of interlaced frames is related to the square of the J_o function whose argument is Ω_t , i. e.,

$$(I_{t_1} - I_{t_3})^2 + (I_{t_2} - I_{t_4})^2 = 16A_o^2A_r^2J_o^2(\Omega_t) \quad (11.5)$$

where the Cartesian coordinates were omitted for simplification.

Quantitative interpretation of the electronically recorded holograms of the vibrating objects depends on determination of Ω_t , from Eq. 11.5. This determination can be done by optical shifting of the J_o fringes. This shifting is achieved by modulating the phase of either the object or the reference beams sinusoidally by addition of a phase bias, B , to the argument of the Bessel function. If the phase of the sinusoidal beam modulation is adjusted to coincide with that of the object vibration, the phasor becomes a simple additive term within the argument of the Bessel function, which can be expressed as²⁹

$$(I_{t_1} - I_{t_3})^2 + (I_{t_2} - I_{t_4})^2 = 16A_o^2A_r^2J_o^2(\Omega_t - B) \quad (11.6)$$

In this approach, the nearly periodic nature of the $J_o^2(\Omega_t - B)$ function is modeled as $\cos^2(\Omega - B)$ function, where Ω represents the fringe-locus function describing the cosinusoidal fringes observed during the reconstruction of a double-exposure hologram, and is utilized to obtain an approximate solution for Ω_t , based on the three irradiance distributions of the type given by Eq. 11.6, corresponding to the zero, the positive, and the negative phase bias shifts, respectively. This approximate solution, $\Omega_{t_{approx}}$, i. e.,

$$\Omega_{t_{approx}} = \frac{1}{2} \tan^{-1} \left\{ \left[\frac{1 - \cos(2B)}{\sin(2B)} \right] \frac{J_o^2(\Omega_t + B) - J_o^2(\Omega_t - B)}{2J_o^2(\Omega_t) - J_o^2(\Omega_t - B) - J_o^2(\Omega_t + B)} \right\} \quad (11.7)$$

differs from the correct value of the argument Ω_t of the J_o function because of inequality between the J_o^2 and the \cos^2 functions, and can be expressed as

$$\Omega_{t_{approx}} = \Omega_t + \varepsilon \quad , \quad (11.8)$$

where ε is the error representing this difference. This error is computed for a range of interest in the values of Ω_t , subject to the specific values of B , to create a lookup table. The lookup table is used to correct the values of $\Omega_{t_{approx}}$ computed from Eq. 11.7. Once correct values of Ω_t are determined, they can be used to compute the displacement using, e. g., Eq. 11.3.

The interferometric information necessary to solve Eq. 11.7 is recorded electronically by the EOH system, at the rate of 30 frames per second. The system processes this information in a pipeline fashion. Currently, this processing yields the results at up to 512×480 pixels per frame.

11.3.2. Description of the EOH system

A typical opto-mechanical configuration of the EOH system is shown in Fig. 11.1. In this system, the laser output is divided into two beams by means of a variable beamsplitter, BS. One of these beams is directed by a fixed mirror M1, and a phase stepper controlled (i. e., movable) mirror, PS1, and is shaped by the spatial filter beam expander assembly, SE1, to illuminate the object uniformly; PS1 can be driven at the same frequency as the object excitation to provide bias modulation necessary for quantitative interpretation of holograms of vibrating objects, as discussed in Section 11.3.1. The beam rotator, BR, located between PS1 and the object, is used to rotate the object illumination to facilitate speckle averaging. The direction of the object illumination is characterized by the vector \mathbf{K}_1 , while the object observation is defined by the vector \mathbf{K}_2 . The other beam, steered by M2 and PS2 and spatially filtered and expanded by SE2, is directed toward the reference input of the speckle interferometer, SI. In this arrangement, PS2 introduces 90° phase steps between the consecutive frames.

The speckle interferometer combines the object beam with the reference beam and directs them collinearly toward the detector array of the CCD camera. The camera detects the interference pattern and sends it to the pipeline processor. The sequential frames are processed to determine quantitative information on the object displacements and/or deformations. All computations are done in a pipeline processor which operates under control of a host computer. The host computer also controls excitation of the object, coordinates it with the bias modulation imposed on the object beam, and keeps track of the 90° phase steps between the sequential frames.

By operating on each input frame and its three predecessors, the pipeline processor produces a hologram, and this hologram is viewed concomitantly on the TV monitor. Such holograms are produced for the zero, as well as the positive, and the negative bias modulations, for each resonance condition of the object. The resulting three electronic holograms are then

processed, by the host computer, to determine spatial distribution of Ω_t , which, in turn, leads to computation of the displacement vectors.

11.4. Test samples

In this study, vibration characteristics of avionic lidded chip modules, surface mounted onto multilayer boards, were investigated. More specifically, two test samples were considered. These test samples were specially developed to represent typical avionic packages. Test sample No. 1 (TS1) consisted of a multilayer board (MLB) with eight identical lidded chip modules which were arranged in two rows with four modules per row, Fig. 11.2. Test sample No. 2 (TS2) consisted of chip modules of different sizes which were mounted onto another MLB forming an assembly shown in Fig. 11.3.

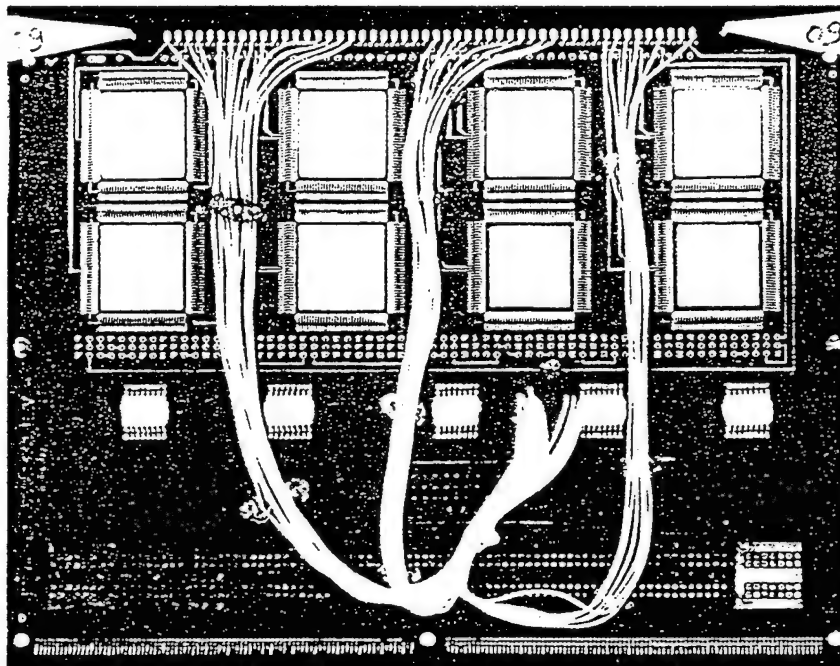


Fig. 11.2. TS1: a multilayer board with eight identical surface mounted chip modules arranged in two rows with four modules per row.

For the measurements, the test samples were fixed at one end in a cantilever configuration, to simulate edge connections. Then, they were excited piezoelectrically, one at a time, by imposing sinusoidal excitation at the "connector" end. The excitation frequencies ranged from zero to approximately 32 kHz.



Fig. 11.3. TS2: a multilayer board with surface mounted chip modules of different sizes.

11.5. Representative results and discussion

Representative results obtained during the study of the TS1 and TS2 are shown in Figs 11.4 to 11.11. All interferograms displayed in these figures were recorded electronically using the EOH system described in Section 11.3.

In this study, the TS1 was first examined in a full field of view, Fig. 11.4. Then, a single lidded chip module was selected and a more detailed study of vibration characteristics of this module was performed, Figs 11.5 to 11.7.

Based on the full field of view examination of the TS1, it was noticed that, at the lower excitation frequencies, all eight modules were exhibiting some response to the excitation as evidenced by the fringe patterns formed on the lids, Fig. 11.4a. However, as the excitation frequency increased, this was not always the case, Figs 11.4b and 11.4c. Using the full field of view results, the most dynamically active module was selected for a more detailed study of its vibration characteristics. This module was the third from the left in the lower row, Fig. 11.4.

Figures 11.5 and 11.6 show a summary of the results of the study of vibration characteristics of a single lidded chip module which is typical of those mounted on the TS1. The fringe patterns shown in Fig. 11.5 were recorded using the EOH system described in Section

11.3. These fringe patterns correspond to all sequential resonance conditions found in the frequency range from zero to 32 kHz, used in this study. Figure 11.6 shows, where applicable, the corresponding finite element results for the same module. In general, agreement between the FEM and the EOH results is good in terms of predictability of the mode shapes. Also, the resonance frequencies, as determined by the two methods, agree to within 2%, Fig. 11.7. However, for the range of the frequencies used in this study, two resonance conditions detected using the EOH method, Figs 11.5g and 11.5h, were not predicted by the FEM model. In the follow up study, the FEM model will be reexamined and an attempt will be made to determine the cause(s) of this discrepancy between it and the EOH results.

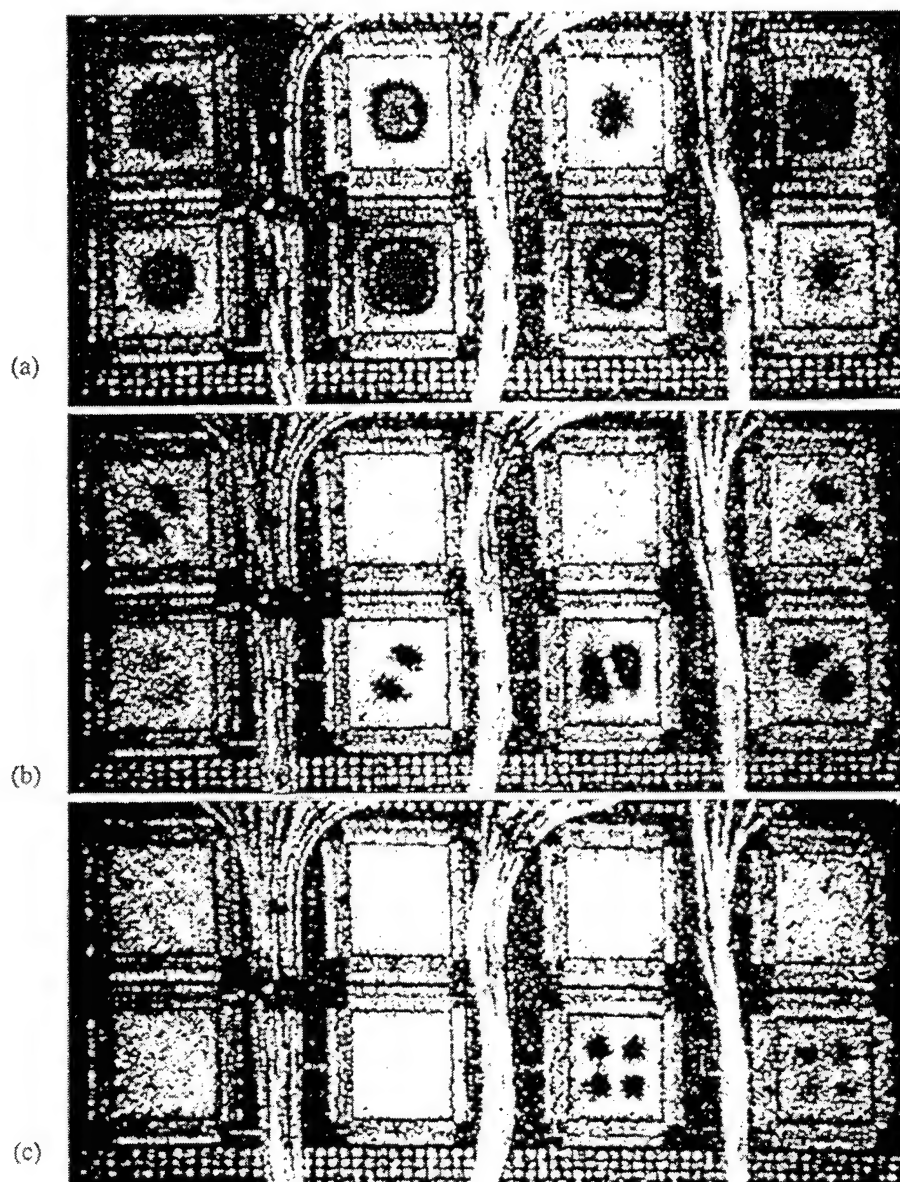


Fig. 11.4. Full field of view EOH images of the TS1 vibrating at:
(a) 6,720 Hz, (b) 13,685 Hz, and (c) 20,011 Hz.

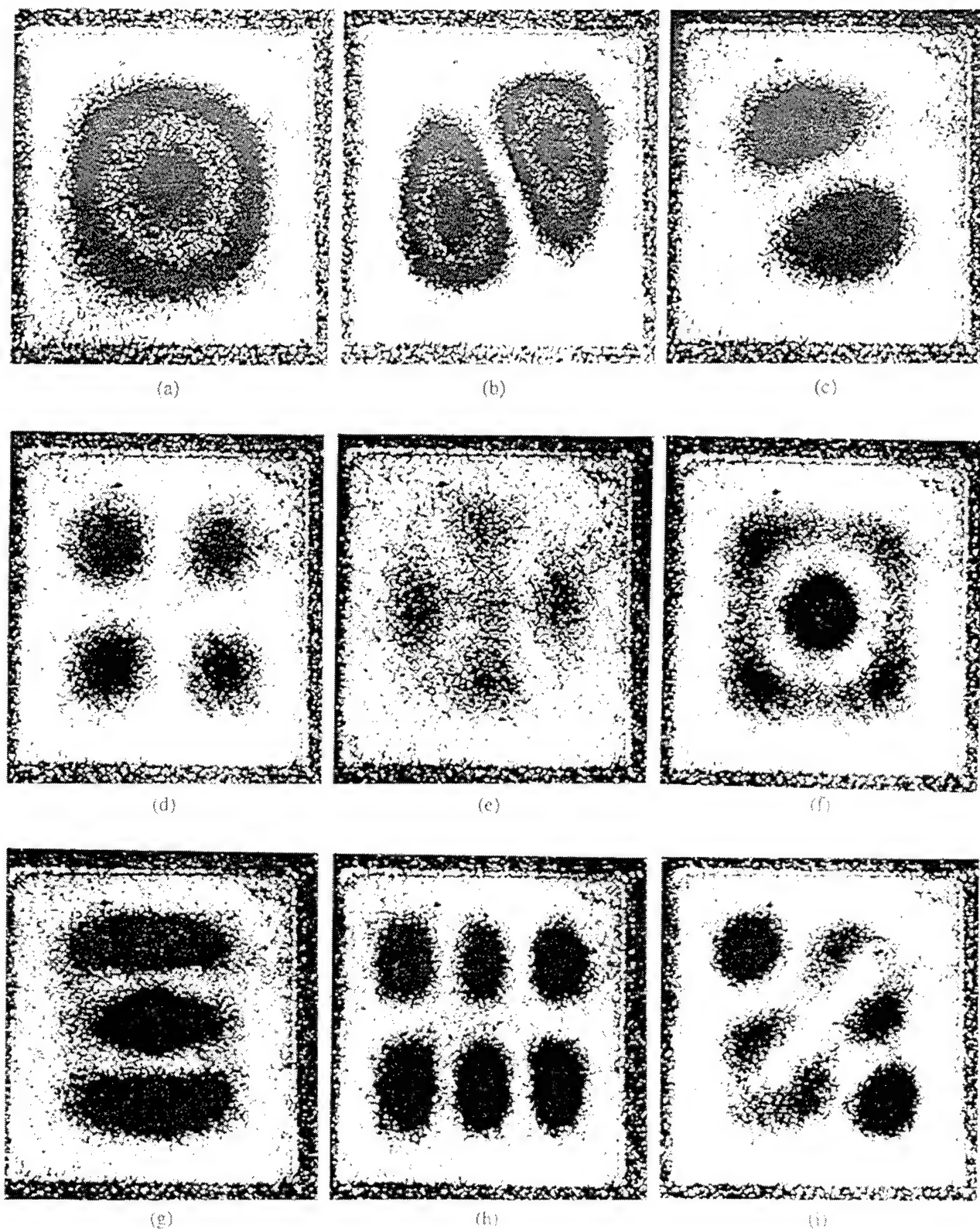


Fig. 11.5. Summary of the EOH images of a single lidded chip module of the TS1 vibrating at resonance frequencies of: (a) 6,720 Hz, (b) 13,685 Hz, (c) 14,006 Hz, (d) 20,011 Hz, (e) 24,600 Hz, (f) 24,980 Hz, (g) 26,000 Hz, (h) 28,990 Hz, and (i) 31,005 Hz.

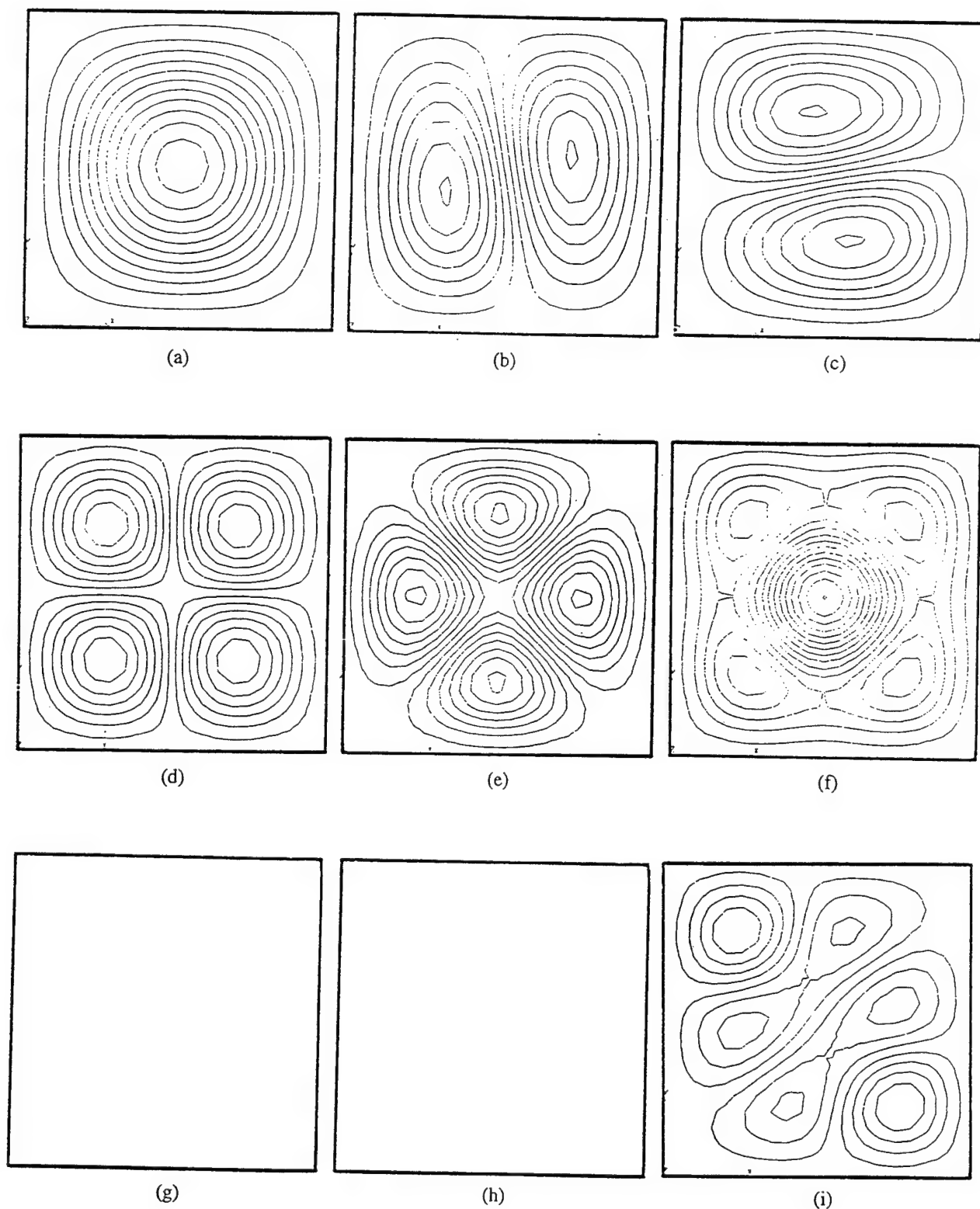


Fig. 11.6. Summary of the FEM results, equivalent to the results shown in Fig. 11.5, for a single lidded chip module of the TS1 vibrating at resonance frequencies of: (a) 6,752 Hz, (b) 13,749 Hz, (c) 13,749 Hz, (d) 20,209 Hz, (e) 24,600 Hz, (f) 24,722 Hz, (g) not determined, (h) not determined, and (i) 30,724 Hz.

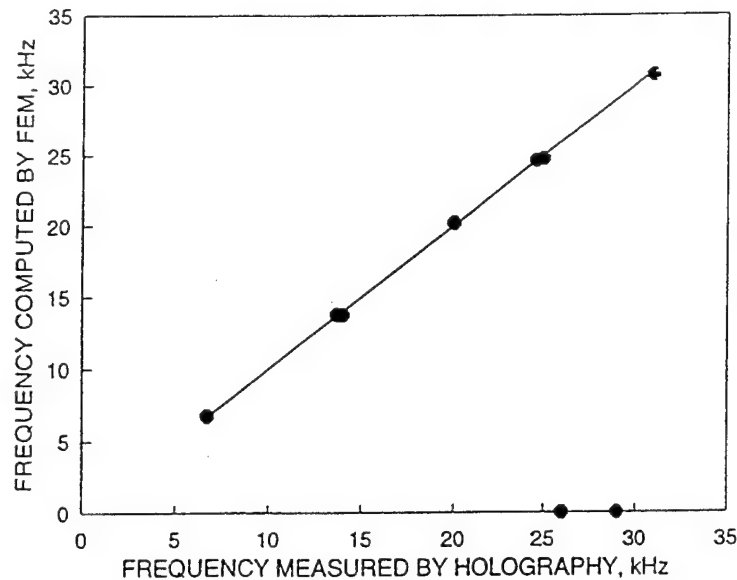


Fig. 11.7. Summary of the measured frequencies for TS1: symbols indicate the actual correlation between the FEM and the EOH results while the line indicates the ideal correlation.

Figures 11.8 to 11.11 show representative results for the TS2. These results indicate that at lower resonance frequencies (below 148 Hz), the TS2 behaves as a cantilever plate without noticeable influence of the surface mounted modules on its mode shapes, Fig. 11.8. That is, the modules neither appear to affect the mode shapes of the multilayer board nor they themselves show any activity that indicates their presence on the TS2. However, as the excitation frequency increases (above 680 Hz), so does the vivid display of the presence of the modules, Figs 11.9 and 11.10. Most pronounced is the presence of the largest, centrally located module.

Figure 11.9 shows that although this module follows the mode shape of the entire TS2, Fig. 11.9a, a close up of the module and the MLB in its vicinity clearly indicates discontinuity between the fringe pattern on the module and the fringe pattern on the MLB. For such a discontinuity to appear, leads attaching the module to the MLB must be deformed in response to the load acting on the TS2, indicating a rigid-body rather than elastic response of the module. In fact, compliant leads should be designed in such a way that they could reliably carry cyclic operating loads during the expected life of the module¹². Figure 11.10 shows that as the excitation frequency increases from 4,690 Hz to 9,330 Hz, the lid on the central module goes from vibration at its first resonance mode, Fig. 11.10a, via no response at the TS2 resonance frequency of 6,890 Hz, Fig. 11.10b, to vibration at its second resonance frequency of 9,330 Hz, Fig. 11.10c. Because of distinct differences in the designs of the modules of the TS1 and the central module of the TS2, their resonance frequencies are significantly different although the mode shapes are similar.

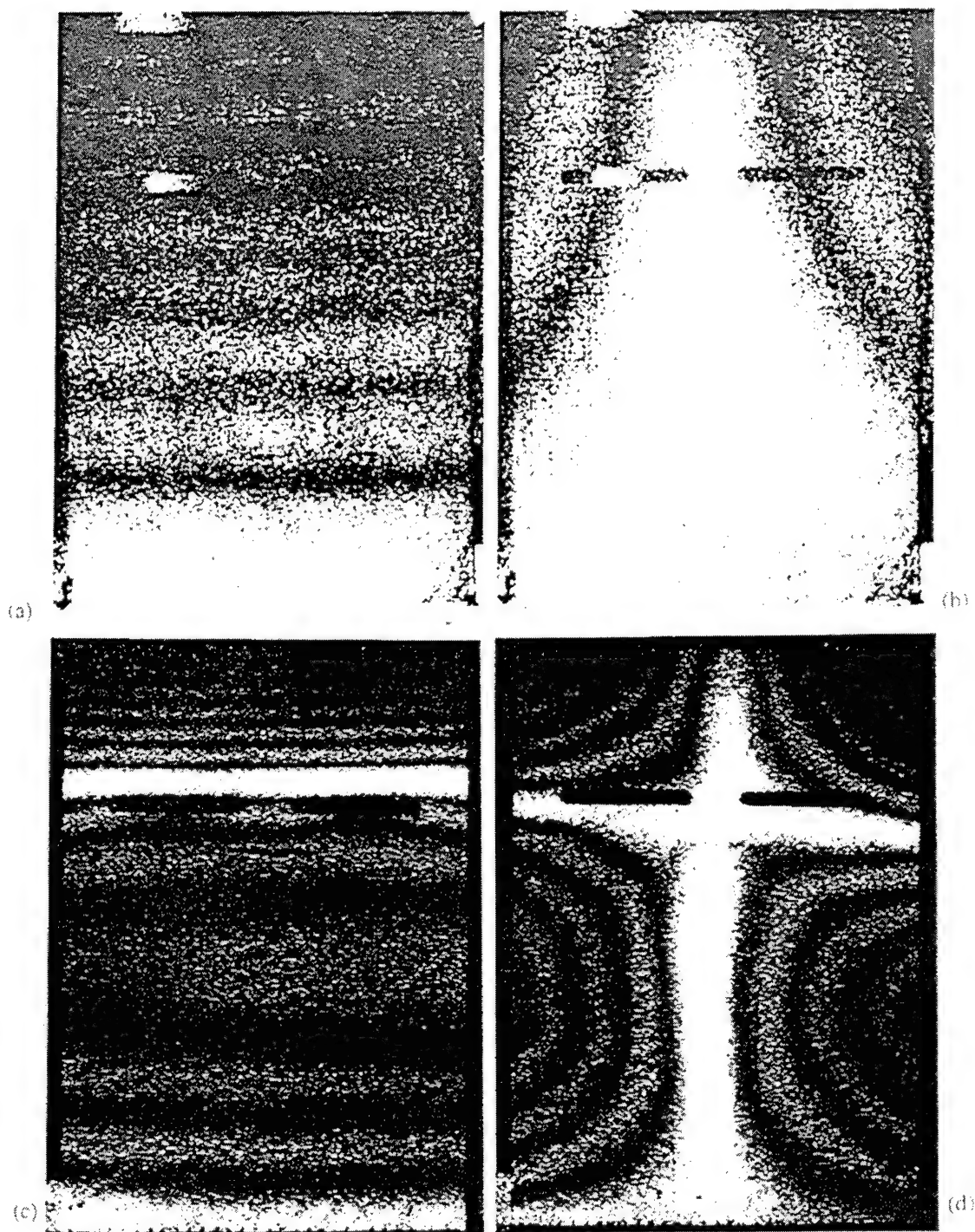


Fig. 11.8. Full field of view EOH images of the TS2 vibrating at:
(a) 18.7 Hz, (b) 39.7 Hz, (c) 117.8 Hz, and (d) 148.0 Hz.

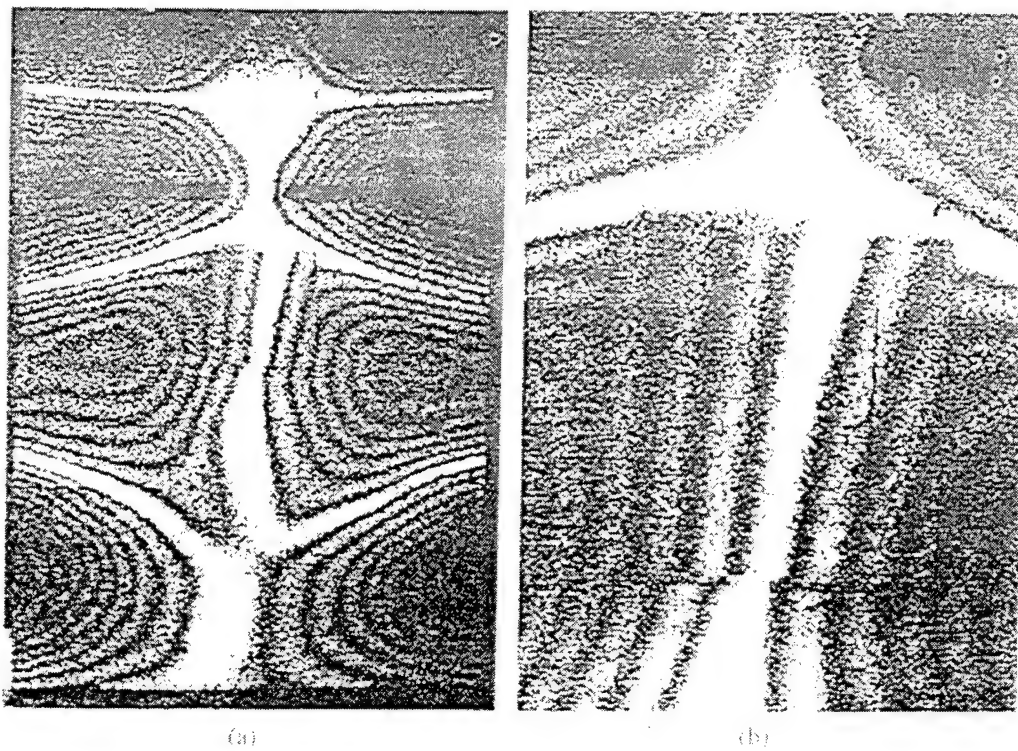


Fig. 11.9. EOH images of the TS2 vibrating at 682 Hz: (a) full field of view, and (b) a close up of the central module and its vicinity.

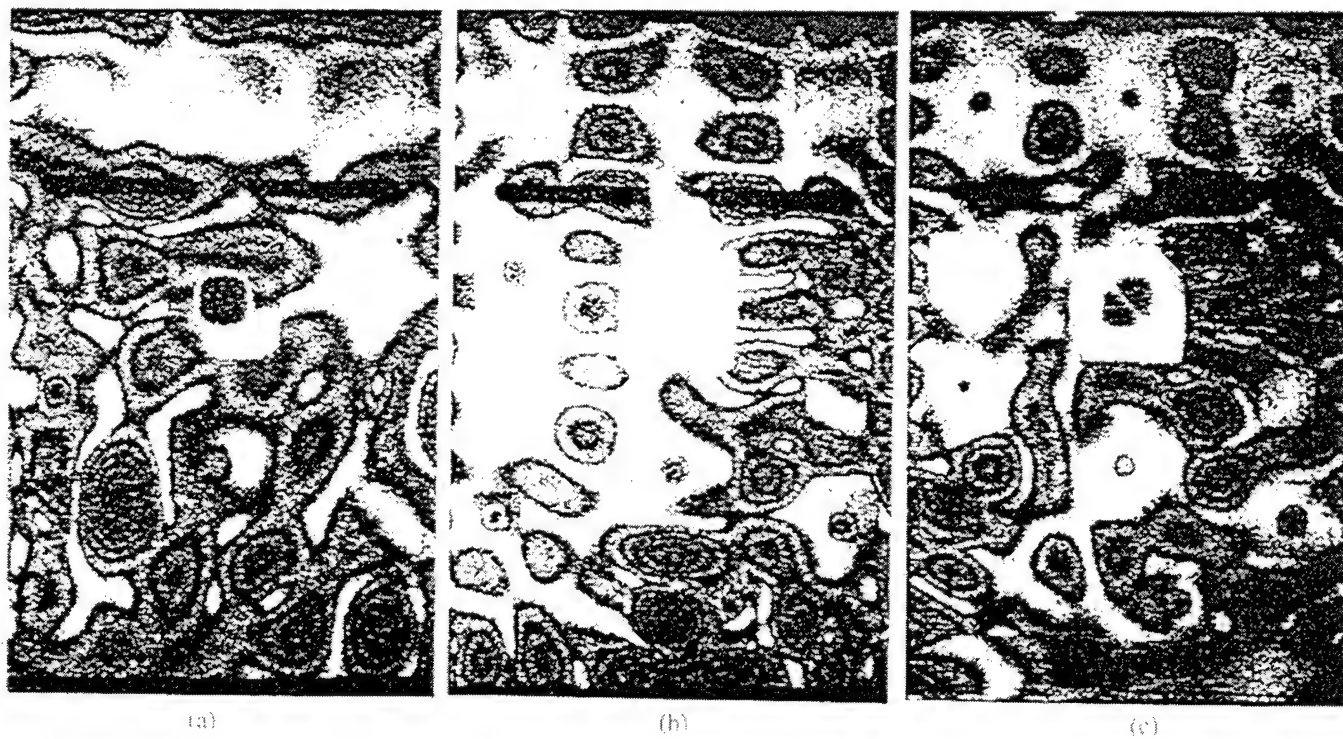


Fig. 11.10. Full field of view EOH images of the TS2 vibrating at: (a) 4,690 Hz, (b) 6,890 Hz, and (c) 9,330 Hz.

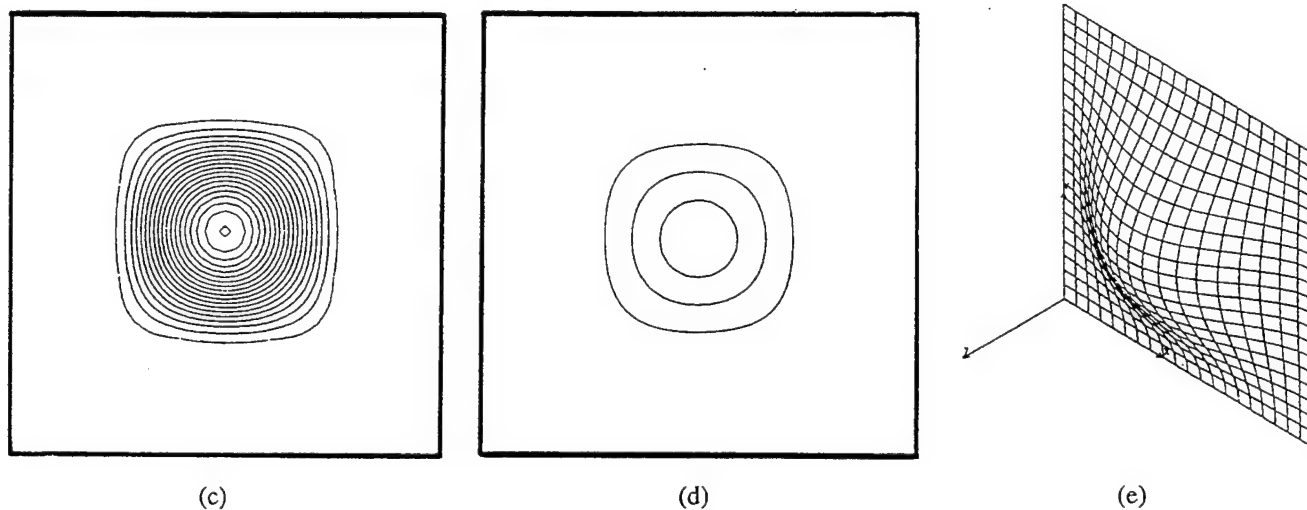
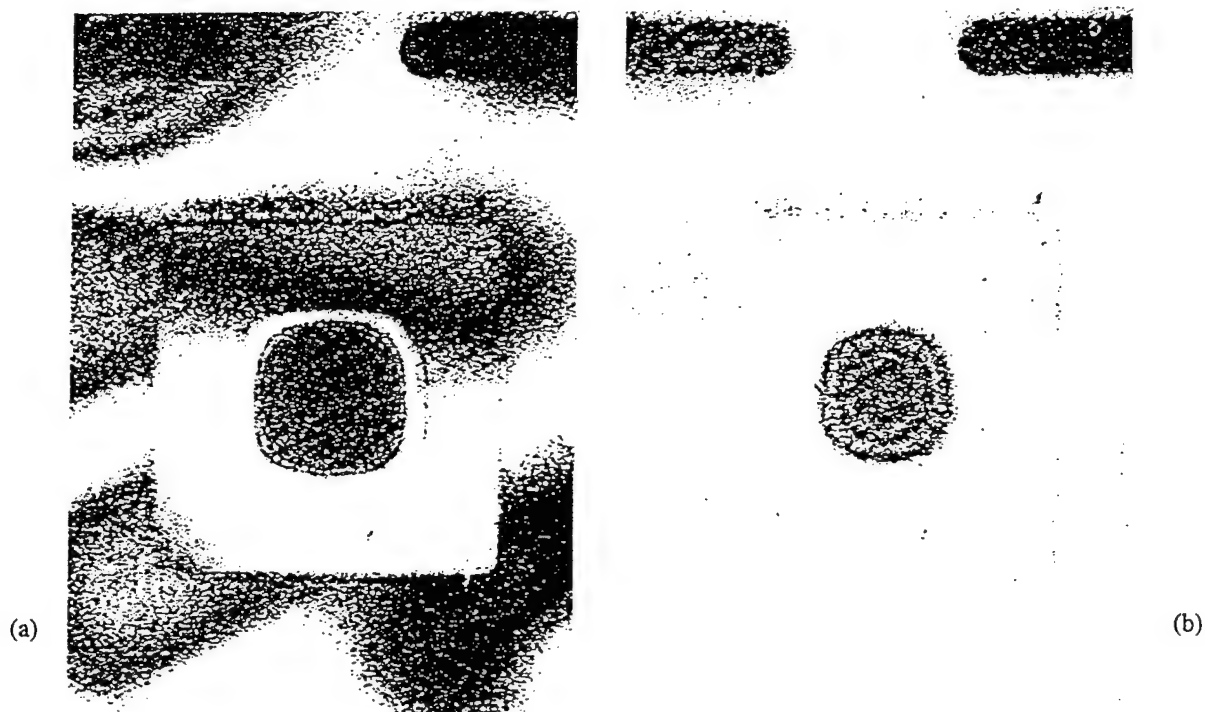


Fig. 11.11. EOH and FEM study of vibration characteristics of the TS2: (a) and (b) represent EOH images recorded at the excitation frequency of 4,830 Hz and at amplitudes lower than that corresponding to Fig. 11.10a, (c) and (d) show equivalent FEM mode shapes determined at 4,809 Hz, and (e) wire frame representation of the fundamental mode shape.

Figures 11.11a and 11.11b display a close up of the central module of the TS2 vibrating at its fundamental resonance frequency of 4,830 Hz, at amplitudes lower than that used to generate the fringe pattern of Fig. 11.10a, vividly showing responsiveness of the module to a change in

the level of the excitation energy. Figure 11.11b clearly shows that at the excitation condition used to generate its fringe pattern there is no apparent activity in the vicinity of the module. Therefore, in order to perform an FEM simulation of the vibration characteristics of the module, development of the corresponding model can be significantly simplified by considering only the module and its immediate vicinity rather than the entire TS2. This is possible by setting the boundary conditions for the MLB in the vicinity of the module to null values as indicated by the EOH image. The FEM simulation of the vibration characteristics of the central module of the TS2, subject to the input from the EOH images, resulted in determination of the resonance frequency of 4,809 Hz which correlated within 0.4% with the experimentally determined value of 4,830 Hz. Also, the FEM determined mode shapes, Figs 11.11c and 11.11d, correlated well with the corresponding EOH results of Figs 11.11a and 11.11b, respectively. A wire frame representation of the fundamental mode shape of the central section of the module, equivalent to Figs 11.11b and 11.11d, is shown in Fig. 11.11e.

11.6. Conclusions and recommendations

In this paper, fundamentals of the TAHI are presented and principles of EOH are reviewed with emphasis on the quantitative study of vibration characteristics of avionics. The quantitative results are illustrated by representative examples from a study of vibration characteristics of two test samples: TS1, consisting of an MLB with eight identical lidded chip modules which were surface mounted in two rows with four modules per row, and TS2, consisting of chip modules of different sizes which were mounted onto another MLB to form an assembly representing typical avionic packages.

Using the EOH, the results are obtained in an automated manner. The interferometric information is recorded electronically at the rate of 30 frames per second, it is processed in a pipeline fashion, and produces results which have very high spatial density, currently at up to 512×480 , or approximately quarter of a million pixels per frame.

The representative results show that the EOH system provides an effective way for recording of the time-average holograms of the vibrating avionics. Using these holograms, eight resonance conditions were identified within the frequency range from zero to 32 kHz, for the TS1. All, except two, of these resonance conditions were predicted by the FEM model used. The correlation between the FEM and the EOH resonance frequencies was within 2% of each other. Investigation of the TS2 vividly revealed the response characteristics of the avionics to various excitation conditions. These results show that at low frequencies the sample behaves as a cantilever plate without any distinctive indication of the presence of the surface mounted modules. However, as the excitation frequency increases so does the display of the presence of the modules. Initially, the modules undergo a rigid-body response. Then, as the excitation frequency increases, they begin to respond elastically exhibiting mode shapes characteristic of a particular design of the avionics subject to the specific boundary conditions and other input parameters.

The ongoing work on combining the methods of hologram interferometry with the finite element methods will lead to a development of new design procedures for avionics. Such hybrid procedures, possessing both experimental and computational capabilities will, in turn, lead to the next generation of tools that will enhance the design and optimization of critical components and structures used in the development of reliable and durable modern avionic packages.

11.7. References

- 11.1. J. Soovere, B. V. Dandawate, and G. A. Garfinkel, *Vibration stress analysis of avionics*, AFWAL-TR-87-3023, 1987.
- 11.2. *Environmental test methods and engineering guidelines*, MIL-STD-810E, 1989.
- 11.3. *Reliability testing for engineering development, qualification, and production*, MIL-STD-781D, 1986.
- 11.4. R. D. Mindlin, "Dynamics of package cushioning," *Bell Syst. Tech. J.*, Vol. 24, pp. 353-461, 1945.
- 11.5. F. T. Flaherty, Jr., "Dynamics of structures," in *Physical design of electronic systems*, Vol. 1, Prentice-Hall, Englewood Cliffs, NJ, 1971.
- 11.6. D. S. Steinberg, *Vibration analysis for electronic equipment*, Wiley, New York, 1973.
- 11.7. J. M. Kallis, K. L. Wong, I. Quzt, L. B. Duncan, K. S. Hill, B. F. Rothschild, D. W. Beuchler, and D. A., Evensen, *Latent defect and life model data*, AFWAL-TR-86-3012, 1986.
- 11.8. D. S. Steinberg, "Tools available for implementing AVIP," *9th Annual IEEE/AESS Dayton Chapter Symp.*, Dayton, OH, 1988.
- 11.9. A. Dasgupta, D. Baker, and M. Pecht, "Reliability prediction of electronic packages," *J. IES*, pp. 36-45, 1990.
- 11.10. D. R. Williams, D. L. Davidson, and J. Lankford, "Fatigue-crack-tip plastic strains by the stereoimaging technique," *Exp. Mech.*, Vol. 20, pp. 134-139, 1980.
- 11.11. C. A. Keely, "Solder joint inspection using laser doppler vibrometry," *Hewlett-Packard J.*, pp. 81-85, 1989.

- 11.12. R. J. Pryputniewicz, "Heterodyne holography applications in studies of small components," *Opt. Engrg.*, Vol. 24, pp. 849-854, 1985.
- 11.13. R. J. Pryputniewicz, "Quantitative electro-optic holography study of dynamics of electronic components," in T. R. Hsu, A. Bar-Cohen, and W. Nakayama, eds, *Advances in electronic packaging*, EEP-Vol. 10-2, Am. Soc. Mech. Eng., New York, pp. 1297-1306, 1995.
- 11.14. W. Bhagat, "Durability life test for avionics/electronics," *Proc. of the IES 38th Annual Technical Mtg.*, Las Vegas, NV, Vol. 2, pp. 174-180, 1987.
- 11.15. J. Soovere, B. V. Dandawante, G. A., Garfinkel, N. Isikbay, and D. S. Steinberg, "Vibration reliability life model for avionics," AFWAL-TR-87-3048, 1987.
- 11.16. J. Kallis, *Reliability assessment of wafer scale integration using finite element analysis*, RL-TR-912-251, 1991.
- 11.17. D. A. Followell, S. L. Liguore, R. Perez, and W. D. Yates, *Computer aided assessment of reliability using finite element methods*, RL-TR-91-155, 1991.
- 11.18. K. J. Bathe, *Finite element procedures in engineering analysis*, Prentice-Hall, Englewood Cliffs, NJ, 1982.
- 11.19. H. Kardestuncer, Editor-in-Chief, *Finite element handbook*, McGraw-Hill, New York, 1987.
- 11.20. W. Weaver, Jr., and P. R. Johnson, *Structural dynamics by finite elements*, Prentice-Hall, Englewood Cliffs, NJ, 1987.
- 11.21. T. J. R. Hughes, *The finite element method: linear static and dynamic finite element analysis*, Prentice-Hall, Englewood Cliffs, NJ, 1987.
- 11.22. O. C. Zienkiewicz and R. L. Taylor, *The finite element method: basic formulations and linear problems*, Vol. 1, McGraw-Hill, New York, 1989.
- 11.23. O. C. Zienkiewicz and R. L. Taylor, *The finite element method: solid and fluid mechanics, dynamics, and nonlinearity*, Vol. 2, McGraw-Hill, New York, 1991.
- 11.24. R. J. Pryputniewicz, "A hybrid approach to deformation analysis," *Proc. SPIE*, Vol. 2342, pp. 282-296, 1994.
- 11.25. A. H. Burkhard and C. E. Leak, "Durability analysis using fracture mechanics for avionics integrity," *J. IES*, pp. 26-32, 1992.

- 11.26. R. J. Pryputniewicz, "Time-average holography in vibration analysis," *Opt. Engrg.*, Vol. 24, pp. 843-848, 1985.
- 11.27. R. J. Pryputniewicz, "Quantitative interpretation of time-average holograms in vibration analysis," in O. D. D. Soares, ed., *Optical metrology*, NATO ASI Series E: Applied Sciences - No. 131, Martinus Nijhoff Publishers, Dordrecht, The Netherlands, pp. 296-316, 1987.
- 11.28. K. A. Stetson and W. R. Brohinsky, "Fringe-shifting technique for numerical analysis of time-average holograms of vibrating objects," *J. Opt. Soc. Am. - A*, Vol. 5, pp. 1472-1476, 1988.
- 11.29. R. J. Pryputniewicz and K. A. Stetson, "Measurement of vibration patterns using electro-optic holography," *Proc. SPIE*, Vol. 1162, pp. 456-467, 1989.
- 11.30. S. Ellingsrud and O. J. Løkberg, "Analysis of high frequency vibrations using TV-holography and digital image processing," *Proc. SPIE*, Vol. 1162, pp. 402-410, 1989.
- 11.31. R. J. Pryputniewicz, "Applications of electro-optic holography in vibration studies," *Proc. Spring Conf. on Experimental Mechanics*, Soc. for Exp. Mech., Bethel, CT, pp. 912-919, 1991.
- 11.32. C. M. Vest, *Holographic interferometry*, Wiley, New York, 1979.
- 11.33. R. J. Pryputniewicz, "Holographic and finite element studies of vibrating beams," *Proc. SPIE*, Vol. 599, pp. 54-62, 1985.
- 11.34. R. J. Pryputniewicz, "Quantitative determination of displacements and strains from holograms," Ch. 3 in Rastogi, P. K., ed., *Holographic interferometry*, Springer-Verlag, Berlin, pp. 33-72, 1994.
- 11.35. K. Oh and R. J. Pryputniewicz, "Application of electro-optic holography in the study of cantilever plate vibration with concentrated masses," in Stetson, K. A., and Pryputniewicz, R. J., eds, *Hologram interferometry and speckle metrology*, Soc. for Exp. Mech., Bethel, CT, pp. 245-253, 1990.
- 11.36. R. J. Pryputniewicz, "Static and dynamics measurements using electro-optic holography," *Proc. SPIE*, Vol. 1554B, pp. 790-798, 1991.
- 11.37. R. J. Pryputniewicz, "Electro-optic holography," in Trolinger, J. D., ed., *Critical reviews of optical science and technology*, SPIE, Vol. CR-46, pp. 148-174, 1993.

12. HYBRID, EOH AND FEM, STUDY AND OPTIMIZATION OF A CANTILEVER PLATE DYNAMICS

In engineering design it is always necessary to use materials and resources in the most efficient and effective way, which is achieved by *optimization*¹. Optimization of structures is usually performed in order to obtain the shape or the layout of the structure of interest that minimizes/maximizes a specific variable of interest, which is known as the *objective function*. The objective function could be weight, displacement, stress, strain, or a specific natural frequency of interest. Frequently, the objective function is limited to physical constraints such as a specific allowed displacement, stress, strain, weight, or natural frequency which are referred to as *constraints*. It is stressed that the above listed parameters are not the only ones used in the process of optimization which, if needed, can also consider such phenomena as heat transfer, fluid flow, electromagnetism, piezoelectricity, etc. Design variables are the parameters that can be changed in order to fulfill the optimization purpose².

12.1. Analytical considerations

Optimization of structures is usually performed in order to obtain the shape or the layout of a structure of interest that makes the most efficient use of materials and resources and that is most capable of meeting the design criteria set by the engineer.

Structural optimization is performed by a combined use of different computational techniques. These techniques include mathematical programming methods, that provide procedures for obtaining optimal conditions, and methods such as finite differences, finite elements, and boundary elements, for evaluation of the response of a structure at different stages of the optimization process.

12.1.1. Terminology

Design optimization can be defined as an iterative redesign process that attempts to minimize or maximize a specific measure of the response of a structure (objective function) subjected to limits or constraints on the response by using a rational mathematical approach to yield improved designs. Design variables are the parameters that can be changed during the optimization process. So, in order to perform optimization of a structure it is necessary to identify a specific objective function and the design variables and constraints. In this chapter the objective function is the dynamic response of a structure having geometric constraints. The objective function is evaluated using modal analyses and is minimized/maximized using

mathematical programming techniques that are capable of taking the design constraints into account.

12.1.2. Mathematical programming methods

The main idea of design optimization presented in this chapter relies on finding a mathematical relationship between an arbitrary objective function, constraints, and the design variables. Such relation is not known in advance. An optimization program makes use of the existing design set that is available out of the initial analyses in order to estimate these approximate mathematical functions using regression analysis procedures. As optimization progresses, new design sets are used to obtain a better approximation. It is this approximation that is minimized/maximized rather than the actual objective function and constraints. Linear, quadratic, cubic, and quadratic cross terms can be used in least squares regression approximations. The general steps for an optimization process are as follows³:

- 1) develop analyses in order to find an initial approximation for the objective function and constraints,
- 2) optimization algorithm,
 - a) form approximations for the objective function and constraints based on regression analysis,
 - b) find the gradient of the objective function and constraints with respect to the design variables,
 - c) use a feasible directions algorithm to determine a new set of design variables,
 - d) build the computational model in terms of these new design variables and totally remesh and reapply boundary conditions to the model,
 - e) perform new analysis,
 - f) check for convergence. This step is needed when the objective function does not improve significantly. If converge is not obtained it is necessary to either repeat steps (a) to (f) or to terminate the algorithm.
- 3) the resultant geometry is an improved design.

12.1.3. Modal analysis

Modal analysis is of particular interest because the optimization process considered in this chapter requires minimization/maximization of specific natural frequencies of a plate. Considering excitation of a structure by a harmonic force the optimization process requires solution of a forced excitation problem. The mathematical solution of this problem indicates that this type of excitation can produce resonance of the structure when the frequency of the forcing

function is equal to any natural frequency of the structure. This indicates that the solution of a free vibrations problem is sufficient for calculating the natural frequencies of a structure.

Consider an undamped free vibrations problem and a discretization of the domain of the structure using the finite element approximation for representing the deformation, y_i , of the structure, i. e.,

$$y_i = \sum_{j=1}^n N_j^i \beta_j^i \quad , \quad (12.1)$$

where N_j^i is the j -th shape function and β_j^i are the nodal coefficients. Then, it is possible to write

$$[M]\{Y\} + [K]\{Y\} = \{0\} \quad , \quad (12.2)$$

where $\{Y\}$ is the deformation vector, $[M]$ is the mass matrix, and $[K]$ is the stiffness matrix. For the free vibrations of the undamped structure, we seek the solution of Eq. 12.2 in the form

$$y_i = a_i \sin(\omega t - \alpha) \quad , \quad i = 1, 2, \dots, n \quad , \quad (12.3)$$

or in a vector form

$$\{Y\} = \{a\} \sin(\omega t - \alpha) \quad , \quad (12.4)$$

where a_i is the amplitude of motion of the i -th coordinate, n is the number of degrees of freedom, ω is the circular frequency of free vibration, t is the time, and α is the phase angle. Substitution of Eq. 12.4 into Eq. 12.2 gives

$$-\omega^2 [M]\{a\} \sin(\omega t - \alpha) + [K]\{a\} \sin(\omega t - \alpha) = \{0\} \quad , \quad (12.5)$$

which yields

$$|[K] - \omega^2 [M]| \{a\} = 0 \quad . \quad (12.6)$$

The formulation of Eq. 12.6 yields an eigenvalue problem. The nontrivial solution of Eq. 12.6 requires that the determinant of the matrix factor of $\{a\}$ be equal to zero, i. e.,

$$|[K] - \omega^2 [M]| = 0 \quad . \quad (12.7)$$

In general, Eq. 12.7 results in a polynomial equation of degree n in ω^2 which should be satisfied for n values of ω^2 . This polynomial equation is called the *characteristic equation* of the system. For each value of ω^2 satisfying the characteristic equation it is possible to solve Eq. 12.6 for a_1, a_2, \dots, a_n in terms of arbitrary constants. In general, for a large number of degrees of freedom it is not possible to solve the polynomial equation in a direct form, so numerical methods are utilized for solving Eq. 12.7 in an iterative fashion. This type of iterative solution is

compatible with the finite element approach since forming of the stiffness and mass matrices is automatic. Therefore, different iterative eigenvalue solvers, such as the Lanczos or subspace iteration methods, can be utilized. The solution of the eigenvalue problem provides information on natural frequencies and mode shapes of the structure^{4,5}.

12.2. Description of the optimization procedure

Optimization of structures can be entirely performed using computational methods. In addition, these methods can be utilized for finding sensitivities of the objective function with respect to the design variables because it is relatively easy to change characteristics of a computational model and to take into account different effects. However, optimization studies may lack any significance if actual boundary conditions, geometry, and/or material properties are not modeled properly. The information necessary to properly model a structure can be obtained by performing experiments.

Experimental methods are very effective tools for testing of components since a correct experimental procedure takes into account the actual boundary conditions, geometry, and material properties of the component being tested. However, experiments alone are not sufficient to optimize a structure because it is impractical to experimentally find the behavior of the objective function under different values of the design variables. An effective approach to optimization of structures is to combine the computational and experimental methodologies since by complementing each other it is possible to take advantage of the unique features of each methodology.

12.2.1. Optimization procedure

The optimization studies presented in this chapter consist of a combined computational and experimental approach¹, Fig. 12.1.

According to Fig. 12.1, computational analyses are performed on the initial design in order to obtain the modal response of the structure before the optimization is performed and its results are compared with the modal response obtained from the holographic interferometry studies of an equivalent initial design model. The comparisons between the computational and the experimental results are based on the eigenvalues/frequencies and eigenvectors/interference patterns of the computational and time-average speckle pattern interferometry modal analyses displayed in real-time. When discrepancies between computational and experimental results are encountered it is necessary to verify both the parameters of the computational model and the experimental conditions. The verifications include boundary conditions, material properties, geometric accuracy, and mechanical and optical setups. The results of these comparisons

provide information on the accuracy of the computational analyses with respect to modeling of the experimental behavior of the structure. When an acceptable degree of accuracy is obtained the computational model is utilized for performing sensitivity analyses of the objective function with respect to the specified design variables as well as shape optimization of the initial design. The geometry obtained from the shape optimization analyses is then used to manufacture a prototype which is experimentally tested in order to obtain computational and experimental comparisons.

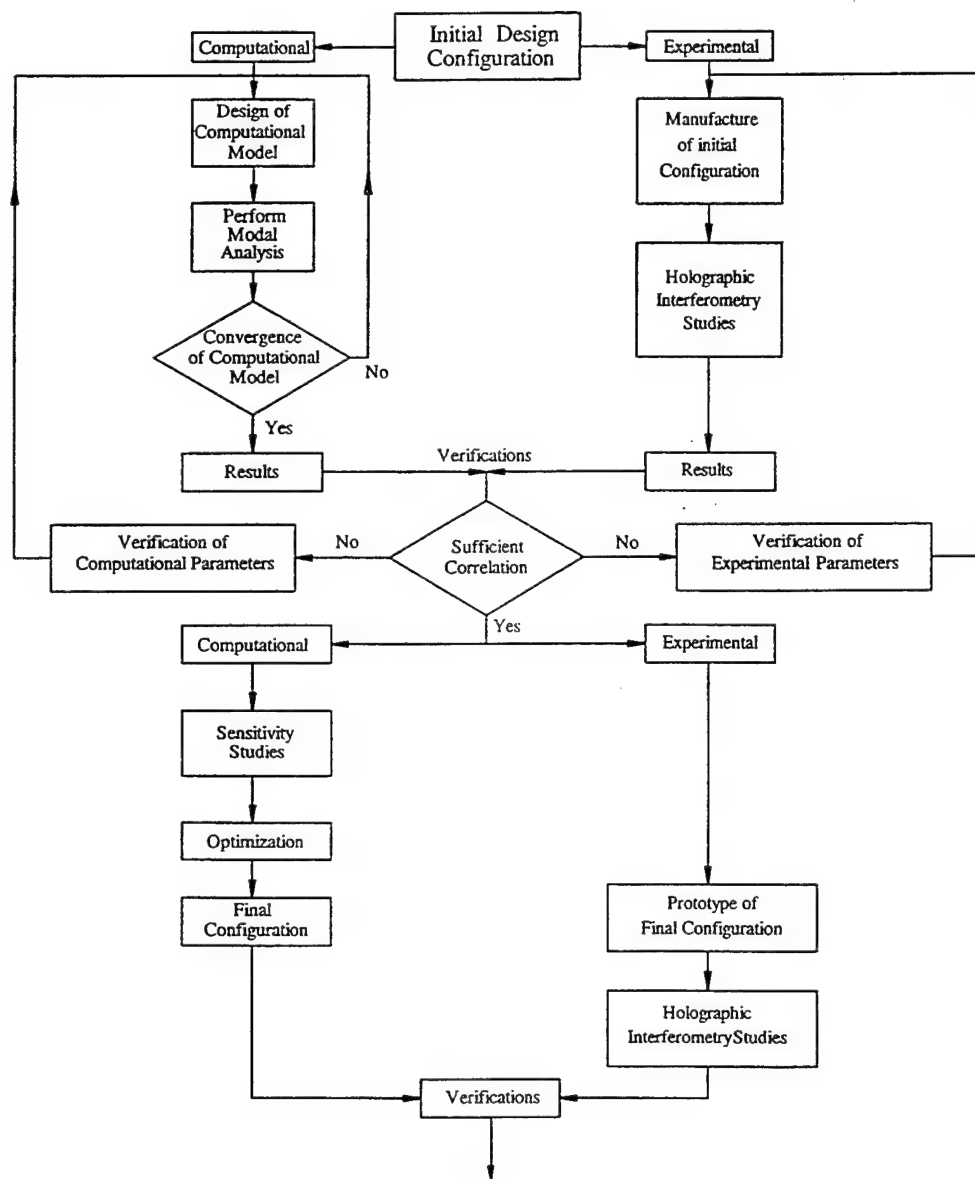


Fig. 12.1. Flowchart of the optimization procedure utilized in the studies presented in this chapter.

12.2.2. Description of the computational model

The computational model utilized for performing the modal analyses and optimization is based on the finite element model (FEM). The input parameters required for the analyses consist of an accurate geometrical representation, domain discretization, boundary conditions, and material properties. Each one of these parameters has to be properly selected in order to obtain a correct modeling of both the modal behavior of the domain and the shape optimization analyses. An important factor is the use of high order polynomial elements since these elements have good convergence properties and higher accuracy than other types of elements⁴⁻⁶.

12.2.3. Description of the experimental model

The electro-optic holography (EOH) system was utilized to performing the experimental modal analyses presented in this chapter. Figure 12.2 shows an optical configuration used in this study. In this system, the laser output is divided into two separate beams by means of a beamsplitter BS. One of the beams is directed towards a beam expander BE to illuminate the object OB uniformly. This beam, modulated by an interaction with an object is transmitted by the object imaging lens IL to the object input of the speckle interferometer SI. The other beam is directed towards a microscope objective MO and then to a fiber-optic probe that is connected to the reference input of SI. The object and reference beams are combined by the SI which is capable of sending the combined signal to a CCD camera. The output of the camera is directed to a pipeline image processor computer which is capable of processing images at a high rate as well as controlling the phase stepper PS1 in order to introduce 90° phase steps between consecutive captured frames^{7,8}.

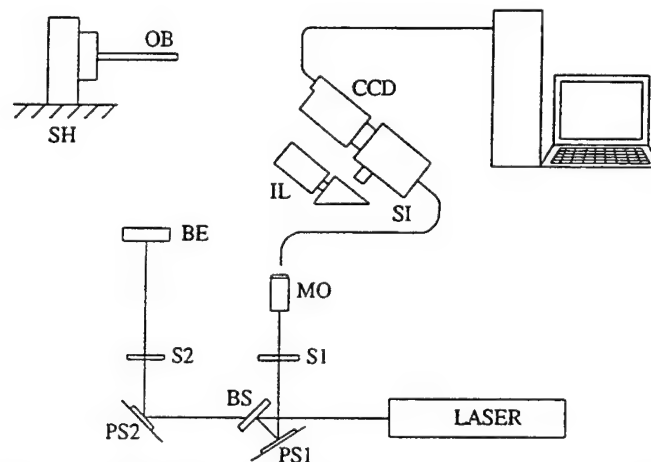


Fig. 12.2. Optical configuration of the EOH system used in the optimization study: OB is the object under investigation, SI is the speckle interferometer, BE is the beam expander, BS is the beamsplitter, MO is the microscope objective, PS1 and PS2 are the piezoelectric phase steppers, S1 and S2 are the beam shutters, IL is the object imaging lens, and SH is the piezoelectric shaker.

In order to perform the experimental modal analyses, the structure of interest is mounted in a fixture that is excited by a piezoelectric shaker SH which, in turn, is driven by a frequency generator. The EOH system is capable of providing real-time speckle interferences when the excitation frequency is modulated. This allows determination of the natural frequencies and mode shapes of the structure being studied.

12.3. Results and discussions

The results that are presented in this chapter include the optimization of an Al-2024 cantilever plate having as objective function the minimization/maximization of its fundamental natural frequencies subjected to different constrained design variables. The cases that are considered include:

- (a) cantilever plate with a single hole having as design variables the vertical location and diameter of the hole,
- (b) cantilever plate with two holes having as design variables the diameters of the holes.

The procedure presented in Section 12.2 is applied to perform the studies for the two cases listed above.

12.3.1. Cantilever plate with a single hole having as design variables the vertical location and diameter of the hole

Figure 12.3 shows the configuration of the cantilever plate considered. In this figure, D and C_y are identified as the constrained design variables that are allowed to vary in a range that permits the manufacture of the optimized geometry within limits that do not change the topology of the plate.

Evaluation of the initial configuration is started by performing convergence studies of the computational model with respect to the number of elements utilized in the discretized plate. These studies are necessary in order to verify the degree of accuracy that is obtained for a specific number of elements. The finite element models are designed based on high accuracy quadratic elements and assumptions of isotropy and homogeneity of the material properties⁹. Figure 12.4 shows a typical finite element model and the convergence behavior of the computational model for predicting the value of the first natural frequency of the cantilever plate.

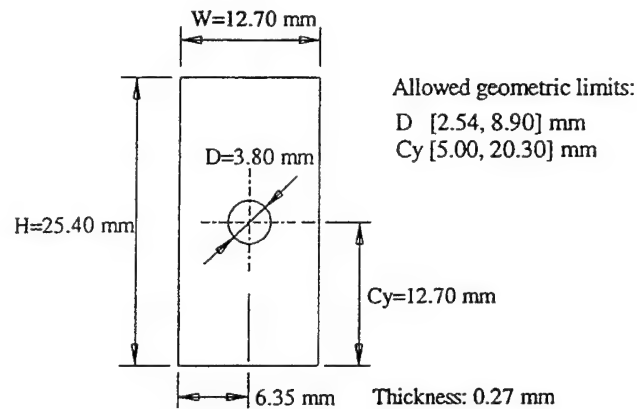


Fig. 12.3. Configuration of the Al-2024 plate with a single hole considered for optimization. The objective function is the minimization/maximization of the fundamental natural frequencies of the plate:
 D and C_y are the constrained design variables.

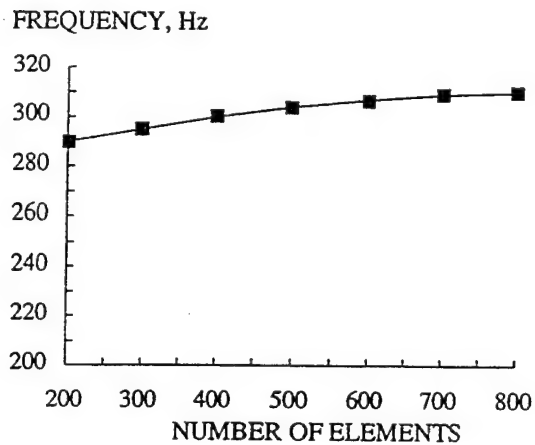
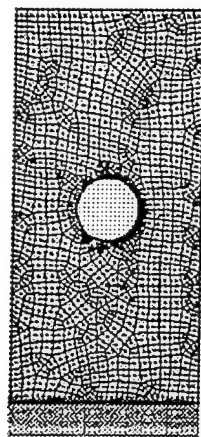


Fig. 12.4. Typical finite element model and convergence behavior to the first resonance frequency with respect to the number of elements utilized for performing the computational modal analyses. The plate is fixed at the base.
 Nine noded elements are utilized.

The EOH studies were performed in parallel with the computational modeling in order to verify that the computational and the experimental studies use equivalent models. Table 12.1 summarizes the computational and experimental results of the first 12 resonance frequencies. As it can be observed, good correlation between the computational and the experimental results was obtained and, therefore, the computational model can be reliably utilized for performing sensitivity and optimization analyses of the plate.

Table 12.1. Summary of computational and experimental values of the first 12 resonance frequencies of the initial configuration of the cantilever plate with a single hole.

Mode	Frequency, Hz		%Diff. *	Mode	Frequency, Hz		%Diff. *
	Computational	Experimental			Computational	Experimental	
1	312.12	319.0	-0.022	7	8994.96	8948.0	0.005
2	1347.27	1300.0	0.036	8	10734.50	11165.0	-0.039
3	1919.75	1978.0	-0.029	9	12193.00	12285.0	-0.007
4	4479.15	4360.0	0.027	10	12364.90	-----	-----
5	5472.95	5650.0	-0.031	11	14017.10	14330.0	-0.022
6	8433.52	8377.0	0.007	12	16890.40	-----	-----

* %Diff.=(computational-experimental)/experimental

Sensitivity analyses and optimization of the plate for minimization and maximization of the objective function are performed on the experimentally validated initial configuration. Figure 12.5 depicts the results of the sensitivity analyses for the first three fundamental natural frequencies with respect to the normalized design variables. The values of the design variables are varied within the allowed constrained design space.

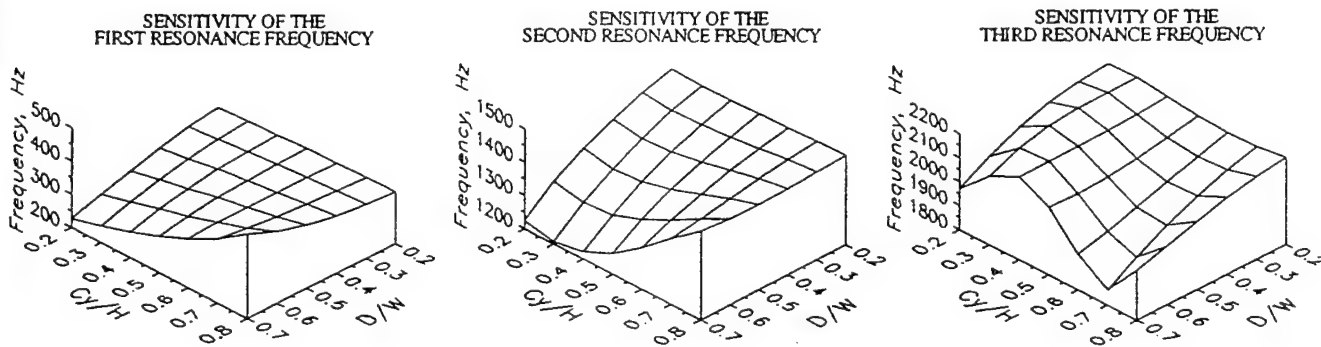


Fig. 12.5. Sensitivity of the first three resonance frequencies with respect to normalized design variables D and C_y . W and H are the width and height of the plate, respectively.

Figure 12.6 shows the EOH patterns and the finite element mode shapes obtained for the first 5 resonance frequencies, while Table 12.2 summarizes the computational and experimental results of the first 12 resonance frequencies for minimization of the objective function. Figure 12.7 and Table 12.3 show equivalent results but for maximization of the objective function.

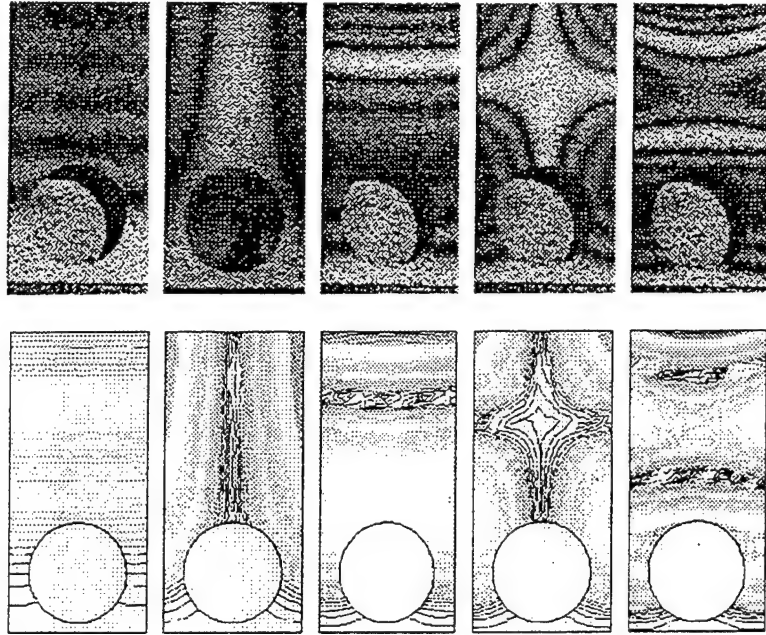


Fig. 12.6. EOH fringe patterns and computational mode shapes of the first five resonance frequencies for *minimization* of the objective function of the cantilever plate with a single hole.

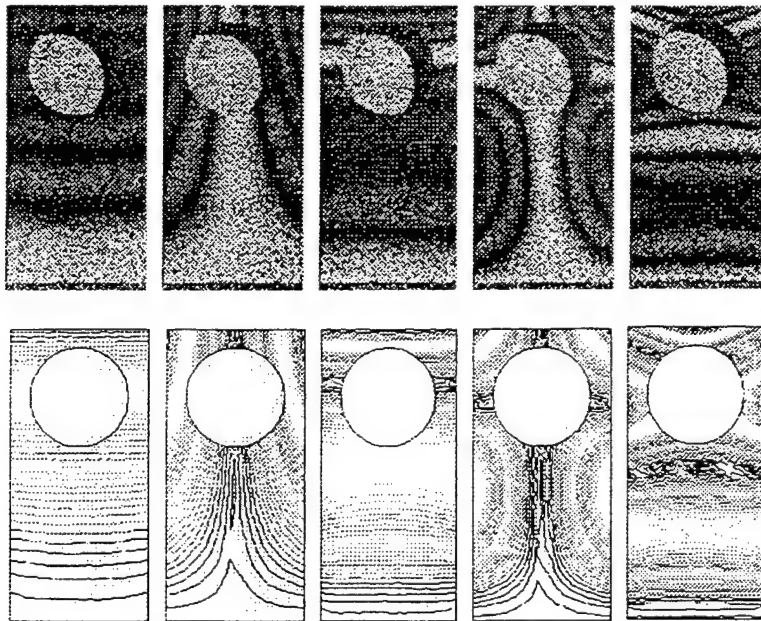


Fig. 12.7. EOH fringe patterns and computational mode shapes of the first five resonance frequencies for *maximization* of the objective function of the cantilever plate with a single hole.

Table 12.2. Summary of computational and experimental values of the first 12 resonance frequencies of the cantilever plate with a single hole optimized for minimization of the objective function.

Mode	Frequency, Hz		%Diff. *	Mode	Frequency, Hz		%Diff. *
	Computational	Experimental			Computational	Experimental	
1	211.64	211.0	0.003	7	8523.48	8355.0	0.020
2	1173.14	1103.0	0.064	8	8890.04	8875.0	0.002
3	1836.79	1831.0	0.003	9	11376.71	10750.0	0.058
4	4345.17	4202.0	0.034	10	12234.77	12340.0	-0.009
5	5578.32	5742.0	-0.029	11	14045.00	13210.0	0.063
6	8502.41	-----	-----	12	17698.43	17840.0	-0.008

$$*\%Diff. = (\text{computational} - \text{experimental}) / \text{experimental}$$

Table 12.3. Summary of computational and experimental values of the first 12 resonance frequencies of the cantilever plate with a single hole optimized for maximization of the objective function.

Mode	Frequency, Hz		%Diff. *	Mode	Frequency, Hz		%Diff. *
	Computational	Experimental			Computational	Experimental	
1	394.93	394.5	0.001	7	7834.96	-----	-----
2	1389.42	1372.0	0.013	8	11058.06	11325.0	-0.024
3	1769.67	1785.0	-0.009	9	11676.75	11835.0	-0.013
4	3795.27	3798.0	-0.0007	10	13279.52	13656.0	-0.028
5	5048.81	5042.0	0.001	11	13667.07	-----	-----
6	7790.43	7770.0	0.003	12	16819.19	16787.0	0.002

$$*\%Diff. = (\text{computational} - \text{experimental}) / \text{experimental}$$

12.3.2. Cantilever plate with two holes having as design variables the diameters of the holes

Figure 12.8 depicts the configuration of the cantilever plate considered. In this figure, $D1$ and $D2$ are identified as the constrained design variables. The same criteria for the limits on the design variables and convergence of the computational model, as explained in Section 12.3.2 are applied. Figure 12.9 shows a typical finite element model and the convergence behavior of the computational model for predicting the value of the first natural frequency of the plate and Table 12.4 summarizes the corresponding computational and experimental results obtained for the initial plate configuration.

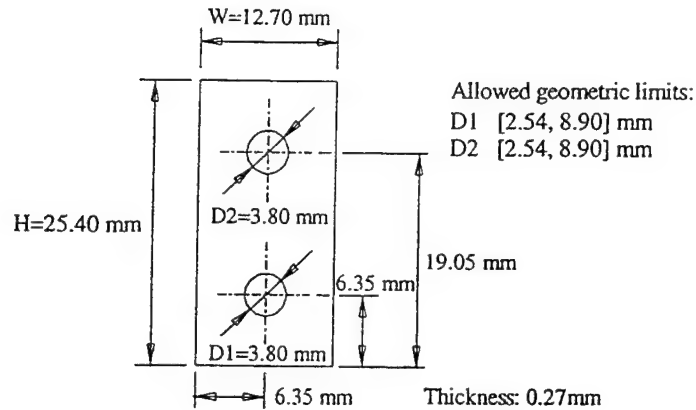


Fig. 12.8. Configuration of the Al-2024 plate with two holes considered for optimization. The objective function is the minimization/maximization of the fundamental natural frequencies of the plate: $D1$ and $D2$ are the constrained design variables.

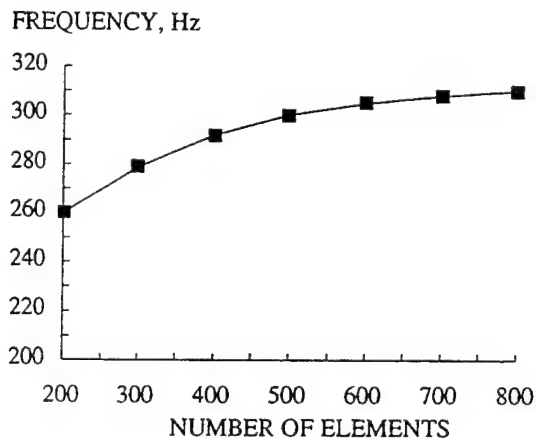
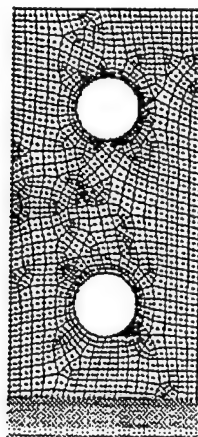


Fig. 12.9. Typical finite element model and convergence behavior to the first resonance frequency with respect to the number of elements utilized for performing the computational modal analyses. The plate is fixed at the base. Nine noded elements are utilized.

Using the validated model, sensitivity analyses and optimization were performed. The results of the sensitivity analyses are presented in Fig. 12.10 where the behavior of the first three resonance frequencies with respect to normalized design variables are shown. Figures 12.11 and 12.12 and Tables 12.5 and 12.6 summarize the results of the optimization studies for the minimization and maximization of the objective function, respectively.

Table 12.4. Summary of computational and experimental values of the first 12 resonance frequencies of the initial configuration of the cantilever plate with two holes.

Mode	Frequency, Hz		%Diff. *	Mode	Frequency, Hz		%Diff. *
	Computational	Experimental			Computational	Experimental	
1	310.08 Hz	313.3 Hz	-0.010	7	8448.76 Hz	-----	-----
2	1321.44	1289.0	0.025	8	11018.76	11155.0	-0.012
3	1959.16	1967.0	-0.004	9	11711.33	11835.0	-0.010
4	4264.66	4220.0	0.011	10	12673.00	-----	-----
5	5415.18	5440.0	-0.005	11	13966.19	14070.0	-0.007
6	8357.92	8455.0	-0.011	12	16947.29	17284.0	-0.019

*%Diff.=(computational-experimental)/experimental

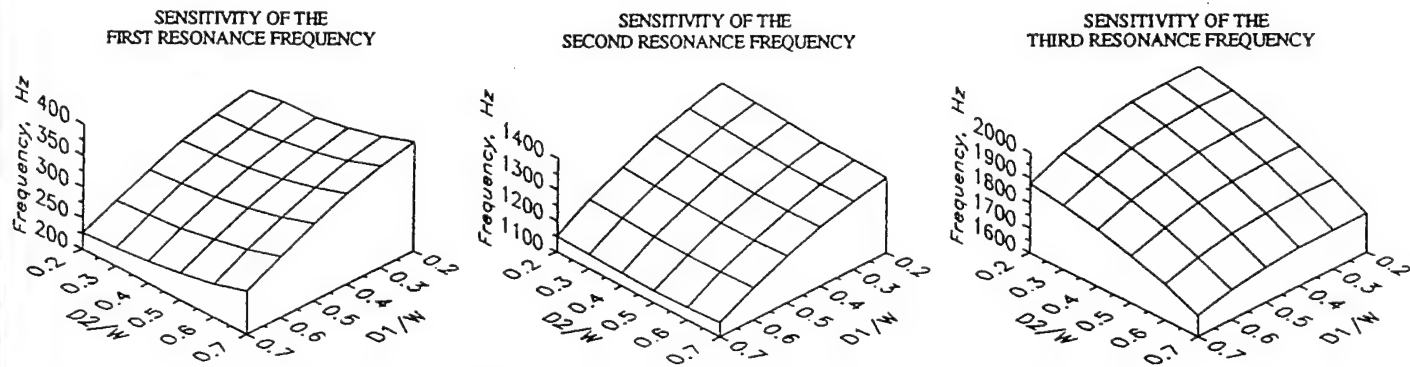


Fig. 12.10. Sensitivity of the first three resonance frequencies with respect to the normalized design variables $D1$ and $D2$, W is the width of the plate.

12.4. Conclusions and recommendations

In this study, a hybrid approach consisting of the finite element method (FEM) and the electro-optic holography (EOH) method was used to optimize a cantilever plate with holes in order to minimize/maximize specific resonance frequencies. This hybrid approach shows that the computational and the experimental methodologies used in this study complement each other and can be applied to optimization of mechanical components yielding results in a very fast, accurate, and efficient manner.

Table 12.5. Summary of computational and experimental values of the first 12 resonance frequencies of the cantilever plate with two holes optimized for minimization of the objective function.

Mode	Frequency, Hz		%Diff. *	Mode	Frequency, Hz		%Diff. *
	Computational	Experimental			Computational	Experimental	
1	218.32 Hz	218.30 Hz	0.0001	7	8302.80 Hz	8170.0 Hz	0.016
2	1139.28	1133.0	0.006	8	8417.12	8460.0	-0.005
3	1847.94	1883.0	-0.019	9	11016.25	11076.0	-0.005
4	4277.73	4266.0	0.003	10	12697.44	12986.0	-0.022
5	5666.00	5948.0	-0.047	11	13822.51	13705.0	0.009
6	8258.61	-----	-----	12	17782.00	18050.0	-0.015

*%Diff.=(computational-experimental)/experimental

Table 12.6. Summary of computational and experimental values of the first 12 resonance frequencies of the cantilever plate with two holes optimized for maximization of the objective function.

Mode	Frequency, Hz		%Diff. *	Mode	Frequency, Hz		%Diff. *
	Computational	Experimental			Computational	Experimental	
1	377.17 Hz	372.5 Hz	0.013	7	7846.09	7940.0	-0.012
2	1346.72	1338.0	0.007	8	10730.0	10670.0	0.006
3	1745.17	1754.0	-0.005	9	11268.16	11160.0	0.010
4	3746.51	3770.0	-0.006	10	13191.61	-----	-----
5	5067.66	5090.0	-0.004	11	13253.0	13420.0	-0.012
6	7786.51	7800.0	-0.002	12	17066.7	17440.0	-0.021

*%Diff.=(computational-experimental)/experimental

12.5. References

- 12.1. C. Furlong and R. J. Pryputniewicz, "Opto-mechanical study and optimization of a cantilever plate dynamics, " *Proc. SPIE*, 2545:192-203, 1995.
- 12.2. T. Haftka and R. V. Grandhi, "Structural shape optimization-a survey," *J. Comp. Meth. in App. Mech. and Engrg.*, 57:91-106, 1986.
- 12.3. P. Y. Papalambros and D. J. Wilde, *Principles of optimal design - modeling and computation*, Cambridge, New York, 1988.
- 12.4. COSMOS/M user guide v. 1.70, Structural Research Analysis Corporation, Santa Monica, CA 1993.

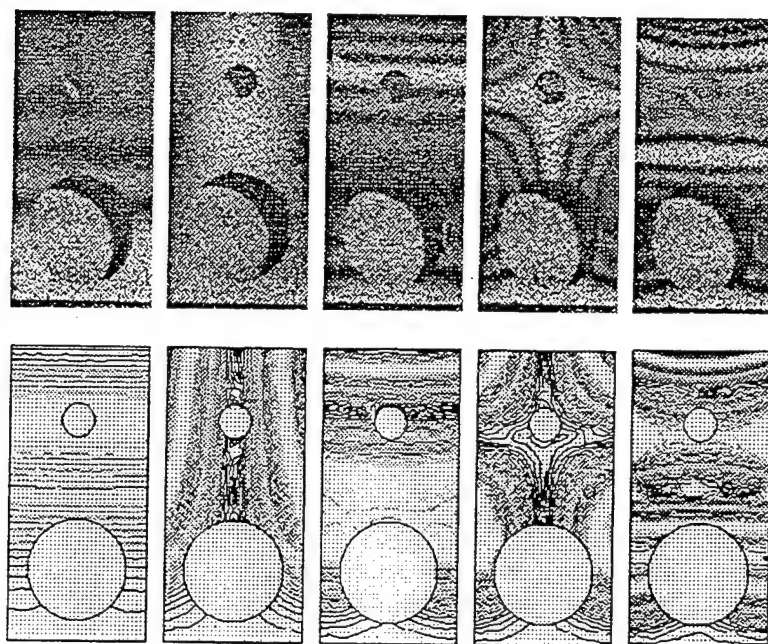


Fig. 12.11. EOH fringe patterns and computational mode shapes for the first five resonance frequencies for *minimization* of the objective function of the cantilever plate with two holes.

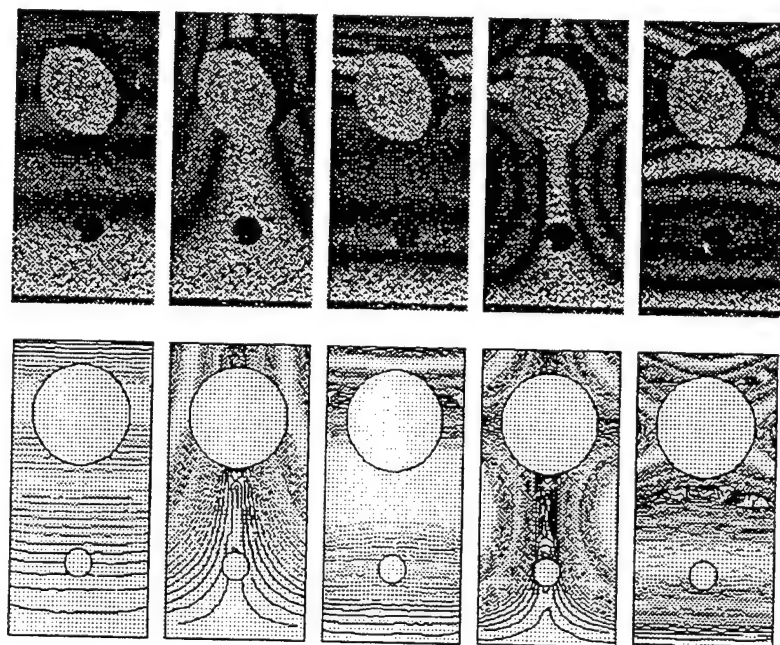


Fig. 12.12. EOH fringe patterns and computational mode shapes for the first five resonance frequencies for the *maximization* of the objective function of the cantilever plate with two holes.

- 12.5. ABAQUS user's guide v. 4.8, Hibbit, Karlsson, and Sorensen, Inc., Palo Alto, CA, 1989.
 - 12.6. N. Kikuchi, "Adaptive grid-design methods for finite element analysis," *J. Comp. Meth. in App. Mech. and Engrg.*, 55:129-160, 1986.
 - 12.7. R. J. Pryputniewicz, "Holographic and finite element studies of vibrating beams," *Optics in Engineering Measurement, Proc. SPIE*, 599:54-62, 1985.
 - 12.8. T. W. Bushman, *Automated fringe unwrapping by energy minimization*, MS Thesis, Worcester Polytechnic Institute, Worcester MA, 1993.
 - 12.9. J. Kiusalaas and R. C. J. Shaw, "An algorithm for shape optimal structural design with frequency constraints," *Int. J. Num. Meth. in Engrg.*, 13:283-295, 1978.
-

13. OVERALL SUMMARY, CONCLUSIONS, AND RECOMMENDATIONS

The objective of this project was to develop and apply, to micro-scale electronic assemblies, a quantitative measurement approach using electro-optic holography (EOH) that is able to simultaneously measure three-dimensional displacements and deformations under either static, quasi-static, or vibration conditions.

The objective of this project was achieved. The results presented in this report describe the EOH system with three cameras, which was developed during this project, the mathematical procedures necessary to use the system for electronic recording, processing, and display of quantitative results on displacement fields of objects subjected to static, quasi-static, and vibration loads, and representative applications of the EOH methodology for avionics durability analysis and validation.

The results presented in this report demonstrate viability of the EOH system for avionics durability analysis and validation.

More specifically, results presented show that the EOH system effectively records high quality electronic holograms of objects at near real-time speeds of 30 holograms per second.

Using the EOH system, developed during this project, results are obtained in a truly totally automated manner. The interferometric information is recorded electronically at the rate of 30 holograms per second, it is processed in a pipeline fashion, and produces results which have very high spatial density - currently at up to 512×480 points per image (frame). These results correlate well with the computational (i. e., FEM) predictions of the displacement fields of the objects subjected to static and dynamic loads.

Continued work is needed to merge, within the host computer, the results obtained from the EOH system with the computational procedures of the FEM. This will result in a hybrid system which will allow totally automated, quantitative approach for avionics durability analysis and validation.

Additionally, during this project, viability of electro-optic shearography for avionics durability analysis and validation was investigated. In this part of the project, the electro-optic holography (EOH) and electro-optic shearography (EOS) were used side by side to study behavior of a cantilever plate under static and dynamic loading conditions. This study examines parameters characterizing EOH and EOS methodologies and relates these parameters to the equations governing recording and quantitative interpretation of the interferograms.

The results presented in this report show that the EOH is a very viable method for accurate determination of the full field displacements. Comparison of the EOH and the FEM results indicates that they correlate to better than 1%. However, because of the EOH's inherently invariant and high sensitivity, fringe frequencies become very high rapidly and often obscure local deformations which are of interest.

The results also show that the EOS is a very viable method for determination of derivatives of the displacement fields. The accuracy of this determination depends on the magnitude of the shear introduced while recording the interferograms. In this study, shears ranging from 3 mm to 25 mm were used. The results show that the difference between the shearographic and the theoretical results decreases as the magnitude of the shear decreases, from approximately 16% for 25 mm shear to approximately 1% for the 3 mm shear.

In addition, the results demonstrate the viability of the EOS for studies of objects under the condition of resonance. It is particularly interesting to see a side by side comparison of the fringe patterns produced electronically while imposing shears in the directions normal to the direction of the predominant component of the displacement vector and how they relate to the conventional mode shapes obtained by the EOH.

Work on side by side developments of electronic holography and electronic shearography should continue. These methodologies complement each other and together provide information that could not be readily obtained in any other way.

Also, this report presents some of the developments relating to hybridization of hologram interferometry and computational methods. This hybrid approach to deformation analysis is a part of what we call ACES methodologies, which emphasize the analogy between analytical, computational, and experimental methodologies and employ them to obtain solutions that may not have been otherwise obtainable, to ease the existing solution procedures, or to attain improvements in the results. Use of these methodologies to solution of real problems is illustrated with representative examples and shows their viability for avionics durability analysis and validation.

Continued advances on hybridization of experimental, especially optical, methods with the computational methods will lead to development of new tools which will facilitate solution of problems hampered by lack of knowledge on behavior of new materials, large deformations, and/or inherent nonlinearities.

As a part of this report, fundamentals of the time-average hologram interferometry (TAHI) are presented and principles of the EOH are reviewed with emphasis on the quantitative study of vibration characteristics of avionics. The quantitative results are illustrated by representative examples from a study of vibration characteristics of selected test samples: TS1, consisting of an MLB with eight identical lidded chip modules which were surface mounted in two rows with four modules per row, and TS2, consisting of chip modules of different sizes which were mounted onto another MLB to form an assembly representing typical avionics packages.

The representative results show that the EOH system provides an effective way for recording of the time-average holograms of the vibrating avionics. Using these holograms, eight resonance conditions were identified within the frequency range from zero to 32 kHz, for the TS1. All, except two, of these resonance conditions were predicted by the FEM model used. The correlation between the FEM and the EOH resonance frequencies was within 2% of each

other. Investigation of the TS2 vividly revealed the response characteristics of the avionics to various excitation conditions. These results show that at low frequencies the sample behaves as a cantilever plate without any distinctive indication of the presence of the surface mounted modules. However, as the excitation frequency increases so does the display of the presence of the modules. Initially, the modules undergo a rigid-body response. Then, as the excitation frequency increases, they begin to respond elastically exhibiting mode shapes characteristic of a particular design of the avionics subject to the specific boundary conditions and other input parameters.

The ongoing work on combining the methods of EOH with the FEM will lead to a development of new design procedures for avionics. Such hybrid procedures, possessing both experimental and computational capabilities will, in turn, lead to the next generation of tools that will enhance the design and optimization of critical components and structures used in the development of reliable and durable modern avionics packages.

Finally, a hybrid approach consisting of the EOH and FEM methodologies was used to optimize a cantilever plate with holes in order to minimize/maximize specific resonance frequencies. This hybrid approach shows that computational and experimental methodologies complement each other and can be applied to optimization of mechanical components yielding results in a very fast, accurate, and efficient manner. We believe that such a hybrid, experimental and computational, approach to structural analysis, in general, and to avionics durability analysis and validation, in particular, will lead to development of new, reliable systems that will be economically desirable.

All in all, the results presented in this report demonstrate viability of the EOH system, developed during this project, for avionics durability analysis and validation. These analysis and validation provide three-dimensional quantitative results in near-real time at 30 holograms per second.

Appendix A

ELECTRO-OPTIC HOLOGRAPHY

ELECTRO-OPTIC HOLOGRAPHY

Ryszard J. Pryputniewicz

Center for Holographic Studies and Laser Technology
Department of Mechanical Engineering
Worcester Polytechnic Institute
Worcester, MA 01609-2280

ABSTRACT

This critical review concentrates on electro-optic holography. First, fundamentals of the electro-optic holography are outlined. Then, mathematical procedures for quantitative interpretation of electronic holograms are presented. This is followed with a description of a system for implementation of procedures for electronic acquisition, storage, processing, and display of optical interference information. This description is illustrated with representative examples relating to static and dynamic loading conditions.

1. INTRODUCTION

Today, the demands for safe, economic, and efficient designs of load resisting structures are greater than ever before. Satisfaction of these demands relies on accurate and precise measurement of displacements and deformations of the structures in response to their loads. These loads are varying in nature and many design problems must be concerned with, both, static and dynamic loading conditions.

In response to the design demands, a number of methods for measurements of displacements/deformations of objects undergoing static and dynamic loads have been developed¹⁻³⁹, based on the principles of hologram interferometry. These methods, in general, require recording of holographic interferograms in photosensitive media which need to be processed and then must be reconstructed in order to produce the images. Although these methods are very functional and have helped to solve many problems, they are "slow" because of the post-exposure processing requirements. As such, these methods are not usually suited for on-line applications. Recently, however, utilizing advances in the phase step hologram interferometry, speckle metrology, and computer technology, novel methods allowing direct electronic recording of holograms and transmission of holographic interferograms by television systems for real-time display of interference fringes have been developed⁴⁰⁻⁵³. One of these methods is known as the Electro-Optic Holography (EOH) method and is the subject of this review.

2. FUNDAMENTALS OF EOH

In the EOH method, also known as Electronic Holography, or TV Holography, the interfering beams are combined by a speckle interferometer, which produces speckles large enough to be resolved by the TV camera⁴². The output of the TV camera is fed to a system that computes and stores the magnitude and phase, relative to the reference beam, of each picture element in the image of the illuminated object.

The EOH method allows automated processing of fringes of statically and dynamically loaded objects^{48, 51-53}. In this method, measurements of irradiances produced by mutual interference of the object and the reference fields are made electronically by a CCD camera, Fig. 1. Processing of this interferometric information and display of the computational results are carried out concomitantly with measurements of irradiation. The EOH method does not depend on recording of holograms in conventional media, but rather relies on electronic acquisition, processing, and display of optical interference information.

In the following sections, principles of the EOH method are outlined and its implementation to static and dynamic measurements is presented.

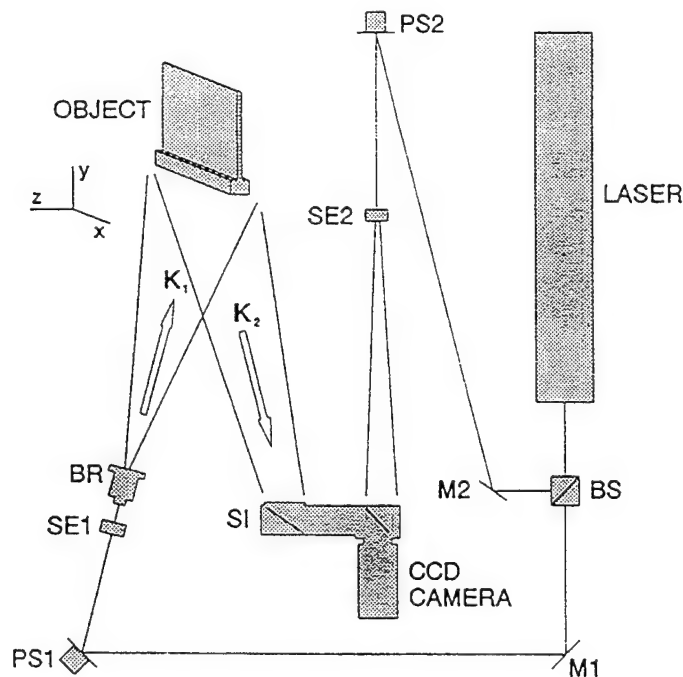


Fig. 1. Optical configuration of the EOH system: BS is the beamsplitter, M1 and M2 are the mirrors, PS1 and PS2 are the phase steppers, SE1 and SE2 are the spatial filter beam expander assemblies, BR is the object beam rotator, SI is the speckle interferometer, and K_1 and K_2 are the directions of object illumination and observation.

2.1. Configuration of the EOH system

Optical configuration of the EOH system is shown in Fig. 1. In this system, the laser output is divided into two beams by means of a continuously variable beamsplitter. One of these beams is directed via a mirror and is shaped by the spatial filter beam expander assembly to illuminate the object uniformly. The other beam, also spatially filtered and expanded, is directed toward the reference input of the speckle interferometer. The speckle interferometer combines the object beam with the reference beam and directs them collinearly toward the detector array of the CCD camera, Fig. 2. The camera detects the irradiance patterns and sends them to the pipeline processor. The sequential frames are processed to determine quantitative information on the object's displacements and/or deformations. All computations are done in the pipeline processor which operates under control of a host computer.

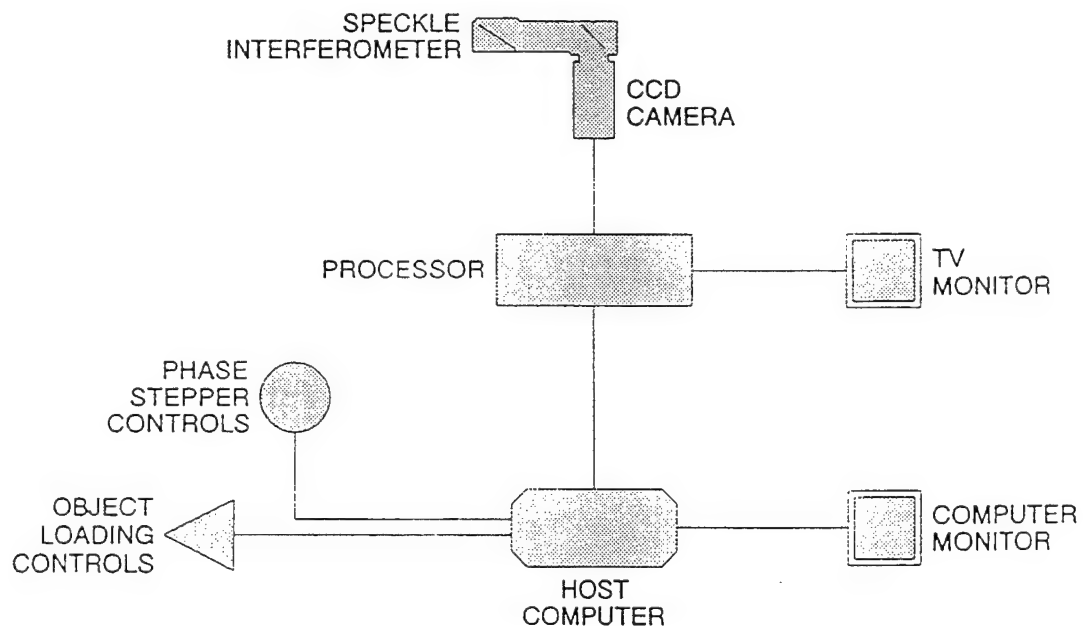


Fig. 2. Electronic configuration of the EOH system.

2.2. Modes of operation

The EOH system is capable of operating in either a viewing mode or a data mode. The viewing mode is used for visual examination of the interference patterns. The data mode is used for quantitative analysis of the electronically recorded holographic images.

The viewing mode produces an 8-bit image, while the data mode produces a 16-bit image. The viewing and data images are produced by lookup tables resident in the EOH system. They can be displayed live on the TV monitor and can be stored and/or printed at any time.

The image storage can be of either of the following two types. If the image is to be recalled in the future for visual observation, then an 8-bit image is stored and occupies approximately one-quarter megabyte of memory. This is image storage. If the image is to be processed quantitatively, then the lookup table for the data mode is loaded into the operating system and produces a data image which is stored as the 16-bit data image and occupies one-half megabyte of memory. This is data storage. Each type of the image may be downloaded to the host computer's memory at any time.

3. QUANTITATIVE INTERPRETATION OF ELECTRONIC HOLOGRAMS

The EOH system is capable of performing either static or dynamic measurements⁵². Static measurements are implemented using double-exposure hologram interferometry method, while dynamic measurements are implemented by time-average method.

3.1. Static measurements

Static measurements are characterized by recording 'single-exposure' holograms of an object at two different states of stress. As a result of interference between a set of two 'single-exposure' holograms, fringes form, if there are any optical path differences between the corresponding points on the object as recorded in the two holograms.

In the EOH, this process is carried out by recording sequential frames of images of the object, corresponding to the two states of stress. Typically, four sequential frames are recorded. These frames are recorded in such a way that a finite phase step is imposed on the reference beam between each frame. In the following discussion, in order to simplify derivation of equations describing the EOH process for static measurements, the object will be initially unstressed.

The image of an unstressed (i. e., unloaded) object can be described by the irradiance distribution for the n -th sequential frame, $I_n(x, y)$, at the detector array of a CCD camera in the EOH system setup, as

$$I_n(x, y) = I_o(x, y) + I_r(x, y) + 2 \cdot I_o(x, y) \cdot I_r(x, y) \cos[\Delta\phi(x, y) + \Delta\theta_n], \quad (1)$$

while the corresponding image of the stressed (i. e., loaded) object can be described by the irradiance distribution, $I_n(x, y)$, as

$$I_n(x, y) = I_o(x, y) + I_r(x, y) + 2A_o(x, y)A_r(x, y)\cos[\Delta\phi(x, y) + \Omega(x, y) + \Delta\theta_n]. \quad (2)$$

In Eqs 1 and 2, x and y identify coordinates of the detectors in the array, I_o and I_r denote irradiances of the object and reference fields, whose amplitudes are A_o and A_r , respectively, $\Delta\phi$ is the phase difference between the two fields, $\Delta\theta_n$ is the n -th finite phase step imposed on the reference beam between sequential frames recording individual images, and Ω is the fringe-locus function, constant values of which define fringe loci on the object's surface.

Since I and I' are measured at known coordinates x and y , Eqs 1 and 2 contain four unknowns, that is, irradiances (which are squares of the amplitudes) of the two fields, the phase differences between these fields, and the fringe-locus function. The goal of the analysis is to determine Ω because it relates directly to displacements and deformations of the object.

In the EOH, $\Delta\phi$ is eliminated by recording sequentially four TV frames with an introduction of a phase step, equal to a multiple of 90° , between each frame. That is, $\Delta\theta_n$, appearing in Eqs 1 and 2, takes on the values of 0° , 90° , 180° , and 270° . This process can be represented by two sets of four simultaneous equations corresponding to Eqs 1 and 2, respectively, that is,

$$I_1 = I_o + I_r + 2A_oA_r\cos(\Delta\phi + 0^\circ), \quad (3)$$

$$I_2 = I_o + I_r + 2A_oA_r\cos(\Delta\phi + 90^\circ), \quad (4)$$

$$I_3 = I_o + I_r + 2A_oA_r\cos(\Delta\phi + 180^\circ), \quad (5)$$

$$I_4 = I_o + I_r + 2A_oA_r\cos(\Delta\phi + 270^\circ), \quad (6)$$

and

$$I'_1 = I'_o + I'_r + 2A'_oA'_r\cos(\Delta\phi + \Omega + 0^\circ), \quad (7)$$

$$I'_2 = I'_o + I'_r + 2A'_oA'_r\cos(\Delta\phi + \Omega + 90^\circ), \quad (8)$$

$$I'_3 = I'_o + I'_r + 2A'_oA'_r\cos(\Delta\phi + \Omega + 180^\circ), \quad (9)$$

$$I_4 = I_o + I_r + 2A_o A_r \cos(\Delta\psi + \Omega + 270^\circ), \quad (10)$$

where the arguments (x, y) were omitted for simplification. Evaluation of Eqs 3 to 10 yields:

$$I_1 = I_o + I_r + 2A_o A_r \cos \Delta\psi, \quad (11)$$

$$I_2 = I_o + I_r + 2A_o A_r \sin \Delta\psi, \quad (12)$$

$$I_3 = I_o + I_r - 2A_o A_r \cos \Delta\psi, \quad (13)$$

$$I_4 = I_o + I_r - 2A_o A_r \sin \Delta\psi, \quad (14)$$

and

$$I_1 = I_o + I_r + 2A_o A_r \cos(\Delta\psi + \Omega), \quad (15)$$

$$I_2 = I_o + I_r + 2A_o A_r \sin(\Delta\psi + \Omega), \quad (16)$$

$$I_3 = I_o + I_r - 2A_o A_r \cos(\Delta\psi + \Omega), \quad (17)$$

$$I_4 = I_o + I_r - 2A_o A_r \sin(\Delta\psi + \Omega), \quad (18)$$

It should be noted that systems of equations similar to Eqs 11 to 14 and Eqs 15 to 18 could be obtained using any value of the phase step, however, use of the 90° phase step results in the simplest computations.

Subtracting Eq. 13 from Eq. 11 and Eq. 14 from Eq. 12, for the case of the unstressed object, we obtain the following set of two equations:

$$(I_1 - I_3) = 4A_o A_r \cos \Delta\psi, \quad (19)$$

and

$$(I_2 - I_4) = 4A_o A_r \sin \Delta\psi. \quad (20)$$

Following the above procedure and subtracting Eq. 17 from Eq. 15 and Eq. 18 from Eq. 16, we generate a set of two equations for the case of the stressed object, that is,

$$(I_1 - I_3) = 4A_o A_r \cos(\Delta\psi + \Omega), \quad (21)$$

and

$$(I_2 - I_4) = 4A_o A_r \sin(\Delta\psi + \Omega). \quad (22)$$

Now, addition of Eqs 19 and 21 yields

$$(I_1 - I_3) + (I_1' - I_3') = 4A_o A_r \cos \Delta \varphi + 4A_o' A_r \cos(\Delta \varphi + \Omega). \quad (23)$$

Because object displacements and deformations are small, it can be assumed that $A_o' \approx A_o$. Therefore, Eq. 23 becomes

$$(I_1 - I_3) + (I_1' - I_3') = 4A_o A_r [\cos \Delta \varphi + \cos(\Delta \varphi + \Omega)]. \quad (24)$$

Recognizing that $\cos(\Delta \varphi + \Omega) = \cos \Delta \varphi \cos \Omega - \sin \Delta \varphi \sin \Omega$, Eq. 24 can be rewritten as

$$\begin{aligned} D_1 &= (I_1 - I_3) + (I_1' - I_3') \\ &= 4A_o A_r [(1 + \cos \Omega) \cos \Delta \varphi - \sin \Delta \varphi \sin \Omega]. \end{aligned} \quad (25)$$

In a similar way, addition of Eqs 20 and 22 simplifies to

$$\begin{aligned} D_2 &= (I_2 - I_4) + (I_2' - I_4') \\ &= 4A_o A_r [(1 + \cos \Omega) \sin \Delta \varphi + \cos \Delta \varphi \sin \Omega]. \end{aligned} \quad (26)$$

Finally, addition of the squares of Eqs 25 and 26 yields

$$\begin{aligned} D_1^2 + D_2^2 &= \{4A_o A_r [(1 + \cos \Omega) \cos \Delta \varphi - \sin \Delta \varphi \sin \Omega]\}^2 \\ &\quad + \{4A_o A_r [(1 + \cos \Omega) \sin \Delta \varphi + \cos \Delta \varphi \sin \Omega]\}^2, \end{aligned}$$

which reduces to

$$D_1^2 + D_2^2 = 16A_o^2 A_r^2 [(1 + \cos \Omega)^2 + \sin^2 \Omega],$$

wherefrom

$$D_1^2 + D_2^2 = 32A_o^2 A_r^2 (1 + \cos \Omega). \quad (27)$$

Furthermore, recognizing that $(1 + \cos \Omega) = 2 \cos^2(\Omega/2)$, Eq. 27 can be rewritten as

$$\sqrt{D_1^2 + D_2^2} = 8A_o A_r \cos\left(\frac{\Omega}{2}\right), \quad (28)$$

which represents the static viewing image displayed by the EOH. In Eq. 28, Ω is the fringe-locus function corresponding to the object's static displacements and/or deformations. The fringe-locus function can be determined by processing the sequential EOH images as described below.

In order to obtain data from the EOH images, we will again employ Eqs 19 to 23 and follow the procedure used to derive Eq. 27. The result of this procedure is

$$\begin{aligned} D_3 &= (I_1 - I_3) - (I'_1 - I'_3) \\ &= 4A_o A_r [(1 - \cos \Omega) \cos \Delta\phi + \sin \Delta\phi \sin \Omega], \end{aligned} \quad (29)$$

$$\begin{aligned} D_4 &= (I_2 - I_4) - (I'_2 - I'_4) \\ &= 4A_o A_r [(1 - \cos \Omega) \sin \Delta\phi - \cos \Delta\phi \sin \Omega], \end{aligned} \quad (30)$$

and

$$D_3^2 + D_4^2 = 32 A_o^2 A_r^2 (1 - \cos \Omega). \quad (31)$$

Subtracting Eq. 31 from Eq. 27 we obtain

$$D = (D_1^2 + D_2^2) - (D_3^2 + D_4^2) = 32 A_o^2 A_r^2 (1 + \cos \Omega) - 32 A_o^2 A_r^2 (1 - \cos \Omega),$$

or

$$D = 64 A_o^2 A_r^2 \cos \Omega. \quad (32)$$

Starting with Eqs 19 to 22, we can also determine

$$\begin{aligned} N_1 &= (I_1 - I_3) + (I'_2 - I'_4) \\ &= 4A_o A_r [(1 + \sin \Omega) \cos \Delta\phi + \sin \Delta\phi \cos \Omega], \end{aligned} \quad (33)$$

$$\begin{aligned} N_2 &= (I_2 - I_4) - (I'_1 - I'_3) \\ &= 4A_o A_r [(1 + \sin \Omega) \sin \Delta\phi - \cos \Delta\phi \cos \Omega], \end{aligned} \quad (34)$$

$$\begin{aligned} N_3 &= (I_1 - I_3) - (I'_2 - I'_4) \\ &= 4A_o A_r [(1 - \sin \Omega) \cos \Delta\phi - \sin \Delta\phi \cos \Omega], \end{aligned} \quad (35)$$

$$N_4 = (I_2 - I_4) + (I_1 - I_3) \\ = 4 A_o A_r [(1 - \sin \Omega) \sin \Delta \phi + \cos \Delta \phi \cos \Omega], \quad (36)$$

$$N_1^2 + N_2^2 = 32 A_o^2 A_r^2 (1 + \sin \Omega). \quad (37)$$

$$N_3^2 + N_4^2 = 32 A_o^2 A_r^2 (1 - \sin \Omega). \quad (38)$$

and

$$N = (N_1^2 + N_2^2) - (N_3^2 + N_4^2) = 64 A_o^2 A_r^2 \sin \Omega. \quad (39)$$

Finally, dividing Eq. 39 by Eq. 32, we obtain

$$\frac{N}{D} = \frac{64 A_o^2 A_r^2 \sin \Omega}{64 A_o^2 A_r^2 \cos \Omega},$$

from which it follows that

$$\Omega = \tan^{-1} \left(\frac{N}{D} \right). \quad (40)$$

It should be noted that Ω , computed from Eq. 40, is a spatial function that depends on coordinates x and y . Therefore, its values are determined for every coordinate pair (x, y) in the object space. Once the values of Ω are determined, they can be used to compute object displacements and deformations using, for example, procedures discussed in references 16, 18, and 23.

3.2. Dynamic measurements

Application of EOH to dynamic measurements is made based on the time-average hologram interferometry³². In this section, in order to facilitate development of the equations governing formation of the images, the time-average recording of a sinusoidally vibrating object will be considered⁵². For this case, the irradiance distribution for the n -th sequential frame, I_{t_n} , can be represented by a relationship similar to those shown in Eqs 1 and 2, that is,

$$I_{t_n} = I_{t_o} + I_r + 2 A_{t_o} A_r \cos(\Delta \phi_t + \Delta \theta_n) M(\Omega_t). \quad (41)$$

In Eq. 41, the arguments (x, y) were omitted for simplification, subscript t indicates time varying parameters, M is the characteristic fringe function⁴ that mod-

ulates the interference of the two fields due to the object's motion, Ω_t is the fringe-locus function defining fringe loci on the surface of a vibrating object, and other parameters are as defined for Eqs 1 and 2.

Equation 41, like Eqs 1 and 2, has four unknowns: I_{t_0} and I_r , which are squares of A_{t_0} and A_r , respectively, $\Delta\phi_t$, and Ω_t . The goal of the analysis is to determine Ω_t because it relates directly to the displacements of the vibrating object.

In order to determine Ω_t from the electronic holograms of a vibrating object, four sequential frames are recorded with the phase steps equal to multiples of 90° imposed on the reference beam between each frame, see also Section 3.1. This process can be represented by the following set of four simultaneous equations:

$$I_{t_1} = I_{t_0} + I_r + 2A_{t_0}A_r \cos(\Delta\phi_t + 0^\circ)M(\Omega_t). \quad (42)$$

$$I_{t_2} = I_{t_0} + I_r + 2A_{t_0}A_r \cos(\Delta\phi_t + 90^\circ)M(\Omega_t). \quad (43)$$

$$I_{t_3} = I_{t_0} + I_r + 2A_{t_0}A_r \cos(\Delta\phi_t + 180^\circ)M(\Omega_t), \quad (44)$$

$$I_{t_4} = I_{t_0} + I_r + 2A_{t_0}A_r \cos(\Delta\phi_t + 270^\circ)M(\Omega_t). \quad (45)$$

Following the procedure used to derive Eqs 19 and 20 and operating on Eqs 42 to 45, we obtain

$$I_{t_1} = I_{t_0} + I_r + 2A_{t_0}A_r \cos(\Delta\phi_t)M(\Omega_t). \quad (46)$$

$$I_{t_2} = I_{t_0} + I_r + 2A_{t_0}A_r \sin(\Delta\phi_t)M(\Omega_t). \quad (47)$$

$$I_{t_3} = I_{t_0} + I_r - 2A_{t_0}A_r \cos(\Delta\phi_t)M(\Omega_t). \quad (48)$$

$$I_{t_4} = I_{t_0} + I_r - 2A_{t_0}A_r \sin(\Delta\phi_t)M(\Omega_t). \quad (49)$$

Then, from Eqs 46 to 49 it follows that

$$(I_{t_1} - I_{t_3}) = 4A_{t_0}A_r \cos(\Delta\phi_t)M(\Omega_t). \quad (50)$$

and

$$(I_{t_2} - I_{t_4}) = 4A_{t_0}A_r \sin(\Delta\phi_t)M(\Omega_t). \quad (51)$$

If the viewing mode is selected, then, based on the input described by Eqs 50 and 51, the EOH system produces an image which can be represented by

$$\sqrt{(I_{t1} - I_{t3})^2 + (I_{t2} - I_{t4})^2} = 4 A_o A_r |M(\Omega_t)|. \quad (52)$$

The image represented by Eq. 52 is displayed live on a TV monitor and it can be stored in processor memory at any time, see Section 2.2.

If the image is to be processed quantitatively, then the EOH system, operating on the input described by Eqs 50 and 51, produces a data image which can be represented by

$$(I_{t1} - I_{t3})^2 + (I_{t2} - I_{t4})^2 = 16 I_o I_r M^2(\Omega_t). \quad (53)$$

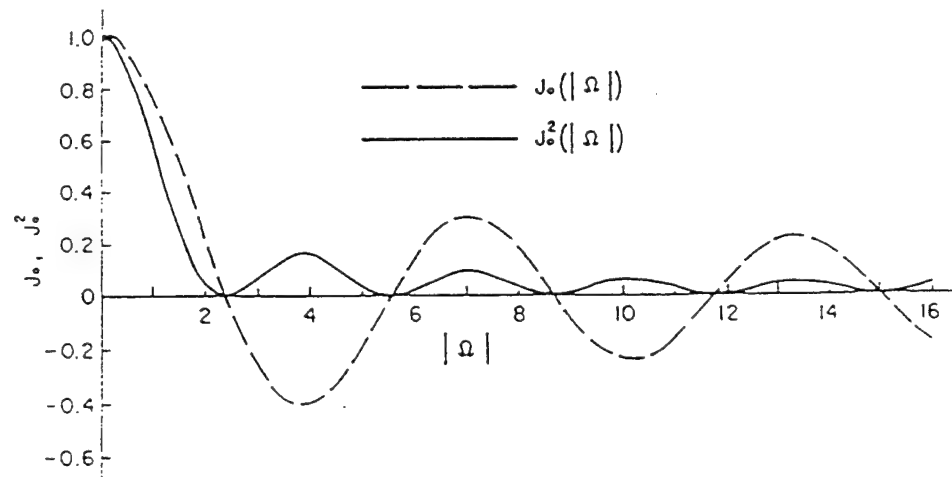


Fig. 3. The zero-order Bessel function of the first kind and its square, defining locations of the centers of dark fringes seen during reconstruction of the time-average holograms of the vibrating objects.

Equations 52 and 53 indicate that the viewing and the data images are proportional to the characteristic function and to the square of the characteristic function, respectively. The characteristic function is determined by the object's temporal motion, and for the sinusoidal vibrations, assuming that the vibration period is much shorter than the TV framing time,

$$M[\Omega_t(x, y)] = J_0[\Omega_t(x, y)]. \quad (54)$$

or, by eliminating the arguments (x, y) for simplification, we can also write

$$M(\Omega_t) = J_0(\Omega_t). \quad (55)$$

where J_0 is the zero-order Bessel function of the first kind, Fig. 3. Therefore, using Eq. 55, Eqs 52 and 53 become

$$\sqrt{(I_{t1} - I_{t3})^2 + (I_{t2} - I_{t4})^2} = 4 A_o A_r |J_0(\Omega_t)|, \quad (56)$$

and

$$(I_{t1} - I_{t3})^2 + (I_{t2} - I_{t4})^2 = 16 I_o I_r J_0^2(\Omega_t). \quad (57)$$

respectively.

Equation 56 represents a viewed image that is modulated by a system of fringes described by the zero-order Bessel function of the first kind, while Eq. 57 shows that the data image is modulated by the square of this function. Thus, centers of the dark fringes are located at those points on the object's surface where $J_0(\Omega_t)$ equals zero, as shown in Fig. 3. This figure indicates that the zero-order Bessel fringe is much brighter than the higher order J_0 fringes.

Since the zero-order fringes represent the stationary points on the vibrating object they allow easy identification of nodes. The brightness of other fringes decreases with increasing fringe order and can be directly related to the mode shapes.

It should be noted that the higher order zeros are nearly equally spaced giving the J_0 function an almost periodic nature. This periodic nature of the Bessel fringes is utilized in quantitative interpretation of images recorded by the EOH system as discussed in Section 3.2.1.

In the EOH system, the data provided by the CCD camera are processed to produce spatial irradiance distribution represented by Eq. 57 for every pixel in the image frame at the rate of 30 frames per second. Each frame contains 512x480 8-bit numbers so that each image consists of 245,760 points.

For visual examination of the vibration modes, the time-average hologram images corresponding to Eq. 56 are displayed on the TV monitor. These images are generated concomitantly by the pipeline processor of the EOH system.

To produce data suitable for quantitative analysis of time-average holograms, 16-bit images represented by Eq. 57 are stored. These data are stored in two 8-bit bytes per pixel and produce a frozen image which can be displayed on the TV monitor one byte at a time, that is, either as a high-byte image or a low-byte image.

3.2.1. Determination of the fringe-locus function for the vibrating object

To interpret electronically recorded time-average holograms quantitatively, the argument of the J_o^2 function, appearing in Eq. 57, must be determined. One method to determine this argument, suitable for the time-average images recorded by EOH, uses the fact that it is possible to shift J_o fringes in a manner similar to that in which phase modulation shifts cosinusoidal fringes in conventional double-exposure hologram interferometry⁴⁵. In time-average holography, this is done by modulating the phase of either the object or the reference beams sinusoidally at the same frequency and phase as the object vibration. Such a process can be represented mathematically by addition of a phasor bias, B , to the argument of the Bessel function, resulting in the characteristic function

$$M(\Omega_t, B) = J_o(\Omega_t - B). \quad (58)$$

For purposes of analysis by this method, the object must be made to vibrate in only one vibration mode at a time so that the motions of its various parts are either in or out of phase with one another. If the phase of the sinusoidal beam modulation is adjusted to coincide with that of the object vibration, the phasor bias becomes a simple additive term within the argument of the Bessel function, that is,

$$M(\Omega_t, B) = J_o(\Omega_t - B). \quad (59)$$

Therefore, Eq. 57 becomes

$$(I_{t1} - I_{t3})^2 + (I_{t2} - I_{t4})^2 = 16 I_o I_r J_o^2(\Omega_t - B). \quad (60)$$

For comparison, the general equation representing the irradiance, I_{ht} , of an image reconstructed from a time-average hologram is

$$I_{ht} = I_{at} + I_{mt} J_o^2(\Omega_t - B). \quad (61)$$

where I_{at} represents local average background irradiance from scattered light and I_{mt} is the local maximum irradiance. Therefore, Eq. 60 is the special case of Eq. 61 with

$$I_{ht} = (I_{t1} - I_{t3})^2 + (I_{t2} - I_{t4})^2 \quad (62)$$

$$I_{at} = 0. \quad (63)$$

and

$$I_{m_t} = 16 I_o I_r. \quad (64)$$

The output of the processor in the data mode, I_{h_t} , is stored in the host computer for different values of B , while I_{a_t} , I_{m_t} , and Ω_t constitute three unknowns, and the goal of the analysis is to determine Ω_t . Unfortunately, the Bessel function is not separable in terms of Ω_t and B , so a straightforward solution is not possible. However, the nearly periodic nature of the J_o function allows an approximate solution for the fringe-locus function. This approximate solution recognizes that Eq. 61 is similar to the general equation for the irradiance distribution, I_h , for an image reconstructed from a conventional double-exposure hologram with cosinusoidal fringes, that is,

$$I_h = I_a + I_m \cos^2(\Omega - B), \quad (65)$$

where J_o^2 in Eq. 61 has been replaced by \cos^2 and Ω_t has been replaced by Ω .

Examination of Eq. 65 shows that it, just like Eq. 61, also has three unknowns: I_a , I_m , and Ω . However, the $\cos^2(\Omega - B)$ term, appearing in Eq. 65, unlike the $J_o^2(\Omega_t - B)$ term of Eq. 61, is separable in its component arguments. To facilitate solution for Ω , Eq. 65 is rewritten as

$$I_h = I_a' + I_m' \cos(2\Omega - 2B), \quad (66)$$

where

$$I_a' = I_a + \frac{I_m}{2} \quad (67)$$

and

$$I_m' = \frac{I_m}{2}. \quad (68)$$

With three values of B , three simultaneous equations of the type of Eq. 66, can be solved uniquely for Ω . The three simultaneous equations are

$$I_{h_1} = I_a' + I_m' \cos(2\Omega), \quad (69)$$

$$I_{h_2} = I_a' + I_m' \cos(2\Omega - 2B), \quad (70)$$

and

$$I_{h_3} = I_a' + I_m' \cos(2\Omega + 2B), \quad (71)$$

corresponding to the zero-, positive-, and negative-shifts, respectively. Solution of Eqs 69 to 71 yields

$$\Omega = \frac{1}{2} \tan^{-1} \left\{ \left[\frac{1 - \cos(2B)}{\sin(2B)} \right] \frac{I_{h_3} - I_{h_2}}{2I_{h_1} - I_{h_2} - I_{h_3}} \right\}. \quad (72)$$

If the three irradiance distributions $I_{h_{t1}}$, $I_{h_{t2}}$, and $I_{h_{t3}}$, corresponding to the three time-average holograms, are substituted into Eq. 72 the result is $\Omega_{t_{approx}}$, that is,

$$\Omega_{t_{approx}} = \frac{1}{2} \tan^{-1} \left\{ \left[\frac{1 - \cos(2B)}{\sin(2B)} \right] \frac{I_{h_{t3}} - I_{h_{t2}}}{2I_{h_{t1}} - I_{h_{t2}} - I_{h_{t3}}} \right\}. \quad (73)$$

The value of $\Omega_{t_{approx}}$, computed from Eq. 73, differs from the correct argument, Ω_t , of the J_o function, because of the inequality between the J_o^2 and the \cos^2 functions, and should be expressed as

$$\Omega_{t_{approx}} = \Omega_t + \epsilon. \quad (74)$$

where ϵ is the error representing this difference.

Equation 73 yields values of $\Omega_{t_{approx}}$ modulo 180° . By adding or subtracting 180° , depending on the sign of the numerator in Eq. 73, whenever the denominator is negative, $\Omega_{t_{approx}}$ can be obtained modulo 360° . The image can be searched by the computer to locate discontinuities to define areas where the missing multiples of the 360° should be added to unwrap function $\Omega_{t_{approx}}$. By further identifying pixels within the zero-order fringe, an overall level shift can be applied to make those pixels have values between $\pm 180^\circ$.

Errors ϵ can be computed for any value of Ω_t for specific values of B to create a lookup table. This lookup table is used to correct the values computed from Eq. 73 that have been unwrapped and level shifted. In this way, vibratory deformations can be obtained from time-average hologram reconstructions with little more mathematical computation than is required for static deformations. Once the correct values of Ω_t are determined, they can be used in any one of the equations for quantitative interpretation of time-average holograms³².

3.2.2. Generation of a lookup table

The lookup table is computed from Eqs 61 and 73. First, the three values of I_{ht} are computed using Eq. 61 for the three values of B , that is,

$$I_{ht1} = I_{at} + I_{mt} J_o^2(\Omega_t), \quad (75)$$

$$I_{ht2} = I_{at} + I_{mt} J_o^2(\Omega_t - B), \quad (76)$$

$$I_{ht3} = I_{at} + I_{mt} J_o^2(\Omega_t + B). \quad (77)$$

The values of B used in Eqs 75 to 77 must be of the magnitude equal to that used while setting bias modulation, see Section 4.2. For example, B can equal to 0 and $\pm \pi/3$.

Substitution of Eqs 75 to 77 into Eq. 73 yields

$$\Omega_{t \text{ approx}} = \frac{1}{2} \tan^{-1} \left\{ \left[\frac{1 - \cos(2B)}{\sin(2B)} \right] \frac{J_o^2(\Omega_t + B) - J_o^2(\Omega_t - B)}{2J_o^2(\Omega_t) - J_o^2(\Omega_t - B) - J_o^2(\Omega_t + B)} \right\}. \quad (78)$$

In order to construct a lookup table corresponding to the specific value of B , Eq. 78 is used to compute $\Omega_{t \text{ approx}}$ for the desired range of values of Ω_t .

Tabulating Ω_t versus $\Omega_{t \text{ approx}}$ produces the lookup table for the given value of the bias modulation. It must be remembered, however, that if the magnitude of the phase modulation of the bias vibration changes, new lookup table must be constructed.

4. EOH SYSTEM AND PROCEDURE

4.1. General description of the EOH system

The EOH system is shown in Fig. 1. In this system, the laser output is divided into two beams by means of a continuously variable beamsplitter. One of these beams is directed via a piezoelectrically driven mirror and is shaped by the spatial filter beam expander assembly to illuminate the object uniformly; this mirror can be driven at the same frequencies as the object excitation to provide bias modulation. The other beam, also spatially filtered and expanded, is directed toward the reference input of the speckle interferometer by another piezoelectrically driven mirror which introduces 90° phase steps between con-

secutive frames. The speckle interferometer combines the object beam with the reference beam and directs them collinearly toward the detector array of the CCD camera, Fig. 2. The camera detects the irradiance patterns and sends them to the pipeline processor. The sequential frames are processed to determine quantitative information on the object's displacements and/or deformations. All computations are done in the pipeline processor which operates under control of a host computer. The host computer also controls excitation of the object, coordinates it with the bias modulation imposed on the object beam, and keeps track of the 90° phase stepping between the frames.

By operating on each input frame and its three predecessors, the pipeline processor produces a hologram which is viewed concomitantly on the TV monitor. Such holograms are produced for the zero, as well as the positive and negative bias modulations, for each loading condition of the object. The resulting three electronic holograms are then processed by the host computer to determine spatial distribution of the displacement vectors which are viewed directly on the computer monitor.

4.2. Setting the bias modulation

In order to interpret electronically recorded time-average holograms quantitatively, both the magnitude and the phase of the bias modulation must be known. One method to set the bias vibration is as follows⁴⁸.

Adjust object excitation so that several J_0 fringes are seen across the object and the zero-order fringe is well identified. Then, increase magnitude of the bias vibration until the zero-order fringe is lost. Following this, adjust phase of the bias vibration until the zero-order fringe is regained and its width is maximum. At this point, phase of the modulation equals the phase of the vibrating object.

Next, turn off the object excitation and reduce magnitude of the bias vibration to zero - do not, however, change the bias phase. Then, slowly increase magnitude of the bias vibration until the entire object goes black, that is, when the first null of J_0 occurs. At this point, the value of B is 2.4048, Fig. 3. Record the voltage output of the bias modulation controller for this condition and reset it by a scaling factor. The scaling factor is the desired magnitude of the bias vibration, e. g., $\pi/3$, divided by 2.4048, the argument of the first zero of the J_0 . The phase of this bias vibration should be recorded; it corresponds to the positive-shift modulation. This completes calibration of the magnitude and the phase of the bias vibration and the sequence of the three holograms can be recorded. Before this is done, the bias excitation should be turned off, the object excitation should be turned on, and the excitation magnitude should be adjusted to the desired level.

When the desired object excitation is achieved, the first time-average hologram is recorded without the bias excitation. This is the zero-bias modulation. Then, the second hologram is recorded after switching on the bias excitation with the magnitude and phase as set above. This is the positive-shift bias modulation. Finally, the phase of the bias excitation is shifted 180° with respect to that used during recording of the second hologram, the bias magnitude is kept the same, and the third hologram is recorded. This is the negative-shift bias modulation. Irradiances of the three time-average holograms recorded in this way are represented by Eqs 75 to 77, respectively.

It should be noted that the bias vibration must be recalibrated for each vibration frequency of the object.

5. REPRESENTATIVE APPLICATIONS OF EOH

Representative results obtained using EOH are shown in Figs 4 to 7. The object used was an aluminum cantilever plate which was rigidly fixed along the bottom edge. All interferograms shown in these figures were produced electronically and were recorded by video printing the displays on the TV monitor. All wire frame displacement plots were based on the irradiances measured from the sets of three holograms corresponding to the zero, the positive, and the negative bias modulations added to the object beam at the object's vibration frequency.

It should be noted that because of the plate's aspect ratio only $(250 \times 400 =)$ 100,000 pixels out of the total available of $(512 \times 480 =)$ 245,760 pixels were used in the interpretation of the images produced by the EOH. Furthermore, in order to produce visually acceptable plots, wire frame grid of 5x5 mm for representation of displacements was selected. In this way, displacements at only a very small number of points $(24 \times 28 = 672)$, out of the total of 100,000 points considered on the object, were displayed.

Figure 4 shows the cosinusoidal fringe patterns of the statically loaded cantilever plate, under four different loads. The electronic hologram corresponding to the maximum load used in this study shows 33 fringes along the plate.

Figure 5 shows the cantilever plate vibrating in its second torsional mode at 966 Hz. More specifically, Fig. 5a shows the time-average hologram produced by the EOH system without the bias modulation of the object beam, whereas Figs 5b and 5c show the holograms with the equal positive and negative bias modulations added to the object beam at the object's vibration frequency, respectively. Note the symmetric location of the zero-order fringe in Fig. 5a and the offsets in the symmetry, due to the bias modulation, in Figs 5b and 5c.

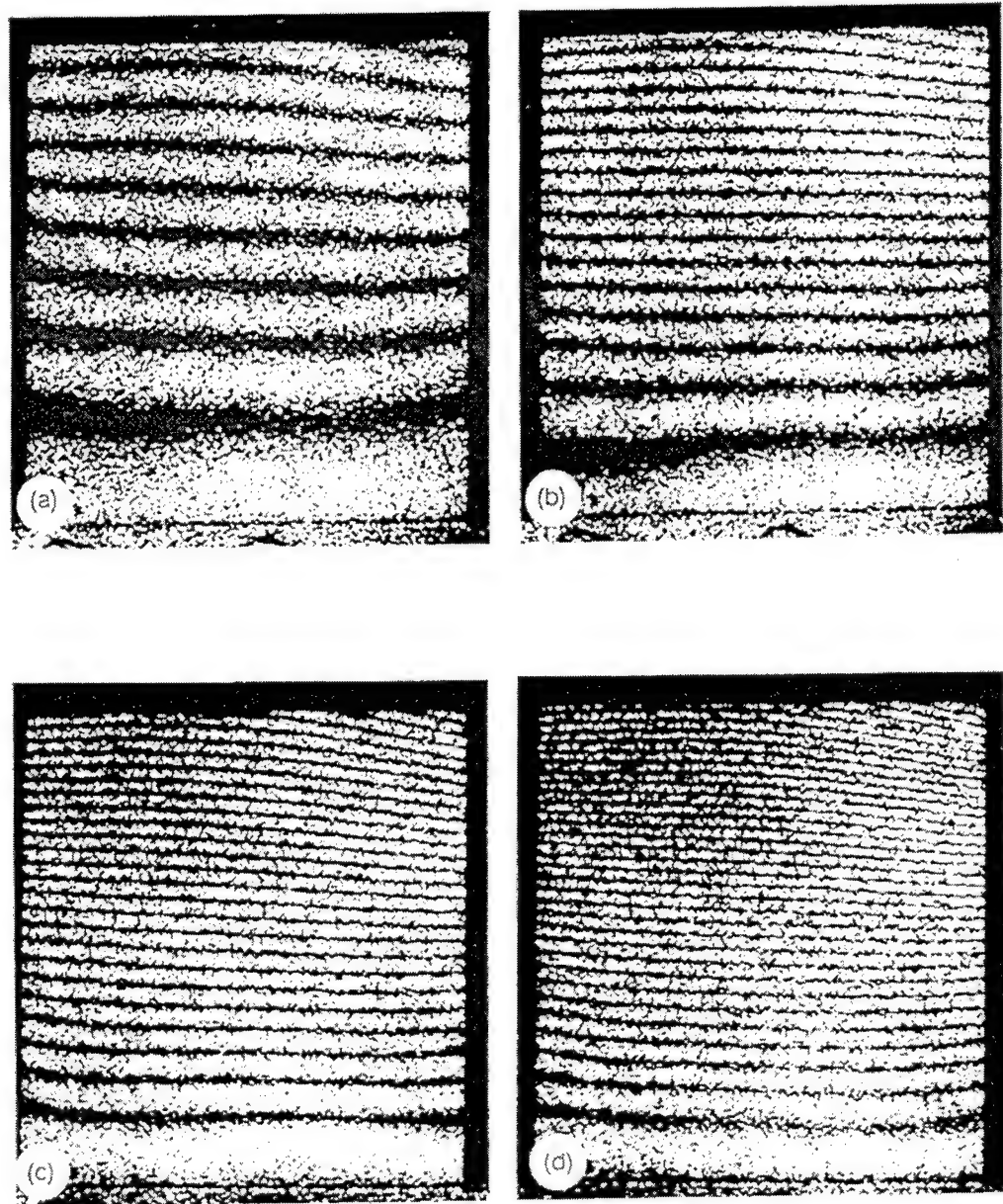


Fig. 4. The EOH images of the double-exposure holograms of the cantilever plate: the static load increases from (a) to (d).

Based on the irradiance values from the corresponding points in Figs. 5a to 5c, displacements were computed as a function of x and y coordinates on the vibrating plate. These displacements are shown in Fig. 5d and correlate well with the image displayed.

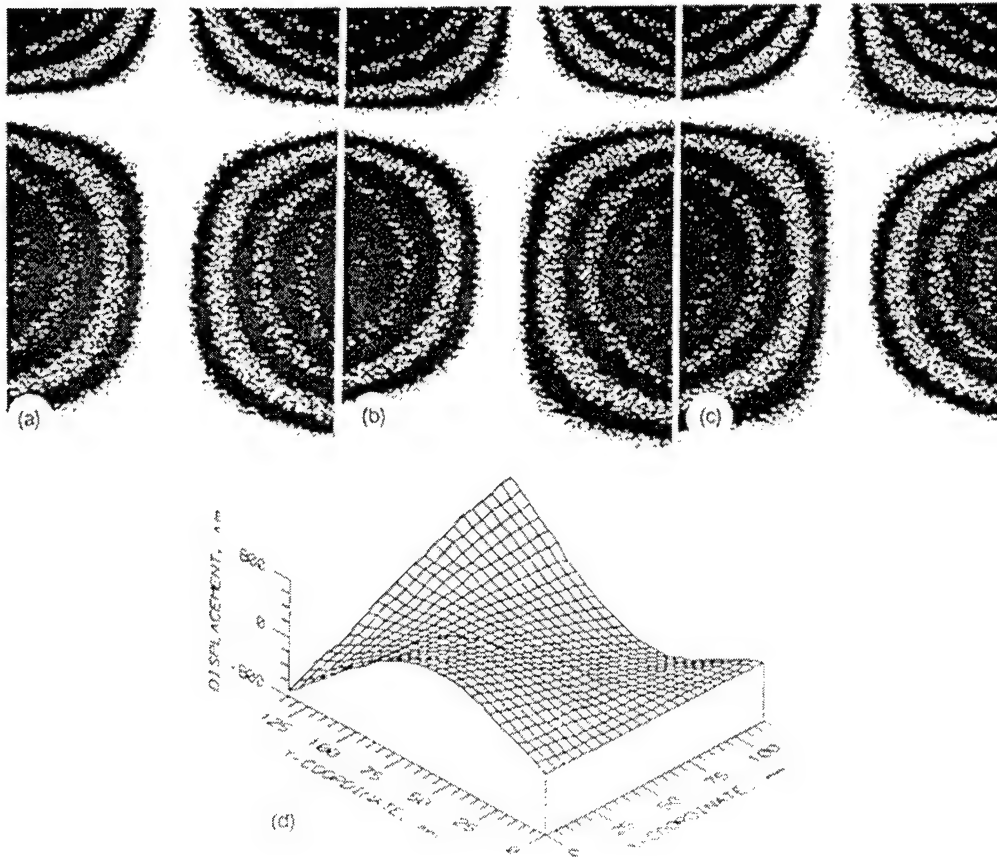


Fig. 5. Cantilever plate vibrating at 966 Hz: (a) image of the plate and the fringe pattern produced by the EOH system during the time-average recording of the plate vibrating at its resonance without the bias modulation of the object beam, (b) the same plate and the vibration as in (a) but with a bias modulation added to the object beam at the object's vibration frequency, (c) the same plate and the vibration as in (a) but with the bias modulation added to the object beam at 180° with respect to (b), (d) wire frame representation of displacements computed from the images shown in (a) to (c).

Figures 6 and 7 show comparison between the wire-frame displacements obtained by the EOH and those computed by the finite element method (FEM). Figures 6a and 7a represent the images of the plate vibrating at 1082 Hz and 3148 Hz, respectively. The displacements determined by the EOH are shown in Figs 6b and 7b, while those determined by the FEM are shown in Figs 6c and 7c. The comparison of the EOH and the FEM results shows good correlation.

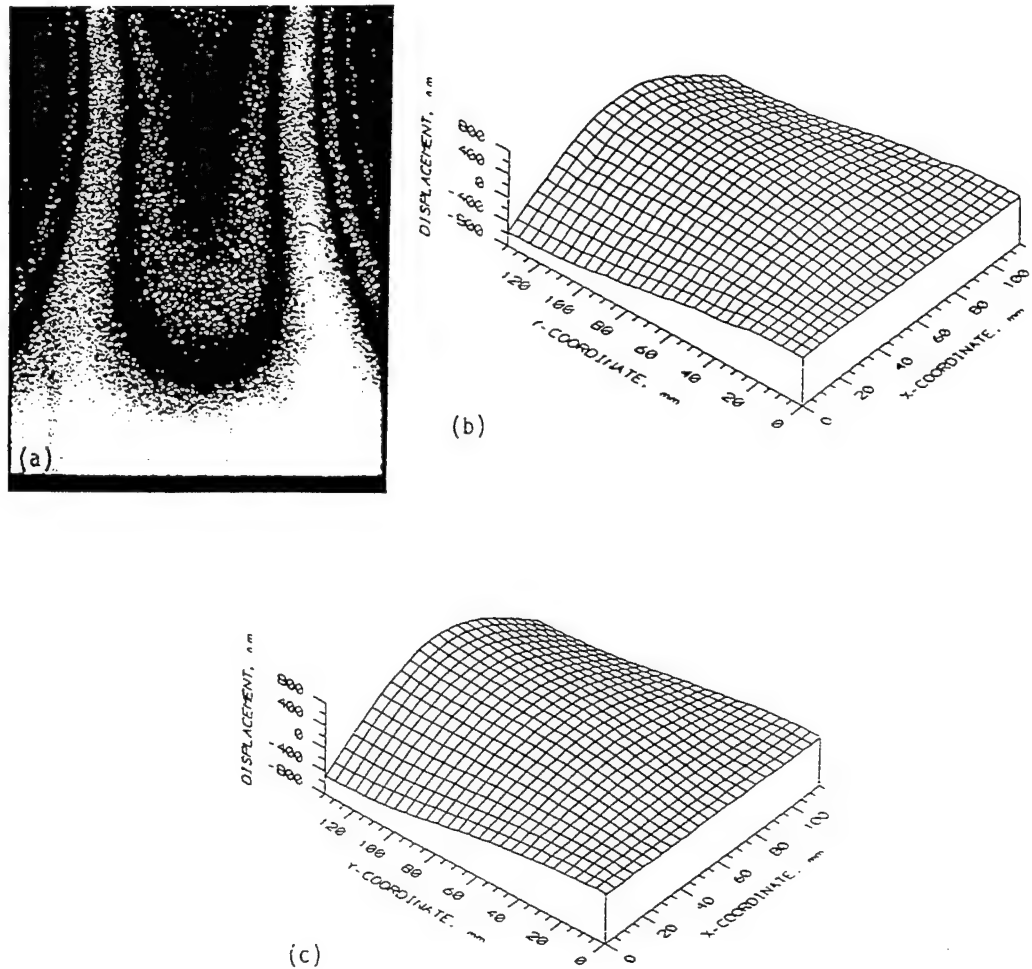


Fig. 6. Comparison of the EOH and the FEM results for the cantilever plate vibrating at 1082 Hz: (a) the EOH image, (b) the EOH displacements, (c) the FEM displacements.

Advances in three-dimensional graphical rendering produce realistic projections of images recorded by EOH⁵³. Figure 8 shows a rendered representation of the displacements determined from the images of Fig. 5. In this representation, all (250x400=) 100,000 pixels are utilized, which allows more complete representation of the results than the wire frame representation of Fig. 5d.

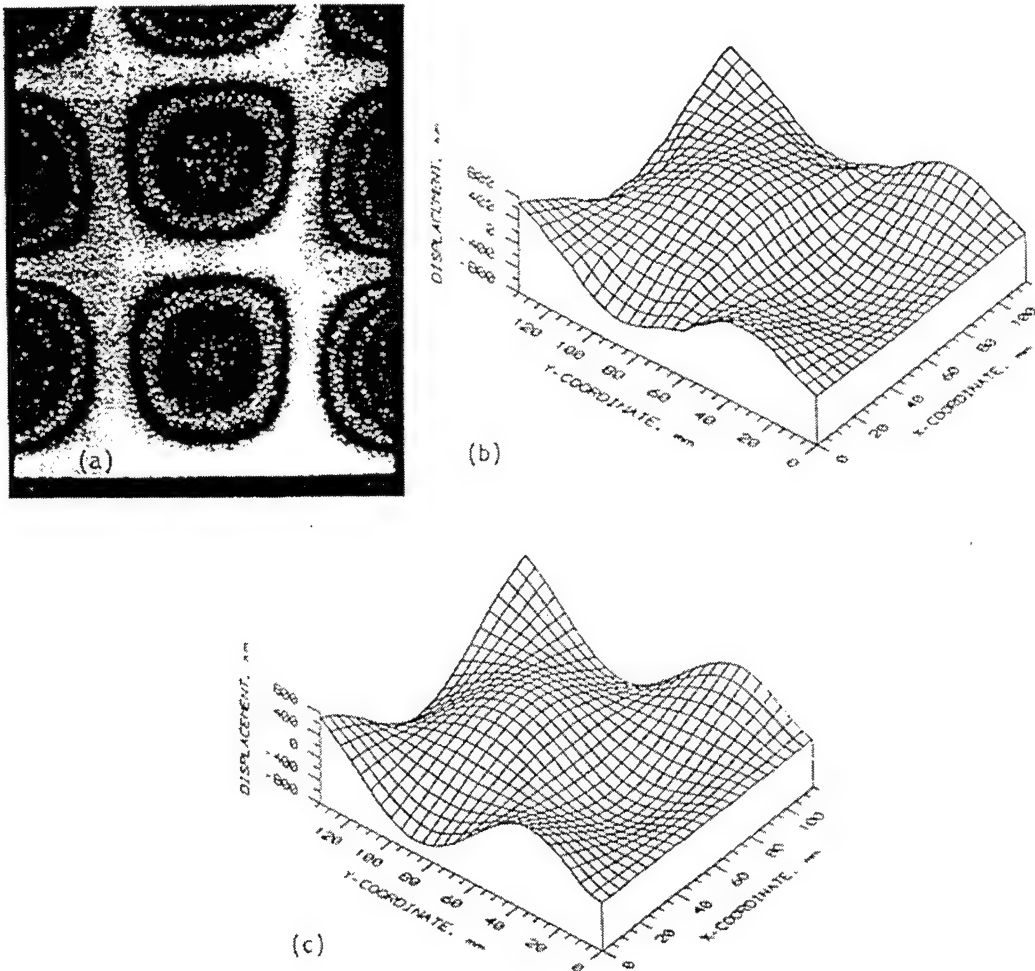


Fig. 7. Comparison of the EOH and the FEM results for the cantilever plate vibrating at 3148 Hz: (a) the EOH image, (b) the EOH displacements, (c) the FEM displacements.

6. CONCLUSIONS

This critical review discusses principles of the electro-optic holography (EOH), presents fundamentals of quantitative interpretation of the electronic holograms recorded under static and dynamic loading conditions, and illustrates application of EOH with representative examples.

The EOH system allows electronic recording, storage, processing, and display of holographic interferograms in real-time. Using this system, the displacements can be extracted from the electronically recorded hologram by a method analogous to optical fringe shifting.

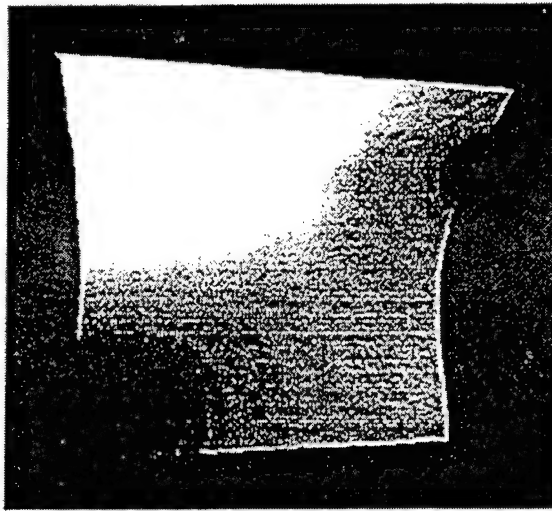


Fig. 8. Rendered representation of the displacements determined from the EOH images of Fig. 5.

Using the EOH system, results are obtained in a truly automated manner. The interferometric information is recorded at the rate of 30 frames per second, it is processed in a pipeline fashion, and produces results which have very high spatial density - currently up to 512x480 points per frame. These results correlate well with the holographically produced fringe patterns and they also correlate well with the FEM predictions of the object's load-displacement characteristics.

Currently, work is underway to merge, or unify, within the host computer, the displacements determined by the EOH system with the computational procedures of FEM. This feat will result in a hybrid system which will allow automated, quantitative analysis of structural deformations. Interpretation of the results of these analysis will be facilitated by the three-dimensional rendering of the holographic data.

7. ACKNOWLEDGMENT

This review was supported by the Flight Dynamics Directorate, Wright Laboratory, Aeronautical Systems Division (AFSC), United States Air Force, Wright-Patterson AFB, OH 45433-6553.

8. REFERENCES

1. E. B. Aleksandrov and A. M. Bonch-Bruевич, "Investigation of surface strains by the hologram technique," *Sov. Phys. Tech. Phys.*, 12:258-265, 1967.
2. A. E. Ennos, "Measurement of in-plane strain by hologram interferometry," *J. Phys. E (Sci. Instr.)*, 1:731-746, 1968.
3. J. E. Sollid, "Holographic interferometry applied to measurements of small static displacements of diffusely reflecting surfaces," *Appl. Opt.*, 8:1587-1595, 1969.
4. K. A. Stetson, "Effects of beam modulation on fringe loci and localization in time-average hologram interferometry," *J. Opt. Soc. Am.*, 60:1378-1384, 1970.
5. K. Shibayama and H. Uchiyama, "Measurement of three-dimensional displacement by hologram interferometry," *Appl. Opt.*, 10:2150-2154, 1971.
6. E. Archbold and A. E. Ennos, "Displacement measurement from double-exposure holography," *Optica Acta*, 19:253-271, 1972.
7. S. K. Dhir and J. P. Sikora, "An improved method for obtaining the general displacement field from a holographic interferogram," *Exp. Mech.*, 12:323-327, 1972.
8. P. M. Boone and L. C. De Backer, "Determination of three orthogonal displacement components from one double-exposure hologram," *Optik*, 37:61-81, 1973.
9. W. Schumann, "Some aspects of the optical techniques of strain measurement," *Exp. Mech.*, 13:225-231, 1973.
10. R. Dändliker, B. Ineichen, and F. M. Mottier, "High resolution hologram interferometry by electronic phase measurement," *Opt. Commun.*, 9:412-416, 1973.
11. K. A. Stetson, "Fringe interpretation for holographic interferometry of rigid-body motions and homogeneous deformations," *J. Opt. Soc. Am.*, 64:1-10, 1974.
12. A. E. Ennos, "Strain measurement," in *Holographic nondestructive testing*, R. K. Erf, ed., Academic Press, New York, pp. 275-287, 1974.
13. V. Fossati Bellani and A. Sona, "Measurement of three-dimensional displacements by scanning a double-exposure hologram," *Appl. Opt.*, 13:1337-1341, 1974.

14. W. Schumann and M. Dubas, "On direct measurement of strain in holographic interferometry using the line of complete localization," *Optica Acta*, 22:807, 1975.
15. K. A. Stetson, "Fringe vectors and observed fringe vectors in hologram interferometry," *Appl. Opt.*, 14:272-273, 1975.
16. K. A. Stetson, "Homogeneous deformations: determination by fringe vectors in hologram interferometry," *Appl. Opt.*, 14:2256-2259, 1975.
17. R. Dändliker and B. Ineichen, "Strain measurement through hologram interferometry," *Proc. SPIE*, 99:90-98, 1976.
18. R. J. Pryputniewicz and K. A. Stetson, "Holographic strain analysis: extension of fringe vector method to include perspective," *Appl. Opt.*, 5:725-728, 1976.
19. R. J. Pryputniewicz, "Determination of the sensitivity vectors directly from holograms," *J. Opt. Soc. Am.*, 67:1351-1353, 1977.
20. L. Ek and K. Biedermann, "Analysis of a system for hologram interferometry with a continuously scanning reconstruction beam," *Appl. Opt.*, 16:2535-2542, 1977.
21. R. J. Pryputniewicz and W. W. Bowley, "Techniques of holographic displacement measurement: an experimental comparison," *Appl. Opt.*, 17:1748-1756, 1978.
22. R. J. Pryputniewicz, "Holographic strain analysis: an experimental implementation of the fringe-vector theory," *Appl. Opt.*, 17:3613-3618, 1978.
23. R. J. Pryputniewicz, "Holographic determination of rigid-body motions," *Appl. Opt.*, 18:1442-1444, 1979.
24. C. M. Vest, *Holographic interferometry*, Wiley, New York, 1979.
24. R. J. Pryputniewicz, "Projection matrices in specklegraphic displacement analysis," *Proc. SPIE*, 243:158-164, 1980.
25. R. J. Pryputniewicz and K. A. Stetson, "Determination of sensitivity vectors in hologram interferometry from two known rotations of the object," *Appl. Opt.*, 19:2201-2205, 1980.
26. K. A. Stetson, "The relationship between strain and derivatives of observed displacement in coherent optical metrology," *Exp. Mech.*, 7:273-275, 1981.
27. K. A. Stetson, "The use of projection matrices in hologram interferometry," *J. Opt. Soc. Am.*, 71:1248-1257, 1981.

28. W. Jüptner, T. Kreis, and H. Kreitlow, "Automatic evaluation of holographic interferograms by reference beam phase shifting," *Proc. SPIE*, 398:22-29, 1983.
29. P. Hariharan, B. F. Oreb, and N. Brown, "Real-time holographic interferometry: a microcomputer system for the measurement of vector displacements," *Appl. Opt.*, 22:876-880, 1983.
30. J. B. Schemm and C. M. Vest, "Fringe pattern recognition and interpolation using nonlinear regression analysis," *Appl. Opt.*, 22:2850-2853, 1983.
31. P. Hariharan, *Optical holography: principles, techniques, and applications*, Cambridge University Press, Cambridge, 1984.
32. R. J. Pryputniewicz, "Time-average holography in vibration analysis," *Opt. Engrg.*, 24:843-848, 1985.
33. W. Schumann, J.-P. Zürcher, and D. Cuhe, *Holography and deformation analysis*, Springer-Verlag, Berlin, 1985.
34. T. Kreis, "Digital holographic interference-phase measurement using the Fourier-transform method," *J. Opt. Soc. Am.*, A3:847-855, 1986.
35. W. Osten, R. Höfling, J. Saedler, "Two computer-aided methods for data reduction from interferograms," *Proc. SPIE*, 863:105-113, 1987.
36. R. J. Pryputniewicz, "Quantitative interpretation of time-average holograms in vibration analysis," in *Optical metrology*, O. D. D. Soares, ed., NATO ASI Series, Martinus Nijhoff, Dordrecht, The Netherlands, pp. 296-316, 1987.
37. R. Thalmann and R. Dändliker, "Strain measurement by heterodyne holographic interferometry," *Appl. Opt.*, 26:1964-1971, 1987.
38. R. Jones and C. Wykes, *Holographic and speckle interferometry*, Cambridge University Press, Cambridge, 1989.
39. Y. I. Ostrovsky, V. P. Shchepinov, and V. V. Yakovlev, *Holographic interferometry in experimental mechanics*, Springer-Verlag, Berlin, 1991.
40. J. E. Berrang, "Television transmission of holograms using narrow-band video signal," *Bell System Technical Journal*, 49:879-887, 1970.
41. A. Makovski, S. D. Ramsey, and L. F. Schaefer, "Time lapse interferometry and contouring with television systems," 10:2711-2727, 1971.
42. K. A. Stetson and W. R. Brohinsky, "Electro-optic holography and its application to hologram interferometry," *Appl. Opt.*, 24:3631-3637, 1985.

43. S. Nakadate, "Vibration measurement using phase-shifting time-average holographic interferometry," *Appl. Opt.*, 25:4162-4167, 1986.
44. K. A. Stetson and W. R. Brohinsky, "An electro-optic holography system for vibration analysis and nondestructive testing," *Proc. SPIE*, 746:44-51, 1987.
45. K. A. Stetson and W. E. Brohinsky, "Fringe-shifting technique for numerical analysis of time-average holograms of vibrating objects," *J. Opt. Soc. Am. - A*, 5:1472-1476, 1988.
46. K. Creath, "Phase-measurement interferometry," in *Progress in optics*, E. Wolf, ed., North-Holland, Vol. 26, 1988.
47. S. Ellingsrud and O. J. Løkberg, "Analysis of high frequency vibrations using TV-holography and digital image processing," *Proc. SPIE*, 1162:402-467, 1989.
48. R. J. Pryputniewicz and K. A. Stetson, "Measurement of vibration patterns using electro-optic holography," *Proc. SPIE*, 1162:456-467, 1989.
49. E. Vilkhagen, "Nondestructive testing by use of TV holography and deformation phase gradient calculation," *Appl. Opt.*, 29:137-144, 1990.
50. G. M. Brown, "Practical phase unwrapping of holographic interferograms," *Proc. SPIE*, 1553:204-208, 1991.
51. R. J. Pryputniewicz, "Application of electro-optic holography in vibration studies," *Proc. Spring Conf. on Exp. Mech.*, SEM, Bethel, CT, pp 912-919, 1991.
52. R. J. Pryputniewicz, "Static and dynamic measurements using electro-optic holography," *Proc. SPIE*, 1554B:790-798, 1991.
53. T. W. Bushman and R. J. Pryputniewicz, "Three-dimensional graphics techniques applied to the rendering of holographic interferometric data," *Proc. SPIE*, 1755:44-52, 1992.

Appendix B

**AUTOMATED FRINGE UNWRAPPING BY
ENERGY MINIMIZATION**

AUTOMATED FRINGE UNWRAPPING BY ENERGY MINIMIZATION

by

Thomas Withington Bushman

A Thesis

Submitted to the Faculty

of the

WORCESTER POLYTECHNIC INSTITUTE

in partial fulfillment of the requirements for the

Degree of Master of Science

in

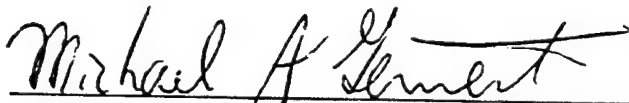
Computer Science

by

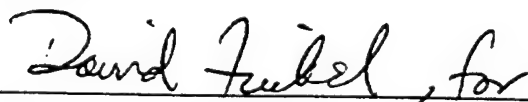


December 1993

Approved:



Dr. Michael A. Gennert, Major Advisor



Dr. Robert E. Kinicki, Head of Department

Abstract

A new method of unwrapping two-dimensional periodically discontinuous phase data is developed in this thesis and results from application of the method to electro-optically generated phase data are presented. The method, whose foundations lie in the minimization of the energy of the surface determined by the unwrapped data, fits planar surface patches to previously processed data, then uses the best fit plane's parameters to estimate the value of the pixel under consideration. At each pixel, a new value composed of the sum of the original value and an integral multiple of the magnitude of the phase discontinuity is assigned. Processing proceeds along an expanding wavefront originating from a seed point chosen as the reference for the measurement. The facet based fringe number selection method has been found to be highly reliable even for incomplete, noisy data.

Preface

The algorithms described in this thesis and the software written to implement them are currently used in the Center for Holographic Studies and Laser Technology (CHSLT), Department of Mechanical Engineering, Worcester Polytechnic Institute. The system, as described here, performs micrometer scale measurements of deformations and vibration amplitudes for the study of the mechanical properties of materials and structures. Those readers who are interested in learning more about the system and techniques presented here should contact Professor Ryszard Pryputniewicz to arrange a visit to the laboratories of the CHSLT. Specific examples of the application areas outlined in *Chapter 1, Section 2* can be found throughout the labs.

Acknowledgments

This thesis was supported by the Flight Dynamics Directorate, Wright Laboratory, Aeronautical Systems Division (AFSC), United States Air Force, Wright-Patterson AFB, OH 45433-6553.

Two members of the faculty of Worcester Polytechnic Institute, Prof. Michael A. Gennert and Prof. Ryszard Pryputniewicz, made this thesis possible. Without their help, support, guidance and encouragement, none of this work could have been done. I am extremely grateful to both of them for their assistance and friendship.

Table of Contents

Chapter 1. Introduction-Holographic Interferometric Measurement.	B - 12
1.1. Purpose of holographic measurement.	B - 12
1.2. Applications of EOH.	B - 13
1.3. Brief description of EOH.	B - 16
1.4. The phase unwrapping problem.	B - 19
1.5. Document Overview.	B - 20
Chapter 2. Overview of EOH, energy minimization and facet based estimation.	B - 22
2.1. Description of a planar light field.	B - 22
2.2. Interference of two coherent light fields.	B - 25
2.3. Laser Speckle.	B - 27
2.4. Coherent light, laser speckle and EOH.	B - 28
2.5. Electro-optic holography system components.	B - 31
2.5.1. Fixtures.	B - 31
2.5.2. Optical system.	B - 32
2.5.3. System electronics.	B - 33
2.6. Mathematical description of holograms.	B - 33
2.7. Static mode data acquisition.	B - 34

2.8. Time average mode data acquisition.	B - 39
2.8.1. Measured intensity modified by the characteristic Bessel function.	B - 40
2.8.2. Time average image capture.	B - 42
2.8.3. Bessel function behavior.	B - 43
2.8.4. Solution for unambiguous phase.	B - 46
2.9. Energy minimization.	B - 52
2.9.1. Image model.	B - 52
2.9.2. Neighborhoods for processing image data.	B - 53
2.9.3. Edge labeling.	B - 53
2.9.4. Energy definitions for labeling and phase unwrapping.	B - 54
2.10. Facet based estimation.	B - 57
Chapter 3. Previous approaches to phase unwrapping.	B - 60
3.1. Basis for two dimensional unwrapping.	B - 60
3.2. Irregular shapes.	B - 61
3.3. Cellular automata.	B - 62
3.4. An image processing techniques based approach.	B - 63
3.5. Other techniques.	B - 64
3.6. Conclusions derived from past implementations of phase unwrappers.	B - 65
Chapter 4. Phase unwrapping by planar facet fitting.	B - 67

4.1. Overview of the technique.	B - 68
4.2. Noise, modulation magnitude and the weighting function.	B - 69
4.3. Seed point selection and initial growth.	B - 71
4.4. Expanding wavefront processing order.	B - 73
4.5. Planar facet fitting to an incomplete, weighted array of data points	B - 75
4.6. Fringe number assignment.	B - 83
4.7. Fitting iterations for energy minimization.	B - 84
4.8. LUT correction for time average holograms.	B - 85
4.9. Data smoothing with planar facets.	B - 85
Chapter 5. Results.	B - 87
5.1. Static mode examples.	B - 87
5.2. Time-average mode examples.	B - 93
Chapter 6. Conclusions and future work.	B - 100
6.1. Benefits and features of the facet based fringe unwrapper.	B - 100
6.2. Suggestions for future improvements and enhancements.	B - 102
6.2.1. Incorporate correction LUT into time average unwrapping directly.	B - 102
6.2.2. Add facilities for interactive drawing of boundaries.	B - 103
6.2.3. Data smoothing.	B - 103
6.2.4. Speed improvements.	B - 104

6.2.5. Noise threshold selection enhancement.	B - 106
6.3. Summation.	B - 106
Appendix A. Mathcad model of the Bessel fringe function.	B - 108
Appendix B. Software Block Diagrams.	B - 111
References.	B - 114

List of Figures

1.1. Simple film-based holographic apparatus.	B - 16
2.1. Two sinusoids of the same frequency.	B - 27
2.2. Electro-optic holography system block diagram.	B - 32
2.3. Static holography 1-D model.	B - 39
2.4. Geometry of incident and reflected light.	B - 41
2.5. One-dimensional Bessel function squared.	B - 44
2.6. Surface plots of the fringe function vs. relative phase and amplitude.	B - 45
2.7. Time-average holography 1-D model.	B - 51
4.1. Processing order for 8-connected FIFO based sequential scan.	B - 74
5.1. Phase unwrapping of a statically loaded wine goblet.	B - 89
5.2. Phase unwrapping of a statically loaded rectangular plate.	B - 92
5.3. Phase unwrapping of time-average hologram of plate vibrating at 6,540 Hz.	B - 95
5.4. Phase unwrapping of time-average hologram of plate vibrating at 34,061 Hz.	B - 98
B.1. Software Block Diagram (Top Level).	B - 111
B.2. Data Acquisition Block Diagram.	B - 111
B.3. Phase Unwrapping Block Diagram.	B - 112
B.4. Energy Minimization Iterations Block Diagram.	B - 112

Chapter 1. Introduction - Holographic Interferometric Measurement.

This master's thesis project develops a new algorithm to unwrap 2π spatial discontinuities in image data consisting of intensity values which correspond to the phase of two interacting light fields. The overall goal of the project can be summarized by the following statement: Given an object whose surface undergoes small deformations or vibrations, and an electro-optic holography (EOH) system whose output is a set of images containing fringe patterns dependent on out-of-plane displacement, find the surface implied by the data which is most likely to depict the actual surface displacement. The surface displacement is directly related to the phase of the fringe locus function which describes the fringe pattern seen on the surface of the object in images created with an EOH system, so, by an inverse operation, the displacements can be derived from observed fringe patterns.

1.1 Purpose of holographic measurement.

The holographic interferometry technique, along with phase unwrapping, generates data sets in the form of images whose values correspond to phase changes of the illuminating light along the viewing axis of a surface under observation. Since data points are produced at every point in the image of the surface, very high density information results. The phase change which the technique measures may be induced by either surface deformations due to stress on the object, or due to the displacement of the surface of the

object during sinusoidal vibrations. Knowledge of the wavelength of the illuminating laser light and the geometry of the illumination and observation angles allows the conversion of measured phase to actual displacements. Surface deformations due to stress are measured with the "static" holography technique while vibration amplitudes are measured with "time-average" holography. In each case, the magnitudes of the measured displacements are very small. The maximum displacement measured in one image is typically on the order of 5×10^{-6} meters or 5 micrometers (assuming there are about 10 fringes in the image). The EOH process thus yields accurate, full field measurements of small surface displacements either due to an applied stress, or due to vibration.

1.2 Applications of EOH.

The data generated with EOH can be used for either qualitative part characterization or to determine exact quantitative responses of a part to known stresses. Applications range from validation of analytical or modeled results to inspection tasks. A brief overview of EOH applications follows.

The use of computer simulation software to determine the behavior of critical parts during mechanical design can lead to greater efficiency in the design process. However, while the programs generate valid results when used properly, even small mistakes in their use can render the results meaningless. In the effort to improve modeling software, experimental validation becomes critical. For example, when searching for the resonant modes of a mechanical part or structure, time average EOH provides real time qualitative feedback. As the part is subjected to a monotonic sinusoidal excitation signal which

sweeps over a range of frequencies, fringes appear and disappear on the surface of the object. The fringe patterns are evident whenever the sweep passes one of the part's resonant modes. The distribution of fringes on the surface indicates how every point on the object moves as it vibrates. These fringes can subsequently be processed to give a topological map of the surface deformation at the extrema of the vibration. The resonant modes found experimentally can be compared to the modes found by the modeling software to determine the validity of the software simulation.

EOH can be used to validate complex new analytical models of mechanical behavior, while simple, well understood analytical models can be used to validate the EOH process itself. Exact solutions for behavior can be found for simple, well understood object geometries. The results generated by empirical tests with the EOH system can be compared to these well known solutions to validate the EOH system's procedures and results. Then, as new analytical models are proposed for more complex geometries, EOH testing can help prove or disprove the model's validity.

The analytical models exist to predict modal frequencies as well as deformations under static loads for simple shapes. The predicted results for modal frequencies can be compared to the resonant modes identified with a frequency sweep using the EOH system in time average mode. Predictions for static deformations can be compared directly to the displacement data generated by the EOH system for quantitative validation. These two approaches allow experimental researchers to prove the reliability of the EOH system's two modes of operation.

For both finite element method (FEM) validation and analytical comparison, quantitative results are required to evaluate the degree to which the models match the experimentally derived data. However, another class of applications makes use only of qualitative results to perform inspection tasks. Most often, EOH is used in inspection to test the quality of the bond between layers of laminated materials. Such inspection can be performed by any of a variety of techniques for stressing the object. Depending on the technique, either time average or static holography may be used. The technique employed depends on the nature of the material to be tested.

Time average EOH is used to inspect the quality of the bond between very stiff parts. The substrate to which a stiff laminate has been bonded is affixed to a piezo electric transducer (PZT shaker) and a white noise signal is applied to shake the part. When the EOH display is viewed, any area where the materials are not bonded properly turns dark or shows a pattern of concentric rings. The area of the bond fault corresponds to the darkened area in the hologram, and can be measured directly.

Static EOH is used to inspect bonding quality in softer materials. Fiberglass or carbon fiber laminates fall in this class. These materials are inspected by a process where first a reference image of the surface of the laminate is captured, then the sample is either heated or subjected to a small drop in pressure. Any failures in the bond between the layers will cause a bubble to form on the surface. The bubble will appear as either a darkening or a bull's eye pattern whose perimeter defines the edge of the poorly bonded area. Each of

these application areas has been investigated in the laboratories at WPI's Center for Holographic Studies and Laser Technologies (CHSLT).

EOH has been used in numerous other applications where extremely small displacements must be measured. Many more applications ranging from analysis of structural dynamics under vibratory, thermal or pressure gradient induced stress to characterization of the operating parameters of micro machines are also likely candidates for empirical testing by EOH methods in the future.

1.3 Brief description of EOH.

The EOH system employs an apparatus similar to that used to generate a film hologram, as shown in Fig. 1.1.

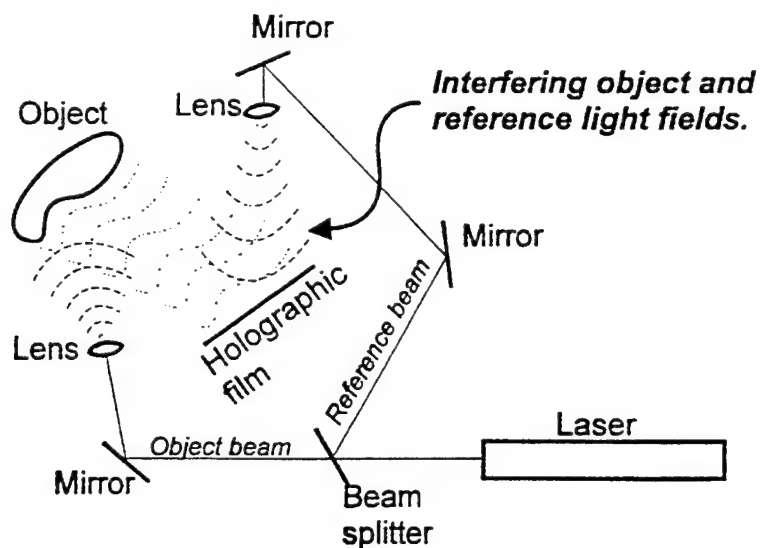


Fig. 1.1 Simple film-based holographic apparatus.

A laser beam is divided into two parts, the object beam, which illuminates the part under scrutiny, and the reference beam, which is recombined with the image of the part to create interference between the two beams. When an object illuminated by laser light is imaged, the finite aperture of the optics causes speckles to appear on the surface of the object in the image. By changing the phase of the reference beam relative to the object beam in a pair of images, the intensity of speckles can be modulated since the relative phases of the interfering light fields change. If either an object is vibrating in the image, or a pair of image sets acquired before and after a small deformation are processed, a system of fringes appears on the surface of the object where the fringes are spaced such that relative surface displacement from one fringe node to the next is $\sim \lambda/2$ (λ is the wave length of the illuminating laser light).

As mentioned above, there are two modes of operation for the EOH system: time average and static modes. Time average mode is used for the study of vibrations, while static mode is used to study displacements of a surface due to some form of loading.

Static mode allows measurement of displacements which do not change over periods of at least 4/30th seconds (See *Chapter 2, Section 8* for a complete description). Two cosinusoidal fringe patterns are produced by the image processor where the phase of one of the two is $\pi/2$ out of phase with the other. Then, the measured phase difference induced by the displacement, Ω' , modulo 2π can be recovered by

$$\Omega' = \arctan\left(\frac{\sin \Omega}{\cos \Omega}\right), \quad 1.1)$$

where Ω is the actual phase difference between the light fields¹. Notice that, though the phase actually varies continuously across the surface, the solution for Ω' is discontinuous and repeats due to the arctan. The phase must therefore be unwrapped to recover the actual surface displacement values.

Time average mode generates three non-overlapping Bessel function fringe patterns in three separate images, where the fringe pattern in each has been offset by a known amount (See *Chapter 2, Section 9* for a complete description). The measured phase difference induced by the displacement, Ω' , modulo π can be recovered by the three bucket technique^{2,4} as expressed in the following equation:

$$\Omega' = 1/2 \arctan \left[\left(\frac{1 - \cos 2B}{\sin 2B} \right) \frac{I_{h_3} - I_{h_1}}{2I_{h_2} - I_{h_3} - I_{h_1}} \right], \quad 1.2)$$

where B is a bias signal introduced to shift the fringes in the images, and I_{h_1} , I_{h_2} and I_{h_3} are the three images containing fringes. To derive this solution for Ω' , the Bessel function has been approximated by a cosine. The resulting phase contains discontinuities at each 2π repetition of the arctan function. These discontinuities must be removed by the phase unwrapper prior to completing the task of recovering the actual displacement values from the phase data. Once the phase has been unwrapped, a correction is applied to account for the difference between the Bessel function fringe spacing in the actual data and the cosine spacing assumed in the derivation of the expression for the phase given above. The correction applies a lookup table (LUT) to map from the cosine

approximation to the actual Bessel function's phase. Then the displacement can easily be computed from the corrected phase.

1.4 The phase unwrapping problem.

For each of the two types of holography, as well as other interference based applications, unwrapping a two dimensional phase map is required to recover the desired physical measurements. Any measurement system which relies on interference effects will require some kind of phase unwrapping since the associated fringe functions will necessarily have a 2π periodicity due to the periodic nature of the fringes. Since the fringes are sinusoidal, or approximated as such, the phase will be recovered by some inverse trigonometric function (usually the arctan), which also has 2π periodicity.

The unwrapping process is complicated by a number of factors including noise, mis-calibration, object discontinuities and shadows. In the simplest case where calibration, discontinuity and shadow effects are ignored, the noise in the image is often sufficient to confuse a phase unwrapper. When phase discontinuities are characterized as intensity transitions greater than some threshold between pairs of pixels, noise can obscure the transition. Then, instead of a single step transition, the step can spread over a number of pixels such that none of the changes between pairs of pixels are larger than the threshold, yet the sum of the steps constitutes a 2π transition. Such a transition will be missed by the unwrapper since none of the pixel pairs show the requisite step size. Conversely, if a noisy pixel occurs in the middle of a fringe such that the difference with

one of its neighbors is greater than the threshold, but the difference is not greater on the opposite side, then a transition will be erroneously introduced. To complicate the problem further still, the offset applied to higher order fringes depends on the number of fringes traversed from a starting point to reach the current point. So, any inappropriate transitions inserted while traversing the path to this point are accumulated and propagated through this pixel to its neighbors. The error then propagates to all the pixels which depend on the neighbors through the remainder of the processing.

While there are many sources of difficulties in the problem, there are also some characteristics which can be exploited to assist in the phase unwrapping task. Specifically, the displacement to be measured is continuous except at borders and its slope will tend not to change rapidly. Though the slope may be discontinuous at an interface between two different materials in one object, the unwrapper can still treat each surface independently since they can subsequently be joined with little difficulty. The continuity of a surface can be used as a constraint on the possible fringe number values which a point can take relative to its neighbors. The use of this constraint is central to the proposed approach for fringe unwrapping, as detailed in *Chapter 4*.

1.5 Document Overview.

This first chapter gives an overview of electro-optic holography and provides the motivation for working to improve on existing phase unwrapping techniques. *Chapter 2* provides detailed background material for EOH, energy minimization techniques used in computer vision labeling software and, by extension, facet based energy minimization. A

discussion of previous techniques employed in phase unwrapping follows in *Chapter 3*. *Chapter 4* develops the facet based unwrapping technique conceived for this project, then *Chapter 5* shows some results and *Chapter 6* draws conclusions and provides a discussion of the strengths and weakness' of the approach.

The appendices contain related information which may be of use. *Appendix A* details the MathCad model used to investigate the behavior of fringes in time-average holography when a bias vibration signal is used to shift the fringe pattern on the surface of the part. *Appendix B* gives a flow diagram of the facet based phase unwrapping software.

Chapter 2. Overview of EOH, energy minimization and facet based estimation.

The following sections outline the theoretical basis for the mathematical description of the electro-optic holographic process.

2.1 Description of a planar light field.

The behavior of light fields can be described by a set of interdependent differential equations deduced in 1861 by Maxwell. Working from the theoretical and experimental efforts of predecessors such as Coulomb, Gauss, Ampere, Faraday and others, Maxwell discovered that the set of equations which now bear his name provided a unified system by which to explain all electro-magnetic behavior. Soon after, the same set of equations was shown to describe the behavior of light giving rise to the description of light as an electro-magnetic phenomenon. Later, with the emergence of quantum theory, Maxwell's description of light as an electro-magnetic wave has been shown to be incomplete.

Phenomena such as the photoelectric effect showed that light also displays particulate behavior and helped to build the quantum model. While Maxwell's equations have been superseded by quantum theory, they still give accurate approximations of electro-magnetic behavior over a broad range of conditions. Planar light fields and their interactions are among the applications for which Maxwell's equations provide a perfectly sufficient description ⁵.

Maxwell's equations applied to electro-magnetic disturbances in a linear, isotropic dielectric media which contains no free charges consist of four second order differential equations as follows:

$$\nabla \mathbf{E} = \frac{\partial E_x}{\partial x} + \frac{\partial E_y}{\partial y} + \frac{\partial E_z}{\partial z} = 0 \quad 2.1)$$

$$\nabla \mathbf{H} = \frac{\partial H_x}{\partial x} + \frac{\partial H_y}{\partial y} + \frac{\partial H_z}{\partial z} = 0 \quad 2.2)$$

$$\begin{aligned} \text{curl } \mathbf{E} &= \left(\frac{\partial E_z}{\partial y} - \frac{\partial E_y}{\partial z} \right) \mathbf{i} + \left(\frac{\partial E_x}{\partial z} - \frac{\partial E_z}{\partial x} \right) \mathbf{j} + \left(\frac{\partial E_y}{\partial x} - \frac{\partial E_x}{\partial y} \right) \mathbf{k} = \\ &= -\mu \frac{\partial \mathbf{H}}{\partial t} = -\mu \frac{\partial H_x}{\partial t} \mathbf{i} - \mu \frac{\partial H_y}{\partial t} \mathbf{j} - \mu \frac{\partial H_z}{\partial t} \mathbf{k} \end{aligned} \quad 2.3)$$

$$\begin{aligned} \text{curl } \mathbf{H} &= \left(\frac{\partial H_z}{\partial y} - \frac{\partial H_y}{\partial z} \right) \mathbf{i} + \left(\frac{\partial H_x}{\partial z} - \frac{\partial H_z}{\partial x} \right) \mathbf{j} + \left(\frac{\partial H_y}{\partial x} - \frac{\partial H_x}{\partial y} \right) \mathbf{k} = \\ &= -\epsilon \frac{\partial \mathbf{E}}{\partial t} = -\epsilon \frac{\partial E_x}{\partial t} \mathbf{i} - \epsilon \frac{\partial E_y}{\partial t} \mathbf{j} - \epsilon \frac{\partial E_z}{\partial t} \mathbf{k} \end{aligned} \quad 2.4)$$

where \mathbf{E} is the electric field, \mathbf{H} is the magnetic field, ϵ is the permittivity of the dielectric medium and μ is the permeability of the dielectric medium.

For linearly polarized light, the electric field \mathbf{E} disappears along two of the three axes.

Assuming a plane wave travels toward $+x$, E_x is zero. Since the light is assumed to be linearly polarized, we can arbitrarily choose one of the two remaining components to be zero as well, say E_z , leaving E_y as the only non-zero component. Similarly, the magnetic field \mathbf{H} then has zero components along x and y leaving only H_z as a non-zero

component. This follows from the fact that a moving charge creates a magnetic field perpendicular to the direction of motion of the charge, and the changing electric field of the light represents a charge in motion along the y axis.

Under the conditions for linear polarization outlined above, Maxwell's equations simplify to:

$$\frac{\partial E_y}{\partial y} = 0 \quad 2.5)$$

$$\frac{\partial H_z}{\partial z} = 0 \quad 2.6)$$

$$\frac{\partial E_y}{\partial z} \mathbf{i} + \frac{\partial E_y}{\partial x} \mathbf{k} = -\mu \frac{\partial H_z}{\partial t} \mathbf{k} \quad 2.7)$$

$$\frac{\partial H_z}{\partial y} \mathbf{i} - \frac{\partial H_z}{\partial x} \mathbf{j} = \epsilon \frac{\partial E_y}{\partial t} \mathbf{j} \quad 2.8)$$

The above system of differential equations can only be satisfied when E_y and H_z are functions of at most x and t . E_y cannot be a function of y due to the condition of Eq. 2.5. Also, E_y cannot be a function of z since the x component of Eq. 2.7 is zero. Similarly, H_z cannot be a function of z or y from Eqs 2.6 and 2.8, respectively.

Given these simplifications, Eqs 2.7 and 2.8 become:

$$\frac{\partial E_y}{\partial x} = -\mu \frac{\partial H_z}{\partial t} \quad 2.9)$$

$$-\frac{\partial H_z}{\partial x} = \epsilon \frac{\partial E_y}{\partial t} \quad 2.10)$$

Differentiation of Eq. 2.9 by x and 2.10 by t followed by the combination of the two gives:

$$\frac{\partial^2 E_y}{\partial x^2} = \mu\epsilon \frac{\partial^2 E_y}{\partial t^2} \quad 2.11)$$

Equation 2.11 is the 1-D wave equation for a wave propagating with speed $c = \frac{1}{\sqrt{\mu\epsilon}}$.

When μ_0 and ϵ_0 , the values of the permeability and permittivity for free space (a vacuum) are substituted, the wave propagation speed is found to be $c = 3.0 \times 10^8$ m/sec - the speed of light in a vacuum, as expected.

The solution of the wave equation above has the form

$$E_y(x, t) = \Re\{A \exp(-i(\omega t - kx))\} = A \cos(\omega t - kx) \quad 2.12)$$

where A is the amplitude of the cosinusoidal wave, ω is the frequency, k is known as the wave number, t is time and x is location along the wave's path.

This specific solution of Maxwell's equations for describing electro-magnetic phenomena implies a sinusoidal wave-like nature to light. Many aspects of light's behavior fit into this framework, and this description of a light field will be used to develop a theoretical description of electro-optic holography later in this chapter.

2.2 Interference of two coherent light fields.

While the solution above applies to the special case of linearly polarized light, a more general solution for other polarization schemes can be derived by similar arguments. The

conclusions of the more generalized argument show that any coherent light source will have some form of elliptically polarized output, where linear polarization is a special case in which the component of the light with polarization perpendicular to the linearly polarized wave is zero. In essence, any polarization can be described as the superposition of two orthogonally polarized components. Therefore, when two coherent fields intersect, only the parallel components from each of the fields will interact.

One essential characteristic of sinusoidal functions is that the superposition of two sinusoids of the same frequency yields a third sinusoid, also of the same frequency, but with a different amplitude and phase from the two original waves as in Fig. 2.1. Thus, depending on the relative phases of the two beams, the fields may interfere constructively, destructively or somewhere in between. That is, the amplitude of the resulting signal depends in part on the amplitudes of the original signals, but also, more importantly for holography, on the relative phases of the originals. This phase dependency of the resulting amplitude will be exploited in the development of the equations used to describe EOH later in this chapter.

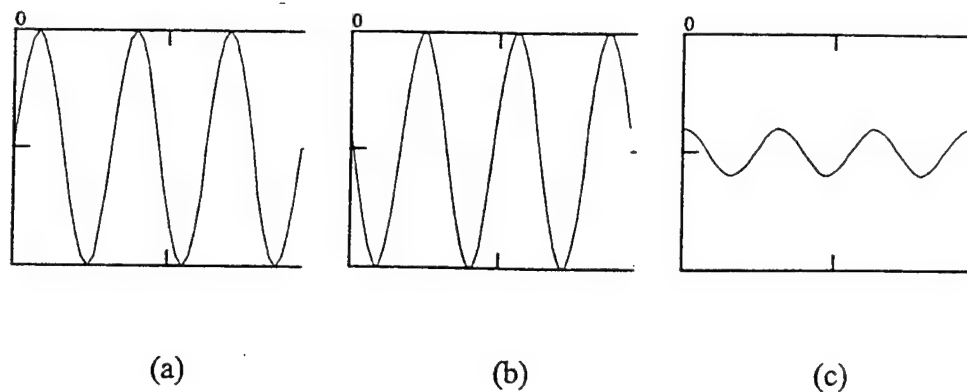


Fig. 2.1 - Two sinusoids of the same frequency, (a) and (b), but out of phase, combine to give another sinusoid of the same frequency but with a different phase and amplitude, (c).

2.3 Laser Speckle.

Most surfaces have some degree of roughness at the scale of the wavelength of light. This surface microstructure causes reflected light to diffuse and bounce in many directions, rather than simply mirror off the surface at an equal but opposite angle to the normal as the incident beam. A point in the image plane of the viewing apparatus (the retina or CCD imaging array) will receive light reflected from appropriately oriented microstructure facets anywhere within the solid angle subtended by the aperture of the imaging optics. Thus, a large number of rays with relative phases varying depending on the relative distances they travel all interfere at any given point on the receiver. Just as two sinusoidal signals of the same frequency interfere to create a new signal as shown in Fig. 2.1, a larger number of beams will show similar behavior. At some locations the interfering superposition of rays gives rise to constructive interference and the location

appears bright. At others, the superposition of the rays gives rise to destructive interference and the location appears dark. While the speckles appear to be randomly distributed over the surface, there is an inverse statistical correlation between average speckle size and imaging aperture size. Thus, for example, an increase in the f-stop of the optics which decreases the size of the aperture causes an increase in the size of the speckles observed on the surface.

An EOH system uses a charge coupled device (CCD) based camera to capture images of parts illuminated with laser light. Ideally, one speckle corresponds to one element of the camera's imaging array. Then, the speckle pattern remains uniform as long as the optical system and test apparatus are stable. Even when the part undergoes small displacements, the speckle pattern continues to stay uniform, as long as the displacements are small compared to the dimensions of the portion of the surface imaged by a single pixel in the camera. This stability of the speckles is critical to the operation of an EOH system, as will be seen later.

2.4 Coherent light, laser speckle and EOH.

The optical front end of an EOH system looks very much like an ordinary holographic setup. The light from a very stable laser is divided into two portions called the object beam and the reference beam. The object beam illuminates the object of interest. As described above, the reflected light from the object contains light and dark speckles. The image of the object is recombined with the reference beam, and the two beams interfere at each speckle.

In order to understand the behavior of the system when the object is quiescent, consider one bright speckle in the object field. If the phase of the speckle and the phase of the reference beam at that point match, then the two fields interfere constructively and a large magnitude signal results. If the phase of the reference beam is subsequently incremented by half a wavelength (π radians) then, at the same point, destructive interference occurs and a low magnitude signal results. When the second result is subtracted from the first, the magnitude of the difference is large. In operation, the EOH system samples the magnitude of the result from the two interfering beams at each pixel in the image created by the camera. The system digitizes and stores the first image, then changes the relative phase of the object and reference beams by π radians and digitizes the second image. Their difference is then computed and bright pixels are seen wherever the object remains stationary.

To extend the example further, consider what happens if the surface illuminated by the laser moves before the system captures the second image. Now, again, the system introduces a π radians phase change in the reference beam relative to the object beam, but, the object has moved, so the path length of the object beam has changed. A change in path length results in a change of the phase of the object beam. If the object moves by exactly one quarter of the wavelength of the illuminating laser light, then the path length which the object beam travels becomes one half wave length longer. As a result, the phase of the object beam changes by π radians, as well. Now, when the two beams combine at the surface of the CCD camera's sensing element, the magnitude of the

interfering signals is again large. When the system computes the difference between the two signals, a small value results. Following this example further along, when the object moves by one half the wavelength of the laser, the phase change in the object beam will be 2π radians, so the difference between the two signals is large. This argument indicates that, where the object is stationary, the speckles appear bright in the computed output. Where the object has moved by a quarter wavelength, the speckles appear dark. Where the object has moved by a half wavelength, the speckles appear bright again. So, the final result of the difference between the two images taken with a phase shift of π radians in the reference beam has alternating light and dark bands on the surface. Each point of the surface covered by a band has moved by nearly the same amount. These bands are commonly referred to as interference fringes or fringe loci.

To improve the system's performance, the subtraction operation is also performed on a second pair of images whose phase difference vector is orthogonal to the phase difference vector of the first pair, as plotted in a polar phase angle versus phase magnitude plot. Given the magnitude of the phase difference along two orthogonal axes, regardless of the phase orientation of the phase vector of the speckle, the square root of the sum of the squares of the magnitudes of the two phase difference vectors gives the modulation magnitude of that speckle. That is, by subtracting images taken at reference beam phases of 0 and π radians to produce a measure of the modulation along one vector, then subtracting images taken at reference beam phases of $\pi/2$ and $3\pi/2$ radians to produce a measure of the modulation along a second, orthogonal vector, then taking the square root

of the sum of the squares, the magnitude of the modulation is recovered, regardless of the absolute phase angle at that speckle.

2.5 Electro-optic holography system components.

The EOH system is composed of: 1) fixturing to hold and stress an object, 2) an optical front end, 3) an image processing subsystem and 4) a host computer to act as the system controller.

2.5.1 Fixtures.

For time average holography, the object of interest must be clamped firmly to a support structure that maintains the object-to-interferometer distance to within a fraction of a wave length of the laser light, but also provides the means to induce small vibrations of known frequency in the object. Two methods are common for coupling the driving signal to the object: 1) Clamp the object firmly by its base, then induce vibration with a speaker, or 2) clamp the object directly onto a piezo electric transducer (PZT) which will shake the entire object with a very small amplitude signal. In either case, a small amplitude driving signal is coupled to the part so that the part undergoes measurable displacement due to vibration only when the signal's frequency matches a resonant mode of the part. When the frequency matches a resonance, the coupling efficiency increases greatly and the structure vibrates sympathetically.

2.5.2 Optical system.

The optical system, as shown in Fig. 2.2, consists of a laser, mirrors, a PZT mirror mount, beam expanding lenses, an imaging lens and a CCD camera. The coherent light beam generated by the laser is split by a partially transmissive mirror, into two portions, the object and the reference beams. The object beam is diverged sufficiently to illuminate the entire object, then the image is focused onto the CCD camera sensor by the imaging lens. Meanwhile, the reference beam is diverged and recombined with the object beam at a second partially transmissive mirror immediately in front of the camera. When the two beams intersect, the coherent light fields interfere. The CCD camera integrates the intensity of the resulting light field over each $\frac{1}{30}$ th second frame time. The image from the CCD camera is then fed to the image processor.

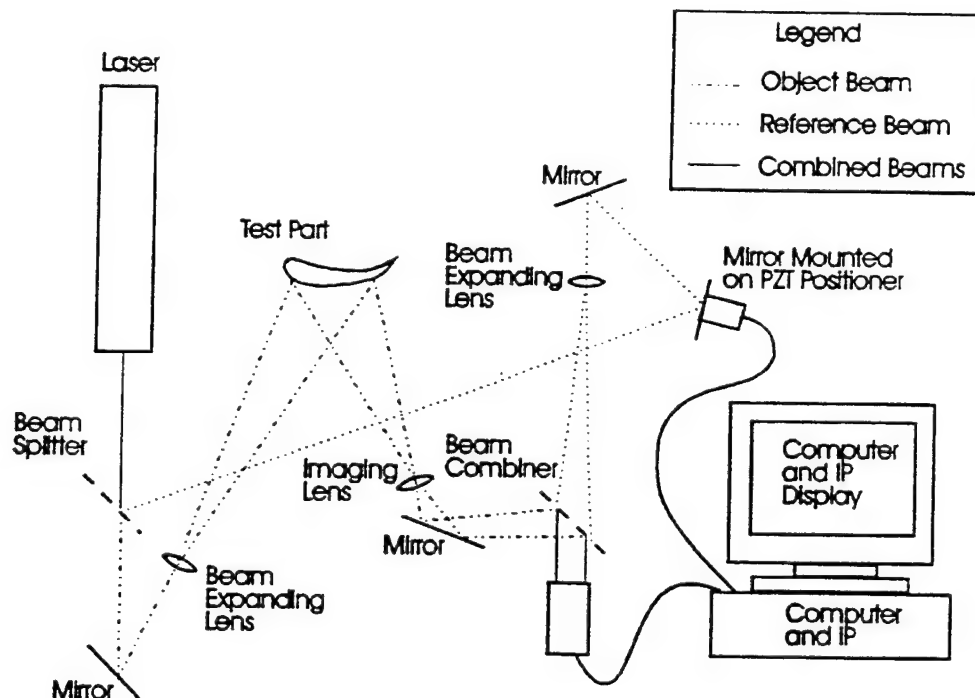


Fig. 2.2 - Electro-optic holography system block diagram.

2.5.3 *System electronics.*

An NEC black and white CCD camera with gamma correction and automatic gain disabled provides RS-170 format video input of the interfering beams at 30 frames per second. To process the image data generated by the camera, the system uses an MV200 image processor from Datacube. The MV200 occupies two VME slots and includes 24MB of image memory, a video analog-to-digital conversion subsystem, a display subsystem which supports the X-Windows environment with live video display inside windows, numerous ALUs, multipliers, shifters, clippers and sign extenders, an 8x8 convolver, a 16-bit lookup table and a 32 channel cross-point switch which allows software control of the configuration of these elements. The image processor is controlled by a Motorola MVME167 single board computer based on a 68040 CPU. A digital function generator provides precise control over the driving signal for exciting the part.

2.6 *Mathematical description of holograms.*

The mathematical description of the interaction of two coherent planar light fields can be derived from the solution to Maxwell's equations given in Eq. 2.12. Either one of the two beams individually can be modeled by

$$F(x, y, t) = \Re\{A(x, y)\exp[-i(\omega t - \varphi(x, y))]\} \quad , \quad 2.13)$$

a complex light field where $\phi(x, y)$ expresses the phase of the light field at every point in the plane, A describes the amplitude and ω is the frequency. We assume that the light is coherent which implies only one frequency and uniform phase.

2.7 Static mode data acquisition.

In static mode, the EOH system generates a hologram whose fringes indicate static deformation of the surface of the object⁶. To produce these results, two sets of images are captured, with the state of stress changed between the two. Each image set is composed of four frames, where a phase increment is added to the reference beam relative to the object beam between each frame in the set¹.

The two beams which interact at the beam combiner can be described by

$$F_o(x, y) = A_o(x, y) \exp[i\phi_o(x, y)] \quad 2.14$$

and

$$F_r(x, y) = A_r(x, y) \exp[i\phi_r(x, y)] \quad , \quad 2.15$$

where F_o and F_r represent the object beam and the reference beam, respectively.

When the two beams interact, the intensity measured at the CCD array of the camera is given by the complex magnitude of the sum of Eqs 2.14 and 2.15, that is,

$$I(x, y) = \Re\{[F_o(x, y) + F_r(x, y)][F_o(x, y) + F_r(x, y)]^*\} \quad 2.16$$

For the following simplification of Eq. 2.16, the field amplitudes A and phases ϕ are each a function of x and y , but the arguments are omitted for greater clarity. So,

$$\begin{aligned} I &= \Re\{[A_o \exp(i\phi_o) + A_r \exp(i\phi_r)][A_o \exp(-i\phi_o) + A_r \exp(-i\phi_r)]\} \\ &= \Re\{A_o^2 + A_r^2 + A_o A_r [\exp(i\phi_o) \exp(-i\phi_r) + \exp(-i\phi_o) \exp(i\phi_r)]\} \\ &= \Re\{A_o^2 + A_r^2 + A_o A_r \{\exp[i(\phi_o - \phi_r)] + \exp[-i(\phi_o - \phi_r)]\}\}. \end{aligned}$$

Now, let $\Delta\phi = \phi_o - \phi_r$. Then

$$\begin{aligned} I &= \Re\{A_o^2 + A_r^2 + A_o A_r (\cos \Delta\phi + i \sin \Delta\phi + \cos \Delta\phi - i \sin \Delta\phi)\} \\ &= A_o^2 + A_r^2 + 2A_o A_r \cos \Delta\phi. \end{aligned}$$

Restoration of the x and y arguments and substitution of $I_o(x, y) = A_o^2(x, y)$ and

$I_r(x, y) = A_r^2(x, y)$ gives

$$I(x, y) = I_o(x, y) + I_r(x, y) + 2A_o(x, y)A_r(x, y)\cos \Delta\phi(x, y) \quad . \quad 2.17)$$

Equation 2.17 represents the pixel intensities of a frame of data captured by the image processing system prior to the introduction of phase shifts.

In the following discussion, the x and y arguments of the functions are again dropped to simplify the mathematical formulation, and constant factors from Eq. 2.17 are grouped so that $C = I_o + I_r$ and $D = 2A_o A_r$. A phase step of $\pi/2$ is introduced between frames of video data by translating the PZT mounted mirror to a new position such that the path length of the reference beam is exactly one quarter wavelength shorter. Then a four image, phase

stepped set of reference images captured prior to the deformation of the object can be described by the following set of equations:

$$\begin{aligned} I_1 &= C + D \cos \Delta\varphi, & I_2 &= C + D \sin \Delta\varphi, \\ I_3 &= C - D \cos \Delta\varphi \text{ and} & I_4 &= C - D \sin \Delta\varphi. \end{aligned} \quad 2.18)$$

The set of images captured after the deformation can be described by four more equations:

$$\begin{aligned} I'_1 &= C' + D' \cos \Delta\varphi', & I'_2 &= C' + D' \sin \Delta\varphi', \\ I'_3 &= C' - D' \cos \Delta\varphi' \text{ and} & I'_4 &= C' - D' \sin \Delta\varphi'. \end{aligned} \quad 2.19)$$

The deformation must be small enough so that the speckle pattern does not decorrelate, and the experimental environment must be stable so that random fluctuations of the phase are held to a minimum. Assuming these conditions to hold, then $C' \approx C$ and $D' \approx D$.

Now, the following combinations of the eight images represented by Eqs. 2.18 and 2.19 can be constructed:

$$P_1 = [(I_1 - I_3) + (I'_1 - I'_3)]^2 = [2D \cos \Delta\varphi + 2D \cos \Delta\varphi']^2, \quad 2.20)$$

$$P_2 = [(I_2 - I_4) + (I'_2 - I'_4)]^2 = [2D \sin \Delta\varphi + 2D \sin \Delta\varphi']^2, \quad 2.21)$$

$$P_1 + P_2 = 8D^2 + 8D^2 \cos \Delta\varphi \cos \Delta\varphi' + 8D^2 \sin \Delta\varphi \sin \Delta\varphi', \quad 2.22)$$

and

$$P_3 = [(I_1 - I_3) - (I'_1 - I'_3)]^2 = [2D \cos \Delta\varphi - 2D \cos \Delta\varphi']^2, \quad 2.23)$$

$$P_4 = [(I_2 - I_4) - (I'_2 - I'_4)]^2 = [2D \sin \Delta\phi - 2D \sin \Delta\phi']^2, \quad 2.24)$$

$$-P_3 - P_4 = -8D^2 + 8D^2 \cos \Delta\phi \cos \Delta\phi' + 8D^2 \sin \Delta\phi \sin \Delta\phi'. \quad 2.25)$$

From Eqs. 2.22 and 2.25

$$\begin{aligned} P_1 + P_2 - P_3 - P_4 &= 16D^2 (\cos \Delta\phi \cos \Delta\phi' + \sin \Delta\phi \sin \Delta\phi') \\ &= 16D^2 \cos(\Delta\phi - \Delta\phi'). \end{aligned} \quad 2.26)$$

Next, let $\Omega = \Delta\phi - \Delta\phi'$. Then

$$\begin{aligned} 16D^2 \cos \Omega &= P_1 + P_2 - P_3 - P_4 \\ &= [(I_1 - I_3) + (I'_1 - I'_3)]^2 + [(I_2 - I_4) + (I'_2 - I'_4)]^2 \\ &\quad - [(I_1 - I_3) - (I'_1 - I'_3)]^2 - [(I_2 - I_4) - (I'_2 - I'_4)]^2. \end{aligned} \quad 2.27)$$

By a similar procedure, a second result proportional to the sine of the phase difference can be generated from the eight images in Eqs 2.18 and 2.19:

$$Q_1 = [(I_1 - I_3) + (I'_2 - I'_4)]^2 = [2D \cos \Delta\phi + 2D \sin \Delta\phi']^2, \quad 2.28)$$

$$Q_2 = [(I_2 - I_4) + (I'_1 - I'_3)]^2 = [2D \sin \Delta\phi + 2D \cos \Delta\phi']^2, \quad 2.29)$$

$$Q_1 + Q_2 = 8D^2 + 8D^2 \cos \Delta\phi \sin \Delta\phi' + 8D^2 \sin \Delta\phi \cos \Delta\phi', \quad 2.30)$$

and

$$Q_3 = [(I_1 - I_3) - (I'_2 - I'_4)]^2 = [2D \cos \Delta\phi - 2D \sin \Delta\phi']^2, \quad 2.31)$$

$$Q_4 = [(I_2 - I_4) - (I'_1 - I'_3)]^2 = [2D \sin \Delta\phi - 2D \cos \Delta\phi']^2, \quad 2.32)$$

$$-Q_3 - Q_4 = -8D^2 + 8D^2 \cos \Delta\phi \sin \Delta\phi' + 8D^2 \sin \Delta\phi \cos \Delta\phi', \quad 2.33)$$

From Eqs 2.30 and 2.33

$$\begin{aligned} Q_1 + Q_2 - Q_3 - Q_4 &= 16D^2(\cos \Delta\phi \sin \Delta\phi' + \sin \Delta\phi \cos \Delta\phi') \\ &= 16D^2 \sin(\Delta\phi - \Delta\phi') . \end{aligned} \quad 2.34)$$

Finally,

$$\begin{aligned} 16D^2 \sin \Omega &= Q_1 + Q_2 - Q_3 - Q_4 \\ &= [(I_1 - I_3) + (I'_2 - I'_4)]^2 + [(I_2 - I_4) + (I'_1 - I'_3)]^2 \\ &\quad - [(I_1 - I_3) - (I'_2 - I'_4)]^2 - [(I_2 - I_4) - (I'_1 - I'_3)]^2 . \end{aligned} \quad 2.35)$$

So, to summarize, the two equations 2.27 and 2.35, composed of combinations of the eight operands described by Eqs 2.18 and 2.19, can be formed which, when simplified, yield results proportional to the sine and cosine of the difference in phase between the light field prior to the deformation and the light field subsequent to the deformation of the object under observation.

The measured change in phase due to the deformation, Ω' , can then be found from the inverse tangent of the ratio of Eqs 2.35 and 2.27 as

$$\Omega' = \arctan \left(\frac{\sin \Omega}{\cos \Omega} \right) , \quad 2.36)$$

where Ω is referred to as the fringe-locus function, constant values of which define fringe loci on the object's surface.

Notice that, due to the arctan function, the measured phase difference function, $\Omega'(x, y)$, wraps back to zero each time the actual phase difference function, $\Omega(x, y)$, passes through $(2N - 1)\pi$, where N is an integer. These discontinuities must be removed by the phase unwrapper to reconstruct a continuous phase function from which actual displacement values can be computed.

Figure 2.3 shows a pair of sinusoidal signals with a $\pi/2$ phase offset between them, along with the wrapped phase which results from applying the arctan to their ratio.

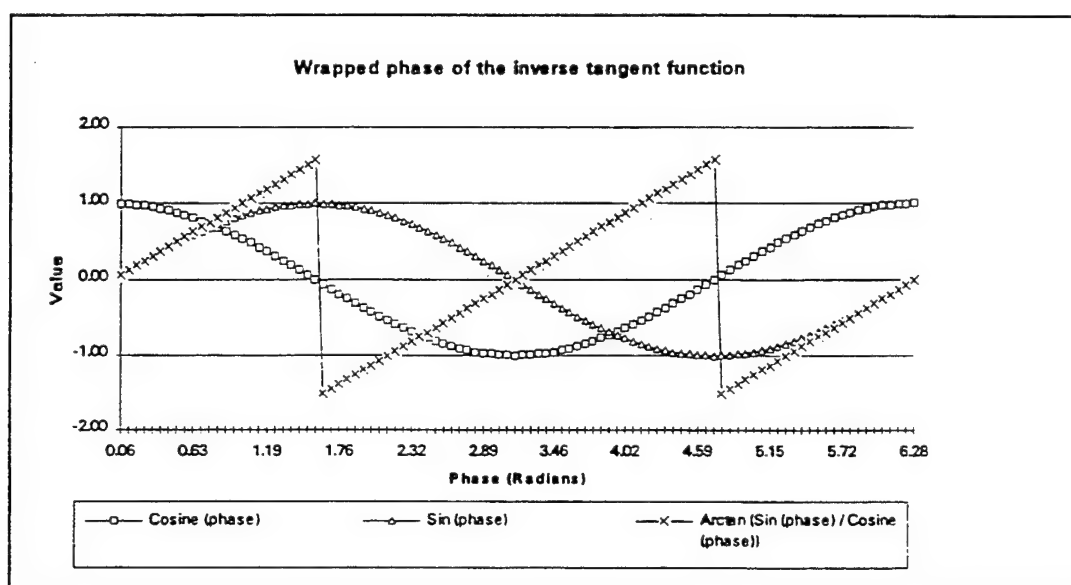


Fig. 2.3. Wrapped phase obtained by solving for the phase given 1-D sine and cosine functions as input.

2.8 Time average mode data acquisition.

In time-average mode, the EOH system generates a hologram whose fringes indicate the amplitude of vibration of the surface of the object⁶. To produce these results, one set of

images is captured as the test part undergoes sinusoidal vibration in a standing wave pattern - a resonant mode. The image set is composed of four images, where a phase increment is added to the reference beam relative to the object beam between each frame in the set ^{2,4,7}.

2.8.1 Measured intensity modified by the characteristic Bessel function.

From the solution to Maxwell's equations, the two beams which interact at the beam combiner can be described by

$$F_o(x,y) = A_o(x,y)\exp\{i[\phi_o(x,y) + \mathbf{K}(x,y) \cdot \mathbf{L}(x,y)\sin \omega t]\} \quad \text{and} \quad 2.37$$

$$F_r(x,y) = A_r(x,y)\exp[i\phi_r(x,y)] \quad . \quad 2.38$$

Equation 2.37 describes the time varying object beam, and Eq. 2.38 describes the reference beam light field which does not vary with time. The second term in the exponential of Eq. 2.37 describes the time dependent variation of the phase of the object light field which results from the sinusoidal motion of the object at frequency ω . The vector \mathbf{K} denotes the sensitivity vector which bisects the angle formed by the illumination and observation vectors. The vector \mathbf{L} denotes the displacement of the object for each point in the image. The sinusoidal term accounts for the motion of the object over the interval during which the camera integrates light to collect a frame of data. Figure 2.4 shows the geometry of the incident beam and a test part.

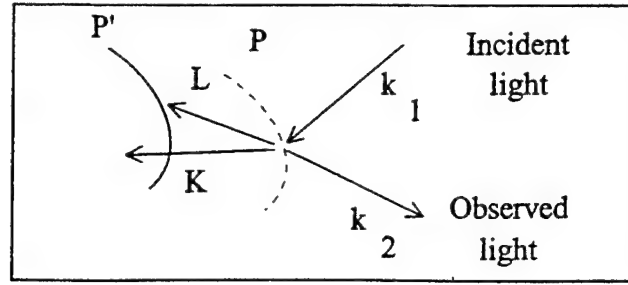


Fig 2.4 - Geometry of incident and reflected light with a moving surface.

When the two beams interact, the intensity measured at the CCD array of the camera is given by the real part of the time-average of the complex magnitude of the sum of the beams' electric fields defined by Eqs 2.37 and 2.38, that is,

$$I(x, y) = \Re \left\{ \frac{1}{T} \int_0^T [F_o(x, y) + F_r(x, y)][F_o(x, y) + F_r(x, y)]^* dt \right\} \quad 2.39$$

Equation 2.39 is expanded and the x and y arguments are dropped for clarity to give

$$\begin{aligned} I &= \Re \left\{ \frac{1}{T} \int_0^T [A_o \exp(i[\varphi_o + \mathbf{K} \cdot \mathbf{L} \sin \omega t]) + A_r \exp(i\varphi_r)] \right. \\ &\quad \left. [A_o \exp(i[\varphi_o + \mathbf{K} \cdot \mathbf{L} \sin \omega t]) + A_r \exp(i\varphi_r)]^* dt \right\} \\ &= \Re \left\{ A_o^2 + A_r^2 + \frac{1}{T} \int_0^T A_o A_r \exp[i(\varphi_o - \varphi_r + \mathbf{K} \cdot \mathbf{L} \sin \omega t)] dt \right. \\ &\quad \left. + \frac{1}{T} \int_0^T A_o A_r \exp[-i(\varphi_o - \varphi_r + \mathbf{K} \cdot \mathbf{L} \sin \omega t)] dt \right\} \quad 2.40 \end{aligned}$$

Substitution of $\Delta\varphi$ for $\varphi_o - \varphi_r$ allows the simplification of the exponential terms to give

$$I = \Re \left\{ A_o^2 + A_r^2 + \frac{A_o A_r \exp(-i\Delta\phi)}{T} \int_0^T \exp[i(\mathbf{K} \cdot \mathbf{L} \sin \omega t)] dt \right. \\ \left. + \frac{A_o A_r \exp(i\Delta\phi)}{T} \int_0^T \exp[-i(\mathbf{K} \cdot \mathbf{L} \sin \omega t)] dt \right\}. \quad (2.41)$$

Finally, taking the real part of Eq. 2.41 gives

$$I = A_o^2 + A_r^2 + 2A_o A_r \cos \Delta\phi \left\{ \frac{1}{T} \int_0^T \cos[\mathbf{K} \cdot \mathbf{L} \sin \omega t] dt \right\}. \quad (2.42)$$

The integral at the end of Eq. 2.42 is often referred to as the characteristic fringe function and denoted by $M[\Omega]$ ⁸. In general,

$$\lim_{T \rightarrow \infty} \frac{1}{T} \int_0^T \cos[\mathbf{K} \cdot \mathbf{L} \sin \omega t] dt = J_0[\Omega] \quad (2.43)$$

is a zero order Bessel function of the first kind, where $\Omega(x, y) = \mathbf{K}(x, y) \cdot \mathbf{L}(x, y)$. For time-average holography, where the integration period, T , is the frame time of the camera, the characteristic fringe function will be $J_0[\Omega(x, y)]$ when $\omega \ll T$, that is, as long as the period of the vibration of the object is much smaller than 1/30th of a second. In practice, frequencies of 60 Hz and higher give good results.

2.8.2 Time average image capture.

For the remainder of the discussion constants in Eq. 2.42 are grouped so that $C = I_o + I_r = A_o^2 + A_r^2$ and $D = 2A_o A_r$. Once again, a phase step of $\pi/2$ is introduced between frames of video data. Then, a phase stepped set of four images as captured by the image processor can be described by the following set of equations:

$$\begin{aligned}
I_1 &= C + D \cos \Delta\phi J_0(\Omega) , & I_2 &= C + D \sin \Delta\phi J_0(\Omega) , \\
I_3 &= C - D \cos \Delta\phi J_0(\Omega) \quad \text{and} & I_4 &= C - D \sin \Delta\phi J_0(\Omega) .
\end{aligned} \tag{2.44}$$

The deformation must be small enough so that the speckle pattern does not decorrelate. Then, all the C 's and all the D 's in Eq. 2.44 are equal and the four equations can be solved to eliminate C and $\Delta\phi$ yielding

$$I_{h_1} = (I_1 - I_3)^2 + (I_2 - I_4)^2 = 4D^2 J_0^2(\Omega) . \tag{2.45}$$

According to Eq. 2.45, the resulting hologram, I_{h_1} , is defined in terms of three unknowns, A_o^2 and A_r^2 comprising D^2 , and Ω contained in the argument of the J_o . In order to solve for Ω , two additional equations must be generated in such a way that the three unknowns are related in three equations. This is accomplished by introducing a bias signal on the reference beam to shift the Bessel function fringe pattern by a known amount, first to one side, then to the other side of the unbiased fringes. The following section describes a mathematical model for the phase bias.

2.8.3 Bessel function behavior.

The phase of the bias signal can be matched to the phase of the vibrating part by a calibration procedure which finds the peak power in the fringes shown in the image where a bias signal is applied. This approach is validated by the following 1-D model for the image fringe function.

The object undergoes sinusoidal vibrations and the light from the vibrations is integrated by the camera to generate the Bessel fringes as explained above. This process can be modeled by

$$I(x) = \frac{1}{T} \int_0^T \exp[-ix \sin(\omega t)] dt , \quad 2.46)$$

where the image intensity I is a function of the position x . As x varies, the intensity value sweeps out a zero order Bessel function of the first kind as shown in the graph in Fig. 2.5. The varying x value corresponds to increasing amplitude of the sinusoidal vibration across the surface moving away from a nodal line at $x = 0$. This varying amplitude term is represented by the x multiplier preceding the sinusoidal term in the integral.

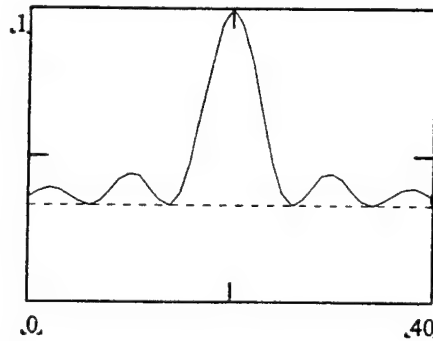


Fig 2.5 - One-dimensional Bessel function squared.

Now, when a second signal of the same frequency but different phase contributes to the function, the model expands to

$$I(x, \phi) = \frac{1}{T} \int_0^T \exp(-i[\sin(\omega t + \phi) + x \sin(\omega t)]) dt . \quad 2.47)$$

Now I depends on both x and ϕ , so a 2-D graph will show how the function varies with changing amplitude along the x axis and how the function varies with changing relative phase of the two signals along the ϕ axis. Figure 2.6(a) shows the 2-D surface plot of I . Notice that there are peaks in the zero order fringe where the phase of the two signals are exactly in or out of phase. Also, the amplitude of the remaining fringes stay constant regardless of the relative phase. This suggests that a calibration routine which detects the peak image energy as the relative phase is changed will find the phase value where the two signals are perfectly in or out of phase.

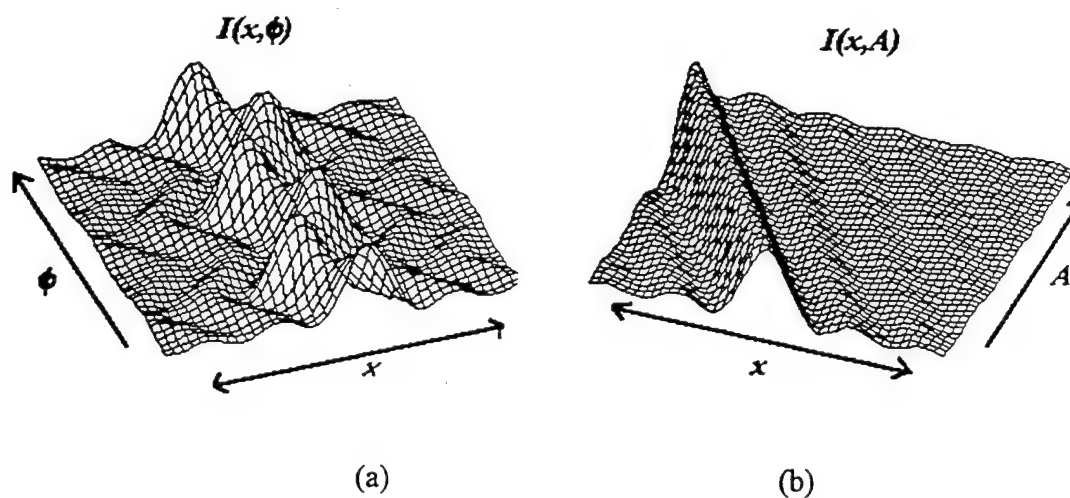


Fig. 2.6 - Surface plots of fringe intensity as a function of displacement in x versus relative phase in (a) and versus bias amplitude in (b).

When the two signals are perfectly in or out of phase, Bessel fringes will still be seen in the image. Now, when the amplitude of the bias signal varies, the location of the peak of

the zero order fringe will vary, without otherwise affecting the shape of the function.

This is illustrated by the modeling the intensity by

$$I(x, A) = \frac{1}{T} \int_0^T \exp(-i(A \sin(\omega t) + x \sin(\omega t))) dt \quad , \quad 2.48)$$

where I is now a function of x and A - the amplitude of the bias signal. A surface plot in Fig. 2.6(b) with x along one axis and A along the other shows the effect of varying the amplitude of the bias signal.

A phase bias can be introduced in the fringes in a hologram by changing the path length of one of the two beams relative to the other with a second signal of the same frequency as the excitation signal, but with variable phase and amplitude. *Appendix A* shows the MathCad model used to investigate the behavior of the Bessel function.

2.8.4 Solution for unambiguous phase.

As discussed earlier, a set of three equations is required to solve for the three unknowns in the equation which describes the hologram images. A bias signal with an amplitude denoted by B , and phase such that the phases of the two beams are identical at the camera, adds a new term to the expression which describes the reference beam so that

$$F_{N,r} = A_r(x, y) \exp \{ i[\phi_r(x, y) + B \sin(\omega t)] \} \quad . \quad 2.49)$$

where the subscript N indicates the negative biased beam and the small subscript r is used to denote the reference beam.

Equation 2.49 represents the electric field of the reference beam modulated by the sinusoidal bias signal for the first of the two biased results called the negative biased hologram. The biased reference beam interacts with the object beam represented in Eq. 2.38 to give an intensity at the camera of

$$I_N = [F_o + F_{N_r}][F_o + F_{N_r}]^* \\ = A_o^2 + A_{N_r}^2 + 2A_o A_{N_r} \cos \Delta\phi \left\{ \frac{1}{T} \int_0^T \cos[(\mathbf{K} \cdot \mathbf{L} - B) \sin \omega t] dt \right\} \quad . \quad 2.50$$

A set of four phase stepped images derived from Eq. 2.50 and identical to Eq. 2.44 except for the bias, is captured. The negative biased hologram is computed from these four images as

$$I_{h_2} = 4D^2 J_0^2(\Omega - B) = (I_{N_1} - I_{N_3})^2 + (I_{N_2} - I_{N_4})^2 \quad . \quad 2.51$$

The third result, called the positive biased hologram, is generated by changing the phase of the bias signal by 180°. Then, the reference beam can be represented by

$$F_{P_r} = A_r \exp \{i[\phi_r + B \sin(\omega t + \pi)]\} = A_r \exp \{i[\phi_r - B \sin(\omega t)]\} \quad . \quad 2.52$$

where the subscript P indicates the positive biased beam and the small subscript r is used to denote the reference beam. The positive biased reference beam interacts with the object beam in Eq. 2.44 to give an intensity at the camera of

$$I_P = [F_o + F_{P_r}][F_o + F_{P_r}]^* \\ = A_o^2 + A_{P_r}^2 + 2A_o A_{P_r} \cos \Delta\phi \left\{ \frac{1}{T} \int_0^T \cos[(\mathbf{K} \cdot \mathbf{L} + B) \sin \omega t] dt \right\} \quad . \quad 2.53$$

Again, the positive biased hologram is computed from a set of four phase stepped images derived from Eq. 2.53 to give

$$I_{h_3} = 4D^2 J_0^2(\Omega + B) = (I_{P_1} - I_{P_3})^2 + (I_{P_2} - I_{P_4})^2 . \quad 2.54)$$

Now we have three equations, given by Eqs 2.45, 2.51 and 2.54, written in terms of the three unknowns. The exact solution for Ω is not simple since the Bessel function is both nonlinear and non-periodic. However, an approximate solution is possible if the fringe function is assumed to be a cosine squared rather than a Bessel function squared. This assumption introduces errors in the computed results, but these errors are directly dependent on the computed phase value and can be corrected after the phase is unwrapped by indexing into an appropriate lookup table (LUT).

To solve for the phase, first approximate the Bessel function squared in Eqs 2.45, 2.51 and 2.54 with the cosine squared:

$$I_{h_1} = 8D^2 \cos^2(\Omega + B) , \quad 2.55)$$

$$I_{h_2} = 8D^2 \cos^2(\Omega) \quad \text{and} \quad 2.56)$$

$$I_{h_3} = 8D^2 \cos^2(\Omega + B) . \quad 2.57)$$

The cosine squared can be replaced by the use of trigonometric identities to give

$$I_{h_1} = 4D^2 + 4D^2 \cos(2\Omega + 2B) = 4D^2 + 4D^2 \cos 2\Omega \cos 2B - 4D^2 \sin 2\Omega \sin 2B, \quad 2.58)$$

$$I_{h_2} = 4D^2 + 4D^2 \cos 2\Omega \quad \text{and} \quad 2.59)$$

$$I_{h_3} = 4D^2 + 4D^2 \cos(2\Omega - 2B) = 4D^2 + 4D^2 \cos 2\Omega \cos 2B + 4D^2 \sin 2\Omega \sin 2B . \quad 2.60)$$

So

$$I_{h_3} - I_{h_1} = 8D^2 \sin 2\Omega \sin 2B \quad \text{and} \quad 2.61)$$

$$2I_{h_2} - I_{h_3} - I_{h_1} = 8D^2 \cos 2\Omega - 8D^2 \cos 2\Omega \cos 2B. \quad 2.62)$$

The ratio of Eqs 2.61 and 2.62 gives

$$\frac{I_{h_3} - I_{h_1}}{2I_{h_2} - I_{h_3} - I_{h_1}} = \left(\frac{\sin 2B}{1 - \cos 2B} \right) \frac{\sin 2\Omega}{\cos 2\Omega} = \left(\frac{\sin 2B}{1 - \cos 2B} \right) \tan 2\Omega. \quad 2.63)$$

Now, the term containing the phase can be isolated as

$$\tan 2\Omega = \left(\frac{1 - \cos 2B}{\sin 2B} \right) \frac{I_{h_3} - I_{h_1}}{2I_{h_2} - I_{h_3} - I_{h_1}}. \quad 2.64)$$

The solution for the phase at each point, assuming the hologram contains cosine squared fringes is therefore

$$\Omega = \frac{1}{2} \arctan \left[\left(\frac{1 - \cos 2B}{\sin 2B} \right) \frac{I_{h_3} - I_{h_2}}{2I_{h_1} - I_{h_3} - I_{h_2}} \right]. \quad 2.65)$$

Notice that, similar to static mode, values for the solution wrap back to zero each time the argument of the arctan function passes across a $(2N - 1)\frac{\pi}{2}$ boundary, where N are integer values. These discontinuities must be removed by unwrapping the phase to build the continuous phase function required to perform the correction and subsequently compute actual displacement values from the data.

The unwrapped Ω values thus computed are corrected by indexing into an LUT generated by finding the inverse mapping to translate from the phase found assuming cosine squared fringes to the correct phase resulting from Bessel squared fringes. To build such

an LUT, first an array is filled with values corresponding to a sampled set of all possible values that the processed data may take. Such an array can be computed by

$$LUT(\Omega_B) = \frac{1}{2} \arctan \left[\left(\frac{1 - \cos 2B}{\sin 2B} \right) \frac{J_0^2(\Omega_B + B) - J_0^2(\Omega_B - B)}{2J_0^2(\Omega_B) - J_0^2(\Omega_B + B) - J_0^2(\Omega_B - B)} \right]. \quad 2.66)$$

Second, the LUT must be inverted to map from the assumed cosine squared fringe domain to the actual Bessel squared fringe domain. Values for the correction LUT are computed at points separated by a fixed interval in the Bessel phase argument, Ω_B . When the LUT is inverted, the intervals between LUT entries are no longer uniform, so care must be taken that an interpolation procedure computes the new values for the inverse LUT at regular intervals in the inverse domain. The inverse LUT is denoted by $LUT^{-1}(\Omega_B)$.

The correction is applied after the phase is unwrapped to compute the actual phase of the Bessel squared fringes, Ω_C , and takes the form of

$$\Omega_C = LUT^{-1}(\Omega_i) \quad 2.67)$$

at every point in the image, where the i subscript indicates that the value of the uncorrected phase is quantized, then used as an index into the correction table.

Finally, the actual displacement of the surface under observation can be calculated from the phase by

$$L = \frac{\lambda}{2\pi(K_2 - K_1)} |\Omega|, \quad 2.68)$$

where L is the displacement, λ is the wave length, K_2 is the observation vector and K_1 is the illumination vector¹.

The upper left image in Fig. 2.7 shows models for three biased Bessel functions with the wrapped phase overlaid. The correction LUT over the same range is shown in the upper right image. The corrected unwrapped data for a low noise case is shown in the lower left and an inconsistently unwrapped phase where large noise was artificially added to the model is shown in the lower right.

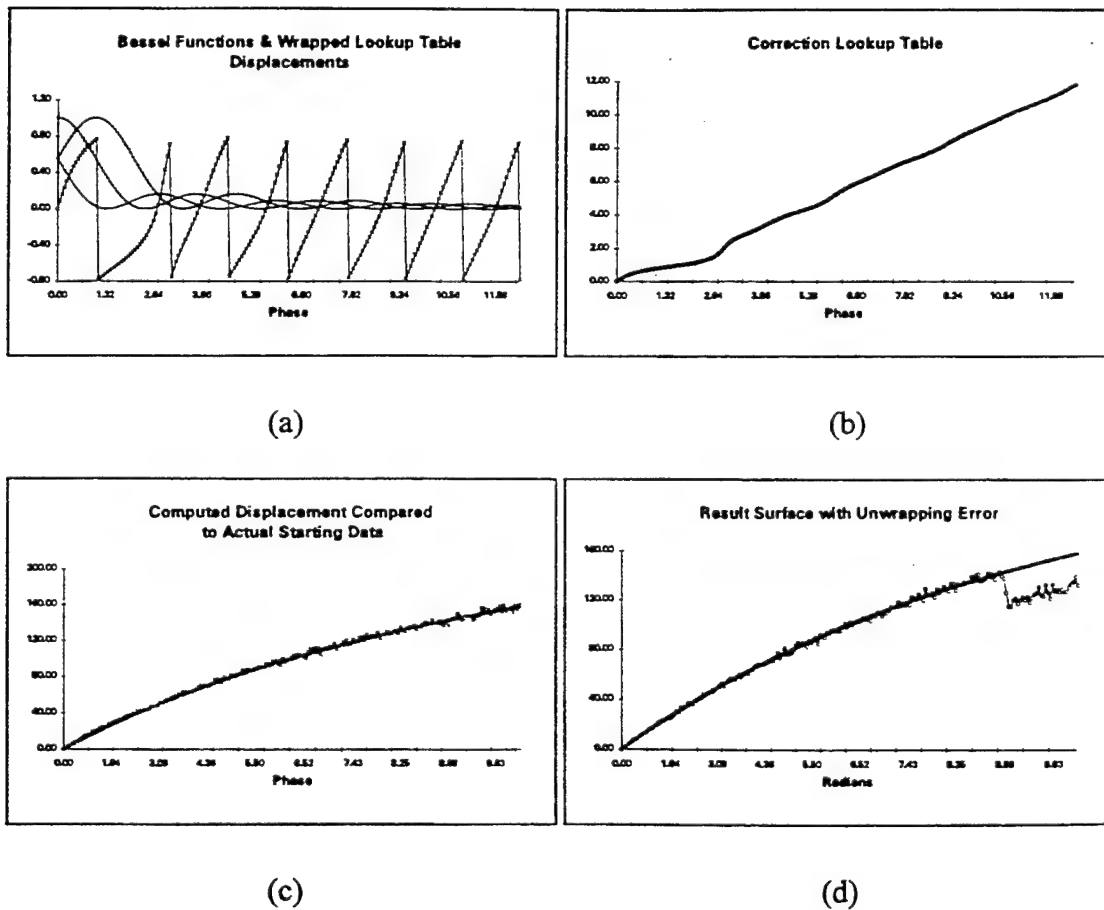


Fig. 2.7 (a) Model of the three biased Bessel function fringes with the wrapped phase overlaid. (b) Model of the correction LUT. (c) Model of the phase recovery process

where fringes were synthesized based on a model surface, noise was added, then the wrapped phase was computed and finally unwrapped to recover the original phase. (d) The same model in another run in which the random errors of 5% of the signal strength were sufficient to confuse a simple nearest-neighbor 1-D phase unwrapper.

2.9 Energy Minimization.

The next sections give a brief overview of energy minimization techniques as applied to image processing problems. Those aspects of energy minimization approaches which pertain to the phase unwrapping problem are emphasized.

2.9.1 Image model.

For the purpose of the phase unwrapper, the image is modeled as a Markov random field (MRF). An MRF model of the image implies that each pixel's probability distribution depends only on a finite set of discrete neighbors. Locations outside of the range of influence for a pixel may still have an effect on that pixel's probability distribution, though, by influencing the pixel's neighbor's values. However, by making the simplifying assumption that the sampled data can be modeled by an MRF, each pixel's value can be computed as a function of the nearby pixels within the pixel's neighborhood. This assumption implies that the values of pixels near each other are more likely to be related than the values of further separated pixels. An MRF corresponds directly to a Gibbs distribution - a description of the interaction potential energy among subsets taken from the set of a pixel's neighbors⁹.

2.9.2 Neighborhoods for processing image data.

Geman and Geman use the formalism of an MRF as the basis for the development of a simulated annealing algorithm for image labeling. To compute the new label for a given pixel, sets of the pixel's neighbors called "cliques" are built. The cliques which contribute to a pixel's new value are culled at the borders of the image so that undefined areas are ignored. For the purpose of image labeling, these cliques are each two or three pixels in extent and the interaction potential within each group provides the energy metric which the annealing process seeks to minimize.

For phase unwrapping, a related, but slightly different definition of a neighborhood is used. Each pixel's neighbors are considered to be those pixels which have previously been visited by the unwrapper so that they contain valid phase data. As the unwrapper serially visits new pixels, some subset of the pixels neighborhood will contain pixels which have previously been processed. This subset can be trimmed at the borders to avoid the inclusion of undefined points beyond the edge of the image. By assuming the image model to be an MRF, the neighborhood of pixels which can influence the current pixel's value is limited, so computationally tractable groups of pixels can be considered when each point is visited.

2.9.3 Edge labeling.

The Geman and Geman model for image labeling also incorporates edge segments which lie between pixels. Any pair of pixels may have an edge between them which cuts their connection. When a connection is cut, the potential of neighborhoods containing the pair

takes a new, lower energy value representative of the fact that the two points are now not associated. Edges are inserted or removed at each processing iteration depending on the energy of the neighborhood. If the introduction of an edge increases the probability of an arrangement, then the edge remains. In order to avoid the degenerate case where edges are introduced between every pair of pixels in the image, a cost is associated with each edge. As a result, edges persist only where very high potential differences are found in the image.

The current implementation of the phase unwrapper does rudimentary edge detection based on a pixel by pixel reliability metric. While this strategy is effective at defining gross borders, it does not take advantage of a priori assumptions of smoothness along borders. With the introduction of edge elements in the facet based strategy, lowest cost edges, that is, straight, smooth edges, could be found by extension of the facet model to minimize fitting error iteratively. Such an extension of the algorithm would also help to provide a mechanism for detection of internal edges within an object.

2.9.4 Energy definitions for labeling and phase unwrapping.

The energy minimization model introduced by Geman and Geman provides a framework for the definition of neighborhoods based on the radius of influence in an MRF. For the labeling problem, energy minimization implies the delineation of uniform regions in the presence of noise. Uniform regions are characterized by the lack of large gray level transitions, just as carefully annealed metal is characterized by the existence of uniformly high potentials in the bonds between particles in the material. To build uniform regions

in images, the annealing algorithm creates flat surface segments with very small gradients where the more uniform the gradient, the higher the potential. This is accomplished by maximizing the probability of the state described by the configuration of the MRF given the observed image. The probability function for any given configuration depends on the exponential of the negative of the energy, that is

$$P = \exp(-E/T)/Z, \quad 2.69)$$

where E is the potential energy, T is a parameter analogous with temperature which controls the annealing schedule and Z is a normalization term. The probability of a particular state of the MRF given the observed image then has a potential function which depends on the difference between the predicted MRF and the observed data as well as on the potential over the neighborhood.

For their labeling scheme, Geman and Geman define the potential of cliques by a few different methods. In each, the potential of pixel pairs with the same value is a constant, while various configurations of edges are assigned varying influences on the potential of the entire clique. As their system converges, areas which are not separated by an edge grow more uniform. The potential energy, E , is approximated by

$$E \approx \sum_{c \in C} K_i, \quad 2.70)$$

where C is the set of all cliques in the neighborhood which are not split by an edge, and K_i is one of a set possible values of the potential depending on the edge site configuration and the data values in the clique. The value of K_i is zero if the pixel values in the clique

are *not equal*. Using this processing model, as the potential of a particular neighborhood increases, the uniformity of the surface increases, so the probability of the given configuration also increases. This force toward uniformity is balanced by a second term in the probability expression which depends on the difference between the observed data and the predicted data contained in the MRF model. The greater the difference between the model and the observed data, the lower the probability for the proposed configuration of the MRF model. When the process converges, the two forces are balanced.

To recover the original displacement of a surface from the wrapped phase computed from a set of holograms, a different set of suppositions hold. While the surface can be assumed to be smooth and planar over local neighborhoods, it cannot be assumed to have zero gradient as is implied by the conditions imposed on Eq. 2.70. Instead, the surface may be tilted, with a maximum gradient, $I_{MaxGrad}$, defined by the minimum fringe spacing which can be resolved in the presence of laser speckle. In this case, the definition of potential energy must be altered so that the potential is maximized when the surface to recover diverges least from the best fit plane determined by the surface. That best fit plane is allowed to have a gradient value bounded by $\pm I_{MaxGrad}$ along both the x and y axes. To define such a potential function, Eq. 2.70 still holds, but a different set of conditions are applied. This time, C is the set of all cliques in the neighborhood and edges are not taken into consideration, only the neighborhood configuration. The value of K_i is then determined solely as a function of the sums of the data values with their corresponding fringe numbers in the neighborhood, such that K_i has a constant positive value for

configurations of cliques which are coplanar. The value of K_i is zero if the pixel values in the clique are *not coplanar*. Clearly, two and three element cliques always pass this test, so cliques of four or more would have to be considered when applying this test for evaluation of the potential.

2.10 Facet based estimation.

Haralick uses a least squares error minimization procedure for fitting parameterized surfaces to noisy data¹⁰. Once a surface has been parameterized, interesting characteristics of the surface can be extracted based on the computed parameter values. The fitting model uses a set of orthogonal polynomials as a basis set for the fit. The minimization procedure finds values for the coefficients of the polynomials.

Haralick uses his facet model fitting procedure for finding the best edges in an image. For this purpose, the polynomial set contains elements up to third order. Thus, his fitted surface is always a third order function and the best edge is then found at the point of inflection on the steepest slope. Furthermore, his neighborhood is defined to be symmetrical about a central point, so an orthogonal polynomial basis set can be found. The use of an orthogonal basis set allows many computational simplifications in the least squares error minimization procedure.

For the purpose of phase unwrapping, the facet model provides a framework for computing an estimate of the phase value of the central pixel in a neighborhood. Complications arise from the lack of complete data within each neighborhood as

processing progresses. The process moves serially through the data tracing out a spiral moving outward from the point chosen to be the starting point or "seed" of the operation. As a result, at each new point, only those points within the neighborhood which have been previously visited by the spiral can contribute to the facet's parameter estimation. Therefore, the estimate must be applied to an arbitrarily populated neighborhood. Under such conditions, no general orthogonal basis set exists to address every possible configuration of weights. This introduces greater computational complexity in the least squares fitting procedure since a square matrix of dimension equal to the number of polynomial coefficients must be inverted to solve for the coefficient values.

Wrapped phase EOH images contain certain characteristics which can be used to simplify the problem. The phase can be assumed to change smoothly over the surface of the object as long as the object does not contain surface discontinuities. Such smoothness implies that the surface deformation due to stress will be continuous. Furthermore, in a local neighborhood in the image, the influence of the stress only changes slowly. Again, this follows from the nature of the mechanical system under observation. That is, the object reacts to stress in such a way that the interaction potential of the bonds from particle to particle in the material remains minimized, which implies that the surface deformation will be smooth and continuous, as long as fractures do not appear. Given this assumption, the facet estimator within a local neighborhood can generate a valid estimate by fitting a planar surface patch to the neighborhood data. A planar surface can be parameterized with three coefficients of a first degree polynomial. The solution for the

coefficient values then requires the inversion of a three by three matrix. Such a matrix can be inverted directly without incurring undue computational complexity.

Haralick's facet model provides the framework used in the estimation procedure for finding discontinuities in phase data within local neighborhoods. The definition of neighborhoods follows from the framework established by Geman and Geman for applying the concept of an MRF to the image labeling problem. These two ideas prove to be central in the development of the phase unwrapping algorithm described in *Chapter 4*.

Chapter 3. Previous approaches to phase unwrapping.

Numerous previous approaches have been applied to the phase unwrapping problem.

Most have been variants of the simple row-wise or column-wise sequential unwrapping approach. The following sections briefly describe notable work from the existing literature.

3.1 Basis for two dimensional unwrapping.

An analysis of both one dimensional and two dimensional unwrapping is provided by Itoh¹¹. The premise of the two dimensional approach is to unwrap along one row and then along all the columns, or along one column and then along all the rows. Itoh proves that 1-D wrapped phase can be unwrapped by integrating wrapped discontinuities in a sweep through the data. The extension to 2-D shows that unwrapping can proceed either in row / column or column / row order.

While Itoh's approach is theoretically valid, it makes no allowance for the noise inherent in any imaging system. With the scan line approach, any mis-assignment propagates to all dependent locations. This results in streaks or discontinuities in the unwrapped phase. This approach also fails for arbitrary shapes, since it relies on the existence of at least one row or column which covers the full width or height of the bounding rectangle of the

object. Furthermore, any discontinuities in the phase will not be recognized, so edges or boundaries within an object will be glossed over with unpredictable results.

Numerous phase unwrappers have been based on the sequential scan method explored by Itoh ^{12, 13}. Each of these approaches exhibits the same weakness of having high sensitivity to noise. Since EOH generated images tend to be highly influenced by systematic noise, a more robust method of phase unwrapping is required for this project.

3.2 Irregular shapes.

Stetson proposed an approach to the phase unwrapping problem which works for arbitrary shaped objects, provided a "mask" can be generated which segments the object of interest from the background ¹². By this approach, the unwrapping progresses along a path around the interior of the border of the object. Unwrapping proceeds sequentially around this path until a dead end is encountered, or the object is filled completely. If an impasse is reached, the routine searches for the upper left-most pixel which has not yet been unwrapped, and restarts the scan around the interior border of unprocessed pixels.

While Stetson's approach solves the problem of processing arbitrary shapes (assuming the shape is known), it still suffers from susceptibility to noise since only two pixels are considered in each decision about whether to introduce a discontinuity at a given point. Also, the spiral processing path works inward from the perimeter where data are most likely to be ambiguous in time average holograms since higher order fringes of the squared Bessel function fringe distribution will be found at the free boundaries of the part

under observation. As a result, the likelihood of creating inappropriate discontinuities increases. Once an erroneous discontinuity is introduced, it propagates through many of the remaining interior points.

3.3 Cellular automata.

Ghiglia, Mastin and Romero implemented a system based on cellular automata¹⁵. By their approach, each pixel location is updated according to its neighborhood's accumulated strength-of-vote. The strength-of-vote for each neighbor is computed from the phase difference of the center pixel versus the neighbor. If the absolute value of the accumulated strength-of-vote is $> \pi$, then add or subtract 2π in the direction of greater strength. The system will converge either to a single, lowest energy configuration, or a pair of states between which it oscillates. When the system reaches a 2-state oscillatory configuration, the two states are averaged pixel by pixel, then the process is restarted. This loop continues until the system converges. For this approach to succeed, inconsistencies in the data due either to excessive noise or edges must be flagged and subsequently ignored in the processing. A preprocessing stage locates noise induced inconsistencies by traversing loops around the neighborhood of each pixel. If the accumulated phase steps encountered while traversing the loop do not equal zero, then an inconsistency exists and is flagged. Edges must be flagged manually.

Since this approach employs an iterative process, it allows elements beyond a given pixel's immediate neighborhood to influence the pixel's fringe number assignment. However, the approach requires many iterations to converge - over 3000 on a relatively

noiseless 512 x 512 image. The algorithm performs its calculations on every pixel in the image for each iteration. Since it is an iterative, full field process, its computational cost is very high. Therefore, the finite automata approach is not a viable alternative for this project. Also, since the algorithm fails to take full advantage of the surface smoothness constraint, it cannot detect edge discontinuities and its reliability is decreased.

3.4 An image processing techniques based approach.

Vrooman and Maas developed a phase unwrapping technique quite similar to the technique described here¹⁴. They use a threshold applied to a measure of the modulation strength of each pixel to eliminate pixels likely to be dominated by noise. To find locations where phase discontinuities need to be unwrapped in the data, they either look for places where the difference between the pixel at the current location and a previously unwrapped neighbor is greater than π or, for noisier images, instead of comparing the current pixel to only one location, they use the average value from a 3 x 3 neighborhood around the pixel. Similarly to the strategy employed in this project, pixels are processed in an expanding four-connected wavefront moving outward from a starting location. Once the phase has been unwrapped using this approach, a subsequent operation is applied which smoothes the data by fitting planar patches to the phase surface. The smoothed results are used in making strain calculations. While the phase assignment procedure used in the Vrooman and Maas approach is more robust than the simple scan line based techniques, their assumption that a 3 x 3 neighborhood is both sufficiently populated and sufficiently representative of the phase in the area of a pixel to fully

determine the value of the phase at the pixel of interest does not hold for the noisy images obtained with the EOH system.

3.5 Other techniques.

Towers unwraps the image in individual sub-blocks, then joins the blocks together by matching the boundaries¹³. He uses this technique to avoid contaminating good data with inconsistencies induced by bad data. The image is divided into a number of small blocks, then each block is unwrapped individually. Subsequently, the borders of each block are joined with their neighbors. Where fringe discontinuities along abutting block borders do not match, the less trustworthy block is marked as containing bad data and discarded. Trustworthiness is proportional to the inverse of the number of phase transitions found in the block. That is, higher fringe densities are assumed to imply lower trustworthiness. This approach relies on the row / column scan technique to unwrap each of the blocks, so it is highly susceptible to noise induced failures. Also, when a block is discarded due to inconsistency, good data are lost with the bad data. For this project, a more robust approach is desired.

Owner-Petersen uses the smoothness constraint to smooth the phase conditionally prior to unwrapping¹⁶. He assumes large noise, and to minimize its effect, he quantizes the phase into four equal sized intervals. Histograms of each pixel's neighborhood are computed to get the number of neighbors of each category. A decision criteria is applied to the results to determine a new smoothed phase value. A phase number is assigned based on this smoothed result. This approach uses the smoothness constraint to good advantage.

However, by discarding the six least significant bits of the measured phase, much information is lost. Furthermore, the use of neighborhood histograms rather than a more robust surface fit compromises the algorithm's robustness in the presence of discontinuous data.

3.6 Conclusions derived from past implementations of phase unwrappers.

Numerous approaches have applied smoothing filters to the original holograms prior to the arctan computation^{12, 17, 18}. While smoothing the original fringe data eliminates some noise, it also averages speckles together which may have markedly different modulation. By spatially averaging, a pixel with a high modulation magnitude may be averaged with a number of pixels with lower modulation magnitudes and, therefore, lower signal to noise ratios. As a result, the best data in the image will invariably be diluted by poorer data values around it. Furthermore, the spatial accuracy of the data will be compromised by averaging so that sharp borders will blend into the background and discontinuities will be smoothed over. To avoid these effects, the approach used here avoids pre-smoothing the data in favor of a system that applies the smoothness constraint to the data by fitting an individual surface patch to the measured data values at each point in order to locate the phase related discontinuities.

Some unwrappers have used row / column based unwrapping or inward spiral scans in processing the hologram data. Both these approaches will unwrap data at the outermost boundary of the object first. By visiting the boundaries first, the unwrapper is susceptible to introducing edge related errors early in the unwrapping process. These errors will

propagate through the remainder of the surface as the unwrapper continues. Furthermore, time average holograms tend to have low amplitude, higher order fringes near the boundaries of the object since the boundaries are most likely to be unconstrained. Low amplitude fringe data has a lower signal to noise ratio, so the unwrapper is more likely to introduce errors when processing these areas. The most reasonable solution to these problems is to start the process from a safe, well defined, interior location and progress outwards.

These ideas are employed in the development of the phase unwrapper presented in *Chapter 4*.

Chapter 4. Phase unwrapping by planar facet fitting.

The phase unwrapping technique introduced in earlier chapters is fully developed here. To accomplish the goal of unwrapping the phase, the energy of the difference of the measured surface from an ideal model of that surface represented by the unwrapped phase must be minimized by adding appropriate multiples of π to each point's phase value. As discussed in *Chapter 2*, the energy can best be minimized when changes in the slope of the surface are minimized, that is, when the difference between the highest potential arrangement of the surface defined by the data values is least different from the model. The potential is highest when the data values are coplanar, where the gradient of the plane is always less than some maximum value. The minimum allowed fringe spacing defines the maximum value that the gradient can take. Fringes containing fewer than three pixels are ambiguous, so the maximum magnitude allowed for the gradient is $2\pi/3$ radians per pixel. The model used to describe the system is a parameterized version of a plane with a limit on the allowable size of the gradient. Thus, the presence of an abrupt transition caused by a phase discontinuity represents a higher energy state than if the transition were removed by the addition of appropriate π multiples. These high energy discontinuities are detected and removed by a planar facet estimator as detailed below.

4.1 Overview of the technique.

Experience indicates that simple scan-line techniques are insufficient for solving the phase unwrapping problem. The large amounts of noise in the images combined with the variable reliability of the data induced by the speckling of the reflected laser light combine to make sequential scan techniques inappropriate. Any effective technique must use data from a neighborhood larger than a point's 4 or 8-connected neighbors to be able to accurately predict the trends in the data which will correctly locate phase transitions.

The technique developed here begins processing from a user selected origin or "seed point." As processing progresses, the pixels along a wavefront growing outward from the seed are considered. As each new pixel is visited, a planar facet is fit to the neighboring phase values which have already been processed. The facet parameters are then used to estimate the correct value for the new pixel based on the trend dictated by the prior pixels. The estimate is then compared to the measured, wrapped phase value at the new pixel and a fringe number is assigned to minimize the difference between the estimate and the measured phase summed with a multiple of π . The data used in each of the facet fits is weighted according to the reliability of the data at each point in the neighborhood. Those pixels whose speckles are bright indicating a large modulation magnitude are given greater influence than darker pixels since the brighter pixels are less affected by the noise in the system.

Once the wavefront has swept over all the data in the area of interest chosen by the user, subsequent iterations can be performed to further minimize the energy of the surface fit.

The extra iteration(s) have larger regions of support on which to fit the planar facets, so, as a result, bring the fringe numbers into the highest potential configuration possible for the given neighborhood size. As a post processing step, the resulting unwrapped phase can be smoothed by another raster scanned application of the facet fits. The facet estimate values are stored in another image to provide as smoothed output. This smoothing constitutes a piece-wise least squares smoothing algorithm. *Appendix A* contains a set of block diagrams showing the software implementation of this algorithm.

4.2 Noise, modulation magnitude and the weighting function.

The phase data to be unwrapped are derived from a set of either 2 or 3 images depending on whether static or time average holograms have been generated, respectively. In either case, an extra image which consists of a hologram of the object without any excitation can provide information about the reliability of the data at each pixel. The bright areas in the image correspond to where the speckle pattern is brightest and so the magnitude of the modulation of the speckles is greatest. That is, as the light from the speckle interferes with the reference beam and the phase of the reference beam is stepped, those speckles with the highest intensity will give the largest change in intensity due to processing, and thus appear to be the brightest pixels in the image. This "modulation map" can be used to eliminate noise dominated speckles in the unwrapping and to give brighter speckles greater influence.

In an ideal system, the magnitude of the modulation would not matter since, if any light were reflected from the object, a valid measurement would result. However, the camera

and image processing system both have limited dynamic range and both introduce noise into the signal. Any CCD camera will introduce increasing "shot noise" as the CCD array heats up. Besides the shot noise, the camera electronics and image processor front end introduce noise to the signal as well. Other sources contribute to the overall noise of the system besides the electronics. Small fluctuations in the intensity of the output of the laser cause large drops in the dynamic range of the measured phase. Air turbulence induced by mixing warm and cold air masses, causes changes of apparent path length in the beams and thereby changes the phase of the beams. Such phase changes can easily cause image degradation. These moving air masses can also act like very weak lenses and change the direction of the beams slightly. Directional changes in the beams, especially in the reference beam, can move the beam's focus as it exits the diverging objective. If the focus point moves, it will no longer pass through the pin-hole filter by the same path. As the pin-hole filter blocks different portions of the beam, the pattern and intensity of the reference light field changes and the differences between frames will include the differences induced in the reference beam as well as the speckle modulation. As a result, still more noise is added to the image.

While many factors contribute to the system noise, it is possible to empirically quantify the noise through a calibration procedure. The procedure consists of the following steps:

1. Capture an image with a 0 degree phase offset in the reference beam.
2. Capture a second image with a 360 degree phase offset in the reference beam.
3. Subtract the second image from the first.

4. Repeat the process and sum the results over a number of frames equal to the number of frames averaged in the hologram acquisition process.
5. Generate a histogram of the resulting difference image.
6. Set the maximum noise level to be the maximum value in the histogram.

The 360 degree phase shift between the pairs of images should not induce any modulation in the speckles. The step is included to account for any inconsistencies in the phase shifter's behavior and to recognize miscalibration of the phase step size. An image generated by this method appears mostly black with Gaussian noise distributed about a small positive mean value.

Once the noise level has been empirically determined, its value is used to convert the modulation magnitude map into a weighting function for the facet fitting. All values in the modulation magnitude map are divided by the noise level and truncated to integer values. Thus, any pixel whose value is less than the noise level is assigned a value of 0 and ignored. All other pixels are assigned a positive integer weight value which is directly related to the brightness of the speckle. Bright speckles get higher weights and influence the facet fit more than dimmer ones. Once computed, this weighting function is stored in an array for use during the remainder of the procedure.

4.3 Seed point selection and initial growth.

The seed point is the starting point from which the unwrapping progresses. A user selects the seed point at a location on a nodal line in a time average hologram or where an object

is known to be fixed in a static hologram. Since the user could accidentally choose a point for which the weight function is zero, a routine must be included to find a valid seed point "near" the chosen point. This routine first tests the chosen location, and, if the chosen pixel has zero weight, spirals outward from this location until a valid pixel is found.

After a valid seed is located, the phase must be unwrapped along an expanding wave-front. However, there is only one pixel of prior data to use to determine the fringe number of the next pixel visited. Unfortunately, the facet fitting routine requires at least 3 non-colinear points to determine a plane, otherwise the matrix employed in estimating the phase value will be singular and not invertable. Therefore, an interim approach is used to get the unwrapping started. In order to build a set of prior data large enough to support facet fits, a traditional difference based technique is employed along the newly established wave front. By this technique, a new pixel's phase value is subtracted from its previously processed neighbor's phase. If the difference between the phases is greater than π , then an appropriate number of π multiples are added to bring the two points within π radians of each other's value. This technique is included in the phase unwrapper as a fallback method to employ whenever there is insufficient support for a planar facet fit.

4.4 Expanding wavefront processing order.

A first-in-first-out (FIFO) circular list structure maintains the addresses of the pixels which lie along the leading edge of the expanding wavefront of processed data. After a pixel is processed, its 8-connected neighbors are each tested as candidates to go into the list. A flag bit in the mask array indicates that the corresponding pixel has already been processed. Another bit indicates that the pixel is currently in the list. All of the current pixels 8-connected neighbors which have neither been processed nor are currently in the list are added at the tail of the list. The flag indicating the pixel has been added to the list is set for each of the new pixels in the list and cleared for the pixel which has just been processed. Finally, the newly processed pixel's processed flag is set. The next pixel to process is removed from the front of the list, its fringe number is assigned based on the fitted facet, and the process repeats.

Processing proceeds along an expanding wavefront emanating from the seed point. The expanding front results directly from the use of the FIFO list. Any new pixel added to the list is an external neighbor of a pixel already on the list. But all the pixels currently in the list must be processed before the new pixel will be serviced. Therefore, a complete circuit around the wavefront is completed before this new addition to the FIFO gets its turn. This visiting order provides nearly the optimal possible region of support, on average, for fitting each new pixel's facet. Figure 4.1 shows the processing of a relatively simple neighborhood. Processing begins at the seed point, then the seed group is formed by comparing the value of each member of the group to the seed's value. If the value

differs by more than π radians, then a phase discontinuity is introduced between the pixels and the proper π multiple is added to the member's phase value. Once a sufficient region of support has been built for the determination of a plane, the planar fitter is used to estimate phase values for subsequent pixels drawn from the head of the FIFO list.

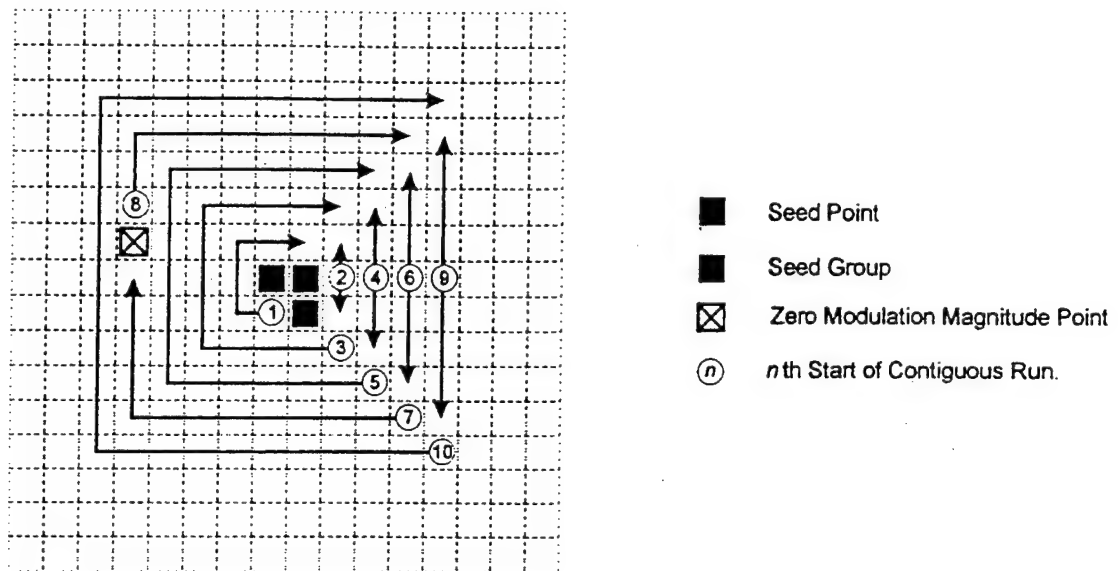


Fig. 4.1 Processing order for 8-connected FIFO based sequential scan.

Expansion of the wavefront will stop for either of two reasons: 1) The expansion stops when the wave reaches the outer boundary for processing defined by a rectangular area of interest (AOI). 2) Expansion stops beyond any given pixel if no further non-zero weighted, unprocessed data points can be found among the 8-connected neighbors of that pixel. So, if the speckle modulation outside the boundary of the part lies beneath the noise threshold, processing stops along the part's edge. Since speckles are generated by laser light reflecting from the object's surface, beyond the edge of the object there will be no speckles. Where there are no speckles, the speckle modulation is near zero and the

weight function automatically clips the facet's region of support, so the wave's expansion stops.

4.5 Planar facet fitting to an incomplete, weighted array of data points.

As the wavefront propagates outward, pixels are visited in a sequential path along the expanding perimeter. Since pixels are put in the wavefront list only when one of their neighbors has been processed, any pixel on the list is guaranteed to have at least one 8-connected neighbor which has already been processed. Because the wavefront can grow around holes in the data or even around interior edges of the object, a given pixel can have anywhere from one to eight 8-connected neighbors which have already been processed. As the region of support for a given pixel is expanded to a larger neighborhood, nearly any arrangement of previously processed pixels is possible. This variability in the population of the region of support at a pixel leads to the requirement for a generalized solution to the fitting problem.

For simplicity, a rectangular region centered on the pixel of interest is used to estimate the value that the pixel should have. The width and height of this region are adjustable parameters. As the neighborhood size grows, processing time increases, but accuracy increases, as well. However, if the neighborhood "radius" gets larger than the smallest surface feature size to be resolved, then larger neighborhoods will result in a worse fit leading to errors. Since the surfaces under investigation are predominantly smooth and slowly changing, errors due to oversize neighborhoods are not a common problem.

Any neighbors of the pixel of interest within the extent of the neighborhood which have already been processed are marked by a flag bit in a "mask" array. Only those neighbors so marked should be considered when fitting the facet. Further, as described previously, a weighting function based on the intensity of the speckle and, thereby, its immunity to noise, is used to give greater credence to the more reliable pixels in the neighborhood. Taking the above factors into consideration, a generalized weighted least squares fit of a planar model to the data values is used to estimate parameters of a surface to describe the data, from which an estimate of the pixels phase can be made.

The planar model used can be expressed as the linear combination of a set of the three polynomials

$$p_0 = 1, \quad p_1 = x, \quad \text{and} \quad p_2 = y. \quad 4.1)$$

Three parameters, A , B , and C , scale the influence of each of the polynomials in the model to give

$$P(x, y) = Ax + By + C, \quad 4.2)$$

where $P(x, y)$ is the value at the point with coordinates (x, y) .

This very simple polynomial is orthogonal over any symmetrical area centered about the origin. An orthogonal set of polynomials is defined as a set for which the inner product of every distinct pair of polynomial terms is zero 19. The inner product for discrete problems can be expressed as

$$\langle p_i, p_j \rangle = \sum_{m=M_l}^{M_h} \sum_{n=N_l}^{N_h} p_i(m) p_j(n), \quad i \neq j, \quad 4.3)$$

where p_i and p_j are the i th and j th polynomials in a polynomial set, and the 2-D region over which the polynomial set is orthogonal is bounded below by (M_l, N_l) and above by (M_h, N_h) . Clearly, for the polynomial set in Eq. 4.1 the requirement for orthogonality is met over any region which is symmetric about the origin since the pairs of scalar products are all zero. Orthogonal systems are characterized by a high degree of numerical stability. This follows because, for problems expressed as matrix equations, the solution depends on inverting a large matrix. With orthogonal systems, this matrix is diagonal, and the inverse of a diagonal matrix is a trivial computation, especially if all the diagonal elements of the array are guaranteed to be non-zero. An orthogonal set has been chosen specifically to reduce the numerical instability of the problem. Unfortunately, the polynomials will no longer display orthogonality when applied to incomplete, weighted matrices, since the weights are not guaranteed to be symmetric about the origin. However, the numerical stability of the system will still be improved by the initial selection of an orthogonal polynomial set since, in general, as the system gets closer to orthogonality, its numerical stability improves. Careful inspection of the matrix inversion required to solve the problem shows the benefits of the use of a nearly orthogonal system, and will be discussed further immediately after the solution is presented.

To find the best fit of the polynomial with the data set, the square of the error of the model data, $P(x, y)$, relative to the actual data, $z(x, y)$, must be minimized. The squared

error, ϵ^2 , is computed from the sum of the squares of the fitting errors at each point, scaled by the weight function, represented by $w(x, y)$, over a neighborhood of horizontal extent $2N+1$ and vertical extent $2M+1$, centered at the point (x, y) , so ¹⁹

$$\begin{aligned}\epsilon^2(x, y) &= \sum_{j=-M}^M \sum_{i=-N}^N \{ [P(i, j) - z(x+i, y+j)] w(x+i, y+j) \}^2 = \\ &= \sum_{j=-M}^M \sum_{i=-N}^N \{ [Ai + Bj + C - z(x+i, y+j)] w(x+i, y+j) \}^2 .\end{aligned}\quad 4.4)$$

Note that $w(x, y)$ will be zero for pixels that have not yet been processed. Also, the model's origin is at the pixel of interest, so the estimated value at that pixel is just C since both x and y equal zero at the origin.

Now the error must be minimized with respect to each of the three variables, so find

$$\min_{A, B, C} \epsilon^2 = \min_{A, B, C} \sum_{j=-M}^M \sum_{i=-N}^N \{ [Ai + Bj + C - z(x+i, y+j)] w(x+i, y+j) \}^2 .\quad 4.5)$$

To minimize Eq. 4.5, create three new equations. In each, set the derivative of the right hand side of Eq. 4.5 with respect to one of the three variables equal to zero to get

$$0 = \frac{\partial \epsilon^2(x, y)}{\partial A} = \sum_j \sum_i 2i w^2(x+i, y+j) [Ai + Bj + C - z(x+i, y+j)], \quad 4.6)$$

$$0 = \frac{\partial \epsilon^2(x, y)}{\partial B} = \sum_j \sum_i 2j w^2(x+i, y+j) [Ai + Bj + C - z(x+i, y+j)], \quad 4.7)$$

$$0 = \frac{\partial \epsilon^2(x, y)}{\partial C} = \sum_j \sum_i 2 w^2(x+i, y+j) [Ai + Bj + C - z(x+i, y+j)]. \quad 4.8)$$

In matrix form, Eqs 4.6 to 4.8 can be expressed in the form $\mathbf{0} = \mathbf{Ax} - \mathbf{b}$ as

$$\begin{bmatrix} 0 \\ 0 \\ 0 \end{bmatrix} = \begin{bmatrix} \sum_j \sum_i i^2 w^2(x+i, y+j) & \sum_j \sum_i ijw^2(x+i, y+j) & \sum_j \sum_i iw^2(x+i, y+j) \\ \sum_j \sum_i ijw^2(x+i, y+j) & \sum_j \sum_i j^2 w^2(x+i, y+j) & \sum_j \sum_i jw^2(x+i, y+j) \\ \sum_j \sum_i iw^2(x+i, y+j) & \sum_j \sum_i jw^2(x+i, y+j) & \sum_j \sum_i 1w^2(x+i, y+j) \end{bmatrix} \begin{bmatrix} A \\ B \\ C \end{bmatrix} - \begin{bmatrix} \sum_j \sum_i iz(x+i, y+j)w^2(x+i, y+j) \\ \sum_j \sum_i jz(x+i, y+j)w^2(x+i, y+j) \\ \sum_j \sum_i z(x+i, y+j)w^2(x+i, y+j) \end{bmatrix} \quad (4.9)$$

Redistributing terms in Eq. 4.9 and multiplying both sides by the inverse of \mathbf{A} gives

$$\begin{bmatrix} A \\ B \\ C \end{bmatrix} = \mathbf{A}^{-1} \begin{bmatrix} \sum_j \sum_i iz(x+i, y+j)w^2(x+i, y+j) \\ \sum_j \sum_i jz(x+i, y+j)w^2(x+i, y+j) \\ \sum_j \sum_i z(x+i, y+j)w^2(x+i, y+j) \end{bmatrix},$$

where

$$\mathbf{A}^{-1} = \begin{bmatrix} \sum_j \sum_i i^2 w^2(x+i, y+j) & \sum_j \sum_i ijw^2(x+i, y+j) & \sum_j \sum_i iw^2(x+i, y+j) \\ \sum_j \sum_i ijw^2(x+i, y+j) & \sum_j \sum_i j^2 w^2(x+i, y+j) & \sum_j \sum_i jw^2(x+i, y+j) \\ \sum_j \sum_i iw^2(x+i, y+j) & \sum_j \sum_i jw^2(x+i, y+j) & \sum_j \sum_i 1w^2(x+i, y+j) \end{bmatrix}^{-1}.$$

The matrix to invert is symmetric about its diagonal, so the its inverse is also symmetric.

Given the assignments

$$\begin{aligned} a(x, y) &= \sum_j \sum_i i^2 w^2(x+i, y+j), & b(x, y) &= \sum_j \sum_i ijw^2(x+i, y+j), \\ c(x, y) &= \sum_j \sum_i iw^2(x+i, y+j), & d(x, y) &= \sum_j \sum_i j^2 w^2(x+i, y+j), \\ e(x, y) &= \sum_j \sum_i jw^2(x+i, y+j) \quad \text{and} & f(x, y) &= \sum_j \sum_i w^2(x+i, y+j), \end{aligned}$$

for the elements of **A**, and

$$g(x,y) = \sum_j \sum_i i z(x+i, y+j) w^2(x+i, y+j) , \quad h(x,y) = \sum_j \sum_i j z(x+i, y+j) w^2(x+i, y+j) \text{ and}$$

$$i(x,y) = \sum_j \sum_i z(x+i, y+j) w^2(x+i, y+j) , \quad 4.10)$$

for the elements of **b**, then the matrix inversion can be written as

$$\begin{bmatrix} a & b & c \\ b & d & e \\ c & e & f \end{bmatrix}^{-1} = \frac{1}{adf - ae^2 - b^2f + 2bce - c^2d} \begin{bmatrix} I_a & I_b & I_c \\ I_b & I_d & I_e \\ I_c & I_e & I_f \end{bmatrix} , \quad 4.11)$$

where

$$\begin{aligned} I_a(x,y) &= d(x,y)f(x,y) - e^2(x,y) , & I_b(x,y) &= c(x,y)e(x,y) - b(x,y)f(x,y) , \\ I_c(x,y) &= b(x,y)e(x,y) - c(x,y)d(x,y) , & I_d(x,y) &= a(x,y)f(x,y) - c^2(x,y) , \\ I_e(x,y) &= b(x,y)c(x,y) - a(x,y)e(x,y) \text{ and } I_f(x,y) = a(x,y)d(x,y) - b^2(x,y) . \end{aligned} \quad 4.12)$$

Solving for the values of the coefficients of the polynomials at each point (x, y) gives

$$A = \frac{I_a g + I_b h + I_c i}{adf - ae^2 - b^2f + 2bce - c^2d} , \quad 4.13)$$

$$B = \frac{I_b g + I_d h + I_e i}{adf - ae^2 - b^2f + 2bce - c^2d} \text{ and} \quad 4.14)$$

$$C = \frac{I_c g + I_e h + I_f i}{adf - ae^2 - b^2f + 2bce - c^2d} . \quad 4.15)$$

An earlier statement suggested that the use of a "nearly" orthogonal polynomial basis set would help improve the numerical stability of the solution in the presence of a non-symmetrical weighting function. The following argument based on inspection of the

solution derived above justifies such a statement. First, notice that the denominator for each of the three coefficients is identical. A solution for the coefficient values will be numerically stable as long as the denominator does not get so small that the error introduced by truncation effects in the computer's internal representation of the numerical value of the denominator causes significant error in the computed results, and, of course, as long as the denominator is not equal to zero. Each term in the denominator is composed of the product of three double summations. Each summation, in turn, is composed of products of neighborhood indices and weighting function values. The neighborhood indices are small integer values, symmetrically distributed about the origin and typically no larger than 32. The weighting function values are also small integers, typically no larger than 100. Since all these terms are integer values, the denominator will also be an integer value. While the degenerate case where the denominator equals zero is possible, it can be caught in the code and handled by using an alternate means to estimate the phase at the poorly behaved point.

For a truly orthogonal basis set, all the off-diagonal elements of the 3×3 matrix become zero. This useful result follows from the fact that each of the off-diagonal elements includes neighborhood indices i and j to the first power. Furthermore, the weighting function becomes a constant. Since the neighborhood is defined to be symmetrical about the origin, and each off-diagonal element is simply the product of the neighborhood indices and a constant, the sum of each positive and corresponding negative pair of indices cancel. When all the off-diagonal elements of a matrix are zero, the matrix is said

to be diagonal. A diagonal matrix is trivial to invert - simply replace each element on the diagonal with its inverse. Now, assuming the neighborhood is defined over a non-zero area, the diagonal elements are guaranteed to be non-zero since they are composed of double sums of the squares of the neighborhood indices, or of a constant. Therefore, the matrix inversion must be numerically stable because the values to invert are never zero.

The question still remains - why does this help in the "nearly" orthogonal case? The answer is that, in general, for a "nearly" orthogonal system, the value of each term of the denominator which depends on the off-diagonal elements of the matrix will be minimized. Then, the term of the denominator in Eqs 4.13 to 4.15 which depends only on the diagonal terms of the matrix is dominant. As a result, the likelihood of finding a neighborhood configuration which leads to a zero valued denominator is minimized.

Also, since only first order polynomials are used in the fit, multiple conflicting solutions cannot exist, as can happen, for example, when fitting sinusoids to data where many very high frequencies could all fit the data under various conditions.

Finally, in order for the fitted coefficients to provide a valid estimator for the new pixel, the fit routine requires sufficient support to fully define a plane. Three non-colinear points are necessary and sufficient to define any plane. To try to insure stability, the fitting procedure for the unwrapper checks that the facet's region of support includes at least four non-colinear points with non-zero weights. The extra point provides some redundancy to limit the influence of any noisy points which might otherwise skew a facet

with little support. Of course, when more data points are available within the facet's extent, they will all be used to improve the facet's fit.

4.6 Fringe number assignment.

The fitting routine transforms the coordinates of the region covered by the facet to a facet based coordinate system where the pixel of interest lies at the origin. Therefore, the facet based estimate for the value of the data at the pixel of interest is simply given by the coefficient of the zero order polynomial. That is, the estimate's value e is given by

$$e = Ax + By + C = C, \quad 4.16)$$

since x and y are both equal to zero.

Given the phase estimate, e , and the measured phase value, $z(x, y)$, a fringe number, n , must be chosen to minimize the difference between e and z , so

$$\min_n \{ |e - [z(x, y) + n\pi]| \} \quad 4.17)$$

must be found, in the case of time average holography or

$$\min_n \{ |e - [z(x, y) + 2n\pi]| \} \quad 4.18)$$

for the case of static holography.

The easiest solution to this problem is

$$n = \text{round}\left(\frac{e - z(x, y)}{\pi}\right), \quad \text{or} \quad n = \text{round}\left(\frac{e - z(x, y)}{2\pi}\right) \quad 4.19)$$

respectively.

Values for n are computed at each point as it is visited to build up a fringe number map. The fringe numbers are stored separately from the phase data to avoid corrupting the original data.

4.7 Fitting iterations for energy minimization.

While the unwrapping outlined above performs quite well, investigation has shown that, based on all the neighbors available after unwrapping is complete, pixel fringe numbers appear to have been occasionally mis-assigned. That is, fringe number assignments based on the partial region of support available at each pixel during the unwrapping are not the lowest energy fringe numbers based on the more completely populated region of support available when the unwrapping is complete. To correct the occasional stray mis-assignments, subsequent iterations of the fitting procedure are applied to the data. Now, since the facets will be fit to each entire neighborhood (except for locations where the weighting function is zero) processing order is irrelevant. Therefore, the minimization fittings are applied in a raster scanned order.

Since the minimization iterations have larger regions of support, more accurate estimates of the phase at each point are made. When a new estimate for the fringe number disagrees with the previous assignment, the new fringe number value is used, instead. Any changes made to one pixel could affect its neighbor's fits. Therefore, the process repeats until no more changes occur. It is conceivable that a pair or group of pixels could

oscillate and never reach a minimum energy configuration. To avoid infinite oscillation, a limit is set on the number of energy minimization iterations to run. In practice, two iterations are usually sufficient to achieve convergence, and the system has never required more than four iterations.

4.8 LUT correction for time average holograms.

When time average holograms of vibrations are processed, the unwrapped phase which results differs slightly from the actual phase due to the assumption of cosine fringes made in the derivation of the equations (see *Chapter 2*). The correction LUT is precomputed and stored for use at this point in the unwrapping procedure. As with any LUT, output mappings are only defined for discrete values of the input. However, the phase is a continuous function. Therefore, the output value is computed by a linear interpolation of the two nearest values in the table.

Use of an LUT also implies integer indexing into the table. The input data values must be scaled and converted to positive integers before being used as indices into the table. The LUT function for negative values is identical, except in sign, to the positive values, so space may be saved by using one table for both ranges with appropriate sign changes.

4.9 Data smoothing with planar facets.

Due to the influence of various noise sources, the unwrapped EOH data generated by the system are generally not smooth. Furthermore, any pixel sites whose weight values were zero contain no data. To fill in the disregarded points and produce a more uniform

surface, the facet fitting routine can be used once again. A new set of smoothed data is created by assigning the value at each point to the value of the estimate returned by the facet fitter. This smoothing technique fills holes in the data and smoothes noisy data.

Whether to smooth the data is a philosophical problem with many ethical ramifications. In general, smoothing or otherwise altering data for presentation should be avoided, but, given that the data measured here correspond to continuous displacements of nearly rigid surfaces, were it not for the noise, the measurements would undoubtedly give smooth results. Therefore, facet based smoothing is provided as an optional element of the algorithm. In using planar facets to perform the fitting, we assume that the size of the features in the data are large compared to the size of the facets. Were we to employ quadratic facet fitting for the smoothing step, this assumption could be relaxed, but the sensitivity to noise would also be increased.

Chapter 5. Results.

This chapter contains examples which show the capabilities of the new phase unwrapping technique as applied to image data generated by an EOH system. The unwrapper has been applied to numerous different objects including the goblet and rectangular plate shown here. The process requires from 2 to 10 minutes to complete depending on the size of the object, the quality of the holographic data and the size of the rectangular boundary used to define the area to process. The samples included here show the algorithm's inherent ability to define the boundaries of objects based on the modulation magnitudes. Examples are included to show the unwrapper's ability to unwrap densely distributed wrapped phase fringes in both the static and time average case. The visual improvements which result due to smoothing are shown as well. Finally, some complex, high frequency time average holograms with compound curving surfaces are shown to demonstrate the algorithm's ability to follow curves in the data.

5.1 Static mode examples.

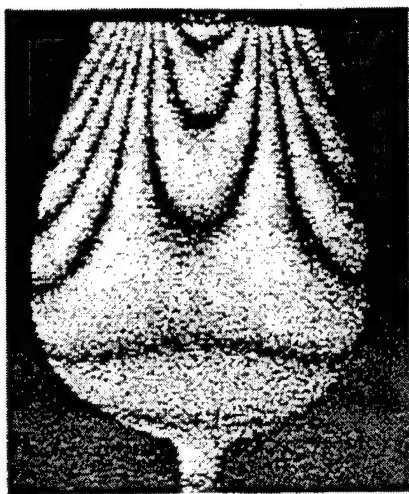
Figures 5.1 and 5.2 show examples of phase unwrapping applied to static mode EOH data. The weighting function provides a means of automatically locating exterior boundaries of objects in the image. Since the weights are computed from the modulation magnitude at all points in the image, and the modulation magnitude is very small anywhere that the object beam does not diffusely reflect from the surface of the object of

interest, the weights outside the object are generally zero. As the unwrapping approaches an object boundary, all the zero weighted points outside the object are ignored. As a result, processing naturally stops at object boundaries. The example in Fig. 5.1 shows the effect of this automatic boundary detection. Wherever the processing wavefront encounters the edge of the cup, the modulation magnitude weighting values fall below the noise threshold and the exterior points are never added to the processing queue. As a result, eventually the processing queue empties before reaching the edges of the rectangular region defined for processing and the unwrapper determines that the area has been completely unwrapped.

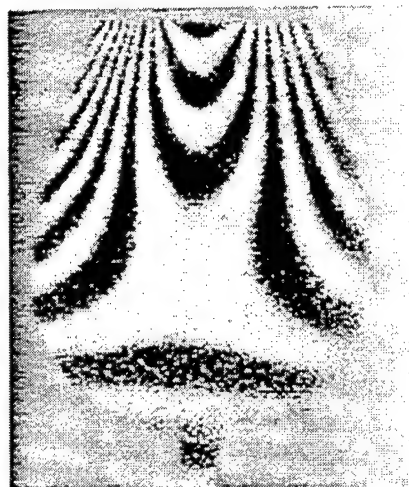
The holograms created for phase unwrapping are not directly displayable since they have a dynamic range of 16-bits and the display is limited to 8-bits. A non-negative representation of static mode fringes can be constructed by taking the square root of Eq. 2.22 to give the displayable image, I_D , described by

$$I_D = \sqrt{8D^2 + 8D^2 \cos \Omega} .$$

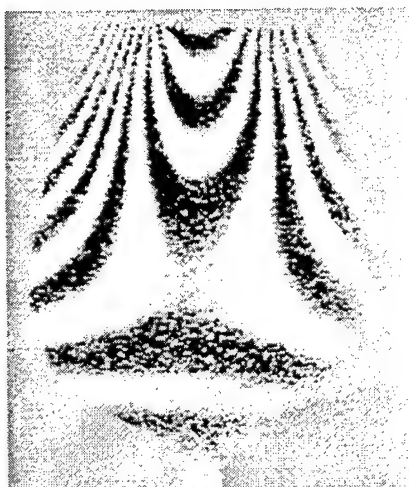
While the 16-bit signed static mode images proportional to the sine and cosine of the phase, Ω , cannot be displayed directly, they can be displayed by scaling the values to lie between -128 and 127. Then, by adding 128 to every pixel, images with zero at neutral gray are produced, where negative values appear as darker fringes and positive values appear as lighter fringes.



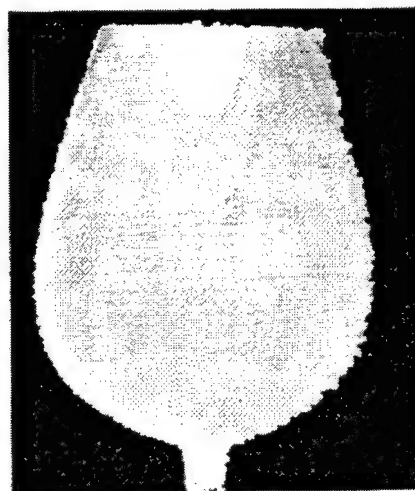
(a) Static display mode hologram.



(b) Sinusoidal static data mode fringes.



(c) Cosinusoidal static data mode fringes.

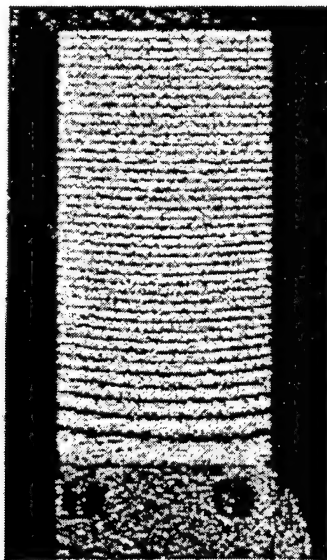


(d) Fringe number map.

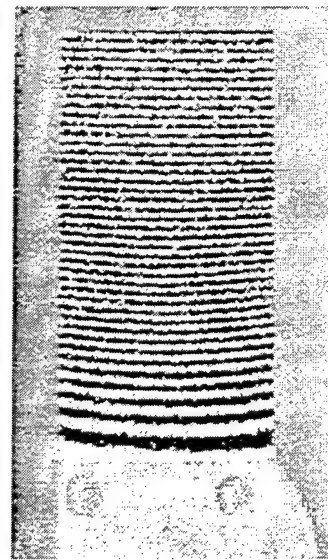
Fig. 5.1 Wine goblet statically loaded with a weight placed across the top of the glass. Image (a) shows the display mode hologram. Images (b) and (c) show the sinusoidal and cosinusoidal data mode fringe patterns,

respectively. Image (d) shows the fringe numbers assigned over the area processed, and illustrates the automatic boundary detection that results from the use of the weighting function (all black regions have been excluded from the object).

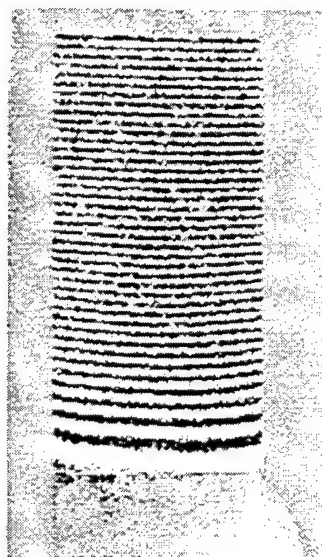
Facet based phase unwrapping has proven to be reliable and effective. In the static mode hologram of a bending beam shown in Fig. 5.2, the unwrapper successfully processed 40 fringes across 288 pixels. This implies that fringes spaced only 7 pixels apart have been interpreted correctly. Figures 5.2a to 5.2d show the image data at various stages during the process of deriving the displacement data and Figs 5.2e to 5.2g show the displacement data.



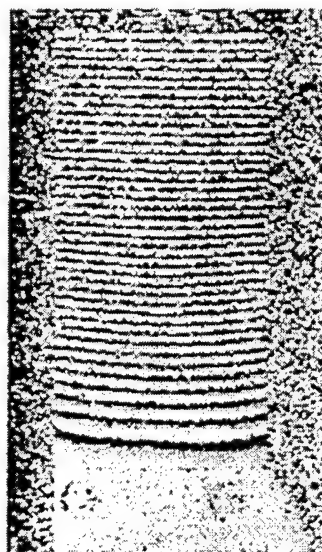
(a) Static display mode hologram.



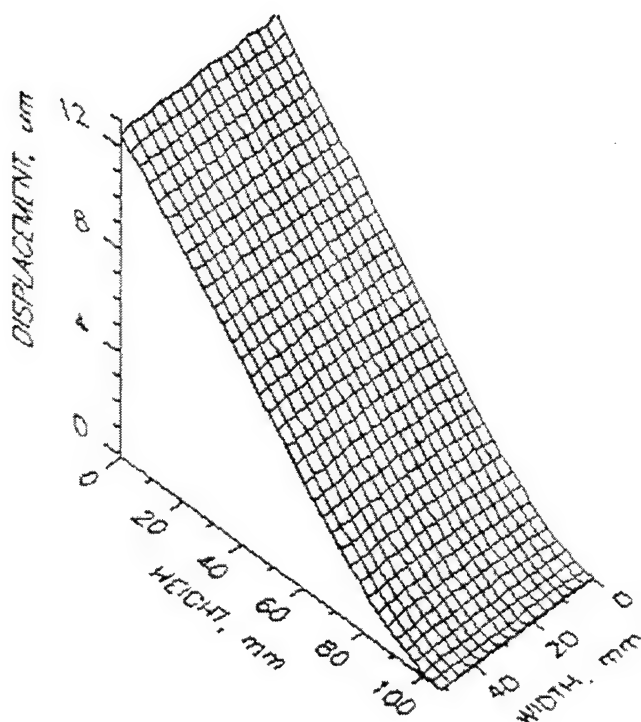
(b) Sinusoidal static data mode fringes.



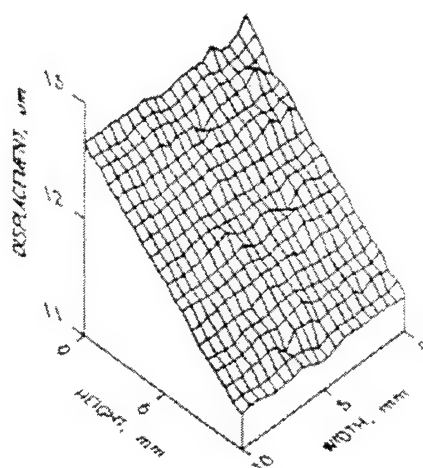
(c) Cosinusoidal static data mode fringes.



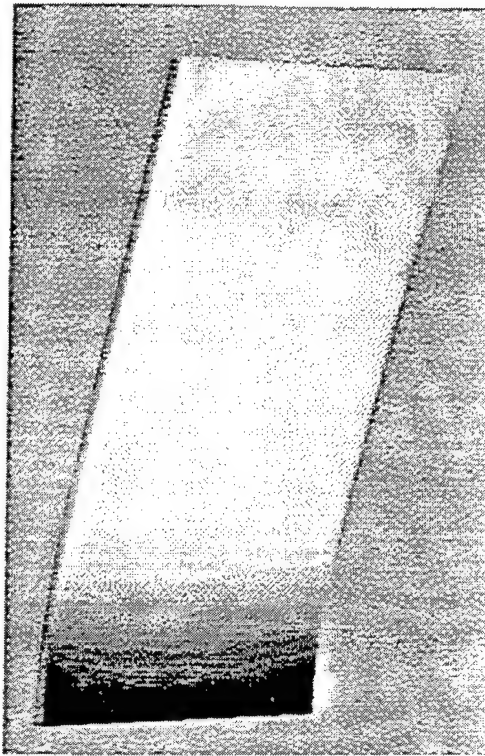
(d) Wrapped phase.



(e) Surface displacements.



(f) Zoomed upper right corner of (e).



(g) Shaded representation of the displaced surface.

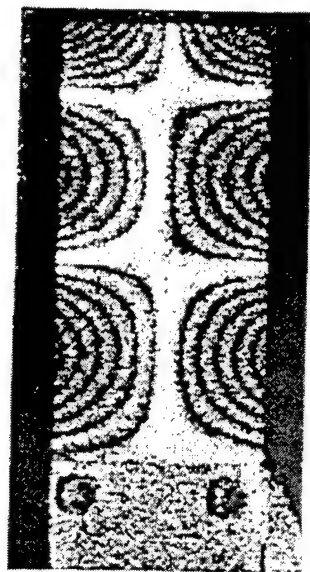
Fig. 5.2 Static bending of a 101.6 mm x 50.8 mm x 3.175 mm aluminum plate. The plate was fixed at the bottom and a force was applied from the back of the plate approximately in its middle and pointing toward the camera. The static display mode hologram is shown in (a) while the sinusoidal and cosinusoidal data mode holograms are shown in (b) and (c). The wrapped phase computed from (b) and (c) is shown in (d). In these images, there are 40 fringes across the 288 pixel height of the plate.

(e) to (g) show renderings of the unwrapped displacement data. The wireframe plot in (e) shows the data converted to metric coordinates and (f) shows a zoomed portion of the upper right corner of the data rendered

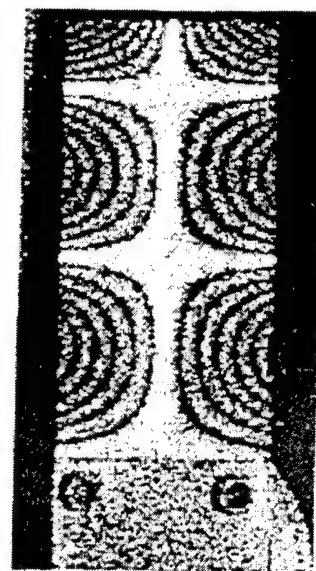
in (e). The small scale random variations visible in (f) are caused by the various sources of noise in the system. The image in (g) is a shaded 3-D rendering of the displacement data mapped onto a rectangular plate.

5.2 Time-average mode examples.

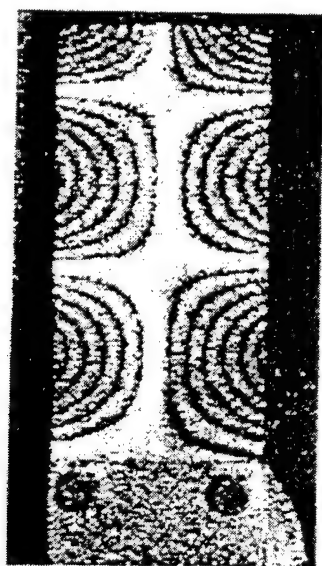
Examples of time-average mode operation are given in Figs 5.3 and 5.4. Time-average mode allows real-time observation of fringe patterns indicative of the displacement of the object's surface in resonant vibration modes, as well as the capture of data for processing. Since the three biased time average hologram images represented by Eqs 2.45, 2.51 and 2.54 each have 16-bits of dynamic range, their square roots are shown in these examples to make 8-bit displayable images and to enhance fringe contrast. In use, as an operator scans through a range of excitation frequencies driving the part under observation, fringe patterns appear and disappear as the driving frequency passes through the part's resonances. The operator can capture image data for quantitative analysis after a resonant mode has been found by this real-time observation.



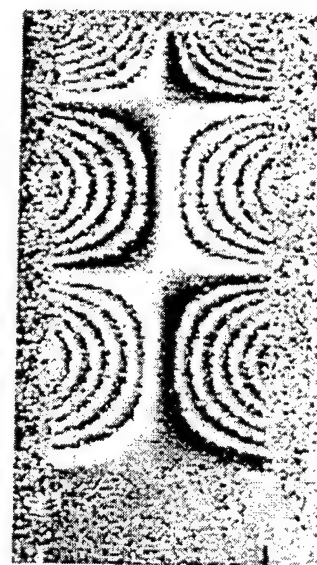
(a) Negative biased time-average hologram.



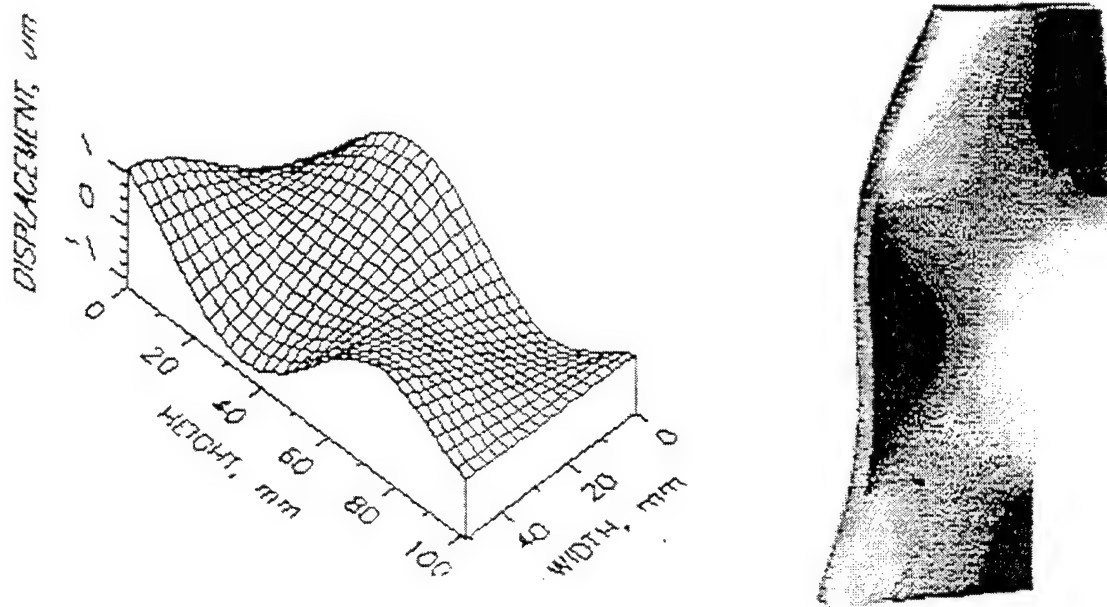
(b) Zero biased time-average hologram.



(c) Positive biased time-average hologram.

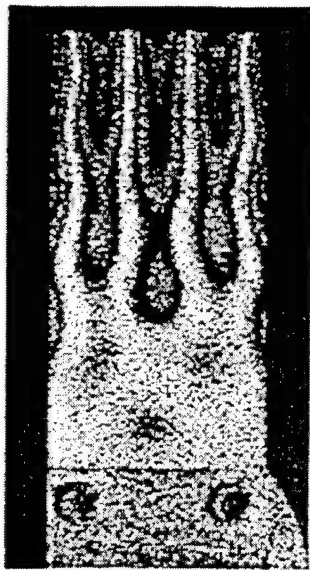


(d) Wrapped phase.

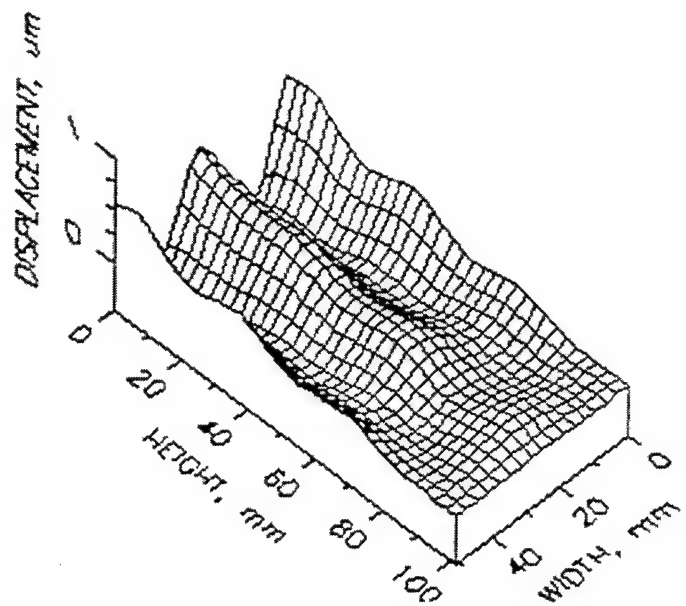


(e) Surface displacement plot. (f) Shaded surface with exaggerated displacements.

Fig. 5.3 Time-average EOH of a plate vibrating in a resonant mode at 6,540 Hz. (a) to (c) images of the negative, zero, and positive biased holograms used to compute the uncorrected phase. (d) image of the wrapped, uncorrected phase, (e) the displacement values plotted on a wireframe grid after facet based smoothing has been applied, and (f) a 3-D shaded rendering of the same data mapped to a rectangular plate. In the shaded image, the primary light source is below and slightly in front of the plate.



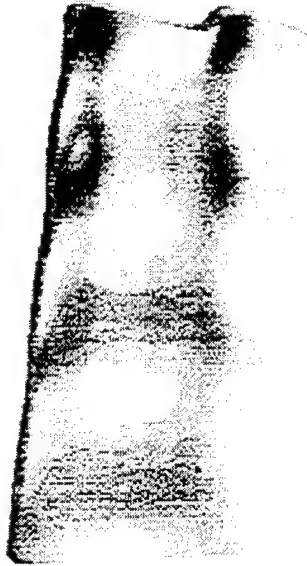
(a) Zero biased time-average hologram.



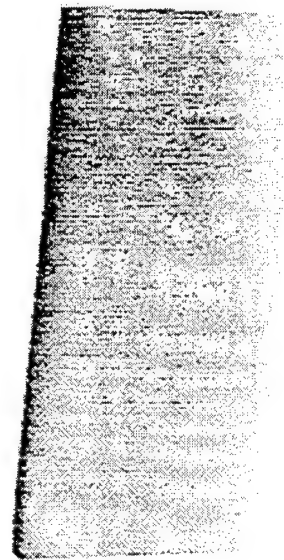
(b) Surface displacement plot.



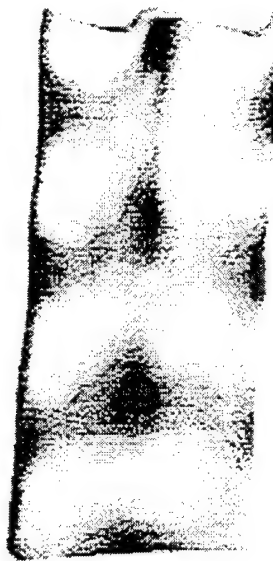
(c) Full scale +



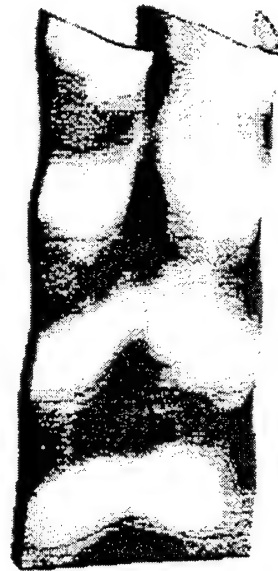
(d) Half scale +



(e) Zero



(f) Half scale -



(g) Full scale -

Fig. 5.4 Time-average EOH of a plate vibrating in a resonant mode at 34,061 Hz. Image

(a) shows the display mode hologram as seen on the image processor screen. The displacements computed from the smoothed phase are displayed in (b). Images (c) to (g) show one half of a cycle of the vibration sampled at five positions during the motion.

Notice that the surface displacements computed from the phase data undergo rapid changes in slope, especially in Fig. 5.4. Even in the presence of such high curvature, the planar facet based unwrapper can make a good local estimate of the expected phase at the next pixel. These images were unwrapped and smoothed with a 9×9 pixel facet which corresponds to roughly 1×1 millimeter in real coordinates. Since this size is small compared to the curving features of the surface, the unwrapper is able to follow the surface faithfully and little distortion is introduced in the smoothed output.

For all the examples, the first stage of processing - the actual unwrapping - required from 1.5 to 2.5 minutes. The energy minimization iterations make relatively small changes to the overall results but require the most time to complete. For these images, 2 or 3 passes were required taking from 6 to 10 minutes. This step can be skipped with no visible impact on the results. Finally, the smoothing step required from 2 to 3 minutes to process and store the data.

In an experiment conducted on 10 images of time-average holograms in various resonant modes, the use of the weighting function consistently decreased the number of iterations required to achieve convergence for the energy minimization stage from three passes to

two. Convergence is achieved when the fringe number assignment for every pixel remains unchanged during the pass. So, since the weighting function places greater emphasis on pixels which are less influenced by noise, the system can converge to its lowest energy state more quickly.

The shaded 3-D renderings of the data were produced by exaggerating the displacements by a user selected scaling factor, then averaging over a neighborhood to choose the value to apply at a grid point in a lower density array of surface displacement values. These displacement values were then mapped to a 3-D rectangular mesh composed of triangular primitives with the same number of grid points. The displacements deform the mesh according to the size and sign of the displacement measured from the phase in the holograms. As a result, when the surface is rendered, an exaggerated representation of the displacement is displayed. To generate the time sequence in Figs 5.4c to 5.4g showing the half cycle of a vibration, the displacements were exaggerated by multiplicative scaling factors of 1000, 500, 0, -500 and -1000.

Chapter 6. Conclusions and future work.

This final chapter presents conclusions based on the results presented in *Chapter 5*, as well as suggestions for future enhancements or improvements of the current phase unwrapper implementation.

6.1 Benefits and features of the facet based fringe unwrapper.

The work performed for this project shows that the planar facet estimator technique for error minimization on wrapped fringe data gives highly reliable unwrapping for continuous surfaces. The unwrapper uses all the information available from the experimental apparatus to perform its function including: 1) The actual data values for the wrapped phase, 2) A modulation magnitude measurement at every pixel, 3) Neighborhood smoothness and continuity constraints imposed on the data around each pixel, modeled as an MRF of limited extent - a justified assumption based on the physical nature of the data to be measured. The results presented in *Chapter 5* show that this approach is robust enough to unwrap dense high order Bessel fringes, as well as phase surfaces with high curvature. As a valuable side effect, this algorithm automatically detects external boundaries at the edges of parts as long as there is a strip of low modulation data at the border. The quality of these experimental results demonstrates that energy minimization by facet based estimation provides a valuable framework for future development of an even more complete system to unwrap phase in the presence of

discontinuities in the data. Use of the weighting function based on the speckle modulation intensity at each point in the image was shown to allow the iterative energy minimization process to converge more quickly and could provide the basis for locating and labeling discontinuities due to surface dislocations in future implementations.

The facet technique requires no prior smoothing of the speckle pattern in the original data to perform the unwrapping. This constitutes a great benefit compared to many of its predecessors. Since the speckle pattern is largely uncorrelated, pre-smoothing has the disadvantages of reducing spatial accuracy and diluting good data with data dominated by noise. Were the operations applied to process the phase data entirely linear, then the same results could be achieved by linear smoothing of the data prior to unwrapping as by smoothing the data after unwrapping. However, the inverse tangent operation on the ratio of a set of fringe patterns is an inherently nonlinear operation. Consequently, the output from the two different processing orders is not identical and errors will be introduced in the data when smoothed prior to processing. The planar estimator operates directly on the wrapped phase data, so it maintains the spatial fidelity of the original data and, by use of the weighting function, gives greater credence to the pixels least likely to be influenced by noise. Data smoothing is performed as a post process to filter out high frequency variations based on the assumption that the phase varies slowly and smoothly over the surface. This same assumption is the basis of the Finite Element Method and associated mathematical modeling techniques; that is, the surface deformations observed result from a physical configuration of the part for which the potential of the system is maximized.

Invariably, a smooth, continuous deformation pattern represents the highest potential energy of the system, provided the part is continuous and free of flaws. For all these reasons, the use of an unwrapper which smoothes the data *after* unwrapping, if at all, is essential.

The technique does not, as yet, locate areas where discontinuities due to surface cracks or other aberrations cause inconsistencies in the fringe pattern. Future implementations of the unwrapper could perform an analysis of the quality of fit computed for each facet to help locate such problem areas, however.

6.2 Suggestions for future improvements and enhancements.

The following subsections detail a number of potential areas for improvement of the existing code and algorithms.

6.2.1 Incorporate correction LUT into time average unwrapping directly.

Results from time average holography show that the nonlinear mapping of the correction LUT occasionally results in inappropriate fringe number assignments. In areas with phase values near changes in the slope of the LUT, the facet will be fit to a section of the data with relatively high curvature. As a result, the estimated planar fit may under or over estimate the actual phase value on the inside of the curvature. Therefore, the energy minimization actually minimizes the energy of the uncorrected data, but not necessarily the energy of the corrected data since the conversion is nonlinear. To truly minimize the corrected data's energy, the algorithm must be modified to 1) fit the facet to data values

which have been pre-corrected through the LUT and 2) find the best match between the estimated phase and the value of the phase added to the appropriate multiple of π then corrected through the LUT. The resulting unwrapped values would then minimize the energy of the actual, corrected phase, not the uncorrected phase.

6.2.2 Add facilities for interactive drawing of boundaries.

For more complex parts with discontinuous surfaces and very irregular shapes, the current implementation cannot distinguish the difference between an actual discontinuity due to a crack in the surface and a phase discontinuity to unwrap. However, with minor modifications, the algorithm could be altered to build neighborhoods for each facet where the neighborhood never extends across a discontinuity line drawn by the user. Such interactive capabilities will undoubtedly be required even with a system for automatically locating discontinuities, since even the best technique will not always succeed.

6.2.3 Data smoothing.

Final smoothing of the data with large facets might be more appropriately implemented with a higher order polynomial fit routine. The use of planar facets results in flattening of hill tops and valleys, but, a higher order fit would be able to better match the curvature of the surface. Specifically, a quadratic fit would allow the model to match simple curves in the data. By using many high order terms, the model might simply "fit the noise". The use of a quadratic polynomial model represents a good compromise. Also, a reasonably accurate representation of an arbitrary curve can always be constructed with piece-wise

quadratic patches. Since the curvature of the surfaces in question is always small compared to the variations due to the noise, a second order fit over a large neighborhood would not be unduly sensitive to the noise.

When the matrix inversion is performed on a higher order polynomial, the matrix is more likely to become ill conditioned. Direct inversion of the first order matrix presents no problem as long as three or more non-coplanar points are defined in the data since the dynamic range of the numbers involved cannot exceed the range available in the double precision floating point numbers used in the inversion routine. For inversion of matrices resulting from a least squares fit to a higher order polynomial, the matrix is larger and the dynamic range required increases. To insure that the inversion remains numerically stable, the matrix inversion must be carried out by a more stable technique such as LU decomposition. Such techniques are appropriate for potentially ill conditioned matrices since they transform poorly behaved matrices into more stable arrangements to reduce the likelihood of encountering "delicately balanced infinities" for which small truncation errors can cause large changes in the results ¹⁹.

6.2.4 Speed improvements.

As with almost any algorithm, special purpose hardware would greatly improve the processing speed. An array processor or i860 based coprocessor board could be used to perform the matrix inversions for the facet fits. The 68040 based host processor would provide data management by both controlling the wavefront ordering and transferring data to the coprocessor.

Another speed gain would be realized by improving the energy minimization iteration algorithm. Instead of performing numerous raster scans through the data, each of which fits a facet at every pixel location repeatedly, a single scan with backtracking could be employed. This technique begins by fitting facets at every point along a raster scan to insure that the phase plus its fringe offset are within a half a fringe of the estimate. Whenever a point is found where the data plus its assigned fringe offset and the estimate are more than half a phase step size different, then the fringe number must be altered to bring the two within a half phase step size of each other. When a point's value is changed, it could affect any member of the neighborhood around the point. Therefore, all the points lying within the current point's neighborhood which have previously been processed must be re-checked. A stack would be implemented to manage the list of pixels requiring reconsideration. As long as points remain in the stack, the next point to consider is popped from the top of the stack. If, in processing a point popped from the stack, another change occurs, then the neighbors of the newly changed point are also placed on the stack, unless they are already somewhere in the stack. Once the stack has been emptied, then the raster scan continues where it left off. Processing is complete when both the stack is empty and the raster scan has been completed. There is a danger that a configuration of pixels could occur in which the fringe number assignments of two pixels cause oscillations in each other's values. A flag could be set for each pixel indicating that the pixel has previously been changed, and indicating the direction of the change. Then, if the routine attempts to change the value back in the opposite direction, a warning could be generated and the location skipped.

6.2.5 Noise threshold selection enhancement.

While the weighting technique improves the operation of the system, the method suffers from high sensitivity to the noise threshold level selected. The user selects a small multiple of the noise threshold level for the system to use as the scaling factor in computing the weighting function from the modulation magnitudes. The higher the measured noise level, the more data get discarded from consideration. But, the noise calibration is sensitive to a wide variety of influences in the system. Even stray air currents can cause significant changes in the measurement. Since all data below the noise threshold are culled, repeated experiments can have varying levels of depopulation of the data set for identical user settings. Until techniques are found to further stabilize the optical system, such variations will continue to be present. Therefore, an interactive technique for selection of the noise threshold where the user is presented with the speckle pattern's histogram and allowed to modify the threshold dynamically may be more appropriate. By such a technique, as the user alters the threshold value, pixels to be discarded can be highlighted dynamically. Thus, the user could use direct feedback to choose a level which would leave sufficient numbers of pixels un-culled to provide reasonable support for the facet fits.

6.3 Summation.

Motivation for the development of this phase unwrapping technique began with the study of energy minimization as applied to the object labeling problem for noisy images in machine vision. Based on this work, a definition of the energy of a surface was

developed such that energy is proportional to the change in slope over a surrounding neighborhood. Since full field iterative techniques were deemed to be inappropriate for the inherently sequential problem of assigning fringe numbers, techniques for estimating surface characteristics based on a set of known neighbor's values seemed the best approach to pursue. Facet based surface modeling provides a means of estimating an unknown location's value based on known neighbors. Haralick's facet model was generalized to work on the sparse, weighted neighborhoods available in the unwrapping problem to construct the facet based phase unwrapper. Energy minimization is accomplished by finding a complete set of fringe number assignments over the non-zero weighted locations such that no other arrangement of assignments can be found to give a smaller total deviation of the surface from planarity. This background gives the technique a solid framework for its construction, and the results show great promise for future applications.

Appendix A. Mathcad model of the Bessel fringe function.

Mathcad model of a 1-D Bessel function

Interval of integration:	$T := 2 \cdot \pi$
Sinusoidal frequency:	$w := 2 \cdot \pi$
Amplitude sweep step size:	$AStep := \frac{\pi}{8}$
Half number of points to evaluate:	$N := 20$
Index for first half:	$i := 0..N$
Index for second half:	$j := N + 1..2 \cdot N \quad k := 0..2 \cdot N$
Arguments for the function scaled by step size:	$A_i := N \cdot AStep - i \cdot AStep$
Arguments for the second half scaled by step size:	$B_j := (j - N) \cdot AStep$

Note: the amplitude of the sinusoid represents increasing amplitude of vibration of the part under observation. Since the vibration will be mirrored and inverse about the nodal line, the second half of the plate is represented by a second equation whose sinusoidal vibration is 180 degrees out of phase with the vibration on the first side of the plate.

Bessel fringe function for first side of plate

$$b(A) := \frac{1}{T} \cdot \int_0^T \exp(-j \cdot A \cdot \sin(w \cdot t)) \, dt$$

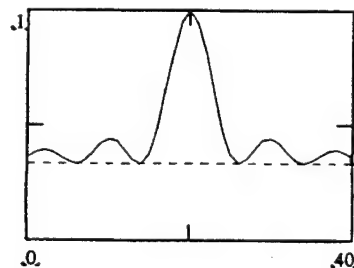
Bessel fringe function for second side of plate

$$c(A) := \frac{1}{T} \cdot \int_0^T \exp(-j \cdot A \cdot \sin(w \cdot t + \pi)) \, dt$$

Functions converted to an array and squared:

$$M_i := b \, A_i^2 \qquad M_j := c \, B_j^2$$

Plot of the Bessel function squared over the two sides of a vibrating objec.



Mathcad model of a biased Bessel function where the bias signal's phase changes.

Amplitude of the bias signal

$$P := 1$$

Phase step size:

$$DStep := \frac{\pi}{8}$$

Array of phase steps:

$$D_k := k \cdot DStep$$

Equation for the computation of the Bessel function with a bias signal of varying phase:

$$f(A, D) := \left(\frac{1}{T} \right) \cdot \int_0^T \exp(-j \cdot (P \cdot \sin(w \cdot t + D) + A \cdot \sin(w \cdot t))) dt$$

2-D array over first half of fringes:

$$M_{i,k} := f(A_i, D_k)^2$$

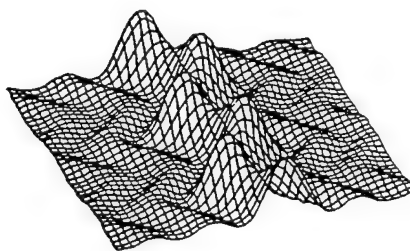
Second equation for the computation of the Bessel function with a bias signal of varying phase:

$$g(A, D) := \left(\frac{1}{T} \right) \cdot \int_0^T \exp(-j \cdot (P \cdot \sin(w \cdot t + D) + A \cdot \sin(w \cdot t + \pi))) dt$$

2-D array over second half of fringes:

$$M_{j,k} := g(B_j, D_k)^2$$

Surface plot of fringe intensity as a plate vibrates sinusoidally and as phase varies.



M

Mathcad model of a biased Bessel function where the bias signal's amplitude changes.

Phase of the bias signal:

$$D := 0$$

Amplitude step size:

$$PStep := \frac{1}{4}$$

Array of amplitude steps:

$$P_k := k \cdot PStep$$

Equation for the computation of the Bessel function with a bias signal of varying amplitude:

$$f(A, P) := \left(\frac{1}{T} \right) \cdot \int_0^T \exp(-j \cdot (P \cdot \sin(w \cdot t + D) + A \cdot \sin(w \cdot t + \pi))) dt$$

2-D array over first half of fringes:

$$N_{i,k} := f(A_i, P_k)^2$$

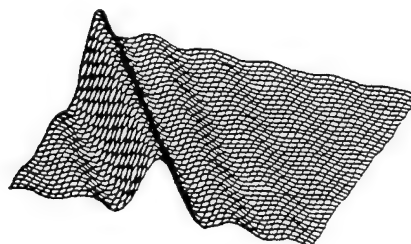
Second equation for the computation of the Bessel function with a bias signal of varying phase:

$$g(A, P) := \left(\frac{1}{T} \right) \cdot \int_0^T \exp(-j \cdot (P \cdot \sin(w \cdot t + D) + A \cdot \sin(w \cdot t))) dt$$

2-D array over second half of fringes:

$$N_{j,k} := g(B_j, P_k)^2$$

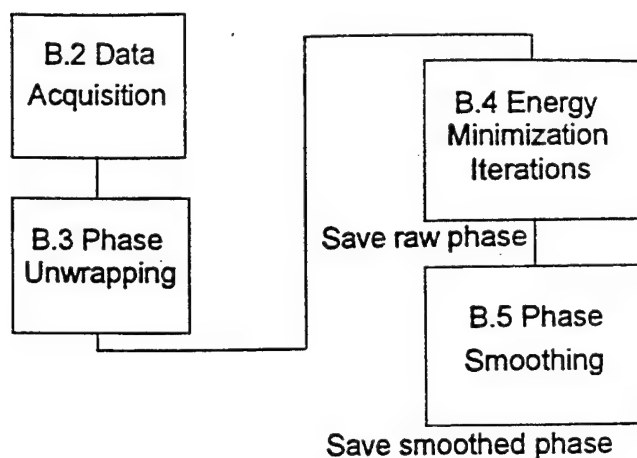
Surface plot of fringe intensity as a plate vibrates sinusoidally and as amplitude varies.



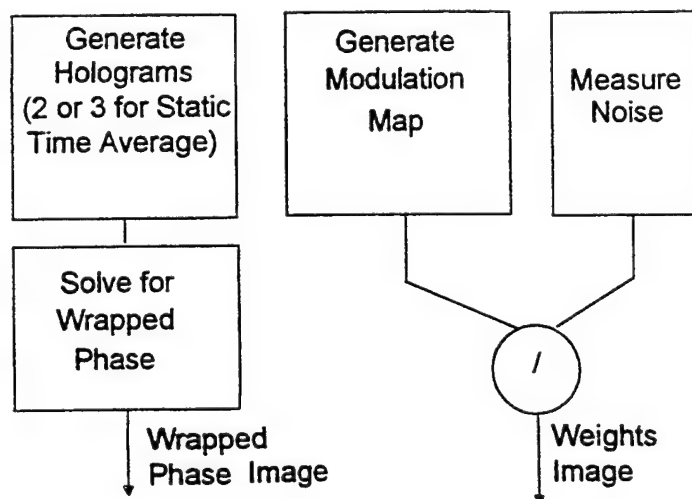
N

Appendix B - Software Block Diagrams

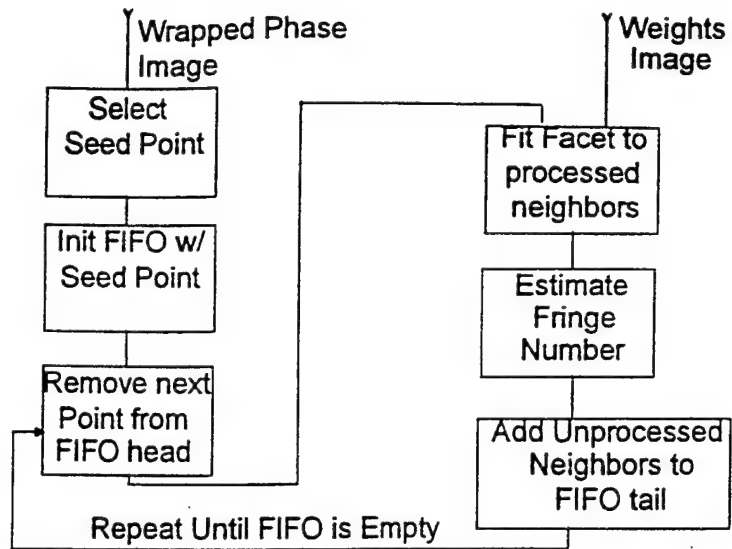
B.1 Software Block Diagram (Top Level)



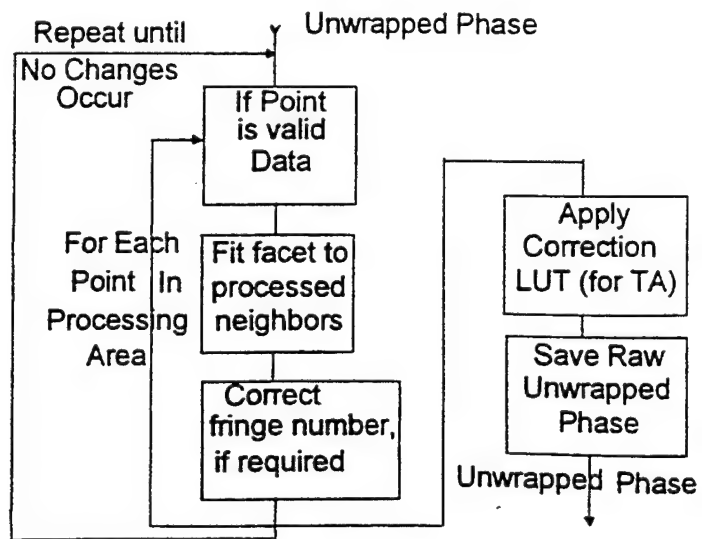
B.2 Data Acquisition Block Diagram.



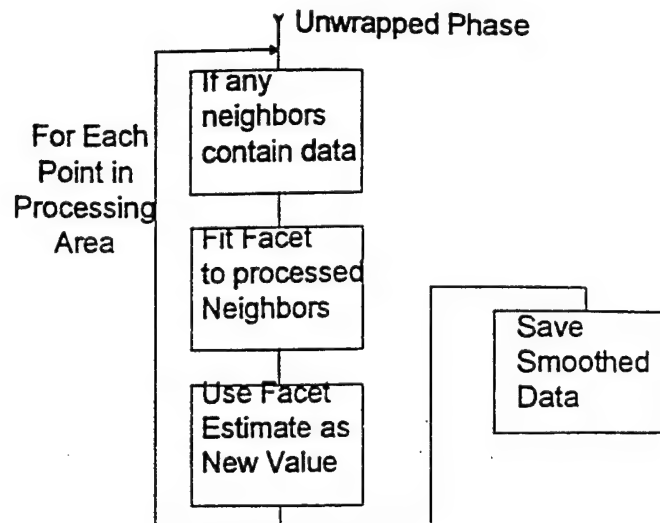
B.3 Phase Unwrapping Block Diagram.



B.4 Energy Minimization Iterations Block Diagram.



B.5 Smoothing Block Diagram.



References

1. R. J. Pryputniewicz, *Holographic Numerical Analysis*, Center for Holographic Studies and Laser Technology, Department of Mechanical Engineering, Worcester Polytechnic Institute, pp. 86-89, 1992.
2. K. A. Stetson and W. R. Brohinsky, "An electro-optic holography system for vibration analysis and nondestructive testing," *Proc. SPIE*, 746:44-51, 1987.
3. K. A. Stetson and W. R. Brohinsky, "Fringe-shifting technique for numerical analysis of time-average holograms of vibrating objects," *J. Opt. Soc. Am. A*, 5:1472-1476, 1988.
4. R. J. Pryputniewicz and K. A. Stetson, "Measurement of vibration patterns using electro-optic holography," *Proc. SPIE*, 1162:456-467, 1989.
5. D. H. Towne, *Wave Phenomena*, Addison-Wesley, Reading, MA, pp. 19-31, 1967.
6. R. J. Pryputniewicz, "Static and dynamic measurements using electro-optic holography," *Proc. SPIE*, 1554B:790-798, 1991.
7. T. W. Bushman, "Development of a holographic computing system," *Proc. SPIE*, 1162:66-77, 1989.
8. K. A. Stetson, "Effects of beam modulation on fringe loci and localization in time-average hologram interferometry," *J. Opt. Soc. Am.*, 60:1378-1384, 1970.
9. S. Geman and D. Geman, "Stochastic relaxation, Gibbs Distributions, and the Bayesian restoration of images," *IEEE PAMI*, 6:721-741, November, 1984.
10. R. M. Haralick, "Digital step edges from zero crossings of second directional derivatives," *IEEE PAMI*, 6:58-68, 1984.

11. K. Itoh, "Analysis of the phase unwrapping algorithm," *Applied Optics*, 21:2470, 1982.
12. K. Stetson, "Phase-step interferometry of irregular shapes by using an edge-following algorithm," *Applied Optics*, 31:5320-5325, 1992.
13. D. P. Towers, "The automatic quantitative analysis of phase stepped interferograms," *Hologram Interferometry and Speckle Metrology*, SEM, pp., 480-487, 1990.
14. H. A. Vrooman and A. A. M. Mass, "Image processing algorithms for the analysis of phase-shifted speckle interference patterns," *Applied Optics*, 30:1636-1641, 1991.
15. D. C. Ghiglia, G. A. Mastin and L. A. Romero, "Cellular-automata method for phase unwrapping," *J. Opt. Soc. Am.*, 4:267-280, 1987.
16. M. Owner-Petersen, "Phase-map unwrapping: a comparison of some traditional methods and a presentation of a new approach," *Industrial Applications of Holographic and Speckle Measuring Techniques - SPIE*, 1508:73-82, 1991.
17. K. Shiloh and A. Saya, "Linearization and flattening techniques for fringe analysis and its application to holographic interferometry," *Nondestructive Testing International*, 21:446-453, 1988.
18. S. Nakadate and H. Saito, "Fringe scanning speckle pattern interferometry," *Applied Optics*, 24:2172-2180, 1985.
19. S. D. Conte and C. deBoor, *Elementary Numerical Analysis - An Algorithmic Approach*, McGraw-Hill, New York, pp. 245-259.

Appendix C

**THREE-DIMENSIONAL GRAPHICS TECHNIQUES APPLIED
TO THE RENDERING OF HOLOGRAPHIC
INTERFEROMETRIC DATA**

PROCEEDINGS REPRINT

 SPIE—The International Society for Optical Engineering

Reprinted from

Interferometry: Techniques and Analysis

20–21 July 1992
San Diego, California



Volume 1755

©1993 by the Society of Photo-Optical Instrumentation Engineers
Box 10, Bellingham, Washington 98227 USA. Telephone 206/676-3290.

THREE DIMENSIONAL GRAPHICS TECHNIQUES APPLIED TO THE RENDERING OF HOLOGRAPHIC INTERFEROMETRIC DATA

Thomas W. Bushman and Ryszard J. Pryputniewicz

Center for Holographic Studies and Laser Technology
Department of Mechanical Engineering
Worcester Polytechnic Institute
Worcester, MA 01609

ABSTRACT

Electro-optic holography (EOH) generates a large array of three-dimensional values (displacement at each x, y location) as its final output. In the past, a number of techniques have been employed to display the displacement data ranging from topographic maps and enhanced versions of the holograms themselves, through fringe skeletonizing, to wire frame surface plots. This paper discusses the application of 3-D shaded rendering techniques to holographic displacement data. Both modeling the object and rendering the model are covered. The resultant shaded images show the displacements of the surface clearly and the software allows the user complete control over the orientation of the view and the characteristics of the light sources. Results are shown for a number of modes of vibrating rectangular plates.

1. INTRODUCTION

Three-dimensional graphical rendering produces realistic two-dimensional projections of objects existing in three dimensions. For any given projection, natural cues provide depth information in the same fashion as an observer perceives when a scene is viewed through a window. The rendering software provides control of the location of the viewing window, the viewer's focus of attention in the world outside, and the strength and location of lights in the world.

To give the user such flexibility requires both a complete 3-D description of the object to view, or world, and a significant number of floating point calculations in the rendering software. As the world becomes more complex or detailed, the computational requirements rise and, more importantly, the buffer space requirements increase, as well. The memory constraints imposed by the PC-DOS environment would not allow any but the simplest world models to be rendered. However, with the advent of MS-Windows, PC software can access all the installed memory in the PC and even use virtual memory to allow large enough buffers for very complex rendering problems. Due to the near universal availability of PCs and their rapidly improving performance, operating software and pricing, we chose to implement our program in this environment.

EOH, also based on the PC environment, generates an array of displacement data over the surface of the object to be measured. These data indicate either the amplitude of vibration or the static deflection at each point in the image. Previous methods used for the representation of EOH data include topographic maps, wire frame surface plots and even shaded surface plots. These techniques all give indications of trends in the data and show varying degrees of detail, but none include the flexibility of 3-D rendering systems for focusing on desired features and highlighting subtle variations in the data. By appropriate selection of the values for the lighting and viewing controls, the operator can focus the viewers' attention on any detail, and use multiple views to show a variety of different features.

The 3-D rendering system also provides a further benefit in that the 3-D model of the object is more compact than the original representation of the 512x480 array of displacement data points, so the results can be stored in a smaller area of a computer's mass storage space.

2. THREE-DIMENSIONAL GRAPHICS TECHNIQUES: AN OVERVIEW

2.1. Two step process

The task of creating 3-D graphics can be conveniently divided into two parts. First, a three-dimensional internal representation of the world called the "world model" is generated. Then, a two-dimensional projection of the three-dimensional model is created as specified by the values of the viewing parameters.

2.2. Modeling

The world model must fully define all the characteristics of the three-dimensional objects to be represented. Since an object is seen due to light interacting with its surface, a natural representation defines objects by their skins shown as joined planar surface patches. By using triangular patches, maximum flexibility for matching the model to the object's geometry results. Triangular patches are necessarily planar, since three points define a plane. Their use as the most primitive level of the representation avoids potential ambiguities that could appear using patches with non-coplanar vertices. Since any surface can be approximated arbitrarily well by a set of increasingly smaller planar patches, the renderer's ability to model curved surfaces is not constrained by its reliance on triangular patches. Furthermore, many rendering sub-tasks are greatly simplified when the world model is constituted solely of such patches.

In the example discussed herein, the modeling process begins by creating a flat rectangular plate whose geometry matches the plate under observation. The operator must supply the plate thickness. Other shapes as well as curved surfaces will be added in future work. After the surface has been created, it is subdivided into smaller regions. Each sub-region's vertices are displaced along the z-axis according to the values of the corresponding data taken from the holographic results. To reduce the effects of noise in the data, the vertex values can be generated by averaging a number of points in a two-dimensional neighborhood around the vertex point. All back surface points are displaced by the same offset value to match the front surface. After the model is generated, the modeling routine finds the deviation between the surface data values and the planar patches used to model the surface. The maximum deviation value is reported to the operator. If the deviation is too large, the operator may choose to re-model the surface with a finer mesh. Figure 1 shows a coarse example mesh.

The model thus generated is stored in a set of three lists: the point list which contains vertex coordinates, the edge list which defines all the edges between pairs of points, and the triangle list composed of sets of edges. As a convenient byproduct of this storage scheme, all edges are shared by exactly two triangles. So, by storing pointers to the two owner triangles sharing a common edge, any triangle's neighbors can easily be located. Quick access to the neighbor triangles is essential for efficient smooth shading later in the rendering process.

2.3. Viewing parameters

Once the model is built, the operator has the opportunity to adjust the viewing parameters. To achieve the most general and complete control of the display, six values are specified: 1) the attention point, which is the spot in the world at which the observer looks, 2) the view reference point (VRP), which is the eye location or point from which the observer views the world, 3) the head tilt, which corresponds to rotations of the viewer's head from side

to side around the axis from the attention point to the VRP, 4) the eye distance, which defines the distance between the eye and the projection plane and thus controls the amount of perspective distortion, 5) the horizontal shear offset, and 6) the vertical shear offset values, which introduce shearing distortion in the image. These last two shear offset values will be neglected for this discussion since perspective shear is neither necessary nor helpful in the generation of unambiguous renderings of the data. Figure 2 shows a schematic representation of the viewing parameters.

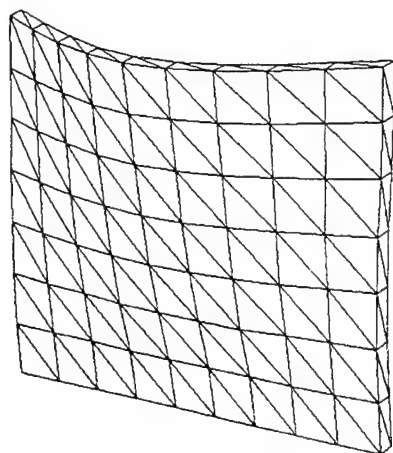


Fig. 1. Coarse triangular surface mesh.

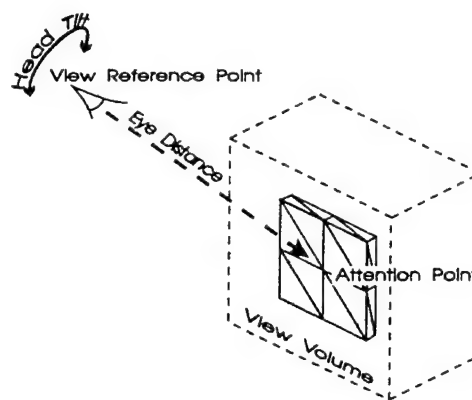


Fig. 2. Generalized viewing parameters and their geometric meaning.

The set of viewing parameters can be expressed succinctly as a single four by four homogeneous affine transformation matrix¹. The transformation converts the coordinates of the world model into a new coordinate system whose coordinate axes are defined by the VRP, attention point, and head tilt.

The transformation from the initial coordinate system (x, y, z) to a new coordinate system (U, V, W) can be expressed in the matrix M_T by placing the U, V , and W unit vectors expressed in the x, y , and z system into the first three columns of the matrix. The displacement of the origin is denoted by the vector \mathbf{r} . To find the displacement expressed in the new coordinate system, find its components along U, V , and W . Place these offset components in the fourth row to get the matrix

$$M_T = \begin{bmatrix} U_x & V_x & W_x & 0 \\ U_y & V_y & W_y & 0 \\ U_z & V_z & W_z & 0 \\ \mathbf{r} \cdot \mathbf{U} & \mathbf{r} \cdot \mathbf{V} & \mathbf{r} \cdot \mathbf{W} & 1 \end{bmatrix}. \quad (1)$$

The perspective distortion, expressed as the distance from the eye to the plane of projection, is given by the scalar distance p . The transformation matrix which applies the perspective distortion, M_p , is given by

$$M_p = \begin{bmatrix} 1 & 0 & 0 & 0 \\ 0 & 1 & 0 & 0 \\ 0 & 0 & 1 & \frac{1}{p} \\ 0 & 0 & 0 & 1 \end{bmatrix}. \quad (2)$$

Now, a single transformation matrix can be generated by combining the matrices M_T and M_p to get the combined transformation matrix M_c , that is,

$$M_c = M_T M_p . \quad (3)$$

All the data points stored in the point list in the world coordinate system can now be transformed to the viewing coordinate system. The transformed points are stored in a new list since the original set of world coordinates must be used later in the shading computation. To perform the transformation, each point is re-expressed as a one by four homogeneous matrix with a 1 appended as the fourth element. Then, each point matrix is multiplied by the combined transformation matrix M_c to get the new point in UVW coordinates. Notice that neither the edge list nor the triangle list is affected by this operation, yet all the edges and triangles have also been transformed to the new coordinate system automatically.

The 2-D projection of the transformed system now follows immediately by simply dropping the z component of the 3-D coordinate of each point. Before disposing of the z component, however, the value is used in the determination of relative depths of points in the new coordinate system. In order to insure that front objects do indeed occlude back objects, all of the triangular faces are ordered according to their distance to the eye. During the rendering process, the faces are drawn in farthest to closest order so that any overlapping objects are rendered such that a closer object's surface overwrites all more distant ones.

2.4. Shading intensity computation

As the triangles are drawn, they must be filled with appropriate intensity values subject to the lighting parameters specified by the operator. The system employs a lighting model which assumes that the intensity at any point on the surface is composed of three parts: 1) reflected ambient glow, 2) diffuse reflection or scattered light, and 3) specular reflection or mirrored light. A set of three reflectivity parameters associated with each surface patch controls the relative contributions of each type of reflection to the total reflected intensity at each point in the patch.

The ambient light contributes a constant intensity, I_A , to the total which depends only on the ambient reflectivity parameter of the surface as

$$I_A = I_b R_A , \quad (4)$$

where I_b is the background intensity of light or ambient glow, and R_A is the ambient reflectivity coefficient of the surface patch.

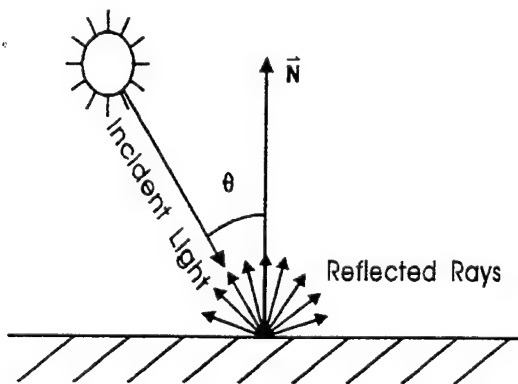


Fig. 3. Diffuse reflection from a surface.

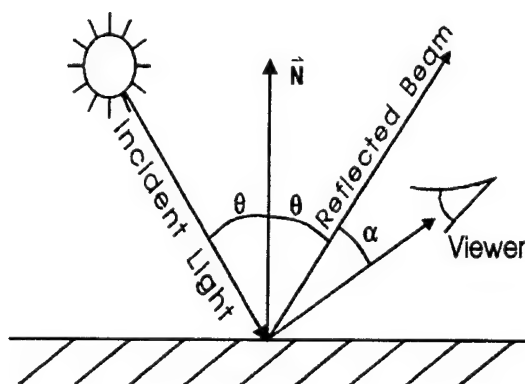


Fig. 4. Specular reflection from a surface.

Diffuse reflected light contributes I_D to the total and is modeled by Lambert's Law which can be expressed as

$$I_D = I_L R_D \cos \theta \quad , \quad (5)$$

where R_D is the percentage of incident light which the surface scatters and θ is the angle between the incident light ray and the normal to the surface at the point as shown in Fig. 3. Thus, a surface diffusely reflects the most light when the light source is directly above the reflection point.

Specular reflected intensity, I_S , shown in Fig. 4 is computed by the Phong model of specular reflection², and it is defined as

$$I_S = I_L R_S \cos^n \alpha \quad . \quad (6)$$

In Eq. 6, R_S is the percentage of incident light which is mirrored and α is the angle between the reflected beam and the line from the viewer to the reflection point. Note that the reflected beam leaves the surface at the same angle with respect to the normal to the surface as the angle of the incident beam. The cosine function is raised to the n th power, where n is an integer value between 50 and 200 (we used 100). As a result, specular reflection is practically zero for all viewing angles except when the viewer's eye is very near the ray produced by the reflected beam. As the eye moves nearer to the beam, the specular component of the total intensity rises quickly. This sharp increase in the intensity due to specular reflection causes glinting highlights on curved surfaces and larger saturated areas on flat planes.

Since the system allows up to ten light sources to contribute to the light reflected from a point, the total intensity, I_T , at a given point can be found from the sum of the ambient intensity with all the diffuse and specular reflected intensities generated by the light sources, that is,

$$I_T = I_A + \sum_{i=1}^N (I_{D_i} + I_{S_i}) = I_A R_A + \sum_{i=1}^N I_{L_i} (R_{D_i} \cos \theta + R_{S_i} \cos^n \alpha) \quad , \quad (7)$$

where N is the number of light sources.

Each triangle's normal is precomputed earlier during the modeling phase. The normal, still in world coordinates, is used during the computation of the intensity for each vertex of the triangle. All the intensity values are computed in the world coordinate system to avoid difficulties introduced by the perspective distortion of the x and y components for varying depths (z distances). To compute the specular reflection, the eye location in the world (x, y, z) coordinate system, is subjected to the inverse of the viewing transformation. By inversely transforming the eye coordinates, the same effect results as does from transforming the entire world. This approach allows easy calculation of the irradiance at each point in the world coordinate system. The irradiances thus computed map directly into the viewing coordinate system for use in rendering.

2.5. Smooth shading

One of two shading strategies may be used in the software: either flat shading or Gouraud shading. For flat shading, the intensity of each triangle is computed at each of its vertices, then averaged. This average intensity is used to fill the entire triangle. Gouraud shading³ smoothes the image by interpolating intensities. First, the intensity at each vertex is computed. However, instead of using the normal to only the current triangle in the computation, the normal used is the average of the normals of each triangle which shares the same vertex point. Then, the intensity values are interpolated between each pair of vertices and along each scan line while filling the area. This smoothing strategy eliminates sharp edges between patches on the same surface at a minimal computational cost.

The combination of MS-Windows and a Super VGA display allows selection of 256 colors from a palette of more than 256 thousand available colors. However, typical D/A converters used in PC video adapters only operate on the most significant 6 bits of the supplied data. As a result, only 64 gray shades can be generated. With only 64 shades available, the smooth shading outlined above produces clearly discernible gradients in the image. Ideally, textured surfaces or variations in a surface's finish would be used to remove the unwanted gradients. A surface finish or pattern can be modeled by introducing small programmed or random changes in the surface normal at each point prior to computing the intensity values. However, since Gouraud shading operates by intensity interpolation, changes to the normals would affect each whole triangular patch. As an alternative to employing a real world model of the surface for gradient banding suppression, these gradients can easily be eliminated by adding a small magnitude, signed random value to each computed pixel's intensity value prior to rendering the pixel.

3. ELECTRO-OPTIC HOLOGRAPHY

The Electro-Optic Holography (EOH) system measures irradiances produced by mutual interference of the object and the reference fields measured electronically by a CCD camera. Processing of this interferometric information and display of results are carried out concomitantly with measurements of the irradiances.^{4,7}

In the EOH system, the laser output is divided into two beams by means of a continuously variable beamsplitter. One of these beams is directed via a piezo-electrically driven mirror and is shaped by the spatial filter beam expander assembly to illuminate the object uniformly; this mirror can be driven at the same frequency as the object excitation to provide bias modulation. The other beam, also spatially filtered and expanded, is directed toward the reference input of the speckle interferometer by another piezo-electrically driven mirror which introduces 90° phase steps between consecutive frames. The speckle interferometer combines the object beam with the reference beam and directs them colinearly toward the detector array of the CCD camera. The camera detects the interference pattern and sends it to the processor which operates under control of the host computer. The host computer also controls excitation of the object, coordinates it with the bias modulation imposed on the object beam, and keeps track of the 90° phase steps between the frames.

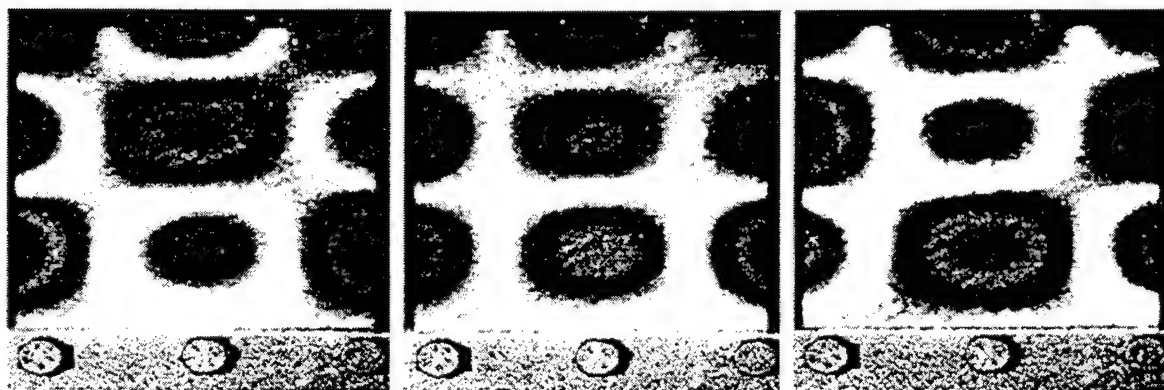


Fig. 5. Displayable versions of data mode holograms used to generate a surface deflection map. A 1/16 inch thick cantilever aluminum plate was clamped to a PZT mount and driven at 2118 Hz. The images were produced with a negative phase bias, zero bias, and a positive phase bias from left to right, respectively. Notice that the two central bullseye patterns are different sizes in the two images with phase biases applied. The shifted fringes carry the information that allows the phase unwrapping software to distinguish areas moving toward the camera from areas moving away.

4. RESULTS

Rendered 3-D shaded images generated by the program are shown in Figs 6 and 7. The laser printer generated images' quality is sufficient to show the points of interest in each example. However, dramatically better print quality is achievable with either 35mm photographs of the monitor or video printer output.

4.1. Source images

In the EOH system, the data provided by the CCD camera are processed for every pixel in the image frame at the rate of 30 frames per second. Each frame contains 512x480 8-bit numbers and consists of 245,760 points.

Quantitative data on the object displacements are obtained by processing the images using procedures of Reference 4. These procedures extract data from electronically recorded holograms by a method of optical fringe shifting. In this approach, the nearly periodic nature of the J_0 fringes is utilized to obtain an approximate solution for the fringe-locus function. This approximate solution recognizes that the general solution representing the irradiance of an image reconstructed from a time-average hologram is similar to the general equation for the irradiance distribution for an image reconstructed from a conventional double-exposure hologram with cosinusoidal fringes. The approximate solution differs from the correct solution because of the inequality between the Bessel and the cosinusoidal fringes and the two are related to each other via an error. This error is computed in terms of the fringe-locus function, for a specific value of the bias modulation, to create a lookup table. The lookup table is used to determine the correct values of the fringe-locus function based on approximate results. Once the correct values of the fringe-locus function are determined, they are used to compute displacements of a vibrating object. Representative results of such computations are shown in Figs 6 and 7.

4.2. Multiple views

Often more than one view of an object leads to a much clearer understanding of its shape and features. The sequence of images in Figs 6 and 7 show two sets of views of the same object under two different conditions of excitation. In Fig. 6, multiple views were generated by changing the scaling factor applied to the data when the model was generated. The resulting set of images shows the motion of the object over one half cycle of the vibration.

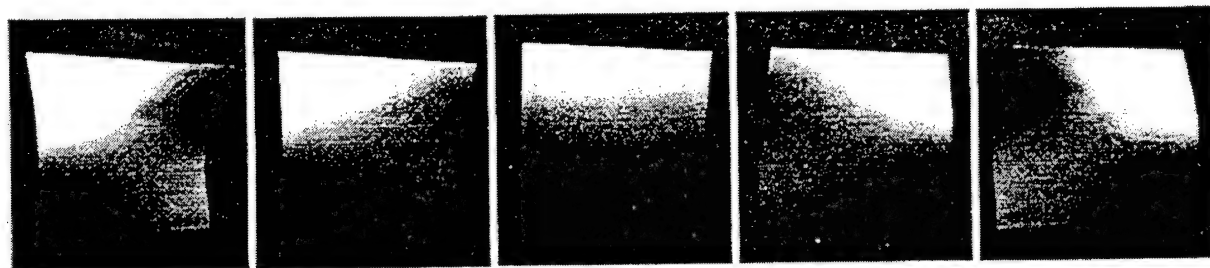


Fig. 6. Shows a set of five images created with z scaling factors, ranging from -1 to 1 by steps of 0.5. The scaling factors were multiplied by the displacement data to compute the displacement of the model's surface for each image. The resulting set of images mimics the displacement that the surface undergoes as the part vibrates at 640 Hz. This capability is particularly useful in animation of the experimental results.

Figure 7 shows a set of images of the same displacement pattern from a range of view points. Notice the extra lump in the upper left corner of the plate in the first image. The phase unwrapping program encountered sufficient noise in the image to introduce an unnecessary 2π transition along a portion of one row of pixels. Such deviations are clearly distinguishable with 3-D rendering, but much less so with other methods of data representation.

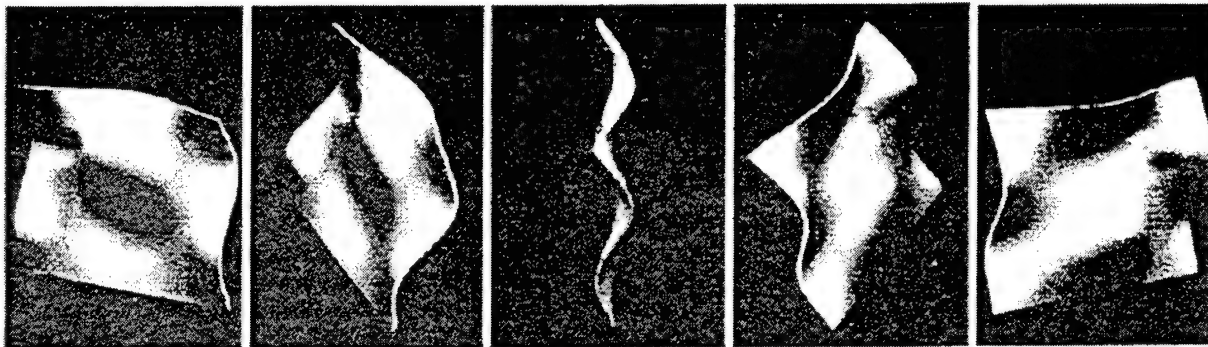


Fig. 7. The set of five images, progressing from left to right, show a "fly-by" as the viewer moves around the object counter-clockwise. The displacements at 2118 Hz were extracted from the holograms shown in Fig. 5. The lighting remains fixed relative to the world of the object.

4.3. Variations of sampling resolution

Finer grid spacing in the triangular mesh reveals increasing amounts of surface texture in the images. The texture results from noise in the source holograms or systematic errors in tuning various experimental parameters. Any changes in the driving frequency among the three holograms due to instability of the excitation source tends to displace the fringes. A similar displacement results from mis-calibration of the phase bias signal. Such displacements manifest themselves as lumpy ridges in the data lying along the fringe lines. Examples of the lumpy ridge effect are shown in Fig. 8.

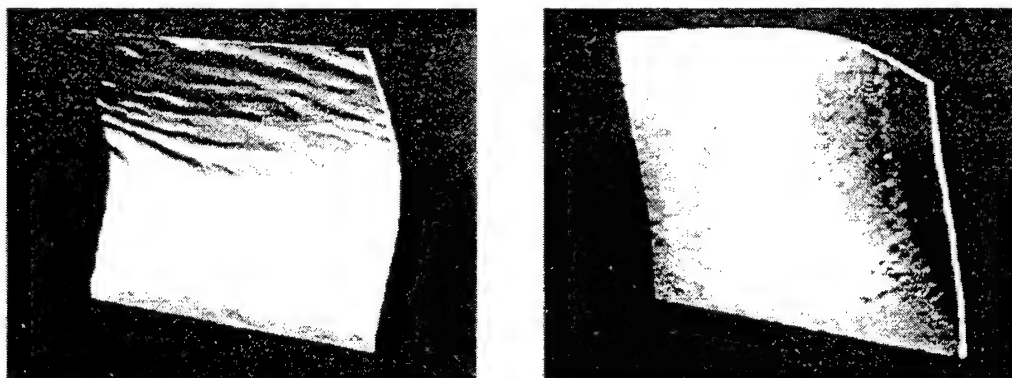


Fig. 8. Two mode shapes of the plate showing ridges that align with the fringes in the holograms from which the displacement maps were created. The result on the left corresponds to the plate driven at 601 Hz and on the right driven at 1082 Hz. The image on the right shows as much surface variation due to noise in the data as to fringe ridges while the image on the left shows very strong fringe ridges. The ridges in the left hand image most likely resulted from inaccurate phase bias settings.

5. CONCLUSIONS

The program outlined in this paper generates exaggerated photo-realistic images of vibratory displacements of rectangular plates. A set of interactive dialog windows give the operator complete control to produce images of the displacements from any viewpoint. As many as ten independent light sources illuminate the object and the user can control their placements and intensities. The resultant images are simple to comprehend, and they contain shading, shape, and occlusion depth cues. Subtle surface features that can easily be lost with other means of data representation are immediately clear and recognizable. The pictures are appealing to the eye, as well. As seen in the results presented in this paper, 3-D rendering can clearly show otherwise unnoticeable patterns such as residual inconsistencies corresponding to fringes in the original holograms. Thus, the more complete data representation which the 3-D images give can help to locate systematic errors or unexpected variations in the data.

While the current program is limited to rectangular flat objects, much of the same code can be applied to non-rectangular surfaces and to curved surfaces. The representation of displacements on curved surfaces introduces new challenges that may require the use of color to indicate movement, translucent undeformed and deformed objects overlapping, or even a combination of the two approaches. Further enhancements will include scaled axes, annotation capabilities, topographic and grid overlays and improved interactive controls for selecting viewing parameters and lighting arrangements.

This three-dimensional data representation approach has already helped to improve the results obtained by EOH and promises to contribute still more to our understanding and presentation capabilities in the future.

6. ACKNOWLEDGMENT

This study was supported by the Flight Dynamics Directorate, Wright Laboratory, Aeronautical Systems Division (AFSC), United States Air Force, Wright-Patterson AFB, OH 45433-6553.

7. REFERENCES

1. F. S. Hill, *Computer graphics*, Macmillan, New York, pp. 384-422, 1990.
2. B-T. Phong, "Illumination for computer generated images," *Communications of the ACM*, 18:311-317, 1975.
3. H. Gouraud, "Continuous shading of curved surfaces," *IEEE Transactions on Computers*, 20:623-629, 1971.
4. R. J. Pryputniewicz and K. A. Stetson, "Measurement of vibration patterns using electro-optic holography", *Laser Interferometry: Quantitative Analysis of Interferograms*, SPIE-1162:456-467, 1989.
5. T. Bushman, "Development of a holographic computing system," *Laser Interferometry: Quantitative Analysis of Interferograms*, SPIE-1162:66-77, 1989.
6. R. J. Pryputniewicz, "Applications of electro-optic holography in vibration studies," *Proc. Spring Conf. on Exp. Mech.*, SEM, Bethel, CT, pp. 912-919, 1991.
7. R. J. Pryputniewicz, "Static and dynamic measurements using electro-optic holography," *Proc. SPIE*, 1554B:790-798, 1991.

Appendix D

**PHASE UNWRAPPING BY LEAST-SQUARES ERROR
MINIMIZATION OF PHASE CURVATURE**

PROCEEDINGS REPRINT

 SPIE—The International Society for Optical Engineering

Reprinted from

Interferometry VI: Techniques and Analysis

12–13 July 1993
San Diego, California



Volume 2003

©1993 by the Society of Photo-Optical Instrumentation Engineers
Box 10, Bellingham, Washington 98227 USA. Telephone 206/676-3290.

Phase unwrapping by least squares error minimization of phase curvature

Thomas W. Bushman, Michael A. Gennert, and Ryszard J. Pryputniewicz

Worcester Polytechnic Institute
Worcester, MA 01609

ABSTRACT

A new method of unwrapping two-dimensional periodically discontinuous phase data is developed in this paper and results from application of the method to electro-optically generated phase data are presented. The method, whose foundations lie in the minimization of the energy of the surface determined by the unwrapped data, fits planar surface patches to previously processed data, then uses the best fit plane's parameters to estimate the value of the pixel under consideration. At each pixel, a new value composed of the sum of the original value and an integral multiple of the magnitude of the phase discontinuity is assigned. Processing proceeds along an expanding wavefront originating from a seed point chosen as the reference for the measurement. The facet based fringe number selection method has been found to be highly reliable even for incomplete, noisy data.

1. INTRODUCTION

This paper describes the phase unwrapping algorithm implemented as a part of a complete, integrated electro-optic holographic interferometry system. The approach, and much of the code are, however, system independent and should provide reliable phase unwrapping for any 2-dimensional array of wrapped phase data which does not contain internal inconsistencies or discontinuities in the phase.

1.1. Problem overview

An electro-optic holography (EOH) system can produce phase maps proportional to surface deformations resulting from either resonant vibration or static displacement of a test part. Vibrations are measured with an electronic form of time-average holography while static displacements are measured with an electronic form of double-exposure holography usually referred to as static EOH. The magnitude of the displacement can be related to the phase by a simple geometric argument, and depends on the orientation of the illumination and viewing vectors as well as the wavelength of the laser light used to illuminate the part. Unfortunately, due to the periodic wavelike nature of light, the solutions by which the phase is derived are inherently discontinuous at regular intervals. The discontinuities follow from the presence of the inverse tangent function in each of the solutions. Each discontinuity corresponds to a 2π or π jump in the phase for static and time-average mode holograms, respectively. These discontinuities must be removed by addition of a fringe number dependent multiple of the magnitude of the phase jump at each point in the image.

To remove discontinuities, the unwrapped phase at any point is calculated to be the data at that point added to the product of the fringe number and the phase jump magnitude. Thus, the value at any point in the unwrapped image depends on the fringe number assigned. The fringe number, in turn, depends on the number of fringes crossed in moving to that point from an initial location chosen to be the origin. Each pixel's dependence on previously processed neighbors suggests that the fringe number at a new location can be determined by the following two step process. First, compute the magnitude of the difference between the new pixel and one of its previously processed neighbors, then, second, assign the new pixel's fringe number to be either the same, one greater or one less than its neighbor's depending on whether the difference between the two is less than a phase jump in magnitude or greater than a phase jump in the positive direction, or in the negative direction, respectively. This solution works when the signal to noise ratio (SNR) of the image is high. However, as the noise increases,

For correspondence please contact: Ryszard J. Pryputniewicz, Center for Holographic Studies and Laser Technology, Dept. of Mechanical Engineering, Worcester Polytechnic Institute, Worcester, MA 01609.

this approach can break down due to rounding of the sharp discontinuities which are expected. Specifically, when one of the phase jumps is rounded, the magnitude of the difference between the new point and its neighbor is no longer greater than the chosen threshold anywhere across the edge. As a result, no phase jump is found and the fringe number assignment is incorrect. Furthermore, since each point's fringe number assignment depends on the assignments made for its previously processed neighbors, errors in the assignments propagate to every subsequent pixel after a mistake has been made.

Further problems result when actual discontinuities exist in the phase data due to abutting or overlapping, but independently moving surfaces in the field of view. At such joints, extra discontinuities appear in the wrapped phase map, further complicating the unwrapping problem. This paper gives a robust algorithm for unwrapping phase in the presence of noisy data, but does not address the difficulties introduced by phase discontinuities created by joints in the object under observation.

1.2. Previous approaches

In a perfect image of wrapped phase, the task of unwrapping is a straight forward operation. Itoh gave a rigorous analysis of the scan line based approach to 2-dimensional phase unwrapping in 1982¹. He showed that, for a consistent set of fringes, first unwrapping along one column, then along each row using the unwrapped value from the initial column as a reference, gives valid results regardless of the location of the initial column. Identical results can also be achieved by operating first on one row, then on all the columns. The unwrapping operation proceeds by comparing successive pairs of pixel values. A threshold value is chosen to be slightly smaller than the magnitude of the wrapped phase jump. Then, whenever the magnitude of the difference is larger than the threshold, the fringe number is incremented or decremented appropriately.

Stetson implemented an algorithm to unwrap phase which works for arbitrarily shaped objects, provided a "mask" can be generated to distinguish the object from the background². Unwrapping proceeds around the interior of the object's border and works its way inward. This approach has the advantage that it can be applied to any shapes, but still suffers from high susceptibility to noise.

A procedure based on cellular automata has been implemented by Ghiglia, Mastin, and Romero³. This iterative procedure operates on the entire image for many iterations before converging. Since the computational burden of this approach is too high for frequent experimentation, another approach was sought in this study.

Vrooman and Maas use an approach that turns out to be very similar to the software described here, but with some important exceptions⁴. Their system uses an expanding wavefront growing out from a starting location, and also uses the magnitude of the modulation at each speckle to weed out bad data. They do not, however, use weighted facets as estimators for the phase.

1.3. Facet based unwrapping

The facet based technique for unwrapping noisy wrapped phase maps can be summarized by the following procedure:

- 1) begin processing by choosing a seed point from which to start the operation,
- 2) at each point along an expanding wavefront growing outward from the seed:
 - 2.1) fit a planar facet to previously processed data within a given neighborhood around the new point,
 - 2.2) use the facet coefficients to estimate the phase at the new point,
 - 2.3) choose a fringe number for the new point to minimize the difference between the estimated and measured values,
- 3) stop when the wavefront hits boundaries or edges.

The procedure outlined above is both robust and reliable for unwrapping noisy wrapped phase maps. The algorithm implementing this procedure consistently succeeds in unwrapping fringes with spacing as small as six pixels. Phase maps created from electronically generated time-average holograms with Bessel function distributed fringe intensities have been unwrapped out to the thirtieth order fringe. In situations where the unwrapper fails, the failure is easily detected within a few pixels of the initial mistake since the fitting error between the facet and the underlying data increases rapidly as the error propagates.

2. ELECTRO-OPTIC HOLOGRAPHY: THEORETICAL OVERVIEW

The EOH system used to capture the data presented here employs techniques previously developed by Stetson and Brohinsky^{5,6}, Stetson and Pryputniewicz⁷, Pryputniewicz⁸, and Bushman⁹. All full field, real-time processing required for the implementation is carried out on an MV200 pipelined image processor in a MaxTD image processing system from Datacube, Inc. The Motorola 68040 VME bus based host computer for the image processing system executes the phase unwrapping algorithm.

2.1. EOH system components

The optical system, Fig. 1, consists of a laser, mirrors, a piezoelectric transducer (PZT) mirror mount, beam expanding lenses, an imaging lens, and a CCD camera. The coherent light beam generated by the laser is split by a half silvered mirror into two portions, the object and the reference beams. The object beam is diverged sufficiently to illuminate the entire object, then the image is focused onto the CCD camera sensor by the imaging lens. Meanwhile, the reference beam is diverged and recombined with the object beam at a partially silvered mirror immediately in front of the camera. When the two beams intersect, the coherent light fields interfere. The CCD camera integrates the intensity of the resulting light field over each 1/30th second frame time. A mirror in the reference beam path is mounted on a PZT positioner such that when a small, computer controlled voltage is applied across the PZT leads, the reference beam's path length is changed by a very small, but carefully controlled amount. A routine within the image processor automatically determines the size of the voltage step required to change the path length of the beam by exactly 1/4 of the wave length of the laser light. This mechanism allows for stepping the phase of one beam relative to the other. The image from the CCD camera is fed to the image processor for capture, manipulation, and display.

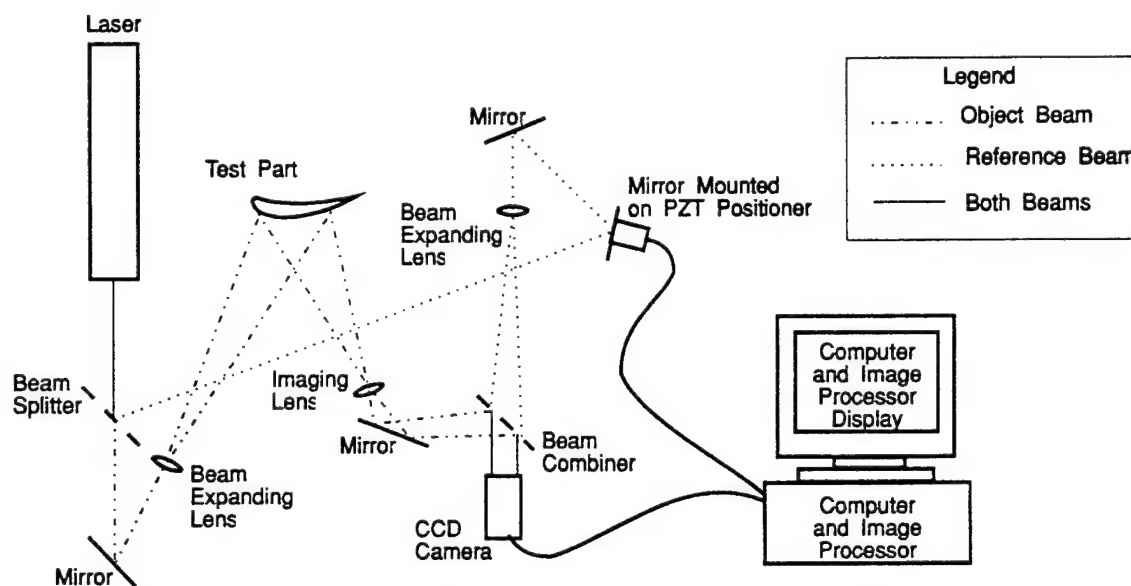


Fig. 1. Electro-optic holography apparatus.

A coherent, linearly polarized planar light field, as generated by the laser, can be described by the solution to Maxwell's equations as

$$F(x, y, t) = \Re\{A(x, y)\exp[-i(\omega t - \phi(x, y))]\}. \quad (1)$$

According to Eq. 1, the electric field, F , along the axis defined by the polarization of the light depends on the amplitude, A , and phase, ϕ , given as a function of absolute position specified by the x, y coordinates. Because of the inherent characteristics of the laser light, the time dependent term in Eq. 1 can safely be ignored, and the resulting formulation provides the basis for the development of the equations for static and time-average holography which follow.

Light reflected from the surface of the object under study is imaged by the camera through the finite aperture of the imaging lens. Facets in the surface microstructure reflect the light in various directions over each small portion of the surface

area. When the image of the surface is formed, each pixel in the sensor receives light from an area of the object surface whose size depends on the size of the aperture. For smaller apertures, fewer distinct facets of the surface microstructure contribute to the light received. This results in a larger scale speckle pattern as viewed by the camera. For EOH systems, each pixel must contain no more than a single speckle. When the phase of the reference beam is deliberately changed relative to the object beam, then the interference between a speckle on the object's surface and the reference beam will also change. For example, if, prior to the phase change, the speckle and the reference beam have identical phase, then the light interferes constructively and the intensity measured at the camera is high. When the phase of the reference beam is changed by 180° , then the speckle and the beam have opposite phase so they interfere destructively. As a result, the intensity at the camera is low. The modulation of speckles by phase shifting one beam relative to the other provides the mechanism which allows the electro-optic systems to function.

2.2. Static mode EOH

In static mode, the EOH system generates a hologram whose fringes indicate static deformation of the surface of the object¹⁰. To produce these results, two sets of images are captured, with the state of stress changed between the two. Each image set is composed of four frames, where a phase increment is added to the reference beam relative to the object beam between each frame in the set⁸.

The two beams which interact at the beam combiner can be described by

$$F_o(x, y) = A_o(x, y)\exp[i\phi_o(x, y)] \quad (2)$$

and

$$F_r(x, y) = A_r(x, y)\exp[i\phi_r(x, y)] , \quad (3)$$

where F_o and F_r represent the object beam and the reference beam, respectively.

When the two beams interact, the intensity measured at the CCD array of the camera is given by the complex magnitude of the sum of Eqs 2 and 3, that is,

$$I(x, y) = [F_o(x, y) + F_r(x, y)][F_o(x, y) + F_r(x, y)]^* = I_o(x, y) + I_r(x, y) + 2A_o(x, y)A_r(x, y)\cos\Delta\phi(x, y) , \quad (4)$$

where $I_o(x, y) = A_o^2(x, y)$, $I_r(x, y) = A_r^2(x, y)$ and $\Delta\phi(x, y) = \phi_o(x, y) - \phi_r(x, y)$. Equation 4 represents the pixel intensities of a frame of data captured by the image processing system prior to the introduction of phase shifts.

In the following discussion, the x and y arguments of the functions are dropped to simplify the mathematical formulation, and constant factors from Eq. 4 are grouped so that $C = I_o + I_r$ and $D = 2A_oA_r$. A phase step of 90° is introduced between frames of video data by translating the PZT mounted mirror to a new position such that the path length of the reference beam is exactly one quarter wavelength shorter. Then a four image, phase stepped set of reference images captured prior to the deformation of the object can be described by the following set of equations:

$$I_1 = C + D \cos \Delta\phi , \quad I_2 = C + D \sin \Delta\phi , \quad I_3 = C - D \cos \Delta\phi \text{ and } I_4 = C - D \sin \Delta\phi . \quad (5)$$

The set of images captured after the deformation can be described by four more equations:

$$I'_1 = C' + D' \cos \Delta\phi' , \quad I'_2 = C' + D' \sin \Delta\phi' , \quad I'_3 = C' - D' \cos \Delta\phi' \text{ and } I'_4 = C' - D' \sin \Delta\phi' . \quad (6)$$

The deformation must be small enough so that the speckle pattern does not decorrelate, and the experimental environment must be stable so that random fluctuations of the phase are held to a minimum. Assuming these conditions to hold, then $C' \approx C$ and $D' \approx D$. Finally, let $\Omega = \Delta\phi - \Delta\phi'$, then the following two combinations of the eight images, described by Eqs 5 and 6, can be formed which, when simplified, yield a pair of images dependent only on the sine and cosine of the difference in phase between the light field prior to the deformation and the light field subsequent to the deformation, that is,

$$16D^2 \sin \Omega = [(I_1 - I_3) + (I'_2 - I'_4)]^2 + [(I_2 - I_4) + (I'_1 - I'_3)]^2 - [(I_1 - I_3) - (I'_2 - I'_4)]^2 - [(I_2 - I_4) - (I'_1 - I'_3)]^2 \quad (7)$$

and

$$16D^2 \cos \Omega = [(I_1 - I_3) + (I'_1 - I'_3)]^2 + [(I_2 - I_4) + (I'_2 - I'_4)]^2 - [(I_1 - I_3) - (I'_2 - I'_4)]^2 - [(I_2 - I_4) - (I'_1 - I'_3)]^2 . \quad (8)$$

The measured change in phase due to the deformation, Ω' , can then be found from the inverse tangent of the ratio of Eqs 7 and 8 as

$$D - 6$$

$$\Omega' = \arctan\left(\frac{\sin \Omega}{\cos \Omega}\right), \quad (9)$$

where Ω is referred to as the fringe-locus function, constant values of which define fringe loci on the object's surface.

Notice that, due to the arctan function, the measured phase difference function, $\Omega'(x, y)$, wraps back to zero each time the actual phase difference function, $\Omega(x, y)$, passes through $(2N - 1)\pi$, where N is an integer. These discontinuities must be removed by the phase unwrapper to reconstruct a continuous phase function from which actual displacement values can be computed.

2.3. Time-average mode EOH

In time-average mode, the EOH system generates a hologram whose fringes indicate the amplitude of vibration of the surface of the object¹⁰. To produce these results, one set of images is captured as the test part undergoes sinusoidal vibration in a standing wave pattern - a resonant mode. The image set is composed of four images, where a phase increment is added to the reference beam relative to the object beam between each frame in the set^{5-7,9}.

The two beams which interact at the beam combiner can be described by

$$F_o(x, y) = A_o(x, y) \exp\{i[\phi_o(x, y) + \mathbf{K}(x, y) \cdot \mathbf{L}(x, y) \sin \omega t]\} \quad \text{and} \quad (10)$$

$$F_r(x, y) = A_r(x, y) \exp[i\phi_r(x, y)] \quad (11)$$

The second term in the exponential of Eq. 10 describes the time dependent variation of the phase of the object beam which results from the sinusoidal motion of the object at frequency ω . The vector \mathbf{K} denotes the sensitivity vector which bisects the angle formed by the illumination and observation vectors, and the vector \mathbf{L} denotes the displacement of the object for each point in the image. The sinusoidal term accounts for the motion of the object over the interval during which the camera integrates light to collect a frame of data.

When the two beams interact, the intensity measured at the CCD array of the camera is given by the real part of the time-average of the complex magnitude of the sum of the beams' electric fields defined by Eqs 10 and 11, that is,

$$I(x, y) = \Re \left\{ \frac{1}{T} \int_0^T [F_o(x, y) + F_r(x, y)][F_o(x, y) + F_r(x, y)]^* dt \right\} \quad (12)$$

Substituting $\Delta\phi$ for $\phi_o - \phi_r$, Eq. 12 can be expanded and simplified to give

$$I(x, y) = A_o^2(x, y) + A_r^2(x, y) + 2A_o(x, y)A_r(x, y) \cos \Delta\phi(x, y) \left\{ \frac{1}{T} \int_0^T \cos[\mathbf{K}(x, y) \cdot \mathbf{L}(x, y) \sin \omega t] dt \right\} \quad (13)$$

The integral at the end of Eq. 13 is often referred to as the characteristic fringe function and denoted by $M[\Omega(x, y)]$. In general,

$$\lim_{T \rightarrow \infty} \frac{1}{T} \int_0^T \cos[\mathbf{K}(x, y) \cdot \mathbf{L}(x, y) \sin \omega t] dt = J_0[\Omega(x, y)] \quad (14)$$

is a zero order Bessel function of the first kind, where $\Omega(x, y) = \mathbf{K}(x, y) \cdot \mathbf{L}(x, y)$. For time-average holography, where the integration period, T , is the frame time of the camera, the characteristic fringe function will be $J_0[\Omega(x, y)]$ when $\omega \ll T$, that is, as long as the period of the vibration of the object is much smaller than 1/30th of a second. In practice, frequencies of 60 Hz and higher give good results.

For the remainder of the discussion, the x and y arguments of the functions are dropped to simplify the mathematical formulation, and constants in Eq. 13 are grouped so that $C = I_o + I_r = A_o^2 + A_r^2$ and $D = 2A_o A_r$. Once again, a phase step of 90° is introduced between frames of video data. Then, a phase stepped set of four images as captured by the image processor can be described by the following set of equations:

$$I_1 = C + D \cos \Delta\phi J_0(\Omega) \quad , \quad I_2 = C + D \sin \Delta\phi J_0(\Omega) \quad , \quad I_3 = C - D \cos \Delta\phi J_0(\Omega) \quad \text{and} \quad I_4 = C - D \sin \Delta\phi J_0(\Omega) \quad (15)$$

The deformation must be small enough so that the speckle pattern does not decorrelate. Then, all the C 's and all the D 's in Eq. 15 are equal and the four equations can be solved to eliminate C and $\Delta\phi$ yielding

$$I_{h_1} = 4D^2 J_0^2(\Omega) = (I_1 - I_3)^2 + (I_2 - I_4)^2. \quad (16)$$

According to Eq. 16, the resulting hologram, I_{h_1} , is defined in terms of three unknowns, A_o^2 and A_r^2 comprising D^2 , and Ω contained in the argument of the J_0 . In order to solve for Ω , two additional equations must be generated in such a way that the three unknowns are related in three equations. This is accomplished by introducing a bias signal on the reference beam to shift the Bessel function fringe pattern by a known amount, first to one side, then to the other side of the unbiased fringes.

A bias signal with an amplitude denoted by B , and phase such that the phases of the two beams are identical at the camera, adds a new term to the expression which describes the reference beam so that

$$F_{N_r} = A_r(x, y) \exp \{ i[\phi_r(x, y) + B \sin(\omega t)] \}. \quad (17)$$

where the subscript N indicates the negative biased beam and the small subscript r is used to denote the reference beam.

Equation 17 represents the electric field of the reference beam modulated by the sinusoidal bias signal for the first of the two biased results called the negative biased hologram. The biased reference beam interacts with the object beam represented in Eq. 10 to give an intensity at the camera of

$$I_N = [F_o + F_{N_r}][F_o + F_{N_r}]^* = A_o^2 + A_{N_r}^2 + 2A_o A_{N_r} \cos \Delta\phi \left\{ \frac{1}{T} \int_0^T \cos[(\mathbf{K} \cdot \mathbf{L} - B) \sin \omega t] dt \right\}, \quad (18)$$

Again, a set of four phase stepped images derived from Eq. 18 and identical to Eq. 15 except for the bias, is captured. The negative biased hologram is computed from these four images as

$$I_{h_2} = 4D^2 J_0^2(\Omega - B) = (I_{N_1} - I_{N_3})^2 + (I_{N_2} - I_{N_4})^2. \quad (19)$$

The third result, called the positive biased hologram, is generated by changing the phase of the bias signal by 180° . Then, the reference beam can be represented by

$$F_{P_r} = A_r \exp \{ i[\phi_r + B \sin(\omega t + \pi)] \} = A_r \exp \{ i[\phi_r - B \sin(\omega t)] \}. \quad (20)$$

where the subscript P indicates the positive biased beam and the small subscript r is used to denote the reference beam. The positive biased reference beam interacts with the object beam in Eq. 10 to give an intensity at the camera of

$$I_P = [F_o + F_{P_r}][F_o + F_{P_r}]^* = A_o^2 + A_{P_r}^2 + 2A_o A_{P_r} \cos \Delta\phi \left\{ \frac{1}{T} \int_0^T \cos((\mathbf{K} \cdot \mathbf{L} + B) \sin \omega t) dt \right\}, \quad (21)$$

Again, the positive biased hologram is computed from a set of four phase stepped images derived from Eq. 21 to give

$$I_{h_3} = 4D^2 J_0^2(\Omega + B) = (I_{P_1} - I_{P_3})^2 + (I_{P_2} - I_{P_4})^2. \quad (22)$$

Now we have three equations, given by Eqs 16, 19 and 22, written in terms of the three unknowns. The exact solution for Ω is not simple since the Bessel function is both nonlinear and non-periodic. However, an approximate solution is possible if the fringe function is assumed to be a cosine squared rather than a Bessel function squared. This assumption introduces errors in the computed results, but these errors are directly dependent on the computed phase value and can be corrected after the phase is unwrapped by indexing into an appropriate lookup table (LUT).

The solution for the phase at each point, assuming the hologram contains cosine squared fringes is

$$\Omega = \frac{1}{2} \arctan \left[\left(\frac{1 - \cos 2B}{\sin 2B} \right) \frac{I_{h_3} - I_{h_2}}{2I_{h_1} - I_{h_3} - I_{h_2}} \right]. \quad (23)$$

Notice that, similar to static mode, values for the solution wrap back to zero each time the argument of the arctan function passes across a $(2N - 1)\frac{\pi}{2}$ boundary, where N are integer values. These discontinuities must be removed by unwrapping the phase to build the continuous phase function required to perform the correction and subsequently compute actual displacement values from the data.

The unwrapped Ω values thus computed are corrected by indexing into an LUT generated by finding the inverse mapping to translate from the phase found assuming cosine squared fringes to the correct phase resulting from Bessel squared

fringes. To build such a LUT, first an array is filled with values corresponding to a sampled set of all possible values that the processed data may take. Such an array can be computed by

$$LUT(\Omega_B) = \frac{1}{2} \arctan \left[\left(\frac{1 - \cos 2B}{\sin 2B} \right) \frac{J_0^2(\Omega_B + B) - J_0^2(\Omega_B - B)}{2J_0^2(\Omega_B) - J_0^2(\Omega_B + B) - J_0^2(\Omega_B - B)} \right]. \quad (24)$$

Second, the LUT must be inverted to map from the assumed cosine squared fringe domain to the actual Bessel squared fringe domain. Values for the correction LUT are computed at points separated by a fixed interval in the Bessel phase argument, Ω_B . When the LUT is inverted, the intervals between LUT entries are no longer uniform, so care must be taken that an interpolation procedure computes the new values for the inverse LUT at regular intervals in the inverse domain. The inverse LUT is denoted by $LUT^{-1}(\Omega_B)$.

The correction is applied after the phase is unwrapped to compute the actual phase of the Bessel squared fringes, Ω_C , and takes the form of

$$\Omega_C = LUT^{-1}(\Omega_i) \quad (25)$$

at every point in the image, where the i subscript indicates that the value of the uncorrected phase is quantized, then used as an index into the correction table. Figure 2 shows the correction LUT over the range of the first four Bessel squared fringes in an unbiased hologram.

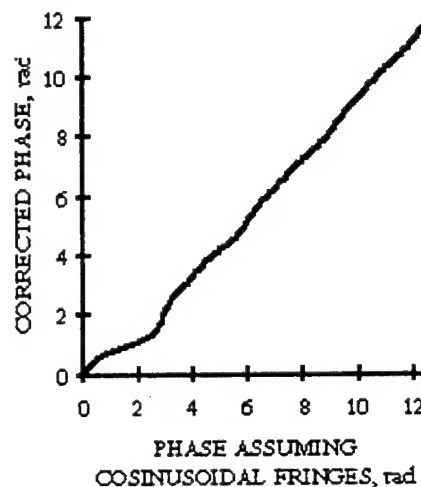


Fig. 2. Correction lookup table.

3. PHASE UNWRAPPING BY FACET BASED ESTIMATION

Motivation for the facet based approach to phase unwrapping grew from a study of energy minimization techniques applied to early vision problems. Geman and Geman used a simulated annealing algorithm to generate the lowest energy configuration of pixel values in the context of recovering the original data from a noise contaminated image¹¹. The simulated annealing algorithm operates on subsets of the neighborhood surrounding a pixel called cliques. Iterations of the algorithm seek to minimize the interaction potential energy among members of each clique. By this definition, higher energy values are assigned as the surface whose height is determined by the pixel values diverges from horizontal and planar. To reconstruct a continuous phase surface from the discontinuous wrapped phase, the energy to be minimized must be redefined to allow surfaces of any slope, as long as the slope changes smoothly. Thus, for phase unwrapping, we wish to minimize the curvature of the phase surface.

To determine the fringe number at a point in the image, we wish to use the noisy, often incomplete data provided by the point's neighbors to "guess" at an appropriate value for the phase at the point. Haralick describes a technique for fitting a facet described by a set of orthogonal polynomials to noisy data in order to subsequently locate the best edge contained within the boundaries of the facet¹². His implementation uses polynomials up to third order to match the polynomial model to the image data, and performs a least squares error fit to determine the values for the coefficients of the polynomials. These coefficients can then be used to find the location and direction of the highest slope in the facet. For our purposes, a first order planar fit is used to fit the facets to the data. By fitting a plane to the phase, the fit's sensitivity to noise is minimized, and the estimate for the phase will be the value which minimizes the curvature of the phase surface.

Based on the foundation of these image processing and machine vision techniques, the phase unwrapping approach outlined in Sections 3.1 through 3.4 has been developed.

3.1. Weighting function

As mentioned at the beginning of Section 2, each pixel in the image is exposed to either one or a portion of one speckle generated by the reflected light from the object. The image created in the EOH process can be conceived of as a measure of the modulation induced in each speckle by changing the phase of one of the two beams relative to the other. Because the

dynamic range of the imaging system is limited and noise is always present due to the electronics in the system as well as other influences, those pixels which have low modulation relative to the noise provide less trustworthy results. In order to make more meaningful estimates for the phase value at each point, the magnitude of each speckle's modulation can be used to weight the speckles in the facet fitting routine.

An image of the magnitude of each speckle's modulation is generated by capturing time-average data of the object at rest. Pixels whose modulation magnitudes do not exceed the system's noise level do not contribute meaningful information to the image. Therefore, they are removed from consideration by setting their weights to zero. This is accomplished by a two step process: first, measure the level of system noise by capturing the difference between frames of data without any phase stepping. Second, divide all the modulation magnitude pixel values by the measured noise level and truncate to integer values. This procedure generates a weight function with zero values where the data cannot be trusted and small integer weights whose values increase with greater reliability.

3.2. Processing order

Unwrapping proceeds along an expanding wavefront emanating from a user selected seed point. The seed is generally chosen to lie within a stationary node in time-average holograms, or within a fringe abutting a fixed boundary in static holograms. The 8-connected neighbors of the seed pixel whose weights are greater than zero are placed in a first-in-first-out (FIFO) list. Processing progresses by removing the next pixel from the head of the list, assigning it a fringe number, then placing all of its 8-connected neighbors whose weights are not zero and who have not previously been put into the list at the tail of the list. This processing order gives the appearance of a wavefront propagating outward from the seed and is guaranteed to visit every pixel which has an 8-connected path back to the seed by way of non-zero weighted pixels. As each pixel is put into the list, it is marked with a flag bit to indicate that it has already been visited and should not be put into the list again. Also, another flag bit is set to indicate that a pixel has had a fringe number assigned. Only those pixels which have been thus marked are used in the facet for estimating the phase of subsequent pixels.

3.3. Planar facet parameter computation

As each pixel is taken from the list to have its fringe number assigned, a rectangular region around the pixel is used to estimate what the phase at that point should be. As the total area of the rectangle increases, processing time also increases, but the estimates become less sensitive to noise. When the facets grow as large as the features of the surface determined by the unwrapped phase, then the estimates will fail to follow the contours of the surface and the unwrapping will fail. Empirical evidence has shown that facets which are no larger than the span of the narrowest fringes, but are at least 7×7 pixels in size, perform well.

Data values are weighted and tend to be clustered in one region of the facet since only those members of the neighborhood which have already been processed are considered when computing the facet parameters. Therefore, a generalized least squares fit must be used, and simplifications which are normally possible with a model composed of an orthogonal polynomial set cannot be made. Planar facets can be modeled by a function composed of the linear combination of a set of 0'th and 1'st order polynomials as

$$P(x, y) = Ax + By + C. \quad (26)$$

To find the best fit of the model with the data, the square of the error of the model, $P(x, y)$, relative to the data, $z(x, y)$, must be minimized. The squared error, ϵ^2 , is computed from the sum of the squares of the deviations at each point, scaled by the weight function, represented by $w(x, y)$, over a neighborhood of horizontal extent $2N+1$ and vertical extent $2M+1$, centered at the point (x, y) , so¹³

$$\begin{aligned} \epsilon^2(x, y) &= \sum_{j=-M}^M \sum_{i=-N}^N \{ [P(i, j) - z(x+i, y+j)] w(x+i, y+j) \}^2 = \\ &= \sum_{j=-M}^M \sum_{i=-N}^N \{ [Ai + Bj + C - z(x+i, y+j)] w(x+i, y+j) \}^2. \end{aligned} \quad (27)$$

Note that $w(x, y)$ will be zero for pixels that have not yet been processed. Also, the model's origin is at the pixel of interest, so the estimated value at that pixel is just C . We wish to find values for A , B , and C which minimize the error. To

find $\min_{A,B,C} \epsilon^2$ three equations are required where, in each, the partial derivative of ϵ^2 is taken with respect to one of the unknowns and set equal to zero:

$$0 = \frac{\partial \epsilon^2(x, y)}{\partial A} = \sum_j \sum_i 2iw^2(x+i, y+j)[Ai + Bj + C - z(x+i, y+j)] , \quad (28)$$

$$0 = \frac{\partial \epsilon^2(x, y)}{\partial B} = \sum_j \sum_i 2jw^2(x+i, y+j)[Ai + Bj + C - z(x+i, y+j)] , \quad (29)$$

$$0 = \frac{\partial \epsilon^2(x, y)}{\partial C} = \sum_j \sum_i 2w^2(x+i, y+j)[Ai + Bj + C - z(x+i, y+j)] . \quad (30)$$

Equations 28 to 30 can be expressed in a single matrix equation of the form $\mathbf{0} = \mathbf{A}\mathbf{x} - \mathbf{b}$, yielding

$$\begin{bmatrix} 0 \\ 0 \\ 0 \end{bmatrix} = \begin{bmatrix} \sum_j \sum_i i^2 w^2(x+i, y+j) & \sum_j \sum_i ijw^2(x+i, y+j) & \sum_j \sum_i iw^2(x+i, y+j) \\ \sum_j \sum_i ijw^2(x+i, y+j) & \sum_j \sum_i j^2 w^2(x+i, y+j) & \sum_j \sum_i jw^2(x+i, y+j) \\ \sum_j \sum_i iw^2(x+i, y+j) & \sum_j \sum_i jw^2(x+i, y+j) & \sum_j \sum_i w^2(x+i, y+j) \end{bmatrix} \begin{bmatrix} A \\ B \\ C \end{bmatrix} - \begin{bmatrix} \sum_j \sum_i iz(x+i, y+j)w^2(x+i, y+j) \\ \sum_j \sum_i jz(x+i, y+j)w^2(x+i, y+j) \\ \sum_j \sum_i z(x+i, y+j)w^2(x+i, y+j) \end{bmatrix} . \quad (31)$$

Redistributing terms in Eq. 31 and multiplying both sides by the inverse of \mathbf{A} gives

$$\begin{bmatrix} A \\ B \\ C \end{bmatrix} = \begin{bmatrix} \sum_j \sum_i i^2 w^2(x+i, y+j) & \sum_j \sum_i ijw^2(x+i, y+j) & \sum_j \sum_i iw^2(x+i, y+j) \\ \sum_j \sum_i ijw^2(x+i, y+j) & \sum_j \sum_i j^2 w^2(x+i, y+j) & \sum_j \sum_i jw^2(x+i, y+j) \\ \sum_j \sum_i iw^2(x+i, y+j) & \sum_j \sum_i jw^2(x+i, y+j) & \sum_j \sum_i w^2(x+i, y+j) \end{bmatrix}^{-1} \begin{bmatrix} \sum_j \sum_i iz(x+i, y+j)w^2(x+i, y+j) \\ \sum_j \sum_i jz(x+i, y+j)w^2(x+i, y+j) \\ \sum_j \sum_i z(x+i, y+j)w^2(x+i, y+j) \end{bmatrix} . \quad (32)$$

Equation 32 can be readily solved at each point (x, y) to obtain

$$A = \frac{I_{aa}g + I_{bh} + I_{ci}}{adf - ae^2 - b^2f + 2bce - c^2d} , B = \frac{I_{bg} + I_{dh} + I_{ei}}{adf - ae^2 - b^2f + 2bce - c^2d} \text{ and } C = \frac{I_{cg} + I_{eh} + I_{fi}}{adf - ae^2 - b^2f + 2bce - c^2d} , \quad (33)$$

where the x and y arguments have been omitted for clarity and the following substitutions have been made:

$$a(x, y) = \sum_j \sum_i i^2 w^2(x+i, y+j) , \quad b(x, y) = \sum_j \sum_i ijw^2(x+i, y+j) , \quad c(x, y) = \sum_j \sum_i iw^2(x+i, y+j) ,$$

$$d(x, y) = \sum_j \sum_i j^2 w^2(x+i, y+j) , \quad e(x, y) = \sum_j \sum_i jw^2(x+i, y+j) , \quad f(x, y) = \sum_j \sum_i w^2(x+i, y+j) ,$$

$$g(x, y) = \sum_j \sum_i iz(x+i, y+j)w^2(x+i, y+j) ,$$

$$h(x, y) = \sum_j \sum_i jz(x+i, y+j)w^2(x+i, y+j) ,$$

$$i(x, y) = \sum_j \sum_i z(x+i, y+j)w^2(x+i, y+j) ,$$

$$I_{aa}(x, y) = d(x, y)f(x, y) - e^2(x, y) , \quad I_{bb}(x, y) = c(x, y)e(x, y) - b(x, y)f(x, y) , \quad I_{cc}(x, y) = b(x, y)e(x, y) - c(x, y)d(x, y) ,$$

$$I_{da}(x, y) = a(x, y)f(x, y) - c^2(x, y) , \quad I_{dc}(x, y) = b(x, y)c(x, y) - a(x, y)e(x, y) \text{ and } I_{fd}(x, y) = a(x, y)d(x, y) - b^2(x, y) .$$

When the coordinates of the pixels in the neighborhood are transformed such that the center pixel, for which the estimated phase value is desired, is at the origin, then the estimated phase value resulting from the facet fit is simply the value of C . Given the estimate C and the measured phase $z(x, y)$, a fringe number, n , must be chosen to minimize the difference between the two; that is, find $\min_n \{|C - [z(x, y) + n\pi]| \}$ for time-average or $\min_n \{|C - [z(x, y) + 2n\pi]| \}$ for static holograms.

3.4. Iterated fitting to achieve minimum curvature

After the phase has been unwrapped by the sweeping wavefront, each pixel's neighborhood is more completely filled in than it was when the fringe number was initially assigned during the unwrapping process. To take advantage of the extra

information available, facets are fit at every point in the data again and any mislabeled pixels are corrected. The points are visited in a raster scanned order. This process is repeated until no more changes occur anywhere in the data over an entire scan. Once this process has converged, the state for which the curvature is minimized has been found.

3.5. Smoothing with facets

Due to the influence of various noise sources, the unwrapped EOH data generated by the system are generally not smooth. Furthermore, any pixel sites whose weight values were zero contain no data. To fill in the disregarded points and produce a more uniform surface, the facet fitting routine can be used once again. A new set of data is created where the value at each point is assigned the value of the estimate returned by the facet fitter.

Whether to smooth the data is a philosophical problem with many ethical ramifications. In general, smoothing or otherwise altering data for presentation should be avoided, but, given that the data measured here correspond to continuous displacements of nearly rigid surfaces, were it not for the noise, the measurements would undoubtedly give smooth results. Therefore, facet based smoothing is provided as an option in the software. In using planar facets to perform the fitting, we assume that the size of the features in the data are large compared to the size of the facets. Were we to employ quadratic facet fitting for the smoothing step, this assumption would be relaxed, but the sensitivity to noise would also be increased. Future versions of the algorithm may include quadratic fitting for the smoothing as an option.

4. RESULTS

This section contains examples which show the capabilities of the new phase unwrapping technique as applied to image data generated by an EOH system. The automatic boundary detection which results from the use of the weighting function is demonstrated in Fig. 3. To show the fringe densities that the system can correctly analyze, a bending example processed with the static mode algorithm in the EOH system is shown in Fig. 4. Figures 5 and 6 show time-average results highlighting the unwrapper's ability to follow compound curves in the data.

4.1. Static mode examples

Figures 3 and 4 show examples of phase unwrapping applied to static mode EOH data.

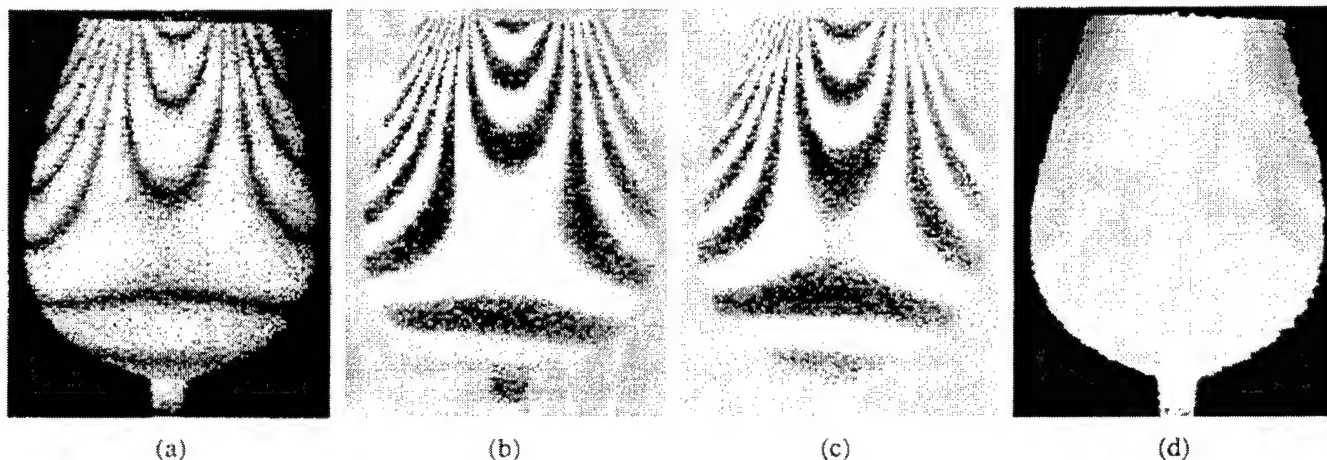


Fig. 3. Wine goblet statically loaded with a weight placed across the top of the glass. Image (a) shows the display mode hologram. Images (b) and (c) show the sinusoidal and cosinusoidal data mode fringe patterns, respectively. Image (d) shows the fringe numbers assigned over the area processed, and illustrates the automatic boundary detection that results from the use of the weighting function.

The weighting function provides a means of automatically locating exterior boundaries of objects in the image. Since the weights are computed from the modulation magnitude at all points in the image, and the modulation magnitude is very small anywhere that the object beam does not diffusely reflect from the surface of the object of interest, the weights outside the object are generally zero. As the unwrapping approaches an object boundary, all the zero weighted points outside the

object are ignored. As a result, processing naturally stops at object boundaries. The example in Fig. 3 shows the effect of this automatic boundary detection.

Facet based phase unwrapping has proven to be reliable and effective. In a static mode hologram of a bending beam, the unwrapper successfully processed 40 fringes across 288 pixels. This implies that fringes spaced only 7 pixels apart can be interpreted correctly. Figures 4a to 4d show the image data at various stages during the process of deriving the displacement data and Figs 4e to 4g show the displacement data.

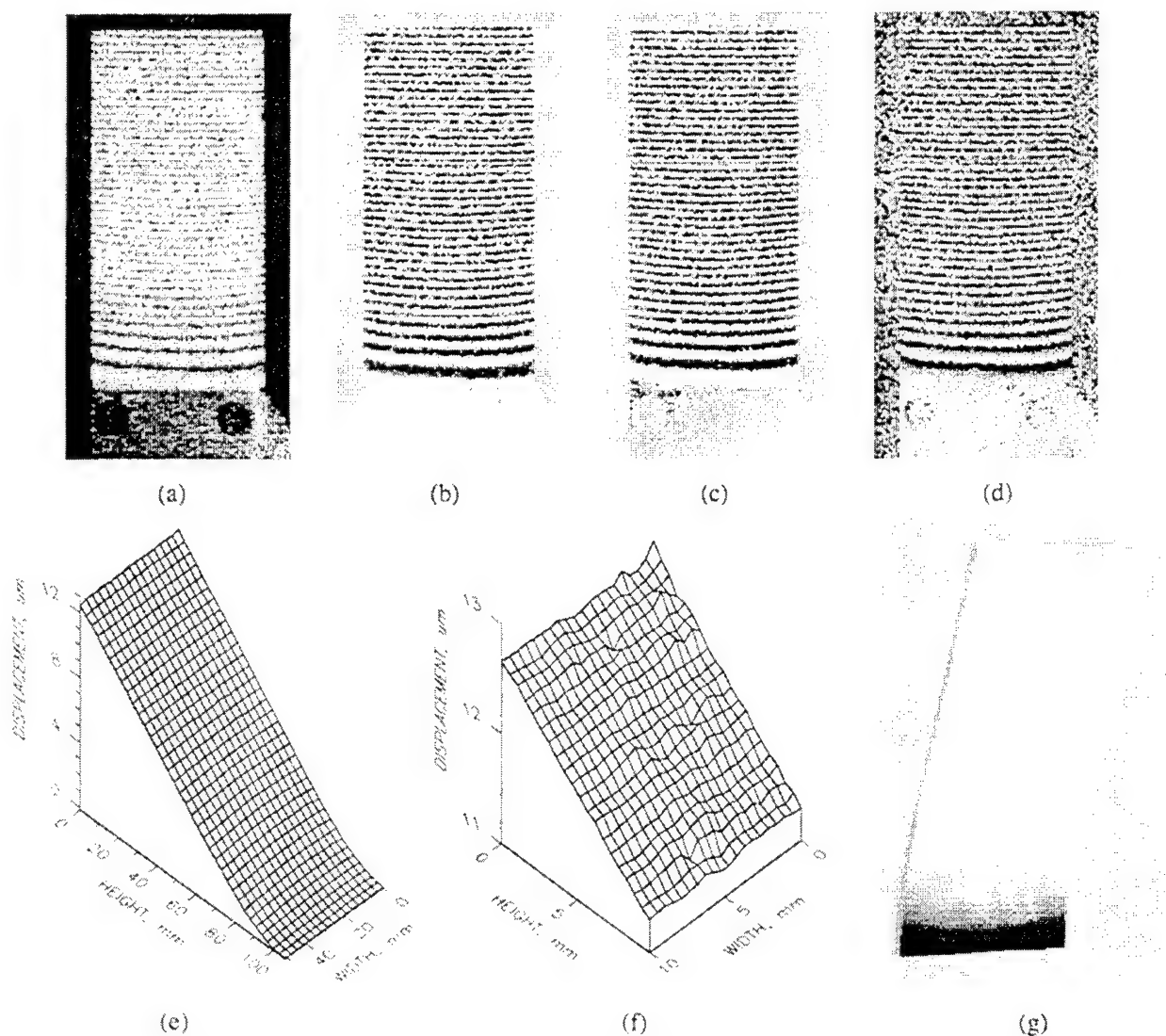


Fig. 4. - Static bending of a 101.6 mm x 50.8 mm x 3.175 mm aluminum plate. The plate was fixed at the bottom and a force was applied from the back of the plate approximately in its middle and pointing toward the camera. The static display mode hologram is shown in (a) while the sinusoidal and cosinusoidal data mode holograms are shown in (b) and (c). The wrapped phase computed from (b) and (c) is shown in (d). In these images, there are 40 fringes across the 288 pixel height of the plate. (e) to (g) show renderings of the unwrapped data. The wireframe plot in (e) shows the data converted to metric coordinates and (f) shows a zoomed portion of the upper right corner of the data rendered in (e). The small scale random variations visible in (f) are caused by the various sources of noise in the system. The image in (g) is a shaded 3-D rendering of the displacement data mapped onto a rectangular plate.

4.2 Time-average mode examples

Examples of time-average mode operation are given in Figs 5 and 6. Time-average mode allows real-time observation of fringe patterns indicative of the displacement of the object's surface in resonant vibration modes, as well as the capture of data for processing. As an operator scans through a range of excitation frequencies driving the part under observation, fringe patterns appear and disappear as the driving frequency passes through the part's resonances. The operator can capture image data for quantitative analysis after a resonant mode has been found by this real-time observation.

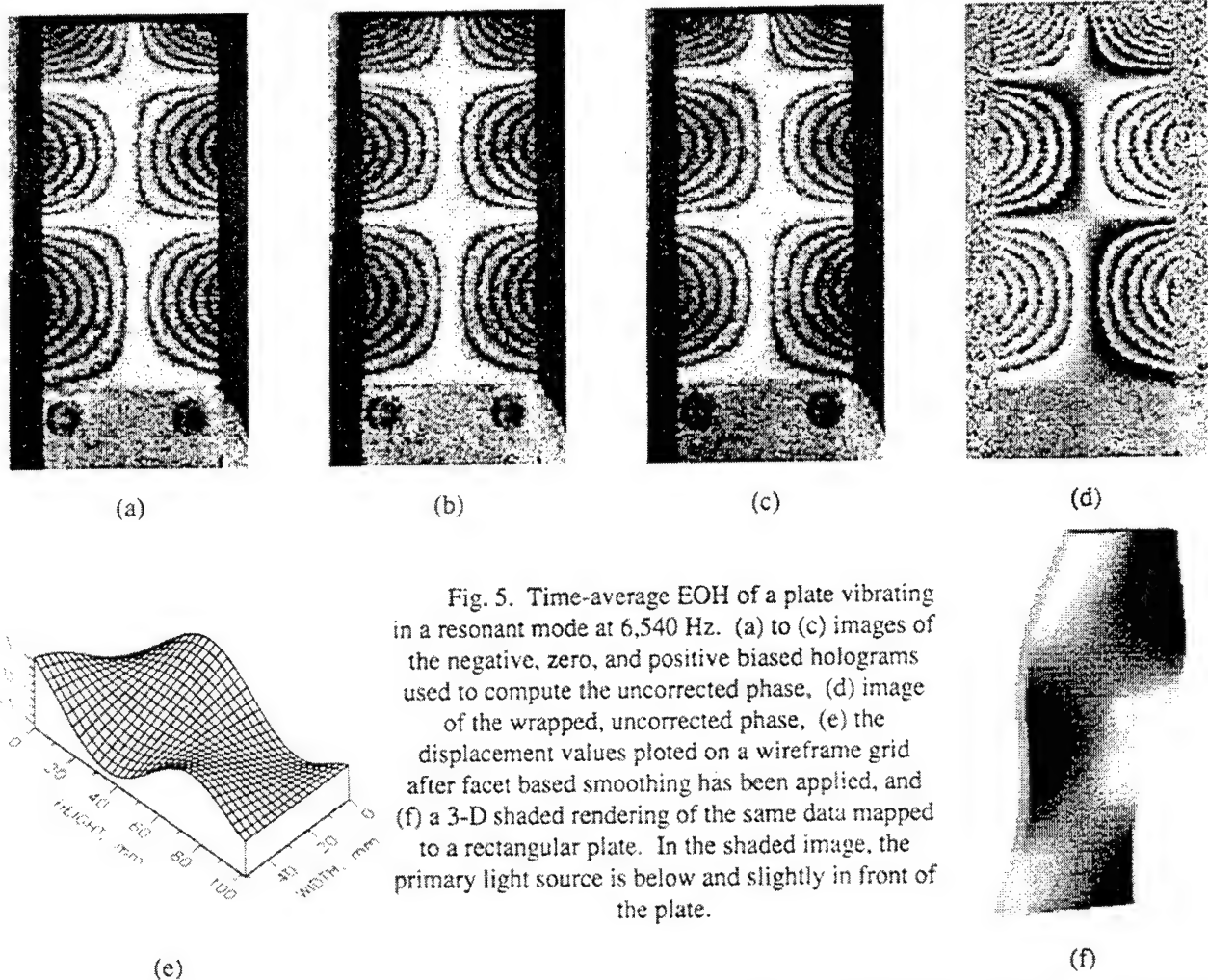
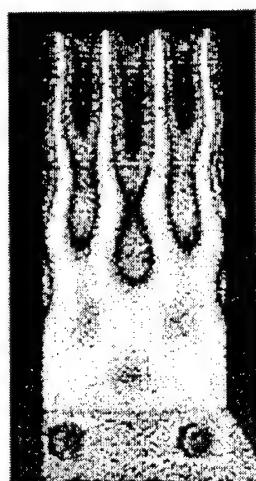


Fig. 5. Time-average EOH of a plate vibrating in a resonant mode at 6,540 Hz. (a) to (c) images of the negative, zero, and positive biased holograms used to compute the uncorrected phase, (d) image of the wrapped, uncorrected phase, (e) the displacement values plotted on a wireframe grid after facet based smoothing has been applied, and (f) a 3-D shaded rendering of the same data mapped to a rectangular plate. In the shaded image, the primary light source is below and slightly in front of the plate.

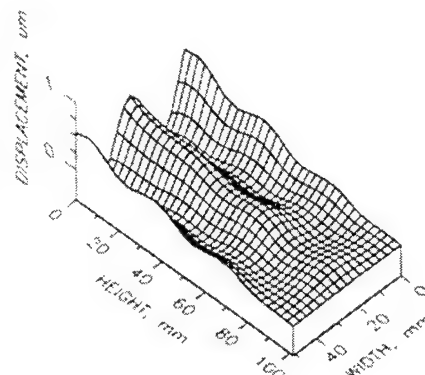
Notice that the surface displacements computed from the phase data undergo rapid changes in slope, especially in Fig. 6. Even in the presence of such high curvature, the planar facet based unwrapper can make a good local estimate of the expected phase at the next pixel. These images were unwrapped and smoothed with a 9x9 pixel facet which corresponds to roughly 1x1 millimeter in real coordinates. Since this size is small compared to the curving features of the surface, the unwrapper is able to follow the surface faithfully and little distortion is introduced in the smoothed output.

For all the examples, the first stage of processing - the actual unwrapping - required from 1.5 to 2.5 minutes. The energy minimization iterations make relatively small changes to the overall results but require the most time to complete. For these images, 2 or 3 passes were required taking from 6 to 10 minutes. This step can be skipped with minimal impact on the results. Finally, the smoothing step required from 2 to 3 minutes to process and save the data.

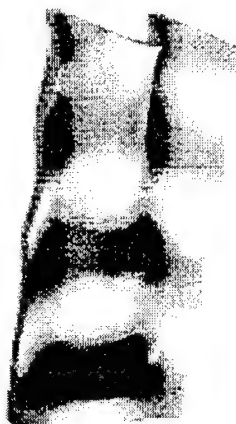


(a)

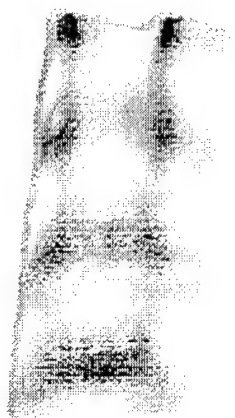
Fig. 6. Time-average EOH of a plate vibrating in a resonant mode at 34,061 Hz. Image (a) shows the display mode hologram as seen on the image processor screen. The displacements computed from the smoothed phase are displayed in (b). Images (c) to (g) show one half of a cycle of the vibration sampled at five positions during the motion.



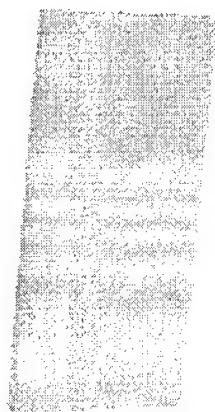
(b)



(c)



(d)



(e)



(f)



(g)

5. CONCLUSIONS AND RECOMMENDATIONS

The results presented in this paper show that the planar facet estimator technique for curvature minimization on wrapped fringe data gives highly reliable unwrapping for continuous surfaces. Experimental results demonstrate that curvature minimization by facet based estimation provides a valuable framework for future development of a more complete system to unwrap phase in the presence of discontinuities in the data.

The facet technique requires no prior smoothing of the speckle pattern in the original data to perform the unwrapping. This constitutes a great benefit compared to many of its precursors. Since the speckle pattern is largely uncorrelated, smoothing has the disadvantages of reducing spatial accuracy and diluting good data with data dominated by noise. In contrast, the technique described in this paper assigns the best fringe number to each data value, then gives the user an option to perform smoothing afterward. The user has the opportunity to study the actual data to determine whether the smoothing is justifiable.

A number of enhancements could be made to improve the present algorithm in the future. These include: 1) improve the speed with an array processor, 2) add facilities for interactive delineation of boundaries and especially discontinuities in the surfaces in the field of view, 3) use the facet fitting error measurement at each point to locate internal discontinuities automatically, and 4) use a quadratic rather than planar model for smoothing the data.

6. ACKNOWLEDGMENT

This study was supported by the Flight Dynamics Directorate, Wright Laboratory, Aeronautical Systems Division (AFSC), United States Air Force, Wright-Patterson AFB, OH 45433-6553.

7. REFERENCES

1. K. Itoh, "Analysis of the phase unwrapping algorithm," *Appl. Opt.*, 21:2470, 1982.
2. K. A. Stetson, "Phase-step interferometry of irregular shapes by using an edge-following algorithm," *Appl. Opt.*, 31:5320-5325, 1992.
3. D. C. Ghiglia, G. A. Mastin, and L. A. Romero, "Cellular-automata method for phase unwrapping," *J. Opt. Soc. Am. A*, 4:267-280, 1987.
4. H. A. Vrooman and A. A. M. Maas, "Image processing algorithms for the analysis of phase-shifted speckle interference patterns," *Appl. Opt.*, 30:1636-1641, 1991.
5. K. A. Stetson and W. R. Brohinsky, "An electro-optic holography system for vibration analysis and nondestructive testing," *Proc. SPIE*, 746:44-51, 1987.
6. K. A. Stetson and W. R. Brohinsky, "Fringe-shifting technique for numerical analysis of time-average holograms of vibrating objects," *J. Opt. Soc. Am. A*, 5:1472-1476, 1988.
7. R. J. Pryputniewicz and K. A. Stetson, "Measurement of vibration patterns using electro-optic holography," *Proc. SPIE*, 1162:456-467, 1989.
8. R. J. Pryputniewicz, *Holographic Numerical Analysis*, Center for Holographic Studies and Laser Technology, Department of Mechanical Engineering, Worcester Polytechnic Institute, pp. 86-89, 1992.
9. T. W. Bushman, "Development of a holographic computing system," *Proc. SPIE*, 1162:66-77, 1989.
10. R. J. Pryputniewicz, "Static and dynamic measurements using electro-optic holography," *Proc. SPIE*, 1554B:790-798, 1991.
11. S. Geman and D. Geman, "Stochastic relaxation, Gibbs distributions, and the Bayesian restoration of images," *IEEE PAMI*, 6:721-741, 1984.
12. R. M. Haralick, "Digital step edges from zero crossing of second directional derivatives," *IEEE PAMI*, 6:58-68, 1984.
13. S. D. Conte and C. deBoor, *Elementary Numerical Analysis - An Algorithmic Approach*, McGraw-Hill, New York, pp. 245-259, 1980.

Appendix E

**VIBRATION STUDIES USING ELECTRO-OPTIC
HOLOGRAPHY AND FINITE ELEMENT METHOD**

VIBRATION STUDIES USING ELECTRO-OPTIC HOLOGRAPHY AND FINITE ELEMENT METHOD

Chris E. Leak

Flight Dynamics Directorate

WL/FIVE

Air Force Systems Command

Wright-Patterson Air Force Base, OH 45433-6553

Ryszard J. Pryputniewicz

Center for Holographic Studies and Laser Technology

Department of Mechanical Engineering

Worcester Polytechnic Institute

Worcester, MA 01609-2280

ABSTRACT

This paper presents fundamentals of the Electro-Optic Holography and reviews basic principles and procedures of the Finite Element Method with special emphasis on quantitative analysis of vibrating objects. The quantitative results are illustrated by representative examples of a vibrating cantilever plate. Comparison of the results obtained using the Electro-Optic Holography and the results produced by the Finite Element Method shows good correlation.

1. INTRODUCTION

The subject of vibrations has a unique fascination. It is a subject explainable by basic principles of mechanics. It is also a subject whose mathematical concepts are all associated with physical phenomena which can be observed experimentally and measured. As such, vibration problems have been subjected to a number of solution methodologies. These methodologies can, in general, be classified as Analytical, Computational, and Experimental Solutions, and constitute, what may be called, **ACES** approach to vibration problems, or, in fact, any type of problems which can be solved either by analytical, or computational, or experimental method, or a combination of these methods¹. Certainly, each methodology has considerable advantage over the others, for a given class of problems, and each makes the use of the others for verification of the results. In many cases, the data furnished by one methodology has been utilized by the other methodologies to make the solutions possible.

Analytical methods are characterized by *exact* closed form solutions and make use of infinitesimal elements. Computational methods employ finite size of elements in discretization of the physical domain and provide *approximate* solutions. Because of increased availability and capability of the number crunching

equipment, in recent years, formulation of problems has shifted from exact to approximate. Experimental methods are the *ultimate tests* of all analytical and computational solutions. They employ actual objects that, in general, are subjected to actual operating conditions to measure their response to the applied loads.

Study of vibrations of a cantilever plate constitutes a classical problem in the field of vibration analysis². It has many applications and acts as a limiting case for more complicated problems, such as, for example, vibrations of turbine blades, aircraft wings, fins of compact heat exchangers in forced convection, or vibrations induced by a flow of fluids used to cool avionics. In these applications, the designer must be concerned with the possibility that large cyclic displacements and stresses may be induced by periodic, or random, time varying loads acting on "plates." Analysis of vibrations of the plates, subjected to such loads, are of primary interest in many design problems.

Today, these design problems are, to a great extent, solved by application of the computational methods, particularly the Finite Element Method³ (FEM). As is often the case with new and powerful methods, FEM have been overused, perhaps even misused⁴. Only recently have we begun to realize that virtually all versions of FEM contain some shortcomings. As a result, the need for unifying (merging, coupling) FEM in the physical and time domains with other methods has begun to manifest itself⁴⁻⁶. What is of particular interest, in this paper, is the unification of FEM with laser methods⁴, especially those relating to studies of vibrations.

Out of a number of laser methods available today, the most widely used for study of vibrations is the method of Time-Average Hologram Interferometry^{7,8} (TAHI), particularly as it is implemented via Electro-Optic Holography^{2,9-11} (EOH).

In the following sections, fundamentals of FEM are presented and basic principles and procedures of TAHI as implemented via EOH are reviewed, with special emphasis on quantitative analysis of vibrating objects. Discussion of this analysis is illustrated by representative examples of a vibrating cantilever plate.

2. FINITE ELEMENT METHOD

The Finite Element Method¹²⁻¹⁷ (FEM) is a computational analysis technique for obtaining approximate solutions to a wide variety of engineering problems. In a continuum problem of any dimension the *field variables*, such as displacement, stress, temperature, etc., possess infinitely many values because they are functions of each generic point in the body, or solution region. Consequently, the problem is one with an infinite number of unknowns. The finite element discretization procedures reduce the problem to one of a finite number of unknowns by dividing the solution into *elements* and by expressing the unknown field variables in terms of *assumed approximate functions* within each element. The approximate functions (sometimes called *interpolation functions*) are defined in terms of the values of the field variables at specified points called *nodes* or *nodal points*. Nodes usually lie on the *element boundaries* where adjacent elements are considered to be *connected*. In addition to *boundary nodes*, an element may also have a number of *internal nodes*. The nodal values of the field variables and the interpolation functions for the elements completely define the behavior of the field variables within the elements. For the finite element representation of a problem the nodal values of the field variables become the unknowns. Once these unknowns are found, the interpolation functions define the field variables throughout the assemblage of elements.

Clearly, the nature of the solution and the degree of approximation depend not only on the size and number of the elements used, but also on the interpolation functions selected. As one would expect, we cannot choose functions arbitrarily, because certain compatibility conditions must be satisfied. Often functions are chosen so that the field variables, or their derivatives, are continuous across adjoining element boundaries.

An important feature of FEM that sets it apart from other computational methods is its ability to formulate solutions for individual elements before putting them together to represent the entire problem. This means that if we are treating a problem in stress analysis, we can find the force-displacement or stiffness characteristics of each individual element and then assemble the elements to find stiffness of the whole structure. In essence, the problem reduces to considering a series of greatly simplified problems.

Another advantage of FEM is the variety of ways in which one can formulate the properties of individual elements. There are basically four different approaches: 1) direct approach, 2) variational approach, 3) weighted residuals approach, and 4) energy balance approach. Regardless of the approach used to find the element properties, the solution of a continuum problem by FEM always follows an orderly step-by-step process.

The fundamental FEM process consists of six steps:

1. *Discretize the continuum.* Finite element analysis is commenced with the division of the continuum, or solution region, into elements.
2. *Select interpolation functions.* Following discretization, nodes are assigned to each element and the type of interpolation function, to represent the variation of the field variables over the elements, is chosen. The magnitude of the field variables as well as the magnitude of their derivatives may be unknowns at the nodes.
3. *Find the element properties.* Once the finite element model has been established, we are ready to determine the matrix equations expressing the properties of the individual elements.
4. *Assemble the element properties to obtain the system equations.* To find the properties of the overall system modeled by the network of elements we must "assemble" all of the element properties. That is, we must combine the matrix equations expressing the behavior of the entire solution region or system. The basis for the assembly procedure stems from the fact that at a node, where elements are interconnected, the value of the variable is the same for each element sharing that node. During this step, the system of equations must also be modified to account for the boundary conditions of the problem.
5. *Solve the system equations.* The assembly process of Step 5 gives a set of simultaneous equations that we can solve to obtain the unknown nodal values of the field variables.
6. *Make additional computations, if desired.*

At the end of Step 5 or Step 6, field variables are known and constitute approximate solution to the problem. However, the most important issue of the resulting FEM solution, or, in general, of any approximate solution in engineering, is the accuracy of the results^{4-6,18}. How good are they? What are the bounds of

errors? Such questions have often been asked though answers have not always been found. The easiest response to these questions has always been the use of a factor of safety (FS) big enough to accommodate all uncertainties. How big should the FS be has, of course, been another question.

In recent years, the availability of computational tools, both in respect to methodology and equipment, has enabled engineers to design very complicated systems by successfully solving difficult problems. Nevertheless, one question raised above still remains: How good are the results?

While examining FEM, it can be noticed that error sources are quite numerous. Basically these sources can be categorized as those related to discretization, mathematical modeling, and manipulation. In addition, each of these has many subdivisions of error sources. Understanding of the error sources and their subsequent control is one of the most challenging tasks in the field of computational methodology, today. One way to approach this task is by unification of FEM with experimental methods.

Unification of FEM with Time-Average Hologram Interferometry, as applied to the study of vibrations of a cantilever plate, is considered in Sections 3 to 5.

3. TIME-AVERAGE HOLOGRAM INTERFEROMETRY

3.1. Recording and reconstruction of time-average holograms

Time-Average Hologram Interferometry (TAHI) is characterized by recording a hologram of an object, undergoing a cyclic vibration, with exposure time long in comparison to one period of the vibration cycle^{7,8,19-21}. In this way, the hologram effectively records an ensemble of images corresponding to the time-average of all positions of the vibrating object. In classical implementation of TAHI, the two-beam off-axis setup, shown in Fig. 1, is used. During reconstruction of such a hologram, interference occurs between the entire ensemble of images, with the images recorded near zero velocity (i. e., maximum displacement) contributing most strongly to the reconstruction. As a result, the image of the object, seen during reconstruction of a time-average hologram, is overlaid with interference fringes of unequal brightness, as discussed in Section 3.2.

3.2. Interpretation of time-average holograms

Time varying displacement, $L_t(x, y, z, t)$, of a vibrating object can be related to temporal changes in the fringe-locus function, $\Omega_t(x, y, z, t)$, constant values of which define fringe loci on the object's surface. Using the holographic setup shown in Fig. 1, this relationship can be written as^{7,8}

$$\Omega_t(x, y, z, t) = K(x, y, z) \cdot L_t(x, y, z, t), \quad (1)$$

where $K(x, y, z)$ is the sensitivity vector defined as the difference between the illumination and observation vectors, $K_1(x, y, z)$ and $K_2(x, y, z)$, respectively, that is,

$$K(x, y, z) = K_2(x, y, z) - K_1(x, y, z). \quad (2)$$

In Eqs 1 and 2, x , y , and z represent rectangular Cartesian coordinates characterizing the holographic system, and t represents time.

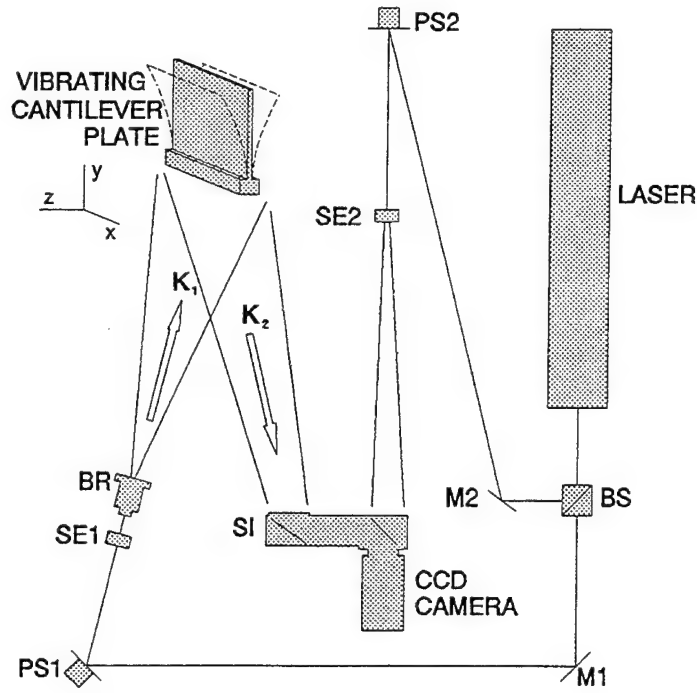


Fig. 1. A two-beam off-axis setup for recording and reconstruction of time-average holograms: BS is the beamsplitter, M1 and M2 are fixed mirrors, PS1 and PS2 are phase stepper controlled mirrors, SE1 and SE2 are spatial filter beam expander assemblies, BR is the beam rotator, and SI is the speckle interferometer. The direction of illumination, during recording of a hologram, is defined by vector K_1 , while the direction of observation is defined by vector K_2 .

The time varying light field, $F_t(x, y, z, t)$, propagating from the vibrating object, along the direction specified by the vector K_2 , shown in Fig. 1, can be represented by

$$F_t(x, y, z, t) = A_o(x, y, z) \exp[i\phi_o(x, y, z) + i\Omega_t(x, y, z, t)], \quad (3)$$

where A_o and ϕ_o are the amplitude and the phase, respectively, of the light field propagating away from the vibrating object, and Ω_t is the fringe-locus function defined by Eq. 1.

The complex reference field, $F_r(x, y, z)$, needed to record a hologram, can be represented by

$$F_r(x, y, z) = A_r(x, y, z) \exp[i\phi_r(x, y, z)], \quad (4)$$

where A_r and ϕ_r are the amplitude and the phase of the reference beam, respectively.

When the light fields defined by Eqs 3 and 4 are brought to interfere with each other in the plane where a hologram is to be recorded, the resulting complex light field in the hologram recording plane, $F_h(x, y, z, t)$, is

$$F_h(x, y, z, t) = A_o(x, y, z) \exp[i\phi_o(x, y, z) + i\Omega_t(x, y, z, t)] + A_r(x, y, z) \exp[i\phi_r(x, y, z)]. \quad (5)$$

The "medium," in which a hologram is recorded, responds to the time-varying intensity, $I_h(x, y, z, t)$, of the field given by Eq. 5. The value of this time-varying intensity is expressed as a product of $F_h(x, y, z, t)$ with its conjugate $F_h^*(x, y, z, t)$, that is,

$$\begin{aligned} I_h(x, y, z, t) &= F_h(x, y, z, t) F_h^*(x, y, z, t) \\ &= \{A_o(x, y, z) \exp[i\phi_o(x, y, z) + i\Omega_t(x, y, z, t)] \\ &\quad + A_r(x, y, z) \exp[i\phi_r(x, y, z)]\} \{A_o(x, y, z) \exp[-i\phi_o(x, y, z) \\ &\quad - i\Omega_t(x, y, z, t)] + A_r(x, y, z) \exp[-i\phi_r(x, y, z)]\} \\ &= A_o^2(x, y, z) + A_r^2(x, y, z) \\ &\quad + F_r(x, y, z) F_t^*(x, y, z, t) + F_r^*(x, y, z) F_t(x, y, z, t). \end{aligned} \quad (6)$$

The image recorded in the medium is the time-average of $I_h(x, y, z, t)$ over the exposure time T and can be expressed as

$$\begin{aligned} \frac{1}{T} \int_0^T I_h(x, y, z, t) dt &= A_o^2(x, y, z) + A_r^2(x, y, z) \\ &\quad + F_r(x, y, z) \frac{1}{T} \int_0^T F_t^*(x, y, z, t) dt \\ &\quad + F_r^*(x, y, z) \frac{1}{T} \int_0^T F_t(x, y, z, t) dt. \end{aligned} \quad (7)$$

When the time-average hologram is developed and illuminated by the original reference field specified by Eq. 4, the result is:

$$\begin{aligned}
F_r(x, y, z) \frac{1}{T} \int_0^T I_h(x, y, z, t) dt &= A_o^2(x, y, z) F_r(x, y, z) + A_r^2(x, y, z) F_r(x, y, z) \\
&+ A_r^2(x, y, z) \exp[2i\phi_r(x, y, z)] \frac{1}{T} \int_0^T F_t^*(x, y, z, t) dt \\
&+ A_r^2(x, y, z) \frac{1}{T} \int_0^T F_t(x, y, z, t) dt.
\end{aligned} \tag{8}$$

The first two terms on the right side of Eq. 8 represent an attenuated undiffracted reconstruction field, the third term gives rise to the conjugate image, while the fourth term is proportional to the time-average of the original field, propagating from the vibrating object, and describes formation of the virtual image. This proportionality constant is the square of the amplitude of the reference field. Therefore, the developed hologram, when illuminated by $F_r(x, y, z)$, produces the object wave which has the complex amplitude proportional to the time-average of $F_t(x, y, z, t)$ over the time interval T . The time-average of $F_t(x, y, z, t)$ can be represented as

$$\begin{aligned}
\frac{1}{T} \int_0^T F_t(x, y, z, t) dt &= \frac{1}{T} \int_0^T A_o(x, y, z) \exp[i\phi_o(x, y, z) + i\Omega_t(x, y, z, t)] dt \\
&= F_o(x, y, z) \frac{1}{T} \int_0^T \exp[i\Omega_t(x, y, z, t)] dt,
\end{aligned} \tag{9}$$

where $F_o(x, y, z)$ represents light field propagating from a stationary object⁸.

The time-average integral appearing in Eq. 9 is called the characteristic function²² and is denoted by $M(x, y, z, t)$, that is,

$$\frac{1}{T} \int_0^T \exp[i\Omega_t(x, y, z, t)] dt = M(x, y, z, t). \tag{10}$$

The integral of Eq. 10 may be evaluated as $J_o[\Omega_t(x, y, z, t)]$, the zero-order Bessel function of the first kind of the argument $\Omega_t(x, y, z, t)$. Therefore, according to Eqs 9 and 10, the reconstructed complex amplitude responsible for formation of the virtual image is proportional to $[F_o(x, y, z)][M(x, y, z, t)]$, while the corresponding intensity, $I_{im}(x, y, z)$, of the reconstructed image is

$$I_{im}(x, y, z) = [F_o(x, y, z)]^2 [M(x, y, z, t)]^2 = A_o^2(x, y, z) J_o^2[\Omega_t(x, y, z, t)],$$

or

$$I_{im} = A_o^2 J_o^2(\Omega_t), \tag{11}$$

where the arguments (x, y, z) and (x, y, z, t) were omitted for simplification.

Equation 11 shows that the virtual image obtained during reconstruction of the time-average hologram is modulated by a system of fringes of unequal brightness described by the square of the zero-order Bessel function of the first kind. Thus, for nontrivial values of A_o , centers of the dark fringes will be located at those points on the object's surface where $J_o(\Omega_t)$ equals zero.

In the case of out-of-plane (transverse) vibration of the object, i. e., when motion of the object is in the direction parallel to the z -axis, Fig. 1, the vibration amplitude L_{tz} can be shown to be⁸

$$L_{tz} = \frac{\lambda}{2\pi(\hat{K}_{2z} - \hat{K}_{1z})} |\Omega_t|. \quad (12)$$

In Eq. 12, L_{tz} is the z -component of the displacement vector L_t , λ is the wavelength of the laser light used to record and reconstruct the holograms, \hat{K}_{1z} and \hat{K}_{2z} are the components of the illumination and the observation unit vectors defining directions of K_1 and K_2 , respectively, and $|\Omega_t|$ is the magnitude of the fringe-locus function.

In order to evaluate Eq. 12, the wavelength of the laser light used must be known, the illumination and the observation geometry must be known in terms of the components of the unit illumination and observation vectors, and the spatial distribution of the fringe-locus function must also be known.

The wavelength of the laser light is known from the manufacturer specifications. The illumination and the observation vectors are computed based on measurements of x , y , and z coordinates of the position vectors specifying locations of the point source of illumination, the point(s) of interest on the object, and the point along the optical axis of the viewing system. Finally, the spatial distribution of Ω_t is determined directly from the holograms and, for the case of TAHI by means of the Electro-Optic Holography, this determination is the subject of Section 4.

4. ELECTRO-OPTIC HOLOGRAPHY

In the Electro-Optic Holography (EOH) irradiances produced by mutual interference of the object and the reference fields are recorded electronically by a CCD camera^{9,10}. Processing of this interferometric information and display of the experimental results are carried out concomitantly with measurements of irradiation. In order to achieve this, the EOH method relies on electronic acquisition, processing, and display of optical interference information, and allows automated processing of fringes of objects subjected to static and dynamic loads²³.

This paper concentrates on quantitative analysis of electronic holograms of objects subjected to the dynamic loads. That is, in the following sections, principles of EOH are outlined and its implementation to study of vibrations is presented. In order to facilitate development of the governing equations, this presentation considers time-average recording of sinusoidally vibrating objects.

4.1. Quantitative analysis of electro-optic holograms

In EOH, the holographic process is carried out by recording sequential frames of images of an object as it vibrates. Typically, four sequential frames are recorded, with a finite phase step, imposed on the reference beam, between each frame. For the case of a sinusoidally vibrating object, the irradiance distribution for the n -th sequential frame, $I_{tn}(x, y)$, at the detector array of a CCD camera in the EOH system can be represented by^{10,23}

$$I_{t_n}(x, y) = I_o(x, y) + I_r(x, y) + 2A_o(x, y)A_r(x, y)\cos[\Delta\phi(x, y) + \Delta\theta_n]M[\Omega_t(x, y, t)]. \quad (13)$$

In Eq. 13, x and y identify coordinates of the detectors in the array, t indicates time, I_o and I_r denote irradiances of the object and reference fields, whose amplitudes are A_o and A_r , respectively, $\Delta\phi$ is the phase difference between the two fields, $\Delta\theta_n$ is the n -th finite phase step, M is the characteristic fringe function²² that modulates the interference of the two fields due to the object's motion, and Ω_t is the time dependent fringe-locus function defining fringe loci on the surface of a vibrating object.

Following procedure used in References 10 and 23, it can be shown that

$$(I_{t_1} - I_{t_3})^2 + (I_{t_2} - I_{t_4})^2 = 16A_o^2A_r^2M^2(\Omega_t) = 16A_o^2A_r^2J_o^2(\Omega_t), \quad (14)$$

where it is seen that the characteristic function, for sinusoidally vibrating object, is equal to the zero-order Bessel function of the first kind.

Quantitative interpretation of electronically recorded holograms of vibrating objects depends on determination of Ω_t from Eq. 14. This determination can be done by optical shifting of the J_o fringes. The shifting of the J_o fringes is achieved by modulating the phase of either the object or the reference beams sinusoidally at the same frequency and phase as the object vibration. Such a process can be represented mathematically by addition of a phasor bias, B , to the argument of the Bessel function. If the phase of the sinusoidal beam modulation is adjusted to coincide with that of the object vibration, the phasor bias becomes a simple additive term within the argument of the Bessel function and Eq. 14 can be represented as¹⁰

$$(I_{t_1} - I_{t_3})^2 + (I_{t_2} - I_{t_4})^2 = 16A_o^2A_r^2J_o^2(\Omega_t - B), \quad (15)$$

where B is the magnitude of the bias modulation imposed on the object beam while recording electronic holograms. In this approach, the nearly periodic nature of the $J_o^2(\Omega_t - B)$ function is modelled as $\cos^2(\Omega - B)$ function, where Ω represents the fringe-locus function describing the cosinusoidal fringes observed during reconstruction of a double-exposure hologram, and is utilized to obtain an approximate solution for Ω_t , based on three irradiance distributions of the type given by Eq. 15, corresponding to the zero-, the positive-, and the negative-shifts, respectively. This approximate solution, $\Omega_{t_{approx}}$, that is,

$$\Omega_{t_{approx}} = \frac{1}{2} \tan^{-1} \left\{ \left[\frac{1 - \cos(2B)}{\sin(2B)} \right] \frac{J_o^2(\Omega_t + B) - J_o^2(\Omega_t - B)}{2J_o^2(\Omega_t) - J_o^2(\Omega_t - B) - J_o^2(\Omega_t + B)} \right\}, \quad (16)$$

differs from the correct argument Ω_t of the J_o function because of inequality between the J_o^2 and the \cos^2 functions, and should be expressed as

$$\Omega_{t_{approx}} = \Omega_t + \epsilon, \quad (17)$$

where ϵ is the error representing this difference. This error is computed for any value of Ω_t , for specific values of B , to create a lookup table. The lookup table is used to correct the values of $\Omega_{t_{approx}}$ computed from Eq. 16. Once the correct values of Ω_t are determined, they can be used to compute object displacements using, e. g., Eq. 12.

The interferometric information necessary to solve Eq. 16 is recorded electronically, by the EOH system, at the rate of 30 frames per second. The system processes this information in a pipeline fashion. This processing yields the results at up to 512x480 points per frame.

4.2. Description of the EOH system

The EOH system is shown in Fig. 1. In this system, the laser output is divided into two beams by means of a continuously variable beamsplitter, BS.

One of these beams is directed by a fixed mirror, M1, and a phase stepper controlled (i. e., moveable) mirror, PS1, and is shaped by the spatial filter beam expander assembly, SE1, to illuminate the object uniformly; PS1 can be driven at the same frequencies as the object excitation to provide bias modulation necessary for quantitative interpretation of holograms of vibrating objects, as discussed in Section 4.1. The beam rotator, BR, located between PS1 and the object, is used to rotate object illumination to facilitate speckle averaging. The direction of object illumination is characterized by the vector K_1 , while the object observation direction is defined by the vector K_2 .

The other beam, steered by M2 and PS2 and spatially filtered and expanded by SE2, is directed toward the reference input of the speckle interferometer, SI. In this arrangement, PS2 introduces 90° phase steps between consecutive frames.

The speckle interferometer combines the object beam with the reference beam and directs them collinearly toward the detector array of the CCD camera. The camera detects the interference pattern and sends it to the pipeline processor. The sequential frames are processed to determine quantitative information on the object's displacements and/or deformations. All computations are done in a pipeline processor which operates under control of a host computer. The host computer also controls excitation of the object, coordinates it with the bias modulation imposed on the object beam, and keeps track of the 90° phase steps between the frames.

By operating on each input image and its three predecessors, the pipeline processor produces a hologram, and this hologram is viewed concomitantly on the TV monitor. Such holograms are produced for the zero, as well as the positive and the negative bias modulations, for each resonance condition of the object. The resulting three electronic holograms are then processed, by the host computer, to determine spatial distribution of Ω_i , which, in turn, leads to computation of the displacement vectors.

5. REPRESENTATIVE RESULTS AND DISCUSSION

Representative results of FEM and EOH study of a vibrating cantilever plate are shown in Figs 2 and 3.

The interferograms shown in these figures were produced using the EOH system and were photographed directly from the displays on the TV monitor. It should be noted that in the current version of the EOH system, 245,760 pixels can be addressed per each frame¹⁰. However, because of the cantilever plate's aspect ratio, only approximately 100,000 pixels were used for interpretation of images produced by EOH. In addition, to facilitate display of experimental and computational results, only a very small fraction of points ($672/100000=0.00672$), out of the total of 100,000 points on the cantilever plate, were selected.

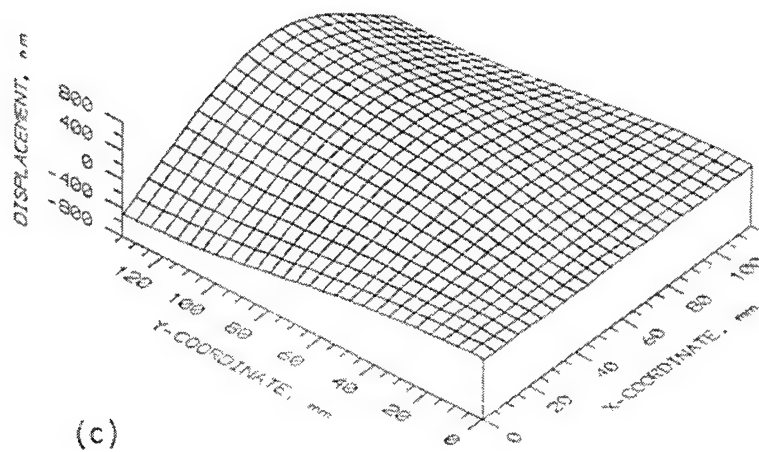
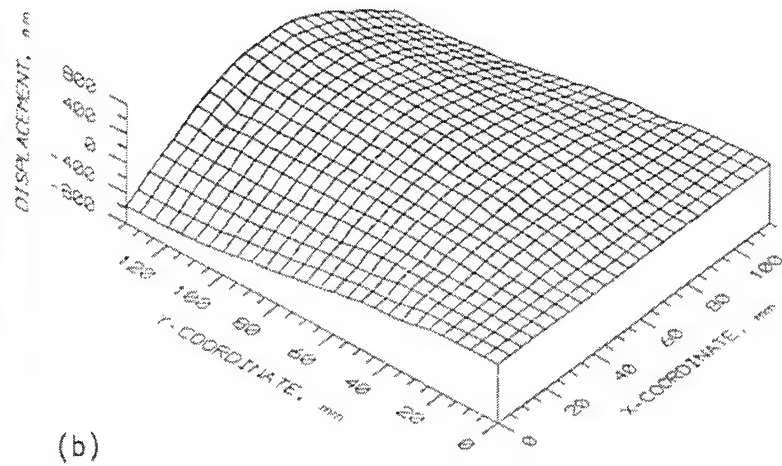
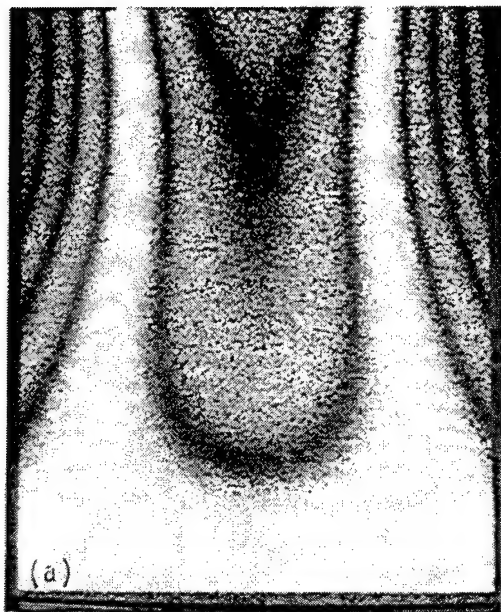


Fig. 2. Cantilever plate: (a) image of the plate and the fringe pattern produced by the EOH system during the time-average recording of the plate vibrating at 1082 Hz, without the bias modulation, (b) wire frame representation of the plate's displacements determined by EOH, (c) wire frame representation of the plate's displacements computed by FEM.

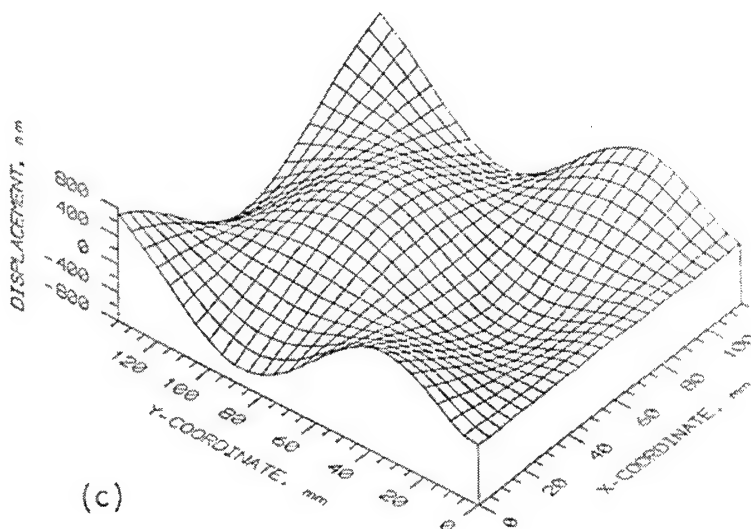
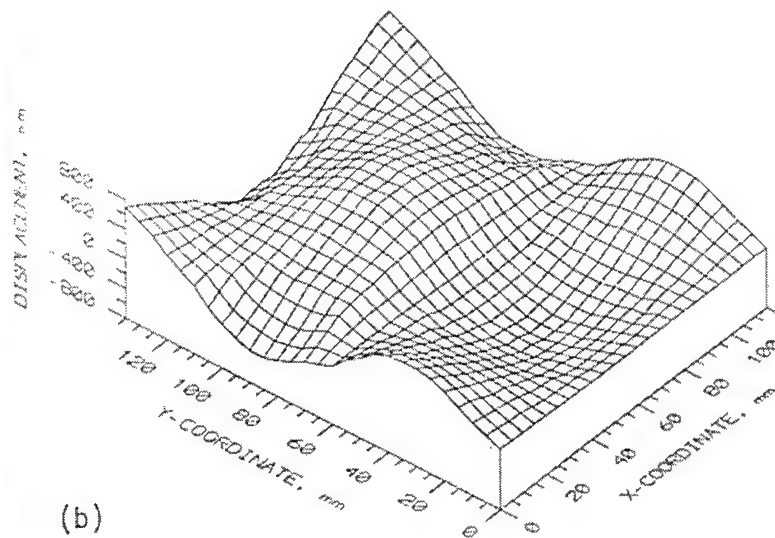
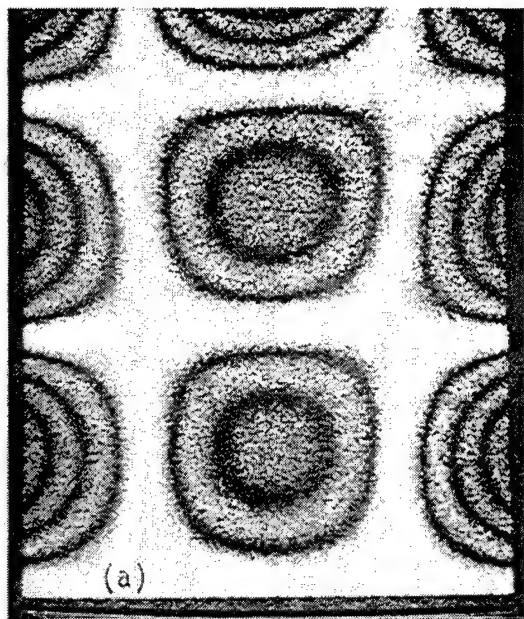


Fig. 3. Cantilever plate: (a) image of the plate and the fringe pattern produced by the EOH system during the time-average recording of the plate vibrating at 3148 Hz, without the bias modulation, (b) wire frame representation of the plate's displacements determined by EOH, (c) wire frame representation of the plate's displacements computed by FEM.

The FEM results shown in these figures were produced by subdividing the cantilever plate into 621 elements defining 672 nodes, each of which, except for the nodes at the fixed end of the cantilever plate, had six-degrees-of-freedom. Therefore, the FEM problem was characterized by solution of a system of 3888 simultaneous equations. It should be noted that the number of nodes at which displacements were computed by FEM was the same as the number of points at which displacements determined by EOH were displayed. It should be also noted that the nodal coordinates used by FEM were the same as the coordinates of the points at which the EOH results were displayed.

Figure 2a shows the image of the cantilever plate and the fringe pattern produced by the EOH system during the time-average recording of the plate vibrating at an experimentally determined resonance frequency of 1082 Hz, without the bias modulation of the object beam. Based on the irradiance values measured from Fig. 2a, corresponding the time-average hologram recorded without the bias modulation, and its two companion images, corresponding to the positive and the negative bias modulations, displacements were determined as a function of x and y coordinates of the vibrating cantilever plate. Figure 2b shows these displacements in wire frame representation. Figure 2c shows the wire frame representation of the FEM computed displacements for the same mode shape as that shown in Figs 2a and 2b. It should be noted that the FEM computed resonance frequency was 1066 Hz. Comparing Figs 2b and 2c it is apparent that the displacements computed by FEM compared well with those measured directly from the EOH images.

Figure 3 shows the EOH and the FEM results for the same cantilever plate, but vibrating at a higher resonant frequency than that shown in Fig. 2. Experimentally measured frequency was 3148 Hz while that computed was 3281 Hz. Again, comparison of the experimentally and the computationally determined displacements shows good correlation.

6. CONCLUSIONS

In this paper, fundamentals of FEM were presented and principles and procedures of EOH were reviewed with special emphasis on quantitative analysis of vibrating objects. The quantitative results were illustrated by representative examples of a cantilever plate vibrating at the specific resonance frequencies.

Using EOH, the results are obtained in an automated manner. The interferometric information is recorded electronically at the rate of 30 frames per second, it is processed in a pipeline fashion, and produces results which have very high spatial density - currently at up to 512x480, or approximately quarter of a million, points per frame. In this specific study, because of the cantilever plate's aspect ratio, only approximately 100,000 points were used for interpretation of images produced by EOH. Out of these points, only 672 were used to represent displacements of the vibrating cantilever plate, in order to facilitate display of the experimental results and for their comparison with the computational results. Furthermore, it should also be noted that EOH is not only capable of operating on vibration interference patterns, but it is also capable to operate on static interference patterns.

The representative results show that the EOH system provides an effective way for recording the time-average holograms of the vibrating objects. As these holograms are being recorded electronically, they can be either viewed directly on the TV monitor or they can be analyzed to obtain quantitative results on the

object's displacements as a function of position on its surface. For the cases presented herein, vibration amplitudes were below 700 nm at experimentally determined plate frequencies up to 3148 Hz. The FEM predictions of the cantilever plate's vibration characteristics correlated well with the EOH results.

The ongoing work in combining methods of hologram interferometry with the finite element methods will lead to a development of new design procedures. Such hybrid procedures, possessing both experimental and computational capabilities will, in turn, lead to the next generation of tools that will enhance design and optimization of critical components and structures.

7. ACKNOWLEDGMENT

This work was sponsored by the Flight Dynamics Directorate, Wright Laboratory, Aeronautical Systems Division (AFSC), United States Air Force, Wright-Patterson AFB, OH 45433-6553.

8. REFERENCES

1. R. J. Pryputniewicz, "Holography and speckle metrology: a state-of-the-art report," *Innovative and Applied Opto-electronics*, Munich, 1991.
2. R. J. Pryputniewicz, "Applications of electro-optic holography in vibration studies," *Proc. SEM Spring Conf. on Experimental Mechanics*, Milwaukee, 1991, pp. 912-919.
3. R. J. Pryputniewicz, "Holographic and finite element studies of vibrating beams," *Proc. SPIE*, 599:54-62, 1985.
4. H. Kardestuncer and R. J. Pryputniewicz, "Unification of FEM with laser experimentation," Ch. 9 in *Unification of Finite Element Methods*, H. Kardestuncer, ed., North-Holland, Amsterdam, pp. 207-234, 1984.
5. H. Kardestuncer, *Discrete Mechanics: a Unified Approach*, Springer-Verlag, Vienna, 1975.
6. O. C. Zienkiewicz, D. W. Kelly, and P. Batters, "The coupling of finite element method and boundary solution procedures," *Internat. J. for Numerical Methods in Engineering*, 11:355-373, 1977.
7. R. J. Pryputniewicz, "Time-average holography in vibration analysis," *Opt. Engrg.*, 24:843-848, 1985.
8. R. J. Pryputniewicz, "Quantitative interpretation of time-average holograms in vibration analysis," *Optical Metrology*, NATO ASI Series E: Applied Sciences - No. 131, Martinus Nijhoff Publishers, Dordrecht, The Netherlands, pp. 296-316, 1987.
9. K. A. Stetson and W. R. Brohinsky, "Fringe-shifting technique for numerical analysis of time-average holograms of vibrating objects," *J. Opt. Soc. Am. - A*, 5:1472-1476, 1988.
10. R. J. Pryputniewicz and K. A. Stetson, "Measurement of vibration patterns using electro-optic holography," *Proc. SPIE*, 1162:456-467, 1989.
11. S. Ellingsrud and O. J. Løkberg, "Analysis of high frequency vibrations using TV-holography and digital image processing," *Proc. SPIE*, 1162:402-410, 1989.
12. K. J. Bathe, *Finite Element Procedures in Engineering Analysis*, Prentice-Hall, Englewood Cliffs, NJ, 1982.

13. H. Kardestuncer, Editor-in-Chief, *Finite Element Handbook*, McGraw-Hill, New York, 1987.
 14. W. Weaver, Jr., and P. R. Johnston, *Structural Dynamics by Finite Elements*, Prentice-Hall, Englewood Cliffs, NJ, 1987.
 15. T. J. R. Hughes, *The Finite Element Method: Linear Static and Dynamic Finite Element Analysis*, Prentice-Hall, Englewood Cliffs, NJ, 1987.
 16. O. C. Zienkiewicz and R. L. Taylor, *The Finite Element Method*, 4th ed., Vol 1: *Basic Formulation and Linear Problems*, McGraw-Hill, New York, 1989.
 17. O. C. Zienkiewicz and R. L. Taylor, *The Finite Element Method*, 4th ed., Vol. 2: *Solid and Fluid Mechanics, Dynamics and Nonlinearity*, McGraw-Hill, New York, 1989.
 18. I. Babuska, O. C. Zienkiewicz, J. Gato, and E. R. de A. Oliveira, *Accuracy Estimates and Adaptive Refinements in Finite Element Computations*, Wiley, New York, 1986.
 19. C. M. Vest, *Holographic Interferometry*, Wiley, New York, 1979.
 20. P. Hariharan, *Optical Holography*, Cambridge University Press, Cambridge, 1984.
 21. Y. I. Ostrovsky, V. P. Shchepinov, and V. V. Yakovlev, *Holographic Interferometry in Experimental Mechanics*, Springer-Verlag, Berlin, 1991.
 22. K. A. Stetson, "Effects of beam modulation on fringe loci and localization in time-average hologram interferometry," *J. Opt. Soc. Am.*, 60:1378-1384, 1970.
 23. R. J. Pryputniewicz, "Static and dynamic measurements using electro-optic holography," *Proc. SPIE*, 1554:670-678, 1991.
-

Appendix F

**QUANTITATIVE ELECTRO-OPTIC HOLOGRAPHY STUDY OF
DYNAMICS OF ELECTRONIC COMPONENTS**



QUANTITATIVE ELECTRO-OPTIC HOLOGRAPHY STUDY OF DYNAMICS OF ELECTRONIC COMPONENTS

Ryszard J. Pryputniewicz

Center for Holographic Studies and Laser Technology
Department of Mechanical Engineering
Worcester Polytechnic Institute
Worcester, Massachusetts

ABSTRACT

Mechanical vibrations of electronic components are of particular interest in electronic packaging because they may lead to a failure and, therefore, may adversely affect durability of the dynamically loaded components. In this paper, computational and experimental methodologies are used to quantitatively study the dynamic behavior of the electronic components. The computational methodology is based on the finite element method. The experimental methodology is based on the electro-optic holography method. This method allows direct electro-optic recording, processing, and display of the laser holograms at the rate of 30 holograms per second, making it capable of producing quantitative data in nearly real-time. Using the electro-optic holography, displacement magnitudes in the submicron range are measured noninvasively over the full field of view, as a function of the resonance frequencies. Although some of the experimentally observed mode shapes were not predicted using the computational model employed in this study, the correlation between the finite element and the electro-optic holography methods was otherwise good and the resonance frequencies agreed to within 2%.

1. INTRODUCTION

One of the major challenges in the development of the electronic components, particularly those for avionic applications, is the requirement to assure their reliable functionality while subjected to the actual operating conditions which are static and dynamic in nature. Of particular interest, to the developments presented in this paper, are the dynamic loading conditions. Because the electronic components have certain mass and elasticity, they respond to the loads encountered during operation with a specific vibration behavior. Therefore, development of reliable electronic packages depends upon our ability to determine the dynamic characteristics which define and control their vibration behavior, particularly as it relates to the dynamic

environment within an aircraft which is a major contributor to the failure of airborne avionic systems. Soovere et al. (1987) estimates that 20% of experienced field failures can be attributed to the damaging influence of vibrations of the vehicle.

As a result of concern over the influence of vibrations on the durability of the electronic components, a number of computational and experimental approaches have been developed to assess the impact of vibrations on the durability of the specific designs. This concern is not new and was recognized some half-a-century ago by Midndlin (1945) and was later continued by Flaherty (1971), among others.

The computational approaches primarily rely on the finite element methods (FEM) as the means to assess the durability of the electronic components in the early stages of their design. Fundamentals of the FEM have been discussed in great detail elsewhere (e. g., Bathe, 1982; Kardestuncer, 1987; Weaver and Johnson, 1987; Hughes, 1987; Zienkiewicz and Taylor, 1989, 1991) and the reader is referred to the appropriate publications. However, for the FEM to be effective, in addition to other input parameters, a priori knowledge of the mechanical properties of the materials used in the construction of the avionics is required for the size of the structures employed in the design (Pryputniewicz, 1994a). In many cases, these properties are neither available nor well defined (Burkhard and Leak, 1992), which is mainly because the traditional measurement techniques cannot be applied to structures on the scale of those used in the construction of the modern electronic components without inherently affecting the outcome. One way to circumvent this difficulty is to employ recent developments in laser holographic interferometry methods which allow noninvasive measurements of the quantities of interest.

Out of a number of the laser methods available today, the most suitable method for the study of vibrations of the electronic components is the method of time-average hologram interferometry (TAHI) (Pryputniewicz, 1985a, 1987), particularly as it is implemented via electro-optic holography (EOH) (Stetson

and Brohinsky, 1988; Pryputniewicz and Stetson, 1989; Ellingsrud and Løkberg, 1989; Pryputniewicz, 1991a).

In the following sections, fundamentals of the TAHI as implemented via EOH are presented, with special emphasis on the quantitative analysis of the vibrating objects. Discussion of this analysis is illustrated by a representative example from a study of dynamics of the electronic components.

2. TIME-AVERAGE HOLOGRAM INTERFEROMETRY

Time-average hologram interferometry is characterized by a single holographic recording of an object undergoing a cyclic vibration. With the continuous exposure time long in comparison to one period of the vibration, the hologram effectively records an ensemble of images corresponding to the time-average of all positions on the vibrating object (Vest, 1979; Pryputniewicz, 1985a, 1987). In a classical implementation of TAHI, the two beam off-axis setup, shown in Fig. 1, is used to record and reconstruct the time-average holograms. During reconstruction of such holograms, the interference occurs between the entire ensemble of images, with the images recorded near zero velocity, i. e., the maximum displacement, contributing most strongly to the reconstruction. As a result, the image of the object, seen during reconstruction of the time-average hologram, is overlaid with interference fringes of unequal brightness. In fact, these fringes vary according to the square of the zero-order Bessel function of the first kind, as discussed later in this section.

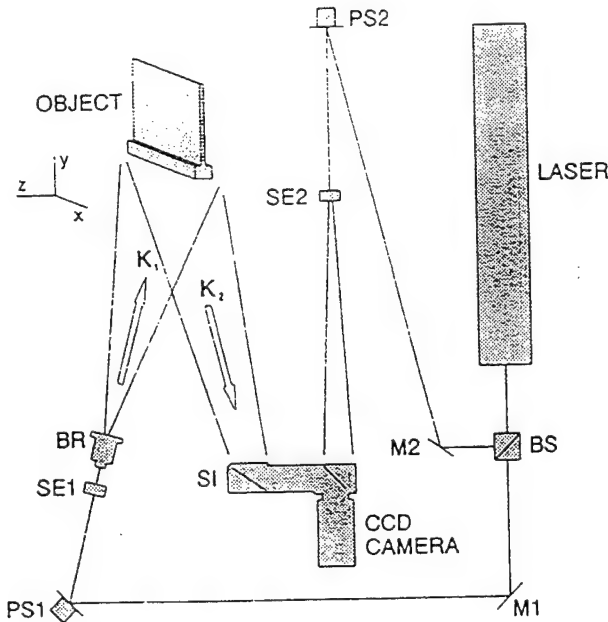


Fig. 1. Opto-mechanical configuration of the EOH system: BS is the beamsplitter, M1 and M2 are the mirrors, PS1 and PS2 are the phase steppers, SE1 and SE2 are the spatial filter beam expander assemblies, BR is the object beam rotator, SI is the speckle interferometer, and K_1 and K_2 are the directions of object illumination and observation.

Time varying displacement, $L_i(x, y, z, t)$, of a vibrating object can be related to temporal changes in the fringe-locus function, $\Omega_i(x, y, z, t)$, constant values of which define fringe loci on the surface of the object. Using the holographic setup shown in Fig. 1, it has been shown by Pryputniewicz (1985a, 1987) that this relationship can be written as

$$\Omega_i(x, y, z, t) = K(x, y, z) \cdot L_i(x, y, z, t), \quad (1)$$

where t is the time and $K(x, y, z)$ is the sensitivity vector defined as the difference between the observation and illumination vectors $K_2(x, y, z)$ and $K_1(x, y, z)$, respectively, with x, y , and z representing the Cartesian coordinates characterizing the holographic setup.

The time varying light field propagating from the vibrating object, along the direction specified by the vector K_2 , interferes with a complex reference field to produce a spatial distribution of image irradiance, $I_{im}(x, y, z)$, which is proportional to the square of the zero-order Bessel function of the first kind of the argument $\Omega_i(x, y, z, t)$, with the proportionality factor being the amplitude squared of the object field, $A_o^2(x, y, z)$, that is,

$$I_{im}(x, y, z) = A_o^2(x, y, z) J_0^2[\Omega_i(x, y, z, t)]. \quad (2)$$

Equation 2 shows that the image obtained during reconstruction of the time-average hologram is modulated by a system of fringes of unequal brightness described by the square of the zero-order Bessel function of the first kind. Thus, for nontrivial values of A_o , centers of the dark fringes will locate at those points on the surface of the object where $J_0(\Omega_i)$ equals zero.

In the case of the out-of-plane (transverse) vibrations of the object, i. e., when motion of the object is in the direction parallel to the z -axis, Fig. 1, the vibration amplitude, L_{ti} , was shown by Pryputniewicz (1985a, 1987) to be

$$L_{ti} = \frac{\lambda}{2\pi(\hat{K}_{2z} - \hat{K}_{1z})} |\Omega_i|. \quad (3)$$

In Eq. 3, L_{ti} is the z -component of the displacement vector, λ is the wavelength of the laser light used to record and reconstruct the holograms, \hat{K}_{1z} and \hat{K}_{2z} are the components of the illumination and observation unit vectors defining directions of K_1 and K_2 , respectively, and $|\Omega_i|$ is the magnitude of the fringe-locus function.

In order to evaluate Eq. 3, the wavelength of the laser light must be known, the illumination and the observation geometry must be known in terms of the components of the unit illumination and observation vectors, and the spatial distribution of the fringe-locus function must also be known. The wavelength of the laser light is usually very well known for the specific type of the laser being used. The illumination and the observation vectors are computed based on the measurements of x, y , and z coordinates of the position vectors specifying locations of the point source of the illumination, the point(s) of interest on the object, and the point along the optical axis of the viewing system (Pryputniewicz, 1985b, 1994b). Finally, the spatial distribution of Ω_i is determined directly from the holograms and, for the case of TAHI by means of EOH, this determination is the subject of Section 3.

3. ELECTRO-OPTIC HOLOGRAPHY

Unlike traditional forms of holographic interferometry, EOH does not use a photographic medium to record the fringe patterns. Rather, a CCD camera is used to convert the light intensity patterns into a digital bit map, making this method capable of producing quantitative data in nearly real-time. That is, in the EOH method, the irradiances produced by mutual interference of the object and the reference fields are recorded electronically by the CCD camera, as discussed by Stetson and Brohinsky (1988) and by Pryputniewicz and Stetson (1989). Processing of this interferometric information and display of the experimental results are carried out concomitantly with the measurements of irradiation. In order to achieve this, the EOH method relies on electronic acquisition, processing, and display of optical interference information, and allows automated processing of fringes of objects subjected to static and dynamic loads (Oh and Pryputniewicz, 1990; Pryputniewicz, 1991b).

In the following sections, principles of the EOH, as they apply to vibrations, are outlined and their implementation to the study of dynamics of the electronic components is presented. In order to facilitate development of the governing equations, this presentation considers time-average recording of sinusoidally vibrating objects.

3.1. Quantitative analysis of electro-optic holograms

In EOH, the holographic process is carried out by recording sequential frames of images of an object as it vibrates. Typically, four sequential frames are recorded, with a finite phase step, imposed on the reference beam, between each frame. It should be noticed that the number of the sequentially recorded frames is equal to the number of unknowns in Eq. 4 which describes irradiance distribution of a typical frame recorded in the EOH system. For the case of a sinusoidally vibrating object, the irradiance distribution for the n -th sequential frame, $I_n(x, y)$, at the detector array of a CCD camera in the EOH system can be represented (Pryputniewicz and Stetson, 1989; Pryputniewicz, 1993) by

$$I_n(x, y) = I_o(x, y) + I_r(x, y) + 2A_o(x, y)A_r(x, y)\cos[\Delta\phi(x, y) + \Delta\theta_n]J_0[\Omega_t(x, y, t)] \quad (4)$$

In Eq. 4, x and y identify the coordinates of the detectors in the CCD array, t indicates the time, I_o and I_r denote the irradiances of the object and reference fields, whose amplitudes are A_o and A_r , respectively. $\Delta\phi$ is the phase difference between the two fields. $\Delta\theta_n$ is the n -th finite phase step - in this study, the phase step equals 90° and is introduced between the sequential frames. J_0 is the zero-order Bessel function of the first kind, and Ω_t is the time dependent fringe-locus function defining loci on the surface of a vibrating object.

Following the procedure used by Pryputniewicz and Stetson (1989), it can be shown that, for any set of the four sequentially recorded frames,

$$(I_1 - I_2)^2 + (I_3 - I_4)^2 = 16A_o^2A_r^2J_0^2(\Omega_t - B) \quad (5)$$

where the Cartesian coordinates were omitted for simplification.

Quantitative interpretation of the electronically recorded holograms of the vibrating objects depends on determination of Ω_t , from Eq. 5. This determination can be done by optical shifting of the J_0 fringes. This shifting is achieved by modulating the phase of either the object or the reference beams sinusoidally by addition of a phase bias, B , to the argument of the Bessel function. If the phase of the sinusoidal beam modulation is adjusted to coincide with that of the object vibration, the phasor becomes a simple additive term in the argument of the Bessel function, as it is shown in Eq. 5. In this approach, the nearly periodic nature of the $J_0^2(\Omega_t - B)$ function is modeled as $\cos^2(\Omega - B)$ function, where Ω represents the fringe-locus function describing the cosinusoidal fringes observed during the reconstruction of a double-exposure hologram, and is utilized to obtain an approximate solution for Ω_t , based on the three irradiance distributions of the type given by Eq. 5, corresponding to the zero, the positive, and the negative phase bias shifts, respectively. This approximate solution, $\Omega_{t, \text{approx}}$, that is,

$$\Omega_{t, \text{approx}} = \frac{1}{2} \tan^{-1} \left\{ \left[\frac{1 - \cos(2B)}{\sin(2B)} \right] \frac{J_0^2(\Omega_t + B) - J_0^2(\Omega_t - B)}{2J_0^2(\Omega_t) - J_0^2(\Omega_t - B) - J_0^2(\Omega_t + B)} \right\} \quad (6)$$

differs from the correct value of the argument Ω_t of the J_0 function because of inequality between the J_0^2 and the \cos^2 functions, and can be expressed as

$$\Omega_{t, \text{approx}} = \Omega_t + \epsilon \quad (7)$$

where ϵ is the error representing this difference. This error is computed for a range of interest in the values of Ω_t , subject to the specific values of B , to create a lookup table. The lookup table is used to correct the values of $\Omega_{t, \text{approx}}$ computed from Eq. 6. Once correct values of Ω_t are determined, they can be used to compute the correct displacement using, e. g., Eq. 3.

The interferometric information necessary to solve Eq. 7 is recorded electronically by the EOH system, at the rate of 30 frames per second. The system processes this information in a pipeline fashion. Currently, this processing yields the results at up to 512x480 points per frame.

3.2. Description of the EOH system

A typical opto-mechanical configuration of the EOH system is shown in Fig. 1. In this system, the laser output is divided into two beams by means of a variable beamsplitter, BS. One of these beams is directed by a fixed mirror M1, and a phase stepper controlled (i. e., moveable) mirror, PS1, and is shaped by the spatial filter beam expander assembly, SE1, to illuminate the object uniformly; PS1 can be driven at the same frequency as the object excitation to provide bias modulation necessary for quantitative interpretation of holograms of vibrating objects, as discussed in Section 3.1. The beam rotator, BR, located between PS1 and the object, is used to rotate the object illumination to facilitate speckle averaging. The direction of the object illumination is characterized by the vector \mathbf{K}_1 , while the object observation is defined by the vector \mathbf{K}_2 . The other beam, steered by M2 and PS2 and spatially filtered and expanded by SE2, is directed toward the reference input of the speckle interferometer, SI. In this arrangement, PS2 introduces 90° phase steps between the consecutive frames.

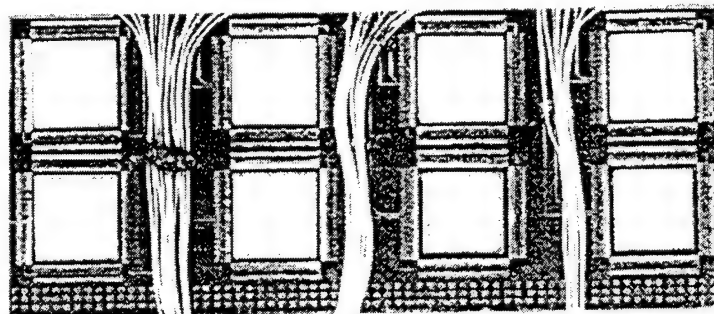


Fig. 2. The test board, used in this study, with eight identical surface mounted lidded components arranged in two rows with four components per row.

The speckle interferometer combines the object beam with the reference beam and directs them collinearly toward the detector array of the CCD camera. The camera detects the interference pattern and sends it to the pipeline processor. The sequential frames are processed to determine quantitative information on the object displacements and/or deformations. All computations are done in a pipeline processor which operates under control of a host computer. The host computer also controls excitation of the object, coordinates it with the bias modulation imposed on the object beam, and keeps track of the 90° phase steps between the sequential frames.

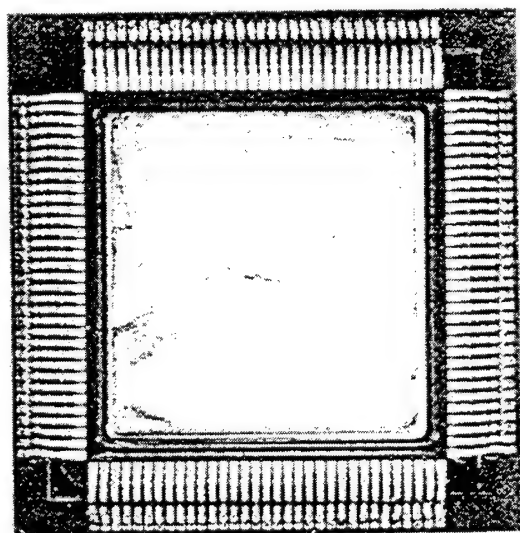


Fig. 3. A typical lidded component.

By operating on each input frame and its three predecessors, the pipeline processor produces a hologram, and this hologram is viewed concomitantly on the TV monitor. Such holograms are produced for the zero, as well as the positive, and the negative bias modulations, for each resonance condition of the object. The resulting three electronic holograms are then processed, by the host computer, to determine spatial distribution of Ω_z , which, in turn, leads to computation of the displacement vectors.

4. TEST SAMPLES

In this study, a multilayer test board with eight identical surface mounted lidded components was used, Fig. 2. A typical component is shown in Fig. 3. The components were arranged in two rows with four components per row.

For the measurements, the test board was fixed at one end in a cantilever configuration, to simulate an edge connection. Then, it was excited piezoelectrically by imposing sinusoidal excitation at the 'connector' end. The excitation frequencies ranged from zero to approximately 32 kHz.

5. REPRESENTATIVE RESULTS AND DISCUSSION

In this study, the test board was first examined in a full field of view, Fig. 4. Then, a single component was selected and a more detailed study of dynamics of this component was performed, Figs 5 to 13. All interferograms shown in Figs 4 to 13 were recorded electronically using the EOH system described in Section 3.

Based on the full field of view examination of the test board, it was noticed that, at the lower excitation frequencies, all eight components were exhibiting some response to the excitation as evidenced by the fringe patterns formed on the lids, Fig. 4a. However, as the excitation frequency increased, this was not always the case, Fig. 4b. Using the full field of view results, the most dynamically active component was selected for a more detailed study. This component was the third from the left in the lower row, Fig. 4.

Figures 5 to 13 show results of the study of dynamics of a single, Fig. 3, lidded component mounted on the test board shown in Fig. 2. The fringe patterns shown in Figs 5 to 13 were recorded by the EOH system described in Section 3. These fringe patterns correspond to all sequential resonance conditions found in the frequency range from zero to 32 kHz, used in this study. Also, Figs 5 to 13 show, where applicable, the finite element results for the same component.

In general, the agreement between the FEM and the EOH results is good in terms of predictability of the mode shapes. Also, the resonance frequencies, as determined by the two methods, agree to within 2%, Fig. 14. However, for the range of the frequencies used in this study, two resonance conditions, shown in Figs 11 and 12 were not predicted by the FEM model. In the follow up study, the FEM model will be reexamined and an attempt will be made to determine the cause(s) of this discrepancy between its and the EOH results.

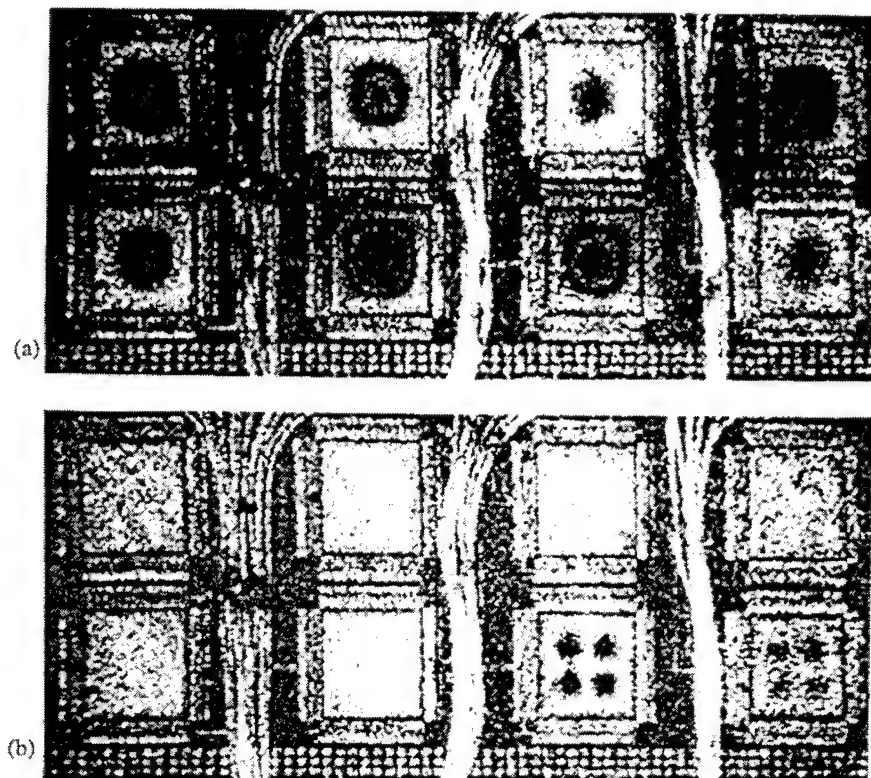


Fig. 4. The EOH images of the test board in full field of view and vibrating at:
(a) 6,720 Hz, and (b) 20,011 Hz.

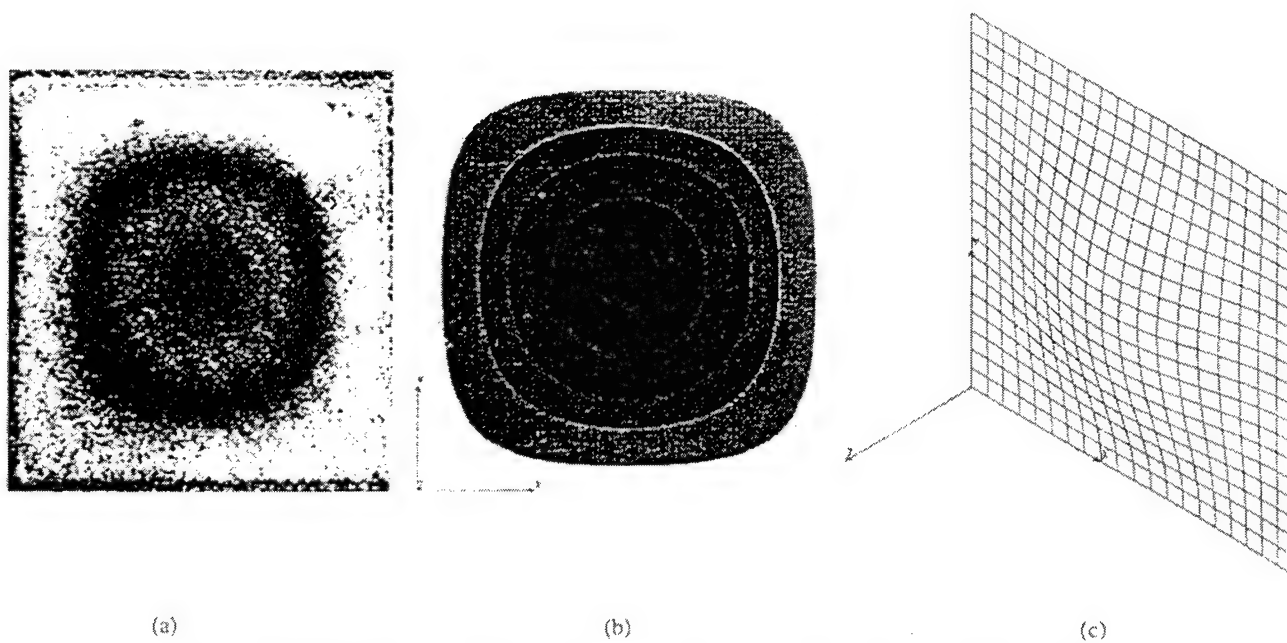


Fig. 5. The study of dynamics of a single component: (a) the EOH image recorded at 6,720 Hz,
(b) the FEM determined mode shape at 6,752 Hz, and (c) the wire frame representation of the displacements.

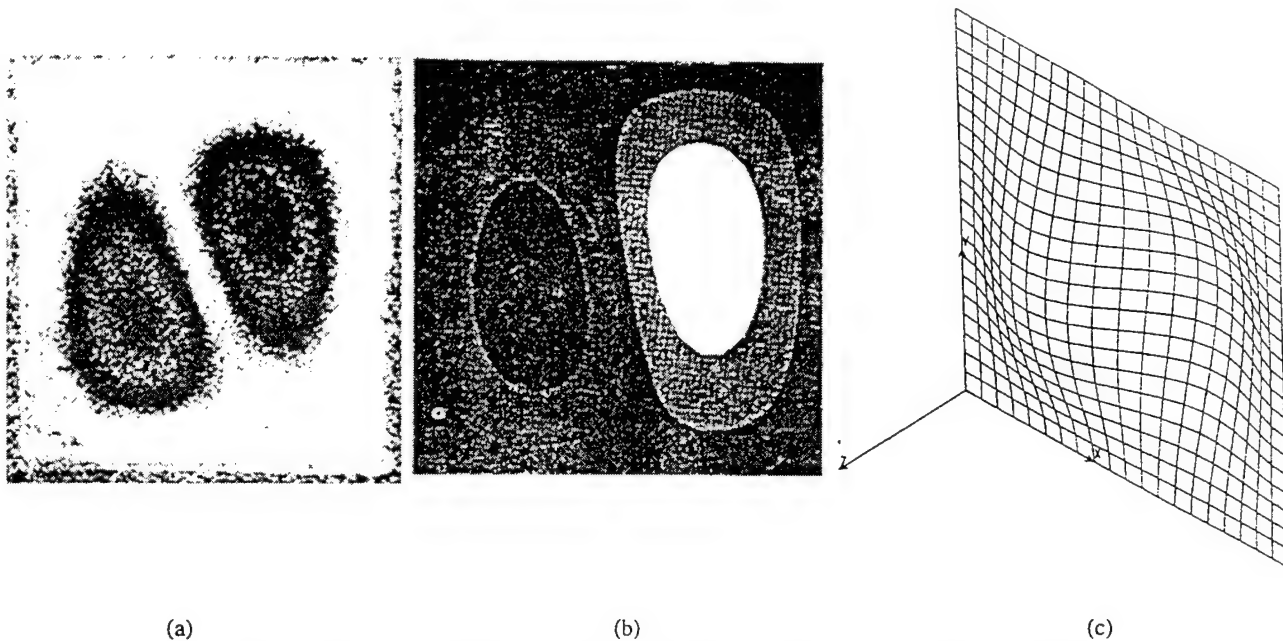


Fig. 6. The study of dynamics of a single component: (a) the EOH image recorded at 13,685 Hz, (b) the FEM determined mode shape at 13,749 Hz, and (c) the wire frame representation of the displacements.

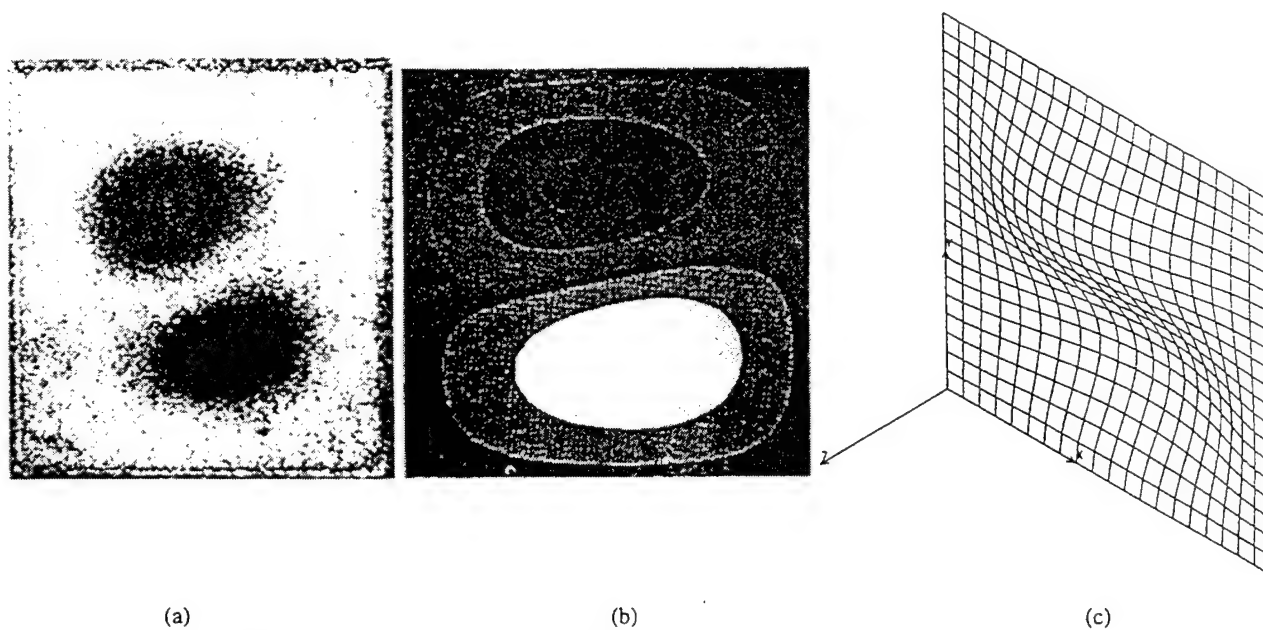


Fig. 7. The study of dynamics of a single component: (a) the EOH image recorded at 14,006 Hz, (b) the FEM determined mode shape at 13,749 Hz, and (c) the wire frame representation of the displacements.

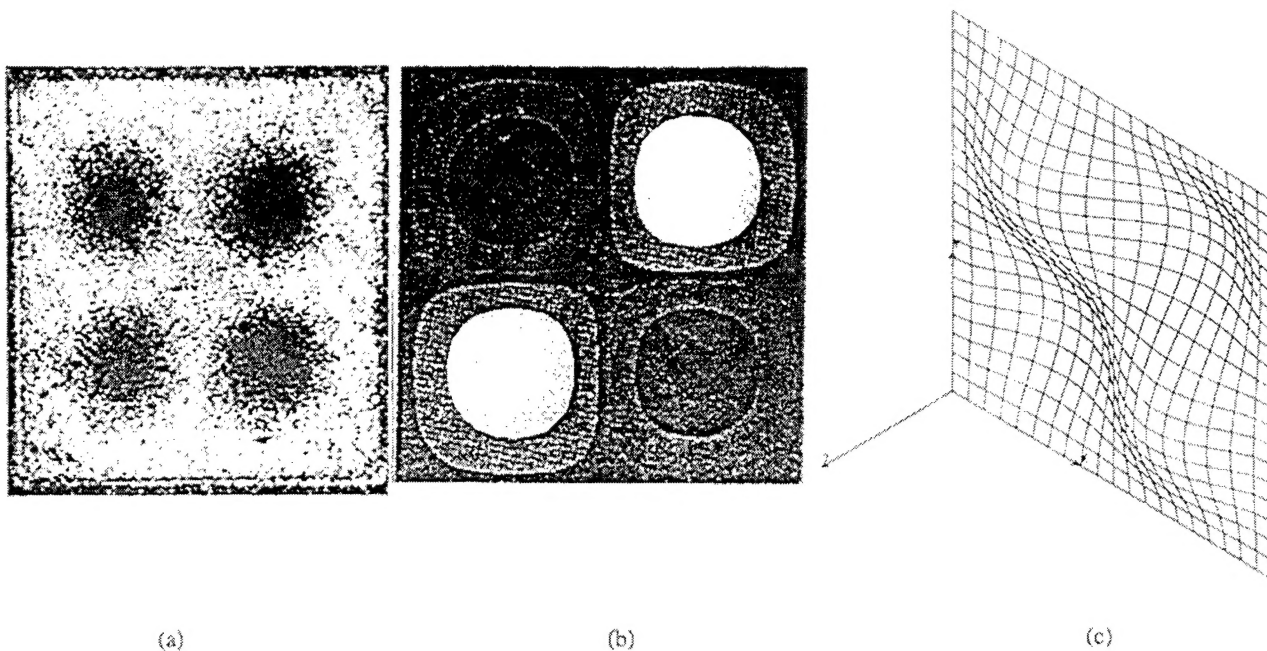


Fig. 8. The study of dynamics of a single component: (a) the EOH image recorded at 20,011 Hz, (b) the FEM determined mode shape at 20,209 Hz, and (c) the wire frame representation of the displacements.

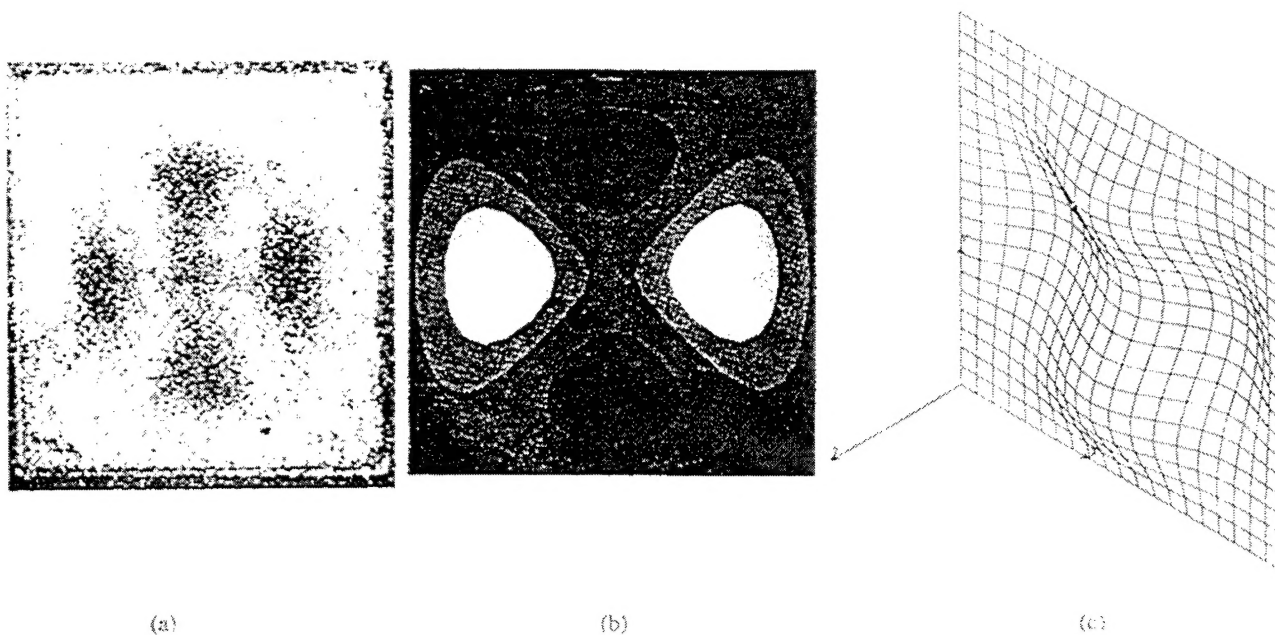


Fig. 9. The study of dynamics of a single component: (a) the EOH image recorded at 24,600 Hz, (b) the FEM determined mode shape at 24,600 Hz, and (c) the wire frame representation of the displacements.

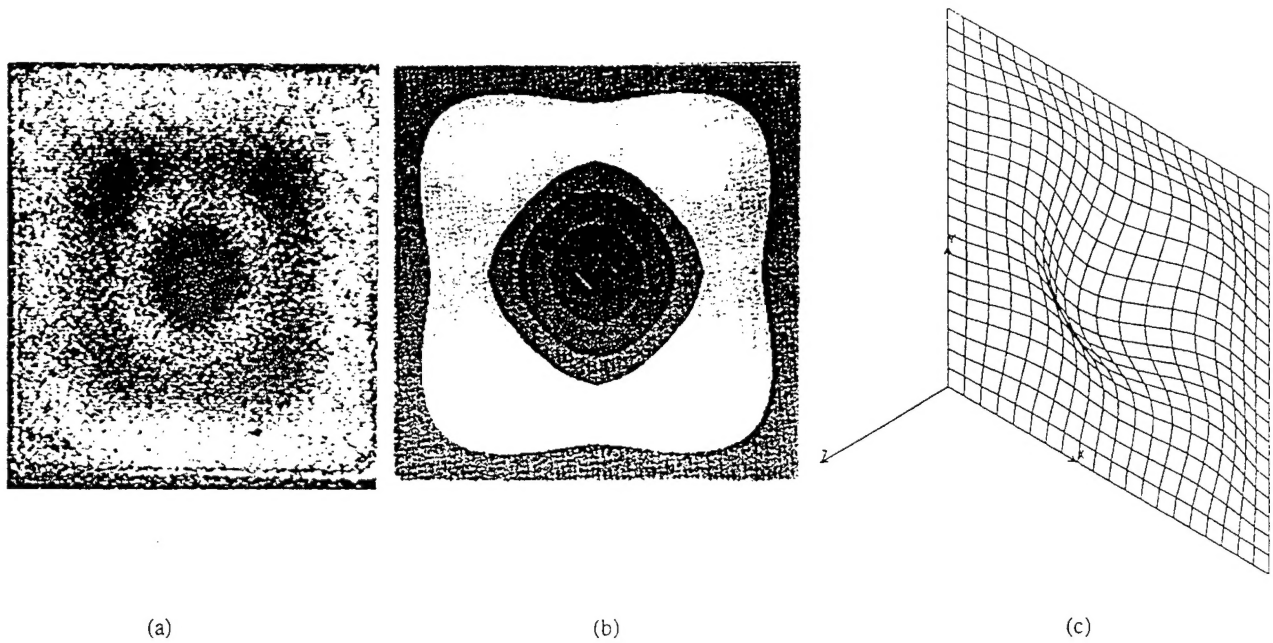


Fig. 10. The study of dynamics of a single component: (a) the EOH image recorded at 24,980 Hz, (b) the FEM determined mode shape at 24,722 Hz, and (c) the wire frame representation of the displacements.

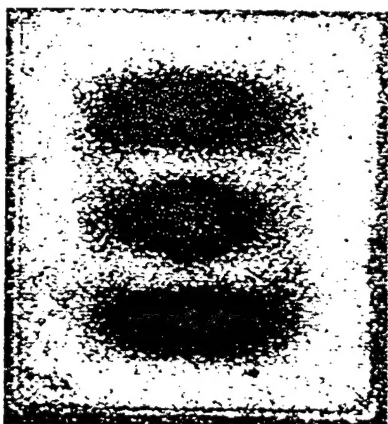


Fig. 11. The study of dynamics of a single component: the EOH image recorded at 26,000 Hz. no corresponding FEM results .

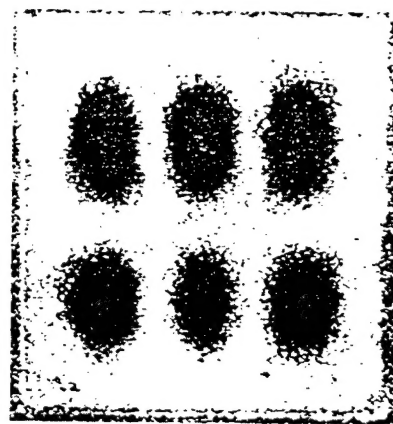


Fig. 12. The study of dynamics of a single component: the EOH image recorded at 28,990 Hz. no corresponding FEM results .

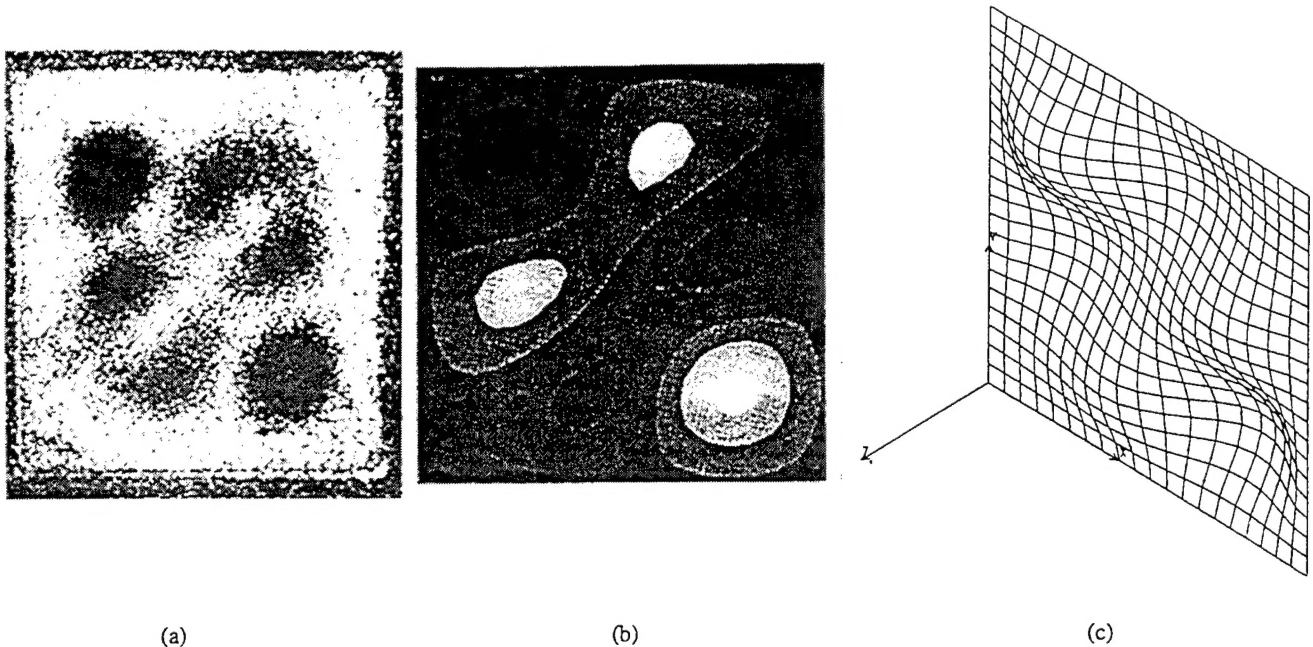


Fig. 13. The study of dynamics of a single component: (a) the EOH image recorded at 31,005 Hz, (b) the FEM determined mode shape at 30,724 Hz, and (c) the wire frame representation of the displacements.

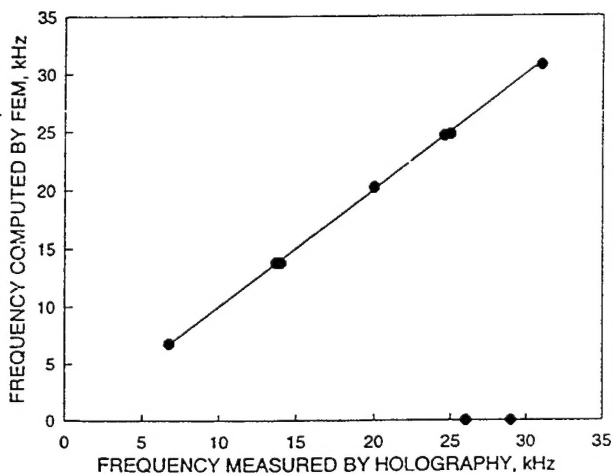


Fig. 14. A summary of the resonance frequencies, the symbols indicate the actual correlation between the FEM and the EOH results while the line indicates the ideal correlation.

6. CONCLUSIONS AND RECOMMENDATIONS

In this paper, fundamentals of the TAHI have been presented and principles of EOH have been reviewed with emphasis on the quantitative analysis of the vibrating objects. The quantitative results were illustrated by representative examples from a study of dynamics of the multilayer board with surface mounted lidded components.

Using the EOH, the results are obtained in an automated manner. The interferometric information is recorded

electronically at the rate of 30 frames per second, it is processed in a pipeline fashion, and produces results which have very high spatial density - currently at up to 512×480 , or approximately quarter of a million points per frame.

The representative results show that the EOH system provides an effective way for recording the time-average holograms of the vibrating electronic components. Using these holograms, eight resonance conditions were identified within the frequency range from zero to 32 kHz, used in this study. All, except two of these resonance conditions were predicted by the FEM model used. The correlation between the FEM and the EOH resonance frequencies was within 2% of each other.

The ongoing work on combining the methods of hologram interferometry with the finite element methods will lead to a development of new design procedures. Such hybrid procedures, possessing both experimental and computational capabilities will, in turn, lead to the next generation of tools that will enhance the design and optimization of critical components and structures used in the development of modern electronic packages, especially those for avionic applications.

8. ACKNOWLEDGMENT

This study was supported by the Flight Dynamics Directorate, Wright Laboratory, Aeronautical Systems Division (AFSC), United States Air Force, Wright-Patterson AFB, OH 45433-6553.

9. REFERENCES

Bathe, K. J., 1982, *Finite element procedures in engineering analysis*, Prentice-Hall, Englewood Cliffs, NJ.

- Burkhard, A. H., and Leak, C. E., 1992, "Durability analysis using fracture mechanics for avionics integrity," *J. IES*, pp. 26-32.
- Ellingsrud, S., and Løkberg, O. J., 1989, "Analysis of high frequency vibrations using TV-holography and digital image processing," *Proc. SPIE*, Vol. 1162, pp. 402-410.
- Flaherty, Jr., F. T., 1971, "Dynamics of structures," in *Physical design of electronic systems*, Vol. 1, Prentice-Hall, Englewood Cliffs, NJ.
- Hughes, T. J. R., 1987, *The finite element method: linear static and dynamic finite element analysis*, Prentice-Hall, Englewood Cliffs, NJ.
- Kardestuncer, H., Editor-in-Chief, 1987, *Finite element handbook*, McGraw-Hill, New York.
- Mindlin, R. D., 1945, "Dynamics of package cushioning," *Bell System Technical Journal*, Vol. 24, pp. 353-461.
- Oh, K., and Pryputniewicz, R. J., 1990, "Application of electro-optic holography in the study of cantilever plate vibration with concentrated masses," in Stetson, K. A., and Pryputniewicz, R. J., eds, *Hologram interferometry and speckle metrology*, Soc. for Exp. Mech., Bethel, CT, pp. 245-253.
- Pryputniewicz, R. J., 1985a, "Time-average holography in vibration analysis," *Opt. Engrg.*, Vol. 24, pp. 843-848.
- Pryputniewicz, R. J., 1985b, "Holographic and finite element studies of vibrating beams," *Proc. SPIE*, Vol. 599, pp. 54-62.
- Pryputniewicz, R. J., 1987, "Quantitative interpretation of time-average holograms in vibration analysis," in O. D. D. Soares, ed., *Optical metrology*, NATO ASI Series E: Applied Sciences - No. 131, Martinus Nijhoff Publishers, Dordrecht, The Netherlands, pp. 296-316.
- Pryputniewicz, R. J., 1991a, "Applications of electro-optic holography in vibration studies," *Proc. Spring Conf. on Experimental Mechanics*, Soc. for Exp. Mech., Bethel, CT, pp. 912-919.
- Pryputniewicz, R. J., 1991b, "Static and dynamics measurements using electro-optic holography," *Proc. SPIE*, Vol. 1554B, pp. 790-798.
- Pryputniewicz, R. J., 1993, "Electro-optic holography," in Trolinger, J. D., ed., *Critical reviews of optical science and technology*, SPIE, Vol. CR-46, pp. 148-174.
- Pryputniewicz, R. J., 1994a, "A hybrid approach to deformation analysis," *Proc. SPIE*, Vol. 2342, pp. 282-296.
- Pryputniewicz, R. J., 1994b, "Quantitative determination of displacements and strains from holograms," Ch. 3 in Rastogi, P. K., ed., *Holographic interferometry*, Springer-Verlag, Berlin, pp. 33-72.
- Pryputniewicz, R. J., and Stetson, K. A., 1989, "Measurement of vibration patterns using electro-optic holography," *Proc. SPIE*, Vol. 1162, pp. 456-467.
- Soovere, J., Dandawate, B. V., and Garfinkel, G. A., 1987, "Vibration stress analysis of avionics," AFWAL-TR-87-3023.
- Stetson, K. A., and Brohinsky, W. R., 1988, "Fringe-shifting technique for numerical analysis of time-average holograms of vibrating objects," *J. Opt. Soc. Am. - A*, Vol. 5, pp. 1472-1476.
- Vest, C. M., 1979, *Holographic interferometry*, Wiley, New York.
- Weaver, W., Jr., and Johnson, P. R., 1987, *Structural dynamics by finite elements*, Prentice-Hall, Englewood Cliffs, NJ.
- Zienkiewicz, O. C., and Taylor, R. L., 1989, *The finite element method: basic formulations and linear problems*, Vol. 1, Mc-Graw Hill, New York.
- Zienkiewicz, O. C., and Taylor, R. L., 1991, *The finite element method: solid and fluid mechanics, dynamics, and nonlinearity*, Vol. 2, Mc-Graw Hill, New York.